Low-dimensional matrices for the delivery of pharmaceutically active agents

Abdessamad Kaassis

A thesis submitted in part fulfilment of the requirements for the degree of Doctor of Philosophy at UCL

UCL School of Pharmacy

29 – 39 Brunswick Square

London, WC1N 1AX

January 2016

Declaration

I, the undersigned, declare that the work described in this thesis was carried out under the supervision of Dr. Gareth Williams at London Metropolitan University between December 2011 and December 2012 and at the UCL School of Pharmacy, University College London, between January 2013 and September 2015. All the molecular dynamics simulation were carried out while I was a visiting student at the Beijing University of Chemical Technology, from October 2013 to December 2013. All the work described is my own unless stated to the contrary, and has not been submitted for any degree at this or any other university.

Abdessamad Kaassis

Abstract

The encapsulation and delivery of drugs using polymeric and inorganic materials is the focus of the work described in this thesis. An introduction to the candidate drugs (non-steroidal anti-inflammatory drugs and others) and drug delivery systems is given in **Chapter 1**.

In the first approach, electrospinning was used to make drug loaded fibres made of polyvinylpyrrolidone (PVP) or poly(ethylene oxide) (PEO), important synthetic polymers known to be safe for human use. They were blended with sodium alginate (SA), a pH-sensitive naturally occurring polymer, to develop targeted drug delivery systems, as reported in **Chapter 2**. Polymer variation permits a range of drug release profiles to be achieved.

In **Chapter 3**, the drugs were intercalated into various hydroxy double salts (HDSs). Initially, known HDSs were used to prove the concept that HDSs can comprise useful delivery systems for these active ingredients. Information about the mechanisms and kinetics of intercalation of the drugs was obtained using non-invasive *in situ* techniques and *ex situ* techniques used to characterise the products. The HDSs reported in the literature have the potential risk of toxicity, however, and so once their utility was established novel biocompatible HDSs were synthesised and loaded with the drugs in **Chapter 4**. Tablets of these systems were also prepared, and drug release in milieu mimicking the human gastrointestinal tract studied.

In **Chapter 5,** the intercalation and release of phosphonoacetic acid and related species from Li/Al based layered double hydroxides was investigated. The mechanisms and kinetics of the intercalation reactions were investigated, using a combination of *in situ* and MD techniques.

The experimental details and characterising techniques utilised in this work are detailed in **Chapter 6**. Additional data are provided in the **Appendices**.

Contents

List of figures

List of tables

Publications from this thesis

[1] A. Y. A. Kaassis, N. Young, N. Sano, H. a. Merchant, D.-G. Yu, N. P. Chatterton, and G. R. Williams, “Pulsatile drug release from electrospun poly(ethylene oxide)–sodium alginate blend nanofibres,” J. Mater. Chem. B, vol. 2, no. 10, p. 1400-1407, 2014. **(Part of Chapter 2)**

[2] A. Y.A. Kaassis, S. Xu, D. G. Evans, M. Wei, G. R. Williams, and X. Duan, “Combined In Situ and In Silico Studies of Guest Intercalation into the Layered Double Hydroxide $[LiAl_2(OH)_6]X{\bullet}yH_2O$,” J. Phys. Chem. C **119,** 18729–18740 (2015)., vol. 32, p., 2015. **(Most of Chapter 5)**

[3] A. Y. Kaassis, S.-M. Xu, S. Guan, D. G. Evans, M. Wei, and G. R. Williams, “Hydroxy double salts loaded with bioactive ions: Synthesis, intercalation mechanisms, and functional performance,” J. Solid State Chem., vol. 238, pp. 129–138, 2016. **(Chapter 3)**

[4] New biocompatible hydroxy double salts and their drug delivery properties (under review). (Chapter 4)

Acknowledgements

First and foremost, I praise and thank God who has granted me this opportunity and given me the ability, strength and ideas all the way through.

I owe many thanks and a tremendous debt of gratitude to many great people who made this doctoral dissertation possible. Their assistance was indispensable in completing this research project.

The list begins with my mentor and doctoral supervisor, **Dr. Gareth Williams** of University College London for accepting me in his team while he was at London Metropolitan University and bringing me to University College London when he moved there and as well for being a supportive advisor. I would like to thank him very much for his time, expertise, wisdom and great guidance. He provided me with advice, enthusiasm and inspiration as well as with valuable information and excellent insight throughout the development of this project. I was able to keep my research focused and on track, which has enabled me to accomplish this goal. Without him, this project would not be what it is.

I would also like to express sincere gratitude to my second supervisor, **Dr. Simon Gaisford** of University College London and to **Dr. Nick Chatterton** of the Open University, for their ability to impart knowledge has been absolutely priceless. To **Prof. Kevin Taylor** of University College London, for his feedback on my work.

I would like to thank NEXUS staff, specially **Dr. Naoko Sano** with her help with XPS analysis Stephen Boyer of London Metropolitan University for elemental microanalysis measurements. To the Deutsches Eleckronen Synchrotron for the provision of beamtime on DORIS, and **Dr. Joern Donges** and **Dr. Andre Rothkirch** for their assistance during in situ experiments on F3; the Diamond

Light Source for the provision of beamtime on I12, and **Dr. Michael Drakopoulos** and **Dr. Christina Reinhard** for their help and advice.

To the institutions, departments, deans, professors, lecturers, department secretaries, university administrators and friends around the globe who helped me in this project. Without their co-operation I would have not been able to complete the research. I owe thanks to people in various departments who provided me with equipment when I needed it most. My sincere thanks are given to all of the people who helped at some stage of my research, even if it was with a few words of sincere advice.

I would like to thanks **Prof. Abdul Basit** at UCL for allowing me to use his equipments and **Dr Alvaro Goyanes** for his assistance with various experiments. I would like to thank as well **Dr. Ahmad Haidery** of London Metropolitan University for their support and guidance in in-vitro cell experiments.

To **Dr. Asma Buanz** and **Dr Bahijja Raimi-Abraham** for thier help with DSC and TGA. To my friends and colleagues especially: **Dr. Upulitha Eranka Illangakoon**, **Dr. Bilal Saeed Ahmad, Mr Sameer Sultan and Ms Daniela Lobo** for their support. Special thanks to **Ms. Zahra Marchant** and **Laxmi Kerai.** I would like to thank **Dr. Urszula Stachewicz** at the SEM facility at the Nanovision Centre, **Mr. David McCarthy** at University College London and **Dr. Neil Young** at the University of Oxford, who helped me in microscopy sessions so many times that I have lost count. I would like to thank all the members of Gareth Williams' lab.

I would like to thank the Beijing University of Chemical Technology staff, specially **Prof. Min Wei, Prof. David G. Evans**, and **Prof. Xue Duan** for their hospitality and help while I was a visiting student. I would like to thank **Ms. Shanyue Guan, Ms. Juyao Zhou, Mr. Jie Liua and Mr. Hao Chen** for the their help with experiments and **Mr. Si-Min Xu** for his help with MD simulations while

I was a visiting student. I would like to thanks them as well for lovely time and memorable moments.

I would like to thank special people for the support **Dr. C.Ma**, **Ms. Y.Yocharan, Mr. K. Shoushou, Ms. K.Tatoum and Mr. K.Shefchenko.**

I also wish to thank my **parents** from the bottom of my heart**,** who have supported me throughout the years. Writing a doctoral thesis is a complex, sophisticated, intellectual endeavour and I survived this only with their love, patience, and understanding. Both of my parents have assisted me to fulfil my and their aspirations and life goals. To everyone else who cheered me up, I extend my sincere appreciation.

Dedication

This dissertation is dedicated to my parents. Their financial and moral support, encouragement, and constant love has sustained me throughout my life.

List of abbreviations

API	Active pharmaceutical ingredient
CA	Contact angle
C_{max}	Maximum concentration
CoZn-NO_3	$Zn_{3.8}Co_{1.2}(OH)_8(NO_3)_2.yH_2O$
DDS	Drug Delivery System
Dic	Diclofenac sodium
DPA	Diethyl phosphonoacetic acid
DSC	Differential scanning calorimetry
EDX	Energy dispersive X-ray spectroscopy
FeZn-Cl	$Fe_{2.4}Zn_{2.6}(OH)_8Cl_2 \cdot yH_2O$
FTIR	Fourier transform infrared spectroscopy
H	hour
HDS	Hydroxy double salt
LDH	Layered double hydroxides
LiAl-Cl	$[LiAl_2(OH)_6]Cl \cdot yH_2O$
LiAl-NO_3	$[LiAl_2(OH)_6]NO_3 \cdot yH_2O$
HPLC	High-performance liquid chromatography
MD	Molecular Dynamics
MgZn-Cl	$Mg_2Zn_3(OH)_8Cl_2.yH_2O$
Min	Minute
Nap	Naproxen sodium
NiZn-NO_3	$Zn_3Ni_2(OH)_8(NO_3)_2.yH_2O$

NMR	Nuclear magnetic resonance
NSAIDs	Non-steroidal anti-inflammatory drugs
PAA	Phosphonoacetic acid
PBS	Phosphate buffer saline
PEO	Poly(ethylene oxide)
PVP	Polyvinylpyrrolidone
SA	Sodium alginate
SAA	Sulfoacetic acid
SEM	Scanning electron microscopy
SI	Sodium Ibuprofen
T	Temperature
Tab	Tablets
TGA	Thermogravimetric analysis
Val	Valproate sodium
XPS	X-ray photoelectron spectroscopy
XRD	X-ray diffraction
Zn-Cl	$Zn_5(OH)_8(Cl)_2.yH_2O$
Zn-NO_3	$Zn_5(OH)_8(NO_3)_2.yH_2O$
TEM	Transmission electron microscopy
T_{max}	Time taken to reach maximum
UV	Ultraviolet

Chapter 1: Introduction

1.1. Non-steroidal anti-inflammatory drugs

1.1.1. History

Historically, the discovery of the anti-inflammatory drugs goes back to the 19th century when the first compound (salicin) was extracted from the *Willow* bark tree, then isolated and identified.[1,2] Its identification led to its chemical synthesis and enabled the development of other non-steroidal anti-inflammatory drugs (NSAIDs), most of which are initially organic acids.[3,4]

It has been more than half century since ibuprofen was developed by Dr. Stewart Adams.[5,6] The aim of this work was to find a drug that would be better tolerated than aspirin and possess comparable properties to ease pain and inflammation. Ibuprofen was commercialised in 1969 and in 1983 an over-the-counter (OTC) form became available. A few years later diclofenac was developed by Dr. Alfred Sallmann and Dr. Rudolf Pfister in late 1960s, while working at Ciba-Geigy (now Novartis).[7–9] Diclofenac was first introduced to the market in 1973. A decade after the discovery of diclofenac, Syntex introduced naproxen to the market in 1976.[10] The compound was synthesised in 1970 by Dr. Harrison and his team.[11] The clinical trial carried out by Lussier and co-workers showed its effectiveness.[12]

1.1.2. Candidate drugs

The NSAIDs are commonly used in the treatment of temporary pains (eg: headache, muscle inflammation) or permanent pains (eg: arthritis, rheumatoid).[13–19] They possess an analgesia ability,[20] hence they are among frequent pain relief medicines used.[21] New formulations are required, due to the safety and tolerability concerns related with actual commercial NSAIDs.[22]

1.1.2.1. Ibuprofen

Ibuprofen ((RS)-2-(4-(2-methylpropyl)phenyl) propanoic acid) is depicted in Figure 1.1. It has a chiral centre, and only the S(+)-isomer is active,[23] although some R(-)-ibuprofen will be transformed to S(+)-Ibuprofen in the human body.[24–27] Its physicochemical properties are summarised in Table 1.1.

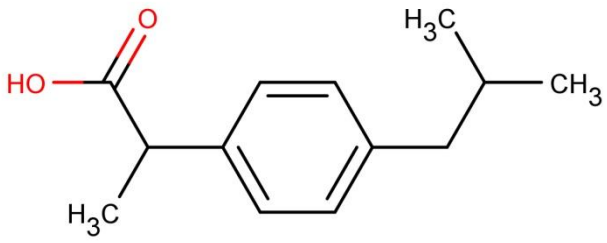

Figure 1.1: The chemical structure of ibuprofen.

Table 1.1: Summary of the main characteristic of ibuprofen and its sodium salt.

	Ibuprofen	**Ibuprofen sodium**
Colour	Colourless	White
Water solubility	Barely soluble	Slightly soluble
Physical form	Solid	Solid
Odour	Characteristic odour	Characteristic odour
Log P	3.97	0.31
pKa	4.91	4.91

Ibuprofen is sold as three therapeutic forms: the acid itself, as salts and as a mixture of both acid and salt forms. Ibuprofen is rapidly absorbed in the gastrointestinal tract with a peak plasma concentration (T_{max}) of around 90 min after tablet ingestion for the acid form and 35 min for sodium ibuprofen.[28] The latter can be deferred when coated or slow-release formulations are used.[29] The drug is present in the plasma (blood) in the ionised form, and has a biological half-life of around 2.3 h.[30] Ibuprofen undergoes extensive amounts of plasma protein binding (more than 90 % is bound),[31] and is mainly metabolised in the liver and the kidney.[32]

1.1.2.2. Diclofenac

Diclofenac (2-[2-(2,6-dichloroanilino)phenyl]acetic acid) is shown in Figure 1.2, and its physicochemical properties are summarised in Table 1.2. Diclofenac is primarily available as the sodium salt.[33,34] It is quickly absorbed in the gastrointestinal tract with a T_{max} of 0.5-2 h after tablet ingestion,[35] or 11 min after ingestion of liquid form.[36] The T_{max} can be delayed by preparing coated or slow-release formulations.[37,38] The drug is present in the plasma in its ionised form. It has a biological half-life between 1 to 2 hours,[35,39] is mainly bound to plasma proteins (more than 98 %),[40] and is primarily metabolised in the liver.[41,42]

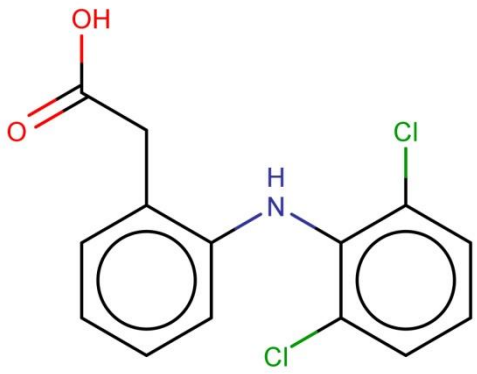

Figure 1.2: The chemical structure of diclofenac.

Table 1.2: Summary of main characteristic of diclofenac and its sodium salt.

	Diclofenac	**Diclofenac sodium**
Water solubility	non soluble	Barely soluble
Physical form	Solid	Solid
Odour	Odourless	Odourless
Log P	4.51	0.73
pKa	4.15	4.15

1.1.2.3. Naproxen

Naproxen ((+)-(S)-2-(6-methoxynaphthalen-2-yl) propanoic acid) (Figure 1.3) is the only NSAID marketed exclusively in an enatiomerically pure form,[10] and its physicochemical properties are summarised in Table 1.3. Naproxen is sold as two therapeutic forms: the acid itself and salts. It is rapidly absorbed in the gastrointestinal tract with a T_{max} 2-4 h after tablet ingestion.[43] The drug is present in the plasma in its ionised form. It has a biological half-life around 18 hours,[44] is mainly plasma protein bound during circulation (more than 98 %),[45] and is primarily metabolised in the kidneys.[46–48]

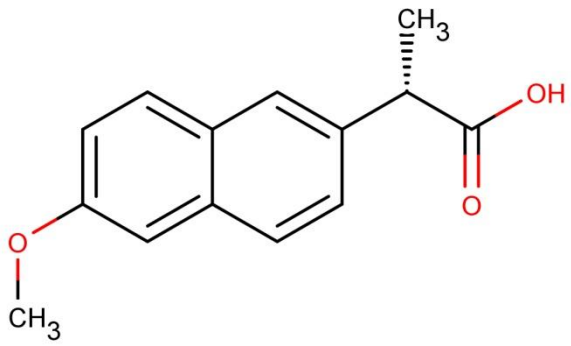

Figure 1.3: The chemical structure of naproxen.

Table 1.3: Summary of the main characteristics of naproxen and its sodium salt.

	Naproxen acid	**Naproxen sodium**
Colour	White to creamy white	White
Water solubility	Non soluble	Slightly soluble
Physical form	Solid	Solid
Odour	Odourless	Odourless
Log P	3.18	-0.54
pKa	4.15	4.15

1.1.3. Mechanism of action and therapeutic effects

When injury arises in the human body, it usually triggers a signal to the nervous system, which is translated into the sensation of pain.[49] Nociceptors are specialised sensory receptors, which are responsible for the detection of noxious stimuli; when they do so, they transform the stimuli into electrical signals and this signal is then transferred to the central nervous system.[50,51] Nociceptors are spread all over the body (skin, muscles, joints) and are stimulated by various factors including mechanical, thermal or chemical events.[52] When tissue is inflamed, injured or damaged it release inflammatory mediators (for instance serotonin, prostaglandins and cytokines), which stimulate the nociceptors.[53] Prostaglandins are considered one of the most important inflammatory mediators, and cause excessive sensitivity to pain (hyperalgesia) through these receptors.[54] The reduction or inhibition of prostaglandin biosynthesis may therefore explain the analgesic effect of the NSAIDs.[55] NSAIDs such as diclofenac, ibuprofen and naproxen, play important roles as anti-inflammatory, analgesic, and antipyretic agents.[56–58]

Their mechanism of action has been mainly explained on the basis of their inhibition of the enzymes that synthesise prostaglandins (PGs) from arachidonic acid, known as the cyclo-oxygenase (COX) enzymes.[59] There are two isoforms of the enzyme (COX-1 and COX-2).[60] COX-1 produces PGs and thromboxane (TxA_2) that regulates gastrointestinal, renal, vascular and other physiological functions. The PGs produced by COX-1 protect the stomach wall from damage by its highly acidic HCl contents.[60] COX-2 is induced in inflammatory cells and produces proinflammatory PGs.[61] Diclofenac, ibuprofen and naproxen are not selective and inhibit both COX-1 and COX-2.[62] While COX-2 inhibition is desired, the inhibition of COX-1 causes side effects in the gastrointestinal system. These side effects include bleeding,[63–65] perforation,[66–68] an upset stomach and abdominal pain.[69,70] They can also affect the hepatic,[71,72] renal,[73] and cardiovascular systems.[74,75]

It has been suggested that the NSAIDs can additionally exert their effects through a variety of other peripheral and central mechanisms such as: inhibition of the lipoxygenase pathway or interference with G-protein-mediated signals.[76] It has been demonstrated that they can be used to reduce risk of or prevent cancer,[77–80] or as an adjuvant in the treatment of the hepatitis virus.[81]

1.2. Other drugs

1.2.1. Valproic acid

Valproic acid was first synthesised in 1882, by Burton.[82] It had been used as an organic solvent in research laboratories for eight decades,[83] before its antiepileptic activity was discovered by Meunier and coworkers in France in 1962.[84] The first clinical trials were reported in 1964.[85] Three years later, it became commercially available in France as an antiepileptic drug, and was sold worldwide by 1979. Its utilisation has widened since to also cover bipolar disorders and migraine.[86]

Valproic acid (di-N-propylacetic acid, 2-propylpentanoic acid, 2-propylvaleric acid) is a C-8 branched-chain fatty acid (Figure 1.4). Its physicochemical properties are summarised in Table 1.4.

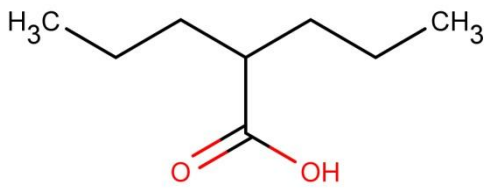

Figure 1.4: The chemical structure of valproic acid.

Table 1.4: Summary of the main characteristic of valproic acid and its sodium salt.

	Valproic acid	**Valproate sodium**
Colour	Clear colourless	White
Water solubility	Barely soluble	Very soluble
Physical form	Liquid	Solid
Odour	Characteristic odour	Odourless
Log P	2.75	-0.73
pKa	4.8	4.8

Valproic acid is sold as three commercially therapeutic forms: the acid itself, salts and mixtures of acid and salt. There are minor pharmacokinetic differences between the various formulations on the market.[87] Valproic acid is rapidly absorbed in the gastrointestinal tract with a T_{max} of 1-4 h after tablet ingestion,[88] or 15-60 min after ingestion of a liquid form.[89] This peak can be delayed by the use of coated or slow-release formulations.[90–93] The drug is present in the plasma (blood) as the valproate ion,[94] and its biological half-life is between 10 to 16 hours.[95] It is heavily bound to plasma proteins (more than 90 %),[96] and is primarily metabolised in the liver.[95]

Initially, it was suggested that valproic acid's mechanism of action is through the gamma-aminobutyric acid (GABA) system, which is a major inhibitory neurotransmitter in nervous system, since has been shown to be able to inhibit major transmitters.[97–99] However, the therapeutic concentrations at which is used are not high enough to inhibit GABA transmitters.[100,101] Winterer and Hermann have suggested that it is unlikely that GABAergic transmission is involved in the action of valproate.[102] There is evidence to show that the valproic acid may act via multiple mechanisms,[103–106] and its mechanism of action remains mysterious.[107]

Valproic acid is indicated in the treatment of mania, social anxiety disorder, panic disorder and mood instability, sleep bruxism (teeth grinding while sleeping),[108] bipolar disorder,[109110] migraines,[111–113] and epilepsy.[114–116] Recent trials hint that valproic acid may be a future candidate in the treatment of cancer,[117–122] viral infections,[123–125] retina diseases,[126–128] Alzheimer's,[129,130] and Parkinson's diseases.[131–133]

The most common side-effects are gastrointestinal disturbances (nausea, vomiting diarrhoea and hepatic dysfunction), hematological disorders (anaemia) and neurologic disorders (tremor, somnolence, dizziness, headache, confusion and sedation).[134,135] In addition to transient hair loss, menstrual disorders, weight gain, lethargy and rashes.[136] Valproic acid also has rare adverse effects such as pancreatitis, hyperammonemia and encephalopathy.[137–140]

1.2.2. Phosphonoacetic acid

Phosphonoacetic acid was first synthesised in 1924, by Nylen.[141] It was subsequently reported to have antiviral activity by Shipkowitz *et al.*[142] but to date only preclinical tests have been carried out.[143–145]

Phosphonoacetic acid (2-phoshonoacetic acid) is depicted in Figure 1.5. Its physicochemical properties are summarised in Table 1.5.

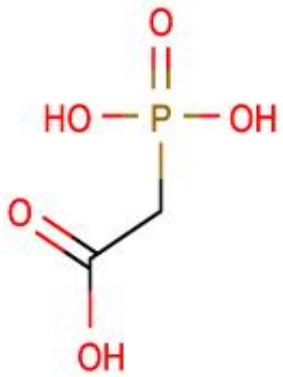

Figure 1.5: The chemical structure of phosphonoacetic acid.

Table 1.5: Summary of main the characteristic of phosphonoacetic acid.

	Phosphonoacetic acid
Colour	Greenish
Water solubility	Very soluble
Physical form	Solid
Odour	Odourless
Log P	-1.6
$pKa_{1,2,3}$	1.7/4.2/8.5

The preclinical studies showed that disodium phosphonoacetate (the acid form was too irritative) can be used locally or by an intravenous route.[146,147] The drug is present in the plasma (blood) as the phosphonoacetate ion, and its biological half-life is estimated to be less than 60 min. It is primarily eliminated in the kidneys.[148]

Phosphonoacetic acid's mechanism of action is by blocking DNA polymerase activity in the infected cell,[149] which blocks virus replication and leads to its death. The reported data showed that the drug was active against a range of viruses (eg: vaccinia virus, African swine fever virus and herpes), with negligible side-effects on the animals themselves.[146,150,151]

1.3. Drug delivery

Rapid progress in drug discovery science over recent years has resulted in a large number of novel molecules with the potential to revolutionise the treatment and/or prevention of disease.[152,153] Nevertheless, their clinical effectiveness is commonly compromised by hurdles to delivering these drugs *in vivo* (e.g. low solubility).[154,155] When an active pharmaceutical ingredient is encapsulated within, or attached to, a carrier, its safety and efficacy can be significantly improved and new therapies are possible.[156] This has led to large numbers of investigations into the design of degradable materials, intelligent delivery systems and new approaches for delivery through diverse portals in the body.[157] The concept of drug delivery to specific sites, which aims to deliver drugs at predetermined rates over predefined periods of time, was enunciated at the beginning of the 20th century by Ehrlich.[158–160] Its goal is to transport appropriate amounts of drug to the targeted sites (such as tumours, inflamed tissues etc.) while minimizing unwanted side effects on other tissues.[161] Systems permitting drug delivery to specific sites were conceptualised in the 1960s,[162] but only in the last few years has the development of such systems become realistic. New drug-delivery systems have had an influence on virtually every field of medicine including cardiology, ophthalmology and pain management.[157]

Development of active pharmaceutical ingredient (API) carriers is an interdisciplinary area of science that requires collaboration between diverse groups of scientists (materials scientists, chemical engineers, pharmaceutical scientists, chemists, biologists, mathematicians, and clinicians) to create novel devices and delivery systems with fundamentally new properties and functions.[163] There exist many type of carrier, including inorganic materials and polymeric vehicles.[164]

Inorganic materials (e.g: layered inorganic solids) are highly promising candidates for drug delivery systems. They can provide scaffolds for the presentation and encapsulation of drugs, biomolecules, and imaging agents.[165–168] Inorganic materials have much to offer in biomedical applications. While there are clearly obstacles to be surmounted in implementing these systems as delivery carriers, several of their attributes (eg: positively charged layers, anionic species may be intercalated, sustained release, biocompatibility and toxicity) and ease of production could make these systems essential additions to the present-day toolkit.[169,170]

Polymer matrices are also deemed good host systems and have been explored extensively.[171–173] In addition to acting as a stabilising environment, polymers are suitable for multifunctional applications for the reason that they can be designed to have diverse structures and functions.[172] Therefore, polymers represent a class of tremendously useful materials for many biomedical and pharmaceutical applications. For any polymer, before being selected for any biomedical application, their interaction and compatibility with the human body must be investigated carefully.[174]

Scientists have been exploring how to get drugs selectively to every part of the body, with the objective of either local delivery to a particular site or non-invasive systemic delivery of drugs utilising that part of the body as a route to the systemic circulation.[157] For many drugs, the route of administration is determined by the therapeutic nature of the drug. For example, for gastrointestinal diseases the most reasonable choice might be oral drug

delivery. Generally the choice of the route depends on the physicochemical and therapeutic properties of the drug. To be therapeutically active, a drug's concentration must be sustained in a precise concentration range (therapeutic window, Figure 1.6).

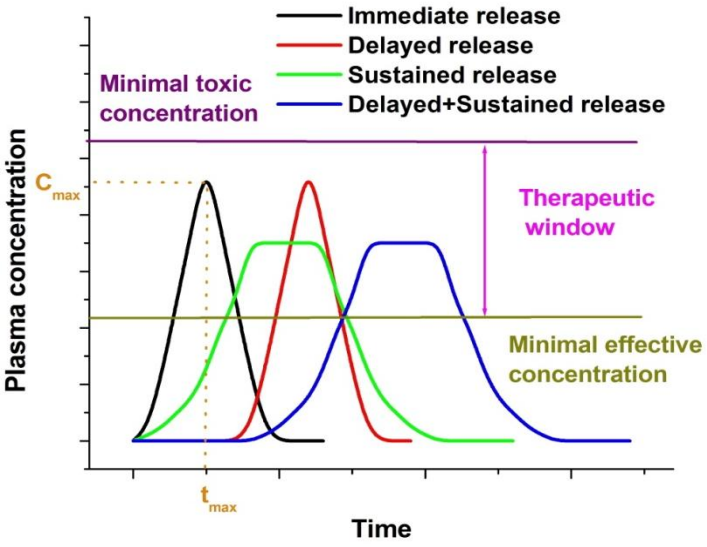

Figure 1.6: A schematic illustrating the different types of drug delivery systems and the plasma concentrations which result

If the drug's solubility is lower than the required concentration, relief of symptoms will be sub-optimal and special efforts must be taken to increase the concentration to the therapeutically active level.[175] The aim of drug delivery is to sustain the drug concentration in the desired therapeutic range for a specific period of time. To achieve this objective there are many possible solutions, depending on the nature of the particular disease being treated. For an acute condition (sudden in onset and disappear with time, ex: Inflammation due to an infection or a physical exercise), this is likely to be by the administration of a single dose that liberates the drug instantly at the site of action. For a chronic disease (a long-developing condition that remains with patients all their life, ex: arthritis), multiple-dose administration is one possible method for providing sustained therapy.[176]

1.4. Electrospun nanofibres

One approach to prepare polymer-based drug delivery systems (DDS) is using electrospinning, where the drug is physically entrapped inside a solid nanofibres that can then be orally administrated or implanted in the body.

1.4.1. Theory and mechanism of electrospinnig

Electrospinning is an effective technique for the generation of polymer fibres with a diameter in the range of 1 – 10^{-3} µm.[177] This technique has attracted much research due to its potential in such areas as tissue engineering and drug delivery.[178] The electrospinning apparatus includes four major components: a high voltage power supply, an electrically conducting spinneret (a metallic needle), a syringe pump and a collector placed at a defined distance from the needle (Figure 1.7). A solution of a polymer in a volatile solvent is loaded into a syringe, and the syringe pump supplies this solution to the spinneret at a constant and controllable rate. The positive electrode from the power supply is connected to the needle to charge the polymer solution and the collector is typically grounded (Figure 1.7).[178]

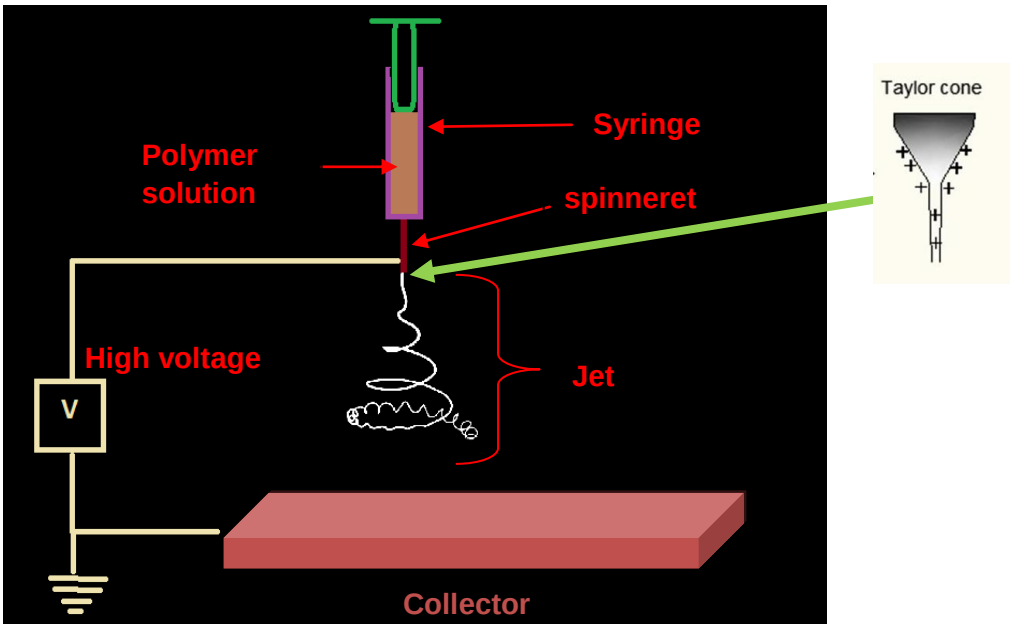

Figure 1.7: The basic electrospinning setup.

A high voltage typically in the range of 1–30 kV is used.[179,180] This causes the surface of the polymer solution at the nozzle of the spinneret to become electrostatically charged. As a result, the droplet comes under the influence of two types of electrostatic forces: the electrostatic repulsion between the surface charges and the Coulombic force applied by the external electric field. These must also compete with the surface tension of the droplet.[181,182] Because of the electrostatic interactions, the liquid drop will be deformed into a conical object known as the Taylor cone (Figure 1.7).

Once the intensity of the electric field reaches a certain level, the electrostatic forces outweigh the surface tension of the polymer solution and force the expulsion of a liquid jet from the nozzle. The liquid jet elongates and the solvent evaporates, so its diameter decreases from hundreds of micrometers to as little as tens of nanometres. The jet is attracted by the grounded collector, resulting in the formation of a randomly oriented, nonwoven mat of thin fibres on the collector.[178,183,184]

Initially, the jet follows a straight trajectory. The width of the jet here diminishes monotonically with distance from the spinneret orifice.[185] However, the jet starts to whip radially outward at particular distance from the tip, which is known as the bending instability (Figure 1.8).[185] This instability is due to electrical forces from the charge carried with the jet causing the jet to follow a diverging helical path, almost perpendicular to its own axis, in such a way that every time the jet intertwines its diameter decreases.[185] Usually, three or more turns (loops) are formed before the jet solidifies.[185]

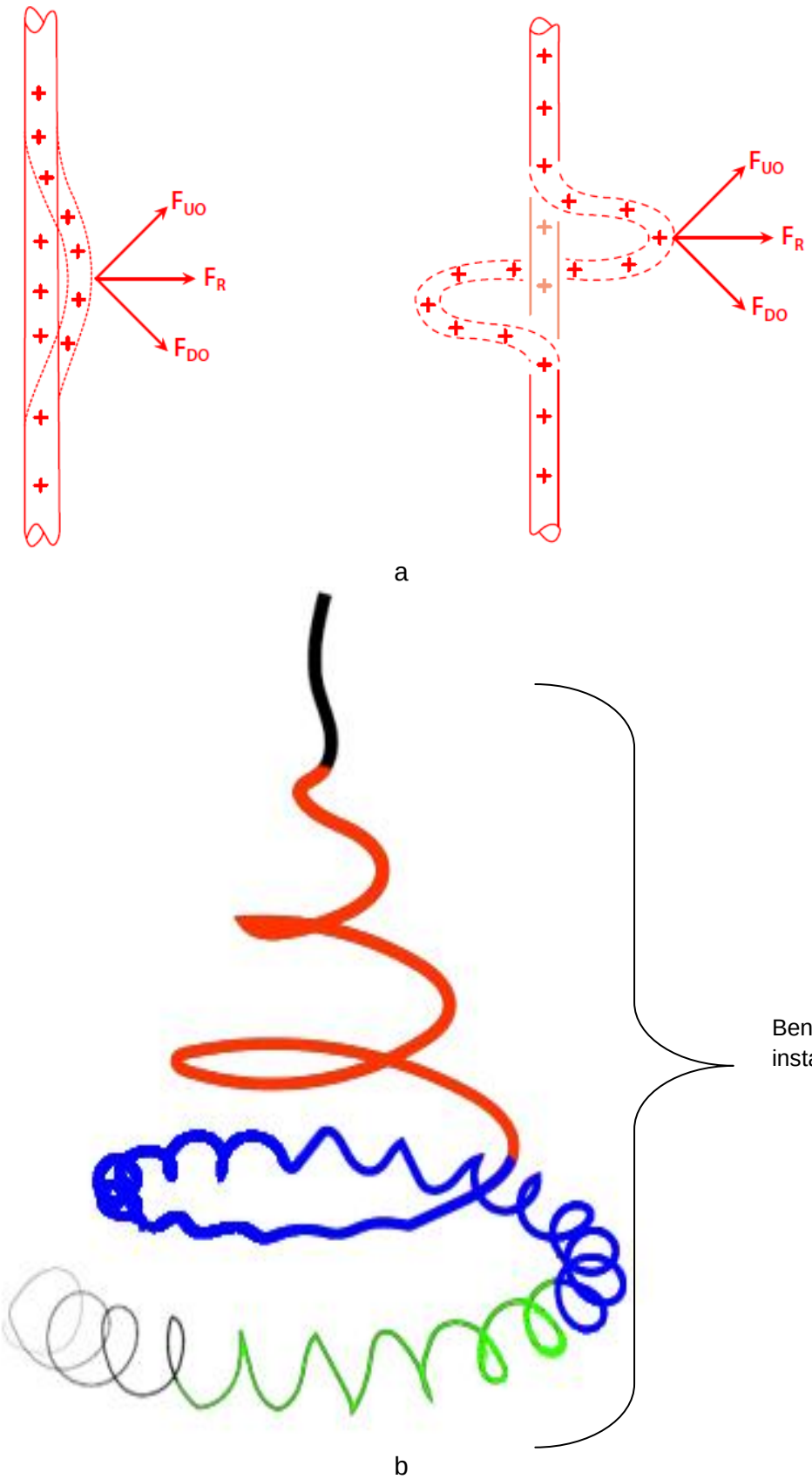

Figure 1.8: Diagrams illustrating the bending instability. **(a)** A depiction of how the bending instability occurs (F_{DO} represents the downward and outward force, and F_{UO} the upward and outward force; F_R is the overall result of these forces). **(b)** A schematic of an electrospinning jet and bending instabilities (redrawn based on diagram reported by Reneker *et al*.)[185].

1.4.2. Applications

It is known that polymers can reduce the crystallisation tendency of APIs, through various mechanisms: forming secondary interactions (van der Waals, H-bonding, etc) with the API molecules, reducing their mobility, and disrupting interactions between the individual API molecules.[186] These effects depend on many factors such as the polymer's chemical structure, molecular weight and glass transition temperature.[187] For instance, it has been reported that blending ibuprofen with alginate, poly(ethylene) oxide (PEO) or polyvinylpyrrolidone (PVP) led to the inhibition of ibuprofen re-crystallisation.[188–191]

The effects of electric current on crystals and crystallisation processes have previously been studied. It was found that electrical forces can accelerate and improve the crystallisation of various materials.[192,193] They have direct influence on the nucleation site, thus influencing the crystal growth.[193] Amorphous materials can also be affected.[194,195] The question that arises is, when polymers and electric current are used simultaneously to generate electrospun nanofibres, what the net effect on crystallisation will be; this will be discussed in the Chapter 2.

Electrospun nanofibres have been explored for a wide variety of purposes, for instance as a storage device for alternative energy sources such as hydrogen,[196,197] or for ecological purposes,[198,199] where nano-sized photocatalysts have been synthesised to improve photocatalytic capacity.[200,201] The biomedical utilisation of nanofibres is a particularly promising research field. Nanofibres are able to contribute to various medical areas such as drug delivery,[202–204] organogenesis,[205] genomic medicine,[206] scaffolds for tissue engineering[207,208] and wound dressings.[209–212]

Usually wounds are covered with bandages and plaster, which are required to be changed quite often till wounds get healed. This procedure sometimes is not convenient for patients and certain wounds. Electrospun nanofibres mat has porous features, where pore sizes are often small and do not allow the bacteria

to pass through while maintaining good ventilation. This process is very important while treating burned skin. Smart dressing mats were developed, which showed better healing, no mats bandage were required, no infections appeared and change colour when an infection occurs or a wound heals.[213–215]

A large number of studies have reported the use of electrospinning to produce drug-loaded fibres for use as engineered drug delivery systems.[216–219] Gatti *et al*[220] have used electrospun PEO nanofibres to improve the retention time of bacteriolytic antibiotics, and found that the fibres were capable of delivering the antimicrobial peptide LL-37 at a constant rate while still maintaining its antimicrobial abilities.[220] Karthikeyan's team have employed electrospun zein/Eudragit, Eudragit is a pH sensitive polymer, nanofibres to generate a dual drug delivery system for the simultaneous delivery of aceclofenac and pantoprazole.[221] The fibres showed efficient sustained release for both drugs, and reduced the gastro-intestinal toxicity induced by these non-steroidal anti-inflammatory drugs.[221] Shen and co-workers have utilised electrospun Eudragit fibres loaded with diclofenac sodium for colon-targeted drug delivery, and observed pH-dependent drug release profiles.[216]

The majority of these studies use one-fluid electrospinning, but even in this simple system it is found that variation of the polymer and processing parameters can result in a wide range of drug release behaviours. More recently, more advanced approaches have been employed to develop bespoke drug delivery profiles; these include coaxial electrospinning (using two concentric needles, one nested inside another) and a process combining electrospinning and spraying.[222,223]

Recent results have also demonstrated that the release of drug from electrospun fibres can be manipulated by surface treatment. For instance, sustained drug release was achieved by using a fluorination treatment to control the swelling rate of poly(vinyl alcohol) nanofibres with drug incorporated.[224] Electrospun nanofiber mats have also extensively been explored for tissue engineering.[225]

1.5. Layered solids

Layered solids are group of materials containing strong bonding connecting atoms in two dimensions, with much weaker bonding in the third dimension.[226] There are many types of layered solids; those which will be used in this work are layered double hydroxides (LDHs), and hydroxy double salts (HDSs). These materials have positively charged layers with charge-balancing anions located between these layers, and exhibit properties such as ion exchange intercalation.[227] These materials may be used to incorporate and deliver drug anions, and being basic have the potential to ameliorate the problems of gastric irritation which frequently arise with NSAIDs. A schematic diagram showing the generic structure of an LDH or HDS is illustrated in Figure 1.9.

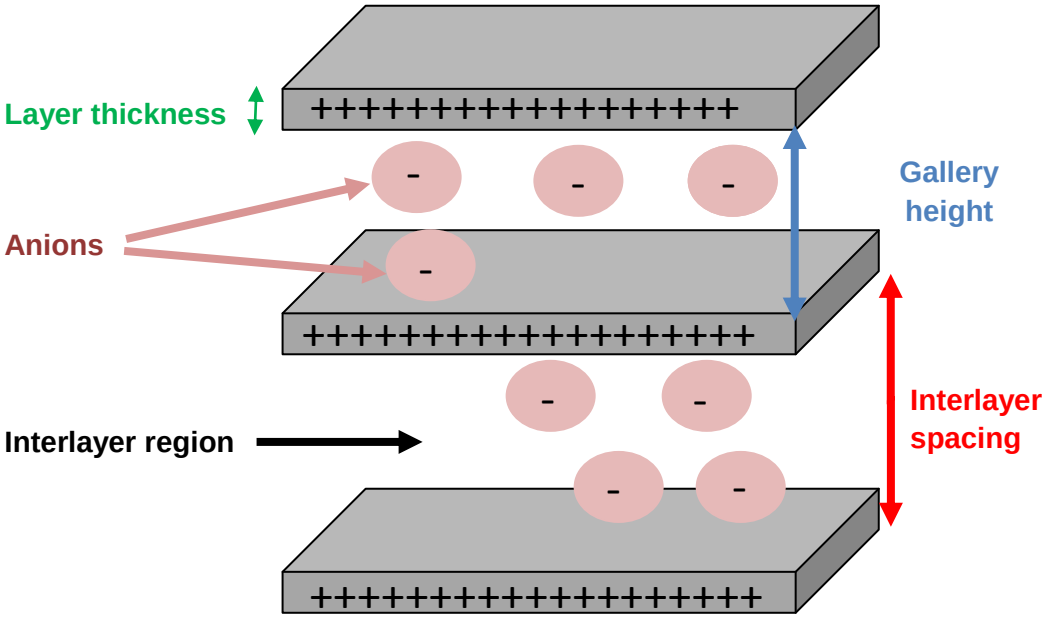

Figure 1.9: A schematic diagram showing the key structural features of LDHs and HDSs.

1.5.1. Layered double hydroxides

Layered double hydroxides (LDHs) were discovered in 1842 in Sweden and synthesised for the first time in the 1940s by Feitknecht.[228] Their main structural features were determined by Allmann and Taylor in the late 1960s.[229,230]

LDHs consist of positively charged metal hydroxide sheets and charge balancing anions in the interlayer region. The general formula of LDHs is $[M^{z+}_{(1-x)}M^{3+}_{x}(OH)_2]^{q+}(X^{n-})_{q/n} \cdot yH_2O$. Generally z=2, and M^{2+} is a divalent metal ion such as Mg^{2+}, Co^{2+}, Ni^{2+}, Cu^{2+}, Zn^{2+} or Ca^{2+}; M^{3+} is a trivalent metal ion such as Al^{3+}; if $q = x$, x is usually between 0.25 and 0.33.[231] There is a unique family of LDHs for which $z = 1$, where $M^{+} = Li^{+}$ and in this case $q = 2x - 1$. The common formula for this family of materials is $[LiAl_2(OH)_6]X \cdot yH_2O$, where y lies in the approximate range 0.5 – 4 and X is a generic anion (*e.g.* Cl, Br, and NO_3).[232] The schematic structure of a LDH is illustrated in Figure 1.10.

1.5.1.1. Structural properties of layered double hydroxides

The simplest way to comprehend the structure of LDHs is to begin from the structure of brucite, $Mg(OH)_2$, where edges are shared by $Mg(OH)_6$ octahedra to form infinite sheets. These sheets are stacked on top of each other and are held together by hydrogen bonding. A positive charge is generated in the hydroxyl sheet once Mg^{2+} ions are substituted by a trivalent ion such as Al^{3+} in an LDH. The positive charge generated is balanced by anions, which are located in the interlayer region. In the free space of this interlayer, water is also commonly found. Both the anion and water are usually randomly loaded in the interlayer region, being free to move by breaking their bonds and forming new ones.[228]

Generally the metals in LDHs are randomly distributed.[233–237] Gibbsite (γ-$Al(OH)_3$) is a naturally occurring mineral (Figure 1.10), where Al atoms fill two thirds of the octahedral sites in the layers in an ordered fashion.[238,239] Gibbsite can be used as a precursor to prepare Li/Al LDH,[240] where Li cations occupy all the octahedral vacancies sites of the gibbsite The structure of the Li/Al LDH, typical of these materials, is depicted in Figure 1.10. The usefulness of uniform metals' distribution in Li/Al LDH is discussed in Section 1.7.

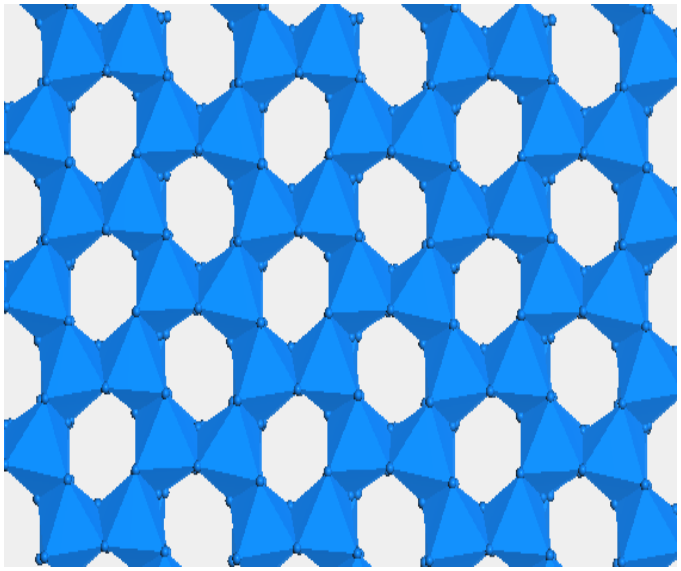

a

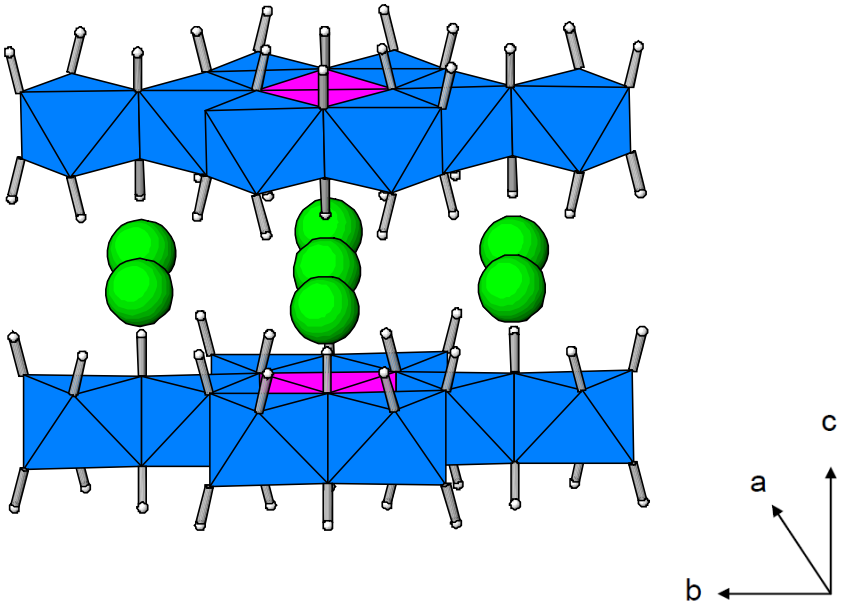

b

Figure 1.10: The structures of. **(a)** gibbsite (H atoms are omitted for clarity). and **(b)** $[LiAl_2(OH)_6]X{\cdot}yH_2O$. $Al(OH)_6$ octahedra are marked in blue, and $Li(OH)_6$ octahedra in magenta. Cl anions are green.

1.5.1.2. Applications

The LDH interlayer anions can be replaced through ion exchange by other functional ions to yield functional systems (see schematic in Figure 1.13). LDHs have high versatility, easily tailored properties and low cost, which make them attractive for the fulfilment of many requirements. LDHs are promising as flame retardants,[241] catalysts and catalyst precursors,[242–244] water and air purifying agents,[245–247] adsorbents,[248–250] as electrical and optical functional materials,[251] and for the separation of organic isomers.[252,253] They have also been shown to have potential as a controlled drug delivery systems,[254,255] and for the stabilisation of APIs. [256]

Del Arco *et al*.[257] have intercalated indomethacin into LDH through two routes (reconstruction and coprecipitation, Section 1.5.3). Intercalation of the drug was accomplished by both routes; however, the amount of drug intercalated, as well as the height of the gallery, were larger by the coprecipitation than by the reconstruction route. Analysis of the animals (Swiss mice) extracted stomachs revealed that oral supply of indomethacin caused gastric hemorrhagic damage. In contrast, the same intercalated dose had less side-effects.[257] In another example Qin and co-workers intercalated an antitumor drug (etoposide VP16), and found that the intercalated product possessed a sustained release profile and exhibited better antitumor efficiency than the drug alone.[258]

In regard to diagnostic imaging applications, several fluorescent compounds have been employed with LDHs for numerous applications such as optical imaging, X-ray computed tomography (CT), magnetic resonance imaging (MRI) and positron emission tomography (PET).[259–261] Xu and co-workers have intercalated Gd–DTPA (gadolinium(III)/di-ethylene triamine pentaacetate) complex into an Mg/Al LDH.[262] They found that the LDH/Gd–DTPA composite enhanced by four times the longitudinal (T1) and 12 times the transverse (T2) relaxation compared to Gd–DTPA on its own, which led to signal improvement in MRI.[262] Wang *el.al* intercalated iobitridol (a contrast agent in X-ray imaging) into a LDH-Gd/Au nanocomposite and injected it to mice.[263] The *in vivo* CT

results obtained showed the organs and their periphery clearly, the images were bright and remained so for a considerable period compared with the free iobitridol.[263] The *in vivo* bio-distribution of a LDH/contrast agent intercalate can be controlled and their accumulation in specific organ or various organs can be efficiently regulated.[264] This property is very desirable *in vivo* imaging for reasons of cost effectiveness, enhancing the MRI signal and the ability to work in a non-invasive manner.[265]

In addition to their ability to deliver APIs and contrast agents, LDHs have another remarkable feature towards the human being immune system. It was shown that they are able to boost the immune response to a vaccine antigen, and the effect observed can be correlated with their physical and chemical properties.[266] It was revealed that the LDHs have the ability to skew T helper cell polarisation to Th1 cells (required for infections by intracellular bacteria and some viruses).[267–270] For example, the LDH systems could be used to enhance the efficacy of vaccination against common diseases, both infectious (e.g: hepatitis B virus) and non-infectious (e.g: cancer).[268–270]

1.5.2. Layered hydroxy double salts

Layered hydroxy double salts (HDSs) occur as natural minerals known as simonkolleite, which is a rare secondary mineral form.[271] HDSs naturally occur from the weathering of zinc-bearing slag that contains native zinc, zincite and hydrozincite.[271,272] Their crystal structure was firstly characterised by Nowacki and Silverman in 1961,[273] and a few years later they were categorised as a new type of mineral.[271]

Layered hydroxy double salts (HDSs) are functionally and structurally similar to LDHs, with the generic formula $[(M^{2+}_{x-1}Me^{2+}_{x})(OH)_{3(1-y)}]X^{n-}_{(1+3y)/n}\cdot zH_2O$ in which M^{2+} and Me^{2+} correspond to divalent metals ions such as Cu^{2+}, Co^{2+}, Ni^{2+}, or Zn^{2+} and X^{n-} is an exchangeable interlayer anion.[274,275]

The radii difference between the divalent metals plays an important role in the formation of HDSs, unlike LDHs where a difference is more tolerable. According to the literature, for a mixture of divalent metals to form successful layer structures, the radii difference between M^{2+} and Me^{2+} should be 0.05 Å or less.[227] However, this not the case all the time, and more details are given the Chapter 4. The divalent metals that were successfully incorporated into HDSs layers structure are illustrated in Table 1.6. There was an attempt by Stahlin and Oswald to synthesise Mn/Zn HDS, but the reaction was not successful.[276]

Table 1.6: Ionic Radii of Metal Ions in HDSs.

HDSs	Radii (Å)	Difference (Å)	Reference
Zn	0.74	0	[277]
Cu	0.73	0	[277]
Ni	0.69	0	[278]
Co	0.745	0	[279]
Zn/Co	0.74/0.745	0.005	[227]
Zn/Cu	0.74/0.73	0.01	[227]
Cu/Co	0.73/0.745	0.015	[227]
Ni/Cu	0.69/0.73	0.04	[227]
Zn/Ni	0.74/0.69	0.05	[227]

1.5.2.1. Structural properties of hydroxy double salts

The HDS structure comprises a brucite-like lattice with some vacant octahedral sites. The surface of the HDS layers is not flat because some metal ions are situated above and below the vacant sites of the hydroxide layer to create tetrahedra. An example of an HDS is the zinc basic salt (ZBS), which has the formula $[Zn_5(OH)_8](NO_3)_2 \cdot 2H_2O$.[280,281] The ZBS can be formulated as $[Zn_{3octa}Zn_{2\ tetra}(OH)_8](NO_3)_2.2H_2O$, and its structure is illustrated in Figure 1.11.

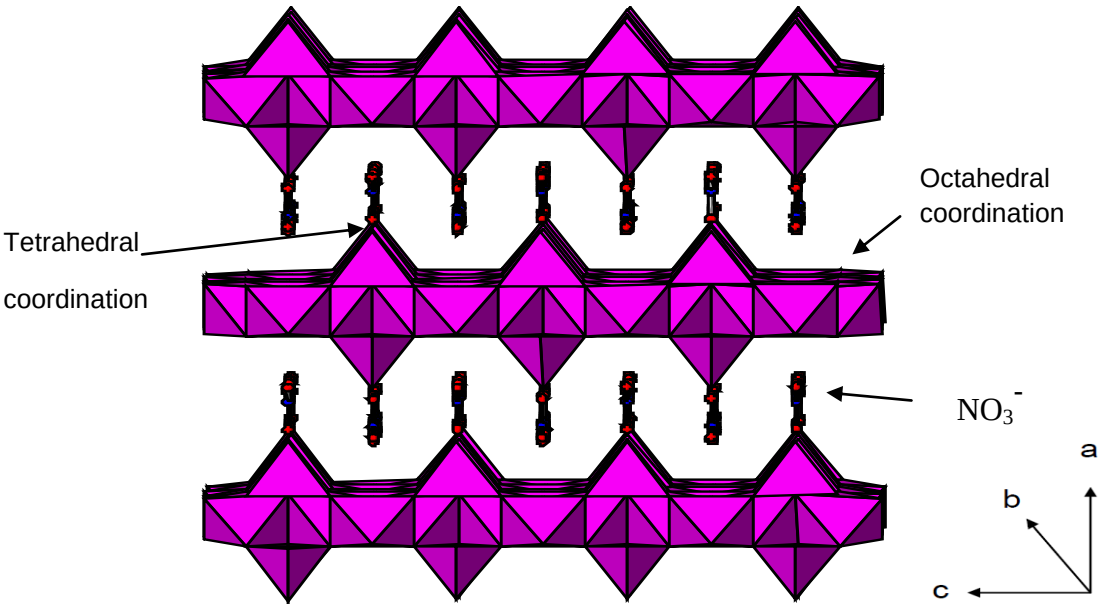

Figure 1.11: The structure of $[Zn_5(OH)_8](NO_3)_2 \cdot 2H_2O$.

The ZBS materials are known to exist as various polytypes, which differ in their layer stacking sequences: for instance, with NO_3 as the interlayer anion they have a two-layer repeat *aba* stacking sequence.[281] On the other hand, with Cl as the anion they possess a three-layer *abca* repeat.[271,273,282] The layers stack in either the a or c–direction for NO_3 and Cl, respectively, and the $[Zn_5(OH)_8]](NO_3)_2 \cdot 2H_2O$ unit cell contains two layers while that of $[Zn_5(OH)_8]](Cl)_2 \cdot 2H_2O$ has three (Figure 1.12).

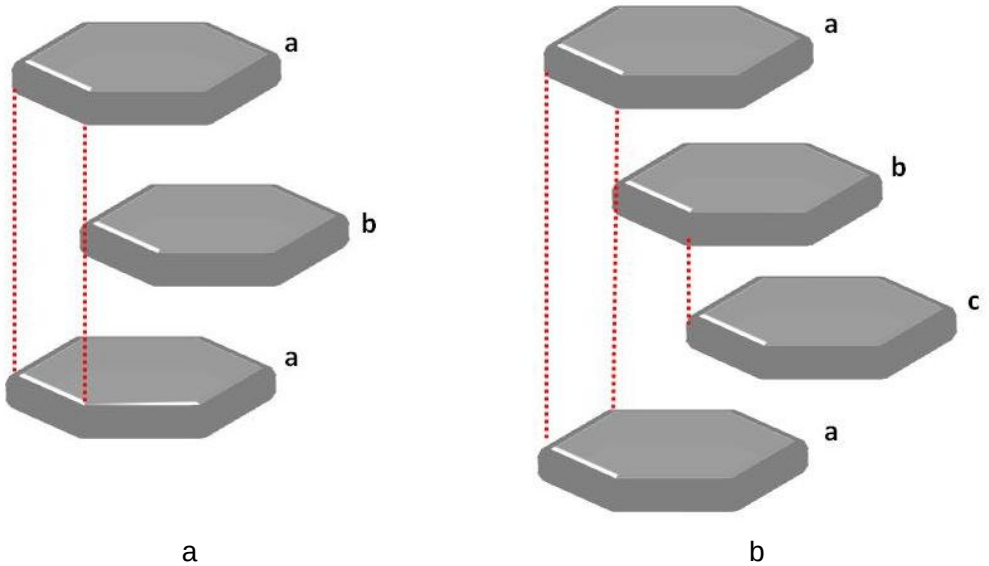

Figure 1.12: Schematics showing two types of ZBS polytypes with different interlayer anions; (a) NO_3 and (b) Cl.

1.5.2.2. Applications of hydroxy double salts

HDSs are generally stable, inert, and biocompatible enough to be employed as drug carriers, as biomolecule reservoirs, and as advanced green materials.[280] They can also used also as antimicrobial agents,[283] antifungal agents,[284] water treatment,[285] anticorrosion agent [286] and photocatalysis agents.[287]

HDSs have also been used as a precursor to synthesise metal–organic frameworks (MOFs); it was found that the transformation reaction was fast even at room-temperature,[288] while common methods to prepare MOFs are slow and require solvothermal conditions.[289] This makes HDSs highly desired for industrial implementation and commercialisation.

There are several examples of commercial systems based on HDSs. The exposure of human skin to sunlight is unavoidable, and has advantages to the human being such as vitamin D activation.[290] However, long exposure is undesirable since it can cause melanoma and other skin cancers.[291–293] Sunscreen is one of the protection options against UV radiation. However, the UV absorber present in sunscreen products can photo-degrade easily, which requires application of sunscreen each few hours, and this is inconvenient for the users. In addition the degraded products can become toxic. When UV absorbers were loaded into HDSs, they showed an increase in their stability, broadening of their absorption wavelength range and an enhancement in the UV absorption.[294,295] For that reason, the HDSs are considered to be good candidate in the cosmetic area. For example, Choy *el.al* have various HDS-based commercial cosmetics products.[296]

In addition to their use in the cosmetic, the HDSs represent good candidates in various domains. They can be utilised for the selective intercalation of certain anions over others, for instance 1,4- over 1,2-benzenedicarboxylate and for 2,6- over 1,5-napthalanedisulfonate.[274] Arulraj *et al*. have intercalated maleate and fumarate into HDS and found that maleate enters as a monoanion, while fumarate enters as a dianion.[297] The HDSs have as well the recognition ability

towards certain carboxylate compounds.[298] Their applications have also been demonstrated in drug delivery: for instance, mefenamic acid and 4-biphenylacetic acid were intercalated into the ZBS and sustained drug release was achieved for both drugs in representative *in vitro* conditions.[299]

HDSs have showed utility in cancer treatment, improving the uptake of loaded drugs compared to the pure drugs, and resulting in enhanced effects.[300–304] For instance, protocatechuic acid loaded into a ZBS showed better results than the free drug towards HeLa, HepG2 and HT29 cell lines. The half maximal inhibitory concentration (IC_{50}) of the protocatechuic acid/ZBS was 50 % lower than the free drug.[300] Hussein Al Ali and co-workers showed that hippuric acid loaded into ZBS also increased its efficacy. When it was combined with other anticancer drugs (doxorubicin, oxaliplatin, cytarabine or tamoxifen) their synergic effects were enhanced toward various cancerous cell lines.[301–303]

1.5.3. Intercalation

Intercalation from chemical sense may be described as the placement of a guest into the interlayer region of a crystal lattice or other structure. The process is usually topotactic, with the preservation of the layered structure during the reaction.[305] Intercalation can be accomplished by a range of different methods such as reconstruction, co-precipitation and ion exchange.[228]

In reconstruction, the layered solid systems are first dehydrated during a calcination process, which results in a mixed metal oxide. Then the mixed metal oxide is stirred in an aqueous solution of a guest, which leads to the reconstruction of layers with the guest in the interlayer region.[306] This phenomenon is known as the ‘memory effect’.[307]

In coprecipitation, two metal salt solutions are added dropwise to a basic solution of the desired guest under vigorous stirring. Generally, the pH and

temperature are kept constant during this process. The preparation is then allowed to age.[308]

Ion exchange, in the context of LDHs and HDSs, involves electrostatic interactions between ions in the boundary layer of the solution and the particle surface, and results in the replacement of an initial interlayer anion with a different species. It is generally rapid and reversible.[309] The process of ion exchange is illustrated in Figure 1.13.

The intercalation of a guest species into the interlayer regions is a heterogeneous process, and for that reason both the kinetics and thermodynamics of the reaction must be taken into account. This means that the activation energy of the process is important, and metastable kinetic products frequently are formed. Intercalation into a layered material passes through three principal steps that require energy. First, the guest must diffuse through the reaction solvent to reach the host. In water, the barrier to diffusion is around 15 kJ mol^{-1}.[232,310] After the guest has reached its destination (the host), the layers must be prised apart to permit the guest entry into the interlayer regions. Finally, the guests must travel all the way through the particles to entirely fill the interlayer regions.[232]

The interlayer anions present in LDHs can be exchanged by other anions, both organic and inorganic. The order of preference for some common inorganic anions is as follows: $I^- < NO_3^- < Br^- < Cl^- < F^- < OH^- < SO_4^{2-} < CO_3^{2-}$ (for Mg/Al LDH).[311] NO_3^- is an anion which can be easily replaced by a more strongly held one like CO_3^{2-}.[231]

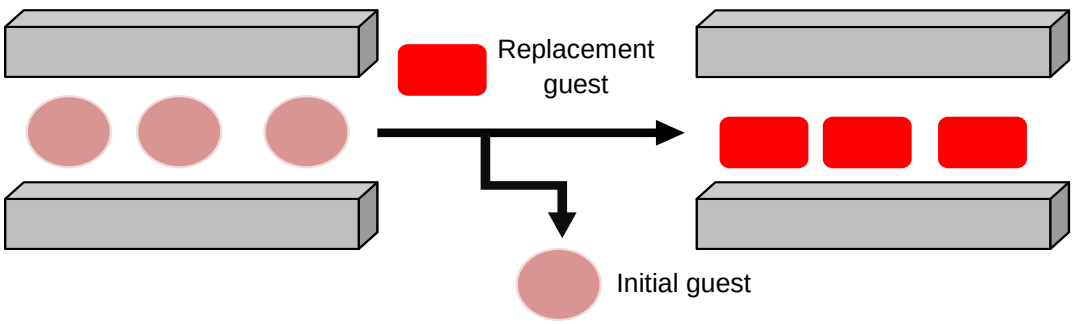

Figure 1.13: Schematic representation of an ion exchange intercalation reaction.

1.6. *In situ* studies

The intercalation process of a guest molecule into a host lattice is a heterogenous process. While the intercalation process is taking place, the standard characterisation techniques are not useful since they cannot penetrate bulky reaction vessels. Thus, little is known about the dynamics and kinetics of intercalation reactions. It is possible to monitor the intercalation process “live” using a non-invasive technique called synchrotron radiation, which allows the extraction of both qualitative and quantitative information.

1.6.1. Introduction to synchrotron radiation

A synchrotron is particular category of cyclic particle accelerator, in which electric and magnetic fields play key roles.[312,313] A synchrotron facility consists of five main components: an electron gun, a linac, a booster, a storage ring and beamlines (Figure 1.14).

Electrons are usually generated by thermionic emission (electron gun) and then injected into the linac (linear accelerator), where they are accelerated to about 100 MeV. Electrons enter the booster (second particle accelerator) where they are accelerated further to the magnitude of GeV, before they are transferred into the storage ring. Once there, they are maintained in a closed loop by the utilisation of straight sections joined by array of magnets (there are various types).[314–317] The electrons inside the ring are moving so quickly that their speed is almost equal to the speed of light. They are maintained under an ultrahigh vacuum (10^{-9} - 10^{-10} Torr) in order to minimise their interactions with air or other molecules. This is essential to provide a long-lasting beam lifetime. As the electrons follow orbit they generate synchrotron radiation (electromagnetic radiation), which leaves the ring through tangential ports called beamlines that permit the radiations to pass to experimental stations located outside the ring.[314–317]

This radiation covers a broad range of wavelengths extending from the infrared through the visible and ultraviolet range, to the soft and hard X-ray parts of the electromagnetic spectrum. This makes synchrotron radiation a powerful tool in biology, chemistry, medicine and physics science investigation.

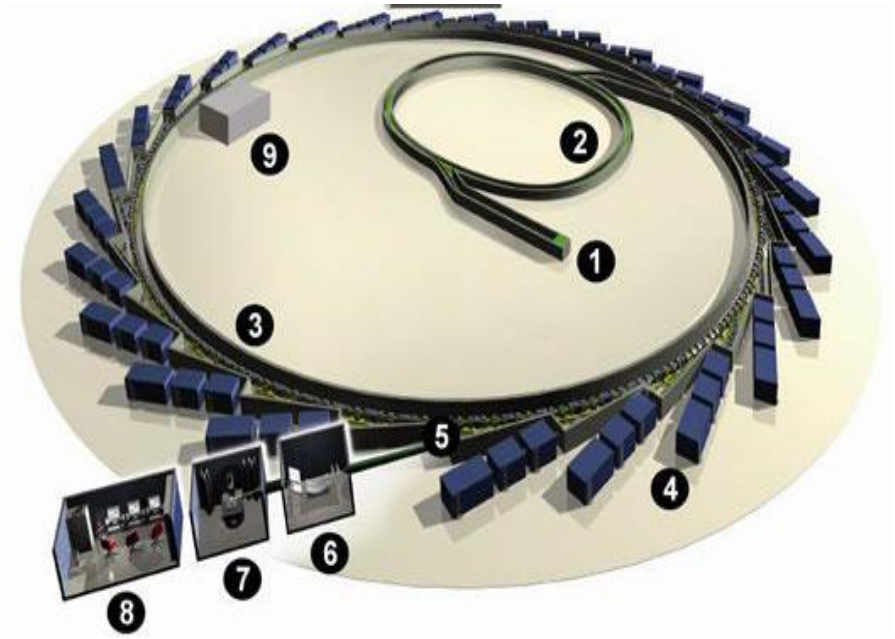

Figure 1.14: A diagram of a synchrotron facility showing the main components (1) injection system and linac; (2) booster synchrotron; (3) storage Ring; (4) beamline; (5) front end; (6) optics hutch; (7) experimental hutch; (8) control cabin and (9) radiofrequency (RF) cavity. (Taken from Diamond light source website)[318]

1.6.2. Time-resolved X-ray diffraction

Synchrotron radiation has been used for years to explain the kinetics and mechanisms of solid-state and heterogeneous liquid/solid or gas/solid reaction processes.[319–326] It comprises a significant non-invasive probe which may be used to monitor solid state reactions, and its use has started to redress the deficit in the comprehension of reactions occurring in the solid state. The high-energy of the synchrotron X-ray beam permits it to traverse large reaction vessels and diffraction patterns can be collected quickly. Therefore, Bragg reflections corresponding to the various materials (host material, any intermediate phases, and the product) present during a reaction can be

recorded simultaneously and the diffraction data can be collected under realistic reaction conditions.

The technique has been widely utilised to investigate a range of solid-state and heterogeneous solid/liquid reaction processes.[327–335] Among these, the intercalation reactions of LDHs and HDSs have been explored.[336–341] The intercalation into HDSs were observed generally to be one step reactions,[336,339] but with lower concentration of guest anions an intermediate phase was detected.[336] For intercalation into LDHs, some reactions were observed to be direct intercalation process (one step reactions) and some went through intermediate phases.[232,337,338,342,343]

1.7. Computer simulation

Computer simulation is considered as a third approach in science, lying between the theoretical and experimental approaches.[344] It has become an indispensable tool for the investigation and prediction of physical and chemical processes. It provides information about structure, dynamic and thermodynamics properties.[345,346] Simulations have been carried out on many systems, for instance: zeolites,[347–350] LDHs,[351–353], HDSs.[354,355] and other porous structures.[356–358]

In order to enhance the understanding of the physical and chemical properties of HDS or LDH/guest combinations, molecular dynamics (MD) computer simulations are seen as a valuable tool for complementing experiments (*ex situ* and *in situ*) and aiding their interpretation. Basically, MD allows the simulation of materials on an atomic scale. The movements and the trajectories of the atoms and molecules (which regulate microscopic and macroscopic behaviours of physical systems) are determined using the Newton's equations of motion.[359] In MD the motion of electrons are not taken in consideration (as opposed to Quantum Mechanics simulations), which results in fast simulation times but

some inaccuracies.[360–363] Those inaccuracies are corrected by the parameterisation of force fields (FFs), which regulate interactions between particles.[364,365]

Very few studies have combined *in situ* time-resolved experiments and MD,[366] but MD has been widely used to probe the interlayer properties of LDHs.[367] It permits the chronological evolution of a model system under near laboratory conditions to be followed as well as providing details regarding the coordinates of all atoms within the model at any moment during the simulation. Therefore, the interlayer arrangement and dynamics of organic and water molecules can be evaluated.[367]

1.7.1. Force fields

The force-field is used to predict the energy of a molecule based on its conformation. This allows predictions of equilibrium geometries and transition states, and relative energies between conformers or between different molecules. The total energy is the sum of bonding and non-bonding interactions.[368,369]

$$E = E_{bonding} + E_{non\text{-}bonding} \quad (1)$$

The bonding term covers stretching, bending and torsional energy.[368,369]

$$E_{bonding} = E_{stretching} + E_{bending} + E_{torsional} \quad (2)$$

The non-bonding term includes van der Waals (VDW), electrostatics (elect) (Coulombic) and polarisation (polar) forces.[368,369]

$$E_{non\text{-}bonding} = E_{VDW} + E_{elect} + E_{polar} \quad (3)$$

1.7.1.1. Bonding terms

1.7.1.1.1. Stretching

$E_{stretching}$ is the energy function for stretching a bond between two atoms A and B (Figure 1.15). $E_{stretching}$ is described by the harmonic bond stretching equation (4), where r is the bond length, r_0 is the equilibrium bond length, and k_s is the force constant.[370,371]

$$E_{stretching} = ½ k_s (r-r_0)^2 \quad (4)$$

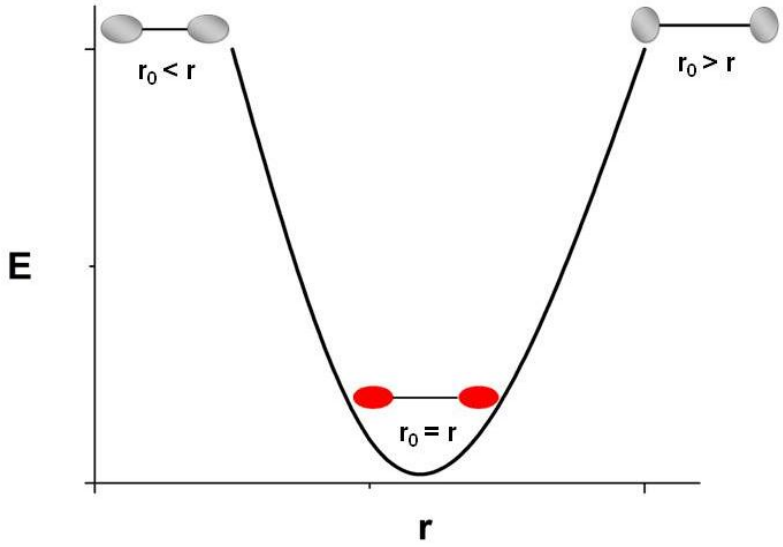

Figure 1.15: The harmonic bond stretching energy term.

1.7.1.1.2. Bending

$E_{bending}$ is the energy required for changing the angle between two bonds formed by three atoms A - B - C, where there is a bond between A and B, and between B and C (Figure 1.16). The $E_{bending}$ is described by a harmonic angle equation (5), where θ is the bond angle, θ_0 is the equilibrium bond angle, and k_b is the force constant.[372,373]

$$E_{bending} = ½ k_b (\theta-\theta_0)^2 \quad (5)$$

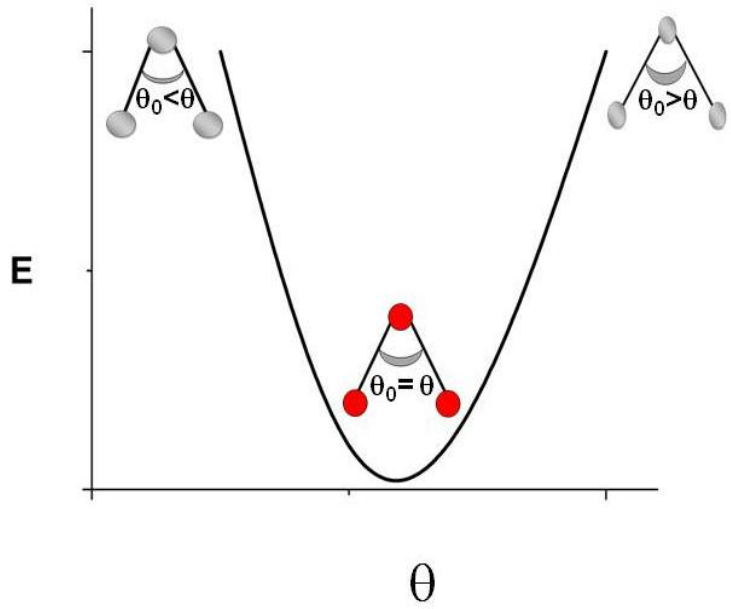

Figure 1.16: The harmonic bond bending energy term.

1.7.1.1.3. Torsion

The third type of bonding term is the term that describes how the energy of a molecule changes as it undergoes a rotation about one of its bonds, i.e. the dihedral or torsion energy for the system. In contrast to the bond and angle terms a harmonic form for the dihedral energy is not usually appropriate. This is because, for many dihedral angles in molecules, the whole range of angles from 0 to 360 can be accessible with relatively small differences in energy. Such effects can be reproduced with a periodic function that is continuous throughout the complete range of possible angles (see Figure 1.17).[374,375] The dihedral energy can then be written as:

$$E_{torsional} = \tfrac{1}{2} V_n[1+\cos(n\phi-\delta)] \quad (6)$$

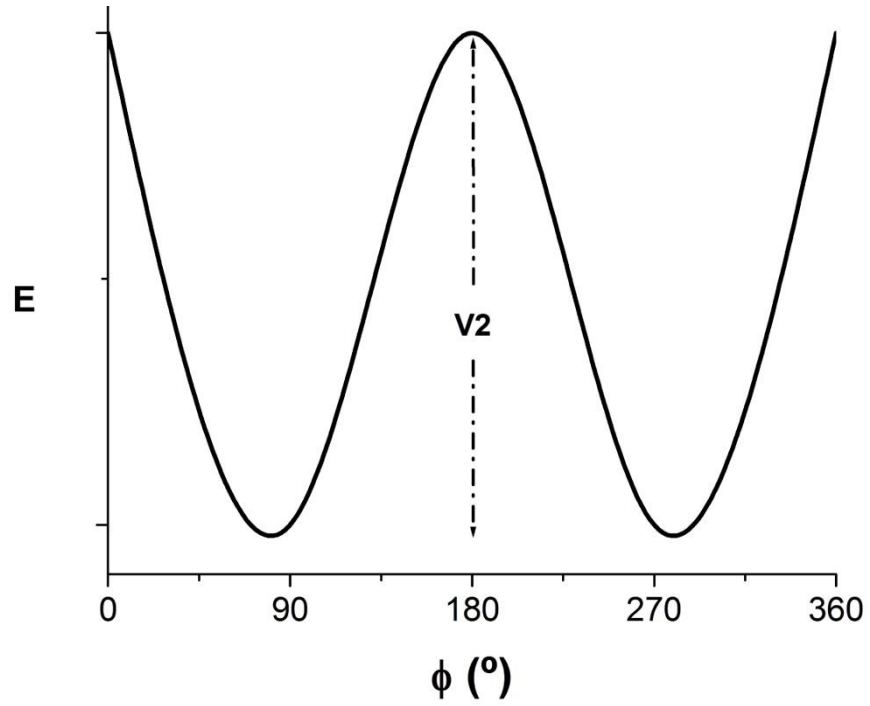

Figure1.17: A torsion angle energy term with a periodicity of 2.

1.7.1.2. Non-bonding terms

By separating out the van der Waals and electrostatic terms, molecular mechanics attempts to make the remaining constants more transferrable between molecules than they would be in a spectroscopic force field.[376]

1.7.1.2.1. Van Der Waals energy interactions

The van der Waals (VDW) energy arises from the interactions between electron clouds around two non-bonded atoms and has correlation with the distance between the two atoms. For instance, if the distance is short the forces become strongly repulsive, while in the intermediate range they become attractive and in the long range they go to zero.[377–380] The VDW general equation is given as follows:

$$E_{VDW} = -\alpha\,(1/r_{ij})^6 \quad (7)$$

The VDW interaction of a force-field computation is often time consuming, and thus usually it is approximated by the Lennard-Jones (LJ) potential as shown in equation (8).[377–380]

$$E_{VDW} = \varepsilon [(r_0/r_{ij})^{12} - 2(r_0/r_{ij})^{6}] \quad (8)$$

ε describes the depth of the potential. r_{ij} is the separation distance between the two atoms i and j, and r_0 is the equilibrium separation distance between the two atoms i and j (Figure 1.18).[377–380]

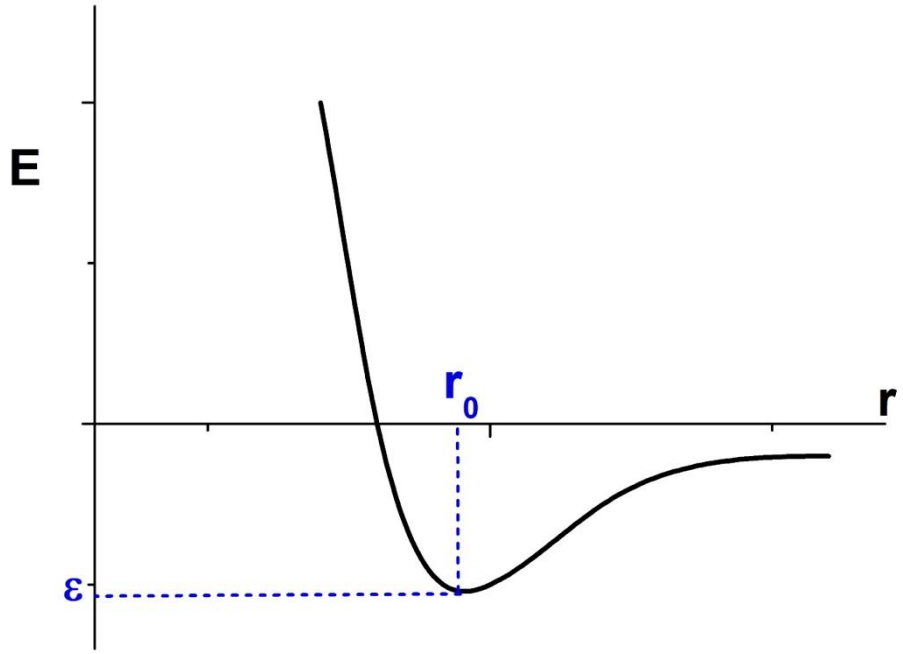

Figure1.18: The Lennard-Jones energy for a pair of atoms.

1.7.1.2.2. Electrostatic interactions

An electrostatic interaction arises due to the unequal distribution of charge in a molecule. A simple example is the water molecule, where the hydrogen atom is slightly positive and the oxygen slightly negative. The common model used is simple, adequately accurate and allows a quick calculation of the electrostatic energy. In this, fractional charges are assigned to each atom, and due to charge

conservation for a neutral molecule these sum to zero: in the previous example qH = -½ qO.[368,381] The electrostatic energy is calculated as

$$E_{elect} = 1/4\pi\varepsilon_0\varepsilon\ (q_i q_j / r_{ij}) \quad (9)$$

where q_i and q_j are the fractional charges on atoms i and j and r_{ij} is the distance between the two atoms (Figure 1.19). The pre-factor $1/4\pi\varepsilon_0$ is the standard term used when calculating electrostatic interactions in the MKSA (metre, kilogram, second, ampere) system of units, and ε is the dielectric constant. The latter is equal to 1 when the system is in vacuum.[368]

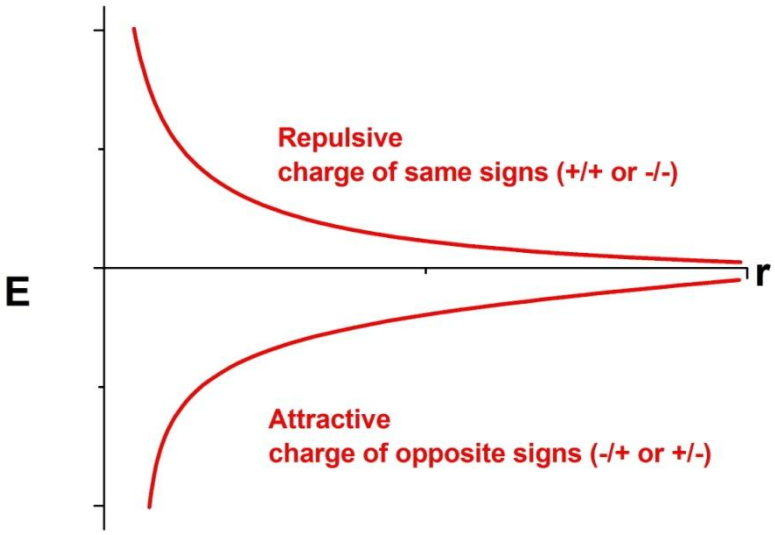

Figure 1.19: A schematic illustrating electrostatic interactions.

Based on the equations 8 and 9 to run the interactions between all possible pairs of atoms in bigger system tends to be challenging and time consuming. Thus, cutoff or truncation methods are usually used to accelerate the calculation, for instance the atom pairs in the system whose distances are greater than a certain distance (r_c) the VDW interaction energy is zero.[382] There are different cutoff methods (e.g: shift and switch) and an example of a switch cutoff method is depicted in Figure 1.20.[368]

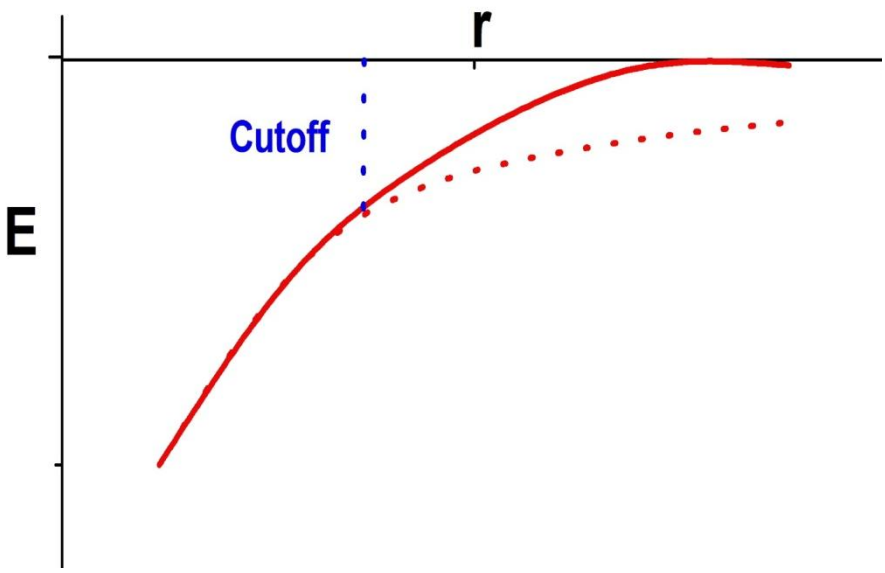

Figure1.20: A switch cutoff for non-bonded interactions.

1.7.1.2.3. Other interactions

There are some interactions that arise from the electrostatic and the VDW interactions simultaneously such as: hydrogen bonding, hydrophilic and hydrophobic effects.[383,384] There are many molecules that generate these effect and the common one is water. Most of the intercalations into LDHs and HDSs were carried out in water, experimental data and MD have shown that water molecules have effects on both the distribution of guests in the interlayer regions and on their interactions with the framework.[385] The NSAIDs and valproic acid cited above have hydrophobic and hydrophilic regions their structures, whereas phosphonoacetic acid does not have hydrophobic region. The hydrophobic effect and hydrogen bonding generated by the water will have effects on these guests orientations, LDHs and HDSs frameworks. Therefore; the presence of water molecules in simulations are important and their number should be closer to the experimental data, the water molecules should not be neglected even if they slowdown the simulation.[386–388]

1.7.2. Other parameters

There exist other parameters that can influence the simulation such as: duration of the simulation, temperature, pressure and thermodynamic ensembles.[389–391]

1.7.2.1. Duration of the simulation

There is a limit to the length of run with MD simulations. In practical, the MD simulations cannot be run for months or years on a supercomputer, because this makes MD simulations useless, costly, more numerical error accumulation and impracticable to analyse the huge data. Any MD simulation run should reach equilibrium first before it can be stopped. The simulation time required to equilibrate a system depends on many factors such as: system size and structure.[392,393] Commonly simulation runs are short, with magnitude of a few nanoseconds of real time,[394–398] and exceptionally to a microsecond in special cases.[398–402]

1.7.2.2. Temperature

As it has been mentioned above, the MD simulation relies on integration of Newton's equations of motion to simulate the trajectories of particles. Thus, the temperature can influences bond length, particle movements and other physicochemical properties in MD simulations.[403] The effect of varying temperature was investigated to mimic the experimental conditions, several physicochemical properties were obtained such as: the activation energy, vibrational frequencies, excitation energies, transition dipole moments, glass transition, defects, atomistic stress, density, volume, bonds length and angle, vaporisation process, guest intercalation/ deintercalation and geometry changes.[358,402,404–407]

Alexiadis and Mavrantzas studied temperature (from 225 to 600 K). effects on regioregular poly-3-hexylthiophene (Rr-P3HT).[408] They investigated the distribution of dihedral angles, radial distribution functions, conformational and configurational properties. They found the transition state of the Rr-P3HT occurs from amorphous to a semicrystalline phase, at 300 k.[408]

1.7.2.3. Pressure

Similar to the temperature, the pressure can have an effect on physicochemical properties of simulated systems. It can affect water molecules movements, hydrophobic interactions, terahertz infrared absorption spectra, crystallization behaviour of amorphous alloys, frequency, structure shape and dynamical properties.[409–413]

Maurin and co-workers simulated the adsorption properties of CH_4 in faujasites at a wide range of pressure and constant temperature, their data were in agreement with the experimental results.[414] It was reported that MD simulations showed correlations between hydrogen bonding, hydrogen bond angle distribution and pressure,[415] which is in harmony with experimental data reported earlier.[416] Hydrogen bonding is a form of dipole-dipole intermolecular force, which can affect the physical properties of a molecule.[417] Zhang *el.al* performed MD simulations of BeO melting point at various pressure series ($0 \leq p \leq 100$ GPa).[418] Zhang *el.al* observed numerous transition phases within the pressure interval and found that BeO melt at 2696.05 K. when $p = 0$.[418] Zhang *el.al* [418] simulations data were in agreement with experimental data reported.[419–431]

1.7.2.4. Thermodynamic ensembles

An ensemble is defined as a collection of a large number of identical systems that imitates the macroscopic thermodynamic system being studied.[432] The common thermodynamic ensembles are : Microcanonical ensemble (NVE), Canonical ensemble (NVT) and Isothermal-isobaric ensemble (NPT).[433–435]

1.7.2.4.1. Microcanonical ensemble (NVE)

Microcanonical ensemble describes a system with constant number of particles (N), constant volume (V), and constant total energy (E), also called the NVE ensemble. The system is isolated with no energy transfer in any form (as heat, as work, with matter, or as radiation) and the thermodynamic driving force in this ensemble is entropy, which attains its maximum in an equilibrated system.[436,437]

1.7.2.4.2. Canonical ensemble (NVT)

Canonical ensemble describes a system with constant number of particles (N), constant volume (V), and constant temperature (T), commonly named the NVT ensemble. It is a closed isothermal isochoric system, where energy transfer is allowed as form of heat only. The thermodynamic driving force in this ensemble is Helmholtz free energy, which attains its minimum in an equilibrated system.[438,439]

1.7.2.4.3. Isothermal-isobaric ensemble (NPT)

Isothermal-isobaric ensemble describes a system with constant number of particles (N), constant pressure (P), and constant temperature (T), also often termed the NPT ensemble. It is a closed isothermal isobaric system, where energy transfer is allowed as heat and work only (no matter, no radiation). The thermodynamic driving force in the NPT ensemble is Gibbs free energy, where it reaches its minimum in an equilibrated system.[440,441]

1.7.3. Setting up a simulation

There have been several MD simulation studies of the interlayer behaviour and arrangement of LDH/guest combinations. MD accuracy depends on many factors, importantly including the quality of the FF used. The common FFs utilised are the modified Dreiding force field and ClayFF force field.[442–444] Regrettably most FFs have limits or obstacles.[367,445] For instance, one of the drawbacks of modified Dreiding force field is a distortion of simulated structure and of ClayFF that central metal atoms may escape from a coordination centre in long time simulation.[367,445] Fruitfully, Zhang and co-workers have developed a new FF denoted LDHFF that could overcome most of those limits and obstacles.[446]

A Li/Al LDH is a good candidate for MD simulations, since the position of all elements are known, in addition the metals (Li/Al) are homogenously distributed (see Section 1.5.1.1). Beside the force field selection, there are certain parameters that should be set before starting MD simulations and these should be preferably close to experimental data. For instance, guests intercalation are usually carried out at constant temperature and pressure, so NPT ensemble should be suitable. Many LDHs MD simulations used NPT ensemble,[447–450] since it allows volume and interlayer spacing to fluctuate.[367] Water content should be as well taken in consideration, because water molecules can have influence on guests orientation and metal hydroxide sheets.[451–453]

1.8. Aims

In this study, both layered solids and electrospinning have been used to develop advanced drug delivery systems. The aims of this work were as follows:

- To prepare electrospun fibres containing ibuprofen, diclofenac, naproxen and valproate sodium salts from blends of sodium alginate, polyvinylpyrrolidone or poly(ethylene oxide), important synthetic polymers known to be safe for human use.
- To characterise the resultant materials and study the drug release from them.
- To investigate the intercalation of selected NSAIDs (diclofenac and naproxen), and an anticonvulsant (valproic acid) into different types of HDS, and study the effect of temperature and other parameters on the reaction processes.
- To synthesise novel biocompatible HDSs and characterise them.
- To load the four NSAIDs and valproate into the novel biocompatible HDSs, characterise the products, and investigate drug release in milieu mimicking the human gastrointestinal tract.
- To prepare tablets from the new biocompatible products and explore the drug release from these.
- To incorporation an antiviral agent (phosphonoacetic acid) drug into a model LDH.
- To undertake a detailed characterisation of the LDH/drug composite materials, including evaluating drug release from the system in representative *in vitro* conditions.

1.9. References

1. Mahdi, J. G. Biosynthesis and metabolism of β-d-salicin: A novel molecule that exerts biological function in humans and plants. *Biotechnol. Reports* **4,** 73–79 (2014).

2. Vlachojannis, J., Magora, F. & Chrubasik, S. Willow species and aspirin: Different mechanism of actions. *Phyther. Res.* **25,** 1102–1104 (2011).

3. Tripathi, K. D. *Essentials of Medical Pharmacology*. (Jaypee Brothers Medical, 2013).

4. Dart, R. C. *Medical toxicology*. (Lippincott Williams & Wilkins, 2004).

5. Adams, S. S. The Propionic Acids: A Personal Perspective. *J. Clin. Pharmacol.* **32,** 317–323 (1992).

6. Adams, S. S. Ibuprofen, the propionics and NSAIDs: personal reflections over four decades. *Inflammopharmacology* **7,** 191–197 (1999).

7. Sallmann, a R. The history of diclofenac. *Am. J. Med.* **80,** 29–33 (1986).

8. Sallmann, A. R. The history of diclofenac. *Semin. Arthritis Rheum.* **15,** 57–60 (1985).

9. Sallmann, A. & Pfister, R. Substituted derivatives of 2-anilinophenylacetic acids and a process of preparation. (1969).

10. Harrington, P. J. & Lodewijk, E. Twenty Years of Naproxen Technology. *Org. Process Res. Dev.* **1,** 72–76 (1997).

11. Harrison, I. T. *et al.* Nonsteroidal antiinflammatory agents. I. 6-Substituted 2-naphthylacetic acids. *J. Med. Chem.* **13,** 203–205 (1970).

12. Lussier, A. *et al.* Long Term Study of Naproxen Challenged by a Short-Term Double Blind Cross-Over Study with Placebo in Rheumatoid Patients. *Scand. J. Rheumatol.* **2,** 113–120 (1973).

13. Kean, W. F. & Buchanan, W. W. The use of NSAIDs in rheumatic disorders 2005: a global perspective. *Inflammopharmacology* **13,** 343–370 (2005).

14. Dahl, J. B. *et al.* Post-operative analgesic effects of paracetamol, NSAIDs, glucocorticoids, gabapentinoids and their combinations: a topical review. *Acta Anaesthesiol. Scand.* **58,** 1165–81 (2014).

15. Hyllested, M. Comparative effect of paracetamol, NSAIDs or their combination in postoperative pain management: a qualitative review. *Br. J. Anaesth.* **88,** 199–214 (2002).

16. Schoenfeld, B. J. The use of nonsteroidal anti-inflammatory drugs for exercise-induced muscle damage: Implications for skeletal muscle development. *Sport. Med.* **42,** 1017–1028 (2012).

17. Taylor, F. R. & Kaniecki, R. G. Symptomatic treatment of migraine: When to use NSAIDs, triptans, or opiates. *Curr. Treat. Options Neurol.* **13,** 15–27 (2011).

18. van de Laar, M. Pain Treatment in Arthritis-Related Pain: Beyond NSAIDs. *Open Rheumatol. J.* **6,** 320–330 (2012).

19. Ong, C. K. S., Lirk, P., Tan, C. H. & Seymour, R. A. An Evidence-Based Update on Nonsteroidal Anti-Inflammatory Drugs. *Clin. Med. Res.* **5,** 19–34 (2007).

20. Kelly, L. E. *et al.* Morphine or Ibuprofen for post-tonsillectomy analgesia: a randomized trial. *Cinahl* **135,** 307–13 (2015).

21. Vanegas, H., Vazquez, E. & Tortorici, V. NSAIDS, opioids, cannabinoids and the control of pain by the central nervous system. *Pharmaceuticals* **3,** 1335–1347 (2010).

22. McCarberg, B. & Gibofsky, A. Need to Develop New Nonsteroidal Anti-Inflammatory Drug Formulations. *Clin. Ther.* **34,** 1954–1963 (2012).

23. Evans, A. M. Comparative pharmacology of S(+)-ibuprofen and (RS)-ibuprofen. *Clin. Rheumatol.* **20 Suppl 1,** S9–S14 (2001).

24. Adams, S. S., Bresloff, P. & Mason, C. G. Pharmacological differences between the optical isomers of ibuprofen: evidence for metabolic inversion of the (-)-isomer. *J. Pharm. Pharmacol.* **28,** 256–257 (1976).

25. Adams, S. S., Cliffe, E. E., Lessel, B. & Nicholson, J. S. Some biological properties of 2-(4-isoburylphenyl)-propionic acid. *J. Pharm. Sci.* **56,** 1686 (1967).

26. Vangiessen, G. J. & Kaiser, D. G. GLC determination of ibuprofen [dl-2-(p-isobutylphenyl) propionic acid] enantiomers in biological specimens. *J. Pharm. Sci.* **64,** 798–801 (1975).

27. Mills, R. F., Adams, S. S., Cliffe, E. E., Dickinson, W. & Nicholson, J. S. The metabolism of ibuprofen. *Xenobiotica.* **3,** 589–598 (1973).

28. Dewland, P. M., Reader, S. & Berry, P. Bioavailability of ibuprofen following oral administration of standard ibuprofen, sodium ibuprofen or ibuprofen acid incorporating poloxamer in healthy volunteers. *BMC Clin. Pharmacol.* **9,** 1–10 (2009).

29. Walter, K., Weiss, G., Laicher, A. & Stanislaus, F. *Pharmacokinetics of ibuprofen following a single administration of a suspension containing enteric-coated microcapsules. Arzneimittelforschung.* **45,** (1995).

30. Legg, T. J., Laurent, A. L., Leyva, R. & Kellstein, D. Ibuprofen Sodium Is Absorbed Faster than Standard Ibuprofen Tablets: Results of Two Open-Label, Randomized, Crossover Pharmacokinetic Studies. *Drugs R. D.* **14,** 283–290 (2014).

31. Lin, J. H., Cocchetto, D. M. & Duggan, D. E. Protein binding as a primary determinant of the clinical pharmacokinetic properties of non-steroidal anti-inflammatory drugs. *Clin. Pharmacokinet.* **12,** 402–432 (1987).

32. Bushra, R. & Aslam, N. An overview of clinical pharmacology of Ibuprofen. *Oman Med. J.* **25,** 155–1661 (2010).

33. Llinàs, A., Burley, J. C., Box, K. J., Glen, R. C. & Goodman, J. M. Diclofenac Solubility: Independent Determination of the Intrinsic Solubility of Three Crystal Forms. *J. Med. Chem.* **50,** 979–983 (2007).

34. Donnelly, R. F., Pascuet, E., Carmen, M. & Vaillancourt, R. Stability of diclofenac sodium oral suspensions packaged in amber polyvinyl chloride bottles. *Can. J. Hosp. Pharm.* **63,** 25–30 (2010).

35. Hinz, B. *et al.* Bioavailability of diclofenac potassium at low doses. *Br. J. Clin. Pharmacol.* **59,** 80–84 (2005).

36. Chen, C., Bujanover, S., Kareht, S. & Rapoport, A. M. Differential Pharmacokinetics of Diclofenac Potassium for Oral Solution vs Immediate-Release Tablets From a Randomized Trial: Effect of Fed and Fasting Conditions. *Headache J. Head Face Pain* **55,** 265–275 (2015).

37. Hooper, I. T., Allen, E., McLaughlin, K., Ward, C. & Sioufi, A. Bioavailability of a Generic Sustained-Release Formulation of Diclofenac Compared with the Standard Sustained-Release Formulation. *Clin. Drug Investig.* **12,** 259–270 (1996).

38. Sahajwalla, C. G. *et al.* Comparative bioavailability of slow release diclofenac (Voveran SR) with enteric coated tablet and internationally used Voltaren Retard. *J. Assoc. Physicians India* **39,** 546–548 (1991).

39. Mustofa, M., Suryawati, S., Dwiprahasto, I. & Santoso, B. The relative bioavailability of diclofenac with respect to time of administration. *Br. J. Clin. Pharmacol.* **32,** 246–247 (1991).

40. Chan, K. K., Vyas, K. H. & Brandt, K. D. In vitro protein binding of diclofenac sodium in plasma and synovial fluid. *J. Pharm. Sci.* **76,** 105–108 (1987).

41. Bort, R. *et al.* Hepatic metabolism of diclofenac: Role of human CYP in the minor oxidative pathways. *Biochem. Pharmacol.* **58,** 787–796 (1999).

42. Tang, W. The metabolism of diclofenac--enzymology and toxicology perspectives. *Curr. Drug Metab.* **4,** 319–329 (2003).

43. Wanwimolruk, S., Lipschitz, S. & Roberts, M. S. Pharmacokinetics and

bioavailability of Naprosyn CR 500 mg tablet, a new controlled-release formulation of naproxen, after single and multiple dosing. *Int. J. Pharm.* **75,** 55–62 (1991).

44. Haberer, L. J., Walls, C. M., Lener, S. E., Taylor, D. R. & McDonald, S. a. Distinct pharmacokinetic profile and safety of a fixed-dose tablet of sumatriptan and naproxen sodium for the acute treatment of migraine. *Headache* **50,** 357–373 (2010).

45. Mortensen, A., Jensen, E. B., Petersen, P. B., Husted, S. & Andreasen, F. The Determination of Naproxen by Spectrofluorometry and its Binding to Serum Proteins. *Acta Pharmacol. Toxicol. (Copenh).* **44,** 277–283 (2009).

46. Runkel, R., Chaplin, M., Boost, G., Segre, E. & Forchielli, E. Absorption, distribution, metabolism, and excretion of naproxen in various laboratory animals and human subjects. *J. Pharm. Sci.* **61,** 703–708 (1972).

47. Segre, E. J. Naproxen sodium (Anaprox): pharmacology, pharmacokinetics and drug interactions. *J. Reprod. Med.* **25,** 222–225 (1980).

48. Segre, E. J. Naproxen metabolism in man. *J. Clin. Pharmacol.* **15,** 316–323 (1975).

49. Acton, A. *Nervous System Trauma: New Insights for the Healthcare Professional*. (ScholaryEditions, 2013).

50. Woolf, C. J. & Ma, Q. Nociceptors-Noxious Stimulus Detectors. *Neuron* **55,** 353–364 (2007).

51. Dubin, A. E. & Patapoutian, A. Nociceptors: the sensors of the pain pathway. *J. Clin. Invest.* **120,** 3760–3772 (2010).

52. Julius, D. Molecular mechanisms of nociception . *Nature* **413,** 203–210 (2001).

53. Dray, a. Inflammatory mediators of pain. *Br. J. Anaesth.* **75,** 125–131 (1995).

54. Ricciotti, E. & FitzGerald, G. A. Prostaglandins and Inflammation. *Arterioscler. Thromb. Vasc. Biol.* **31,** 986–1000 (2011).

55. Ferreira, S. H., Moncada, S. & Vane, J. R. Prostaglandins and the mechanism of analgesia produced by aspirin-like drugs. *Br. J. Pharmacol.* **120,** 399–400 (1997).

56. Peterson, K. *et al. Durg Class Review: Nonsteroidal Antiinflammatory Drugs (NSAIDs)*. *Oregon Heal. Sci. Univ.* (2010).

57. Day, R. O. & Graham, G. G. Non-steroidal anti-inflammatory drugs (NSAIDs). *BMJ* **346,** f3195 (2013).

58. Bacchi, S., Palumbo, P., Sponta, A. & Coppolino, M. F. Clinical pharmacology of non-steroidal anti-inflammatory drugs: a review. *Antiinflamm. Antiallergy. Agents Med. Chem.* **11,** 52–64 (2012).

59. Simmons, D. L., Wagner, D. & Westover, K. Nonsteroidal Anti-Inflammatory Drugs, Acetaminophen, Cyclooxygenase 2, and Fever. *Clin. Infect. Dis.* **31,** S211–S218 (2000).

60. Vane, J. R., Bakhle, Y. S. & Botting, R. M. Cyclooxygenases 1 and 2. *Annu. Rev. Pharmacol. Toxicol.* **38,** 97–120 (1998).

61. Meade, E. a, Smith, W. L. & Dewitt, D. L. Differential Inhibition of Prostaglandin Endoperoxide Synthase (Cyclooxygenase) Isozymes by Aspirin and Other inflammatory Drugs. *Biochemistry* **268,** 6610–6614 (1993).

62. Peterson, K. *et al. Durg Class Review: Nonsteroidal Antiinflammatory Drugs (NSAIDs)*. (2010).

63. Lawrence, C., Sakuntabhai, A. & Tiling-Grosse, S. Effect of aspirin and nonsteroidal antiinflammatory drug therapy on bleeding complications in dermatologic surgical patients. *J. Am. Acad. Dermatol.* **31,** 988–992 (1994).

64. Schjerning Olsen, A.-M. *et al.* Association of NSAID use with risk of bleeding and cardiovascular events in patients receiving antithrombotic therapy after myocardial infarction. *JAMA* **313,** 805–14 (2015).

65. Slawson, D. NSAID Use Associated with Increased Risk of Serious Bleeding and CV Events After MI. *Am. Fam. Physician* **92,** 60 (2015).

66. Goh, H. & Bourne, R. Non-steroidal anti-inflammatory drugs and perforated diverticular disease: A case-control study. *Ann. R. Coll. Surg. Engl.* **84,** 93–96 (2002).

67. Collier, D. S. & Pain, J. a. Non-steroidal anti-inflammatory drugs and peptic ulcer perforation. *Gut* **26,** 359–363 (1985).

68. Forshaw, M. J., Zayyan, K. & Power, D. M. *NSAID-induced small bowel perforation. ANZ J. Surg.* **71,** 255–256 (2001).

69. Becker, J. C., Domschke, W. & Pohle, T. Current approaches to prevent NSAID-induced gastropathy - COX selectivity and beyond. *Br. J. Clin. Pharmacol.* **58,** 587–600 (2004).

70. Iwabuchi, T. *et al.* Increased gastric mucus secretion alleviates non-steroidal anti-inflammatory drug-induced abdominal pain. *Tohoku J. Exp. Med.* **231,** 29–36 (2013).

71. Boelsterli, U. A. Mechanisms of NSAID-induced hepatotoxicity: focus on nimesulide. *Drug Saf.* **25,** 633–648 (2002).

72. Bessone, F. Non-steroidal anti-inflammatory drugs: What is the actual risk of liver damage? *World J. Gastroenterol.* **16,** 5651 (2010).

73. Murray, M. D. & Brater, D. C. Renal toxicity of the nonsteroidal anti-inflammatory drugs. *Annu. Rev. Pharmacol. Toxicol.* **33,** 435–465 (1993).

74. Feenstra, J., Grobbee, D. E., Remme, W. J. & Stricker, B. H. C. Drug-induced heart failure. *J. Am. Coll. Cardiol.* **33,** 1152–1162 (1999).

75. Bleumink, G. S., Feenstra, J., Sturkenboom, M. C. J. M. & Stricker, B. H. C. Nonsteroidal anti-inflammatory drugs and heart failure. *Drugs* **63,** 525–534 (2003).

76. Cashman, J. N. The Mechanisms of Action of NSAIDs in Analgesia. *Drugs* **52,** 13–23 (1996).

77. Ulrich, C. M., Bigler, J. & Potter, J. D. Non-steroidal anti-inflammatory drugs for cancer prevention: promise, perils and pharmacogenetics. *Nat. Rev. Cancer* **6,** 130–140 (2006).

78. Harris, R. E., Beebe-Donk, J., Doss, H. & Burr Doss, D. Aspirin, ibuprofen, and other non-steroidal anti-inflammatory drugs in cancer prevention: a critical review of non-selective COX-2 blockade (review). *Oncol. Rep.* **13,** 559–583 (2005).

79. Shebl, F. M. *et al.* Aspirin but not ibuprofen use is associated with reduced risk of prostate cancer: a PLCO Study. *Br. J. Cancer* **107,** 207–214 (2012).

80. Muranushi, C., Olsen, C. M., Pandeya, N. & Green, A. C. Aspirin and Nonsteroidal Anti-Inflammatory Drugs Can Prevent Cutaneous Squamous Cell Carcinoma: a Systematic Review and Meta-Analysis. *J. Invest. Dermatol.* **135,** 975–983 (2015).

81. Fiorino, S. *et al.* The pharmacology and activity of non-steroidal anti-inflammatory drugs (NSAIDs): a review of their use as an adjuvant treatment in patients with HBV and HCV chronic hepatitis. *Ital. J. Med.* **5,** 82–89 (2011).

82. Burton, B. S. On the propyl derivatives and decomposition products of ethylacetoacetate. *Am. Chem. J.* **3,** 385– 395. (1882).

83. Henry, T. R. The history of valproate in clinical neuroscience. *Psychopharmacol. Bull.* **37 Suppl 2,** 5–16 (2003).

84. MEUNIER, H., CARRAZ, G., NEUNIER, Y., EYMARD, P. & AIMARD, M. Pharmacodynamic properties of N-dipropylacetic acid. *Therapie* **18,** 435–438

85. Carraz, G., Farr, R., Chateau, R. & Et.Al. First clinical trials of the antiepileptic activity of n-dipropylacetic acid. *Ann Med Psychol* **(Paris)122,** 577–84 (1964).

86. Levy, R. H., Mattson, R. H., Meldrum, B. S. & Perucaa, E. *Antiepileptic drugs*. (Lippincott Williams & Wilkins, 2002).

87. Schwartz, T. L. *et al.* Divalproex Sodium Versus Valproic Acid in Hospital Treatment of Psychotic Disorders. *Prim. Care Companion J. Clin. Psychiatry* **2,** 45–48 (2000).

88. Shorvon, S. D., Perucca, E. & Engel, J. J. *The Treatment of Epilepsy*. (John Wiley & Sons, 2009).

89. Franke, G. *et al. Relative bioavailability of different valproic acid formulations. Int. J. Clin. Pharmacol. Ther.* **33,** (1995).

90. Carrigan, P. J., Brinker, D. R., Cavanaugh, J. H., Lamm, J. E. & Cloyd, J. C. *Absorption characteristics of a new valproate formulation: divalproex sodium-coated particles in capsules (Depakote Sprinkle). J. Clin. Pharmacol.* **30,** (1990).

91. Rha, J. H. *et al.* Pharmacokinetic comparison of two valproic acid formulations--a plain and a controlled release enteric-coated tablets. *J. Korean Med. Sci.* **8,** 251–256 (1993).

92. Fujisaki, Y. *et al. Development of sustained-release tablets containing sodium valproate: in vitro and in vivo correlation. Drug Dev. Ind. Pharm.* **32,** (2006).

93. Phaechamud, T., Mueannoom, W., Tuntarawongsa, S. & Chitrattha, S. Preparation of Coated Valproic Acid and Sodium Valproate Sustained-release Matrix Tablets. *Indian J. Pharm. Sci.* **72,** 173–183 (2010).

94. Vázquez, M. *et al.* Hyperammonemia associated with valproic acid concentrations. *Biomed Res. Int.* **2014,** 1–7 (2014).

95. Benjamin J. Sadock, V. A. S. *Kaplan & Sadock's Concise Textbook of Clinical Psychiatry - Third Edition*. (Lippincott Williams & Wilkins, 2008).

96. Löscher, W. Serum protein binding and pharmacokinetics of valproate in man, dog, rat and mouse. *J. Pharmacol. Exp. Ther.* **204,** 255–261 (1978).

97. Fawcett, J. *Valproate use in acute mania and bipolar disorder: an international perspective. J. Clin. Psychiatry* **50 Suppl,** (1989).

98. Sawaya, M. C., Horton, R. W. & Meldrum, B. S. Effects of anticonvulsant drugs on the cerebral enzymes metabolizing GABA. *Epilepsia* **16,** 649–655 (1975).

99. Godin, Y., Heiner, L., Mark, J. & Mandel, P. Effects of DI-n-propylacetate, and anticonvulsive compound, on GABA metabolism. *J. Neurochem.* **16,** 869–873 (1969).

100. Ko, G. N., Korpi, E. R., Freed, W. J., Zalcman, S. J. & Bigelow, L. B. *Effect of valproic acid on behavior and plasma amino acid concentrations*

in chronic schizophrenic patients. Biol. Psychiatry **20,** (1985).

101. Löscher, W. Effect of Inhibitors of GABA Aminotransferase on the Metabolism of GABA in Brain Tissue and Synaptosomal Fractions. *J. Neurochem.* **36,** 1521–1527 (1981).

102. Winterer, G. & Hermann, W. M. Valproate and the symptomatic treatment of schizophrenia spectrum patients. *Pharmacopsychiatry* **33,** 182–188 (2000).

103. Buchhalter, J. R. & Dichter, M. A. Effects of valproic acid in cultured mammalian neurons. *Neurology* **36,** 259–262 (1986).

104. Bolaños, J. P. & Medina, J. M. Effect of valproate on the metabolism of the central nervous system. *Life Sci.* **60,** 1933–1942 (1997).

105. Wang, J. F., Bown, C. & Young, L. T. Differential display PCR reveals novel targets for the mood-stabilizing drug valproate including the molecular chaperone GRP78. *Mol. Pharmacol.* **55,** 521–527 (1999).

106. Zeise, M. L., Kasparow, S. & Zieglgänsberger, W. Valproate suppresses N-methyl-D-aspartate-evoked, transient depolarizations in the rat neocortex in vitro. *Brain Res.* **544,** 345–348 (1991).

107. Schloesser, R. J., Huang, J., Klein, P. S. & Manji, H. K. Cellular plasticity cascades in the pathophysiology and treatment of bipolar disorder. *Neuropsychopharmacology* **33,** 110–133 (2008).

108. Lin, X.-L. & Tang, S.-Y. Sodium valproate may be a treatment for sleep bruxism. *J. Child Adolesc. Psychopharmacol.* **23,** 636–7 (2013).

109. Cipriani, A., Reid, K., Young, A. H., Macritchie, K. & Geddes, J. in *Cochrane Database Syst. Rev.* 1–73 (2013).

110. Smith, L. A. *et al.* Valproate for the treatment of acute bipolar depression: Systematic review and meta-analysis. *J. Affect. Disord.* **122,** 1–9 (2010).

111. Rovers, J. M. & Roks, G. Electroconvulsive therapy-induced migraine successfully treated with valproic acid. *J ECT* **28,** 64–65 (2012).

112. Frazee, L. A. & Foraker, K. C. Use of intravenous valproic acid for acute migraine. *Ann. Pharmacother.* **42,** 403–407 (2008).

113. Linde, M., Mulleners, W. M., Chronicle, E. P. & McCrory, D. C. in *Cochrane Database Syst. Rev.* (Linde, M.) **6,** 1–52 (John Wiley & Sons, Ltd, 2013).

114. Perucca, E. The new generation of antiepileptic drugs: advantages and disadvantages. *Br. J. Clin. Pharmacol.* **42,** 531–543 (1996).

115. Perucca, E. An introduction to antiepileptic drugs. *Epilepsia* **46,** 31–37 (2005).

116. Carmona-Vazquez, C. R., Ruiz-Garcia, M., Pena-Landin, D. M., Diaz-Garcia, L. & Greenawalt, S. R. The prevalence of obesity and metabolic syndrome in paediatric patients with epilepsy treated in monotherapy with valproic acid. *Rev. Neurol.* **61,** 193–201 (2015).

117. Venkataramani, V. *et al.* Histone deacetylase inhibitor valproic acid inhibits cancer cell proliferation via down-regulation of the alzheimer amyloid precursor protein. *J. Biol. Chem.* **285,** 10678–10689 (2010).

118. Ryu, C. H. *et al.* Valproic acid enhances anti-tumor effect of mesenchymal stem cell mediated HSV-TK gene therapy in intracranial glioma. *Biochem. Biophys. Res. Commun.* **421,** 585–590 (2012).

119. Masoudi, A. *et al.* Influence of valproic acid on outcome of high-grade gliomas in children. *Anticancer Res.* **28,** 2437–2442 (2008).

120. Michaelis, M., Doerr, H. W. & Cinatl, J. Valproic acid as anti-cancer drug. *Curr. Pharm. Des.* **13,** 3378–3393 (2007).

121. Shi, P. *et al.* Valproic acid sensitizes pancreatic cancer cells to natural killer cell-mediated lysis by upregulating MICA and MICB via the PI3K/Akt signaling pathway. *BMC Cancer* **14,** 370 (2014).

122. Fortunati, N. *et al.* Valproic acid is a selective antiproliferative agent in estrogen-sensitive breast cancer cells. *Cancer Lett.* **259,** 156–164 (2008).

123. White, M. C. & Frampton, A. R. The histone deacetylase inhibitor valproic acid enhances equine herpesvirus type 1 (EHV-1)-mediated oncolysis of human glioma cells. *Cancer Gene Ther.* **20,** 88–93 (2013).

124. Vázquez-Calvo, A., Saiz, J.-C., Sobrino, F. & Martín-Acebes, M. A. Inhibition of enveloped virus infection of cultured cells by valproic acid. *J. Virol.* **85,** 1267–1274 (2011).

125. Routy, J. P. *et al.* Valproic acid in association with highly active antiretroviral therapy for reducing systemic HIV-1 reservoirs: Results from a multicentre randomized clinical study. *HIV Med.* **13,** 291–296 (2012).

126. Charles, S. J., Moore, a T., Davison, B. C., Dyson, H. M. & Willatt, L. Flecked retina associated with ring 17 chromosome. *Br. J. Ophthalmol.* **75,** 125–127 (1991).

127. Bhalla, S. *et al.* Long-term follow-up for efficacy and safety of treatment of retinitis pigmentosa with valproic acid. *Br. J. Ophthalmol.* **97,** 895–9 (2013).

128. Clemson, C. M. *et al.* Therapeutic potential of valproic acid for retinitis pigmentosa. *Br. J. Ophthalmol.* **95,** 89–93 (2011).

129. Mellow, A. M., Solano-Lopez, C. & Davis, S. Sodium Valproate in the Treatment of Behavioral Disturbance in Dementia. *J. Geriatr. Psychiatry Neurol.* **6,** 205–209 (1993).

130. Takahashi, M. & Akagi, M. *Case report of sodium valproate treatment of aggression associated with Alzheimer's disease*. *No To Shinkei* **48,** 757–760 (1996).

131. Khwaja, G. A., Ranjan, R., Gupta, M., Chowdhry, D. & Hirve, M. Valproate-induced Reversible ' Parkinsonism Plus ' Syndrome. *Indian Acad. Clin. Med.* **11,** 235–238 (2010).

132. Schreur, L., Middeljans-Tijssen, C. W., Hengstman, G. J. D. & Olde Rikkert, M. G. M. *Cognitive impairment and parkinsonism due to use of sodium valproate*. *Tijdschr. Gerontol. Geriatr.* **40,** 29–33 (2009).

133. Christian Machado Ximenes, J., Crisóstomo Lima Verde, E., da Graça Naffah-Mazzacoratti, M. & Socorro de Barros Viana, G. Valproic Acid, a Drug with Multiple Molecular Targets Related to Its Potential Neuroprotective Action. *Neurosci. Med.* **03,** 107–123 (2012).

134. Fagundes, B. S. R. Valproic Acid : Review. *Rev Neurocienc* **16,** 130–136 (2008).

135. Mattson, R. H., Cramer, J. a, Williamson, P. D. & Novelly, R. a. Valproic acid in epilepsy: clinical and pharmacological effects. *Ann. Neurol.* **3,** 20–25 (1978).

136. Haddad, P. M., Das, A., Ashfaq, M. & Wieck, A. A review of valproate in psychiatric practice. *Expert Opin. Drug Metab. Toxicol.* **5,** 539–551 (2009).

137. Wadzinski, J., Franks, R., Roane, D. & Bayard, M. *Valproate-associated hyperammonemic encephalopathy. J. Am. Board Fam. Med.* **20,** 499–502

138. Gerstner, T. *et al.* Valproic acid-induced pancreatitis: 16 new cases and a review of the literature. *J. Gastroenterol.* **42,** 39–48 (2007).

139. Werlin, S. L. & Fish, D. L. The spectrum of valproic acid-associated pancreatitis. *Pediatrics* **118,** 1660–1663 (2006).

140. Gerstner, T. *et al.* Valproic acid induced encephalopathy - 19 new cases in Germany from 1994 to 2003 - A side effect associated to VPA-therapy not only in young children. *Seizure* **15,** 443–448 (2006).

141. Nylén, P. Beitrag zur Kenntnis der organischen Phosphorverbindungen. *Berichte der Dtsch. Chem. Gesellschaft (A B Ser.* **57,** 1023–1038 (1924).

142. Shipkowitz, N. L. *et al.* Suppression of herpes simplex virus infection by phosphonoacetic acid. *Appl. Microbiol.* **26,** 264–7 (1973).

143. Overby, L. R., Duff, R. G. & Mao, J. C. Antiviral potential of phosphonoacetic acid. *Ann. N. Y. Acad. Sci.* **284,** 310–320 (1977).

144. Boezi, J. A. The antiherpesvirus action of phosphonoacetate. *Pharmacol. Ther.* **4,** 231–243 (1979).

145. Reno, J. M., Lee, L. F. & Boezi, J. a. Inhibition of herpesvirus replication and herpesvirus-induced deoxyribonucleic acid polymerase by phosphonoformate. *Antimicrob. Agents Chemother.* **13,** 188–192 (1978).

146. Gordon, Y. J., Lahav, M., Photiou, S. & Becker, Y. Effect of phosphonoacetic acid in the treatment of experimental herpes simplex keratitis. *Br. J. Ophthalmol.* **61,** 506–9 (1977).

147. Roboz, J., Suzuki, R., Bekesi, G. & Hunt, R. Preclinical toxicological study of phosphonoacetic acid: determination in blood by selected ion monitoring. *Biomed. Mass Spectrom.* **4,** 291–296 (1977).

148. Chadwick, M. *et al.* Comparative physiological disposition of N-(phosphonacetyl)-L-aspartate in several animal species after intravenous and oral administration. *Cancer Res.* **42,** 627–632 (1982).

149. Gil-Fernández, C., Páez, E., Vilas, P. & Gancedo, A. G. Effect of disodium phosphonoacetate and iododeoxyuridine on the multiplication of African swine fever virus in vitro. *Chemotherapy* **25,** 162–169 (1979).

150. Smee, D. F., Bailey, K. W., Wong, M.-H. & Tarbet, E. B. Topical treatment of cutaneous vaccinia virus infections in immunosuppressed hairless mice with selected antiviral substances. *Antivir. Chem. Chemother.* **21,** 201–8 (2011).

151. Villinger, F., Genovesi, E. V, Gerstner, D. J., Whyard, T. C. & Knudsen, R. C. Inhibition of African swine fever virus in cultured swine monocytes by phosphonoacetic acid (PAA) and by phosphonoformic acid (PFA). *Arch. Virol.* **115,** 163–84 (1990).

152. Kaul, P. N. *et al. Progress in Drug Research*. (Birkhäuser Basel, 1998).

153. Jones, C. L. *et al.* Drug discovery for the developing world: progress at the Novartis Institute for Tropical Diseases. *Nat. Rev. Drug Discov.* **14,** 442–444 (2015).

154. van de Waterbeemd, H. & Testa, B. *Drug Bioavailability*. **40,** (Wiley-VCH Verlag GmbH & Co. KGaA, 2008).

155. Savjani, K. T., Gajjar, A. K. & Savjani, J. K. Drug Solubility: Importance and Enhancement Techniques. *ISRN Pharm.* **2012,** 1–10 (2012).

156. Hillery, A., Lloyd, A. & Swarbrick, J. *Drug delivery and targeting for pharmacists and pharmaceutical scientists*. *Nature* (Taylor & Francis, 2001).

157. Langer, R. Drug delivery and targeting. *Nature* **392,** 5–10 (1998).

158. Ehrlich, P. Address in Pathology, ON CHEMIOTHERAPY: Delivered before the Seventeenth International Congress of Medicine. *BMJ* **2,** 353–359 (1913).

159. Bennett, M. R. The concept of transmitter receptors: 100 years on. *Neuropharmacology* **39,** 523–46 (2000).

160. Parascandola, J. & Jasensky, R. Origins of the receptor theory of drug action. *Bull. Hist. Med.* **48,** 199–220 (1974).

161. Tran, P. a, Zhang, L. & Webster, T. J. Carbon nanofibers and carbon nanotubes in regenerative medicine. *Adv. Drug Deliv. Rev.* **61,** 1097–114 (2009).

162. Lee, V. H. L. & Ghandehari, H. Advanced drug delivery: perspectives and prospects. Preface. *Adv. Drug Deliv. Rev.* **65,** 1–2 (2013).

163. Nicolaou, K. C. The Chemistry-Biology-Medicine Continuum and the Drug Discovery and Development Process in Academia. *Chem. Biol.* **21,** 1039–1045 (2014).

164. Safari, J. & Zarnegar, Z. Advanced drug delivery systems: Nanotechnology of health design A review. *J. Saudi Chem. Soc.* **18,** 85–99 (2014).

165. Fayyazbakhsh, F. *et al.* Biological Evaluation of a Novel Tissue Engineering Scaffold of Layered Double Hydroxides (LDHs). *Key Eng. Mater.* **493-494,** 902–908 (2011).

166. Chen, C., Yee, L. K., Gong, H., Zhang, Y. & Xu, R. A facile synthesis of strong near infrared fluorescent layered double hydroxide nanovehicles with an anticancer drug for tumor optical imaging and therapy. *Nanoscale* **5,** 4314 (2013).

167. Khan, S. B. *et al.* Nanohybrid based on antibiotic encapsulated layered double hydroxide as a drug delivery system. *Appl. Biochem. Biotechnol.* **175,** 1412–28 (2015).

168. Shi, W., Wei, M., Jin, L. & Li, C. Calcined layered double hydroxides as a 'biomolecular vessel' for bromelain: Immobilization, storage and release. *J. Mol. Catal. B Enzym.* **47,** 58–65 (2007).

169. Rotello, V. M. Advanced drug delivery reviews theme issue. Preface. *Adv. Drug Deliv. Rev.* **60,** 1225 (2008).

170. Bi, X., Zhang, H. & Dou, L. Layered Double Hydroxide-Based Nanocarriers for Drug Delivery. *Pharmaceutics* **6,** 298–332 (2014).

171. Zhong, Z., Yin, Y., Gates, B. & Xia, Y. Preparation of Mesoscale Hollow Spheres of TiO2 and SnO2 by Templating Against Crystalline Arrays of Polystyrene Beads. *Adv. Mater.* **12,** 206–209 (2000).

172. Wang, J., Zhang, C., Liu, Z., Ding, K. & Yang, Z. A Simple and Efficient Route to Prepare Inorganic Compound/Polymer Composites in Supercritical Fluids. *Macromol. Rapid Commun.* **27,** 787–792 (2006).

173. Shchukin, D. G., Sukhorukov, G. B. & Möhwald, H. Smart inorganic/organic nanocomposite hollow microcapsules. *Angew. Chem. Int. Ed. Engl.* **42,** 4472–5 (2003).

174. Coulembier, O., Degée, P., Hedrick, J. L. & Dubois, P. From controlled ring-opening polymerization to biodegradable aliphatic polyester: Especially poly(β-malic acid) derivatives. *Prog. Polym. Sci.* **31,** 723–747 (2006).

175. Wang, B., Siahaan, T. & Soltero, R. *Drug delivery: principles and applications*. **1,** (John Wiley& Sons, 2005).

176. Rasala, T. M., Govind K, L., Kale, V. V & Avari, J. G. Comparative Study of Ionotropic Gelation Technique To Entrap Diltiazem HCl In Mucoadhesive Microparticulate System. *J. Pharm. Res.* **3,** 1531–1534 (2010).

177. Yao, J., Bastiaansen, C. & Peijs, T. High Strength and High Modulus Electrospun Nanofibers. *Fibers* **2,** 158–186 (2014).

178. Li, D. & Xia, Y. Electrospinning of Nanofibers: Reinventing the Wheel? *Adv. Mater.* **16,** 1151–1170 (2004).

179. Garg, K. & Bowlin, G. L. Electrospinning jets and nanofibrous structures. *Biomicrofluidics* **5,** 013403 (2011).

180. Baştürk, E. & Kahraman, M. V. Thermal and morphological properties of PVA/4-vinylbenzene boronic acid hybrid nanofibrous. *Polym. Compos.* **33,** 829–837 (2012).

181. Ramakrishna, S., Fujihara, K., Teo, W.-E., Lim, T.-C. & Ma, Z. *An Introduction to Electrospinning and Nanofibers*. (WORLD SCIENTIFIC, 2005).

182. Fridrikh, S. V., Yu, J. H., Brenner, M. P. & Rutledge, G. C. Controlling the Fiber Diameter during Electrospinning. *Phys. Rev. Lett.* **90,** 144502 (2003).

183. Hohman, M. M., Shin, M., Rutledge, G. & Brenner, M. P. Electrospinning and electrically forced jets. I. Stability theory. *Phys. Fluids* **13,** 2201 (2001).

184. Hohman, M. M., Shin, M., Rutledge, G. & Brenner, M. P. Electrospinning and electrically forced jets. II. Applications. *Phys. Fluids* **13,** 2221 (2001).

185. Reneker, D. H. & Yarin, A. L. Electrospinning jets and polymer nanofibers. *Polymer (Guildf).* **49,** 2387–2425 (2008).

186. Taylor, L. S. in *Pharm. Amorph. Solid Dispersions* (Newman, A.) 179–217 (John Wiley & Sons, 2015).

187. Ilevbare, G., Marsac, P. & Mitra, A. in *Discov. Dev. Mol. with Optim. Drug-*

Like Prop. (Templeton, A. C., Byrn, S. R., Haskell, R. J. & Prisinzano, T. E.) **15,** 287–343 (Springer New York, 2015).

188. Ramesh Babu, V. *et al.* pH sensitive interpenetrating network microgels of sodium alginate-acrylic acid for the controlled release of ibuprofen. *J. Appl. Polym. Sci.* **99,** 2671–2678 (2006).

189. Ivanov, I. T. & Tsokeva, Z. Effect of chirality on PVP/drug interaction within binary physical mixtures of ibuprofen, ketoprofen, and naproxen: a DSC study. *Chirality* **21,** 719–27 (2009).

190. Bogdanova, S., Pajeva, I., Nikolova, P., Tsakovska, I. & Müller, B. Interactions of poly(vinylpyrrolidone) with ibuprofen and naproxen: experimental and modeling studies. *Pharm. Res.* **22,** 806–15 (2005).

191. Marsac, P. Formation and stabilisation of amorphous molecular level solid dispersions. (2007).

192. Tseng, Y.-W. *et al.* Electrical Crystallization Mechanism and Interface Characteristics of Nanowire ZnO/Al Structures Fabricated by the Solution Method. *J. Nanomater.* **2012,** 1–6 (2012).

193. Shichiri, T. & Nagata, T. Effect of electric currents on the nucleation of ice crystals in the melt. *J. Cryst. Growth* **54,** 207–210 (1981).

194. Takemoto, R. & Hizubayashi, H. Effects of passing electric current on the structural relaxation and crystallization in amorphous alloys. *Mater. Sci. Eng. A* **179-180,** 275–278 (1994).

195. Takemoto, R. & Mizubayashi, H. Effects of passing electric current on structural relaxation, crystallization and elastic property in amorphous Cu50 Ti50. *Acta Metall. Mater.* **43,** 1495–1504 (1995).

196. Hansen, N. S., Ferguson, T. E., Panels, J. E., Park, A. A. & Joo, Y. L. Inorganic nanofibers with tailored placement of nanocatalysts for hydrogen production via alkaline hydrolysis of glucose. *Nanotechnology* **22,** 325302 (2011).

197. Chinnappan, A., Kang, H.-C. & Kim, H. Preparation of PVDF nanofiber composites for hydrogen generation from sodium borohydride. *Energy* **36,** 755–759 (2011).

198. Thavasi, V., Singh, G. & Ramakrishna, S. Electrospun nanofibers in energy and environmental applications. *Energy Environ. Sci.* **1,** 205 (2008).

199. Filatov, Y., Budyka, A. & Kirichenko, V. *Electrospinning of Micro-and Nanofibers: Fundamentals in Separation and Filtration Processes*. *J. Eng. Fibers* (Begell House Publishers, 2007).

200. Im, J. H., Yang, S. J., Yun, C. H. & Park, C. R. Simple fabrication of carbon/TiO2 composite nanotubes showing dual functions with adsorption

and photocatalytic decomposition of Rhodamine B. *Nanotechnology* **23,** 035604 (2012).

201. Liu, L., Liu, Z., Bai, H. & Sun, D. D. Concurrent filtration and solar photocatalytic disinfection/degradation using high-performance Ag/TiO2 nanofiber membrane. *Water Res.* **46,** 1101–12 (2012).

202. Mickova, A. *et al.* Core/Shell Nanofibers with Embedded Liposomes as a Drug Delivery System. *Biomacromolecules* **13,** 952–962 (2012).

203. Son, Y. J., Kim, W. J. & Yoo, H. S. Therapeutic applications of electrospun nanofibers for drug delivery systems. *Arch. Pharm. Res.* **37,** 69–78 (2014).

204. Hu, X. *et al.* Electrospinning of polymeric nanofibers for drug delivery applications. *J. Control. Release* **185,** 12–21 (2014).

205. Walpoth, B. H. Vascular organogenesis: dream or reality? *Organogenesis* **6,** 158–60 (2010).

206. Andrady, A. L. in *Sci. Technol. Polym. Nanofibers* 183–223 (John Wiley & Sons, Inc., 2007).

207. Ma, B., Xie, J., Jiang, J., Shuler, F. D. & Bartlett, D. E. Rational design of nanofiber scaffolds for orthopedic tissue repair and regeneration. *Nanomedicine (Lond).* **8,** 1459–81 (2013).

208. Venugopal, J., Low, S., Choon, A. T. & Ramakrishna, S. Interaction of cells and nanofiber scaffolds in tissue engineering. *J. Biomed. Mater. Res. B. Appl. Biomater.* **84,** 34–48 (2008).

209. Rujitanaroj, P., Pimpha, N. & Supaphol, P. Wound-dressing materials with antibacterial activity from electrospun gelatin fiber mats containing silver nanoparticles. *Polymer (Guildf).* **49,** 4723–4732 (2008).

210. Sadri, M., Arab-Sorkhi, S., Vatani, H. & Bagheri-Pebdeni, A. New wound dressing polymeric nanofiber containing green tea extract prepared by electrospinning method. *Fibers Polym.* **16,** 1742–1750 (2015).

211. Abdelgawad, A. M., Hudson, S. M. & Rojas, O. J. Antimicrobial wound dressing nanofiber mats from multicomponent (chitosan/silver-NPs/polyvinyl alcohol) systems. *Carbohydr. Polym.* **100,** 166–178 (2014).

212. Unnithan, A. R. *et al.* Wound-dressing materials with antibacterial activity from electrospun polyurethane–dextran nanofiber mats containing ciprofloxacin HCl. *Carbohydr. Polym.* **90,** 1786–1793 (2012).

213. Brocklesby, K. L., Johns, S. C., Jones, A. E., Sharp, D. & Smith, R. B. Smart bandages--a colourful approach to early stage infection detection & control in wound care. *Med. Hypotheses* **80,** 237–40 (2013).

214. Kossovich, L. Y., Salkovskiy, Y. & Kirillova, I. V. in *6th World Congr.*

Biomech. (Lim, C. . & Goh, J. C. .) 1212–1214 (Springer, 2010).

215. Abrigo, M., McArthur, S. L. & Kingshott, P. Electrospun nanofibers as dressings for chronic wound care: advances, challenges, and future prospects. *Macromol. Biosci.* **14,** 772–92 (2014).

216. Shen, X. *et al.* Electrospun diclofenac sodium loaded Eudragit® L 100-55 nanofibers for colon-targeted drug delivery. *Int. J. Pharm.* **408,** 200–7 (2011).

217. Wu, X., Branford-White, C. J., Zhu, L., Chatterton, N. P. & Yu, D. Ester prodrug-loaded electrospun cellulose acetate fiber mats as transdermal drug delivery systems. *J. Mater. Sci. Mater. Med.* **21,** 2403–11 (2010).

218. Yu, D.-G., Zhang, X.-F., Shen, X.-X., Brandford-White, C. & Zhu, L.-M. Ultrafine ibuprofen-loaded polyvinylpyrrolidone fiber mats using electrospinning. *Polym. Int.* **58,** 1010–1013 (2009).

219. Cui, W. *et al.* Investigation of drug release and matrix degradation of electrospun poly(DL-lactide) fibers with paracetanol inoculation. *Biomacromolecules* **7,** 1623–9 (2006).

220. Gatti, J. W., Smithgall, M. C., Paranjape, S. M., Rolfes, R. J. & Paranjape, M. Using electrospun poly(ethylene-oxide) nanofibers for improved retention and efficacy of bacteriolytic antibiotics. *Biomed. Microdevices* (2013).

221. Karthikeyan, K., Guhathakarta, S., Rajaram, R. & Korrapati, P. S. Electrospun zein/eudragit nanofibers based dual drug delivery system for the simultaneous delivery of aceclofenac and pantoprazole. *Int. J. Pharm.* **438,** 117–22 (2012).

222. Jiang, Y.-N., Mo, H.-Y. & Yu, D.-G. Electrospun drug-loaded core-sheath PVP/zein nanofibers for biphasic drug release. *Int. J. Pharm.* **438,** 232–9 (2012).

223. Yu, D.-G. *et al.* Dual drug release nanocomposites prepared using a combination of electrospraying and electrospinning. *RSC Adv.* **3,** 4652 (2013).

224. Im, J. S., Yun, J., Lim, Y.-M., Kim, H.-I. & Lee, Y.-S. Fluorination of electrospun hydrogel fibers for a controlled release drug delivery system. *Acta Biomater.* **6,** 102–9 (2010).

225. Lee, Y. & Im, J. *Preparation of Functionalized Nanofibers and Their Applications*. (2010).

226. Trifiro, F. & Vaccari, A. Comprehensive supramolecular chemistry. *Compr. Supramol. Chem.* **34,** 34–5097–34–5097 (1996).

227. Meyn, M., Beneke, K. & Lagaly, G. Anion-exchange reactions of hydroxy double salts. *Inorg. Chem.* **32,** 1209–1215 (1993).

228. Cavani, F., Trifirò, F. & Vaccari, A. Hydrotalcite-type anionic clays: Preparation, properties and applications. *Catal. Today* **11,** 173–301 (1991).

229. Allmann, R. The crystal structure of pyroaurite. *Acta Crystallogr. Sect. B Struct. Crystallogr. Cryst. Chem.* **24,** 972–977 (1968).

230. Taylor, H. Segregation and cation-ordering in sjogrenite and pyroaurite. *Miner. Mag* **37,** 338–42 (1969).

231. Meyer, P. D. T. J. & Sauvage, H. W. R. J. *Layered Double Hydroxides*. *J. Infect. Dis.* **119,** (Springer-Verlag, 2006).

232. Williams, G. R., Fogg, A. M., Sloan, J., Taviot-Guého, C. & O'Hare, D. Staging during anion-exchange intercalation into [LiAl2(OH)6]Cl.yH2O: structural and mechanistic insights. *Dalton Trans.* **2,** 3499–506 (2007).

233. de Roy, A., Forano, C. & Besse, J. P. in *Layer. Double Hydroxides Present Futur.* (Rives, V.) 1–39 (Nova Science Pub Inc, 2011).

234. Marappa, S. & Kamath, P. V. Structure of the Carbonate-Intercalated Layered Double Hydroxides: A Reappraisal. *Ind. Eng. Chem. Res.* **54,** 11075–11079 (2015).

235. Rosenberg, S. P. & Armstrong, L. in *Essent. Readings Light Met.* (Donaldson, D. & Raahauge, B. E.) 235–239 (John Wiley & Sons, Inc., 2013).

236. Long, X., Wang, Z., Xiao, S., An, Y. & Yang, S. Transition metal based layered double hydroxides tailored for energy conversion and storage. *Mater. Today* 1–14 (2015).

237. Vucelic, M., Jones, W. & Moggridge, G. D. Cation Ordering in Synthetic Layered Double Hydroxides. *Clays Clay Miner.* **45,** 803–813 (1997).

238. Ksenofontov, D. A. & Kabalov, Y. K. Structure refinement and thermal stability of gibbsite. *Inorg. Mater.* **48,** 142–144 (2012).

239. Megaw, H. D. The crystal structure of hydrargillite, Al(OH)3. *Zeitschrift fuer Krist.* **87,** 185–204 (1934).

240. Besserguenev, A. V *et al.* Synthesis and Structure of the Gibbsite Intercalation Compounds [LiAl 2 (OH) 6]X {X = Cl, Br, NO 3 } and [LiAl 2 (OH) 6]Cl·H 2 O Using Synchrotron X-ray and Neutron Powder Diffraction. *Chem. Mater.* **9,** 241–247 (1997).

241. Wang, Z., Han, E. & Ke, W. Influence of nano-LDHs on char formation and fire-resistant properties of flame-retardant coating. *Prog. Org. Coatings* **53,** 29–37 (2005).

242. Kagunya, W., Hassan, Z. & Jones, W. Catalytic Properties of Layered Double Hydroxides and Their Calcined Derivatives. *Inorg. Chem.* **35,**

5970–5974 (1996).

243. Gong, M. *et al.* An advanced ni-fe layered double hydroxide electrocatalyst for water oxidation. *J. Am. Chem. Soc.* **135,** 8452–5 (2013).

244. He, S., An, Z., Wei, M., Evans, D. G. & Duan, X. Layered double hydroxide-based catalysts: nanostructure design and catalytic performance. *Chem. Commun. (Camb).* **49,** 5912–20 (2013).

245. M. J. Kang, S. W. Rhee, H. Moon, V. Neck, T. F. *Radiochim Acta*. (oldenbourg-verlag, 1996).

246. Theiss, F. L., Sear-Hall, M. J., Palmer, S. J. & Frost, R. L. Zinc aluminium layered double hydroxides for the removal of iodine and iodide from aqueous solutions. *Desalin. Water Treat.* **39,** 166–175 (2012).

247. Jin, S., Bland, A. E. & Brown, T. H. Bioagent Air Filtration Systems. (2005).

248. Dutta, P. K. & Robins, D. S. Pyrene Sorption in Organic-Layered Double-Metal Hydroxides. *Langmuir* **10,** 1851–1856 (1994).

249. Monash, P. & Pugazhenthi, G. Utilization of calcined Ni-Al layered double hydroxide (LDH) as an Adsorbent for removal of methyl orange dye from aqueous solution. *Environ. Prog. Sustain. Energy* **33,** 154–159 (2014).

250. Bruna, F. *et al.* Layered double hydroxides as adsorbents and carriers of the herbicide (4-chloro-2-methylphenoxy)acetic acid (MCPA): systems Mg-Al, Mg-Fe and Mg-Al-Fe. *J. Hazard. Mater.* **168,** 1476–81 (2009).

251. Ogawa, M. & Kuroda, K. Photofunctions of Intercalation Compounds. *Chem. Rev.* **95,** 399–438 (1995).

252. Millange, F., Walton, R. I., Lei, L. & O'Hare, D. Efficient Separation of Terephthalate and Phthalate Anions by Selective Ion-Exchange Intercalation in the Layered Double Hydroxide Ca 2 Al(OH) 6 ·NO 3 ·2H 2 O. *Chem. Mater.* **12,** 1990–1994 (2000).

253. Ragavan, A., Khan, A. I. & O'Hare, D. Isomer selective ion-exchange intercalation of nitrophenolates into the layered double hydroxide $[LiAl_2(OH)_6]Cl{\cdot}xH_2O$. *J. Mater. Chem.* **16,** 602 (2006).

254. Khan, A. I., Lei, L., Norquist, A. J. & O'Hare, D. Intercalation and controlled release of pharmaceutically active compounds from a layered double hydroxide. *Chem. Commun. (Camb).* 2342–3 (2001).

255. Yang, J. *et al.* New Inorganic-Based Drug Delivery System of Indole-3-Acetic Acid-Layered Metal Hydroxide Nanohybrids with Controlled Release Rate. *Chem. Mater.* **19,** 2679–2685 (2007).

256. Hwang, S., Han, Y. & Choy, J. Intercalation of Functional Organic

Molecules with Pharmaceutical , Cosmeceutical and Nutraceutical Functions into Layered Double Hydroxides and Zinc Basic Salts. *Bull. Korean Chem. Soc.* **22,** 1019–1022 (2001).

257. Del Arco, M. *et al.* Mg,Al layered double hydroxides with intercalated indomethacin: synthesis, characterization, and pharmacological study. *J. Pharm. Sci.* **93,** 1649–58 (2004).

258. Qin, L. *et al.* The in vitro sustained release profile and antitumor effect of etoposide-layered double hydroxide nanohybrids. *Int. J. Nanomedicine* **8,** 2053–64 (2013).

259. Shi, S. *et al.* Chelator-Free Labeling of Layered Double Hydroxide Nanoparticles for in Vivo PET Imaging. *Sci. Rep.* **5,** 1–10 (2015).

260. Park, D.-H., Choi, G. & Choy, J.-H. in *Photofunct. Layer. Mater.* (Yan, D. & Wei, M.) 137–175 (Springer International Publishing, 2015).

261. Gu, Z., Atherton, J. J. & Xu, Z. P. Hierarchical layered double hydroxide nanocomposites: structure, synthesis and applications. *Chem. Commun.* **51,** 3024–3036 (2015).

262. Xu, Z. P., Kurniawan, N. D., Bartlett, P. F. & Lu, G. Q. Enhancement of Relaxivity Rates of Gd–DTPA Complexes by Intercalation into Layered Double Hydroxide Nanoparticles. *Chem. - A Eur. J.* **13,** 2824–2830 (2007).

263. Wang, L. *et al.* A Gd-doped Mg-Al-LDH/Au nanocomposite for CT/MR bimodal imagings and simultaneous drug delivery. *Biomaterials* **34,** 3390–401 (2013).

264. Wei, P.-R. *et al.* Synthesis of chitosan-coated near-infrared layered double hydroxide nanoparticles for in vivo optical imaging. *J. Mater. Chem.* **22,** 5503 (2012).

265. Hillman, E. M. C. *et al.* In vivo optical imaging and dynamic contrast methods for biomedical research. *Philos. Trans. R. Soc. A Math. Phys. Eng. Sci.* **369,** 4620–4643 (2011).

266. Williams, G. R. *et al.* Immunity induced by a broad class of inorganic crystalline materials is directly controlled by their chemistry. *J. Exp. Med.* **211,** 1019–25 (2014).

267. Romagnani, S. Th1/Th2 cells. *Inflamm. Bowel Dis.* **5,** 285–94 (1999).

268. Li, A. *et al.* The use of layered double hydroxides as DNA vaccine delivery vector for enhancement of anti-melanoma immune response. *Biomaterials* **32,** 469–477 (2011).

269. Yan, S. *et al.* Polarized immune responses modulated by layered double hydroxides nanoparticle conjugated with CpG. *Biomaterials* **35,** 9508–16 (2014).

270. Wang, J. *et al.* The enhanced immune response of hepatitis B virus DNA vaccine using SiO2@LDH nanoparticles as an adjuvant. *Biomaterials* **35,** 466–78 (2014).

271. Hawthorne, F. C. & Sokolova, E. SIMONKOLLEITE, Zn5 (OH)8 Cl2 (H2O), A DECORATED INTERRUPTED-SHEET STRUCTURE OF THE FORM [M 2]4. *Can. Mineral.* **40,** 939–946 (2002).

272. Lichtenegger, H. C., Birkedal, H. & Waite, J. H. in *Biomineralization* (Sigel, A., Sigel, H. & Sigel, R. K. O.) 295–325 (John Wiley & Sons, Ltd, 2010).

273. Nowacki, W. & Silverman, J. N. Die Kristallstruktur von Zinkhydroxychlorid II, $Zn_5(OH)_8Cl_2 \cdot 1H_2O$*. *Zeitschrift für Krist.* **115,** 21–51 (1961).

274. Williams, G. R., Crowder, J., Burley, J. C. & Fogg, A. M. The selective intercalation of organic carboxylates and sulfonates into hydroxy double salts. *J. Mater. Chem.* **22,** 13600 (2012).

275. Sathisha, T. V., Kumara Swamy, B. E., Chandrashekar, B. N., Thomas, N. & Eswarappa, B. Selective determination of dopamine in presence of ascorbic acid and uric acid at hydroxy double salt/surfactant film modified carbon paste electrode. *J. Electroanal. Chem.* **674,** 57–64 (2012).

276. Stählin, W. & Oswald, H. R. The topotactic reaction of zinc hydroxide nitrate with aqueous metal chloride solutions. *J. Solid State Chem.* **3,** 256–264 (1971).

277. Feitknecht, W. Die Struktur der basischen Salze zweiwertiger Metalle. *Helv. Chim. Acta* **16,** 427–454 (1933).

278. Oliva, P. *et al.* Review of the structure and the electrochemistry of nickel hydroxides and oxy-hydroxides. *J. Power Sources* **8,** 229–255 (1982).

279. Ma, R. *et al.* Tetrahedral Co(II) Coordination in α-Type Cobalt Hydroxide: Rietveld Refinement and X-ray Absorption Spectroscopy. *Inorg. Chem.* **45,** 3964–3969 (2006).

280. Oh, J.-M., Biswick, T. T. & Choy, J.-H. Layered nanomaterials for green materials. *J. Mater. Chem.* **19,** 2553 (2009).

281. Stählin, W. & Oswald, H. R. The crystal structure of zinc hydroxide nitrate, $Zn_5(OH)_8(NO_3)_2.2H_2O$. *Acta Crystallogr. Sect. B Struct. Crystallogr. Cryst. Chem.* **26,** 860–863 (1970).

282. Allmann, R. Verfeinerung der Struktur des Zinkhydroxidchlorids II, $Zn_5(OH)_8Cl_2 \cdot 1H_2O$. *Zeitschrift für Krist.* **126,** 417–426 (1968).

283. Saifullah, B. *et al.* Antimycobacterial, antimicrobial, and biocompatibility properties of para-aminosalicylic acid with zinc layered hydroxide and Zn/Al layered double hydroxide nanocomposites. *Drug Des. Devel. Ther.* **8,** 1029–1036 (2014).

284. Polson, G. A., Roberts, K. P., Lou, K. K. & Dinicola, K. N. Compositions and methods for nail fungus treatment. (2009).

285. Kozai, N., Ohnuki, T. & Komarneni, S. Selenium oxyanions: Highly selective uptake by a novel anion exchanger. *J. Mater. Res.* **17,** 2993–2996 (2002).

286. Boshkov, N., Petrov, K., Vitkova, S. & Raichevsky, G. Galvanic alloys Zn–Mn—composition of the corrosion products and their protective ability in sulfate containing medium. *Surf. Coatings Technol.* **194,** 276–282 (2005).

287. Ma, W. *et al.* Layered zinc hydroxide nanocones: synthesis, facile morphological and structural modification, and properties. *Nanoscale* **6,** 13870–13875 (2014).

288. Zhao, J. *et al.* Facile Conversion of Hydroxy Double Salts to Metal–Organic Frameworks Using Metal Oxide Particles and Atomic Layer Deposition Thin-Film Templates. *J. Am. Chem. Soc.* **137,** 13756–13759 (2015).

289. Stock, N. & Biswas, S. Synthesis of Metal-Organic Frameworks (MOFs): Routes to Various MOF Topologies, Morphologies, and Composites. *Chem. Rev.* **112,** 933–969 (2012).

290. Ross, A., Taylor, C., Yaktine, L. & Del Valle, H. *Dietary Reference Intakes for Calcium and Vitamin D*. *Diet. Ref. Intakes Calcium Vitam. D* (National Academies Press, 2011).

291. Newton-Bishop, J. A. *et al.* Relationship between sun exposure and melanoma risk for tumours in different body sites in a large case-control study in a temperate climate. *Eur. J. Cancer* **47,** 732–41 (2011).

292. Armstrong, B. K., Kricker, A. & English, D. R. Sun exposure and Skin Cancer. *Australas. J. Dermatol.* **38,** S1–S6 (1997).

293. Gallagher, R. P. *et al.* Sunlight exposure, pigmentary factors, and risk of nonmelanocytic skin cancer. I. Basal cell carcinoma. *Arch. Dermatol.* **131,** 157–63 (1995).

294. Biswick, T., Park, D. H. & Choy, J. H. Enhancing the UV A1 screening ability of caffeic acid by encapsulation in layered basic zinc hydroxide matrix. *J. Phys. Chem. Solids* **73,** 1510–1513 (2012).

295. Mohsin, S. M. N. *et al.* Synthesis of (cinnamate-zinc layered hydroxide) intercalation compound for sunscreen application. *Chem. Cent. J.* **7,** 26 (2013).

296. Choy, J.-H., Han, Y.-S., HWANG, S.-H. & LEE, C.-W. Cosmetic raw material having improved properties and processes for preparing the same. *WO/2003/011233* 1–10 (2003).

297. Arulraj, J., Rajamathi, J. T., Prabhu, K. R. & Rajamathi, M. Anionic clays

as hosts for anchored synthesis: Interlayer bromination of maleate and fumarate ions in nickel–zinc layered hydroxy double salt. *Solid State Sci.* **9,** 812–816 (2007).

298. Tagaya, H., Sasaki, N., Morioka, H. & Kadokawa, J. Preparation of New Inorganic—Organic Layered Compounds, Hydroxy Double Salts, and Preferential Intercalation of Organic Carboxylic Acids into Them. *Mol. Cryst. Liq. Cryst. Sci. Technol. Sect. A. Mol. Cryst. Liq. Cryst.* **341,** 413–418 (2000).

299. Richardson-Chong, S. S. D., Patel, R. & Williams, G. R. Intercalation and Controlled Release of Bioactive Ions Using a Hydroxy Double Salt. *Ind. Eng. Chem. Res.* **51,** 2913–2921 (2012).

300. Barahuie, F., Hussein, M. Z., Abd Gani, S., Fakurazi, S. & Zainal, Z. Anticancer nanodelivery system with controlled release property based on protocatechuate-zinc layered hydroxide nanohybrid. *Int. J. Nanomedicine* **9,** 3137–3149 (2014).

301. Al Ali, S. H. H., Al-Qubaisi, M., Hussein, M. Z., Zainal, Z. & Hakim, M. N. Preparation of hippurate-zinc layered hydroxide nanohybrid and its synergistic effect with tamoxifen on HepG2 cell lines. *Int. J. Nanomedicine* **6,** 3099–3111 (2011).

302. Hussein Al Ali, S. H., Al-Qubaisi, M., El Zowalaty, M., Hussein, M. Z. & Ismail, M. Antimicrobial activity of hippurate nanocomposite and its cytotoxicity effect in combination with cytarabine against HL-60. *J. Nanomater.* **2013,** 1–9 (2013).

303. Hussein Al Ali, S. H., Al-Qubaisi, M., Hussein, M. Z., Ismail, M. & Bullo, S. Hippuric acid nanocomposite enhances doxorubicin and oxaliplatin-induced cytotoxicity in MDA-MB231, MCF-7 and Caco2 cell lines. *Drug Des. Devel. Ther.* **7,** 25–31 (2013).

304. Barahuie, F., Hussein, M. Z., Arulselvan, P., Fakurazi, S. & Zainal, Z. Development of the Anticancer Potential of a Chlorogenate-Zinc Layered Hydroxide Nanohybrid with Controlled Release Property Against Various Cancer Cells. *Sci. Adv. Mater.* **5,** 1983–1993 (2013).

305. Schöllhorn, R. Reversible Topotactic Redox Reactions of Solids by Electron/Ion Transfer. *Angew. Chemie Int. Ed. English* **19,** 983–1003 (1980).

306. Duan, X., Lu, J. & Evans, D. G. in *Mod. Inorg. Synth. Chem.* 375–404 (Elsevier, 2011).

307. Tiwari, A. & Raj, B. *Reactions and Mechanisms in Thermal Analysis of Advanced Materials*. (John Wiley & Sons, Inc., 2015).

308. Wang, D. *et al.* in *Adv. Polyolefin Nanocomposites* (Mittal, V.) 225–246 (CRC Press, 2010).

309. Sparks, D. *Environmental soil chemistry*. (Academic press, Elsevier Science (USA), 2003).

310. M. J. Pilling and P. W. Seakins. *Reaction Kinetics*. (Oxford University Press, 1995).

311. Miyata, S. Anion-Exchange Properties of Hydrotalcite-Like Compounds. *Clays Clay Miner.* **31,** 305–311 (1983).

312. Nunes, M. d'Ávila. in *Hadron Ther. Phys. Simulations* (Nunes, M. d'Ávila) 35–63 (Springer, 2014).

313. Durrant, A. *Quantum Physics of Matter*. (CRC Press, 2000).

314. Winick, H. *Synchrotron Radiation Sources: A Primer*. (World Scientific, 1995).

315. Willmott, P. *An Introduction to Synchrotron Radiation*. (John Wiley & Sons, Ltd, 2011).

316. Williams, G. P. A general review of synchrotron radiation, its uses and special technologies. *Vacuum* **32,** 333–345 (1982).

317. Bienenstock, A. & Winick, H. Synchrotron radiation research—An overview. *Phys. Today* **36,** 48 (1983).

318. http://www.diamond.ac.uk.

319. Sa, J.-H., Kwak, G.-H., Han, K., Ahn, D. & Lee, K.-H. Gas hydrate inhibition by perturbation of liquid water structure. *Sci. Rep.* **5,** 11526 (2015).

320. Mukherjee, R., McCaddon, A., Smith, C. A. & Brasch, N. E. Synthesis, Synchrotron X-ray Diffraction, and Kinetic Studies on the Formation of a Novel Thiolatocobalamin of Captopril: Evidence for cis - trans Isomerization in the β-Axial Ligand. *Inorg. Chem.* **48,** 9526–9534 (2009).

321. Zahn, G. *et al.* Insight into the mechanism of modulated syntheses: in situ synchrotron diffraction studies on the formation of Zr-fumarate MOF. *CrystEngComm* **16,** 9198–9207 (2014).

322. Cai, B. *et al.* Time-resolved synchrotron tomographic quantification of deformation-induced flow in a semi-solid equiaxed dendritic Al–Cu alloy. *Scr. Mater.* **103,** 69–72 (2015).

323. Yoshigoe, A. & Teraoka, Y. Synchrotron Radiation Photoelectron Spectroscopy Study on Oxide Evolution during Oxidation of a Si(111)-7 × 7 Surface at 300 K: Comparison of Thermal Equilibrium Gas and Supersonic Molecular Beams for Oxygen Adsorption. *J. Phys. Chem. C* **118,** 9436–9442 (2014).

324. Zhao, H., Nenoff, T. M., Jennings, G., Chupas, P. J. & Chapman, K. W.

Determining Quantitative Kinetics and the Structural Mechanism for Particle Growth in Porous Templates. *J. Phys. Chem. Lett.* **2,** 2742–2746 (2011).

325. You, H. & Nagy, Z. Applications of Synchrotron Surface X-Ray Scattering Studies of Electrochemical Interfaces. *MRS Bull.* **24,** 36–40 (1999).

326. Prasad, A., McDonald, S. D., Yasuda, H., Nogita, K. & StJohn, D. H. A real-time synchrotron X-ray study of primary phase nucleation and formation in hypoeutectic Al-Si alloys. *J. Cryst. Growth* (2015).

327. Rau, J. V. *et al.* Energy dispersive X-ray diffraction study of phase development during hardening of calcium phosphate bone cements with addition of chitosan. *Acta Biomater.* **4,** 1089–1094 (2008).

328. Rey, F. *et al.* Synchrotron-Based Method for the Study of Crystallization: Templated Formation of CoALPO-5 Catalyst. *Chem. Mater.* **7,** 1435–1436 (1995).

329. Davies, A. T., Sankar, G., Catlow, C. R. A. & Clark, S. M. Following the Crystallization of Microporous Solids Using EDXRD Techniques. *J. Phys. Chem. B* **101,** 10115–10120 (1997).

330. Walton, R. I., Loiseau, T., O'Hare, D. & Férey, G. An in Situ Energy-Dispersive X-ray Diffraction Study of the Hydrothermal Crystallizations of Open-Framework Gallium Oxyfluorophosphates with the ULM-3 and ULM-4 Structures. *Chem. Mater.* **11,** 3201–3209 (1999).

331. Ragon, F. *et al.* In Situ Energy-Dispersive X-ray Diffraction for the Synthesis Optimization and Scale-up of the Porous Zirconium Terephthalate UiO-66. *Inorg. Chem.* **53,** 2491–2500 (2014).

332. Francis, R. J. *et al.* Hydrothermal Synthesis of Microporous Tin Sulfides Studied by Real-Time in Situ Energy-Dispersive X-ray Diffraction. *Chem. Mater.* **8,** 2102–2108 (1996).

333. Jensen, K. M. Ø., Tyrsted, C., Bremholm, M. & Iversen, B. B. In Situ Studies of Solvothermal Synthesis of Energy Materials. *ChemSusChem* **7,** 1594–1611 (2014).

334. Muncaster, G. *et al.* An in Situ Microcrystal X-ray Diffraction Study of the Synthetic Aluminophosphate Zeotypes DAF-1 and CoAPSO-44. *Chem. Mater.* **11,** 158–163 (1999).

335. Simmance, K., Sankar, G., Bell, R. G., Prestipino, C. & Beek, W. van. Tracking the formation of cobalt substituted ALPO-5 using simultaneous in situ X-ray diffraction and X-ray absorption spectroscopy techniques. *Phys. Chem. Chem. Phys.* **12,** 559–562 (2010).

336. Du, Y. & O'Hare, D. Observation of staging during intercalation in layered alpha-cobalt hydroxides: a synthetic and kinetic study. *Inorg. Chem.* **47,** 11839–46 (2008).

337. Fogg, A. M., Dunn, J. S. & O'Hare, D. Formation of Second-Stage Intermediates in Anion-Exchange Intercalation Reactions of the Layered Double Hydroxide [LiAl 2 (OH) 6]Cl·H 2 O As Observed by Time-Resolved, in Situ X-ray Diffraction. *Chem. Mater.* **10,** 356–360 (1998).

338. Taviot-Guého, C., Feng, Y., Faour, A. & Leroux, F. Intercalation chemistry in a LDH system: anion exchange process and staging phenomenon investigated by means of time-resolved, in situ X-ray diffraction. *Dalton Trans.* **39,** 5994–6005 (2010).

339. Williams, G. R., Crowder, J., Burley, J. C. & Fogg, A. M. The selective intercalation of organic carboxylates and sulfonates into hydroxy double salts. *J. Mater. Chem.* **22,** 13600 (2012).

340. Tarasov, K. A., Isupov, V. P., Chupakhina, L. E. & O'Hare, D. A time resolved, in-situ X-ray diffraction study of the de-intercalation of anions and lithium cations from [LiAl2(OH)6]nX.qH2O (X = Cl, Br, NO_3, SO_4^2). *J. Mater. Chem.* **14,** 1443 (2004).

341. Millange, F., Walton, R. I. & O'Hare, D. Time-resolved in situ X-ray diffraction study of the liquid-phase reconstruction of Mg–Al–carbonate hydrotalcite-like compounds. *J. Mater. Chem.* **10,** 1713–1720 (2000).

342. Francis, R. J. *et al.* Time-Resolved In-Situ Energy and Angular Dispersive X-ray Diffraction Studies of the Formation of the Microporous Gallophosphate ULM-5 under Hydrothermal Conditions. *J. Am. Chem. Soc.* **121,** 1002–1015 (1999).

343. Ellmer, K., Mientus, R., Wei, V. & Rossner, H. In situ energy-dispersive x-ray diffraction system for time-resolved thin-film growth studies. *Meas. Sci. Technol.* **14,** 336–345 (2003).

344. Sadiku, M. N. O. *Monte Carlo Methods for Electromagnetics*. (CRC Press, 2009).

345. Wilfred, B., Gunsteren, V. & Berendsen, C. Computer simulation of molecular dynamics: Methodology, applications, and perspectives in chemistry. *Angew. Chemie Int. Ed. English* **29,** 992–1023 (1990).

346. Allen, M. P. Introduction to Molecular Dynamics Simulation. *Comput. Soft Matter From Synth. Polym. to Proteins* **23,** 1–28 (2004).

347. Maurin, G., Bell, R. G. & Llewellyn, P. L. in 955–962 (2005).

348. Torrisi, A., Bell, R. G. & Mellot-Draznieks, C. Functionalized MOFs for Enhanced CO 2 Capture. *Cryst. Growth Des.* **10,** 2839–2841 (2010).

349. Fischer, M. & Bell, R. G. Modeling CO 2 Adsorption in Zeolites Using DFT-Derived Charges: Comparing System-Specific and Generic Models. *J. Phys. Chem. C* **117,** 24446–24454 (2013).

350. Catlow, R., Bell, R., Cora, F. & Slater, B. in *Introd. to Zeolite Sci. Pract.*

(Cejka, J., van Bekkum, H., Corma, A. & Schueth, F.) 659–700 (Elsevier, 2007).

351. Kovář, P., Pospíšil, M., Nocchetti, M., Čapková, P. & Melánová, K. Molecular modeling of layered double hydroxide intercalated with benzoate, modeling and experiment. *J. Mol. Model.* **13,** 937–942 (2007).

352. Zhang, H., Xu, Z. P., Lu, G. Q. & Smith, S. C. Computer Modeling Study for Intercalation of Drug Heparin into Layered Double Hydroxide. *J. Phys. Chem. C* **114,** 12618–12629 (2010).

353. Pisson, J., Morel, J. P., Morel-Desrosiers, N., Taviot-Guého, C. & Malfreyt, P. Molecular Modeling of the Structure and Dynamics of the Interlayer Species of ZnAlCl Layered Double Hydroxide. *J. Phys. Chem. B* **112,** 7856–7864 (2008).

354. Demel, J. *et al.* Insight into the Structure of Layered Zinc Hydroxide Salts Intercalated with Dodecyl Sulfate Anions. *J. Phys. Chem. C* **118,** 27131–27141 (2014).

355. Demel, J. *et al.* Inorganic−Organic Hybrid Materials: Layered Zinc Hydroxide Salts with Intercalated Porphyrin Sensitizers. *J. Phys. Chem. C* **114,** 16321–16328 (2010).

356. Catlow, C. R. A., Bell, R. G. & Slater, B. in *Comput. Model. Microporous Mater.* (Catlow, C. R. ., Smit, B. & van Santen, R. A.) 1–24 (Elsevier, 2004).

357. Torrisi, A., Bell, R. G. & Mellot-Draznieks, C. Predicting the impact of functionalized ligands on CO2 adsorption in MOFs: A combined DFT and Grand Canonical Monte Carlo study. *Microporous Mesoporous Mater.* **168,** 225–238 (2013).

358. Salles, F. *et al.* Molecular Dynamics Simulations of Breathing MOFs: Structural Transformations of MIL-53(Cr) upon Thermal Activation and CO 2 Adsorption. *Angew. Chemie Int. Ed.* **47,** 8487–8491 (2008).

359. Field, M. J. *A Practical Introduction to the Simulation of Molecular Systems*. (Cambridge University Press, 2007).

360. Hinchliffe, A. *Molecular Modelling for Beginners*. (John Wiley & Sons, Ltd, 2008).

361. Solomon, E. I., Scott, R. A. & King, R. B. *Computational Inorganic and Bioinorganic Chemistry*. (Wiley, 2009).

362. Leach, A. R. *Molecular Modelling: Principles and Applications*. (Pearson Education Limited, 2001).

363. Elder, A. & Fort, R. C. J. in *Lignin Lignans Adv. Chem.* (Heitner, C., Dimmel, D. & Schmidt, Jo.) 321–348 (CRC Press, 2010).

364. Balbuena, P. B. & Seminario, J. M. *Molecular Dynamics From Classical to Quantum Methods*. (Elsevier, 1999).

365. Rocchia, W. & Spagnuolo, M. *Computational Electrostatics for Biological Applications*. (Springer International Publishing, 2015).

366. Johnson, M. *et al.* Cation exchange, dehydration, and calcination in clinoptilolite: In situ x-ray diffraction and computer modeling. *J. Phys. Chem. B* **107,** 942–951 (2003).

367. Newman, S. P., Greenwell, H. C., Coveney, P. V. & and Jones, W. in *Layer. Double Hydroxides Present Futur.* 101–125 (Nova Science Pub Inc, 2001).

368. Field, M. J. in *A Pract. Introd. to Simul. Mol. Syst.* 81–109 (Cambridge University Press, 2007).

369. Hopfinger, a J. & Pearlstein, R. a. Molecular mechanics force-field parameterization procedures. *J. Comput. Chem.* **5,** 486–499 (1984).

370. Wise, O. M., Xu, L. & Coskuner, O. in *Met. Syst. A Quantum Chem. Perspect.* (Thomas, C. A., Coskuner, O. & Carlos, A. G.) 29–82 (CRC Press, 2011).

371. Wylie, W. in *Mol. Model. Drug Des.* (Vinter, J. G. & Gardner, M.) 1–52 (CRC Press, 1994).

372. Smith, J. S., Borodin, O. & Smith, G. D. A Quantum Chemistry Based Force Field for Poly(dimethylsiloxane). *J. Phys. Chem. B* **108,** 20340–20350 (2004).

373. Flores, T. P. & Moss, D. S. in *Mol. Dyn. Appl. Mol. Biol.* (Goodfellow, J.) 1–26 (CRC Press, 1990).

374. Griebel, M., Knapek, S. & Zumbusch, G. in *Numer. Simul. Mol. Dyn.* 151–209 (Springer Berlin Heidelberg, 2007).

375. VLUGT, T. J. H. & SMIT, B. in *Mol. Dyn. Parallel Comput.* (Esser, R., Grassberger Johannes Grotendorst, P. & Lewerenz, M.) 108–119 (WORLD SCIENTIFIC, 2000).

376. Arno, J., Bauder, A., Bettens, F. L., Bettens, R. P. A. & Bevan, J. W. *Jet Spectroscopy and Molecular Dynamics*. (Springer Netherlands, 1995).

377. Buehler, M. in *At. Model. Mater. Fail.* 31–94 (Springer US, 2008).

378. Griebel, M., Knapek, S. & Zumbusch, G. in *Numer. Simul. Mol. Dyn.* 17–36 (Springer Berlin Heidelberg, 2007).

379. Alvo, S., Lambert, P., Gauthier, M. & Regnier, S. in *Adhes. Asp. MEMS/NEMS* (Kim, S. H., Dugger, M. T. & Mittal, K. L.) 77–93 (CRC Press, 2011).

380. Li, J. in *Handb. Mater. Model.* (Yip, S.) 565–588 (Springer Netherlands, 2005).

381. *Multiscale Modeling of Particle Interactions*. (John Wiley & Sons, Inc., 2010).

382. Field, M. J. in *A Pract. Introd. to Simul. Mol. Syst.* 195–224 (Cambridge University Press, 2007).

383. Schnabel, T. *Molecular Modeling and Simulation of Hydrogen Bonding Pure Fluids and Mixtures*. (Logos Verlag Berlin, 2008).

384. Chandler, D. Interfaces and the driving force of hydrophobic assembly. *Nature* **437,** 640–647 (2005).

385. Maurin, G., Bell, R. G., Devautour, S., Henn, F. & Giuntini, J. C. in *Stud. Surf. Sci. Catal.* 1606–1611 (2004).

386. Padma Kumar, P., Kalinichev, A. G. & Kirkpatrick, R. J. Hydration, swelling, interlayer structure, and hydrogen bonding in organolayered double hydroxides: insights from molecular dynamics simulation of citrate-intercalated hydrotalcite. *J. Phys. Chem. B* **110,** 3841–4 (2006).

387. Xu, Q., Ni, Z., Yao, P. & Li, Y. Molecular dynamics simulation of anionic clays containing glutamic acid. *J. Mol. Struct.* **977,** 165–169 (2010).

388. Varela, L. M. *et al.* Solvation of molecular cosolvents and inorganic salts in ionic liquids: A review of molecular dynamics simulations. *J. Mol. Liq.* **210,** 178–188 (2015).

389. Field, M. J. in *A Pract. Introd. to Simul. Mol. Syst.* 225–261 (Cambridge University Press, 2007).

390. Heinecke, A., Eckhardt, W., Horsch, M. & Bungartz, H.-J. in *Supercomput. Mol. Dyn. Simulations* 11–29 (Springer, 2015).

391. Sandler, S. I. *An Introduction to Applied Statistical Thermodynamics*. (John Wiley & Sons, 2010).

392. Kandt, C., Ash, W. L. & Peter Tieleman, D. Setting up and running molecular dynamics simulations of membrane proteins. *Methods* **41,** 475–488 (2007).

393. Chernatynskiy, Aleksandr Clarke, D. R. & Phillpot, S. R. in *Handb. Nanosci. Eng. Technol.* (Goddard, W. A., Brenner, D., Lyshevski, S. E. & Iafrate, G. J.) 545–566 (CRC Press, 2012).

394. Xu, S.-M. *et al.* Understanding the thermal motion of the luminescent dyes in the dye–surfactant cointercalated ZnAl-layered double hydroxides: a molecular dynamics study. *RSC Adv.* **4,** 47472–47480 (2014).

395. Vital de Oliveira, O. Molecular Dynamics and Metadynamics Simulations

of the Cellulase Cel48F. *Enzyme Res.* **2014,** 1–7 (2014).

396. Pang, A., Arinaminpathy, Y., Sansom, M. S. P. & Biggin, P. C. Interdomain dynamics and ligand binding: molecular dynamics simulations of glutamine binding protein. *FEBS Lett.* **550,** 168–174 (2003).

397. Tai, K., Shen, T., Börjesson, U., Philippopoulos, M. & McCammon, J. A. Analysis of a 10-ns Molecular Dynamics Simulation of Mouse Acetylcholinesterase. *Biophys. J.* **81,** 715–724 (2001).

398. *Computational Molecular Dynamics: Challenges, Methods, Ideas*. **4,** (Springer Berlin Heidelberg, 1999).

399. Koshy, C., Parthiban, M. & Sowdhamini, R. 100 ns molecular dynamics simulations to study intramolecular conformational changes in Bax. *J. Biomol. Struct. Dyn.* **28,** 71–83 (2010).

400. Duan, Y. & Kollman, P. A. Pathways to a protein folding intermediate observed in a 1-microsecond simulation in aqueous solution. *Science* **282,** 740–4 (1998).

401. Karplus, M. & McCammon, J. A. Molecular dynamics simulations of biomolecules. *Nat. Struct. Mol. Biol.* **9,** 646–652 (2002).

402. Tsolou, G., Harmandaris, V. A. & Mavrantzas, V. G. Temperature and Pressure Effects on Local Structure and Chain Packing incis-1,4-Polybutadiene from Detailed Molecular Dynamics Simulations. *Macromol. Theory Simulations* **15,** 381–393 (2006).

403. Chen, W.-H. & Cheng, H.-C. in *Trends Nanoscale Mech.* (Harik, V.) 45–109 (Springer Netherlands, 2014).

404. Sun, Y. *et al.* Molecular dynamics simulation of temperature effect on dendrimer / NanoGs / PPy interface material. *Comput. Mater. Sci.* **46,** 162–166 (2009).

405. Sugden, I. J., Plant, D. F. & Bell, R. G. Thermal rearrangement mechanisms in icosahedral carboranes and metallocarboranes. *Chem. Commun. Chem. Commun* **49,** 975–977 (2013).

406. Kwasniewski, S. P., François, J. P. & Deleuze, M. S. Temperature effects on the UV-Vis electronic spectrum of trans-stilbene. *Int. J. Quantum Chem.* **85,** 557–568 (2001).

407. Chen, W.-H. & Cheng, H.-C. in *Trends Nanoscale Mech.* (Harik, V.) 45–109 (Springer Netherlands, 2014).

408. Alexiadis, O. & Mavrantzas, V. G. All-atom molecular dynamics simulation of temperature effects on the structural, thermodynamic, and packing properties of the pure amorphous and pure crystalline phases of regioregular P3HT. *Macromolecules* **46,** 2450–2467 (2013).

409. Pereverzev, A. & Sewell, T. D. Molecular dynamics study of the effect of pressure on the terahertz-region infrared spectrum of crystalline pentaerythritol tetranitrate. *Chem. Phys. Lett.* **515,** 32–36 (2011).

410. Rino, J. P., Pizani, P. S. & Costa, S. C. Interaction potential for InSb: a molecular dynamics study. *Brazilian J. Phys.* **34,** 347–353 (2004).

411. Ducut, M. R. D. *et al.* Molecular dynamics study on the effects of varying temperature and pressure on phosphatidylcholine lipids for microalgae drying. in *2014 Int. Conf. Humanoid, Nanotechnology, Inf. Technol. Commun. Control. Environ. Manag.* 1–4 (IEEE, 2014).

412. Kazanc, S. Molecular dynamics study of pressure effect on crystallization behaviour of amorphous CuNi alloy during isothermal annealing. *Phys. Lett. A* **365,** 473–477 (2007).

413. Ghosh, T., García, a E. & Garde, S. Molecular dynamics simulations of pressure effects on hydrophobic interactions. *J. Am. Chem. Soc.* **123,** 10997–1003 (2001).

414. Maurin, G., Bourrelly, S., Llewellyn, P. L. & Bell, R. G. Simulation of the adsorption properties of CH4 in faujasites up to high pressure: Comparison with microcalorimetry. *Microporous Mesoporous Mater.* **89,** 96–102 (2006).

415. Root, L. J. & Berne, B. J. Effect of pressure on hydrogen bonding in glycerol: A molecular dynamics investigation. *J. Chem. Phys.* **107,** 4350 (1997).

416. Cook, R. L., King, H. E., Herbst, C. A. & Herschbach, D. R. Pressure and temperature dependent viscosity of two glass forming liquids: Glycerol and dibutyl phthalate. *J. Chem. Phys.* **100,** 5178 (1994).

417. Parthasarathi, R., Subramanian, V., Buemi, G. & Pacios, L. F. *Hydrogen Bonding—New Insights*. (Springer Netherlands, 2006).

418. Li, D., Zhang, P. & Yan, J. Ab initio molecular dynamics study of high-pressure melting of beryllium oxide. *Sci. Rep.* **4,** 4707 (2014).

419. Iwanaga, H., Kunishige, A. & Takeuchi, S. Anisotropic thermal expansion in wurtzite-type crystals. *J. Mater. Sci.* **35,** 2451–2454 (2000).

420. Victor, A. C. & Douglas, T. B. Thermodynamic properties of magnesium oxide and beryllium oxide from 298 to 1,200 °K. *J. Res. Natl. Bur. Stand. Sect. A Phys. Chem.* **67A,** 325–329 (1963).

421. Loh, E. Optical Phonons in BeO Crystals. *Phys. Rev.* **166,** 673–678 (1968).

422. Hazen, R. M. & Finger, L. W. High-pressure and high-temperature crystal chemistry of beryllium oxide. *J. Appl. Phys.* **59,** 3728 (1986).

423. Roessler, D. M., Walker, W. C. & Loh, E. Electronic spectrum of crystalline beryllium oxide. *J. Phys. Chem. Solids* **30,** 157–167 (1969).

424. Slack, G. A. Thermal Conductivity of BeO Single Crystals. *J. Appl. Phys.* **42,** 4713 (1971).

425. Bosak, A., Schmalzl, K., Krisch, M., van Beek, W. & Kolobanov, V. Lattice dynamics of beryllium oxide: Inelastic x-ray scattering and ab initio calculations. *Phys. Rev. B* **77,** 224303 (2008).

426. Song, H.-F., Liu, H.-F. & Tian, E. Structural and thermodynamic properties of hexagonal BeO at high pressures and temperatures. *J. Phys. Condens. Matter* **19,** 456209 (2007).

427. Sahariah, M. B. & Ghosh, S. Dynamical stability and phase transition of BeO under pressure. *J. Appl. Phys.* **107,** 083520 (2010).

428. Yu, B.-R., Yang, J.-W., Guo, H.-Z., Ji, G.-F. & Chen, X.-R. Phase transition and elastic properties of BeO under pressure from first-principles calculations. *Phys. B Condens. Matter* **404,** 1940–1946 (2009).

429. Amrani, B., Hassan, F. E. H. & Akbarzadeh, H. First-principles investigations of the ground-state and excited-state properties of BeO polymorphs. *J. Phys. Condens. Matter* **19,** 436216 (2007).

430. Jephcoat, A. P., Hemley, R. J., Mao, H. K., Cohen, R. E. & Mehl, M. J. Raman spectroscopy and theoretical modeling of BeO at high pressure. *Phys. Rev. B* **37,** 4727–4734 (1988).

431. Camp, P. E. Van & Doren, V. E. Van. Ground-state properties and structural phase transformation of beryllium oxide. *J. Phys. Condens. Matter* **8,** 3385–3390 (1996).

432. Laurendeau, N. in *Stat. Thermodyn.* 7–22 (Cambridge University Press, 2005).

433. Gibbs, J. W. *Elementary Principles in Statistical Mechanics*. (Cambridge University Press, 1902).

434. BRYAN, G. H. Elementary Principles in Statistical Mechanics. *Nature* **66,** 291–292 (1902).

435. Gallavotti, G. *Statistical Mechanics*. (Springer Berlin Heidelberg, 1999).

436. Beard, D. A. in *Biosimulation* 145–177 (Cambridge University Press, 2012).

437. Phillies, G. D. J. in *Elem. Lect. Stat. Mech.* 28–38 (Springer New York, 2000).

438. Lelièvre, T., Rousset, M. & Stoltz, G. in *Free Energy Comput.* 1–60 (IMPERIAL COLLEGE PRESS, 2010).

439. Van Vliet, C. M. in *Equilib. Non-Equilibrium Stat. Mech.* 93–169 (WORLD SCIENTIFIC, 2008).

440. Leach, A. *Molecular Modelling: Principles and Applications*. (Dorset press, 2001).

441. Tuckerman, M. E. in *Stat. Mech. Theory Mol. Simul.* 218–264 (Oxford University Press, 2010).

442. Newman, S. P., Di Cristina, T., Coveney, P. V. & Jones, W. Molecular Dynamics Simulation of Cationic and Anionic Clays Containing Amino Acids. *Langmuir* **18,** 2933–2939 (2002).

443. Cygan, R. T., Liang, J.-J. & Kalinichev, A. G. Molecular Models of Hydroxide, Oxyhydroxide, and Clay Phases and the Development of a General Force Field. *J. Phys. Chem. B* **108,** 1255–1266 (2004).

444. Mayo, S. L., Olafson, B. D. & Goddard, W. A. DREIDING: a generic force field for molecular simulations. *J. Phys. Chem.* **94,** 8897–8909 (1990).

445. Lin, F. & Wang, R. Systematic derivation of AMBER force field parameters applicable to zinc-containing systems. *J. Chem. Theory Comput.* **6,** 1852–1870 (2010).

446. Zhang, S. T., Yan, H., Wei, M., Evans, D. G. & Duan, X. Valence force field for layered double hydroxide materials based on the parameterization of octahedrally coordinated metal cations. *J. Phys. Chem. C* **116,** 3421–3431 (2012).

447. Hou, Kalinichev, A. G. & Kirkpatrick, R. J. Interlayer Structure and Dynamics of Cl-−LiAl2-Layered Double Hydroxide: 35Cl NMR Observations and Molecular Dynamics Modeling. *Chem. Mater.* **14,** 2078–2085 (2002).

448. Bell, I. S., Kooli, F., Jonesl, W. & Coveney, P. V. Thermal Characteristics of Layered Double Hydroxide Intercalates - Comparison of Experiment and Computer Simulation. *MRS Proc.* **435,** 73 (1996).

449. Rad, F. A., Rezvani, Z. & Khodam, F. Molecular design confirmation for proposition of improved photophysical properties in a dye-intercalated layered double hydroxides. *RSC Adv.* **6,** 11193–11203 (2016).

450. Pisson, J., Morel, J. P., Morel-Desrosiers, N., Taviot-Guého, C. & Malfreyt, P. Molecular modeling of the structure and dynamics of the interlayer species of ZnAlCl layered double hydroxide. *J. Phys. Chem. B* **112,** 7856–64 (2008).

451. Newman, S. P. & Jones, W. in *Supramol. Organ. Mater. Des.* (Jones, W. & Rao, C. N. R.) 295–331 (Cambridge University Press, 2001).

452. Yan, D. *et al.* A combined study based on experiment and molecular dynamics: perylene tetracarboxylate intercalated in a layered double

hydroxide matrix. *Phys. Chem. Chem. Phys.* **11,** 9200 (2009).

453. Kumar, P. P., Kalinichev, A. G. & Kirkpatrick, R. J. Molecular Dynamics Simulation of the Energetics and Structure of Layered Double Hydroxides Intercalated with Carboxylic Acids. *J. Phys. Chem. C* **111,** 13517–13523 (2007).

Chapter 2: Electrospun Nanofibres

2.1. Introduction

Electrospinning is a facile top-down technique permitting the fabrication of a wide variety of functional nanocomposites. A solution of a polymer and a functional component is prepared, usually in a volatile solvent, and expelled from a needle (spinneret) towards a metal collector at a controlled rate. A high potential difference is applied between the two and this electrical energy causes rapid evaporation of the solvent, resulting in polymer-based one-dimensional objects with diameters on the nm scale.[1–4] These fibres have a number of desirable properties (*e.g.* high surface area) which may be tuned by controlling the processing parameters (voltage applied, needle-to-collector distance, flow rate, solution concentration, *etc*).[2]

A large number of studies have reported the use of electrospinning to produce drug-loaded fibres for use as engineered drug delivery systems.[2,5–9] The majority of these studies use one-fluid electrospinning, but even in this simple system it is found that variation of the polymer and processing parameters can result in a wide range of drug release behaviours. More recently, more advanced approaches have been employed to develop bespoke drug delivery profiles; these include coaxial electrospinning (using two concentric needles, one nested inside another) and a combination with other technique.[10,11]

The electrospinning of polymer blends has been explored reasonably widely, and has been applied to drug delivery to deliver modulated release profiles.[12–14] Electrospun materials have successfully been used to modify the rate of drug release,[13] to target release to a particular part of the body such as the gastrointestinal tract,[6] or to deliver biphasic or dual-stage drug release.[10,11] While such release profiles can be very useful in the development of advanced pharmaceutics, they are inappropriate if a drug has a high first-pass effect or to be effective requires very time- and site-specific delivery.[15] Time-controlled pulsatile release, in which the drug is released after a predefined time period, is more appropriate for such applications.

A number of disease states follow biological rhythms.[16] For instance, asthma attacks tend to happen mainly late at night, following the body's natural circadian cycle, and pain from rheumatoid arthritis is most intense in the morning. Epilepsy also oscillates in its implications for patients, in response to melatonin secretion. To effectively treat these conditions, precise time-controlled release profiles are required. Pulsatile delivery systems of drugs such as sodium valproate (indicated for the treatment of epilepsy) or diltiazem (angina) are hence much sought after to enhance patient compliance and improve clinical outcomes. To date, there are no reports of time-resolved pulsatile release from electrospun nanofibres.

The formation of a system comprising two polymers mixed, with a drug component loaded, offers the potential to deliver novel drug release profiles even from a single fluid electrospinning process. If one of these polymers has pH-sensitive characteristics, then targeted drug release should be possible. One such polymer is alginic acid, commonly available as its sodium salt, which dissolves only at elevated pHs. In order to incorporate sodium alginate (SA) into nanofibres, it is necessary to blend it with a carrier polymer.[17] A number of researchers have developed electrospun fibres containing SA blended with poly(ethylene oxide) (PEO).[18–21] Alborzi *et al.* have used SA-pectin-PEO fibres to stabilise folic acid,[22] and Lee's team have coated poly(vinyl alcohol) fibres with alginate for pH sensitive release.[23] In 2012, two sets of researchers

independently reported the formation of electrospun fibres comprising PEO and sodium alginate (SA).[24,25] Although both teams used the same building blocks and similar synthetic processes, very different results were obtained: Ma *et al.* created core-shell nanofibres with a PEO shell and a SA core,[25] while Bonino and co-workers noted the formation of a "mountain" of fibres on the collector plate instead of the flat mat normally seen, which they attributed to the aggregation of SA on the exterior of the fibres.[24]

It is clear therefore that blended PEO/SA fibres have interesting properties from an academic viewpoint; in addition, PEO is a highly suitable polymer for drug delivery systems because it is classified by the FDA as a "generally regarded as safe" excipient, and since it is hydrophilic can aid the solubilisation of poorly water soluble drugs. Variation in the molecular weight of the polymer can result in tuning of the drug release properties from PEO composites.[26] Furthermore, SA has been exploited for many years as a pH-responsive drug release system.[27–29]

Another commonly used FDA-approved polymer is poly(vinyl pyrrolidone) (PVP). PVP has many favourable properties such as its capacity to interact with a large range of hydrophilic and hydrophobic materials. It has minimal immunogenicity, and is used in the drug and food fields as a chelating agent.[30] PVP nanofibres have been used to prepare a number of immediate release / fast dissolving drug delivery systems by electrospinning.[31–34]

In this work, these properties were exploited to develop drug delivery systems based on PEO/SA blend fibres; systems based on PVP and PVP/SA were also explored. A series of fibres loaded with the non-steroidal anti-inflammatory drugs ibuprofen sodium (SI), diclofenac sodium (Dic), naproxen sodium (Nap) and sodium valproate (Val) were generated and their drug delivery properties explored.

2.2. Results and discussion

Solutions were prepared by co-dissolving PEO and SA in deionised water to give final concentrations of 5 % and 1.5 % w/v respectively. In the same way, solutions of PVP and SA were prepared with final concentrations of 20 % and 2 % w/v, respectively (again by dissolving both in water). 10 mL of each solution was then combined with certain amounts of SI, Nap, Val and Dic. In addition, a pure PVP solution at 10 % w/v was also prepared by dissolving it in ethanol. Details of the solutions prepared are given in Table 2.1.

Table 2.1: The compositions of the fibres prepared in this study.

Fiber ID	Drug	% SA in solution (w/v)	% PEO in solution (w/v)	% Drug in solution (w/v)
F0	-	1.5	5.0	0
Fi10	SI	1.5	5.0	10.0
Fi2	SI	1.5	5.0	2.0
Fi1	SI	1.5	5.0	1.0
Fn10	Nap	1.5	5.0	10.0
Fn5	Nap	1.5	5.0	5.0
Fn1	Nap	1.5	5.0	1.0
Fv10	Val	1.5	5.0	10.0
Fv5	Val	1.5	5.0	5.0
Fv2	Val	1.5	5.0	2.0
Fv1	Val	1.5	5.0	1.0
Fd1	Dic	1.5	5.0	1.0

Fiber ID	Drug	% SA in solution (w/v)	% PVP in solution (w/v)	% SI in solution (w/v)
FP	-	0	10.0	0
FPi1	SI	0	10.0	1.0
FPS	-	2.0	20.0	0
FPSi1	SI	2.0	20.0	1.0

2.2.1. Effect of processing parameters on fibre morphology

The effect of voltage, polymer concentration, the distance between the needle and collector, and the solution flow rate on the fibre morphology were investigated in previous studies.[35–38] Based on these, a series of optimisation experiments were undertaken to select the most appropriate processing parameters before fibre manufacture commenced. These are detailed in Chapter 6, Section 6.2.

2.2.2. Characterisation of drug-free fibres

2.2.2.1. Fibre morphology

A photograph of the F0 (PEO/SA) fibres is given in Figure 2.1. It is immediately clear that the fibres form a three-dimensional "mountain" structure rather than a flat mat on the collector plate: our results thus agree with those of Bonino *et al*.[24] Scanning electron microscopy (SEM) images were recorded on samples taken from different points of the 3D fibre structure (base and tip); data for the base and tip are included in Figure 2.1. The SEM data show the fibres throughout the 3D structure to have smooth and uniform structures. There is no obvious "bead-on-string" morphology visible in any of the images. Each fibre appears to have a constant diameter, although there seems to be a difference in size between the top and bottom of the structure (221.3 ± 48.2 nm and 197.3 ± 20.3 nm, respectively).

The observation of core-shell structure by Ma[25] led us to record scanning transmission electron microscopy (STEM) images of the fibres (Figure 2.1). No core-shell structure is visible in any of the fibres, but there are regions of high- and low-density present throughout them.

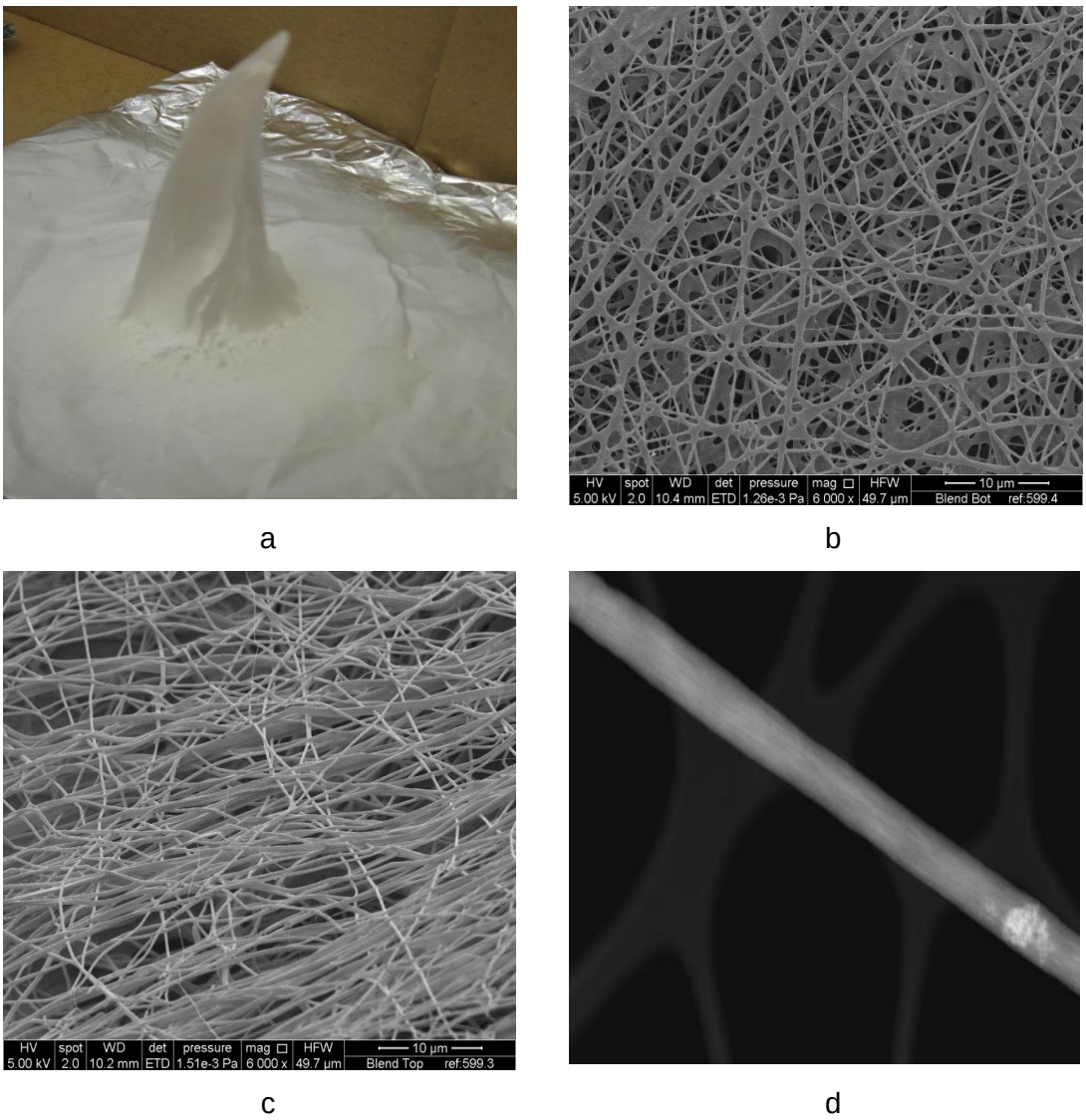

Figure 2.1: Images of the F0 (PEO/SA) fibres. **(a)** Digital photograph; **(b)** SEM images of the base of the 3D structure; **(d)** SEM images of the tip of the 3D fibre network and **(b)** STEM data for a sample collected on a lacey C coated Cu grid.

The PVP (FP) and PVP/SA (FPS) systems resulted in flat mats of fibres being obtained on the collector. The nanofibres have smooth surfaces and almost uniform structures (see Figure 2.2). The average fiber diameter was around 405 nm ± 166 nm and 477 ± 95 nm, respectively.

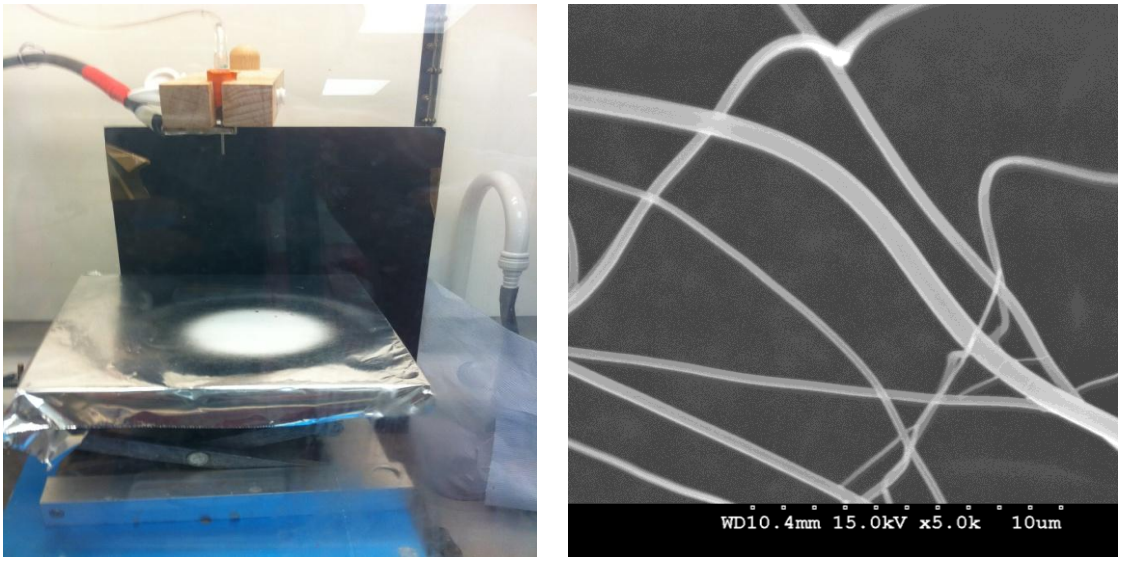

a b

Figure 2.2: Images of the FP fibres **(a)** Digital photograph and **(b)** SEM image.

2.2.2.2. Contact angle study

The contact angle (CA) is a helpful measure to determine the hydrophobic or hydrophilic characteristics of a surface. The most wettable surfaces have low values (Θ <20º) and hydrophobic surfaces have high values (Θ >70º) of the contact angle.[39] The wettability of a surface depends on the nature of the surface, and is influenced by the pH of the solution interacting with.[39–41]

The pure PVP nanofibres (FP) transferred water faster than PVP/SA (FPS) and PEO/SA (F0) (Table 2.2), and a water droplet on their surface exhibited a contact angle below 20º. The FP nanofibres are more hydrophilic than FPS and F0 (both CA > 45º), as a result of FP having more polar groups in its structure (Appendix I).[42,43] However, F0 fibres are seen to be more hydrophilic than FPS. This could potentially be explained by the presence of both SA and PVP at the surface of the FPS nanofibres, while the PEO fibres might have only PEO at their surfaces (this has been suggested before in the literature).[44–46] Measurements were recorded both at the top and bottom of the “mountain” structure, and the CA values observed to be approximately the same, indicating that the fibre mountain has a consistent fibre morphology and composition

throughout. Similar water CA data have previously been reported for PVP/SA blended films .[42,46]

For the first droplet added to F0, the CA was below 50º (Table 2.2). If SA was on the surface, the contact angle would be expected to be higher.[45] The CA of water and ethylene glycol on the F0 fibres were similar to data reported by Çaykara *et al* for 100 % PEO layers.[45] Small differences arising may be due to different PEO molecular weights, the shape of the surface, and the porous structure of the nanofibre mat. From the data presented, it appears that both PVP and SA are present on the surface of the FPS nanofibres. On the other hand, the surface of F0 seems to be mainly composed of PEO, with the SA present inside the fibres.

Table 2.2:Contact angle results of F0, FP and FPS nanofibres.

	Water	**Methanol**	**Ethylene glycol**	**Acidic water**
FP	12.39 ± 3.5	10.42 ± 4.2	11.49 ± 2.5	-
FPS	51.25 ± 2.3	7.84 ± 3.7	40.05 ± 3.4	-
F0 Bottom 1st drop	47.85 ± 2.5	11.97 ± 3.2	35.17 ± 2.6	-
F0 Top 1st drop	47.93 ± 2.1	13.20 ± 2.8	35.2 ± 3.1	-
F0 Top 2nd drop after drying	79.29 ± 1.8	21.16 ± 2.0	47.47 ± 2.1	99.0 ± 1.9

The CA values of the liquids used were evaluated to determine the surface free energy (SFP) components of the nanofibres (Table 2.3). The CA values observed with FPS were different from those of FP only. The FP nanofibres showed a basic (Lewis Acid-Base indices above 50) character but FPS had acidic character (Lewis Acid-Base indices below 50).[47,48] This means that the surfaces of the two sets of nanofibres were composed of different materials, which is due to the presence of acidic SA on the surface of the blend fibres (FPS).[45] The data in Table 2.3 show that the surface of F0 also has a basic character, suggesting that no SA was present.

The CA for the F0 fibres is very different when the first droplet added is allowed to dry and a second is placed on the surface in the same location (Table 2.2). Furthermore, the data in Table 2.3 demonstrate that the surface of the F0 nanofibres changes from basic to acidic after the first droplet was allowed to dry. This is thought to be because the first droplet caused the dissolution of some PEO, exposing some SA at the surface. The CA results thus all indicate that SA is encapsulated by PEO in the F0 fibres .

Table 2.3: Surface free energy components of F0, FP and FPS nanofibres.

	F0 Bottom	**F0 Top 1st drop**	**F0 Top 2nd drop after drying**	**FPS**	**FP**
Method	γ^{tot} [mN/m]	γ^{tot}[mN/m]	γ^{tot}[mN/m]	γ^{tot} [mN/m]	γ^{tot} [mN/m]
Acid-Base	50.95	51.01	25.86	46.51	77.56

A simple visual experiment was carried out to confirm this hypothesis: the as-formed material is white in colour (as is PEO), but when a drop of an acidic solution is placed upon its surface, the PEO dissolves revealing brown SA within (see Figure 2.3).

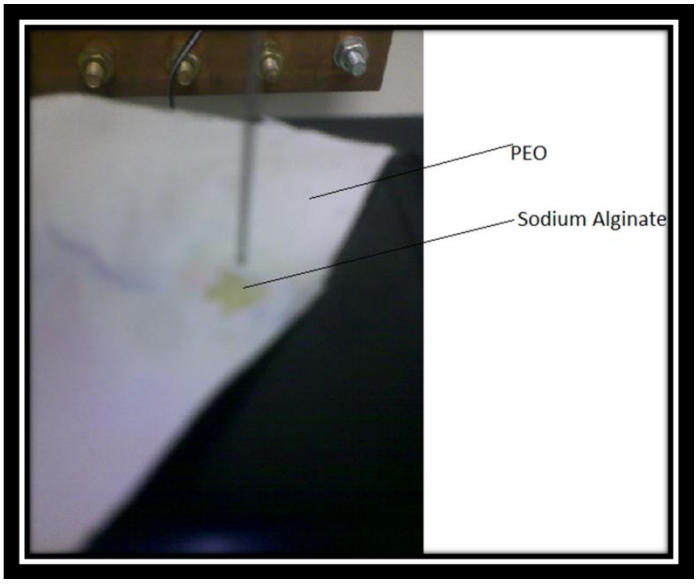

Figure 2.3: Digital photograph of F0 after adding an acidic droplet**.**

In a further experiment to confirm that SA is encapsulated by PEO, F0 was placed in an oven for a few hours at 70 ºC, to let the PEO melt. The PEO melting point is around 69 ºC while SA melts at > 300 ºC (see Section 2.2.3.3). The digital photograph before heating (Figure 2.4a) showed a white colour while after heating the sample is brown in colour (Figure 2.4b,c). Pure PEO does not caramelise after such heating (Figure 2.4d,e). Thus, these visual observations confirm that SA is enclosed by PEO.

Figure 2.4: Digital photographs of F0 **(a)** before heating; after heating at 70 ºC for **(b)** 3 hours and **(c)** 3 days; PEO before **(d)** and **(e)** after heating for 3 h at 70 ºC.

2.2.2.3. X-ray photoelectron spectroscopy

X-ray photoelectron spectroscopy (XPS) is a surface analysis technique, which measures the binding energy of electrons in atoms. It is used to analyse the surface of materials and obtain their chemical composition. Its penetration limit is between 5-10 nm.[47] XPS analyses were used to investigate the F0 fibres, and the results are given in Table 2.4.

The XPS data show that SA has two C peaks and PEO one C peak. The data additionally show that there is only one C peak for F0, and almost no Na is present on the surface of these fibres. This suggests that SA was completely enveloped by PEO, and the thickness of the PEO layer is at least beyond the detection depth of XPS.

Table 2.4: The ratios of C, O, and Na at the surface of raw materials (PEO and SA) and the F0 fibres, calculated from XPS data. Samples were taken from the top of the 3D fibre structure

	C	**O**	**Na**
PEO (Peak position)	42.5 ± 0.3 % (286.3 ± 0.2 (eV))	57.5 ± 0.3 % (532.6 ± 0.2 (eV))	-
SA (Peak positions)	70.3 ± 1.3 % (284.9 ± 0.4 (eV) 286.5 ± 0.3 (eV))	27.9 ± 1.5 % (532.8 ± 0.3 (eV))	1.8 ± 0.2 % (1071.6 ± 0.3 (eV))
F0 (Peak position)	68.8 ± 0.2 % (286.5±0.4 (eV))	31.0 ± 0.2 % (532.0 ± 0.6 (eV))	0.2 ± 0.0 % (1071.6 ± 0.3 (eV))

The data obtained in this work are similar to those recorded by Ma *et al*., and in distinct disagreement with the data reported Bonino *et al*.[24,50] Bonino and co-workers used PEO with a higher molecular weight (600 kDa, while 400 kDa was used in this work), SA with a lower molecular weight (37 kDa *cf.* 120 kDa here) and the ratio between PEO/SA was different to the one used in this study.[24] This presumably affected the surface composition and hence changed the chemical interactions and binding properties.

The sputter depth profile (Figure 2.5) of the top of the 3D F0 fibre structure shows an increase in the concentration of Na moving from the surface to the interior of the fibres, which confirms that SA is enrobed by the PEO.

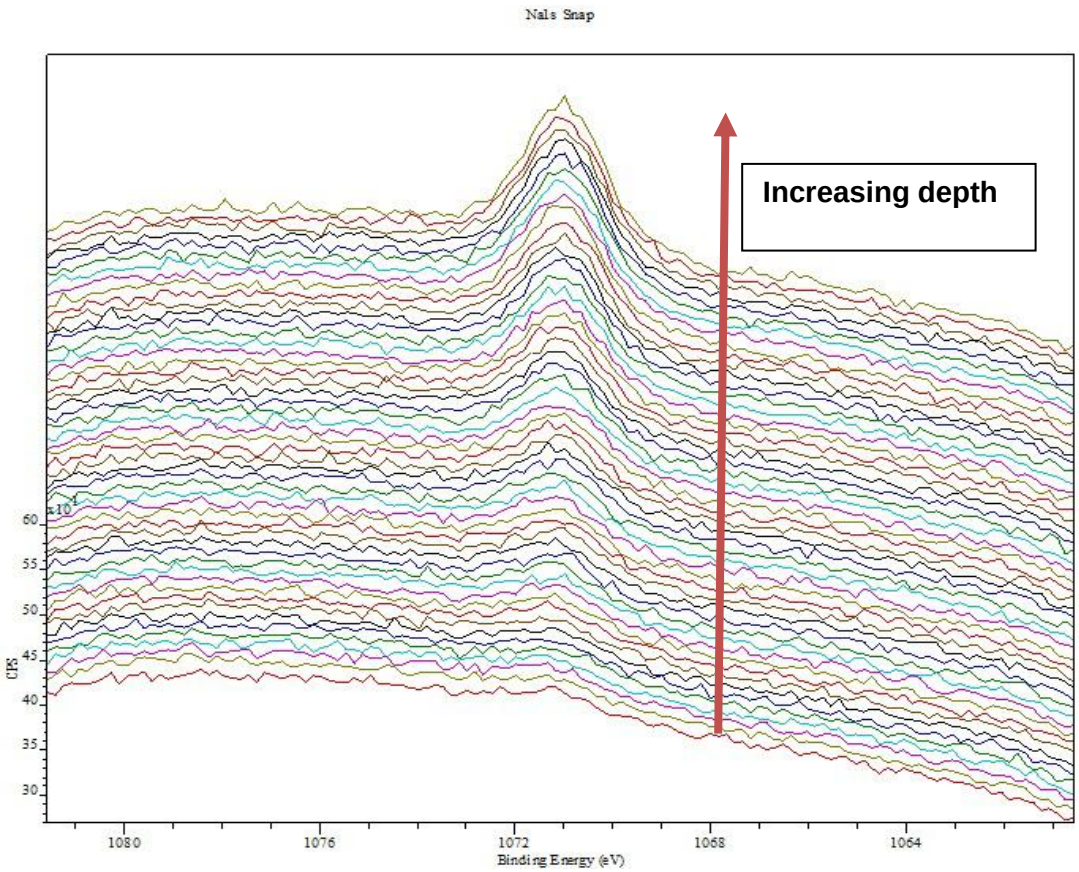

Figure 2.5: The Na depth profile of the top of the F0 fibre structure .

2.2.2.4. Detailed SEM analysis

A sample of the F0 (PEO/SA) fibres was broken, and SEM used to investigate the cross sections of the individual samples. The SEM cross sections (Figure 2.6) shows that the fibres appear to consist of bundles of very small sub-fibres. The latter are estimated to be around 17.5 ± 2.0 nm in size. These small fibres could be SA or blends of PEO/SA.

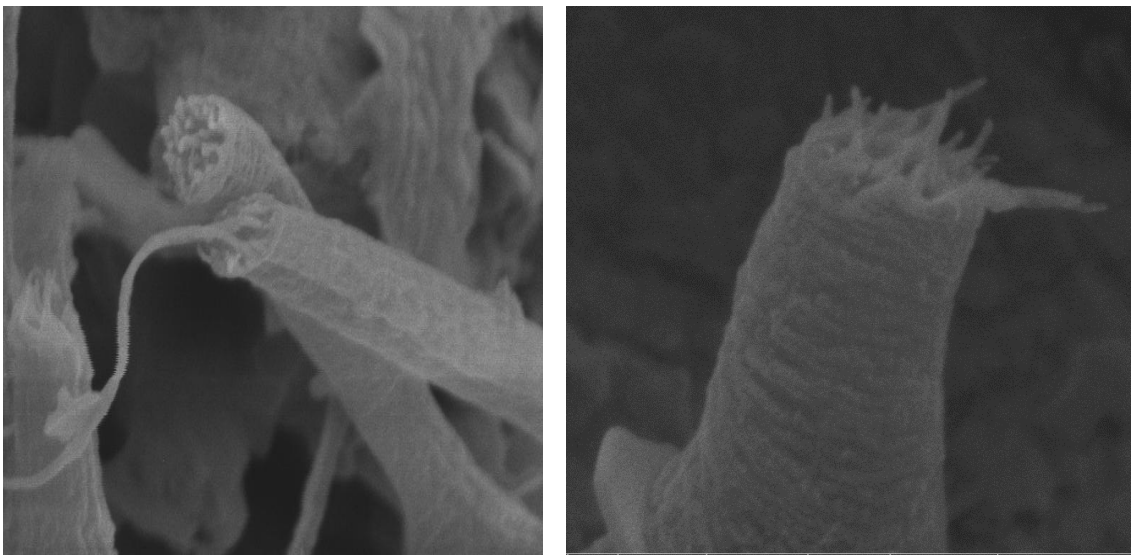

Figure 2.6: SEM images of the cross sections of F0.

There are two simple models which can be conceived to understand how the SA is contained inside the PEO; these are depicted in Figure 2.7. The PEO is white in colour, and as demonstrated in the sections above is essentially the only material present at the surface of the fibres. The SA is brown in colour, and it is not visible at the surface to the eye, or to surface analysis techniques. On the basis of the SEM data, model B in Figure 2.7 is more likely than model A.

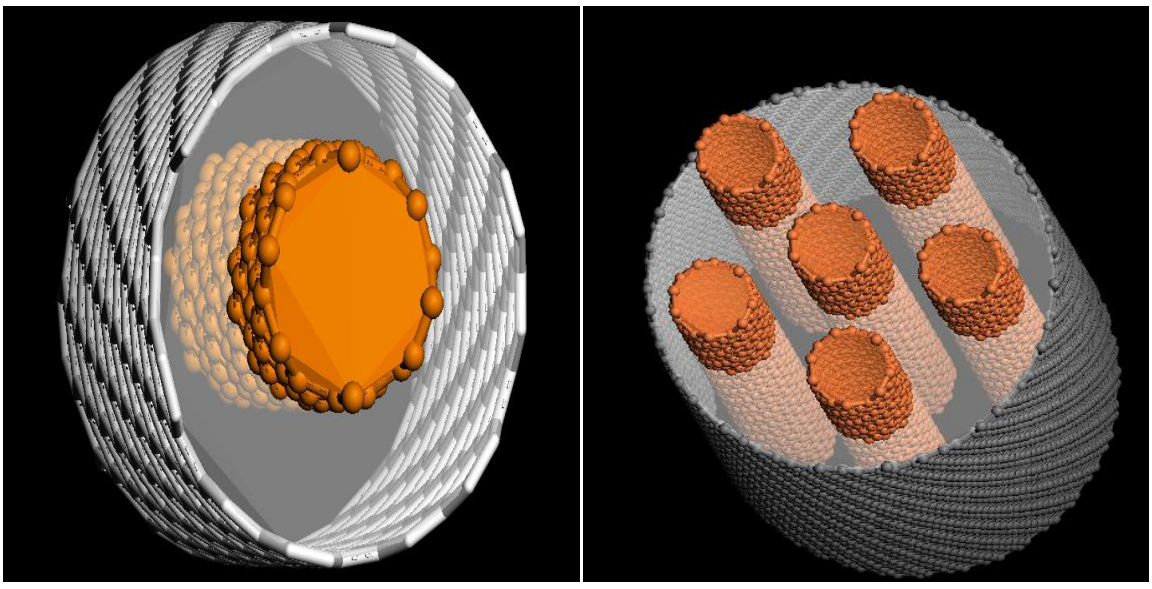

a b

Figure 2.7 : Schematic structures illustrating the possible locations of SA (orange) and PEO (white) in the F0 fibres.

2.2.3. Drug-loaded fibre characterisation

2.2.3.1. Morphology

2.2.3.1.1. Sodium ibuprofen fibres

The SI-loaded fibres Fi10 retained the 3D structure of the drug-free analogue (Figure 2.8a). Each Fi10 fibre appears to have a constant diameter, although there seems to be a difference in size between the top and bottom of the structure (318 ± 53 nm and 233 ± 44 nm respectively). Looking at the outside of the structure, there are no visible particles; however, bisection through the centre reveals a number of small particles inside the structure at its apex (see Figure 2.8C). The diameters of the PEO/SA/SI fibres lie in the order Fi10 > Fi2 > Fi1, there thus appears to be a decline in fibre diameter as the SI content is reduced.

To find out the chemical composition of the crystallites observed at the top of the 3D structure with Fi10, these crystallites were investigated by energy-dispersive X-ray spectroscopy (EDX). The resultant data show that those crystallites are SI particles (see Figure 2.9).The weight ratio of carbon and sodium were close to that calculated for SI (Table 2.5).

The crystallite size is found to be *ca.* 1.3 ± 0.2 μm. Prior to dissolution and electrospinning, the SI particles had sizes of approximately 3.0 ± 1.5 μm (Appendix I) and hence there has been a significant reduction in particle size as a result of the processing.

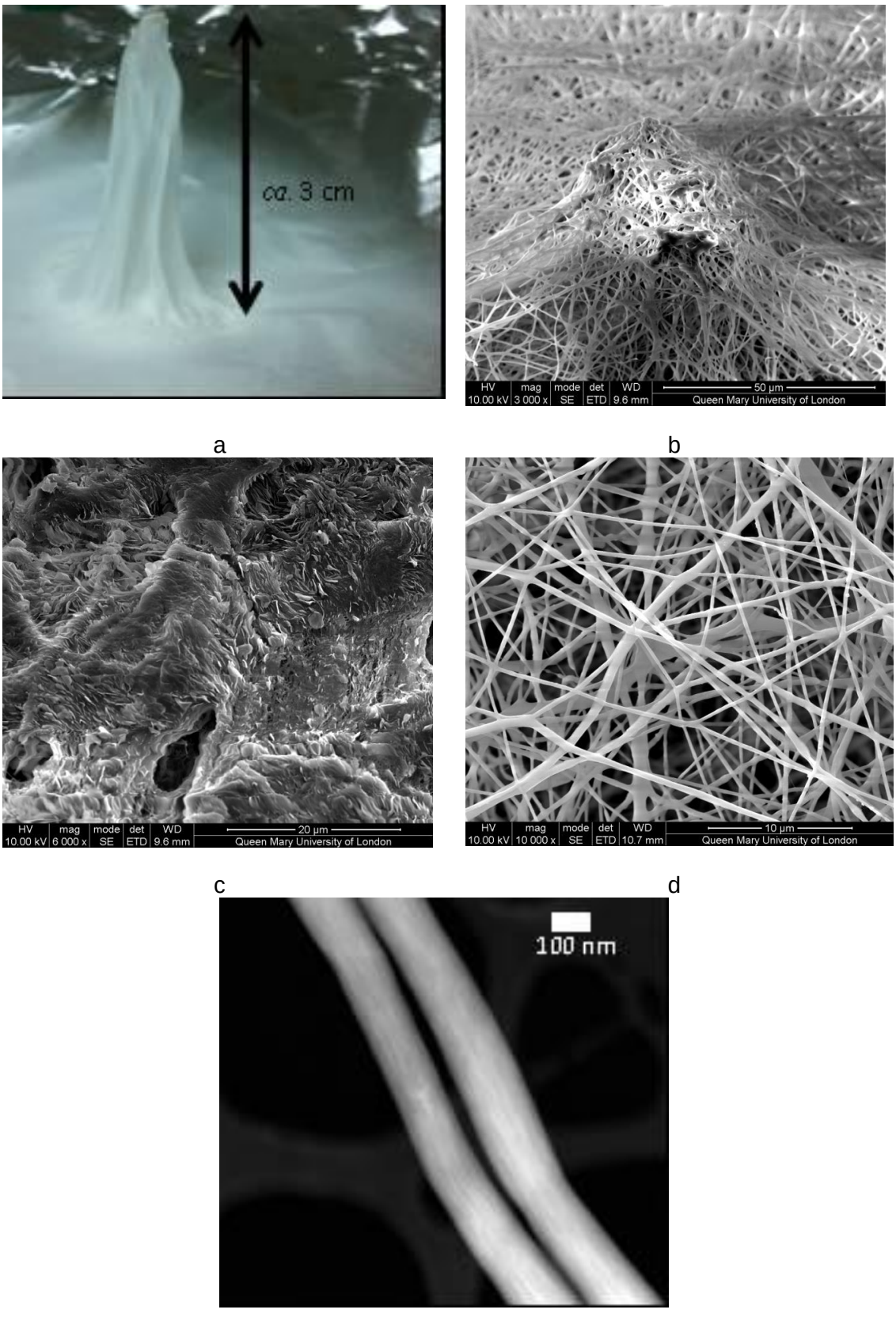

Figure 2.8 : Images of the Fi10 fibres. **(a)** a digital photograph; SEM images of **(b)** the exterior of the tip of the 3D fibre network; **(c)** the interior of the tip of the 3D fibre network; **(d)** the base of the 3D structure and **(e)** STEM data for a sample of Fi2 collected on a lacey C coated Cu grid.

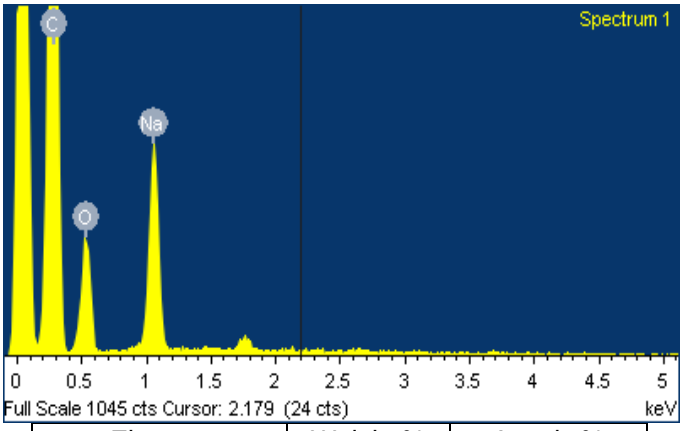

Element	Weight %	Atomic %
C K	67.02	74.41
O K	25.48	21.23
Na K	7.50	4.35
Totals	100.00	

Figure 2.9: EDX data on the crystallites observed in the top of the Fi10 fibres.

Table 2.5: Elements theoretical atomic weight ratio of the SI, SA and PEO.

	C	O	Na
SI	73.93	15.17	10.90
SA	37.70	50.26	12.04
PEO	60.00	40.00	-

2.2.3.1.2. Naproxen sodium fibres

As for the SI fibres, the Nap/SA/PEO materials again formed a 3D mountain structure. The individual fibres had a constant diameter, although as before there seems to be a difference in size between the top and bottom of the structure (432.0 ± 106.7 nm and 351.0 ± 114.4 nm for Fn10) (Figure 2.10). A bisection through the centre of the 3D structure reveals a number of small particles inside (see Figure 2.10a,b). No visible particles could be seen when the concentration of Nap was decreased (Fn1 and Fn2).

The crystallites have rectangular shape with width around 0.4 ± 0.1 μm and thickness of 77.4 ± 24.7 nm (the length could not be measured, since part of the Nap crystallite was inside the fibres). Prior to dissolution and electrospinning, the Nap particles formed agglomerates, as shown in Figure 2.10d.

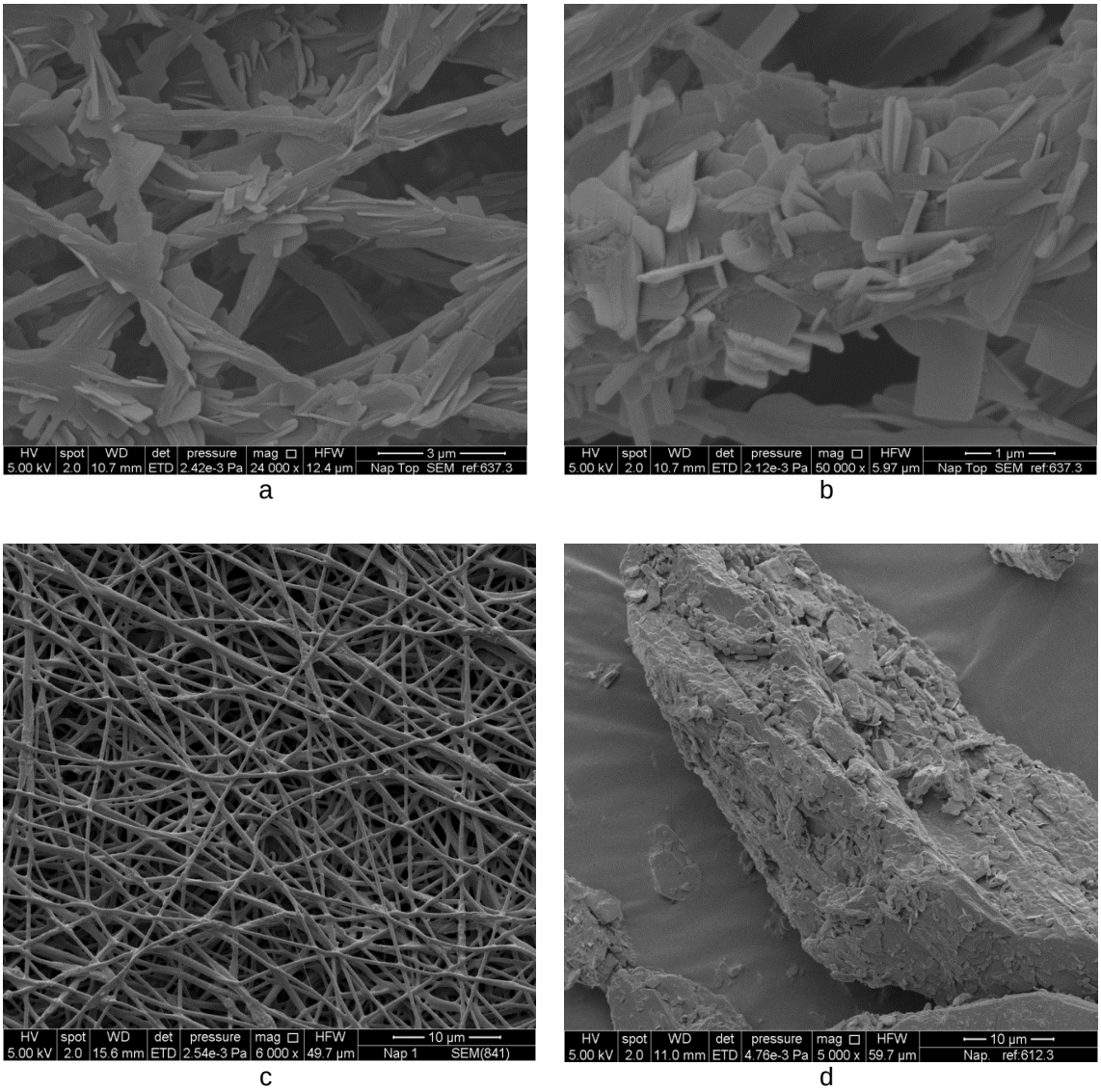

Figure 2.10: SEM images of Fn10 **(a)** the interior of the tip of the 3D fibre network;**(b)** with higher magnefication; **(c)** the exterior of the tip of the 3D fibre network of Fn2 and **(d)** Nap.

2.2.3.1.3. Diclofenac sodium fibres

PEO/SA fibres with Dic also appear individually to have a constant diameter (Figure 2.11), again with a difference in size between the top and bottom of the structure (318 ± 53 nm and 233 ± 44 nm, Fd1). The bisection through the centre of Fd1 reveals the presence of some crystallites (these were difficult to find, however, and many sections were mapped to find them; see Figure 2.11). These have hexagonal shapes with 471.0 ± 164.9 nm diameter and 66.8 ± 5.7 nm width. Increasing the concentration of Dic to obtain higher loading fibres was not possible because this took the drug beyond its solubility limit and led to the spinning solution being less viscous and non-spinnable. Prior to dissolution and electrospinning, the Dic particles formed agglomerates, as shown in Figure 2.11d.

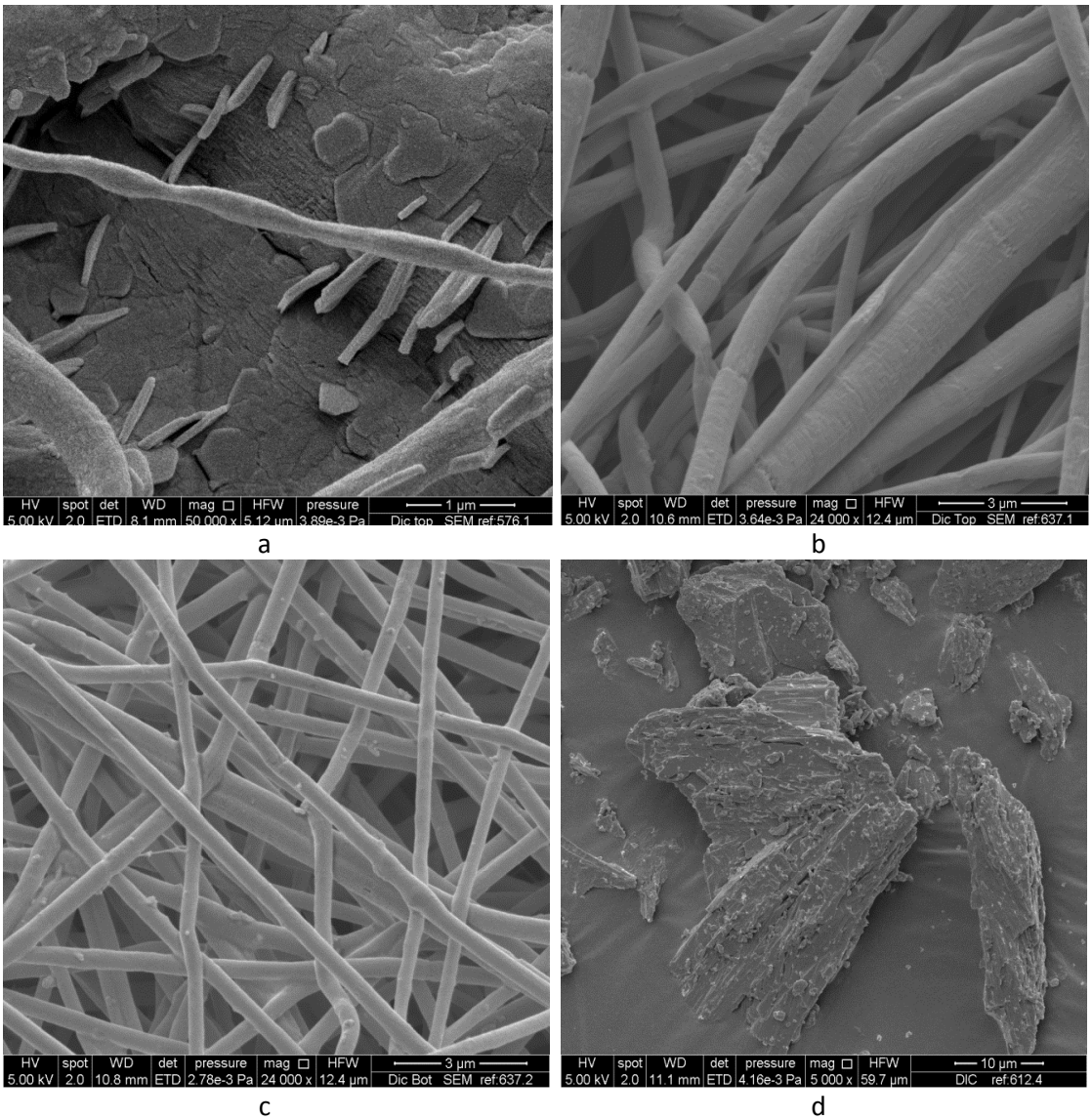

Figure 2.11: SEM images of Fd1 **(a, b)** the interior of the tip of the 3D fibre network**; (c)** the base of the 3D structure and **(d)** Dic.

2.2.3.1.4. Valproate sodium fibres

As for the other samples, the PEO/SA/Val fibres show a small difference in size between the top and bottom of the 3D structure which forms after electrospinning. The bisection through the centre of fibres Fv1, with low concentration, reveals the presence of plain fibres (no crystallites were seen, see Figure 2.12). Higher concentrations of Val (Fv5 and Fv10) led to the disappearance of the 3D structure and only flat mats were obtained.

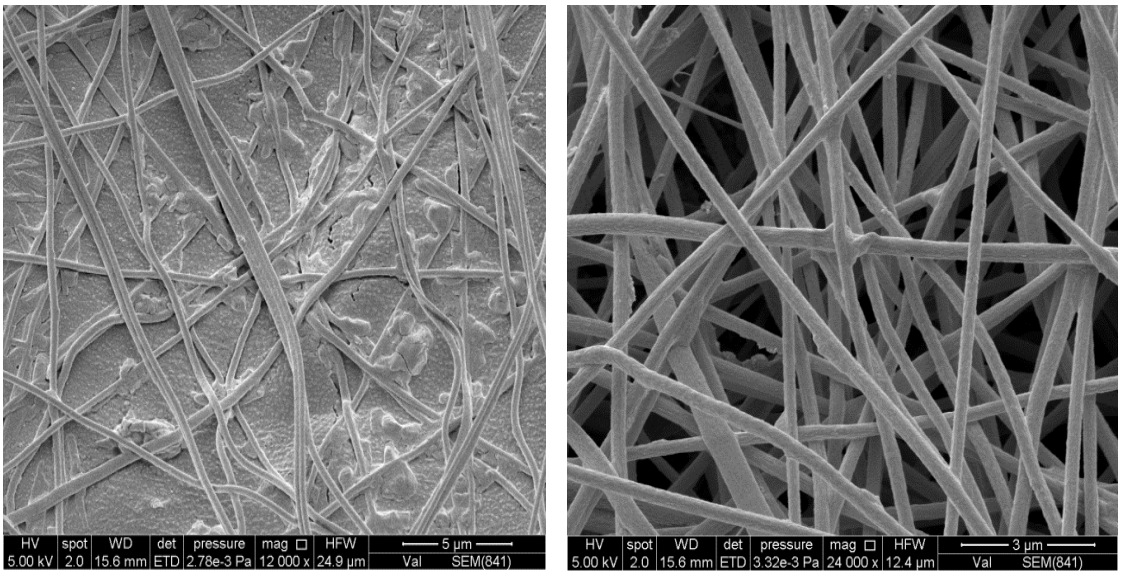

Figure 2.12: SEM images of the interior of the tip of the 3D fibre network the Fv1.

2.2.3.1.5. PVP based fibres

The FPi1 and FPSi1 nanofibres resulted in flat mats of fibres being obtained on the collector. The nanofibres have smooth surfaces and almost uniform structures (Figure2.13). The average fibre diameter was around 400 ± 65 nm and 530 ± 80 nm, respectively. Larger PVP/ibuprofen fibres were previously reported by Yu *et al.*[51]; these differences are ascribed to the previous authors using a higher flow rate and lower voltage.

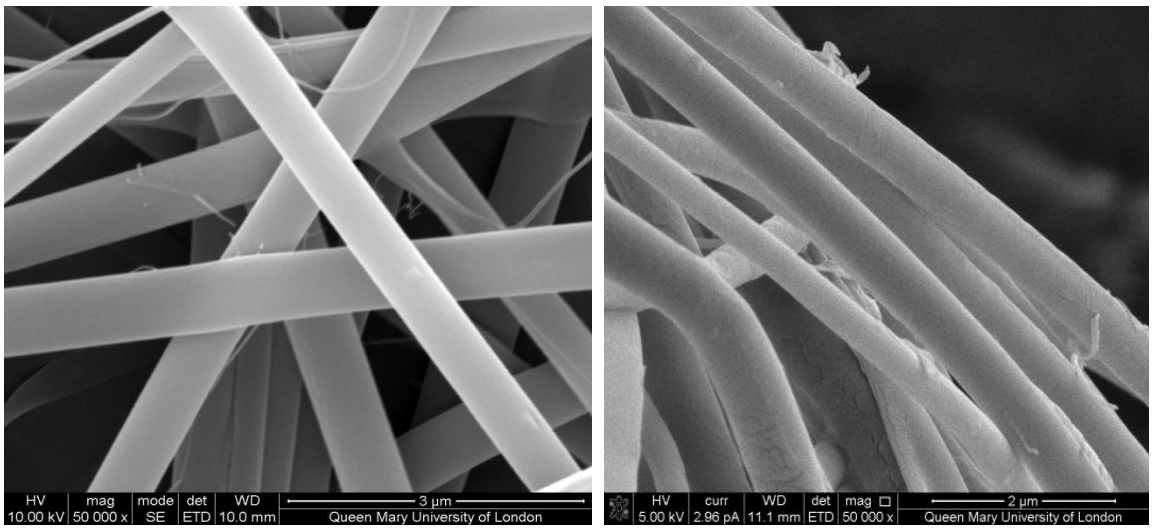

a b

Figure2.13: SEM images of **(a)** FPi1 and **(b)** FPSi1

2.2.3.1.6. Discussion of SEM data

Crystallites were visible only with higher concentrations of drug, and were seen only inside the “mountain” and not outside or on the base of the 3D structure. The SI, Dic and Nap crystallites formed after electrospinning show significant differences in crystal habit and size from the starting materials (Figure 2.8, Figure 2.10 and Figure 2.11). These factors both influence the flowability and solubility of drugs, and thus this processing method could potentially be used to enhance the performance of these active ingredients.[52,53]

2.2.3.1.7. Arrangement of SA and PEO

To confirm the SA and PEO arrangement, a set of fibres were slightly stretched and then examined by TEM and SEM. The SEM images show that there are small fibres inside the nanofibres (Figure 2.14). Their size was hard to measure, since they are very tiny. The estimated Fi10 and Fi2 diameters are around 100.0 ± 13.5 nm and 79.5 ± 12.1 nm, respectively. The TEM additionally

showed small fibres inside the nanofibres, the small fibres has lighter colour than the main nanofibres. This suggests that these small fibres could not be PEO, they might be SA or mixture PEO/SA.

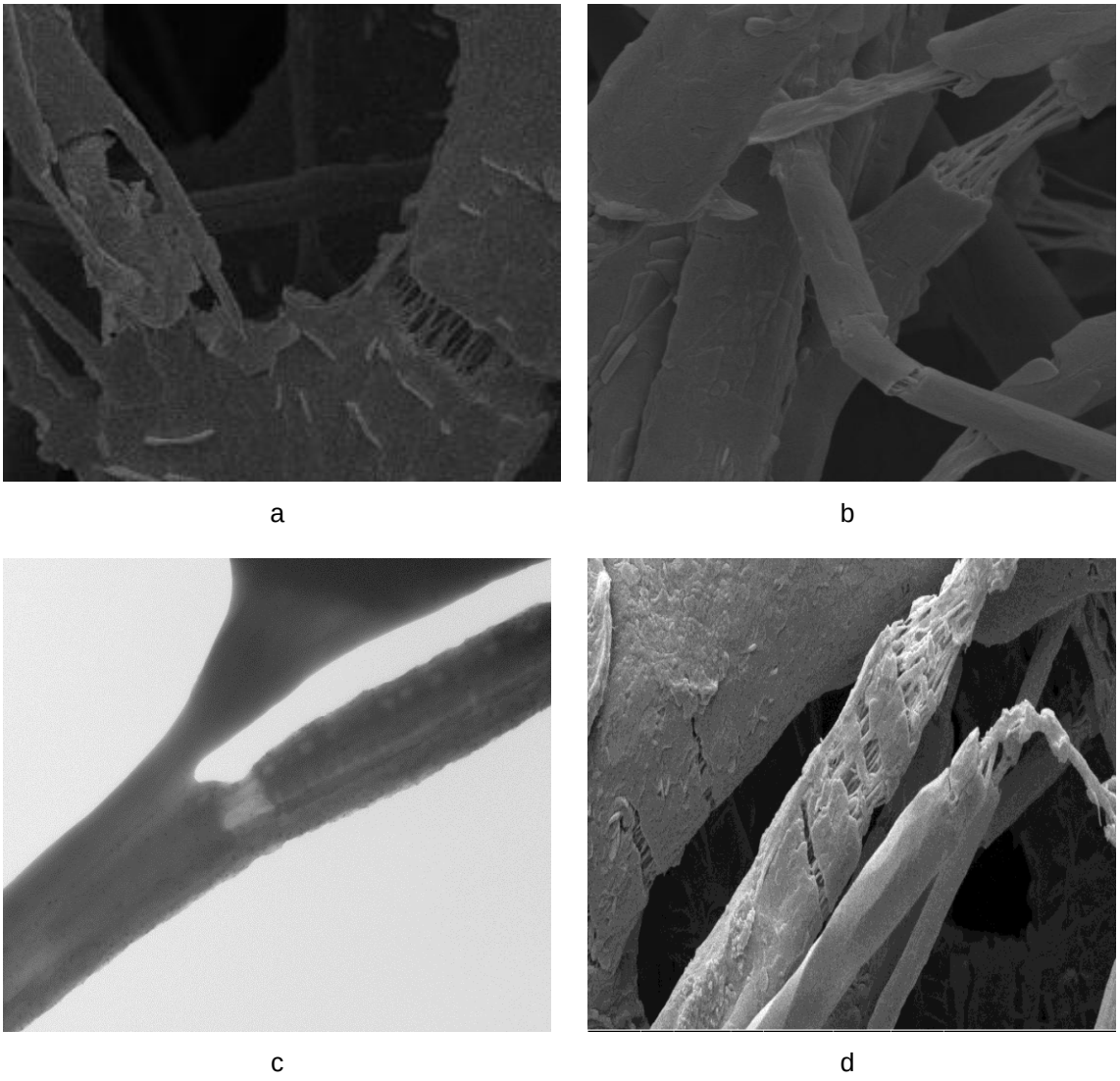

Figure 2.14: Images of nanofibres after stretching **(a)** SEM image of Fi2; **(b)** SEM image of Fi10; **(c)** TEM image of Fi10 and **(d)** SEM image of Fn10

2.2.3.2. X-ray diffraction

X-ray diffraction (XRD) patterns for samples taken from various set of fibres prepared are given in Figure 2.15, together with patterns for the starting materials. PEO is a crystalline polymer, and hence shows two distinct

reflections at 19º and 23º. The four drugs are also crystalline, and exhibit numerous reflections. SA is amorphous (see Appendix I). Both the top and base of the Fi10 structure show the presence of a number of Bragg reflections (see Figure 2.15a). These appear to occur at approximately the same positions as the SI and PEO reflections, although the reflection positions are considerably broadened and also shifted to higher angle. The increased broadness of the SI reflections is consistent with the presence of SI crystallites with reduced size (*cf.* the pure drug) in the fibre structure. The position of the reflections implies that crystallites could be in hydrated form,[54–56] as opposed to the anhydrous starting material.

The Fn10 XRD pattern for the top of the structure (Figure 2.15b) shows a shift of the first reflections from 4.24º to 3.96º and the presence of two new reflections at 7.82º and 11.94º. The base shows same similarity with little bit higher angles. Di Martino *et al.* and Kim *et al.* have reported similar patterns for dihydrated naproxen sodium,.[57,58] while different patterns are seen for the mono-and tetrahydrated forms.[57,59]

The top of the Fd1 structure (Figure 2.15c) shows a small broad reflection at 9.42º and another at 22.00º, merging with a PEO reflection. There is no sign of the intense reflection of anhydrous Dic at 6.56º. By comparing these data to those reported for various hydrated forms, it is thought that Dic could be in the hydrated form.[60–64] The Fv2 (3D structure) shows three broad reflections at 9.55º, 15.17º and 26.43º (Figure 2.15d), which disappear with the 3D structure when the concentration of Val was increased (Fv10). Similar values were reported for hydrated Val crystals,[65] also suggesting that Val might exist in a hydrated form in the 3D structure. The reflections of Fv10 peaks were comparable to those of pure Val.

The XRD patterns of FPi1 (PVP/SI) and FPSi1 (PVP/SA-SI) (Figure 2.15e) are characterised by the complete disappearance of SI peaks. This means that the drug is present in its amorphous form in these systems.

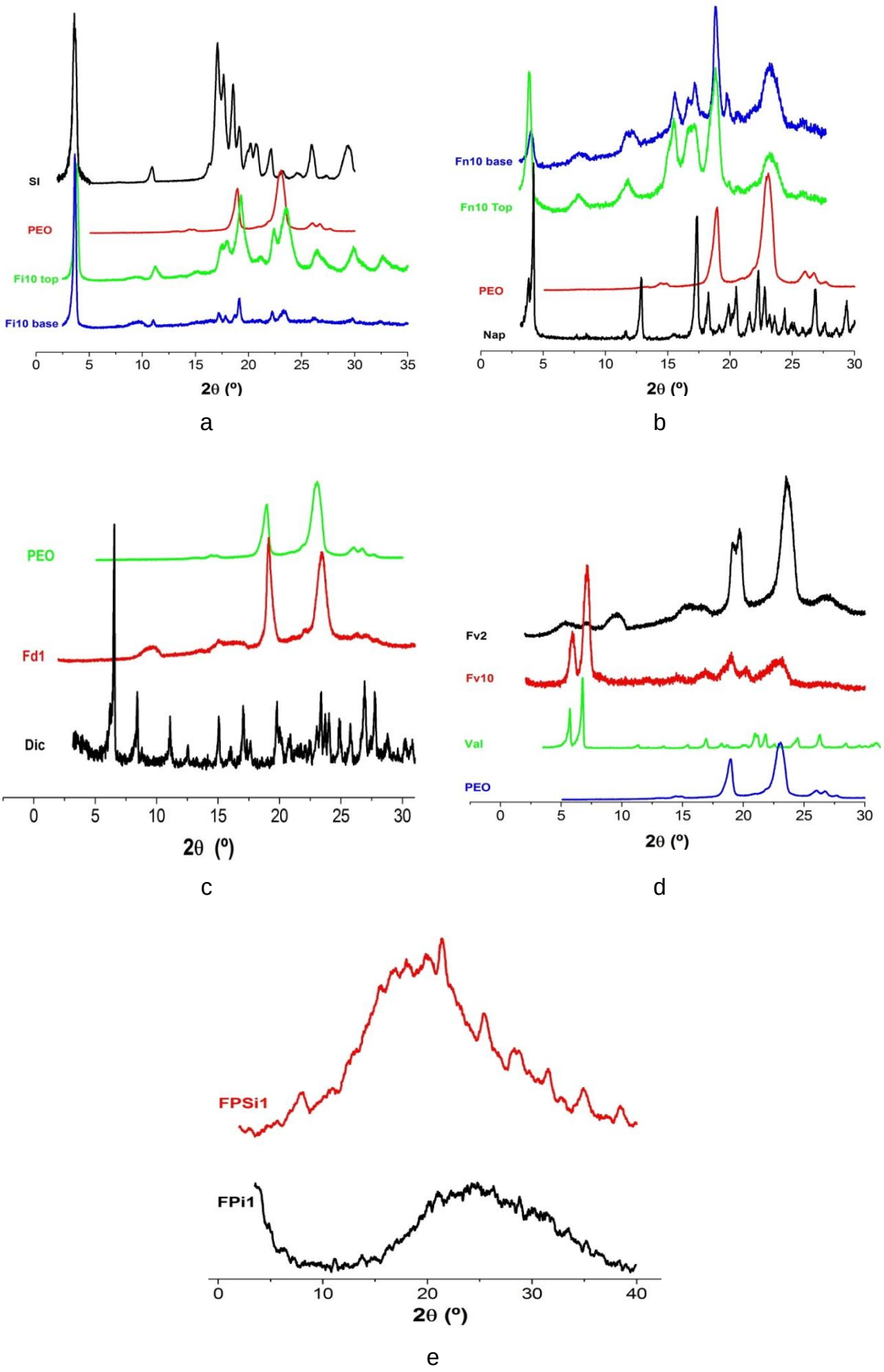

Figure 2.15: XRD patterns of of **(a)** Fi10,PEO and SI;**(b)** Fn10, PEO and Nap; **(c)** Fd1 PEO and Dic; **(d)** Fv2 and Fv10 with PEO and Val and **(e)** FPi1 and FPSi1.

2.2.3.3. Differential scanning calorimetry

Differential scanning calorimetry (DSC) traces of the raw PEO reveals a melting endotherm peak at 69.3 ºC (Figure 2.16). The data in Figure 2.16 show the presence of crystalline PEO in the F0 fibres, with a decrease in the melting point. The decrease in the melting point is related to the ratio of PEO/SA, with an increasing SA concentration causing a lower melting point. It has previously been reported that the PEO melting point goes down as the SA concentration increases in PEO/SA fibres.[66] The broad endothermic peak at around 80 ºC corresponds to the loss of water (incomplete evaporation of the water solvent used for electrospinning will result in some being incorporated into the nanofibres). The nature of the last peak around 144 ºC remains unclear, but it could be related to another dehydration of the SA.[67] SA melts at T > 300 ºC, and hence is not seen in the DSC traces.

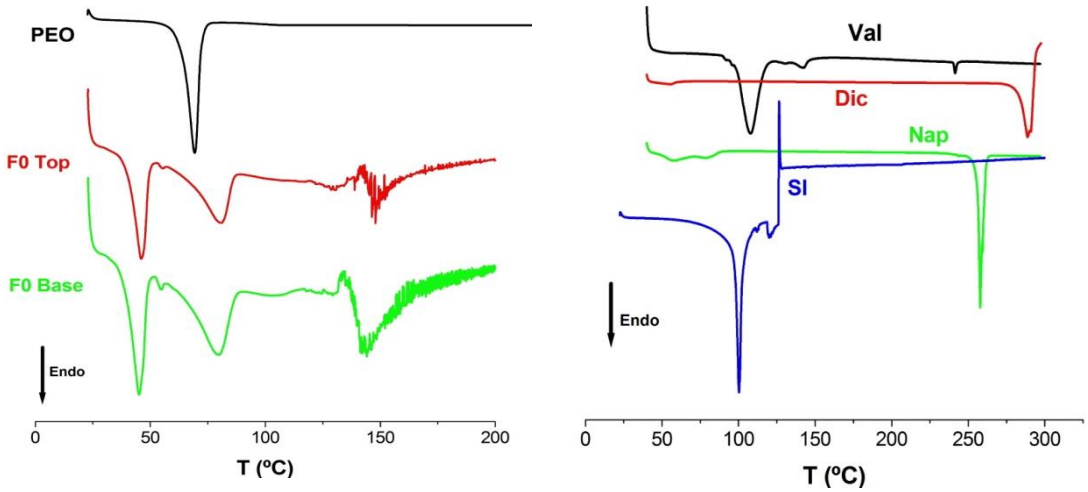

Figure 2.16: DSC curves of **(a)** the top and base of the F0 fibres and PEO and **(b)** pure Val, Dic, Nap and SI.

The DSC data for Fi10 and Fi2 can be found in Figure 2.17. The data confirm the presence of crystalline SI and PEO in the nanofibres. The traces exhibit a sharp endotherm at 62–63 ºC, attributed to the melting of PEO. It is thus clear that the PEO retains its crystalline nature even after the incorporation of SI into nanofibres. A second sharp endotherm is visible at 92.5–93.5 ºC; this latter feature is superimposed on a broad endotherm with an apex at ca. 105–110 ºC. These two features are respectively believed to correspond to the SI melting peak and the loss of water. The nature of the last peak around 190 ºC (Fi10 top 188.0 ºC and Fi10 base 189.3 ºC) remains unclear; it might correspond to the melting of SI hydrate (this is reported to melt at 105 and 208 ºC).[68] The decline in SI melting point could be attributed as well to the diminishing of particles size from 3.0 ± 1.5 µm to 1.3 ± 0.2 µm, since it is known that the melting point is correlated with particles shape and size.[69–73] Alternatively, the presence of polymers (PEO and SA) could cause this effect. There is a small exothermic peak around 230 ºC, which is discussed in more detail below.

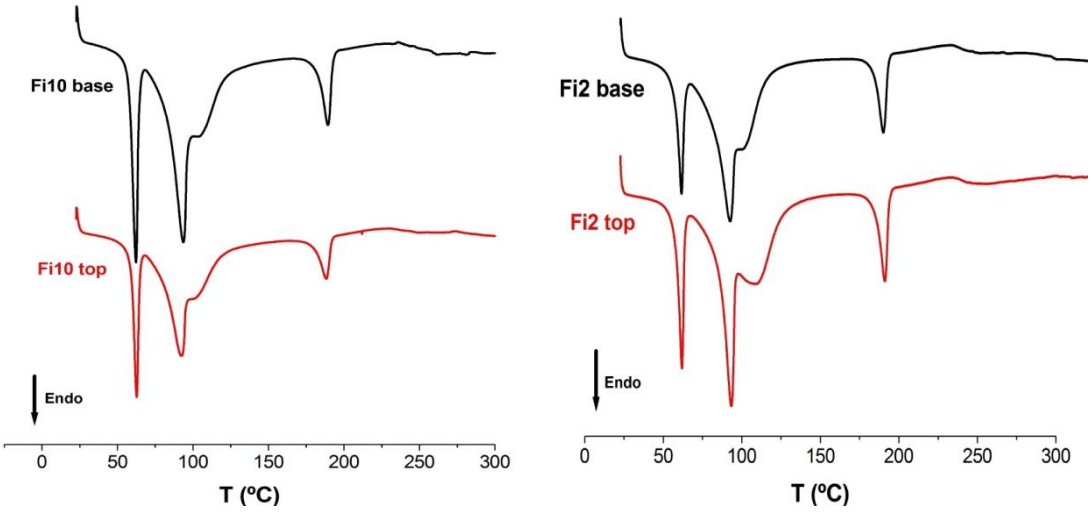

Figure 2.17: DSC thermograms of **(a)** Fi10 top and base and **(b)** Fi2 top and base.

DSC thermograms of the Nap system Fn1 showed melting of PEO at 62.2 ºC, followed by water loss (Figure 2.18). No Nap melting point could be seen and only a broad exothermic peak is detected around 226.2 ºC. On the other hand, the higher drug-loaded Fn5 showed endotherms centred at 134.6 and 224.1 ºC,

which could be due to water evaporation and Nap melting, respectively. DSC traces of the raw material reveal that Nap melts at 257.8 ºC (Figure 2.16). The decline in Nap melting point could be attributed to the diminishing of the particle size, shape uniformity and hydrated form. Nap crystallites showed even lower melting point than hydrate Nap crystals reported in literature, which have melting point around 244-255 ºC.[57,58]

The DSC data for Fd1 is depicted in Figure 2.18. Again a clear PEO melting endotherm is visible at 60.8 ºC. The exothermic peak around 226.0 ºC could be a polymorphic transition or decomposition.[74,75]

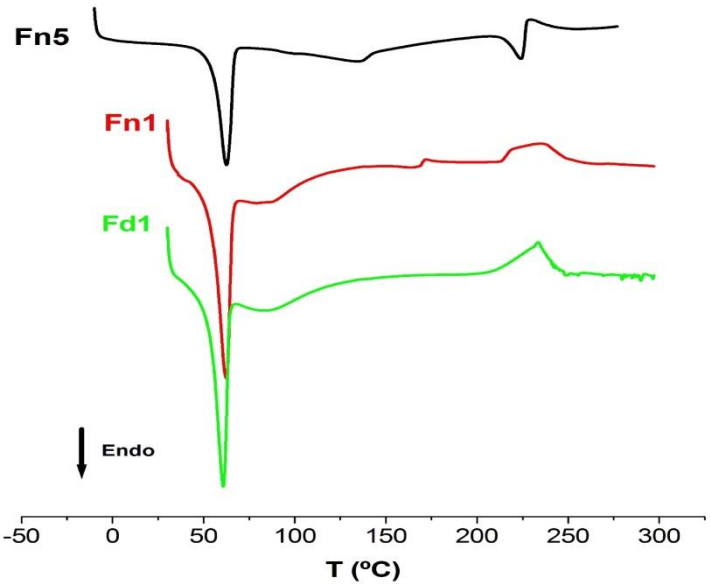

Figure 2.18 : DSC thermograms of Fn5, Fn1 and Fd1

The DSC Data for Fv10 and Fv2 can be found in Figure 2.19. Fv2 shows similar patterns to Fn1 and Fd1. Fv10 formed a flat mat, and showed different thermal behaviour compared to Fv2 (3D structure). The traces exhibit a sharp endotherm at 61.0 ºC, attributed to the melting of PEO, in addition to small endothermic peaks located at 70.3, 99.1, 116.7, 132.5 and 229 ºC.DSC traces of the raw material reveal melting endotherms for Val at 107.9, 130.5, 142.2 and 241.4 ºC. The peak at 70.3 ºC could be attributed to water loss and the rest to the drug. All the Val peaks in Fv10 have shifted to lower temperature compared

to the pure drug. The Val crystallites in Fv2 and Fv10 are completely different in their DSC signals, which is in agreement with XRD data. Fv2 and Fv10 show different thermal behaviour compared to the reported literature.[76]

DSC thermograms of the FPi1 and FPSi1 nanofibres (Figure 2.19b) showed broad endothermic peaks ranging from 30 to 130 °C, with no clear melting endotherms present. This suggested that the drug is no longer present in its crystalline form and was converted into an amorphous state.[51] The DSC data hence confirm the XRD and SEM analysis.

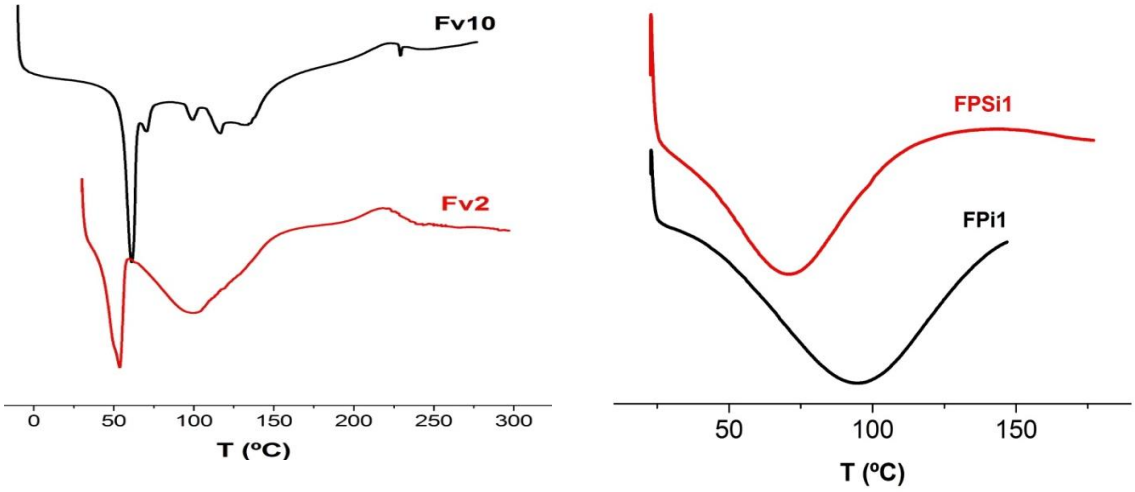

Figure 2.19: DSC thermograms of **(a)** Fv2 and FV10; **(b)** FPi1 and FPSi1.

2.2.3.4. FTIR spectroscopy

2.2.3.4.1. PEO/SA system

FTIR spectra for Fi10, PEO, SA and SI are included in Figure 2.20. The spectrum of SI contains distinct peaks around 3000–3500 cm^{-1} (H-bonded OH stretches, arising from the presence of some water in the material), 3000–2850 cm^{-1} (alkane C-H stretches), and characteristic peaks at 1545 and 1408 cm^{-1} (respectively asymmetric and symmetric carboxylate stretches). The SA spectrum also shows a broad band from *ca.* 3700–2850 cm^{-1}, corresponding to

H-bonded OH groups and C-H stretches. Carboxylate peaks can be seen at 1589 and 1403 cm^{-1}, and C-O vibrations are at 1020 cm^{-1}. The PEO spectrum has a distinct peak at *ca.* 2875 cm^{-1} arising from C-H stretches, and the C-O stretch is centred around 1095 cm^{-1}. The spectra recorded from the top and bottom of Fi10 are essentially identical, and contain features from each of the component molecules. A broad feature from 3500–3000 cm^{-1} arises from H-bonded OH groups, and peaks at 2950 and 2875 cm^{-1} from the SI and SA alkyl C-H peaks. The SI carboxylate groups are visible at 1549 and 1408 cm^{-1}. Although the latter has not moved, the asymmetric stretch has shifted in wavenumber, indicating the existence of interactions between SI and the other components of the fibres. The PEO C-O stretch is seen at 1095 cm^{-1}.

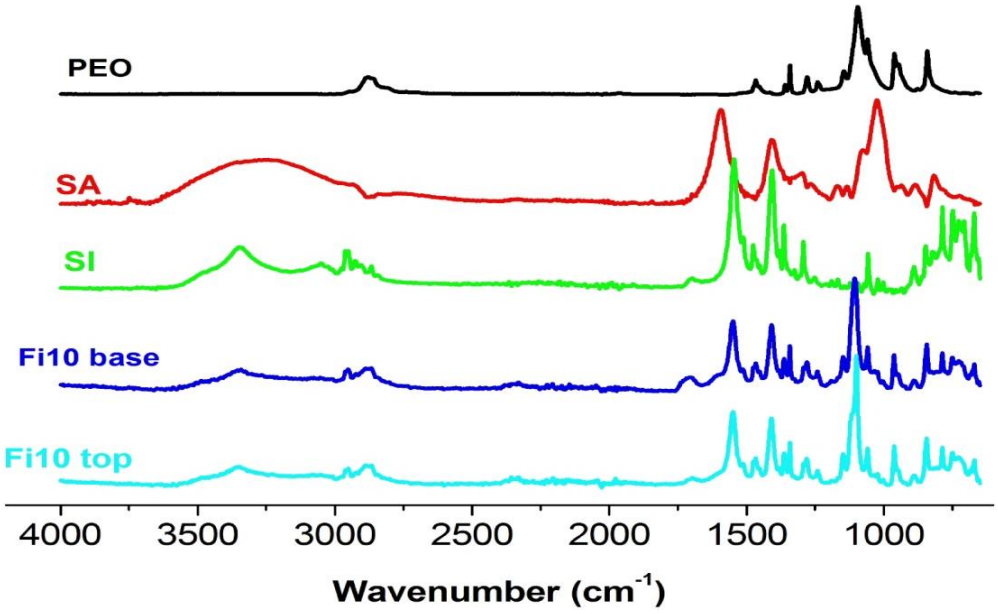

Figure 2.20: IR spectra of the Fi10 fibres and associated starting materials.

Overall, therefore, the IR data indicate the successful incorporation of all three components into the fibres, and suggest that SI is interacting with the other components, most likely through the formation of H-bonds. The IR spectra of the other PEO/SA/SI materials show largely analogous features, confirming the successful formulation of fibres containing all three components intact.The IR spectra for the other drugs also display analogous features: all the characteristic peaks of the drug ions are present after electrospinning, and demonstrate that the intact drugs are successfully loaded into the nanofibres.

2.2.3.4.2. PVP and PVP/SA systems

The spectra of the PVP-based nanofibres (Figure 2.21) showed bands at 2950 cm^{-1} (C–H stretch) and 1640 cm^{-1} (C=O). A very broad peak centred at 3407 cm^{-1} corresponds to the presence of H-bonded OH groups of water. These results are similar to the findings reported by Yu *et al*. [51] The comparison between the spectra of the drug, PVP, and PVP/SI showed shifts in the peaks of the carboxylate anions to higher wave numbers. The carboxymethyl groups appearing at 1327 cm^{-1} for SI and 1330 cm^{-1} for PVP were fused together in a band at intermediate wavenumber for the composite fibres. These peaks also diminished in intensity, which suggests that there hydrogen bonds formed between the C=O of PVP and the OH groups of SI.[51] The characteristic peaks of SA are $–COO^-$ (1553 cm^{-1} and 1412 cm^{-1}) and –C–OH (O–H stretching vibration at 3450 cm^{-1}, C–O stretching vibration of secondary alcohol at 1023 cm^{-1}, C–O stretching vibration of tertiary alcohol is 1082 cm^{-1}).[77] A comparison between the spectra of the FPi1 and FPSi1 (Figure 2.21) showed similar features except that the PVP/SA-SI system showed two extra peaks, at 1548 and 1418 cm^{-1}, which are assigned to asymmetric and symmetric stretching peaks of SA carboxylate groups. The SI peaks diminished in intensity, again suggesting that hydrogen bonds form between C=O and OH groups in the three-component systems. The spectra of raw materials PVP and SA are shown in Appendix I.

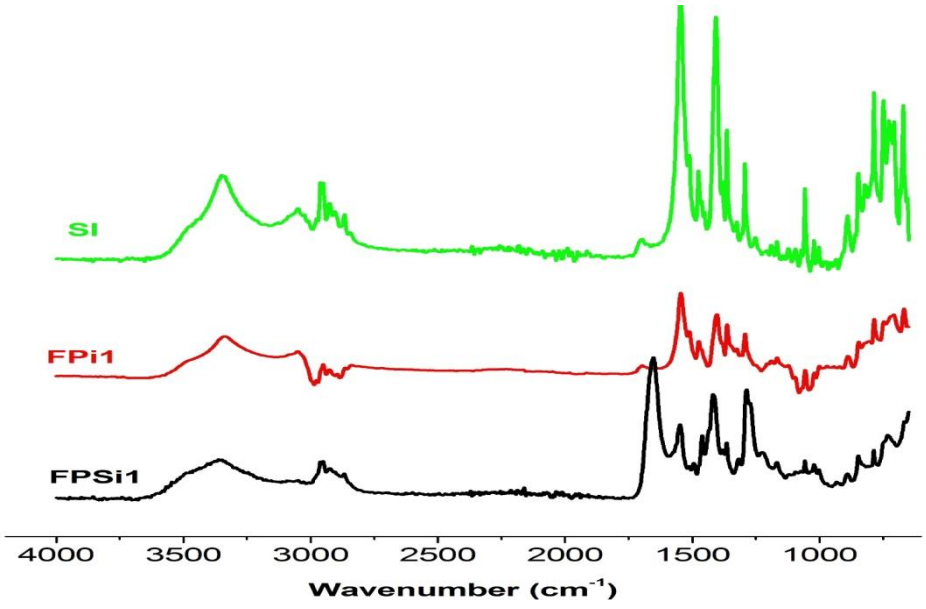

Figure 2.21: The IR spectra of SI, FPi1 fibres and FPSi1 fibres.

2.2.3.5. X-ray photoelectron spectroscopy

XPS spectra of selected fibre materials were recorded. The C 1s spectra of the fibres were then peak fitted using the C 1s spectra of the starting materials as reference spectra to determine the relative amounts of SI at the fibre surfaces. The results of this analysis are given in Table 2.6. The fractions of the surface comprising SI are, within the error of the measurements, identical to those calculated from the weight ratios of the components. The XPS spectra were recorded for Fd1 and Fv1 also (Appendix I).

Table 2.6: The ratio of SI at the surface of the fibres, calculated from XPS data.. Samples were taken from the top of the 3D fibre structure

Fibre ID	% SI in fibre (w/w)	Drug Surface composition (%)
F0	0	0
Fi1	13.3	12.0 ± 2.5
Fi2	23.5	24.3 ± 1.5
Fi10	60.6	60.3 ± 3.0

2.2.3.6. High-performance liquid chromatography

The drug loading into the fibres was verified by high-performance liquid chromatography (HPLC), and found to be 100 % within the error of the measurement. For Fi10, the values observed were 101 ± 2.1 % for the top of the fibre structure and 99 ± 1.7 % for the base (Figure 2.22). The chromatogram of the top of Fi10 showed an extract peak at 1.76 min, however. This fraction was isolated and investigated by NMR; the details of the study are below.

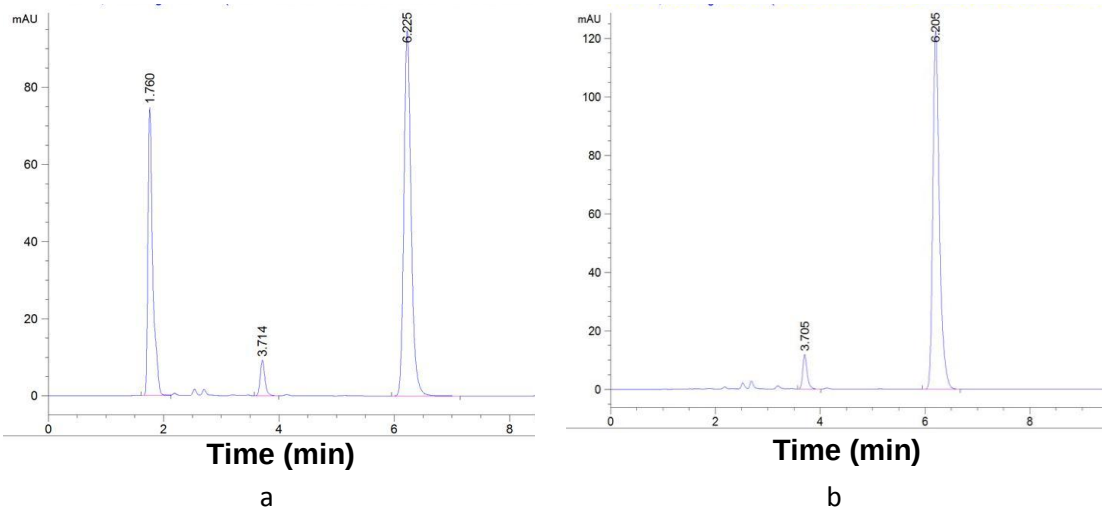

Figure 2.22: Chromatograms of Fi10 **(a)** top and **(b)** base.

2.2.3.7. NMR spectroscopy

NMR spectroscopy was performed on samples of the fibre mats dissolved in D_2O. The ^1H NMR spectrum of SI exhibited the following resonances: at 0.9 ppm corresponding to the methyl protons of the isobutyl group; at 1.39 ppm, ascribed to the α-methyl protons; at 2.47 ppm, originating from the methylene adjacent to the phenyl group; at 1.83 ppm, arising from the methine proton of the isobutyl moiety; at 3.62 ppm, due to the α-methine proton; and at 7.24 ppm, resulting from the four benzene protons (Figure 2.23). The spectra after dissolution of the fibres are observed to contain all the features of the SI starting material, confirming that the structural integrity of SI molecule is retained after electrospinning (Figure 2.23). The resonances from 3.57 to 3.72 ppm correspond to PEO and SA. The spectra after dissolution of the fibres are observed to contain all the features of the Dic, Nap and Val starting materials, confirming that the structural integrity of drugs molecule is retained after electrospinning.

The ^{13}C NMR spectrum of 1.76 min fraction isolated from HPLC reveals that contains carbonate. The origin of the carbonate is not certain, but it is expected to arise from the water used for the experiments or the air.

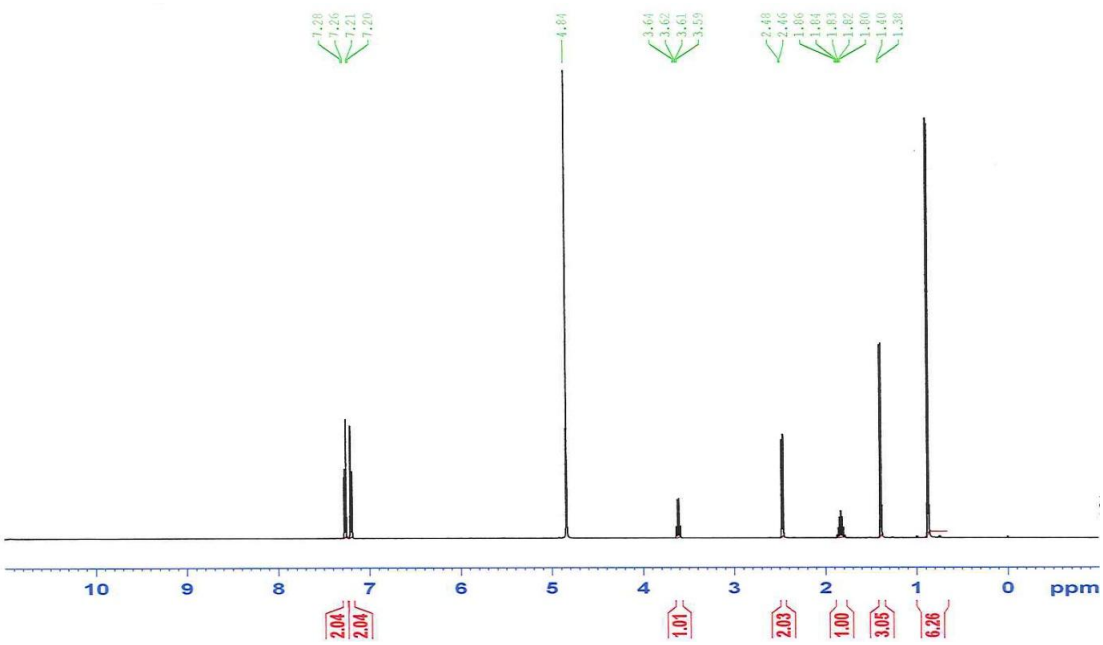

a

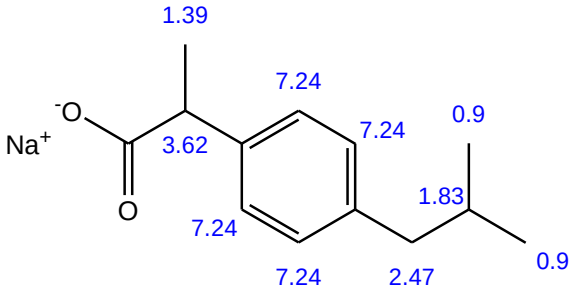

b

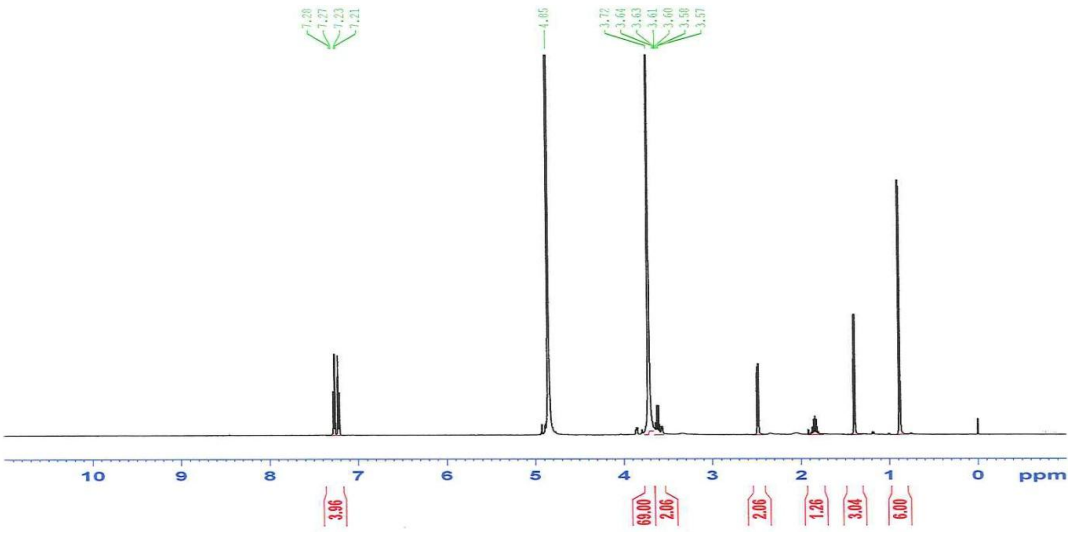

c

Figure 2.23: ^{1}H NMR spectrum of SI **(a)**, chemical structure with details of the resonances **(b)** and ^{1}H NMR spectrum of Fi10 **(c)**.

2.2.4. Drug release

Since the four drugs remain intact after spinning, the fibre structures may have utility as drug delivery systems. Dissolution tests for the formulations have been carried out under experimental conditions as close as possible to the gastrointestinal tract and following pharmacopeia requirements.[78] The fibres were placed in 750 mL of 0.1 N hydrochloric acid in a vessel held at 37 ± 0.5 ºC and stirred at 50 r.p.m. After 2 hours, the pH of the medium was adjusted to 6.8 ± 0.1 by adding 250 mL of 0.20 M tribasic sodium phosphate. Experiments were carried out for 22 h at this pH. All the experiments were carried out in darkness (except for Val, because manual sampling was required). Dissolution tests were carried out in triplicate from the various sets of fibres in an automated apparatus (equipped with autosampler and inline UV spectrometer) to monitor release from the formulations which had a UV chromophore. A different protocol for Val was required: since it does not have a distinct UV chromophore, manual sampling was required, and HPLC used to measure the amount of Val released.

At pH 1.0, which mimics the stomach, there is a very rapid burst release of SI within the first 5–60 min after the fibres are added to the release medium. The amount of drug released in this stage is dependent on the SI content of the fibres, with a greater burst release being seen as the SI loading increases. There is then a plateau in which no further drug is released, and after the adjustment of pH to 6.8 (mimicking the pH of the intestine), the rest of the SI is freed rapidly from the fibres at an almost linear rate (Figure 2.24a). The Fi1, Fi2 and Fi10 fibres thus comprise time-controlled drug delivery systems, where there is an “on/off” pattern of drug release (bursts of release with a lag period between them).

In contrast, in the pH 6.8 buffer, fast SI release over *ca.* 15 min is seen (Figure 2.24b), with essentially identical release profiles regardless of the SI loading in the fibres. By appropriate selection of the fibre composition it would be possible to deliver a desired loading dose of drug in the stomach, with the remainder retained in the fibres for longer than the typical stomach transit time

(2 h), permitting release in the intestinal tract. The percentage of SI released in the first stage is approximately the same as the w/w percentage of SI in the fibres, meaning it would be facile to design materials to release a given amount of SI in the stomach. Colon-targeted delivery of SI is hence possible with these systems.

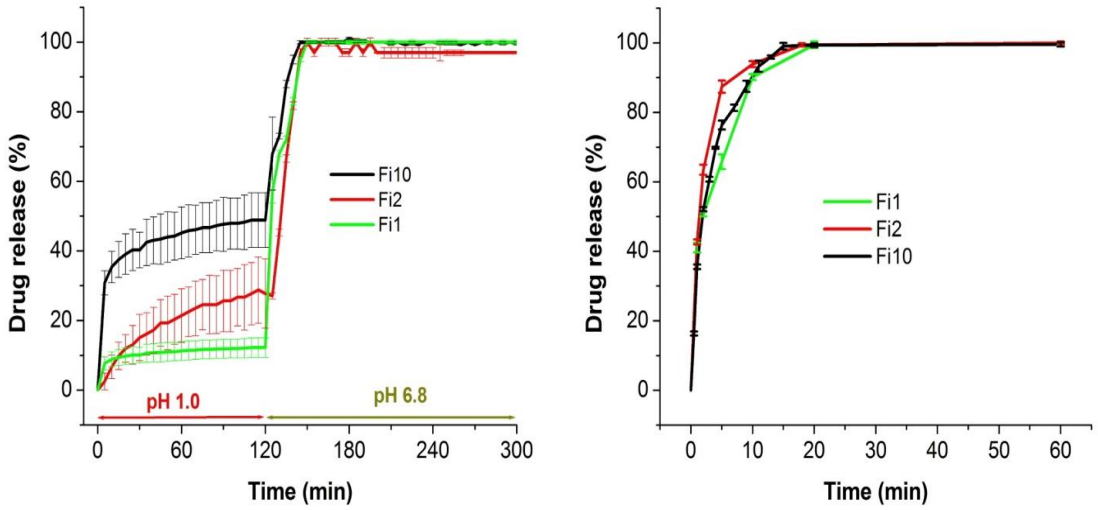

Figure 2.24: SI release at **(a)** pH 1.0 and 6.8 and **(b)** pH 6.8 from the Fi10, Fi2 and Fi1 nanofibres; these contain respectively 60.6, 23.5, and 13.3 % w/w SI. Three independent experiments were performed (each with a separate fibre mat), and results are reported as mean ± S.D.

The drug release from Fd1 and Fv1 nanofibres showed similar patterns to the Fi nanofibres (Figure 2.25), although with different amounts of release in the low pH conditions. A summary of the results is given in Table 2.7. Once the pH was adjusted, the Fv1 and Fd1 released their remaining loading. The XPS data (Appendix I) show that the surfaces of Fd1 and Fv1 contain 10 % Dic and 46.3 % Val, respectively. All the XPS data (Fi10, Fi2, Fi1, Fd1 and Fv1) are in agreement with drug release, where approximately these amounts of drug release are seen at pH 1. It seems that the amount released during the first stage is influenced by the amount of the drug on the surface of the nanofibres. The latter appears to have a close relation with solubility (Val > SI > Dic).[79–81]

Table 2.7: Summary of drug release from Fd1, Fi1 and Fv1.

Time	Drug release %		
	Fd1	**Fi1**	**Fv1**
After 15 min	5.1	9.4	40.0
After 120 min	9.1	12.2	60.4
After 180 min	85.8	100	100

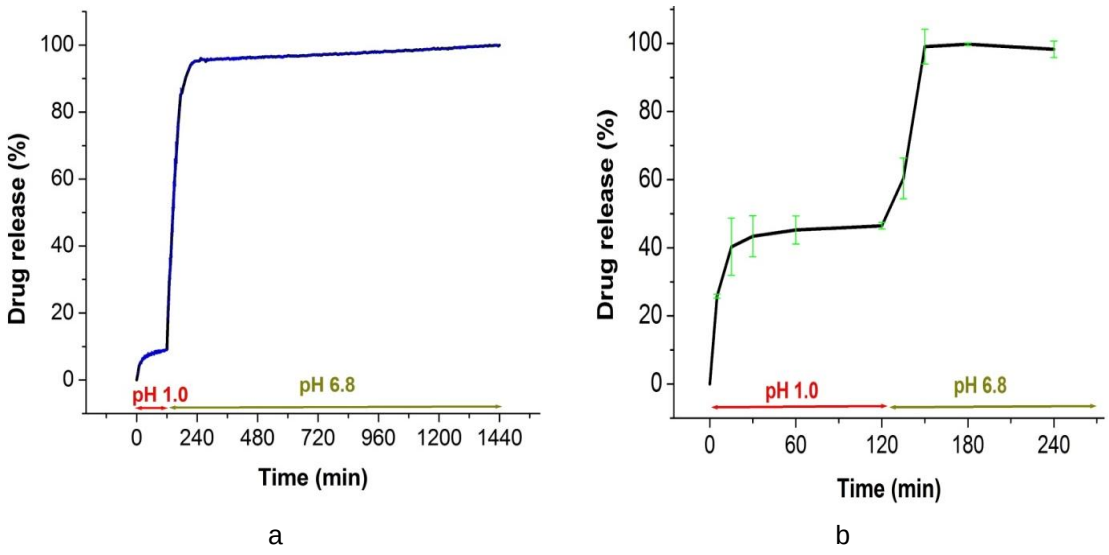

Figure 2.25: Drug release at pH 1.0 and 6.8 from (a) Fd1 and (b) Fv1 nanofibres. Three independent experiments were performed (each with a separate fibre mat), and results are reported as mean ± S.D. (There are error bar (blue) on Dic release black line but they are too small (< 1%) and thus cannot clearly be seen).

A dissolution study showed that the release rate of the SI from the FPi1 nanofibres was very fast, reaching 100% in less than 10 seconds. Release from the FPSi1 fibres was slightly slower (100% release was reached in less than 60 seconds).

2.2.5. Drug release mechanism

The drug release trends identified above for the PEO/SA systems can be explained by a simple model. The STEM data indicate that there are regions of the fibres which are relatively high density, and others where less contrast is present. This suggests that there are some areas of the fibres which are more SA rich than others; the presence of fine structure within the fibres was also confirmed with SEM images of their cross sections. SI particles are also seen to be present at the fibre surfaces by SEM. PEO is freely soluble at this pH, while SA is not. It is hypothesised that SI particles on the surface, and also SI ion pairs at the fibre edges are freed into solution very rapidly at this low pH, and at the same time the PEO molecules will disentangle and begin to dissolve, freeing the SI linked to PEO through an erosion mechanism. The greater the SI content, the more SI we expect to exist as particles or near the surface, and hence the larger the percentage of drug released in the initial burst phase.

The SA will be insoluble, and so its strands might be expected to cluster together while the other components of the fibre dissolve. Similar results have been reported in the literature: SA is known to aggregate at low pH (*ca.* 3) into core-shell micelle-like structures.[82] The different residues in SA have different pK_a values (3.38 and 3.64 respectively for the *β*-D-mannuronic and *α*-L-guluronic acids[83]), which results in some portions of its polymer chain becoming hydrophobic and others hydrophilic at this low pH. It is hypothesised that such effects might also be involved in the fibre systems. To explore this, Fi10 fibres were exposed to the pH 1.0 medium for 60 minutes, sufficient time for the first release stage to be complete, recovered by filtration, and assessed by SEM. The results are given in Figure 2.26. A similar experiment was carried out at pH 3.0 and the resultant SEM image is shown in Appendix I.

The images shows that upon addition of the pH 1.0 medium (Figure 2.26), the fibres swell and begin to dissolve and disentangle as the PEO absorbs water. In the centre of the image in Figure 2.26, where individual fibres can be resolved, the average fibre diameter is of the order of 88.6 nm, somewhat smaller than the initial material and close to the diameter of the fine structure features observed in Figure 2.14. The initial 3D structure of Fi10 and Fd1 was white, but it changes colour to brown shortly after immersion in the acidic media pH 1.0 (Figure 2.26b,c). The SEM image and colour change suggest that the PEO is dissolving, and the SA-rich parts of the fibres remain. This could be SA fibres identified in the PEO/SA system, as their diameter is almost similar to the sub-fibres visible in Fi10 (Figure 2.14). The insolubility of SA at pH 1.0 means that the drug in SA-rich areas of the fibres is hindered in dissolution.

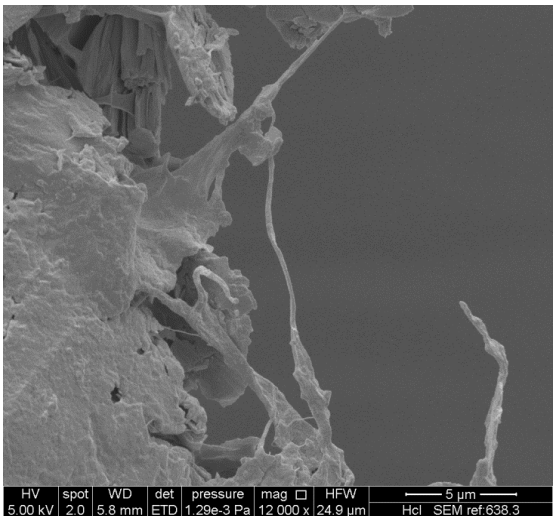

a

b

c

Figure 2.26: SEM images of Fi10 fibres after suspension in 1 L of medium pH 1.0 for 60 minutes**(a)** and digital photographs of Fi10 **(b)** and Fd1 **(c)** after immersion in milieu pH 1.0

This model is consistent with the observed results, and is depicted in Figure 2.27. At pH 6.8 both PEO and SA are freely soluble, and so the fibre mat dissolves completely, releasing all the embedded SI very rapidly.

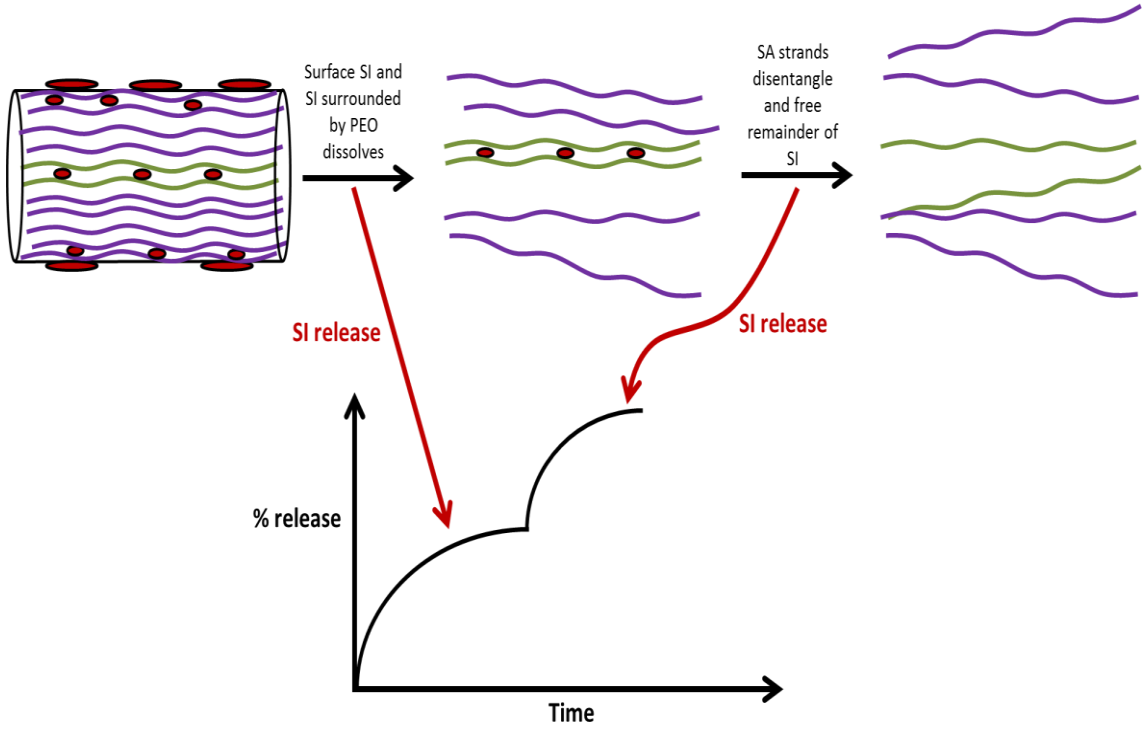

Figure 2.27: A schematic illustrating the proposed mechanism responsible for two-stage drug release at pH 1.0.

2.3. Conclusion

This chapter reports for the first time blended fibres containing PEO, SA and SI, Dic, Nap and Val. The PEO/SA/drug fibre aggregates in general exhibit novel 3D network structures, although elevated concentrations of Val led to the generation of a flat mat. The fibres were uniform and had cylindrical shape with a smooth surface. Electron microscopy data indicated the presence of regions of high and low SA density in the fibres. It seems that the SA is present as tiny fibres enrobed inside larger PEO nanofibres. SI, Nap and Dic were present as crystallite materials in the fibres, with their particles smaller than the pure drug materials. In contrast, the FPi1 and FPSi1 fibre systems formed flat mats on the collector, and SI was present in the amorphous form in these materials.

At low pH, there is a very rapid burst release of drug within the first 5–60 min. The amount of drug released in this stage is dependent on the drug content of the fibres, with a greater burst release being seen as the drug loading increases. There is then a plateau in which no further drug is released, and after the adjustment of pH to 6.8, the rest of the drug is freed from the fibres at an almost constant rate. The PEO/SA/drug fibres thus comprise time-controlled drug delivery systems, where there is an “on/off” pattern of drug release (bursts of release with a lag period between them). The release profile may be precisely tuned by varying the drug contents of the fibres. The materials may hence be used for colon-targeted drug delivery, and/or to deliver a desired amount of drug into the stomach in the fed state.

2.4. References

1. Luo, C. J., Stoyanov, S. D., Stride, E., Pelan, E. & Edirisinghe, M. Electrospinning versus fibre production methods: from specifics to technological convergence. *Chem. Soc. Rev.* **41,** 4708 (2012).

2. Williams, G. R. *et al.* Electrospun nanofibers in drug delivery: recent developments and perspectives. *Ther. Deliv.* **3,** 515–533 (2012).

3. Huang, Z.-M., Zhang, Y.-Z., Kotaki, M. & Ramakrishna, S. A review on polymer nanofibers by electrospinning and their applications in nanocomposites. *Compos. Sci. Technol.* **63,** 2223–2253 (2003).

4. Chakraborty, S., Liao, I.-C., Adler, A. & Leong, K. W. Electrohydrodynamics: A facile technique to fabricate drug delivery systems. *Adv. Drug Deliv. Rev.* **61,** 1043–1054 (2009).

5. Cui, W. *et al.* Investigation of drug release and matrix degradation of electrospun poly(DL-lactide) fibers with paracetanol inoculation. *Biomacromolecules* **7,** 1623–1629 (2006).

6. Shen, X. *et al.* Electrospun diclofenac sodium loaded Eudragit® L 100-55 nanofibers for colon-targeted drug delivery. *Int. J. Pharm.* **408,** 200–207 (2011).

7. Wu, X., Branford-White, C. J., Zhu, L., Chatterton, N. P. & Yu, D. Ester prodrug-loaded electrospun cellulose acetate fiber mats as transdermal drug delivery systems. *J. Mater. Sci. Mater. Med.* **21,** 2403–2411 (2010).

8. Yu, D.-G., Zhang, X.-F., Shen, X.-X., Brandford-White, C. & Zhu, L.-M. Ultrafine ibuprofen-loaded polyvinylpyrrolidone fiber mats using electrospinning. *Polym. Int.* **58,** 1010–1013 (2009).

9. Verreck, G. *et al.* Incorporation of drugs in an amorphous state into electrospun nanofibers composed of a water-insoluble, nonbiodegradable polymer. *J. Control. Release* **92,** 349–360 (2003).

10. Jiang, Y.-N., Mo, H.-Y. & Yu, D.-G. Electrospun drug-loaded core–sheath PVP/zein nanofibers for biphasic drug release. *Int. J. Pharm.* **438,** 232–239 (2012).

11. Yu, D.-G. *et al.* Dual drug release nanocomposites prepared using a combination of electrospraying and electrospinning. *RSC Adv.* **3,** 4652 (2013).

12. El-Newehy, M. H., Al-Deyab, S. S., Kenawy, E.-R. & Abdel-Megeed, A. Fabrication of electrospun antimicrobial nanofibers containing metronidazole using nanospider technology. *Fibers Polym.* **13,** 709–717 (2012).

13. Meng, Z. X., Zheng, W., Li, L. & Zheng, Y. F. Fabrication, characterization and in vitro drug release behavior of electrospun PLGA/chitosan nanofibrous scaffold. *Mater. Chem. Phys.* **125,** 606–611 (2011).

14. Shanmuga Sundar, S. & Sangeetha, D. Fabrication and evaluation of electrospun collagen/poly(N-isopropyl acrylamide)/chitosan mat as blood-contacting biomaterials for drug delivery. *J. Mater. Sci. Mater. Med.* **23,** 1421–1430 (2012).

15. Bussemer, T., Otto, I. & Bodmeier, R. Pulsatile drug-delivery systems. *Crit. Rev. Ther. Drug Carrier Syst.* **18,** 433–458 (2001).

16. Kalantzi, L. E., Karavas, E., Koutris, E. X. & Bikiaris, D. N. Recent advances in oral pulsatile drug delivery. *Recent Pat. Drug Deliv. Formul.* **3,** 49–63 (2009).

17. Saquing, C. D. *et al.* Alginate–Polyethylene Oxide Blend Nanofibers and the Role of the Carrier Polymer in Electrospinning. *Ind. Eng. Chem. Res.* **52,** 8692–8704 (2013).

18. Bonino, C. A. *et al.* Electrospinning alginate-based nanofibers: From blends to crosslinked low molecular weight alginate-only systems. *Carbohydr. Polym.* **85,** 111–119 (2011).

19. Rošic, R. *et al.* The role of rheology of polymer solutions in predicting nanofiber formation by electrospinning. *Eur. Polym. J.* **48,** 1374–1384 (2012).

20. Moon, S., Ryu, B.-Y., Choi, J., Jo, B. & Farris, R. J. The morphology and mechanical properties of sodium alginate based electrospun poly(ethylene oxide) nanofibers. *Polym. Eng. Sci.* **49,** 52–59 (2009).

21. Nie, H. *et al.* Effect of poly(ethylene oxide) with different molecular weights on the electrospinnability of sodium alginate. *Polymer (Guildf).* **50,** 4926–4934 (2009).

22. Alborzi, S., Lim, L.-T. & Kakuda, Y. Encapsulation of folic acid and its stability in sodium alginate-pectin-poly(ethylene oxide) electrospun fibres. *J. Microencapsul.* **30,** 64–71 (2013).

23. Im, J. S., Lee, S. K., Bai, B. C. & Lee, Y.-S. Prediction and characterization of drug release in a multi-drug release system. *J. Ind. Eng. Chem.* **18,** 325–330 (2012).

24. Bonino, C. a *et al.* Three-dimensional electrospun alginate nanofiber mats via tailored charge repulsions. *Small* **8,** 1928–36 (2012).

25. Ma, G., Fang, D., Liu, Y., Zhu, X. & Nie, J. Electrospun sodium alginate/poly(ethylene oxide) core–shell nanofibers scaffolds potential for tissue engineering applications. *Carbohydr. Polym.* **87,** 737–743 (2012).

26. Maggi L, Segale L, Torre ML, Machiste EO, C. U. *Biomater*. *ScL, Polym. Edn* **6,** (2002).

27. Balasubramaniam, J., Rao, V. U., Vasudha, M., Babu, J. & Rajinikanth, P. S. Sodium alginate microspheres of metformin HCl: formulation and in vitro evaluation. *Curr. Drug Deliv.* **4,** 249–56 (2007).

28. Rajinikanth, P. S., Sankar, C. & Mishra, B. Sodium alginate microspheres of metoprolol tartrate for intranasal systemic delivery: development and evaluation. *Drug Deliv.* **10,** 21–8 (2003).

29. Rahman, Z. *et al.* In-vivo evaluation in rats of colon-specific microspheres containing 5-fluorouracil. *J. Pharm. Pharmacol.* **60,** 615–23 (2008).

30. Xu, F. *et al.* Improvement of cytocompatibility of electrospinning PLLA microfibers by blending PVP. *J. Mater. Sci. Mater. Med.* **20,** 1331–8 (2009).

31. Illangakoon, U. E. *et al.* Fast dissolving paracetamol/caffeine nanofibers prepared by electrospinning. *Int. J. Pharm.* **477,** 369–379 (2014).

32. Illangakoon, U. E., Nazir, T., Williams, G. R. & Chatterton, N. P. Mebeverine-Loaded Electrospun Nanofibers: Physicochemical Characterization and Dissolution Studies. *J. Pharm. Sci.* **103,** 283–292 (2014).

33. Yu, D. G. *et al.* Electrospun biphasic drug release polyvinylpyrrolidone/ethyl cellulose core/sheath nanofibers. *Acta Biomater.* **9,** 5665–5672 (2013).

34. Wu, Y.-H., Yu, D.-G., Li, X.-Y., Diao, A.-H. & Illangakoon, Upulitha Eranka Williams, G. R. Fast-dissolving sweet sedative nanofiber membranes. *J. Mater. Sci.* **50,** 3604–3613 (2015).

35. Yu, D. G. *et al.* A modified coaxial electrospinning for preparing fibers from a high concentration polymer solution. *Express Polym. Lett.* **5,** 732–741 (2011).

36. Deitzel, J. ., Kleinmeyer, J., Harris, D. & Beck Tan, N. . The effect of processing variables on the morphology of electrospun nanofibers and textiles. *Polymer (Guildf).* **42,** 261–272 (2001).

37. Homayoni, H., Ravandi, S. A. H. & Valizadeh, M. Electrospinning of chitosan nanofibers: Processing optimization. *Carbohydr. Polym.* **77,** 656–661 (2009).

38. Deuk Yong, L. *et al.* Titania Nanofibers Prepared by Electrospinning. *J. Korean Phys. Soc.* **48,** 1686–1690 (2006).

39. Carneiro-da-Cunha, M. G. *et al.* Physical and thermal properties of a chitosan/alginate nanolayered PET film. *Carbohydr. Polym.* **82,** 153–159 (2010).

40. Chau, T. T. A review of techniques for measurement of contact angles and their applicability on mineral surfaces. *Miner. Eng.* **22,** 213–219 (2009).

41. Eral, H. B., 'T Mannetje, D. J. C. M. & Oh, J. M. Contact angle hysteresis: A review of fundamentals and applications. *Colloid Polym. Sci.* **291,** 247–260 (2013).

42. Zhu, T. *et al.* Study of pervaporation for dehydration of caprolactam through blend NaAlg–poly(vinyl pyrrolidone) membranes on PAN supports. *Sep. Purif. Technol.* **74,** 242–252 (2010).

43. Oss, C. Van. in *Interface Sci. Technol.* (Carel J. van Oss) 59–72 (Elsevier, 2008).

44. Xu, J., Wang, J., Dong, X., Liu, G. & Yu, W. Preparation of PVP/PLLA Ultrafine Blend Fibers by Electrospinning. *Int. J. Chem.* **3,** 57–60 (2011).

45. Çaykara, T., Demirci, S., Eroğlu, M. S. & Güven, O. Poly(ethylene oxide) and its blends with sodium alginate. *Polymer (Guildf).* **46,** 10750–10757 (2005).

46. Çaykara, T., Demirci, S., Eroğlu, M. S. & Güven, O. Surface properties of binary blend films of poly(N-vinyl-2-pyrrolidone) and poly(vinyl alcohol) with sodium alginate. *J. Polym. Sci. Part B Polym. Phys.* **44,** 426–430 (2006).

47. Della Volpe, C. & Siboni, S. Acid–base surface free energies of solids and the definition of scales in the Good–van Oss–Chaudhury theory. *J. Adhes. Sci. Technol.* **14,** 235–272 (2000).

48. Çaykara, T., Alaslan, A., Eroğlu, M. S. & Güven, O. Surface energetics of poly(N-vinyl-2-pyrrolidone)/chitosan blend films. *Appl. Surf. Sci.* **252,** 7430–7435 (2006).

49. Li, X. *et al.* Self-accelerated biodegradation of electrospun poly(ethylene glycol)–poly(l-lactide) membranes by loading proteinase K. *Polym. Degrad. Stab.* **93,** 618–626 (2008).

50. Ma, G., Fang, D., Liu, Y., Zhu, X. & Nie, J. Electrospun sodium alginate/poly(ethylene oxide) core–shell nanofibers scaffolds potential for tissue engineering applications. *Carbohydr. Polym.* **87,** 737–743 (2012).

51. Yu, D.-G., Zhang, X.-F., Shen, X.-X., Brandford-White, C. & Zhu, L.-M. Ultrafine ibuprofen-loaded polyvinylpyrrolidone fiber mats using electrospinning. *Polym. Int.* **58,** 1010–1013 (2009).

52. Rasenack, N. & Müller, B. W. Properties of ibuprofen crystallized under various conditions: a comparative study. *Drug Dev. Ind. Pharm.* **28,** 1077–89 (2002).

53. Saritha, D., Bose, P. S. C., Reddy, P. S., Madhuri, G. & Nagaraju, R. Improved dissolution and micromeritic properties of naproxen from spherical agglomerates: preparation, in vitro and in vivo characterization. *Brazilian J. Pharm. Sci.* **48,** 683–690 (2012).

54. Dun, W. *et al.* Solubility of Ibuprofen Sodium Dihydrate in Acetone + Water Mixtures: Experimental Measurement and Thermodynamic Modeling. *J. Chem. Eng. Data* **59,** 3415–3421 (2014).

55. Lee, T., Chen, Y. H. & Wang, Y. W. Effects of Homochiral Molecules of (S)-(+)-Ibuprofen and (S)-(−)-Sodium Ibuprofen Dihydrate on the Crystallization Kinetics of Racemic (R,S)-(±)-Sodium Ibuprofen Dihydrate. *Cryst. Growth Des.* **8,** 415–426 (2008).

56. Zhang, G. G. Z., Paspal, S. Y. L., Suryanarayanan, R. & Grant, D. J. W. Racemic species of sodium ibuprofen: Characterization and polymorphic relationships. *J. Pharm. Sci.* **92,** 1356–1366 (2003).

57. Kim, Y. S. & Rousseau, R. W. Characterization and solid-state transformations of the pseudopolymorphic forms of sodium naproxen. *Cryst. Growth Des.* **4,** 1211–1216 (2004).

58. Di Martino, P., Barthélémy, C., Palmieri, G. F. & Martelli, S. Physical characterization of naproxen sodium hydrate and anhydrate forms. *Eur. J. Pharm. Sci.* **14,** 293–300 (2001).

59. Martino, P. Di *et al.* A new tetrahydrated form of sodium naproxen. *J. Pharm. Sci.* **96,** 156–167 (2007).

60. Rodomonte, A. *et al.* Different crystal morphologies arising from different preparation methods of a same polymorphic form may result in different properties of the final materials: The case of diclofenac sodium trihydrate. *J. Pharm. Biomed. Anal.* **48,** 477–481 (2008).

61. Bartolomei, M., Bertocchi, P., Antoniella, E. & Rodomonte, A. Physico-chemical characterisation and intrinsic dissolution studies of a new hydrate form of diclofenac sodium: Comparison with anhydrous form. *J. Pharm. Biomed. Anal.* **40,** 1105–1113 (2006).

62. Bartolomei, M., Rodomonte, A., Antoniella, E., Minelli, G. & Bertocchi, P. Hydrate modifications of the non-steroidal anti-inflammatory drug diclofenac sodium: Solid-state characterisation of a trihydrate form. *J. Pharm. Biomed. Anal.* **45,** 443–449 (2007).

63. Palomo, M. E., Ballesteros, M. P. & Frutos, P. Analysis of diclofenac sodium and derivatives. *J. Pharm. Biomed. Anal.* **21,** 83–94 (1999).

64. Fini, A. *et al.* Diclofenac salts. III. Alkaline and earth alkaline salts. *J. Pharm. Sci.* **94,** 2416–2431 (2005).

65. Petruševski, G., Naumov, P., Jovanovski, G. & Ng, S. W. Unprecedented sodium-oxygen clusters in the solid-state structure of trisodium

hydrogentetravalproate monohydrate: A model for the physiological activity of the anticonvulsant drug Epilim®. *Inorg. Chem. Commun.* **11,** 81–84 (2008).

66. Hu, C., Gong, R. H. & Zhou, F. L. Electrospun Sodium Alginate/Polyethylene Oxide Fibers and Nanocoated Yarns. *Int. J. Polym. Sci.* **2015,** 1–12 (2015).

67. Cheng, W. T. & Lin, S. Y. Processes of dehydration and rehydration of raffinose pentahydrate investigated by thermal analysis and FT-IR/DSC microscopic system. *Carbohydr. Polym.* **64,** 212–217 (2006).

68. Abioye, A. O. & Kola-Mustapha, A. Formulation studies on ibuprofen sodium–cationic dextran conjugate: effect on tableting and dissolution characteristics of ibuprofen. *Drug Dev. Ind. Pharm.* **00,** 1–21 (2015).

69. Pan, D., Liu, L. M., Slater, B., Michaelides, A. & Wang, E. Melting the ice: On the relation between melting temperature and size for nanoscale ice crystals. *ACS Nano* **5,** 4562–4569 (2011).

70. Xue, Y., Zhao, Q. & Luan, C. The Thermodynamic Relations between the Melting Point and the Size of Crystals. *J. Colloid Interface Sci.* **243,** 388–390 (2001).

71. Smith, M. *Organic Chemistry: An Acid-Base Approach*. (CRC Press, 2010).

72. Wronski, C. R. M. The size dependence of the melting point of small particles of tin. *Br. J. Appl. Phys.* **18,** 1731–1737 (2002).

73. Antoniammal, P. & Arivuoli, D. Size and Shape Dependence on Melting Temperature of Gallium Nitride Nanoparticles. *J. Nanomater.* **2012,** 1–11 (2012).

74. Ribeiro, Y. A., Oliveira, J. D. S., Leles, M. I. G., Juiz, S. A. & Ionashiro, M. Thermal decomposition of some analgesic agents. *J. Therm. Anal.* **46,** 1645–1655 (1996).

75. Tudja, P., Khan, M. Z., Mestrović, E., Horvat, M. & Golja, P. Thermal behaviour of diclofenac sodium: decomposition and melting characteristics. *Chem. Pharm. Bull. (Tokyo).* **49,** 1245–1250 (2001).

76. Petruševski, G., Naumov, P., Jovanovski, G., Bogoeva-Gaceva, G. & Seik, W. N. Solid-state forms of sodium valproate, active component of the anticonvulsant drug epilim. *ChemMedChem* **3,** 1377–1386 (2008).

77. Tan, R., Niu, X., Gan, S. & Feng, Q. Preparation and characterization of an injectable composite. *J. Mater. Sci. Mater. Med.* **20,** 1245–53 (2009).

78. US Pharmacopeia USP 38NF33. The United States Pharmacopeial Convention, (711) Dissolution. *Rockville,MD.* 486–496 (2015).

79. Shao, Y., Li, L., Gu, X., Wang, L. & Mao, S. Evaluation of chitosan–anionic polymers based tablets for extended-release of highly water-soluble drugs. *Asian J. Pharm. Sci.* **10,** 24–30 (2015).

80. Levis, K. a., Lane, M. E. & Corrigan, O. I. Effect of buffer media composition on the solubility and effective permeability coefficient of ibuprofen. *Int. J. Pharm.* **253,** 49–59 (2003).

81. Llinàs, A., Burley, J. C., Box, K. J., Glen, R. C. & Goodman, J. M. Diclofenac Solubility: Independent Determination of the Intrinsic Solubility of Three Crystal Forms. *J. Med. Chem.* **50,** 979–983 (2007).

82. Cao, Y. *et al.* pH-induced self-assembly and capsules of sodium alginate. *Biomacromolecules* **6,** 2189–2196 (2005).

83. Huguet, M. L., Groboillot, A., Neufeld, R. J., Poncelet, D. & Dellacherie, E. Hemolglobin encapsulation in chitosan/calcium alginate beads. *J. Appl. Polym. Sci.* **51,** 1427–1432 (1994).

Chapter 3: The intercalation of valporate, naproxen and diclofenac sodium into hydroxy double salts.

3.1. Introduction

3.1.1 General overview

Both hydroxy double salts (HDSs) and layered double hydroxides (LDHs) belong to the layered solids family, but HDSs have received much less attention than LDHs. Both have the same key structural features of positively charged layers and charge-balancing anions located in the interlayer region, but they differ in their layer compositions. LDHs contain a mixture of trivalent and mono or divalent metal cations.[1–4] In contrast, HDSs contain only divalent metal cations; they are usually called layered hydroxide (or basic) salts (LHS or LBS) when they contain only one type of divalent metal.[5–7] The generic formula of an HDS is $[(M^{2+}_{x-1}Me^{2+}_{x})(OH)_{3(1-y)}]\ X^{n-}_{(1+3y)/n}\cdot zH_2O$. M and Me are divalent metal ions such Zn, Cu, Ni, or Co.[8,9] The interlayer anions can be either monovalent (e.g. Cl^-, NO_3^-) or divalent, such as CO_3^{2-}.[9,10] The interlayer anions can be replaced, through an ion exchange route, with a variety of anions (inorganic and organic anions).[11–14]

LDHs have drawn the interest of many researchers for their potential as drug delivery systems. They have been widely explored *in vitro* and *in vivo* for drug delivery and have the resultant nanocomposites have shown much improved properties over the free drugs in terms of solubility, absorption, bioavailability and cells uptake.[15–22] Much less attention has been paid to HDSs in general and specifically to their potential as delivery system.

The charge-balancing anions located in the interlayer region of HDSs can easily be replaced, and since a number of well known anti-epileptic, anti-inflammatory and analgesic agents are either carboxylic acids or carboxylic derivatives they comprise good candidates to be intercalated into the HDS host matrix.

Non-steroidal anti-inflammatory drugs (NSAIDs), such as Diclofenac (Dic) and Naproxen (Nap), play important roles as anti-inflammatory, analgesic, and antipyretic agents.[23,24] Valproic acid (Val) (otherwise known as 2-propylvaleric acid, 2-propylpentanoic acid or n-dipropylacetic acid) is used as an anticonvulsant and mood stabilizing drug.[25,26] The chemical structures of these drugs are given in Figures 1.2,1.3 and 1.4.

3.1.2 Scope of this chapter

In this chapter, the intercalation of Dic, Nap and Val into HDSs is explored for the first time. These guests have been incorporated into a range of Zn-containing HDSs, and the resulting products were characterized by X-ray diffraction, IR spectroscopy and elemental analysis. An *in situ* X-ray diffraction study was performed to investigate the intercalation mechanisms and kinetics. Molecular dynamics simulations were undertaken to aid interpretation of the *in situ* data, in addition gain more insight into the interactions between the layer and the guest ions. The release of the drugs from the HDSs system was studied in representative physiological conditions.

3.2 Results and Discussion

3.2.1. Intercalation into $Co_{1.2}Zn_{3.8}(OH)_8(NO_3)_2 \cdot 2H_2O$

It proved easy to intercalate the organic species Dic, Nap and Val into $Co_{1.2}Zn_{3.8}(OH)_8(NO_3)_2 \cdot 2H_2O$ (CoZn-NO_3) through an anion exchange method. Successful intercalation was confirmed by X-ray diffraction (XRD) and IR spectroscopy. Both before and after intercalation the materials are found to consist of roughly hexagonal platelets. An SEM image of the Dic intercalate (CoZn-Dic) is shown in Figure 3.1.

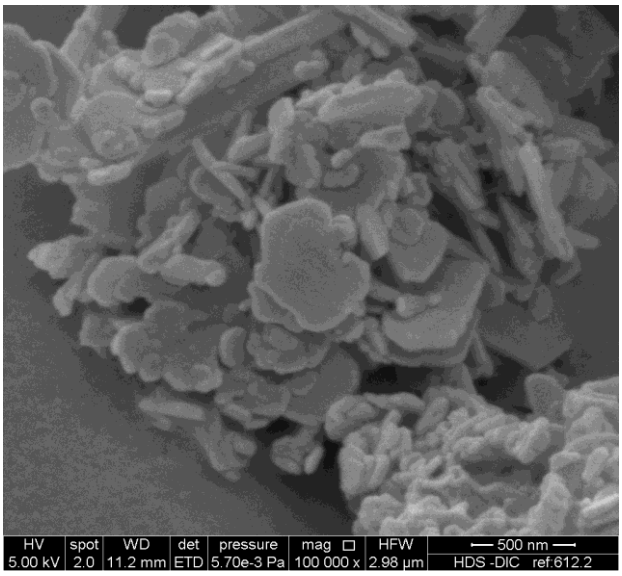

Figure 3.1: An SEM image of CoZn-Dic.

3.2.1.1. X-ray diffraction

XRD patterns of the drug intercalates of CoZn-NO_3 are given in Figure 3.2. The reaction products show no characteristic basal reflections of the starting material, and a shift of the *h00* basal reflections to lower angles; this corresponds to an increase in interlayer distance, which is indicative of the intercalation of a larger anion (Dic, Nap and Val) into the interlayer galleries of the HDS by anion exchange for NO_3^-. The interlayer spacing increases from 9.7 Å with CoZn-NO_3 to 19.4 Å, 22.3 Å and 24.1Å for the Val, Dic and Nap intercalates, respectively. These are in good agreement with previous results for LDHs: Khan *et al*. recorded d-spacings of 22.3 Å for Dic, 21.5 Å for Nap and 18.7 Å for Val. [27] All the diffraction patterns illustrate peak broadening, indicative of stacking defects. Full data are included in Table 3.1.

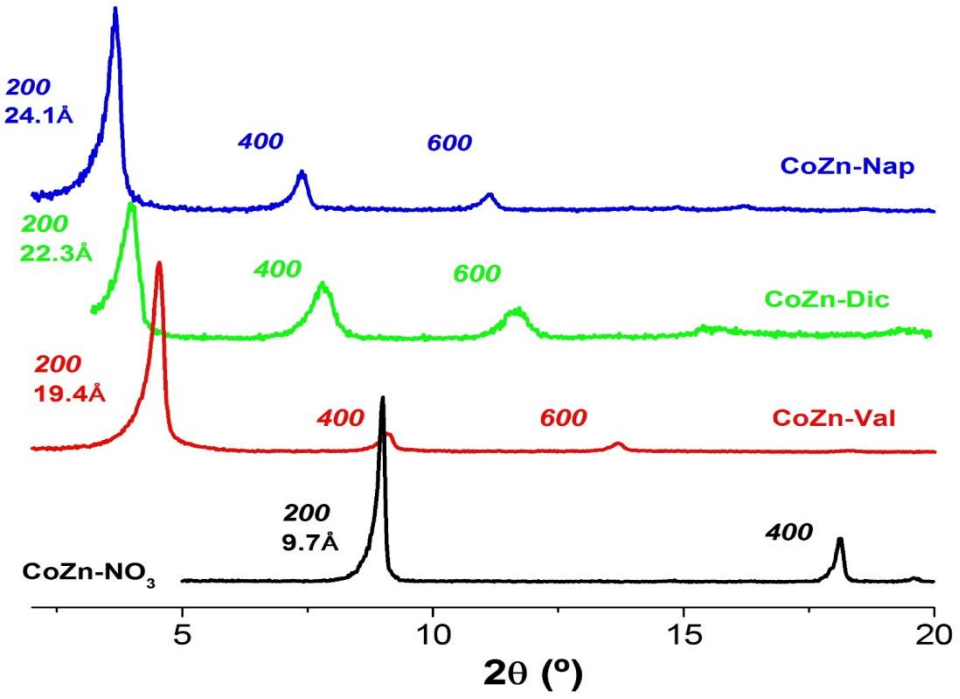

Figure 3.2: XRD patterns of CoZn–NO_3; CoZn-Dic; CoZn-Nap and CoZn-Val.

3.2.1.2. IR spectroscopy

The intercalated compounds were also characterised by IR spectroscopy. Spectra of the CoZn-NO_3, Dic, and the reaction product of CoZn-NO_3 and Dic are shown in Figure 3.3. The spectrum of CoZn-NO_3 shows typical features of an HDS. A broad peak centred at around 3250 cm^{-1} corresponds to H-bonded OH groups of the HDS layers. The δ-vibration of the interlayer water molecules is located at 1636 cm^{-1}, the NO_3^- vibrations at *ca.* 1373 cm^{-1}, and Zn–O vibrations from the HDS layers are visible below 1000 cm^{-1}.

The spectrum of Dic (Figure 3.3a) displays distinctive symmetric and asymmetric carboxylate bands at 1397 and 1572 cm^{-1} respectively. An additional peak at 746 cm^{-1} corresponds to the C-Cl group. The IR spectrum from the intercalation compound is a combination of those from the HDS and Dic. The spectrum of CoZn-NO_3, provided in Figure 3.3a, contains a broad OH absorption band at around 3400 cm^{-1}, and distinctive carboxylate vibrations at 1572 and 1397 cm^{-1} as well as a C-Cl vibration at 746 cm^{-1}. This indicates that the intercalation of Dic anion was successful. There is no visible peak at 1373 cm^{-1} for the intercalate, implying that the nitrate ions have been displaced from the structure. The shift in the position of the asymmetric carboxylate band from 1572 cm^{-1} in Dic to 1580 cm^{-1} in CoZn-Dic may be attributed to the electrostatic interactions between the COO^- groups of Dic anions and the hydroxide layers. The IR spectra for the other HDS intercalates also show the disappearance of the nitrate absorption and the presence of characteristic bands from the guest ions (Figure 3.3b). Thus, all three drug ions are stable after intercalation into CoZn-NO_3.

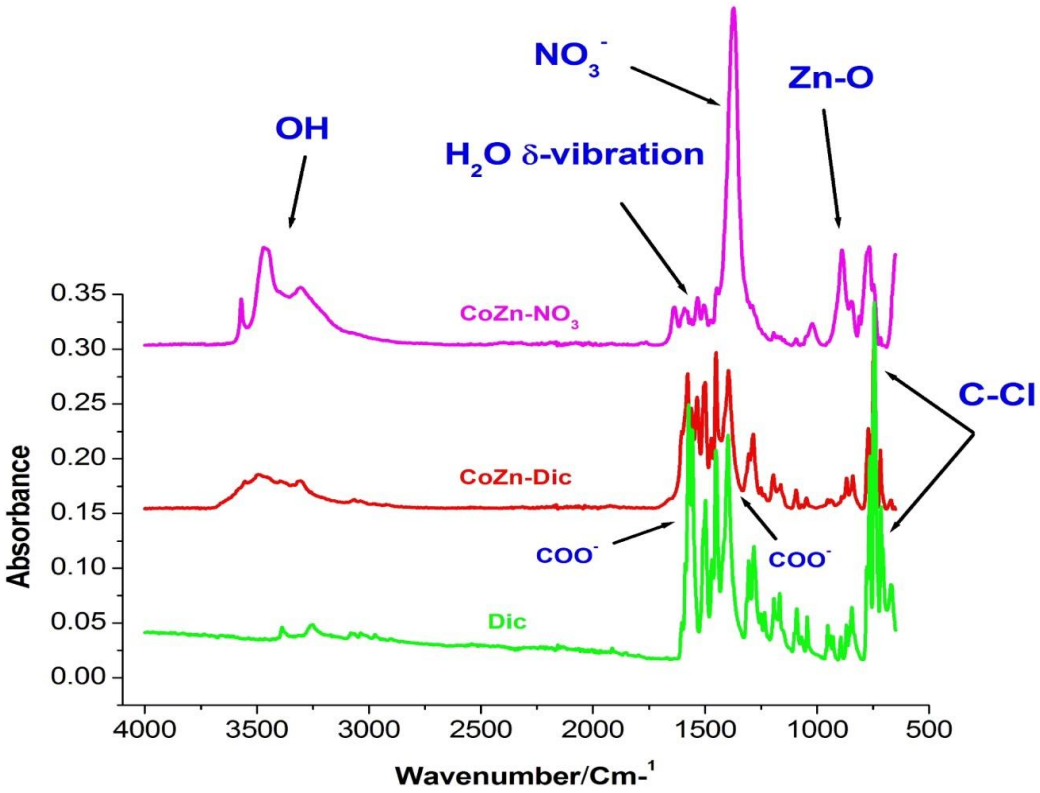

a

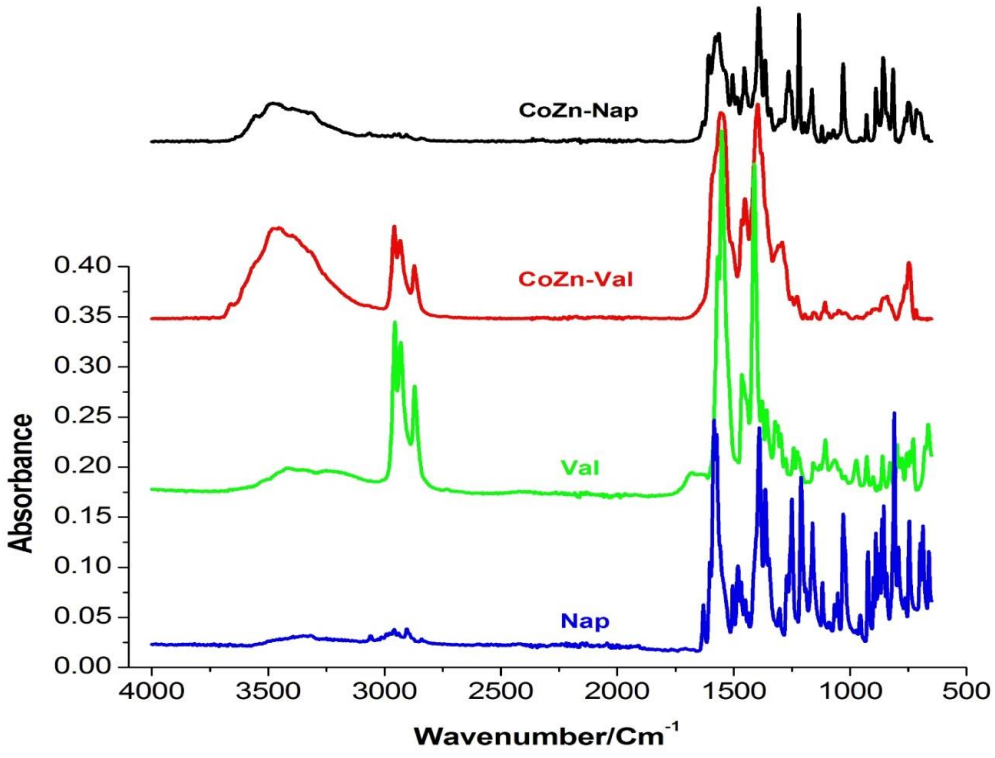

b

Figure 3.3: IR spectra of **(a)** CoZn-NO_3, CoZn-Dic and Dic; **(b)** CoZn-Nap, CoZn-Val, Val and Nap.

3.2.2. Intercalation into other hydroxy double salts

The influence of the initial interlayer anion and the layer composition on intercalation was explored with Val, Dic and Nap and three further HDSs: $[Zn_5(OH)_8]Cl_2.yH_2O$ (Zn-Cl), $[Zn_5(OH)_8](NO_3)_2.yH_2O$ (Zn-NO_3) and $[Ni_2Zn_3(OH)_8](NO_3)_2.yH_2O$ (NiZn-NO_3). The XRD data (Table 3.1) show that the intercalation compounds are largely analogous to those prepared from CoZn-NO_3. The exception to this was Val, where intercalation into Zn-Cl and Zn-NO_3 was not successful and only ZnO powder was recovered. XRD and IR spectroscopy (see Appendix II) demonstrated successful intercalation of the Dic and Nap anions into all the HDSs.

Table 3.1: The interlayer spacings and chemical formulae of the various HDS-drug composites prepared.

ID	d_{200} (Å)	Formula[a]	Elemental analysis/% Obsd (calcd)
CoZn-NO_3	9.7	$Co_{1.2}Zn_{3.8}(OH)_8(NO_3)_2{\cdot}2H_2O$	-
CoZn-Val	19.4	$Co_{1.2}Zn_{3.8}(OH)_8(C_8H_{15}O_2)_2{\cdot}2.5H_2O$	C 24.46 (24.43) H 5.55 (5.51) N 0.0 (0.0)
CoZn-Dic	22.3	$Co_{1.2}Zn_{3.8}(OH)_8(C_{14}H_{10}Cl_2NO_2)_{1.6}(CO_3)_{0.2}{\cdot}$ $2H_2O$	C 28.25 (28.83) H 2.77 (2.89) N 1.44 (2.30)
CoZn-Nap	24.1	$Co_{1.2}Zn_{3.8}(OH)_8(C_{14}H_{13}O_3)_{1.8}(CO_3)_{0.1}{\cdot}$ $3.4H_2O$	C 32.21 (32.50) H 4.12 (4.12) N 0.0 (0.0)
NiZn-NO_3	9.7	$Ni_2Zn_3(OH)_8(NO_3)_2{\cdot}2H_2O$	-
NiZn-Dic	21.2	$Ni_2Zn_3(OH)_8(C_{14}H_{10}Cl_2NO_2)_{1.65}(NO_3)_{0.35}$ $2H_2O$	C 27.91 (27.9) H 2.42 (2.89) N 3.31 (2.82)
NiZn-Nap	24.2	$Ni_2Zn_3(OH)_8(C_{14}H_{13}O_3)_{1.72}\ (CO_3)_{0.14}{\cdot}2.7H_2O$	C 32.21 (32.29) H 4.03 (4.00) N 0.0 (0.0)
Zn-NO_3	9.7	$Zn_5(OH)_8(NO_3)_2{\cdot}2H_2O$	-
Zn-Nap	24.6	$Zn_5(OH)_8(C_{14}H_{13}O_3)_2{\cdot}2H_2O$	C 34.87 (35.12) H 3.90 (4.00) N 0.0 (0.0)
Zn-Dic	22.3	$Zn_5(OH)_8(C_{14}H_{10}Cl_2NO_2)_{2.4}.2H_2O$	C 33.68 (33.43) H 1.67 (3.01) N 3.05 (2.78)

3.2.3. Guest recovery

The CoZn-Dic, CoZn-Nap and CoZn-Val intercalates were reacted with Na_2CO_3 in D_2O, and NMR spectra recorded of the filtrate from these reactions. The spectra after deintercalation are observed to be identical to those of the Dic, Nap and Val starting materials, confirming that the structural integrity of these drug molecules is retained.

The ^1H NMR spectrum of Val, shown in Figure 3.4, contains resonances at 0.83, 1.22, 1.32 and 1.41 ppm, which are characteristic of an aliphatic n-propyl chain ($CH_3CH_2CH_2$); their assignment is displayed in Figure 3.5c. The fourth signal at 2.19 ppm is attributed to CH. Similar findings (using $CDCl_3$ as the solvent) were reported by Badawi et al.[28]

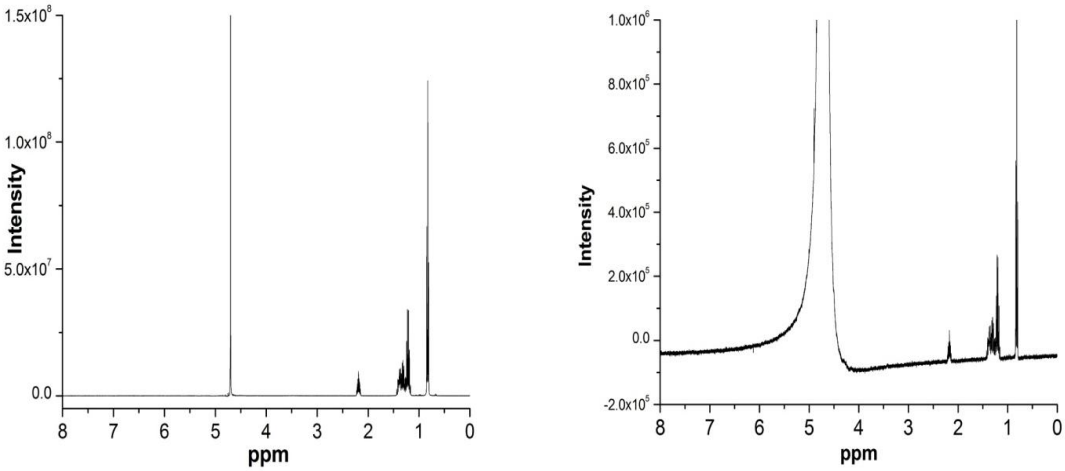

Figure 3.4: ^1H NMR of Val (a) pure drug, (b) after intercalation and deintercalation from CoZn-NO_3 and (c) the chemical structure with chemical shifts (calculated in ChemDraw).

3.2.4. Guest orientation

The layer thickness of the HDS is around 8.5 Å (from end to end of tetrahedral sites). The lengths of the guest ions are calculated (using the Marvin software [29]) to be 7.09 Å (Val); 11.76 Å (Dic); and 12.88 Å (Nap). Comparing the lengths of the guests with the gallery height (the interlayer spacing minus the HDS layer thickness) suggests that the gallery height is between 1.5 and 2 times the length of the intercalated ions. This indicates that the guests adopt intertwined bilayer or bilayer arrangements. For Val, the gallery height is around twice the size of the ions, suggesting a perpendicular bilayer arrangement. A schematic of the guest orientation adopted with Val is provided in Figure 3.5. For Dic and Nap, the gallery height is greater than the size of one molecule and less than the length of two, indicating an intertwined bilayer arrangement. There are various possibilities of intertwined bilayer guest arrangements, and common ones that have been published are illustrated in Figure 3.5b (I, II).[7,9,10]

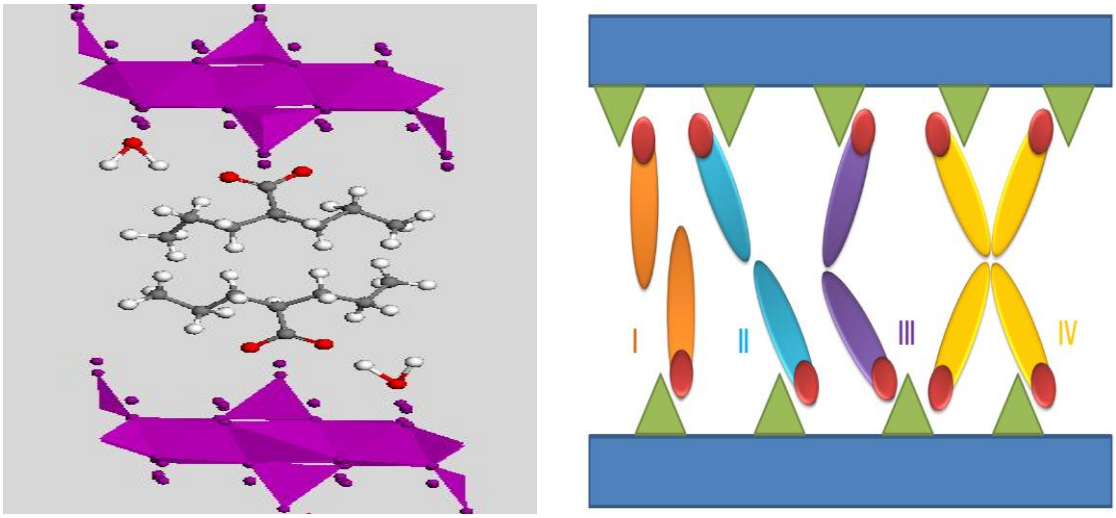

a b

Figure 3.5: Schematics showing the arrangement of Val in CoZn-Val **(a)** and **(b)** the various possible intertwined bilayer guest arrangements. The carboxylate group of the guest is highlighted in red and the layer tetrahedral in green.

To understand more about the intercalation process, a series of molecular dynamics (MD) simulations were undertaken (Figure 3.6). The simulation was allowed to run until the energy of the system was minimised. This resulted in a bilayer of drugs ions model given in Figure 3.6a. The Val ions can be seen to form a bilayer, resulting in an interlayer spacing of 19.1 ± 0.1 Å. This result is in good agreement with the experimental value (19.4 Å), with the small difference between experimental and simulation being well within the range of deviations reported in previous LDH modelling studies (very little modelling work has been done using HDSs).[30–34] The Val ions adopt a perpendicular position in the interlayer regions, with their carboxylates facing the HDS layer and the aliphatic chains towards the centre. The simulation shows that H-bonding occurs between the COO^- group of Val, water and the HDS layer.

As for Val, MD simulations were used to acquire more insight into the intercalation processes, and the results are presented in Figure 3.6. When the simulations for Dic and Nap were allowed to run until an energy minimum was reached, the result is the Nap ions forming a bilayer arrangement between the HDS layers, with a *d*-spacing of 24.0 ± 0.1 Å (Figure 3.6b). This is in good agreement with the experimental value of 24.1 Å. The Nap ions form an "X" shape in three dimensions (Figure 3.6b), in which the hydrophobic regions are close to each other in the centre and the hydrophilic regions (carboxylate) are close to the tetrahedral Zn and facing the positively charged layers. Demel.*et al*. reported the MD simulation of dodecyl sulphate intercalated into an HDS (Zn-NO_3) using the Dreiding force field (different from that utilised in this work), and found that the ions formed a bilayer arrangement similar to that in Figure 3.5b(I).[35]

MD simulation shows that Dic ions form an "X" shape in 3D (Figure 3.6c), very similar to Nap, leading to an interlayer spacing of 22.0 ± 0.3 Å.

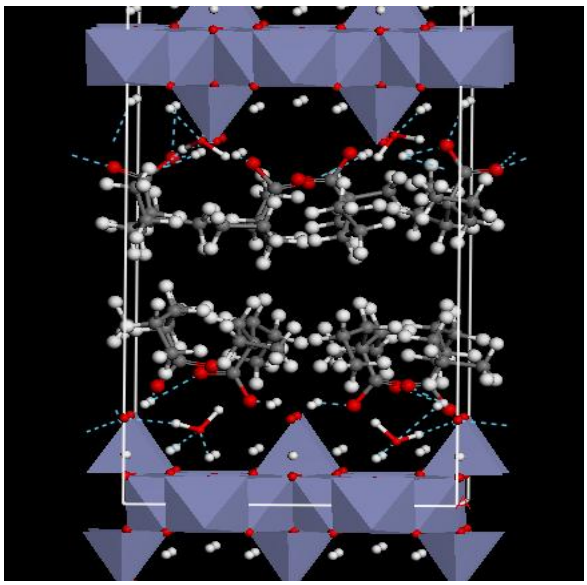

a

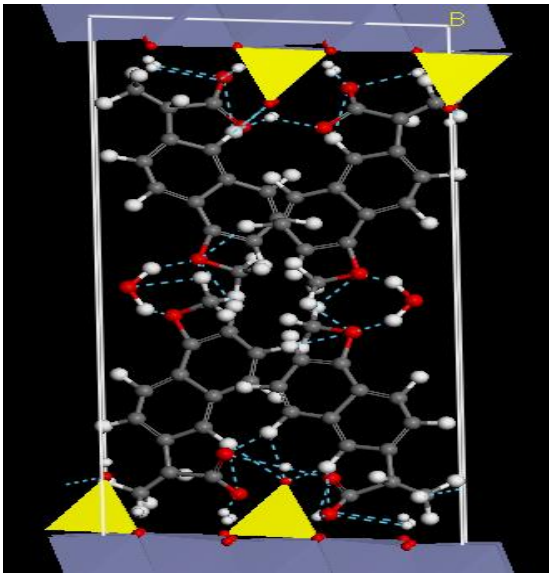

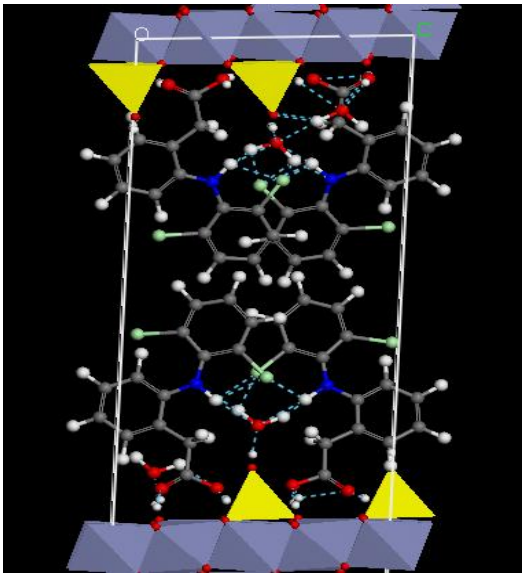

b c

Figure 3.6: MD results for the intercalates of Val, Nap and Dic into Zn-NO_3 in the energy minimised structure. **(a)** Val with H-Bonds in blue;**(b)** Nap and **(c)** Dic.

3.2.5. *In situ* diffraction

The intercalation of Dic, Nap, and Val into the HDSs was studied using *in situ* diffraction. The reactions were observed to be too slow for effective monitoring at 60 ºC. At 70 ºC and above, the reactions were faster, and thus kinetic and mechanistic parameters could be extracted.

3.2.5.1. Intercalation of Val into CoZn-NO_3

At all temperatures, the intercalation of Val was seen to be a one stage process, proceeding directly from the CoZn-NO_3 starting material to the CoZn-Val product. No crystalline intermediate phases were visible in the diffraction data (Figure 3.7a).

A comparison of the datasets for Val reveals that the intercalate exhibits virtually the same d-spacing *in situ* and *ex situ* (19.8 and 19.4 Å respectively). The intensities of the *200* reflections of the CoZn-NO_3 and CoZn-Val materials were integrated, and converted into extent of reaction vs. time, α:

$$\alpha = I_{hkl}(t)/I_{hkl}(max) \qquad \textbf{(1)}$$

where $I_{hkl}(t)$ is the intensity of a reflection hkl at time t, and I_{hkl} (max) is the maximum intensity of that reflection. A plot illustrating the change in intensity of the *200* reflections for the intercalation of Val into CoZn-NO_3 is illustrated in Figure 3.7b.

The α vs t curves in Figure 3.7b cross at α ≈ 0.45 which indicates a one stage transformation. This crossing point reveals that the diffracted intensity lost from the starting material is matched by the diffracted intensity gained by the product, and therefore the intercalation reaction has not passed through an intermediate

phases (NB: there is an overlap between the *200* reflection of CoZn-NO_3 with the *400* of CoZn-Val; therefore, the change in intensity of the starting material reflection was not plotted after 10 min). If there is an intermediate stage, the starting material and product curves should cross close to $\alpha \approx 0$.

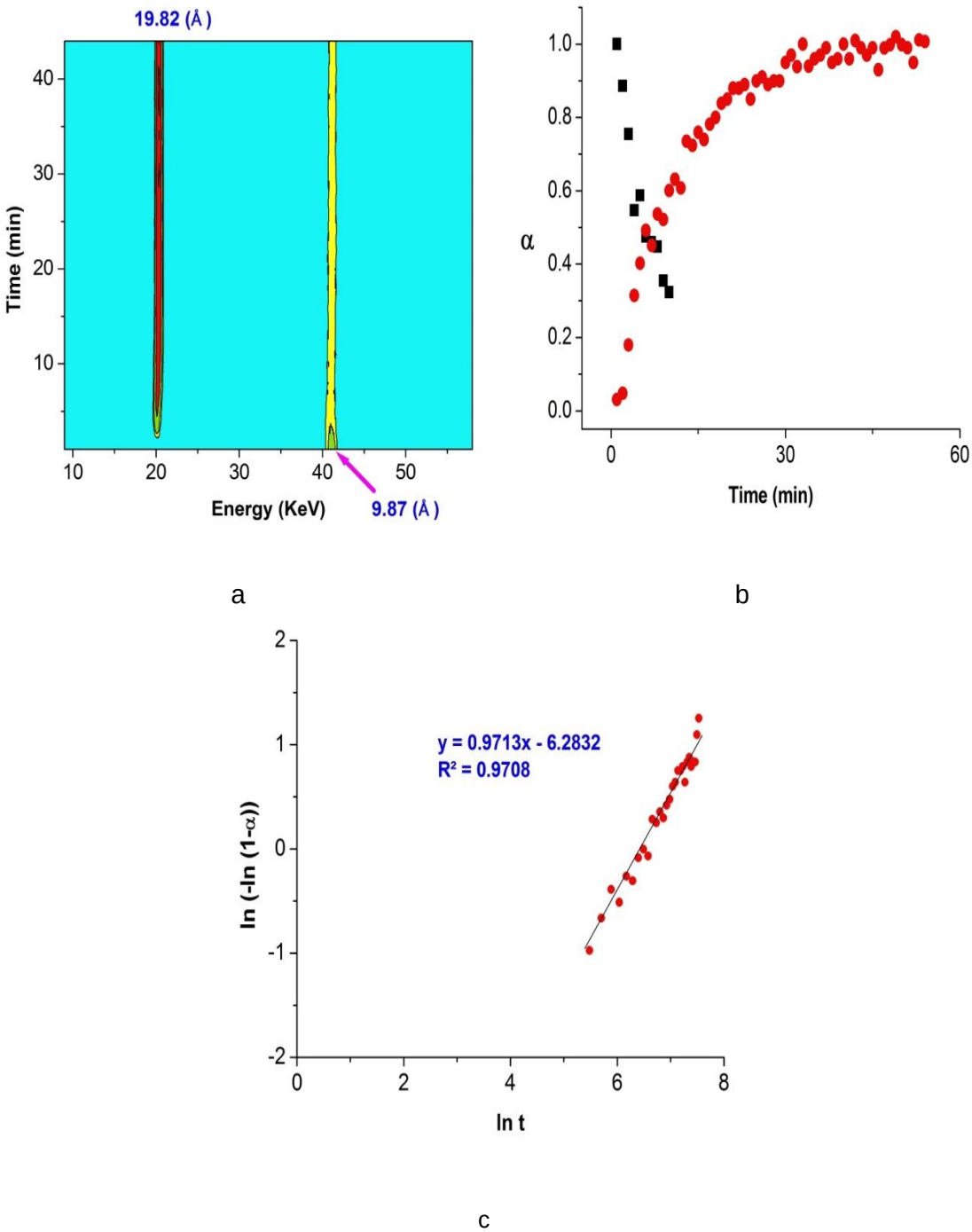

Figure 3.7: *In situ* data for the intercalation of Val into CoZn-NO_3 at 80 ºC. **(a)** A contour plot of the raw data; **(b)** Extent of reaction vs time data showing the changes in intensity of the host (■) and product (●) *200* reflections; and **(c)** a Sharp–Hancock plot of the product *200* reflection.

The study of the kinetics of solid-state reactions is helpful, because it enables us to obtain quantitative information (such as half-lives, rate constants, *etc*) about the reactions and the factors affecting them. Moreover, it allows the deduction of mechanistic information about the reactions investigated.[36] Generally, kinetic analysis can be obtained by fitting the experimental data to a theoretical expression relating the extent of reaction (α) and time. It is possible to derive specific forms of *f*(α) for a range of possible mechanistic scenarios, by making assumptions about the nucleation as well as growth processes (such as the number of dimensions in which growth takes place and the relative importance of nucleation and diffusion as the reaction progresses). Kinetic analysis generally involves comparison of the experimental data with the theoretical models.[36] In solid-state kinetics, one of the most commonly used kinetic expressions is the Avrami-Erofe'ev expression.[37–39,40] This expression divides the reaction into separate stages of product nucleation and nuclei growth. An automated Gaussian fitting routine is usually utilised to calculate the peak areas of the Bragg reflections. These values are then converted to the extent of reaction at time t, α(t), defined as

The Avrami–Erofe'ev model has the general functional form:

$$\alpha = 1 - e^{-[k(t-t0)]n} \quad \textbf{(2)}$$

where α is the extent of reaction, t_0 is the induction time, k is the rate, and n (the reaction exponent) encloses information on the reaction mechanism.[10] This expression can conveniently be rearranged to give:

$$\ln(-\ln(1 - \alpha)) = n \ln k + n \ln(t - t_0) \quad \textbf{(3)}$$

t_0 is an optional term used to take into account any induction time or zero error and is found to be zero for these systems.

This expression is mostly applicable in the range $0.15 < \alpha < 0.8$.[41] The exponent n can be exploited to infer information about the rate of nucleation and the mechanism of nuclei growth,[42] k is the rate of reaction. The value of n can most easily be obtained using a Sharp-Hancock plot,[43] which is a plot of $\ln[-\ln(1 - \alpha)]$ *vs* $\ln(t)$ and gives a straight line of gradient n and intercept $n \ln k$ if the Avrami method is valid. Therefore, testing the linearity of a Sharp-Hancock plot is a good way of determining if a reaction proceeds via a consistent mechanism, and since each of the theoretical models has a characteristic value of the exponent, n, the values of n extracted from such plots can be used to infer information about the mechanism of crystallization (Table 3.2).

Table 3.2: Functional forms of the common rate equations used to model solid-state reactions.[42]

Dimension of growth	**Nucleation rate**	**Exponent value (n)**	
		Phase boundary controlled	**Diffusion controlled**
1	Zero (instantaneous)	1	0.5
	Deceleratory	**1-2**	**0.5-1.5**
	Constant	2	1.5
2	**Zero (instantaneous)**	**2**	**1**
	Deceleratory	**2-3**	**1-2**
	Constant	3	2
3	Zero (instantaneous)	3	1.5
	Deceleratory	3-4	1.5-2.5
	Constant	4	2.5

A Sharp–Hancock plot was generated for Val intercalation at 80 ºC, and is given in Figure 3.7c. The plot is linear, indicating that the reaction proceeds via a consistent mechanism over almost the entire course of the reaction, and that the Avrami–Erofe'ev model is suitable for this system. The reaction exponent n can be calculated from the gradient, and the rate constant k from the intercept of the graph. The reaction exponent n is observed to be ca. 1 at 80 ºC (Table 3.3). This means that the reaction mechanism is a nucleation–growth type, with instantaneous nucleation and two dimensional diffusion control thereafter. The layer edges are the nucleation sites, and ''instantaneous'' nucleation is observed since all these are present at the beginning of the reaction. Two-dimensional diffusion control indicates that, when a pair of layers has been prised apart (''nucleation''), the diffusion of the new guest molecules into the interlayer space is easy: thus, diffusion control operates thereafter.[10]

The intercalation of Val into NiZn-NO_3 gave similar results to the CoZn-NO_3 reaction, with a one stage reaction observed and reflections arising at essentially the same d-spacings as for CoZn-NO_3 (see Appendix II). The reaction with Zn-NO_3 could not be explored due to the limited availability of synchrotron time.

Table 3.3: Summary of the kinetic data for Val.

	Temperature (ºC)	*n*	*k* ($10^{-3}.s^{-1}$)
NiZn-NO_3	80	1.043	2.955
CoZn-NO_3	80	0.971	1.525

3.2.5.2. Intercalation of Dic

3.2.5.2.1. Intercalation into CoZn-NO_3

In situ data for Dic intercalation at 80 ºC into CoZn-NO_3 are given in Figure 3.8. No intermediates are observed: the starting material is converted directly to the product. However, there is a peak (9.2 Å) which appeared after the product *200* reflection began to grow in. The latter peak moves to lower d-spacing with time. The identity of this reflection is uncertain, and it is thought it might be an artefact in the beginning and is discussed below. Plots of α *vs.* time are depicted in Figure 3.8b. The α *vs.* t curves of the starting material and final product cross close to α ≈ 0.45, which confirms a one-step transformation. There is very large difference between the intercalate interlayer spacing observed *in situ* and *ex situ* (16.5 Å vs 22.3 Å). The reasons behind this are not completely clear, but this may be a result of the guests reorienting on drying.

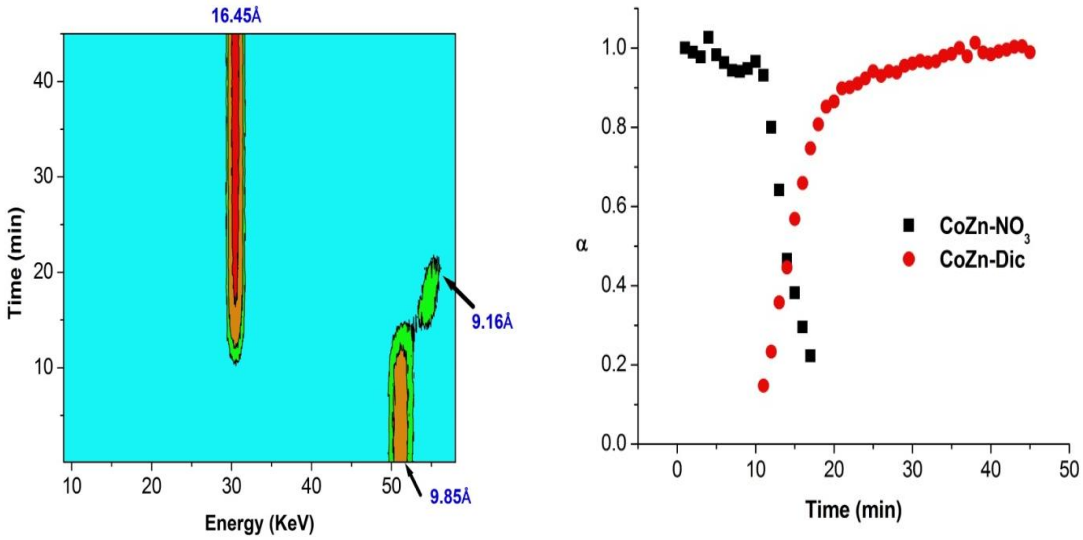

a b

Figure 3.8: *In situ* data for the intercalation of Dic into CoZn-NO_3 at 80 ºC. (a) a contour plot of the raw data; and, (b) an extent of reaction vs time plot showing the changes in intensity of the host (■),and product (●) 200 reflections.

A Sharp–Hancock plot for the product *200* reflection is given in Figure 3.9. The plot is not linear, and shows that there are at least two distinctive segments in the reaction with a change in reaction mechanism part way through the intercalation process. The values of n and k are given in Table 3.4. The values for n calculated here do not appear consistent with any of the likely mechanisms for intercalation into a layered material, and so no conclusions may be drawn here.

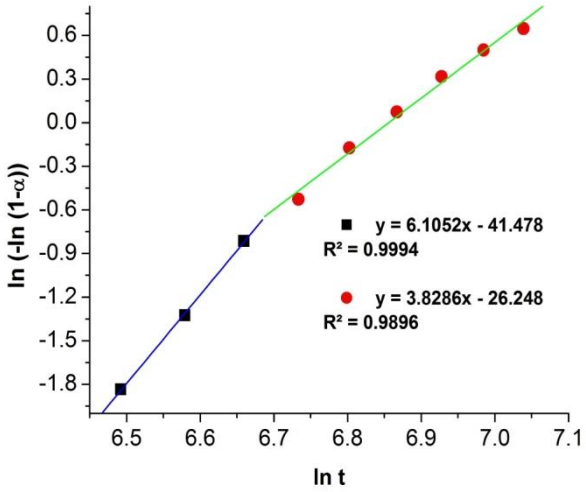

Figure 3.9: A Sharp–Hancock plot of the product *200* reflection for the intercalation of Dic into CoZn-NO_3

3.2.5.2.2. Intercalation into Zn-NO_3

In situ diffraction data for the intercalation of Dic into Zn-NO_3 are shown in Figure 3.10. The product *200* reflection *in situ* is located at 16.3 Å, a much smaller interlayer spacing than observed ex situ (22.3 Å). In addition to the starting material and product reflections, another (low intensity) reflection can be seen at around 9.2 Å. This is believed to be some sort of reaction intermediate rather than an artefact, since it appeared in all the reactions studied. Intermediate phases have previously been observed during the intercalation of guests into LDHs and HDSs.[44–47] Plots of α *vs.* time for intercalation are depicted in Figure 3.10b. The α *vs.* t curves of the starting material and final product cross close to α ≈ 0.4, and the intermediate and final product curves also intersect at α ≈ 0.4. From these data, it is thus hard to confirm whether the reaction occurs in one step, with an artefact present in the data, or if this is a true two-step transformation.

All the *in situ* work described thus far was performed on Beamline F3 of the DORIS facility at the Deutsches Elektronen-Synchrotron (DESY) in Hamburg. To explore the intercalation of Dic into Zn-NO_3 in more detail and to determine whether a one or two step process is operational we undertook additional experiments on Beamline I12 of the Diamond facility. This has a much higher resolution area detector, with a wider angular detection range, than the Ge detector present on F3. The raw data (see Figure 3.10) show the product peak *200* reflection to arise at around 16.3 Å, similar to the DESY data. In addition, further peaks can be observed, including the *400* at 8.2 Å and *600* at 5.4 Å.

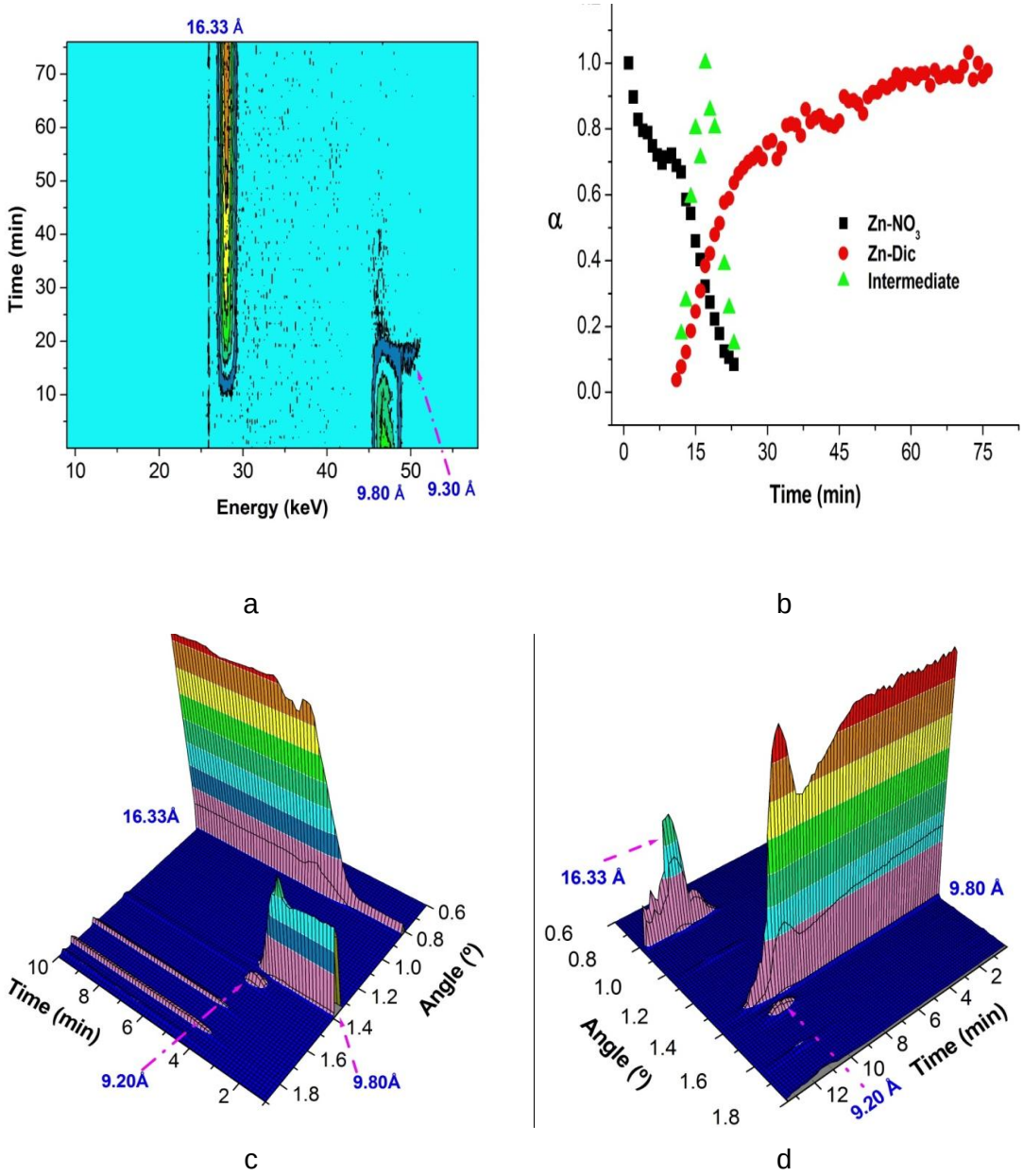

Figure 3.10: *In situ* data for the intercalation of Dic into Zn-NO_3. **(a)** Raw data obtained at DESY at 80 ºC; **(b)** an extent of reaction *vs.* time plot showing the changes in intensity of the host, intermediate and product *200* reflections from the DESY data, and data obtained using Diamond **(c)** at 80 ºC, and **(d)** at 70 ºC.

Both *in situ* experiments hence show the Zn-Dic product to have a *200* reflection with a lower d-spacing than that observed *ex situ*, which led us to carry out a quenching reaction under the same conditions. In this we halted the reaction after 80 min. The XRD pattern of the quenched product (Figure 3.11) shows a virtually identical interlayer spacing to that observed *in situ* (15.6 Å), with an intense *200* reflection and weak *400 & 600* reflections. Afterwards, the quenched product was returned to the Dic solution and left to stir for 12 h at 80 ºC. The XRD pattern of the material recovered shows a very intense reflection at 20.5 Å, while the phase at 15.6 Å has almost vanished. Based on this data, the *in situ* phase seen at 16.3 Å appears to be a long-lived intermediate. The CHN analysis data of the quenched material shows that only 65 % of the nitrate ions (NO_3^-) were replaced by Dic ions. However, for the final product (Table 3.1) the data demonstrate that all the initial nitrate ions were replaced by Dic.

The intercalation of Dic into Zn-NO_3 showed a strange phenomenon: a drop in the intensity of the host *200* reflection, followed by a subsequent increase. This was initially assumed to be the result of a stirring problem. However, comparing the Diamond data (at 70 ºC and 80 ºC, see Figure 3.10c, d) with DESY data (Figure 3.10a) shows that this occurred at roughly the same time in all experiments. This led us to re-examine the previously studied intercalation into CoZn and it shows a similar trend (Figure 3.8). Since this phenomenon is observed in a number of experiments, it is highly unlikely to be related to a stirring problem. It is unlikely to be some sort of phenomenon involving the layers coming into better register and thus giving greater intensity, since the intercalation of Nap into Zn-NO_3 (below) does not show this phenomenon and no one has reported this phenomena previously, even though there have been a number of *in situ* studies of intercalation into Zn-NO_3 and Zn-Cl.[10] Hence, it is proposed that some sort of an intermediate phase with the same d-spacing as the starting material may be forming.

To confirm this suggestion, experiments were performed with Zn-Cl, since it has a different initial interlayer spacing (7.8 Å) to that of Zn-NO_3. If the phenomenon seen with Zn-NO_3 is not related to an intermediate, no peak should be seen around 9.8 Å. Quenching reactions were conducted in the same conditions as were deployed *in situ*, with the reaction halted after a range of different times. The XRD patterns shown in Figure 3.11 demonstrate that the *in situ* phenomenon seen during the intercalation of Dic into Zn-NO_3 is caused by an intermediate that has a d-spacing of 9.8 Å. In addition, the peak seen at 9.2 Å is a genuine reflection and not an artefact.

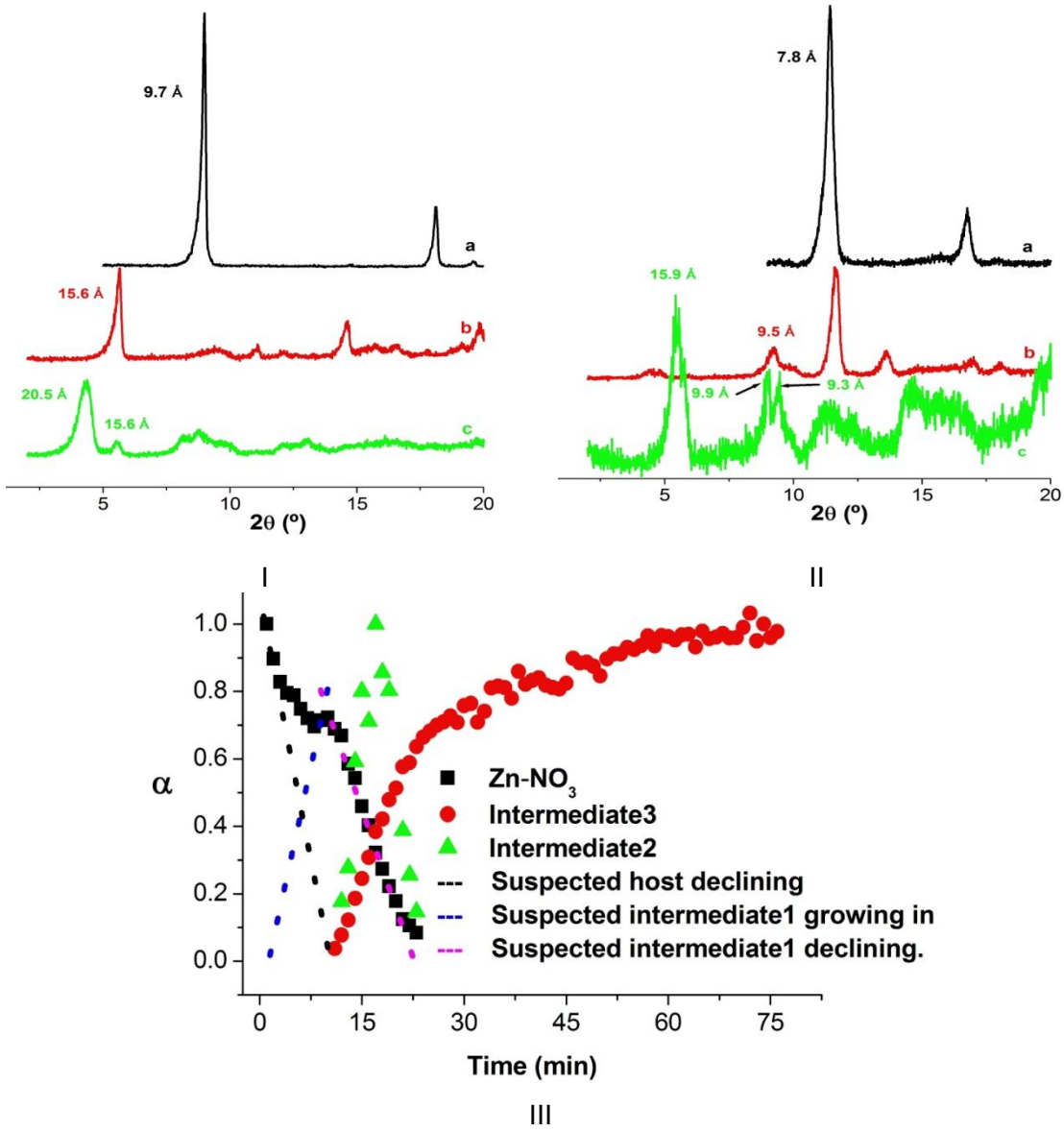

Figure 3.11: The intercalation of Dic into all-Zn HDS systems. XRD patterns of the quenched products obtained for intercalation into the (I) Zn-NO_3 system for **(a)** 0 min, **(b)** 80 min and **(c)** 12 h; **(II)** Zn-Cl system after **(a)** 0 min; **(b)** 120 min and **(c)** 24 h. **(III)** depicts an extent of reaction vs time plot showing the changes in intensity of the host, intermediate and product *200* reflections, in addition to lines illustrating where an intermediate is suspected to be overlapping with the host *200* reflection.

It is not immediately obvious from the d-spacings observed exactly what the nature of the intermediate is; it does not appear to be a classical staging intermediate as has been observed previously for LDHs. Molecular dynamics simulations were performed to investigate this in more detail, and the results are presented in Section 3.2.7.

Plots of α *vs.* time for Dic intercalation into Zn-NO_3, which illustrates the suspected trends, are depicted in Figure 3.11. The reaction process for Dic intercalation can thus be summarised as follows:

Zn-NO_3 (9.80 Å) → Intermediate 1 (9.80 Å) → Intermediate 2 (9.20 Å) → Intermediate 3 (16.33 Å) → Product (22.30 Å).

The intercalation reaction is 4-steps transformation, which has gone via three intermediates phases.

A Sharp–Hancock plot for the Zn-NO_3 and Zn-Dic *200* reflections is given in Figure 3.12. Both plots are non-linear, and show that there are at least two distinctive phases during the reaction. This indicates that the reaction proceeds *via* a changing mechanism, in agreement with the above analysis. The *n* values calculated indicate that the mechanism which takes place as the starting material *200* reflection approaches zero (Figure 3.12a) is the same as that when the product begins to grow in (see Figure 3.12b). It seems that the first stage in the plot given in Figure 3.12a is related to the starting material (Zn-NO_3) and the second to an intermediate phase. The values of n and k calculated are summarised in Table 3.4.

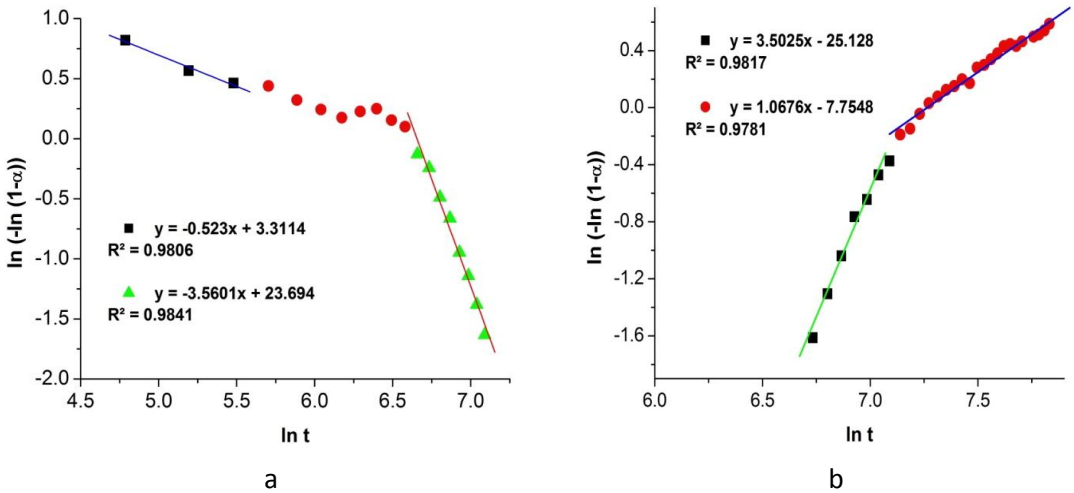

Figure 3.12: Sharp–Hancock plots of the **(a)** host and **(b)** product *200* reflections for the intercalation of Dic into Zn-NO_3.

3.2.5.2.3. Intercalation into NiZn-NO_3

The intercalation of Dic into NiZn-NO_3 appears more straightforward process than its reactions with the other HDSs studied. The raw data (Figure 3.13a) show the product peak *200* reflection to arise at around 24.3 Å (*400*: 12.2 Å, *600*: 8.2 Å). The d-spacing *in situ* is similar to that observed *ex situ* (21.2 Å). The starting material *200* reflection shifts from 9.8 Å to 9.5 Å during the reaction, which was not seen with the intercalation of Val into NiZn-NO_3. Plots of α *vs.* time for intercalation are depicted in Figure 3.13b. The α *vs.* t curves of the starting material and final product cross close to α = 0.5, confirming a one-step transformation.

A Sharp–Hancock plot for the product *200* reflection of NiZn-Dic is given in Figure 3.13c. The plot is linear, indicating that the reaction proceeds via a consistent mechanism over the entire course of the reaction. The reaction exponent n is observed to be ca. 1 at 80 ºC. This means that the reaction mechanism is of nucleation–growth type, with instantaneous nucleation and two dimensional diffusion control thereafter, as seen for the intercalation of Val into CoZn-NO_3 and NiZn-NO_3.

Table 3.4: Summary of the kinetic data for Dic intercalation.

	***Temperature* (ºC)**	***n***	***k* ($10^{-3}.s^{-1}$)**
Zn-NO_3	80	3.503 (a)	0.766
		1.068 (b)	0.701
CoZn-NO_3	80	6.105 (a)	1.053
		3.829 (b)	1.121
NiZn-NO_3	80	1.004	1.183

(a) The first stage of reaction
(b) The second stage of reaction

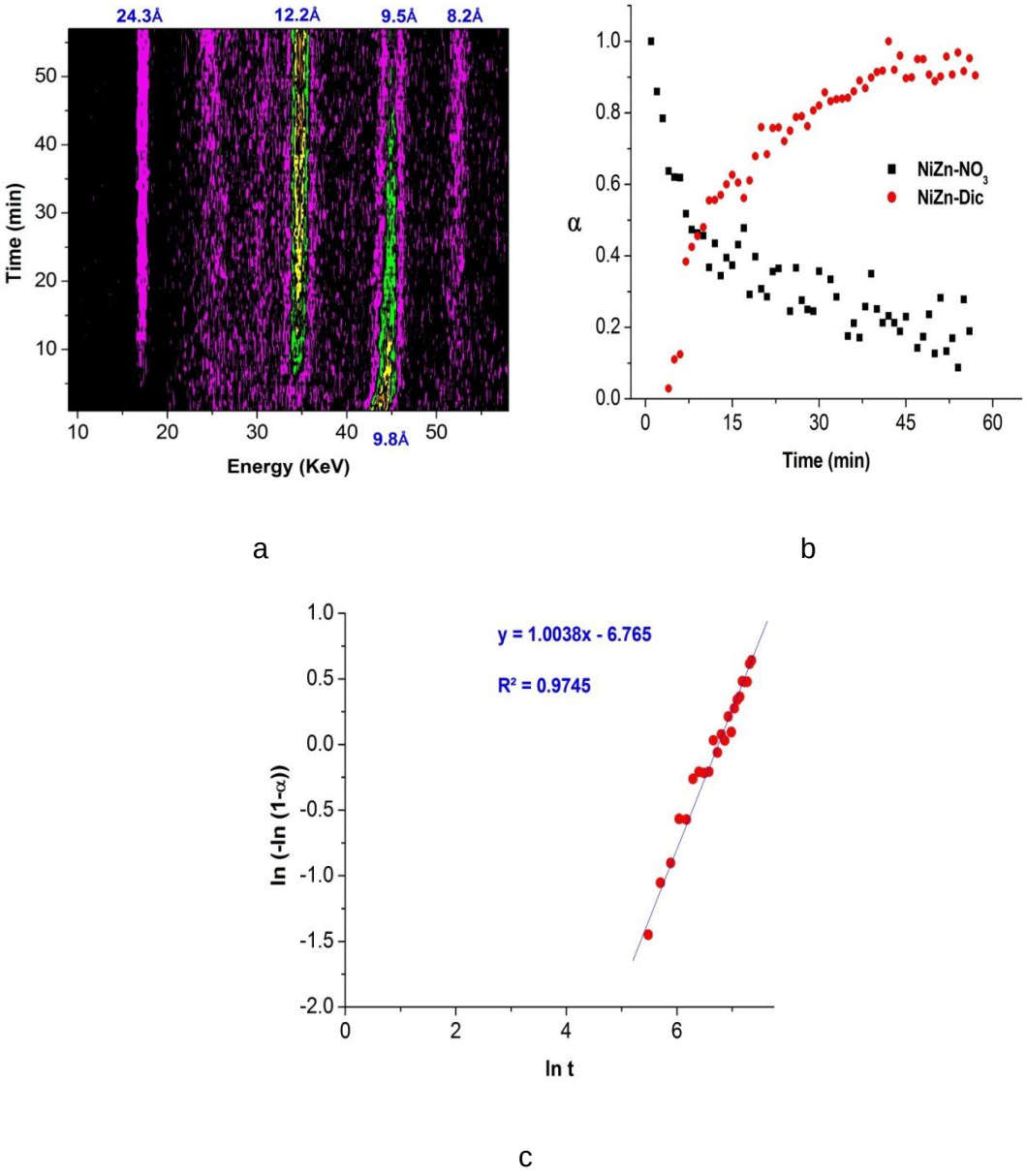

Figure 3.13: *In situ* data for the intercalation of Dic into NiZn-NO_3 .**(a)** Raw data collected at 80 ºC **(b)** an extent of reaction *vs* time plot showing the changes in intensity of the host and product *200* reflections, **(c)** a Sharp–Hancock plot of the product *200* reflection.

3.2.5.3. Intercalation of Nap

3.2.5.3.1. Intercalation into CoZn-NO_3

In situ diffraction data for the intercalation of Nap are given in Figure 3.14. Experiments were performed both at Diamond and DESY to ensure the reproducibility of the results obtained. The intercalation of Nap into CoZn-NO_3 at 80 ºC shows that the intercalate has essentially the same interlayer spacing *in situ* and *ex situ* (24.3 Å *vs.* 24.1 Å). A clear crystalline intermediate phase was observed in the diffraction data, with two distinctive reflections that appear and disappear virtually at the same time (the *400* and *600* reflections were clearly observed but the *200* was beyond the detection window). The intermediate possesses a higher d-spacing than the final CoZn-Nap product.

The intensities of the CoZn-NO_3 *200,* CoZn-Nap *400* and the intermediate *400* reflections were integrated and are plotted as *α* vs t curves in Figure 3.14c. The reflections from CoZn-NO_3 and CoZn-Nap cross at α ≈ 0, consistent with the observation of an intermediate. The starting material *vs* intermediate curves cross at α ≈ 0.5, as do the intermediate *vs* product curves. This indicates a two stage transformation, since the diffracted intensity lost from the starting material is matched by diffraction intensity gained by the intermediate, and that lost from the intermediate is gained by the product; hence the intercalation reaction has gone *via* an intermediate phase. It should be noted that there is an overlap of the *200* reflection from CoZn-NO_3 with the *600* of the intermediate. Therefore, the change in the intensity of the host reflection was not plotted after 4 min.

The Sharp–Hancock plot for CoZn-Nap is given in Figure 3.14d. The plot is not linear (it shows that there are two distinctive phases), indicating that the intercalation process proceeds via an inconsistent mechanism. The *n* and *k* values are summarised in Table 3.5. The values for n calculated here do not appear consistent with any of the likely mechanisms for intercalation into a layered material, and so no conclusions may be drawn here. Molecular dynamics simulations were performed to investigate this in more detail the intermediate phase, and the results are presented in Section 3.2.7.

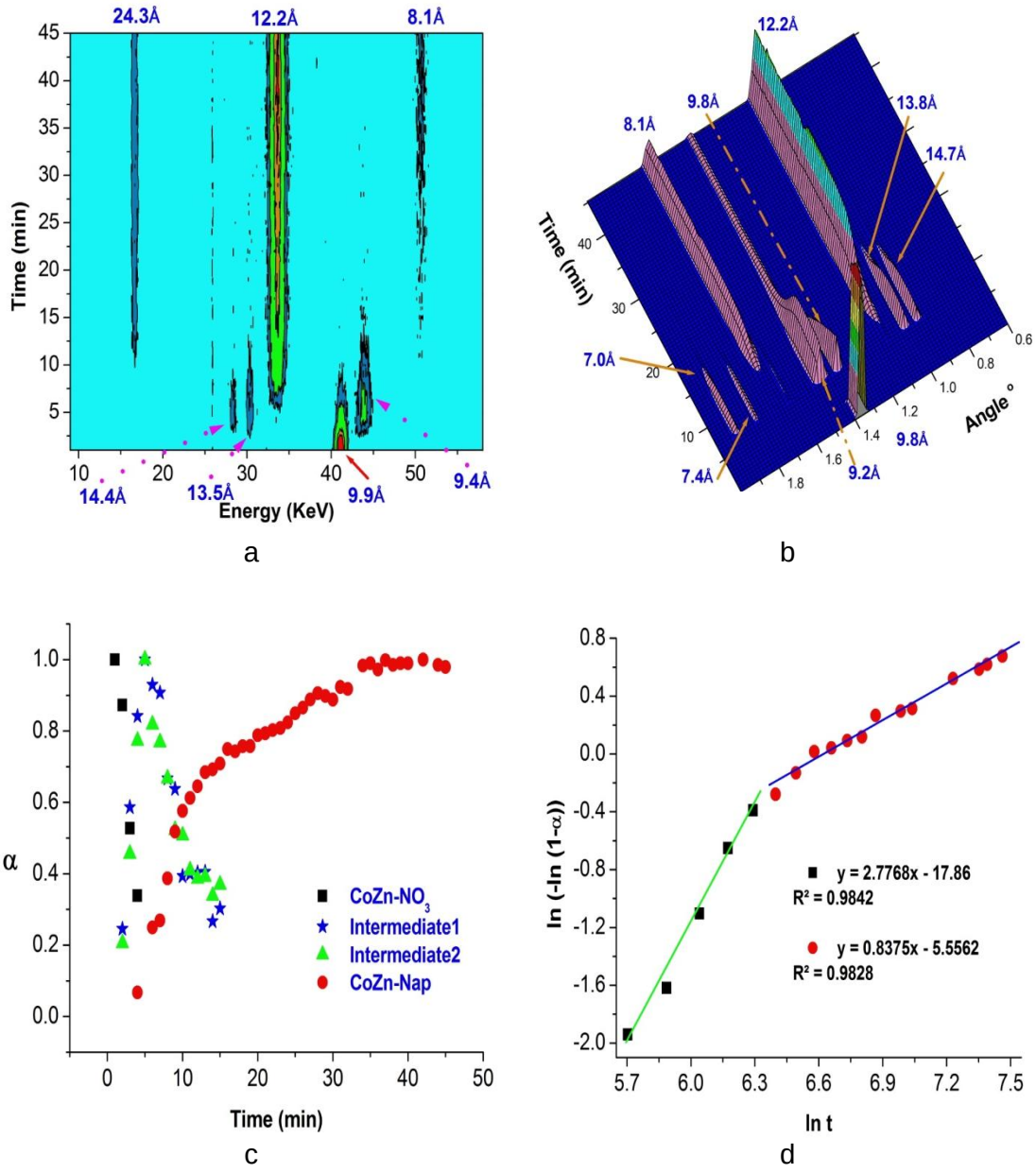

Figure 3.14: *In situ* data for the intercalation of Nap into CoZn-NO_3 at 80 ºC. Raw data obtained at **(a)** DESY and **(b)** Diamond; **(c)** an extent of reaction vs time plot showing the changes in intensity of the host *200*,intermediate and product *400* reflections; **(d)** a Sharp–Hancock plot for the product *400* reflection.

3.2.5.3.2. Intercalation into Zn-NO_3

The intercalation of Nap into Zn-NO_3 (Figure 3.15a, b) also seems to proceed *via* a crystalline intermediate phase. In Figure 3.15b, a small peak can be seen at 21.5 Å in the data (*400*: 10.7 Å, *600*: 7.1 Å). This was not observed when the experiment was performed at DESY, probably due to the poorer resolution of the latter detector. A further intermediate peak is located at 9.2 Å; this appears after the first intermediate. It seems that there are two product phases, one at 24.0 Å (product 1) and a second around 20.8 Å (product 2). This could be correlated with the existence of two different arrangements of Nap ions inside the Zn-Nap system here. The product 1 reflection appeared after the disappearance of both intermediates. It seems that there is a direct relationship between this product and the intermediates, but no connection between the other product and the intermediates, since they emerge practically at same time. After drying the product, the XRD pattern (Appendix II) contains a very intense reflection at around 24.0 Å, while the peak around 20.8 Å had virtually vanished. This is in agreement with the data observed *ex situ,* where the Zn-Nap system show an interlayer spacing of 24.6 Å.

The Sharp–Hancock plot for the two product (Zn-Nap) *200* reflections are given in Figure 3.15d,e. The plot for the product 2 peak shows linearity, so the reaction proceeds via a consistent mechanism over its entire course. The plot for the product 1 peak is not linear (it shows that there are two distinctive phases), indicating that the reaction proceeds via an inconsistent mechanism. The *n* and *k* values are summarised in Table 3.5. The values for n calculated here do not appear consistent with any of the likely mechanisms for intercalation into a layered material, and so no conclusions may be drawn here.

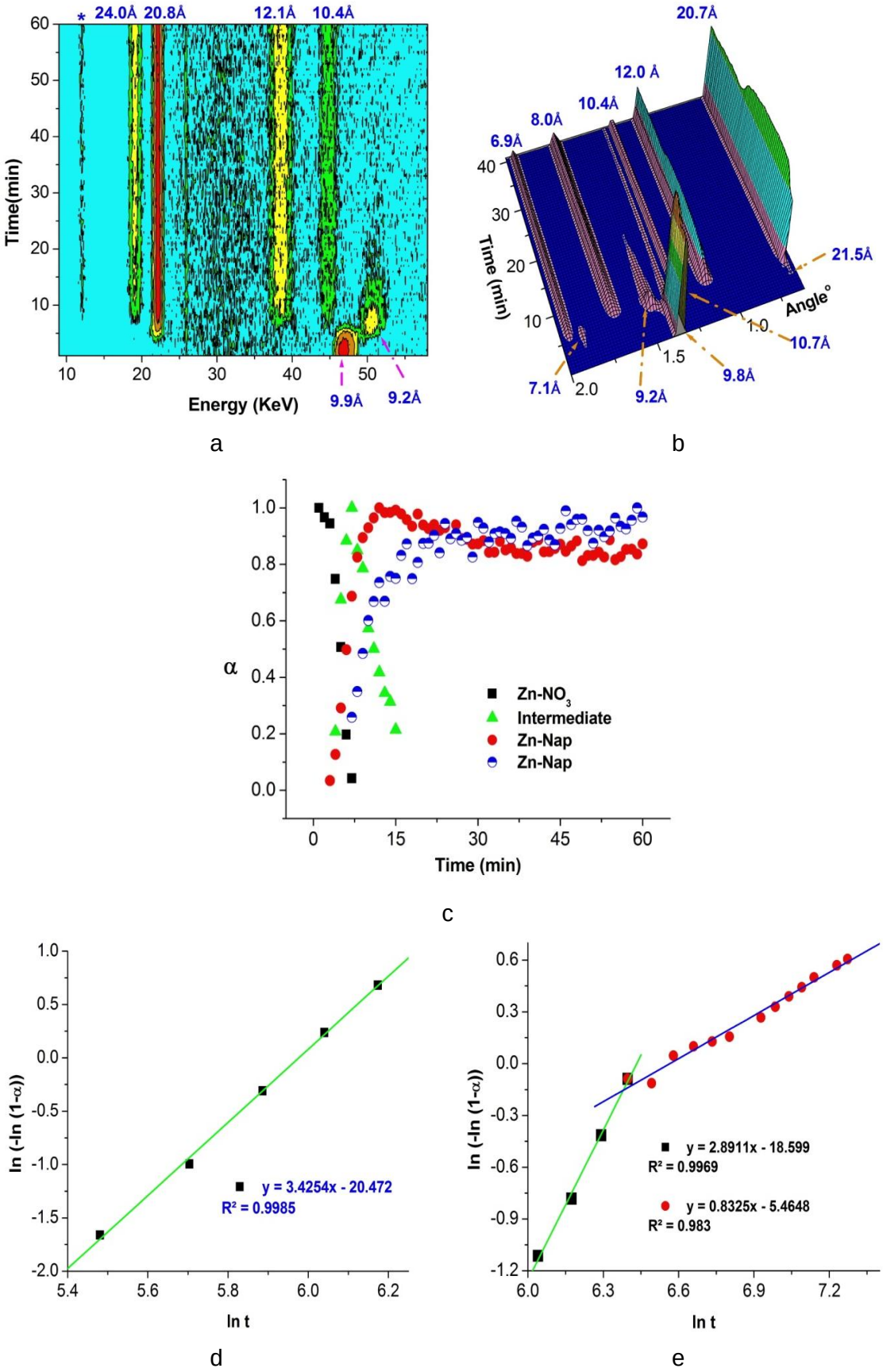

Figure 3.15: *In situ* data for the intercalation of Nap into Zn-NO_3 at 80 ºC **(a)** raw data obtained at DESY, **(b)** the raw dataset from Diamond, **(c)** Extent of reaction vs time data showing the changes in intensity of the host, intermediate and product 200 reflections, Sharp–Hancock plot for the *200* reflections of the two product phases observed **(d)** product 2 (20.8 Å) and **(e)** product 1 (24.0 Å)

3.2.5.3.3. Intercalation into NiZn-NO_3

In situ data for Nap intercalation into NiZn-NO_3 at 80 ºC are given in Figure 3.16a. No intermediates are observed, and the α vs t curves in Figure 3.16b cross at α ≈ 0.5 which indicates a one step process, as seen for the intercalation of Val and Dic into this system. The raw data show the product *200* reflection to arise at around 24.6 Å (*400*: 12.4 Å, *600*: 8.3 Å). The d-spacing *in situ* is very similar to that observed *ex situ* (24.2 Å).

A Sharp–Hancock plot for the product *200* reflection is given in Figure 3.16c. The plot is not linear, and shows that there are at least two distinctive phases. The reaction was also studied at lower temperatures (60, 70 and 75 ºC). Below 80 ºC, all the Sharp-Hancock plots are linear, indicating that at these temperatures a consistent mechanism over the entire course of the reaction. The reaction exponent *n* is observed to be *ca.* 1 when temperature is lower than 80 ºC (see Table 3.5). Williams and co-workers saw similar results when they intercalated 1,2 benzenedicarboxylate into Zn-NO_3 at 90 ºC: non-linear Sharp–Hancock plots were obtained with two distinctive phases, and the exponent values of 0.65 and 1.28. At 80 ºC, the Sharp–Hancock plot was linear and $n \approx 1$.[10]

The activation energy (E_a) for the intercalation of Nap into NiZn-NO_3 is estimated to be around 45 kJ mol^{-1} from the *k* values (Table 3.5). Based on the reaction exponent *n* (Table 3.5), the intercalation of Nap is a complex process, with a number of different mechanisms being operational depending on the HDS (Zn-NO_3, NiZn-NO_3 and CoZn-NO_3) and the reaction temperature.

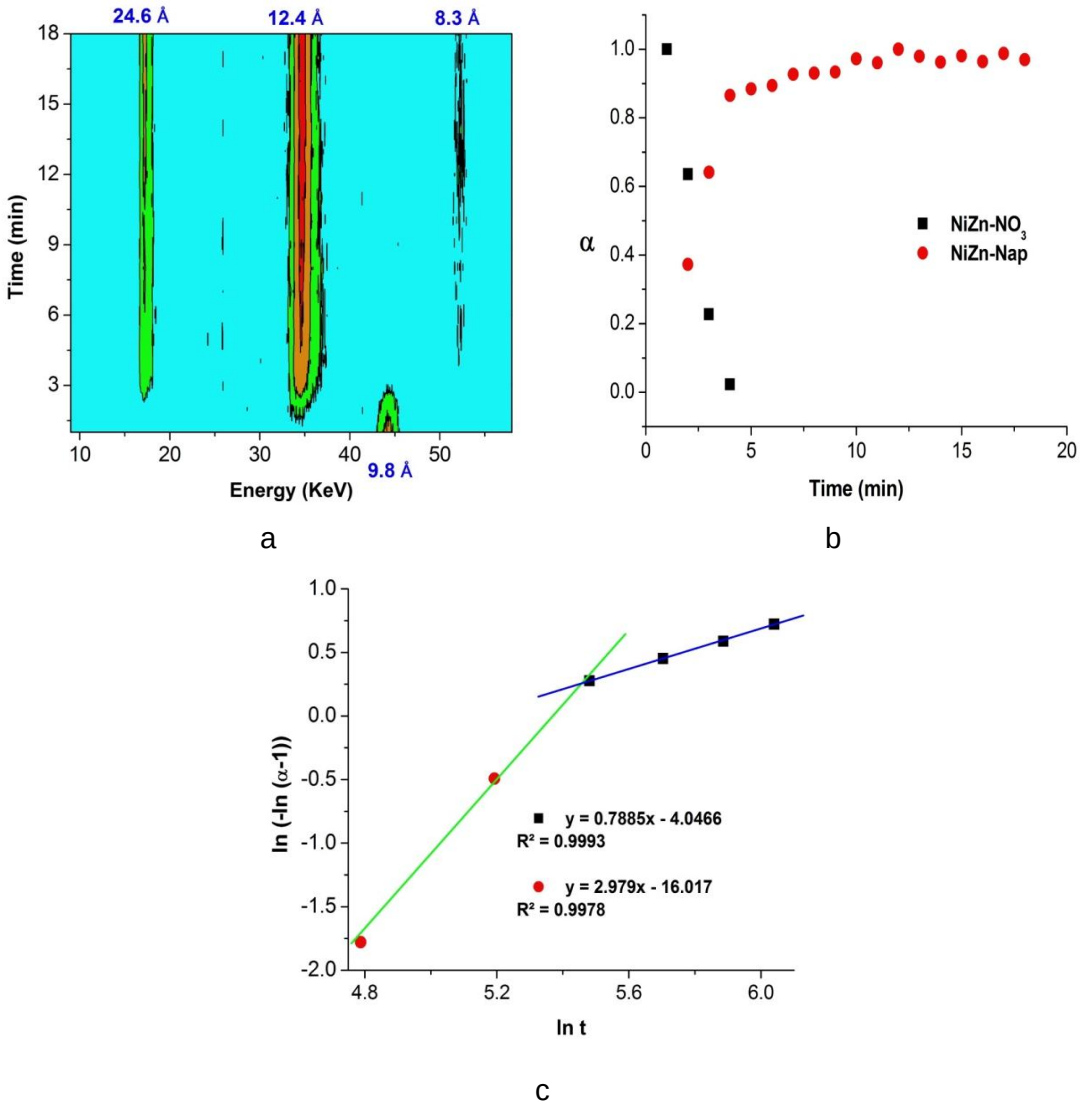

Figure 3.16: *In situ* data for the intercalation of Nap into NiZn-NO_3 at 80 ºC **(a)** the raw data obtained at DESY, **(b)** an extent of reaction vs time plot showing the changes in intensity of the host and product *200* reflections and **(c)** a Sharp–Hancock plot for the product *200* reflection.

Table 3.5: Summary of the kinetic data for Nap.

HDS	Temperature (ºC)	*n*	*k* ($10^{-3}.s^{-1}$)	Activation energy (Ea) (kJ mol^{-1})
CoZn-NO_3	80	2.777[(a)]	1.610	
		0.838[(b)]	1.315	
NiZn-NO_3	60	0.978	1.222	44.673
	70	0.978	1.630	
	75	1.185	2.089	
	80	2.979[(a)]	4.623	
		0.789[(b)]	5.905	
Zn-NO_3	80	3.425[(2)]	2.538	
		2.891[(1)(a)]	1.607	
		0.833[(1)(b)]	1.410	

(1) product 1, (2) product 2.
(a) The first stage of reaction,(b) The second stage of reaction

3.2.6. Comparison of in situ datasets

The reaction exponent values for all the intercalation reactions are collated in Table 3.6. The reaction exponent n for the intercalation of Dic, Nap and Val into NiZn-NO_3 is observed to be ca. 1 at the different temperatures studied. This means that the reaction mechanism is a nucleation–growth type, with instantaneous nucleation and two dimensional diffusion control thereafter. It seems the intercalation process into NiZn-NO_3 goes *via* this same mechanism for all the guests studied and is rapid process. The intercalation of Val into both CoZn-NO_3 and NiZn-NO_3 occurs by the same mechanism. The majority of the one step intercalation reactions show linear Sharp–Hancock plots (the exception being NiZn-Nap at 80 ºC), while the more complex multi-step processes have distinctly non-linear Sharp–Hancock plots.

Table 3.6: A summary of reaction exponent data for Dic, Nap and Val intercalation.

HDS	Guest	Temperature (ºC)	n	Sharp–Hancock plot linearity	Presence of intermediate
CoZn-NO_3	Val	80	0.971	linear	-
NiZn-NO_3	Val	80	1.043	linear	-
Zn-NO_3	Dic	80	3.503$^{(a)}$	non-linear	yes
			1.068$^{(b)}$		
CoZn-NO_3	Dic	80	3.829$^{(a)}$	non-linear	yes
			6.105$^{(b)}$		
NiZn-NO_3	Dic	80	1.004	linear	-
Zn-NO_3	Nap	70	1.026	linear	-
		80	3.425$^{(2)}$	linear	-
			2.891$^{(1)(a)}$	non-linear	yes
			0.833$^{(1)(b)}$		
CoZn-NO_3	Nap	70	2.866	linear	-
		80	2.777$^{(a)}$	Non-linear	yes
			0.838$^{(b)}$		
NiZn-NO_3	Nap	60	0.978	linear	-
		70	0.978	linear	-
		75	1.185	linear	-
		80	2.979$^{(a)}$	non-linear	-
			0.789$^{(b)}$		

(1) product 1, (2) product 2.
(a) The first stage of reaction,(b) The second stage of reaction.

3.2.7. Molecular dynamics for the *in situ* data

As was revealed in Section 3.2.5, a number of the reactions studied proceeded *via* crystalline intermediate phases. To obtain more insight into the precise nature of these, molecular dynamics (MD) simulations were undertaken. Modelling of the CoZn and NiZn mixed systems was not undertaken because of uncertainty as to the precise arrangement of metal ions in the systems. XPS data revealed that the Co^{2+} and Ni^{2+} both occupy octahedral sites in the HDS, Since no crystal structure is known here it would have been very difficult to establish an acceptable model. Thus, MD was performed for the all-Zn HDS.

The intercalation of Nap into Zn-NO_3 showed there to be intermediate phases at 27.0 and 28.8 Å. MD simulation of the higher d-spacing intermediate phase shows that the Nap ions are arranged in a perpendicular bilayer arrangement (Figure 3.17a). This yields a d-spacing of 28.0 Å. This arrangement is unstable, and thus the Nap ions rearrange themselves in an intertwined bilayer to give a phase with an interlayer spacing of 24.3 Å as discussed in Section 3.2.5.3.1.

The MD of the Dic intermediate phase shows that the guest ions are arranged in a perpendicular monolayer arrangement (Figure 3.17b) with a d-spacing of 16.0 Å. The carboxylate groups of Dic and NO_3 ions are close to Zn_{tetra}. This arrangement becomes unstable when number of Dic ions in the interlayer region increases and the amount of NO_3 ions declines. As a result, at a critical Dic content the ions rearrange themselves in an intertwined bilayer arrangement to give a phase with an interlayer spacing of 22 Å.

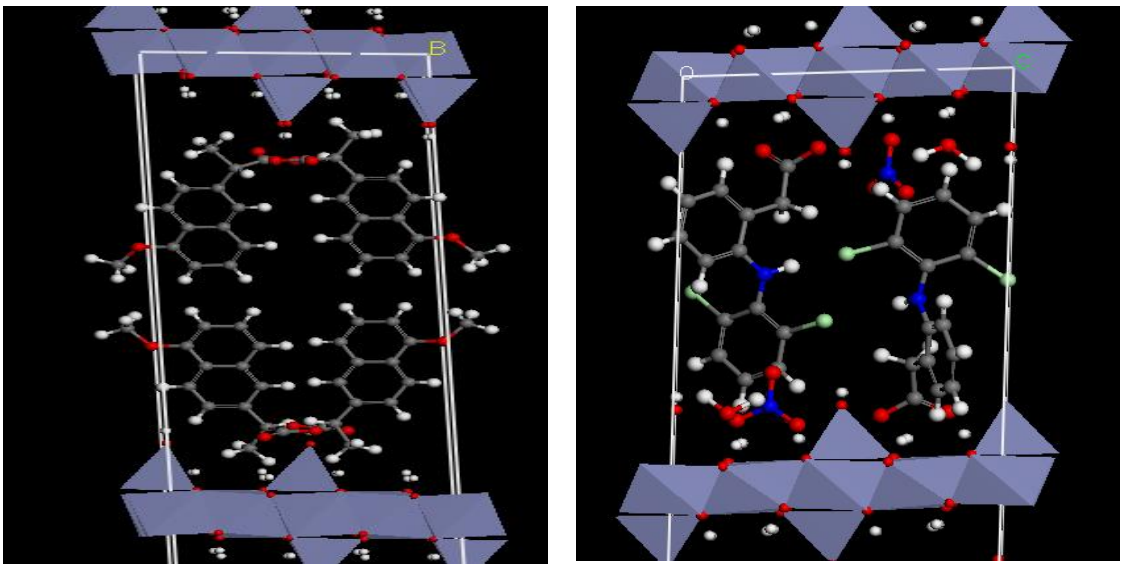

a b

Figure 3.17: MD results for the orientation in the intermediate phase of **(a)** Nap at 28.0 Å and **(b)** Dic at 16.0 Å.

3.2.8. Drug release

A drug release study was carried out on selected samples in a phosphate buffer saline (PBS) (pH 7.4) to explore the potential of the HDS systems for drug delivery. Dic release (see Figure 3.18a) was faster from the all Zn HDS (Zn-NO_3) than from those containing a mixture of divalent metals (CoZn-NO_3 and NiZn-NO_3). Dic was released fully within 6 h from Zn-Dic (Figure 3.18a). Dic release from CoZn-Dic was slightly faster than from NiZn-Dic and the full loading was released within 24 h. However, a maximum of around 75 % release was observed from NiZn-Dic after 6 h, after which the release rate decreased and only 85 % release was reached after 24 h (Figure 3.18). The Dic release from the different HDSs shows a fast release rate in the beginning, followed by a more moderate rate. This two-stage release behaviour has previously been reported from LDH and HDS systems for various drugs, including NSAIDs.[48–52]

The Nap release profile from CoZn-Nap is given in Figure 3.19b; the full drug loading was released within 5 h. Nap release thus occurred faster than Dic from the CoZn system. This could be explained by its higher solubility than Dic.[53,54] As a result of these preliminary experiments, it is clear that the intercalates seem to have promise for sustained release.

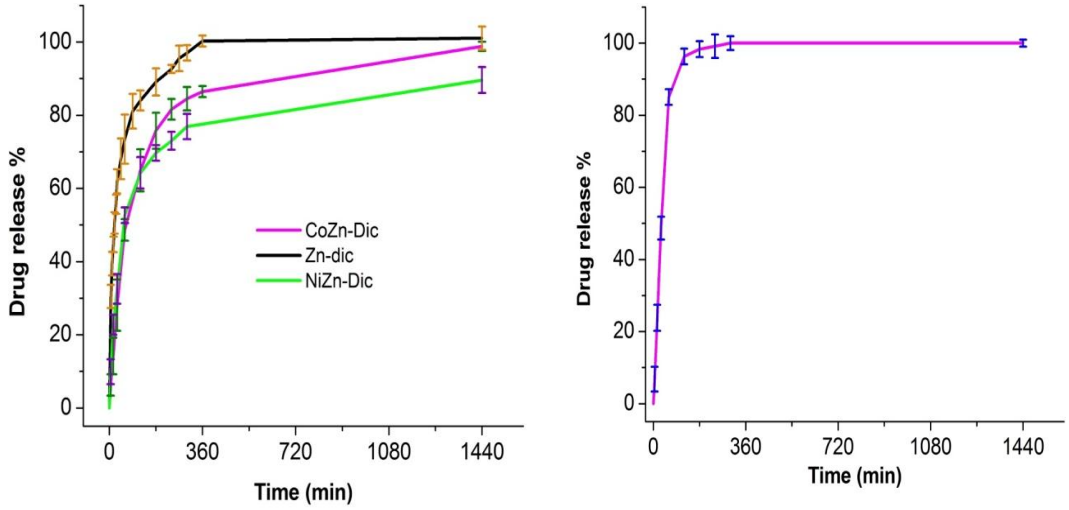

a b

Figure 3.18: Drug release in a PBS buffer. **(a)** Dic from Zn-Dic, NiZn-Dic and CoZn-Dic; **(b)** Nap from CoZn-Nap.

In the second step, a trial drug release was carried out in conditions that mimic passage through the human gastrointestinal tract (see Appendix II). The carrier Zn-Dic released only 2 % of its drug loading in acidic media (2 h). The release rate was faster once the pH was increased to 6.8, and Zn-Dic released most of its loading within 9 h. The drug release from CoZn-Dic was slower, as seen at pH 7.4 (in PBS), and was complete after around 21 h. Dic release from both Zn-Dic and CoZn-Dic shows a slower rate at pH 6.8 than 7.4; the correlation between the rate of release from layered systems and pH has been reported previously.[55,56] On the basis of the data obtained to date, HDSs seem to have promise for sustained release and the release profiles observed comply with the pharmacopeia requirements for intestinal drug targeting.[57–59]

3.2.9. Drug delivery potential of HDSs

The release data obtained above show that the CoZn, NiZn and Zn-based HDSs have great potential as sustained release drug delivery systems. There has been a small amount of work using HDSs for drug delivery prior to this.[60,61] Much more attention has been paid to LDHs, however. For instance, Mg/Al based layered double hydroxides loaded with omeprazole have been used in the treatment of ulcers and showed better therapeutic effects than omeprazole on its own.[62] LDHs intercalated with drug molecules can reduce the side-effects of NSAIDs significantly, owing to their basic nature.[63,64] Zinc and aluminium have almost the same LD_{50} (lethal dose, 50 %),[65–70] and in experiments looking into Mg/Al-NSAID intercalates no animals died prior to sacrifice.[62,63] Both the LDH and HDS materials are basic, and so it is hoped that HDSs will reduce the side-effects of NSAIDs in a similar manner to LDHs.

However, free metals can be absorbed during their passage through gastro-intestinal tract,[71] and since it has been reported that metals can leach from HDSs it is important to consider the possible uptake of metals into the body and their concentration. Zinc is an essential trace element in humans and animals, because it is crucial for the function of a large number of metalloenzymes.[65–67,69] Therefore, oral uptake of small amounts of zinc is indispensable for endurance. The recommended dietary allowance (RDA) for zinc is 11 mg/day for men, 8 mg/day for women, and lower for infants (2–3 mg/day) and children (5–9 mg/day) because of their lower average body weights.[72] This is significantly below the LD_{50} value, which has been estimated to be 27 g/day for humans, based on comparison with equivalent studies in rats and mice.[67]

Usually, the daily maximum dose of diclofenac is around 200 mg (the required dose depends on many factors such as the nature of a diseased being treated, age of the patient, etc). The chemical formulae of the intercalates are $Zn_5(OH)_8$-$(Dic)_2$.$(H_2O)_2$ (for 200 mg diclofenac, there is 110 mg of zinc). The HDS are unlikely to be absorbed in the intestine due to their size, charge and insolubility in aqueous media.[73,74] In any event, even if they were fully absorbed, the

amount of zinc would be far below the LD_{50} (27g) for an adult (Table 3.8). Thus, the Zn-based systems are expected to be safe as drug delivery systems.

Acute oral lethality investigations imply that soluble nickel compounds are more toxic than its less-soluble compounds. LD_{50} values are between 39-139 mg/kg. In rats the oral LD_{50} values for the less soluble nickel compounds such as nickel oxide and subsulphide were >3,930 and >3,665 mg / kg, respectively.[75–79] Cobalt is another essential mineral required, in the composition of vitamin B_{12}, in very small amounts: the daily required dose is 1.5 µg for adults.[80] The LD_{50} for Cobalt ranges from 42.4 - 418 mg cobalt/kg. An LD_{50} of 3,672 mg cobalt/kg was determined for tricobalt tetraoxide, a highly insoluble cobalt compound.[81–84]

HDSs remain stable after intercalation and deintercalation. In addition, the *in vitro* tests show that HDSs are unlikely to break down during gastro-intestinal transit, and only small amounts of metal ions are observed to leach from the systems. If the HDS structure was fully disintegrated during gastro-intestinal transit, and all the metals were absorbed then drug delivery systems based on all three HDSs would in many cases remain non-toxic: calculated exposure values are summarised in Table 3.7.

Table 3.7: The amounts of Zn, Co, and Ni required per day to deliver a therapeutic dose of Dic, Nap, or Val, together with LD_{50} values for the metals.

HDS	Drug	Daily dose of drug (mg)	Amount of metals (mg) required for daily dose	LD_{50}(Zn) mg/Kg/day	LD_{50}(Ni) mg/Kg/day	LD_{50}(Co) mg/Kg/day
$Zn\text{-}NO_3$	Dic	25 - 200	Zn:14-111	186-623	-	-
	Nap	250-1500	Zn:178-1069	186-623	-	-
	Val	200-2500	Zn:228-2853	186-623	-	-
$NiZn\text{-}NO_3$	Dic	25-200	Zn:8-66 Ni:5-40	186-623	39-139	-
	Nap	250-1500	Zn:107-856 Ni:64/512	186-623	39-139	-
	Val	200-2500	Zn:137-1712 Ni:82-1025	186-623	39-139	-
$CoZn\text{-}NO_3$	Dic	25-200	Zn:10-80 Co:3-27	186-623	-	42.4-418
	Nap	250-1500	Zn:135-813 Co:39-231	186-623	-	42.4-418
	Val	200-2500	Zn:174-2169 Co:49-617	186-623	-	42.4-418

3.3. Conclusion

Dic and Nap were intercalated into several Zn-based HDSs. The intercalation of Val into Zn-NO_3 and Zn-Cl could not be achieved successfully, and led to the destruction of the HDS layers to yield ZnO. In contrast, the presence of Co^{2+} or Ni^{2+} in the HDS appears to stabilise the layers and resulted in the successful intercalation of Val into CoZn-NO_3 and NiZn-NO_3. *In situ* time resolved X-ray diffraction experiments showed that the intercalation of Dic and Nap into CoZn-NO_3 and Zn-NO_3 proceeds by distinct intermediates, while the intercalation of the three drugs into NiZn-NO_3 is a simple one step reaction proceeding directly from the starting material to product. Sharp–Hancock plots were linear for all the one step intercalation reactions but non-linear for the intercalation reactions that proceed via intermediate(s) phase.

Molecular dynamics (MD) simulations were employed to gain more insight into the arrangement of ions in the interlayer space, and it was found that the Dic and Nap ions were arranged in an “X” shape, forming a bilayer arrangement in the HDS interlayer space. Val was determined to adopt a position with its aliphatic groups parallel to the HDS layer, and again form a bilayer. The drug release from Zn-Dic, CoZn-Dic and NiZn-Dic showed a sustained release profile; the HDSs thus seem to have promise for sustained release and comply with pharmacopeia requirements.

3.4. References

1. Besserguenev, A. V *et al.* Synthesis and Structure of the Gibbsite Intercalation Compounds $[LiAl_2(OH)_6]X$ {X = Cl, Br, NO_3 } and $[LiAl_2(OH)_6]Cl{\cdot}H_2O$ Using Synchrotron X-ray and Neutron Powder Diffraction. *Chem. Mater.* **9,** 241–247 (1997).

2. Vialat, P. *et al.* High-performing monometallic cobalt layered double hydroxide supercapacitor with defined local structure. *Adv. Funct. Mater.* **24,** 4831–4842 (2014).

3. Britto, S. & Kamath, P. V. Polytypism in the Lithium–Aluminum Layered Double Hydroxides: The $[LiAl_2(OH)_6]$ + Layer as a Structural Synthon. *Inorg. Chem.* **50,** 5619–5627 (2011).

4. Merchán, M. *et al.* Photostability and photobactericidal properties of porphyrin-layered double hydroxide–polyurethane composite films. *J. Mater. Chem. B* **1,** 2139 (2013).

5. Oh, J.-M., Biswick, T. T. & Choy, J.-H. Layered nanomaterials for green materials. *J. Mater. Chem.* **19,** 2553 (2009).

6. Thomas, N. Mechanochemical synthesis of layered hydroxy salts. *Mater. Res. Bull.* **47,** 3568–3572 (2012).

7. Yang, J. *et al.* New Inorganic-Based Drug Delivery System of Indole-3-Acetic Acid-Layered Metal Hydroxide Nanohybrids with Controlled Release Rate. *Chem. Mater.* **19,** 2679–2685 (2007).

8. Kandare, E. & Hossenlopp, J. M. Hydroxy double salt anion exchange kinetics: Effects of precursor structure and anion sizet. *J. Phys. Chem. B* **109,** 8469–8475 (2005).

9. Morioka, H., Tagaya, H., Karasu, M., Kadokawa, J. & Chiba, K. Preparation of hydroxy double salts exchanged by organic compounds. *J. Mater. Res.* **13,** 848–851 (1998).

10. Williams, G. R., Crowder, J., Burley, J. C. & Fogg, A. M. The selective intercalation of organic carboxylates and sulfonates into hydroxy double salts. *J. Mater. Chem.* **22,** 13600 (2012).

11. Morioka, H., Tagaya, H., Kadokawa, J. I. & Chiba, K. Studies on layered basic zinc acetate. *J. Mater. Sci. Lett.* **18,** 995–998 (1999).

12. Rajamathi, J. T., Britto, S. & Rajamathi, M. Synthesis and anion exchange reactions of a layered copper-zinc hydroxy double salt, $Cu_{1.6}Zn_{0.4}(OH)_3(OAc){\cdot}H_2O$. *J. Chem. Sci.* **117,** 629–633 (2005).

13. Tagaya, H., Sasaki, N., Morioka, H. & Kadokawa, J. Preparation of New Inorganic—Organic Layered Compounds, Hydroxy Double Salts, and Preferential Intercalation of Organic Carboxylic Acids into Them. *Mol.*

Cryst. Liq. Cryst. Sci. Technol. Sect. A. Mol. Cryst. Liq. Cryst. **341,** 413–418 (2000).

14. Hara, T., Kurihara, J., Ichikuni, N. & Shimazu, S. Size Control of Catalytic Reaction Space by Intercalation of Alkylcarboxylate Anions into Ni–Zn Mixed Basic Salt Interlayer: Application for Knoevenagel Reaction in Water. *Chem. Lett.* **39,** 304–305 (2010).

15. Dong, L., Gou, G. & Jiao, L. Characterization of a dextran–coated layered double hydroxide acetylsalicylic acid delivery system and its pharmacokinetics in rabbit. *Acta Pharm. Sin. B* **3,** 400–407 (2013).

16. Al Ali, S. H. H. *et al.* Controlled release and angiotensin-converting enzyme inhibition properties of an antihypertensive drug based on a perindopril erbumine-layered double hydroxide nanocomposite. *Int. J. Nanomedicine* **7,** 2129–2141 (2012).

17. Hussein, S. H. *et al.* Comparative study of Mg/Al- and Zn/Al-layered double hydroxide-perindopril erbumine nanocomposites for inhibition of angiotensin-converting enzyme. *Int. J. Nanomedicine* **7,** 4251–4262 (2012).

18. Saifullah B, Hussein MZ, Hussein-Al-Ali SH, et al. Antituberculosis nanodelivery system with controlled-relase properties based on para-amino-salicylate-zinc amlunium-layered double-hydroxide nanocomposites. *Drug Des Devel Ther* **7,** 1365–1375 (2013).

19. Barahuie, F. *et al.* Preparation and controlled-release studies of a protocatechuic acid-magnesium/aluminumlayered double hydroxide nanocomposite. *Int. J. Nanomedicine* **8,** 1975–1987 (2013).

20. Berber, M. R., Minagawa, K., Katoh, M., Mori, T. & Tanaka, M. Nanocomposites of 2-arylpropionic acid drugs based on Mg-Al layered double hydroxide for dissolution enhancement. *Eur. J. Pharm. Sci.* **35,** 354–360 (2008).

21. Cao, F., Wang, Y., Ping, Q. & Liao, Z. Zn-Al-NO3-layered double hydroxides with intercalated diclofenac for ocular delivery. *Int. J. Pharm.* **404,** 250–256 (2011).

22. Choi, S. J. *et al.* In vivo anticancer activity of methotrexate-loaded layered double hydroxide nanoparticles. *Curr Pharm Des* (2013).

23. Peterson, K. *et al. Durg Class Review: Nonsteroidal Antiinflammatory Drugs (NSAIDs)*. *Oregon Heal. Sci. Univ.* (2010).

24. Day, R. O. & Graham, G. G. Non-steroidal anti-inflammatory drugs (NSAIDs). *BMJ* **346,** f3195 (2013).

25. Haddad, P. M., Das, A., Ashfaq, M. & Wieck, A. A review of valproate in psychiatric practice. *Expert Opin. Drug Metab. Toxicol.* **5,** 539–551 (2009).

26. Cipriani, A., Reid, K., Young, A. H., Macritchie, K. & Geddes, J. in *Cochrane Database Syst. Rev.* 1–73 (2013).

27. Khan, A. I., Lei, L., Norquist, A. J. & O'Hare, D. Intercalation and controlled release of pharmaceutically active compounds from a layered double hydroxide. *Chem. Commun. (Camb).* 2342–3 (2001).

28. Badawi, H. M., Förner, W. & Ali, S. A. A study of the experimental and theoretical infrared, Raman, 1H and 13C NMR spectra of the biochemicals valeric and valproic acids. *J. Mol. Struct.* **1075,** 494–503 (2014).

29. ChemAxon. Marvin 6.0.1. (2013). at <http://www.chemaxon.com>

30. Mohanambe, L. & Vasudevan, S. Anionic clays containing anti-inflammatory drug molecules: comparison of molecular dynamics simulation and measurements. *J. Phys. Chem. B* **109,** 15651–8 (2005).

31. Newman, S. P., Di Cristina, T., Coveney, P. V. & Jones, W. Molecular Dynamics Simulation of Cationic and Anionic Clays Containing Amino Acids. *Langmuir* **18,** 2933–2939 (2002).

32. Greenwell, H. C. *et al.* Interlayer Structure and Bonding in Nonswelling Primary Amine Intercalated Clays. *Macromolecules* **38,** 6189–6200 (2005).

33. Wang, J., Kalinichev, A. G. & Kirkpatrick, R. J. Effects of substrate structure and composition on the structure, dynamics, and energetics of water at mineral surfaces: A molecular dynamics modeling study. *Geochim. Cosmochim. Acta* **70,** 562–582 (2006).

34. Xu, S.-M. *et al.* Understanding the thermal motion of the luminescent dyes in the dye–surfactant cointercalated ZnAl-layered double hydroxides: a molecular dynamics study. *RSC Adv.* **4,** 47472–47480 (2014).

35. Demel, J. *et al.* Insight into the Structure of Layered Zinc Hydroxide Salts Intercalated with Dodecyl Sulfate Anions. *J. Phys. Chem. C* **118,** 27131–27141 (2014).

36. Francis, R. J. *et al.* Time-Resolved In-Situ Energy and Angular Dispersive X-ray Diffraction Studies of the Formation of the Microporous Gallophosphate ULM-5 under Hydrothermal Conditions. *J. Am. Chem. Soc.* **121,** 1002–1015 (1999).

37. Avrami, M. Kinetics of Phase Change. I General Theory. *J. Chem. Phys.* **7,** 1103 (1939).

38. Avrami, M. Kinetics of Phase Change. II Transformation-Time Relations for Random Distribution of Nuclei. *J. Chem. Phys.* **8,** 212 (1940).

39. Avrami, M. Granulation, Phase Change, and Microstructure Kinetics of Phase Change. III. *J. Chem. Phys.* **9,** 177 (1941).

40. Erofe'ev, B. Generalized equation of chemical kinetics and its application in reactions involving solids. *Compt Rend Acad Sci USSR* 511–14 (1946).

41. Williams, G. R., Norquist, A. J. & O'Hare, D. Time-Resolved, In Situ X-ray Diffraction Studies of Staging during Phosphonic Acid Intercalation into $[LiAl_2(OH)_6]Cl \cdot H_2O$. *Chem. Mater.* **16,** 975–981 (2004).

42. Hulbert, S. Models for solid-state reactions in powder compacts: A review. *J Brit Ceram Soc* **6,** 11–20 (1969).

43. Hancock, J. D. & Sharp, J. H. Method of Comparing Solid-State Kinetic Data and Its Application to the Decomposition of Kaolinite, Brucite, and $BaCO_3$. *J. Am. Ceram. Soc.* **55,** 74–77 (1972).

44. Du, Y. & O'Hare, D. Observation of staging during intercalation in layered alpha-cobalt hydroxides: a synthetic and kinetic study. *Inorg. Chem.* **47,** 11839–46 (2008).

45. Du, Y., Ok, K. M. & O'Hare, D. A kinetic study of the phase conversion of layered cobalt hydroxides. *J. Mater. Chem.* **18,** 4450 (2008).

46. Iyi, N., Fujii, K., Okamoto, K. & Sasaki, T. Factors influencing the hydration of layered double hydroxides (LDHs) and the appearance of an intermediate second staging phase. *Appl. Clay Sci.* **35,** 218–227 (2007).

47. Taviot-Guého, C., Feng, Y., Faour, A. & Leroux, F. Intercalation chemistry in a LDH system: anion exchange process and staging phenomenon investigated by means of time-resolved, in situ X-ray diffraction. *Dalton Trans.* **39,** 5994–6005 (2010).

48. Perioli, L., Ambrogi, V., di Nauta, L., Nocchetti, M. & Rossi, C. Effects of hydrotalcite-like nanostructured compounds on biopharmaceutical properties and release of BCS class II drugs: The case of flurbiprofen. *Appl. Clay Sci.* **51,** 407–413 (2011).

49. Del Arco, M., Fernández, a., Martín, C. & Rives, V. Solubility and release of fenbufen intercalated in Mg, Al and Mg, Al, Fe layered double hydroxides (LDH): The effect of Eudragit® S 100 covering. *J. Solid State Chem.* **183,** 3002–3009 (2010).

50. Perioli, L. *et al.* Intercalation and release of antiinflammatory drug diclofenac into nanosized ZnAl hydrotalcite-like compound. *Appl. Clay Sci.* **53,** 374–378 (2011).

51. Gu, Z., Thomas, A. C., Xu, Z. P., Campbell, J. H. & Lu, G. Q. In vitro sustained release of LMWH from MgAl-layered double hydroxide nanohybrids. *Chem. Mater.* **20,** 3715–3722 (2008).

52. Barahuie, F., Hussein, M. Z., Abd Gani, S., Fakurazi, S. & Zainal, Z. Anticancer nanodelivery system with controlled release property based on protocatechuate-zinc layered hydroxide nanohybrid. *Int. J. Nanomedicine* **9,** 3137–3149 (2014).

53. Delgado, D. R., Ruidiaz, M. A., Gómez, S. M., Gantiva, M. & Martínez, F. Thermodynamic study of the solubility of sodium naproxen in some ethanol + water mixtures. *Quim. Nova* **33,** 1923–1927 (2010).

54. Llinàs, A., Burley, J. C., Box, K. J., Glen, R. C. & Goodman, J. M. Diclofenac Solubility: Independent Determination of the Intrinsic Solubility of Three Crystal Forms. *J. Med. Chem.* **50,** 979–983 (2007).

55. Panda, H. S., Srivastava, R. & Bahadur, D. In-vitro release kinetics and stability of anticardiovascular drugs-intercalated layered double hydroxide nanohybrids. *J. Phys. Chem. B* **113,** 15090–15100 (2009).

56. Berber, M. R., Hafez, I. H., Minagawa, K., Mori, T. & Tanaka, M. Nanocomposite formulation system of lipid-regulating drugs based on layered double hydroxide: Synthesis, characterization and drug release properties. *Pharm. Res.* **27,** 2394–2401 (2010).

57. Kinget, R., Kalala, W., Vervoort, L. & van den Mooter, G. Colonic drug targeting. *J. Drug Target.* **6,** 129–49 (1998).

58. Li, J. *et al.* In vitro evaluation of dissolution behavior for a colon-specific drug delivery system (CODES) in multi-pH media using United States Pharmacopeia apparatus II and III. *AAPS PharmSciTech* **3,** E33 (2002).

59. The United States Pharmacopeia. *In Vitro and In Vivo Evaluation of Dosage form*. (1995).

60. Richardson-Chong, S. S. D., Patel, R. & Williams, G. R. Intercalation and Controlled Release of Bioactive Ions Using a Hydroxy Double Salt. *Ind. Eng. Chem. Res.* **51,** 2913–2921 (2012).

61. Bull, R. M. R., Markland, C., Williams, G. R. & O'Hare, D. Hydroxy double salts as versatile storage and delivery matrices. *J. Mater. Chem.* **21,** 1822 (2011).

62. Schmassmann, a *et al.* Antacid provides better restoration of glandular structures within the gastric ulcer scar than omeprazole. *Gut* **35,** 896–904 (1994).

63. Silion, M. *et al.* In vitro and in vivo behavior of ketoprofen intercalated into layered double hydroxides. *J. Mater. Sci. Mater. Med.* **21,** 3009–18 (2010).

64. Del Arco, M. *et al.* Mg,Al layered double hydroxides with intercalated indomethacin: synthesis, characterization, and pharmacological study. *J. Pharm. Sci.* **93,** 1649–58 (2004).

65. Robbins, S. L. & Cotran, R. S. *Robbins pathologic basis of disease*. (Saunders Company, 1989).

66. Commission, E. Opinion of the Scientific Committee on Food on the Tolerable Upper Intake Level of Zinc. *SCF/cs* **62 Final,** (2003).

67. DPHHS, U. S. Agency for Toxic Substances and Disease Registry (ATSDR). Toxicological Profile for Zinc (update). Atlanta, GA: US Department of Public Health and Human Services. *Public Heal. Serv.* 1–2 (2005).

68. Plum, L. M., Rink, L. & Haase, H. The essential toxin: impact of zinc on human health. *Int. J. Environ. Res. Public Health* **7,** 1342–65 (2010).

69. Friberg, L., Nordberg, G. F. & Vouk, V. B. *Handbook on the Toxicology of Metals: Specific Metals*. (Elsevier ; New York, NY : Sole distributors for the USA and Canada, Elsevier Science Publishing Company, 1986).

70. Llobet, J. M., Domingo, J. L., Gómez, M., Tomás, J. M. & Corbella, J. Acute toxicity studies of aluminium compounds: antidotal efficacy of several chelating agents. *Pharmacol. Toxicol.* **60,** 280–3 (1987).

71. Powell, J. J., Jugdaohsingh, R. & Thompson, R. P. The regulation of mineral absorption in the gastrointestinal tract. *Proc. Nutr. Soc.* **58,** 147–153 (1999).

72. Trumbo, P., Yates, A. A., Schlicker, S. & Poos, M. Dietary reference intakes: vitamin A, vitamin K, arsenic, boron, chromium, copper, iodine, iron, manganese, molybdenum, nickel, silicon, vanadium, and zinc. *J. Am. Diet. Assoc.* **101,** 294–301 (2001).

73. Buzea, C., Pacheco, I. I. & Robbie, K. Nanomaterials and nanoparticles: sources and toxicity. *Biointerphases* **2,** MR17–71 (2007).

74. Hoet, P. H., Brüske-Hohlfeld, I. & Salata, O. V. Nanoparticles - known and unknown health risks. *J. Nanobiotechnology* **2,** 12 (2004).

75. Agency for Toxic Substances and Disease Registry (ATSDR). Toxicological Profile for Nickel. *US Dep. Heal. Hum. Serv. Atlanta, US* (2005).

76. Mastromatteo, E. Yant memorial lecture. Nickel. *Am. Ind. Hyg. Assoc. J.* **47,** 589–601 (1986).

77. Haro, R. T., Furst, A. & Falk, H. L. Studies on the acute toxicity of nickelocene. *Proc. West. Pharmacol. Soc.* **11,** 39–42 (1968).

78. England Public Health/The Toxicology Department CRCE. *Nickel Toxicological Overview*. (2001).

79. World Health Organization (WHO). *Chemical Environmental Health Criteria 108: Nickel*. *Int. Program. Chem. Saf.* (1991).

80. Froese, D. S. & Gravel, R. A. Genetic disorders of vitamin B12 metabolism: eight complementation groups – eight genes. *Expert Rev. Mol. Med.* **12,** e37 (2010).

81. Kim, J. H., Gibb, H. J. & Howe, P. Cobalt and inorganic coblat compounds. (2006).

82. Speijers, G. J., Krajnc, E. I., Berkvens, J. M. & van Logten, M. J. Acute oral toxicity of inorganic cobalt compounds in rats. *Food Chem. Toxicol.* **20,** 311–4 (1982).

83. Singh, P. & Junnarkar, A. Behavioural and toxic profile of some essential trace metal salts in mice and rats. *Indian J. Pharmacol.* **23,** 153–159 (1991).

84. Faroon, O. *et al.* Toxicological profile for cobalt. *Agency Toxic Subst. Dis. Regist.* **41,** (2004).

Chapter 4: New biocompatible inorganic drug delivery systems

4.1. Introduction

Drug delivery can take many forms, such as ingestion, inhalation and injection. To achieve the ingestion of medicines, tablet, capsule or liquid formulations are commonly used. Tablets are the most frequently used dosage form for oral delivery and they occupy two thirds of the global drug market.[1] The oral route is preferred over other methods of applying medicines because it is the most simple and results in high levels of patient compliance.[2] We cannot just ask the patient to take the drug (active ingredient) alone, however: often it tastes very bitter, may be unstable on storage, and/or be difficult to process. Furthermore, it is very hard to ensure that the patient gets the correct dose of medicine if they were to take a simple drug powder. Thus, when drugs are processed into medicines such as tablets a number of additional materials known as "excipients" are added. Excipients are inactive ingredients that are blended with the active pharmaceutical ingredient (API) to facilitate the delivery, manufacturability and stabilisation of the API in tablets or other pharmaceutical dosage forms.[3] They are sub-divided into various functional classifications such as: diluents (it is added to increase the bulk prior the compression), disintegrants (which facilitate tablets break up and their disintegration inside gastrointestinal tract), binders (added to boost cohesiveness within powders and enhance the flowability) and lubricants (which reduce friction between the powder and the tableting equipment).[4–7]

Tablets are made by compressing the API and the excipients, and there a number of techniques including wet and direct compression.[8] Direct compression (DC) is the simplest method for tablet manufacturing. It is cheap, easy and does not require the use of water (unlike wet granulation, with both requires water and additional, expensive, processing steps). The tablets are manufactured by directly compressing a blend of the API powder and excipients.[8]

Tablets have proved to be a remarkably versatile dosage form, and there are many types of different drug delivery profile which can be delivered using them. Tablets may for instance be immediate release, delayed release, or sustained release; in all cases, the excipients play an important role in controlling drug release.[9] The effect of the different types tablets on bioavailability (the availability of the drug in the body) is shown in Figure 4.1.

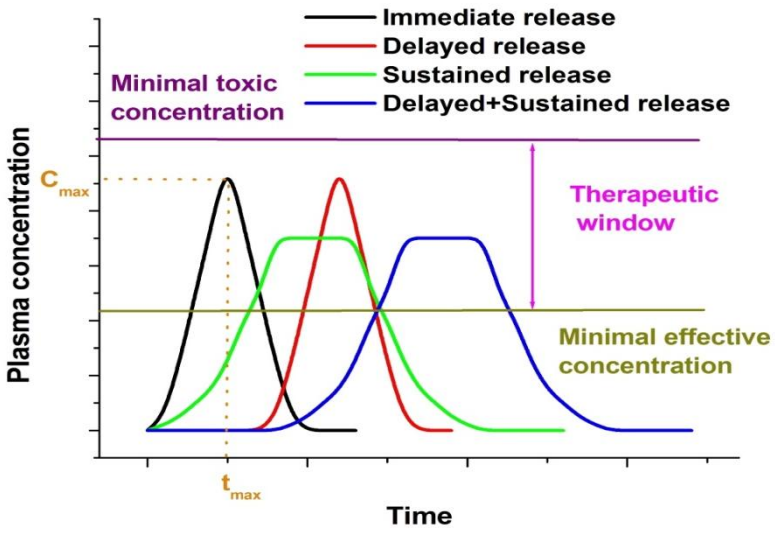

Figure 4.1: The effect of different type tablets on bioavailability.

It has been established that a drug's efficacy can be improved and its side effects reduced if it is released in a sustained, manner rather than through conventional "burst" (immediate) release.[10,11] Moreover, from the pharmacoeconomic perspective, sustained release dosage forms are meanwhile better than immediate release formulations, since they improve efficacy and reduce treatment costs.[12] In the consideration of controlled release oral drug delivery systems, it is important to consider the human gastrointestinal transit time. This can vary from a few hours to around 3 days, and is influenced by many factors such as the age, sex, or ethnicity of the patient. It even varies significantly in the same person depending on diet, environment, or mood. The transit time tends to be faster in the fasting state than the fed state.[13–17] In this chapter, a fast transit time is taken to mean 12 h or below, a normal transit time is taken to mean 24 h and a slow transit time as being 48 h or above.

The challenge is to deliver both existing and new drugs in a way that benefits patients, healthcare workers and the healthcare system. Most carriers employed to modulate drug release are pH sensitive,[18,19] allowing release to occur only under certain pH conditions. Since these vary from person to person, and indeed for the same person depending on whether they have eaten, there can be variations in the efficacy of a formulation from person to person. A good carrier should deliver its loading depending on the environment composition, rather than relying on pH only. Modern controlled release systems are usually polymer based;[20,21] much less attention has been paid to inorganic delivery systems, even though they have a number of promising features. Layered double hydroxides (LDHs) are probably the most widely explored inorganic systems for the delivery of pharmaceutical active compounds,[22,23] but many are cytotoxic and often their drug release profile is very rapid.

There are a number of serious concerns regarding the accumulation of inorganic materials in the body with repeated applications, and their potential systemic toxicity.[24] Any potential inorganic drug delivery system must hence be composed of metals that are part of the natural composition of the human body. In case the component metals are absorbed or accumulated, it is vital that they do not have any potential systemic toxicity. Thus, while the HDS systems studied in the previous chapter have shown good release profiles, the toxic nature of the metals they contain means they are highly unlikely to be acceptable in a medical product.

In this chapter, we looked to develop the results from Chapter 3 to produce analogous biocompatible hydroxy double salt (HDS) systems to deliver commonly used drugs in a tuneable manner. The sodium salts of ibuprofen, naproxen, diclofenac and valproic acid were loaded into biocompatible analogues of the zinc basic hydroxide salt ($[Zn_5(OH)_8](Cl)_2 \cdot 2H_2O$) through an ion-exchange route. The resulting products were characterized by X-ray diffraction, IR spectroscopy, NMR and elemental analysis. The materials obtained were formulated into tablets and drug release studies were carried out under conditions that mimic the human gastrointestinal tract. The inorganic-based tablets were compared to tablets currently available on the market.

4.2. Results and discussion

4.2.1. Characterisation of new HDSs

New HDSs made from the biocompatible metal ions Fe^{2+}, Zn^{2+}, and Mg^{2+} were prepared (as detailed in Chapter 6), using $FeCl_2$, $MgCl_2$ and ZnO as starting materials. These are henceforth denoted MZn-Cl (M = Mg, Fe) or Zn-Cl. The aim was to prepare systems that host Cl^- ions rather than NO_3^-, since Cl^- is present in the human body and NO_3^- is toxic.[25–29] Since it is the first time that these new HDSs have been prepared, the new materials have been thoroughly characterised to ensure their preparation was successful. FeZn-Cl (Figure 4.2a) has a dark green colour. This implies that the Fe^{2+} has not been oxidised to Fe^{3+}, and remains in the divalent oxidation state. Other tests were carried out to check the oxidation state of Fe, and will be discussed further below (section 4.2.1.6). MgZn-Cl has a white colour similar to Zn-Cl, but it has smoother texture and finer particles which make it easy to distinguish from Zn-Cl (Figure 4.2 b, c).

Figure 4.2: Digital photographs of the HDSs: (a) FeZn-Cl; (b) MgZn-Cl and (c) Zn-Cl

4.2.1.1. X-ray diffraction

The XRD patterns (Figure 4.3) show that materials prepared are indeed HDSs (MgZn-Cl and FeZn-Cl). The MgZn-Cl and FeZn-Cl materials have slightly higher d-spacings than Zn-Cl (interlayer spacing data are summarised in Table 4.1). The MgZn-Cl and Zn-Cl patterns have a flat baseline, in contrast to FeZn-Cl where the baseline is inclined. This could be caused by Fe fluorescence, where Fe^{2+} is excited at 7.11 keV by Cu Kα-radiation of 8.04 keV in the laboratory diffractometer.[30–33] The formulae of the guests were calculated with the aid of EDX and TGA data (see Table 4.1 and the discussion below), and found to be consistent with HDS systems having formed.

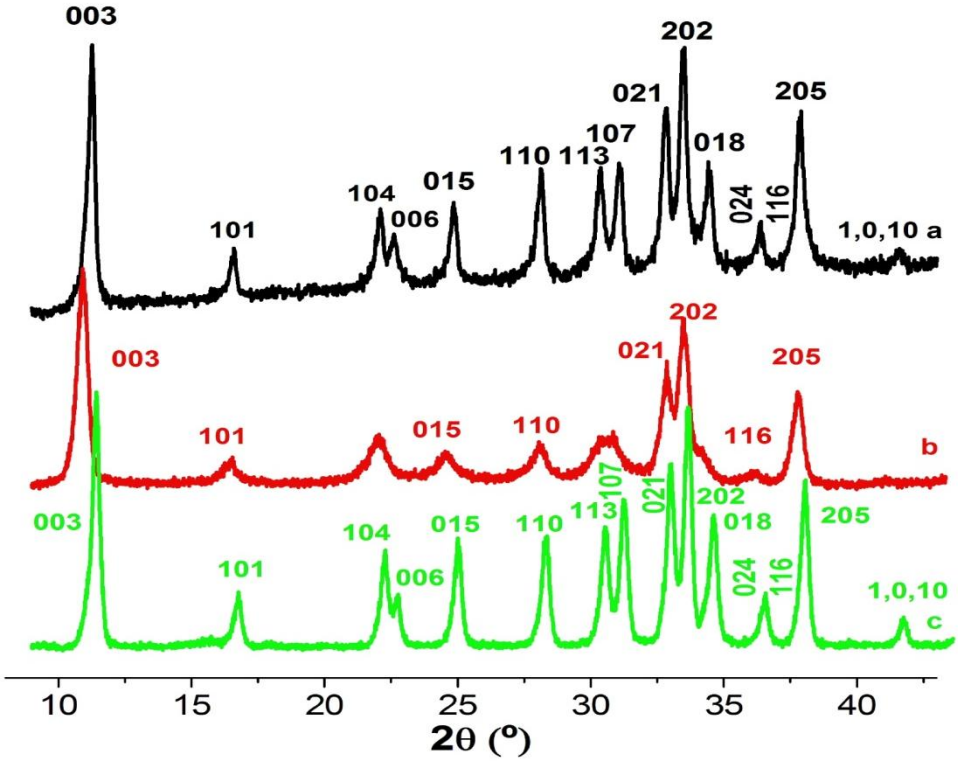

Figure 4.3 : XRD patterns of (a) FeZn-Cl; (b) MgZn-Cl and (c) Zn-Cl

Table 4.1: The interlayer spacings, ratio Zn/Fe or Mg and chemical formulae of the new biocompatible HDSs prepared.

	d-spacing (Å)	Zn (%)	Fe (%)	Mg (%)	Formula[a]
FeZn-Cl	7.8	1.1	1.0	-	$Fe_{2.4}Zn_{2.6}(OH)_8Cl_2{\cdot}2H_2O$
MgZn-Cl	8.1	1.4	-	1.0	$Mg_2Zn_3(OH)_8Cl_2{\cdot}3.4H_2O$

[a] Metals contents were determined by EDX, and the H_2O content from TGA.

4.2.1.2. Scanning electron microscopy

The samples consist largely of hexagonal platelets (Figure 4.4). This is as expected for HDS systems, and the morphology observed here agrees well with the literature.[34,35] Their sizes and zeta potentials are summarised in Table 4.2 (and Appendix III).

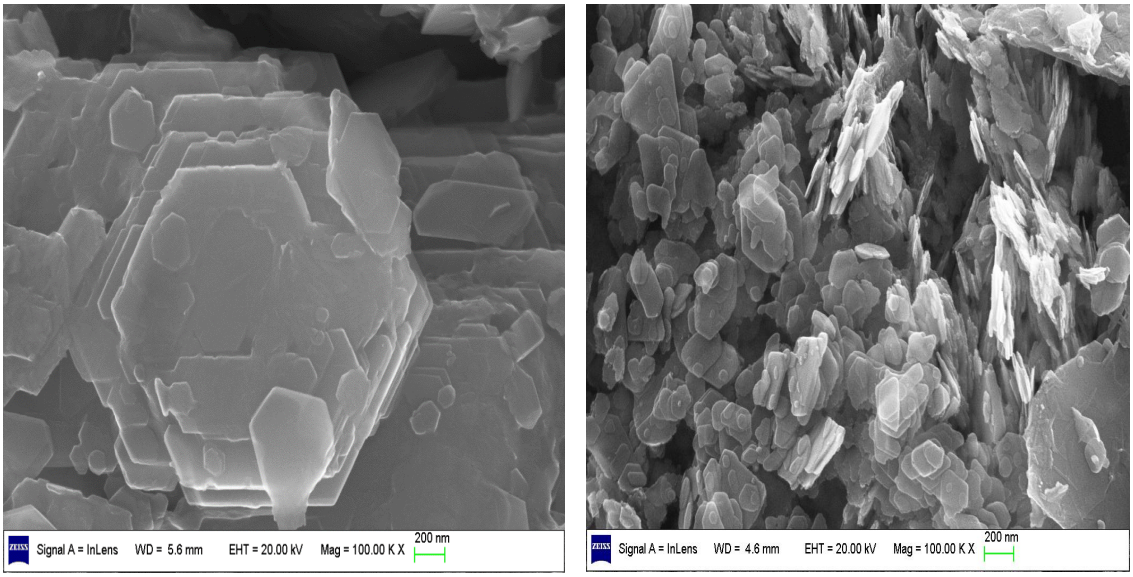

a b

Figure 4.4: Scanning electron microscopy images of **(a)** MgZn-Cl and **(b)** FeZn-Cl

Table 4.2: Size and zeta potential in water of the new HDSs

	Size (nm)	Zeta Potential (mV)
FeZn-Cl	403.5 ± 238.9	45.1 ± 14.0
MgZn-Cl	359.9 ± 138.5	43.0 ± 13.9

4.2.1.3. Energy dispersive X-ray spectroscopy analysis

Energy dispersive X-ray (EDX) spectroscopy analysis (Figure 4.5) reveals the existence of a mixture of divalent metals (Fe/Zn and Mg/Zn) in the samples. The elemental composition of MgZn-Cl and FeZn-Cl, and the resultant formulae calculated, are given in Table 4.1.

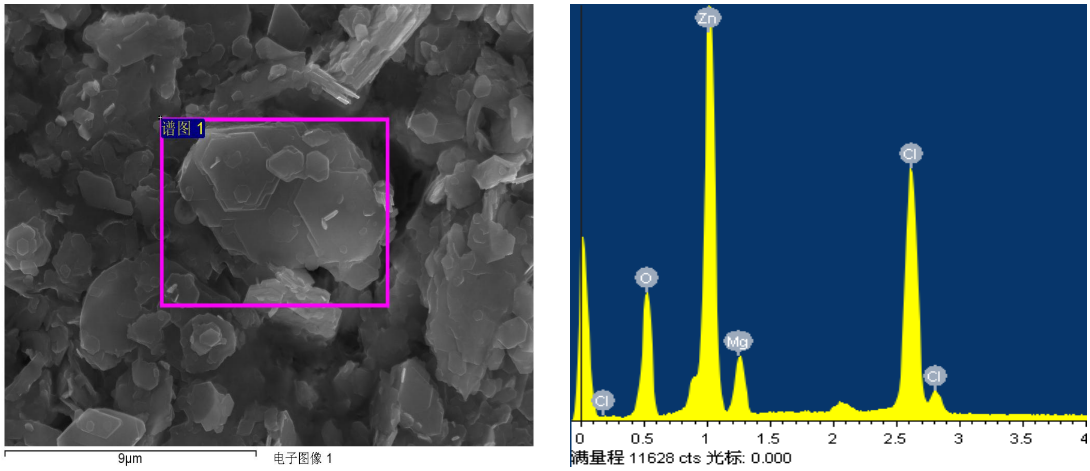

a

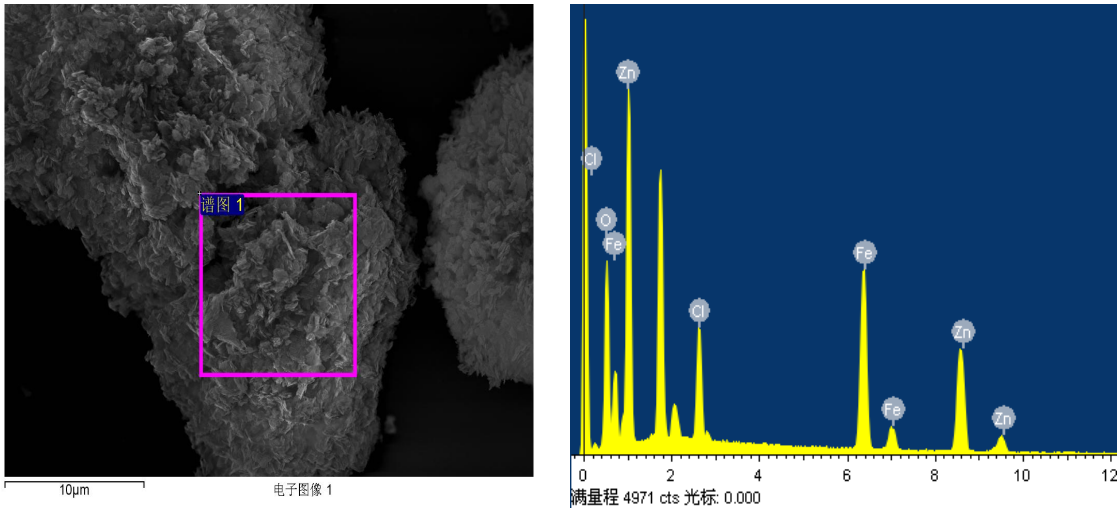

b

Figure 4.5: EDX data obtained on **(a)** MgZn-Cl and **(b)** FeZn-Cl

4.2.1.4. IR spectroscopy

The IR spectra of MgZn-Cl, FeZn-Cl and Zn-Cl (Figure. 4.6) all look similar. MgZn-Cl and FeZn-Cl show broadened peaks (two merged peaks) at 3448 cm^{-1}, which correspond to stretches of the OH groups in the layers and water. In addition, the band around 1635 cm^{-1} is assigned to the δ-bend of water molecules in the interlayer, and physically adsorbed water. Zn-Cl shows a less intense and sharper band at 3448 cm^{-1} (stretching of OH groups in the layers) and a small band at 1605 cm^{-1} arising from water bending motions.

The M–O and O–M–O (M = Mg, Fe and Zn) vibration bands appear in the region of 700 cm^{-1},[36] while bands around 1030 and 900 cm^{-1} correspond to the bending of OH groups attached to the divalent metal. Based on the IR spectra in Figure 4.6, MgZn-Cl appears to contain the highest amount of water, followed by FeZn-Cl, while Zn-Cl incorporates the smallest amount.

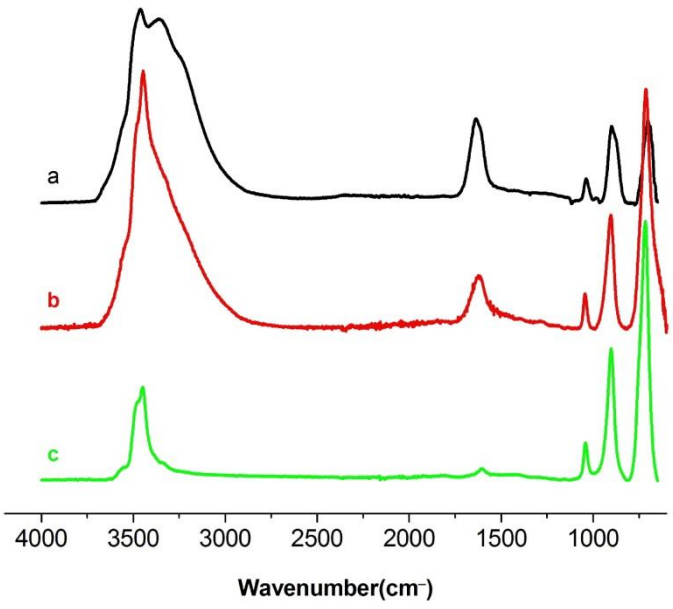

Figure 4.6: IR spectra of **(a)** MgZn-Cl, **(b)** FeZ and **(c)** Zn-Cl

4.2.1.5. Thermogravimetric analysis

Thermogravimetric analysis (TGA) was performed to check the amount of water contained in the new HDS materials. TGA traces are given in Figure 4.7. Mass loss goes through two or three stages, which is common for LDH and HDS materials.[37–39] For Zn-Cl and FeZn-Cl (Figure 4.7a,b), the initial mass loss of *ca.* 4 – 7 % is complete by 160 ºC and this corresponds to the loss of the two water molecules binding to tetrahedral metal. For MgZn-Cl (Figure 4.7c), the initial mass loss of *ca.* 5 % commences below 100 ºC, and ends by 150 ºC. This related to the loss of interlayer water, to give the dehydrated HDS material. After that the two water molecules binding to tetrahedral metal are lost. The percentage mass losses observed in the TGA analysis agree very well with the FTIR data.

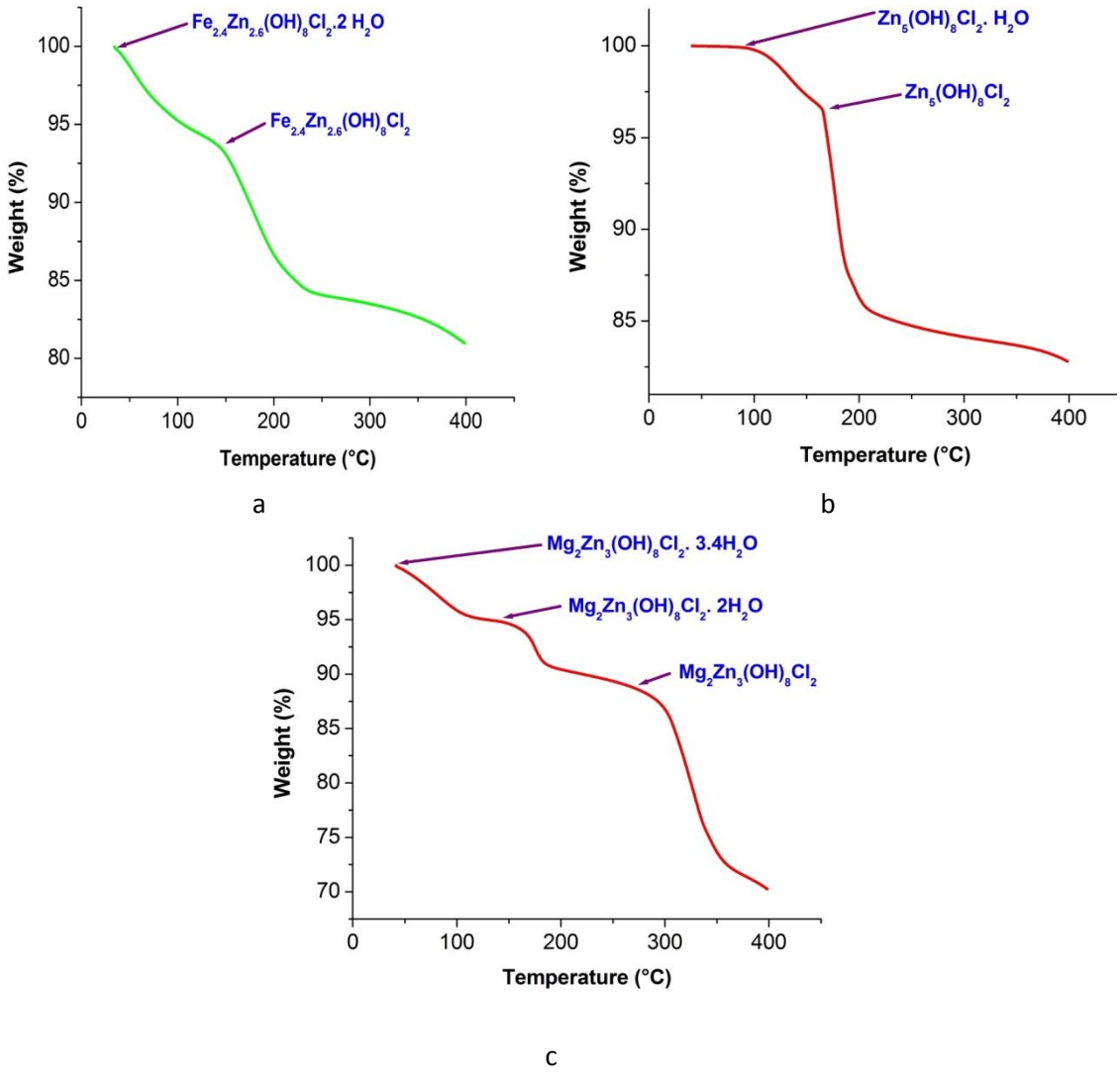

Figure 4.7: TGA traces for **(a)** FeZn-Cl, **(b)** Zn-Cl and **(c)** MgZn-Cl

4.2.1.6. X-ray photoelectron spectroscopy

The X-ray photoelectron (XPS) spectra of the Fe 2p region (Figure 4.8) yield information about the oxidation state of iron in the FeZn-Cl HDSs. The data in Figure 4.8a show the Fe $2p_{1/2}$ peak has a shoulder with a satellite peak (SS), and thus it was fitted with two peaks positioned at 725.4 and 734.0 eV (Table 4.3). The other principal peak, Fe $2p_{3/2}$, is located at 712.0 eV and similarly is associated with a small satellite peak at 718.8 eV. The binding energy (B.E.) difference between the Fe $2p_{3/2}$ peak and its satellite is 6.8 eV. For Fe^{2+} and Fe^{3+} the difference should be 6 and 8.5 eV; respectively.[40] The literature reports a B.E. difference of 8.5 eV for a Ca/Fe LDH containing iron in the Fe^{3+} oxidation state.[41] Thus, it appears that Fe in the FeZn-Cl HDS exists in the Fe^{2+} oxidation state with possibly a small amount of oxidation having taken place. The chemical shifts in the B.E.s of photoelectrons originating from the same energy level can be influenced by a range of factors such as the environment around the atom(s).[42,43] If there is any shift due to the environment factor, all elements peaks should shift simultaneously, and thus the energy difference between the main peaks and their satellites is one of the most robust way to verify oxidation state.

Another common method for the determination of oxidation states of metals in their oxides was employed to confirm the oxidation state of Fe in the HDS systems.[44,45] This involves calculating

$$\text{B.E. (Fe } 2p_{3\text{-}2}) - \text{B.E. } (O_{1s}) = 180 \text{ eV (Figure 4.8b)}$$

Comparing this value to the calibration curve reported by Hadnadjev and co-workers verifies that Fe is present in the Fe^{2+} state,[46] agreeing with the analysis above and also the initial visual observations made.

There are not any XPS data reported for Fe^{2+} occupying octahedral and tetrahedral sites simultaneously. The only available data are for Fe^{3+} and by comparing the FeZn-Cl XPS data to Fe^{3+}XPS data,[47] is thought that Fe^{2+} occupies both octahedral and tetrahedral positions, which is in agreement with UV spectroscopy analysis (Appendix III).

Table 4.3: Fe binding energies for the specimens analysed.

	Fe $2p_{3/2}$	SS	Fe $2p_{1/2}$	SS	References
FeO	710.1	715.1	723.8	730.0	[48,49]
Fe_2O_3	710.9	719.3	724.4	733.0	This work
$FeCl_2$	710.8	716.2	724.5	730.3	This work
FeZn-Cl	712.0	718.8	725.4	734.0	This work
LDH-Ca/Fe	710.4	718.8	724.8	332.5	[41]

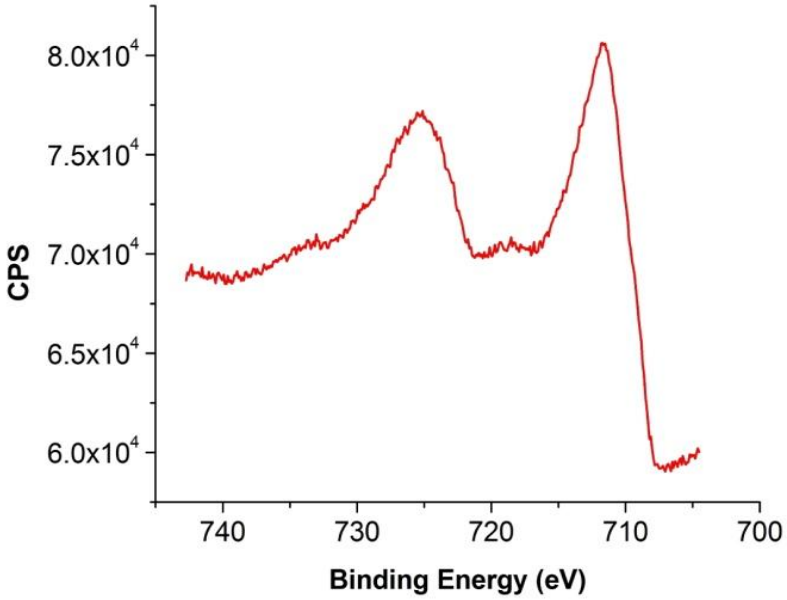

a

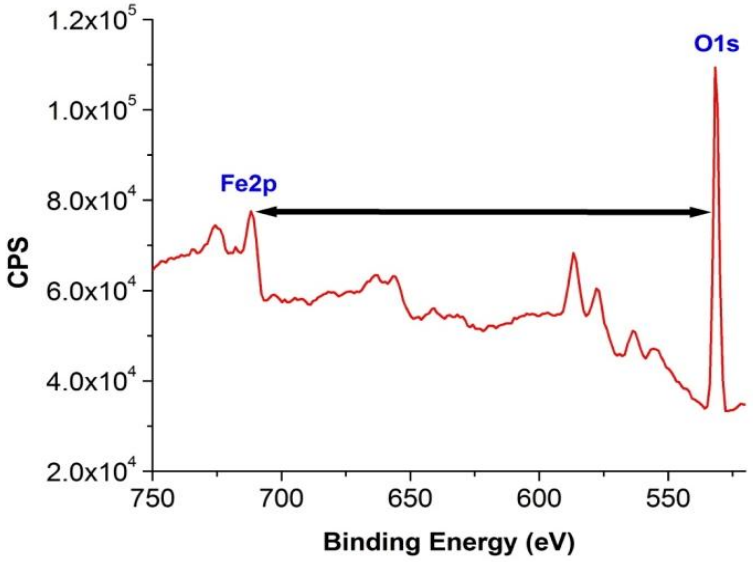

b

Figure 4.8: XPS of FeZn-Cl depicting **(a)** the Fe 2p region and **(b)** a section of the survey spectrum showing the splitting between the O 1s and Fe $2p_{3/2}$ peaks.

Figure 4.9 shows the Mg 2p XPS spectra of MgZn-Cl; there are two peaks with shoulders, present in the area ratio of 1:1.9. The first is located at around 49.9 eV, similar to the value recorded for Mg^{2+} in the MgO structure (Table 4.4).[50] It corresponds to Mg^{2+} in an octahedral site, and its position is in agreement with values reported for Mg/Al LDHs where Mg is also octahedrally coordinated.[51,52] The second peak, situated at 55.0 eV is linked to Mg^{2+} in a tetrahedral site. Similar B.E.s have been seen for $MgAl_2O_4$ (56.0 eV was reported),[53] where Mg occupies tetrahedral sites.[54] Mg 2p XPS spectra thus demonstrate that Mg atoms occupy both octahedral and tetrahedral sites in the MgZn-Cl HDS. A schematic of the MgZn-Cl structure is depicted in Figure 4.9b.

Table 4.4: Mg binding energies for the specimen analysed

	Mg 2p (eV)	References
MgO	49.6	[50]
$MgAl_2O_4$	56.0	[53]
LDH Mg/Al	49.7/49.9	[51,52]
MgZn-Cl	49.9/55.0	This work

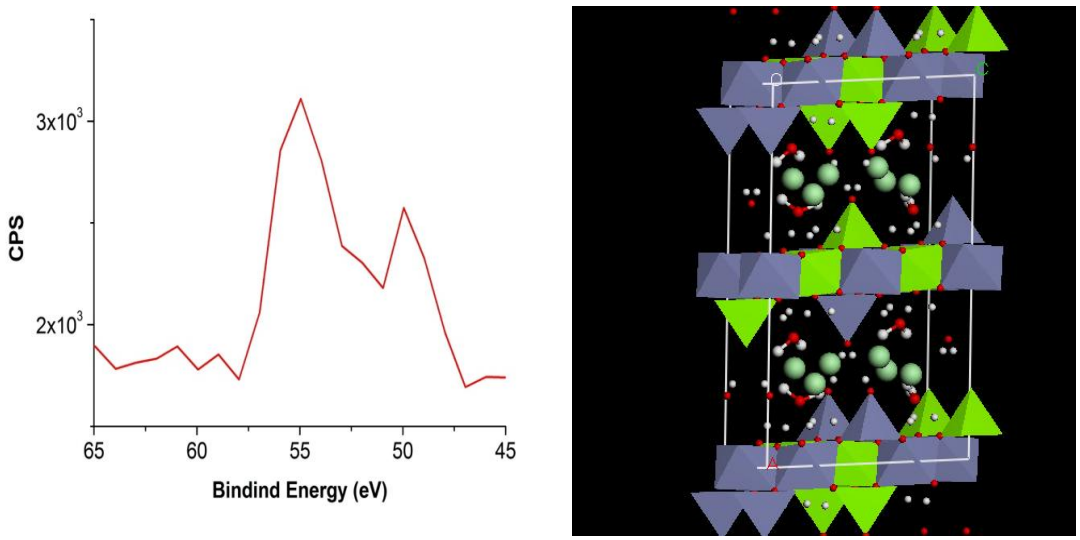

a b

Figure 4.9: Data for MgZn-Cl **(a)** The XPS of spectrum of the Mg 2p region and **(b)** a schematic structure.

4.2.2. Characterisation of drug intercalates

It proved possible to intercalate the organic species diclofenac sodium (Dic), naproxen sodium (Nap), ibuprofen sodium (SI) and valproate sodium (Val) into the new HDSs $Mg_2Zn_3(OH)_8(Cl)_2{\cdot}3.4H_2O$ (MgZn-Cl) and $Fe_{2.4}Zn_{2.6}(OH)_8(Cl)_2{\cdot}2H_2O$ (FeZn-Cl) through an anion exchange method. Successful intercalation was confirmed by X-ray diffraction (XRD) and IR spectroscopy.

4.2.2.1. Intercalation into $Mg_2Zn_3(OH)_8(Cl)_2{\cdot}3.4H_2O$

XRD patterns of the drug intercalates of MgZn-Cl are given in Figure 4.10. The reaction products show no basal reflections characteristic of the starting material, and a shift of the *h00* basal reflections to lower angles; this corresponds to an increase in interlayer distance, which is indicative of the intercalation of a larger anion (Dic, SI, Nap and Val) into the interlayer galleries of the HDS by anion exchange for Cl. The interlayer spacing increases from 8.1 Å with MgZn-Cl to 22.8 Å 24.4 Å, 27.0 Å, and 18.8 Å for the Dic, Nap, SI and Val intercalates; respectively. These are in good agreement with the results detailed in Chapter 3 and the literature on LDH and HDS drug intercalates: d-spacings have been reported of 22.5 Å for Dic,[55] 27.0 Å for SI,[56] 23.5 Å for Nap,[57] and 18.5 Å for Val.[58,59] For SI, most d-spacing values reported for LDH systems are below 23 Å, but a value of 28.5 Å has also been reported.[60] All the diffraction patterns illustrate peak broadening, indicative of stacking defects, except that of MgZn-Dic. Full data are included in Table 4.5.

Table 4.5: The interlayer spacings and chemical formulae of the various MgZn-drug composites prepared.

ID	d-spacing (Å)	Formula	Elemental analysis (%) Obsd (calcd)[a]
MgZn-Cl	8.1	$Mg_2Zn_3(OH)_8(Cl)_2{\cdot}3.4H_2O$	
MgZn-Val	18.8	$Mg_2Zn_3(OH)_8(C_8H_{15}O_2)_{1.1}(CO_3)_{0.45}{\cdot}3.4H_2O$	C 17.43 (17.73) H 4.02 (5.04)
MgZn-Dic	22.8	$Mg_2Zn_3(OH)_8(C_{14}H_{10}Cl_2NO_2)_{2.17}.2.1H_2O$	C 34.46 (34.45) H 2.77 (3.22) N 1.44 (2.87)
MgZn-Nap	24.4	$Mg_2Zn_3(OH)_8(C_{14}H_{13}O_3)_{1.7}Cl_{0.3}{\cdot}2.1H_2O$	C 35.41 (35.43) H 4.09 (4.45)
MgZn-Sl	27.0	$Mg_2Zn_3(OH)_8(C_{13}H_{17}O_2)_{1.7}(CO_3)_{0.15}{\cdot}3.0H_2O$	C 33.61 (33.71) H 4.52 (5.45)

[a]C and H contents were determined by quantitative combustion, and the H_2O content from TGA

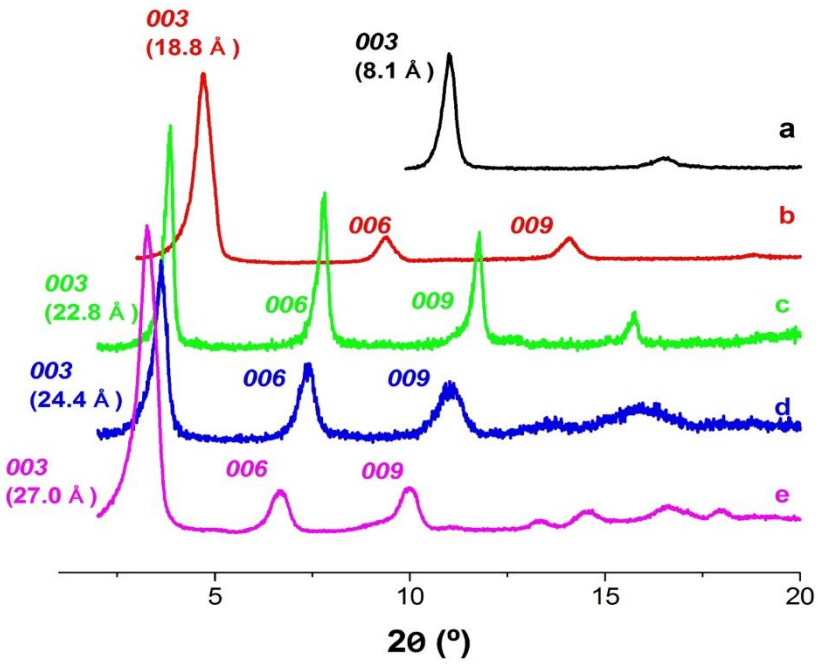

Figure 4.10: XRD patterns for **(a)** MgZn-Cl, **(b)** MgZn-Val, **(c)** MgZn-Dic, **(d)** MgZn-Nap and **(e)** MgZn-Sl

4.2.2.2. Intercalation into $Fe_{2\cdot4}Zn_{2.6}(OH)_8(Cl)_2\cdot2H_2O$

The intercalation of the guests into the Fe-containing HDS was challenging, as the drug-loaded system tended to oxidise easily when in contact with air. This could be overcome by draining water from the preparation quickly after reaction, then drying the drug intercalates in a vaccum oven. The process is detailed in Chapter 6. The digital photographs of the two FeZn products, (with and without rapid drying) are depicted in Figure 4.11. The oxidised form is labelled $Fe_{ox}Zn$.

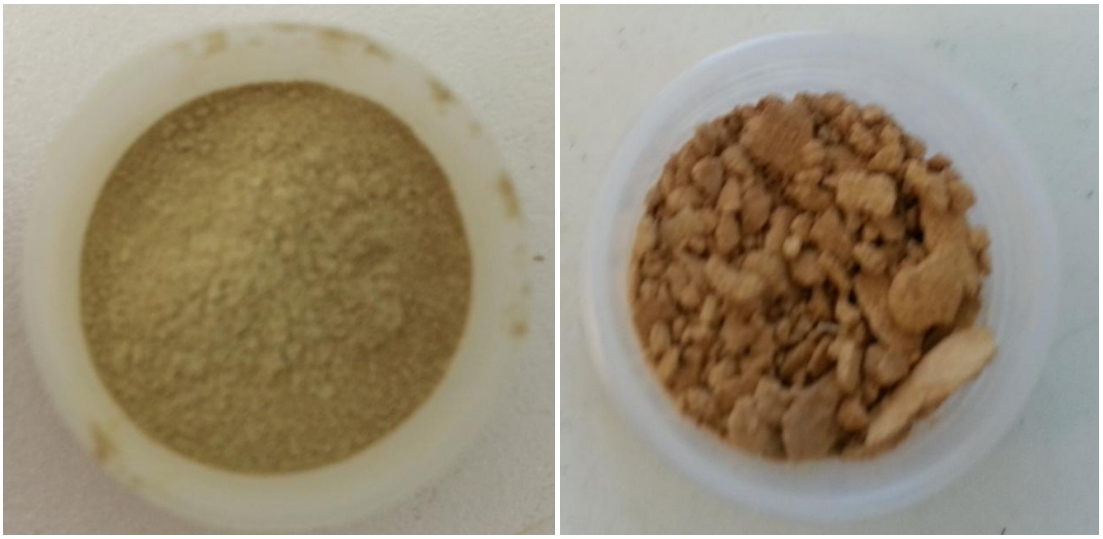

a b

Figure 4.11: FeZn-Dic **(a)** protected and **(b)** non protected

Similar to the MgZn-Cl HDS, the basal reflections of the host can no longer be seen after intercalation (Figure 4.12), except for the intercalation of Val where the presence of the starting material could be seen (reflections of the host are marked with *****). The interlayer spacing increases from 7.8 Å with FeZn-Cl to 22.4 Å, 26.6 Å, 24.5 Å, and 18.6 Å for the, Dic, SI, Nap and Val intercalates, respectively. These are similar to the results reported above using the MgZn-Cl system. No difference in the d-spacing was noticed between FeZn-Dic and $Fe_{ox}Zn$-Dic. Full data are included in Table 4.6. For the Dic intercalation there appear to be two different intercalate phases; it is thought that one contains a bilayer of the guest and the other a monolayer. A small reflection believed to correspond to the latter is marked #.This finding was also seen in Chapter 3.

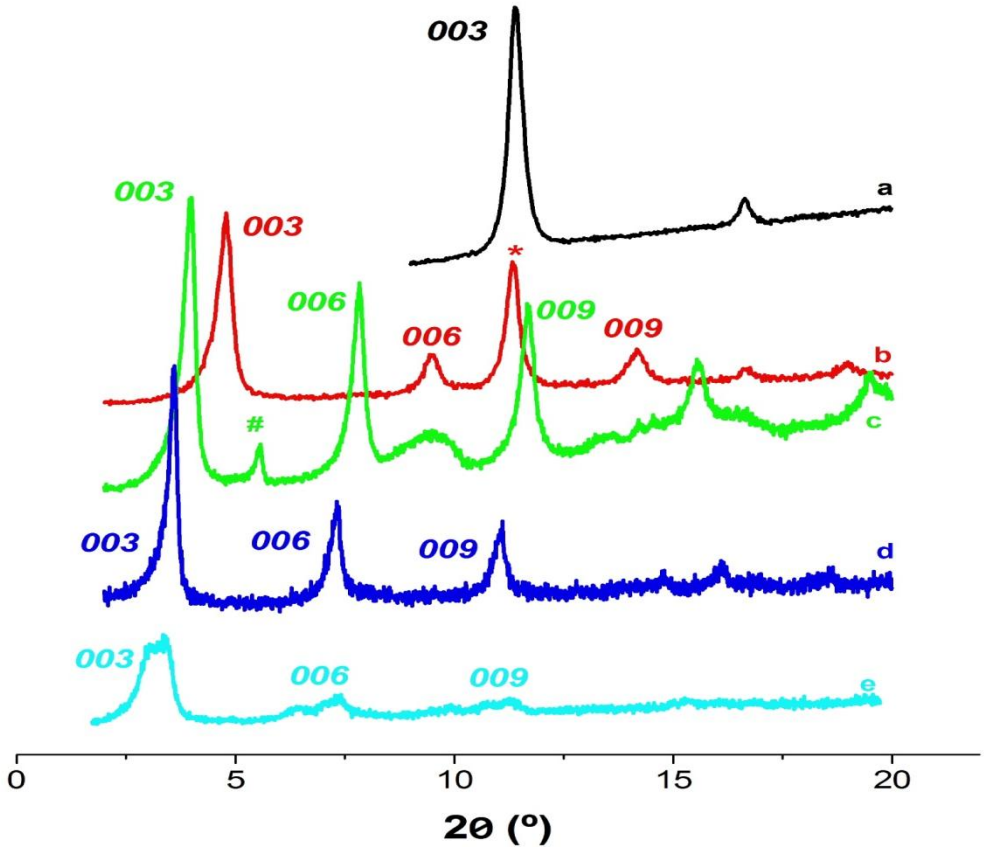

Figure 4.12: XRD spectra of **(a)** FeZn-Cl, **(b)** FeZn-Val, **(c)** FeZn-Dic, **(d)** FeZn-Nap and **(e)** FeZn-SI.

There are broad lumps in the FeZn-Dic pattern indicative of some amorphous material, but exactly what it is unknown.

Table 4.6: The interlayer spacings and chemical formulae of the various FeZn-drug composites prepared.

ID	d-spacing (Å)	Formula[a]	Elemental analysis (%) Obsd (calcd)[b]
FeZn-Cl	7.8	$Fe_{2.4}Zn_{2.6}(OH)_8Cl_2{\cdot}2H_2O$	
FeZn-Val	18.6	$Fe_{1.6}Zn_{3.4}(OH)_8(C_8H_{15}O_2)_{0.61}(Cl)_{1.39}{\cdot}3.4H_2O$	C 9.12 (9.08) H 2.18(3.74)
FeZn-Dic	22.4	$Fe_{2.4}Zn_{2.6}(OH)_8(C_{14}H_{10}Cl_2NO_2)_{1.62}(CO_3)_{0.19}$ $4.3H_2O$	C 27.32 (27.28) H 2.72 (3.28) N 2.34 (2.25)
FeZn-Nap	24.5	$Fe_{2.4}Zn_{2.6}(OH)_8(C_{14}H_{13}O_3)_{0.8}(CO_3)_{0.6}{\cdot}3.6H_2O$	C 19.57 (19.59) H 2.47 (3.39)
FeZn-SI	26.6	$Fe_{2.4}Zn_{2.6}(OH)_8(C_{13}H_{17}O_2)_{0.88}(CO_3)_{0.56}.4.2H_2O$	C 19.83 (19.74) H 3.16 (4.33)

[a] Metals contents were determined by EDX.
[b]C and H contents were determined by quantitative combustion, and the H2O content from TGA.

4.2.2.3. IR spectroscopy

The IR spectrum of Nap in Figure 4.13 shows four main regions. Stretching at 3059 cm^{-1} can be assigned to CH groups, and adsorption bands at 2959 and 2905 cm^{-1} are generated by stretching vibrations of the CH_3 groups. Bands at 1603, 1584 and 1482 cm^{-1} are assigned to aromatic ring vibrations. Peaks at 1573 and 1384 cm^{-1} are attributed to carboxylate groups. The bands in the region 1250-1000 and 900-750 cm^{-1} are due to CH vibrations in and out of the plane, respectively.[61]

The infrared spectra of the Nap intercalation products (MgZn-Nap and FeZn-Nap) are given in Figure 4.13b,c. They present a very broad adsorption band centred at around 3400 cm^{-1} that can be assigned to the OH stretching vibration of hydroxyl groups, from water molecules and those in the layer. There is a shift of the OH band to higher wavenumber compared with pure naproxen (acid form), which has a broad and strong adsorption band around 3100-3200 cm^{-1}. [62,63] This shift could be due to hydrogen bonding between Nap and OH groups of the HDS layers.

All the characteristic peaks of Nap remained after intercalation, confirming successful intercalation of intact Nap ions. Some of the peaks shifted to slightly different wavenumbers due to interactions between guest Nap ions and the host layers: the intercalated Nap anions can bind by electrostatic interactions and hydrogen bonding to the HDS layers.[57,64]

The IR spectra for the other intercalation compounds all display analogous features: all the characteristic peaks of the drug ions are present after intercalation, and demonstrate that the intact guests are successfully intercalated into the HDS hosts (MgZn-Cl and FeZn-Cl).

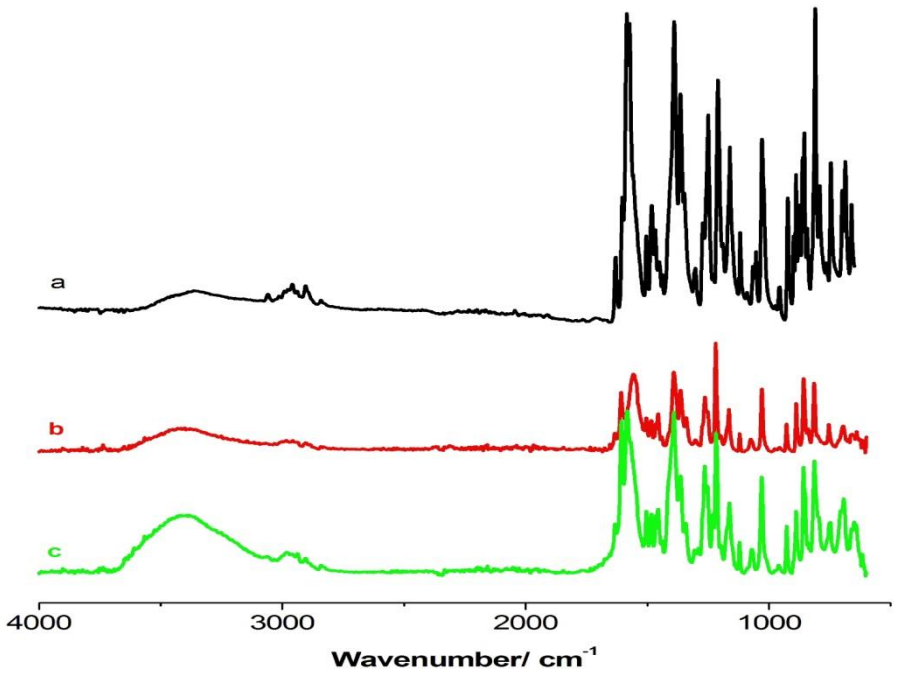

Figure 4.13: IR spectra of **(a)** Nap, **(b)** FeZn-Nap and **(c)** MgZn-Nap.

4.2.2.4. Thermogravimetric analysis

TGA traces of the intercalates (Figure 4.14) reveal mass loss in three stages, except for MgZn-Dic (Figure 4.14f). This is usual for organic guests intercalated into HDS materials.[65,66] The initial mass loss of *ca.* 3.5 – 5 % is complete by 150 ºC, and is expected to correspond to the loss of interlayer water. The second mass loss is linked to the two water molecules binding to tetrahedral metal. For MgZn-Dic (Figure 4.14f), the first mass loss of *ca.* 4 % is complete by 90 ºC and this corresponds to the loss of the two water molecules binding to tetrahedral metal as well as in the interlayer region. MgZn-Dic and MgZn-Val showed more rapid decomposition than FeZn-Dic and FeZn-Val.

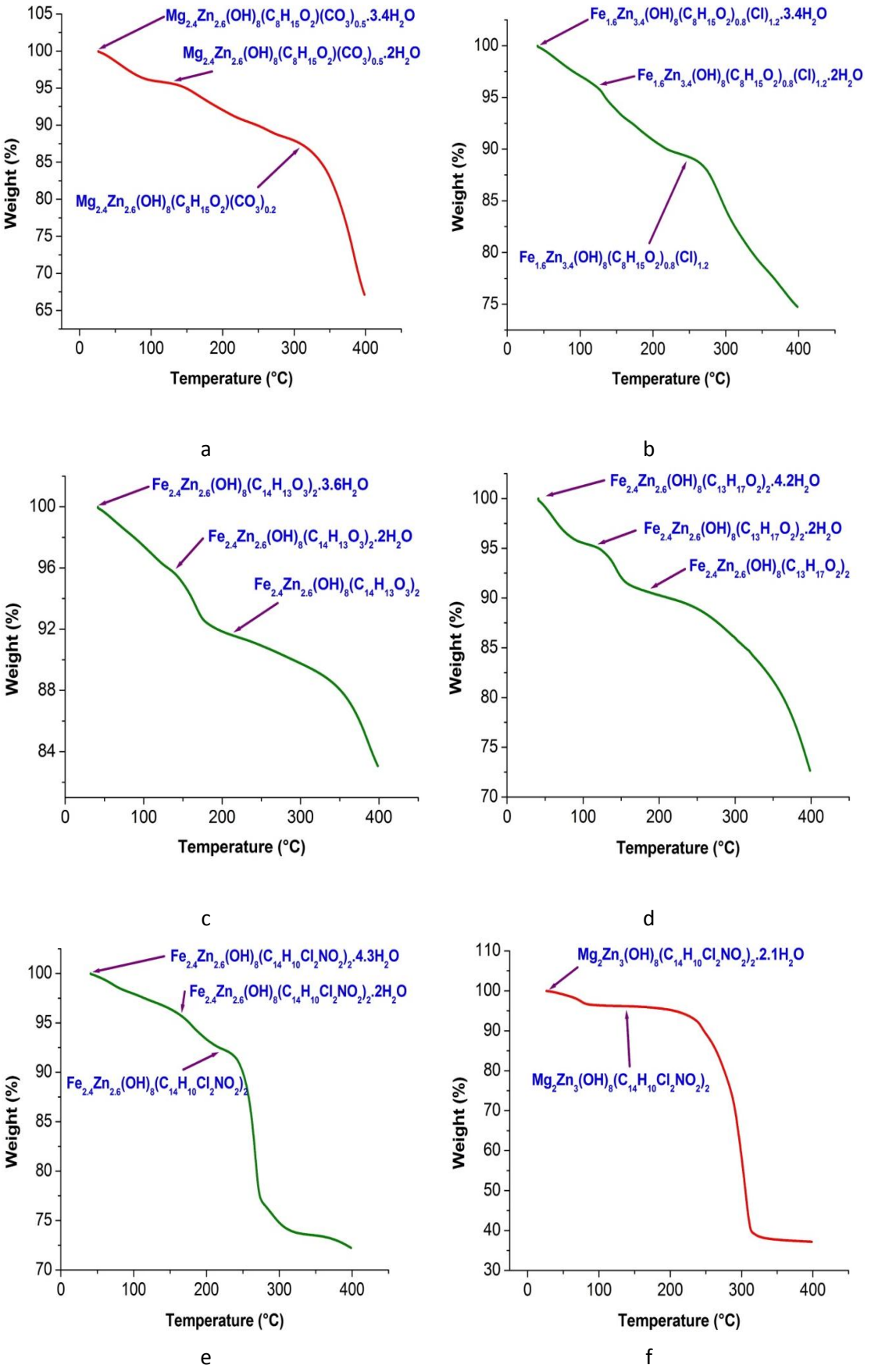

Figure 4.14: TGA traces for **(a)** MgZn-Val, **(b)** FeZn-Val, **(c)** FeZn-Nap, **(d)** FeZn-SI, **(e)** FeZn-Dic and **(f)** MgZn-Dic

4.2.2.5. Guest Orientation

The layer thickness of the HDS is around 8.5 Å (from end to end of the tetrahedral units), while the thickness of octahedral layers is around 5 Å. The lengths of the guest ions are calculated (using the Marvin software[67]) to be 4.48 Å (Val); 10.02 Å (Dic); and 11.56 Å (Nap), and 10.38 Å (SI). Comparing the lengths of the guests with the gallery height (the interlayer spacing minus the HDS layer thickness) suggests that the gallery height is between 1.5 and 2 times the length of the intercalated ions. This suggests that the guests adopt intertwined bilayer or bilayer arrangements, with the carboxylic acid groups pointing towards the positively charged layers. For SI and Val, the gallery height is around twice the size of the molecules, suggesting a perpendicular bilayer arrangement of ions. For Dic and Nap, the gallery height is greater than the size of one molecule and less than the length of two, indicating an intertwined bilayer arrangement. A schematic of the guest orientations in the MgZn system is provided in Figure 4.15. The FeZn system has very similar interlayer spacings, and thus analogous arrangements are envisaged.

Unfortunately, full molecular dynamics simulations could not be performed with these systems since the exact location of Mg^{2+}, Fe^{2+}, and Zn^{2+} are unknown.

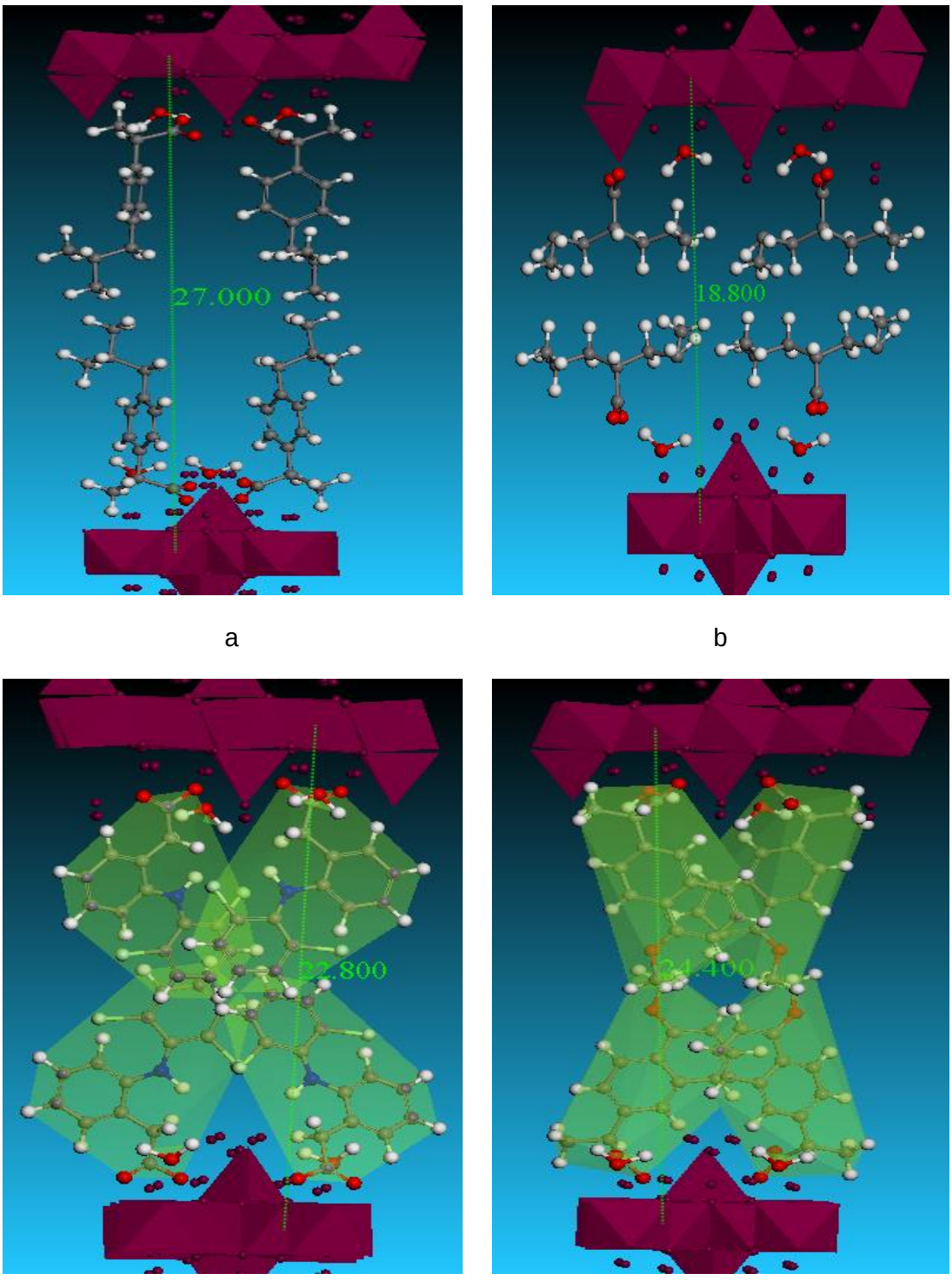

Figure 4.15: A schematic showing the arrangement of guests in MgZn **(a)** MgZn-SI, **(b)** MgZn-Val, **(c)** MgZn-Dic and **(d)** MgZn-Nap.

4.2.2.6. Guest recovery

The MgZn-Dic, MgZn-Nap, MgZn-SI, MgZn-Val, FeZn-Dic, FeZn-Nap, FeZn-SI and FeZn-Val intercalates were each reacted with Na_2CO_3 in D_2O, and NMR spectra recorded of the filtrate from these reactions. The spectra after deintercalation are observed to be identical to those of the Dic, Nap, SI and Val starting materials, confirming that the structural integrity of these drug molecules are retained.

The ^{13}C NMR spectrum of de-intercalated Nap, shown in Figure 4.16a, illustrates resonances at 18.36, 48.48, 55.47, 106.31, 118.38, 125.30, 126.98, 127.05, 128.92, 129.44, 132.99, 139.09, 156.71 and 183.88 ppm; their assignment is displayed in Figure 4.16b. Because a large excess of Na_2CO_3 was used to replace the drug guest, there was residual Na_2CO_3 in the filtrate after the solid HDS was removed; this results in the presence of an additional singlet peak (*cf.* the drug spectrum) at 167.61 ppm.

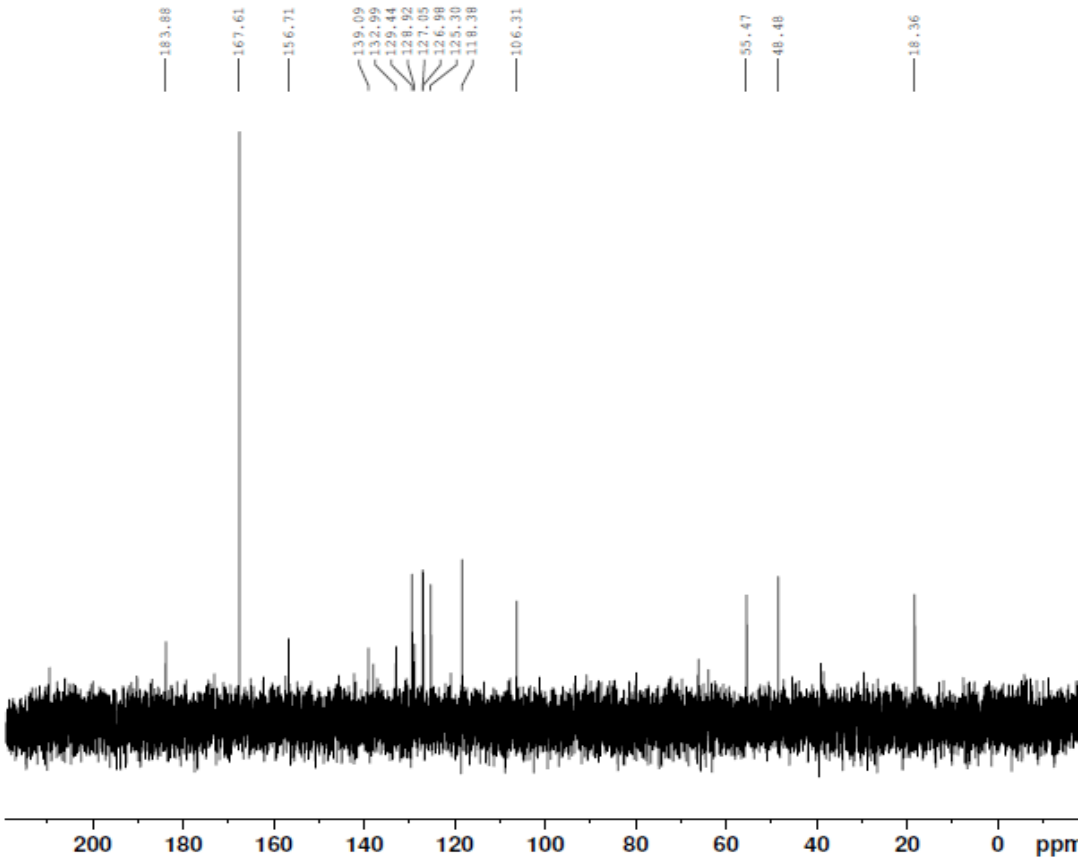

a

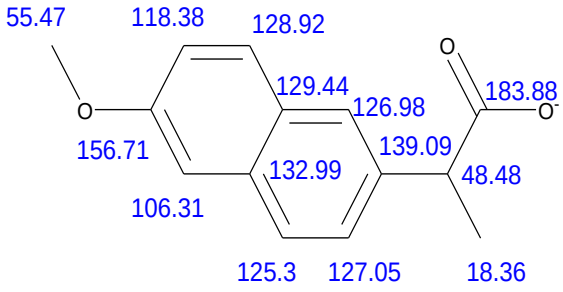

b

Figure 4.16: **(a)** ^{13}C NMR spectrum of Nap after deintercalation and **(b)** chemical structure with resonances.

4.2.2.7. Scanning Electron Microscopy

SEM was performed on selected samples and data are given in Figures 4.17 and 18. The FeZn-Val particles can be seen to have remained hexagonal after intercalation. On the other hand, the intercalation of Dic and Nap into the MgZn-Cl and FeZn-Cl led to rod shaped particles, completely different from the initial shapes. The width of the FeZn-Nap rods is around 63 ± 12 nm. There are also some additional small particles visible on top of certain of the FeZn-Nap rods (Figure 4.18b), and their estimated width is around 21.70 ± 4.25 nm. This will be discussed further below (Section 4.2.2.9).

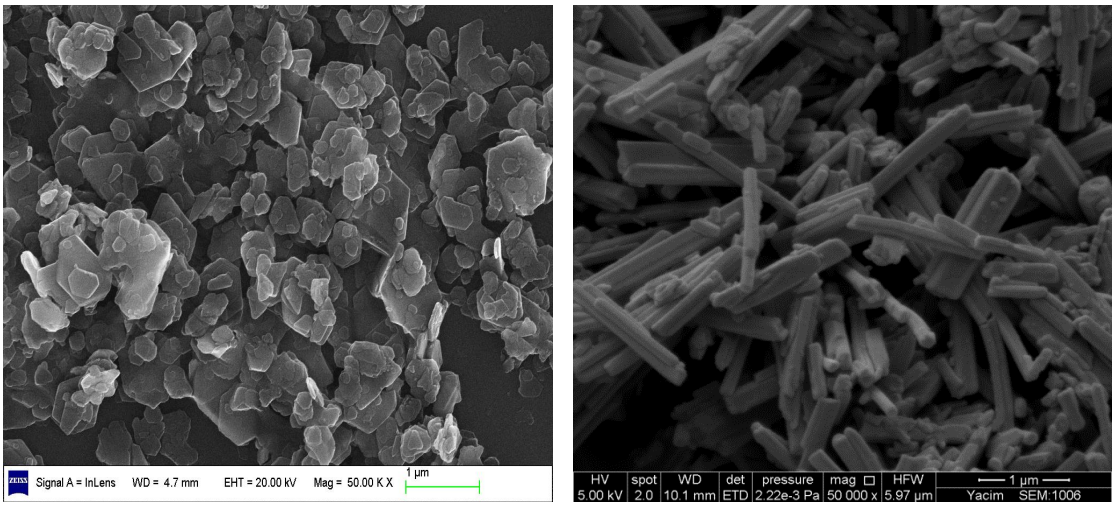

Figure 4.17: SEM images of **(a)** FeZn-Val and **(b)** MgZn-Dic.

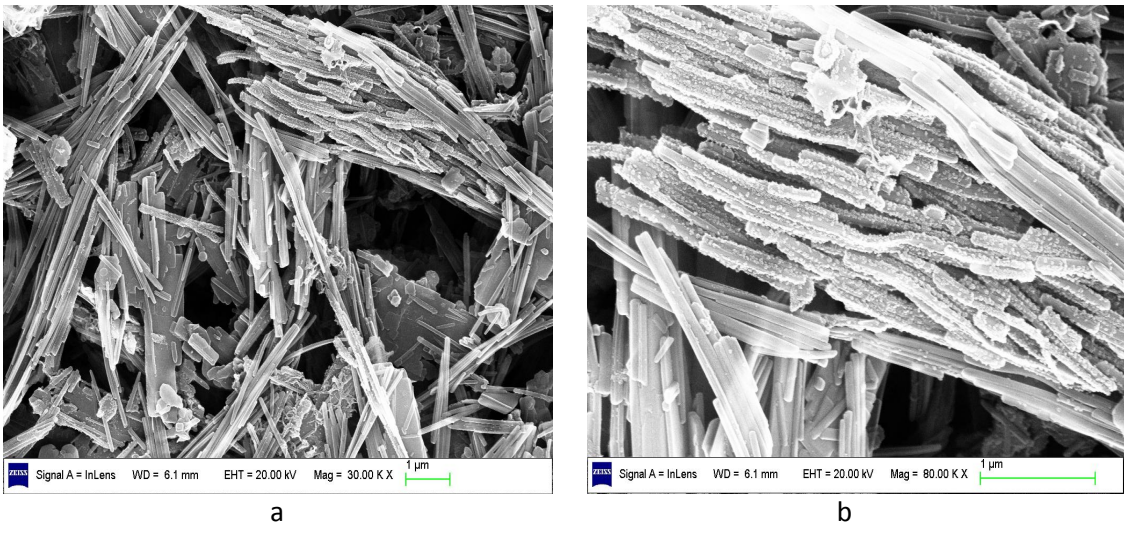

Figure 4.18: SEM images of **(a)** FeZn-Nap, **(b)** an enlargement of a section of the main image of FeZn-Nap.

4.2.2.8. Energy dispersive X-ray spectroscopy

Because of instrument access constraints, EDX could only be run on a few selected samples. However, the spectra of the intercalated products (Figure 4.19 and Table 4.7) show that ratios between Mg/Zn and Fe/Zn do not change substantially during intercalation, except for the intercalation of Val into FeZn-Cl, where the ratio of Fe/Zn dropped, presumably because of some HDS dissolution .

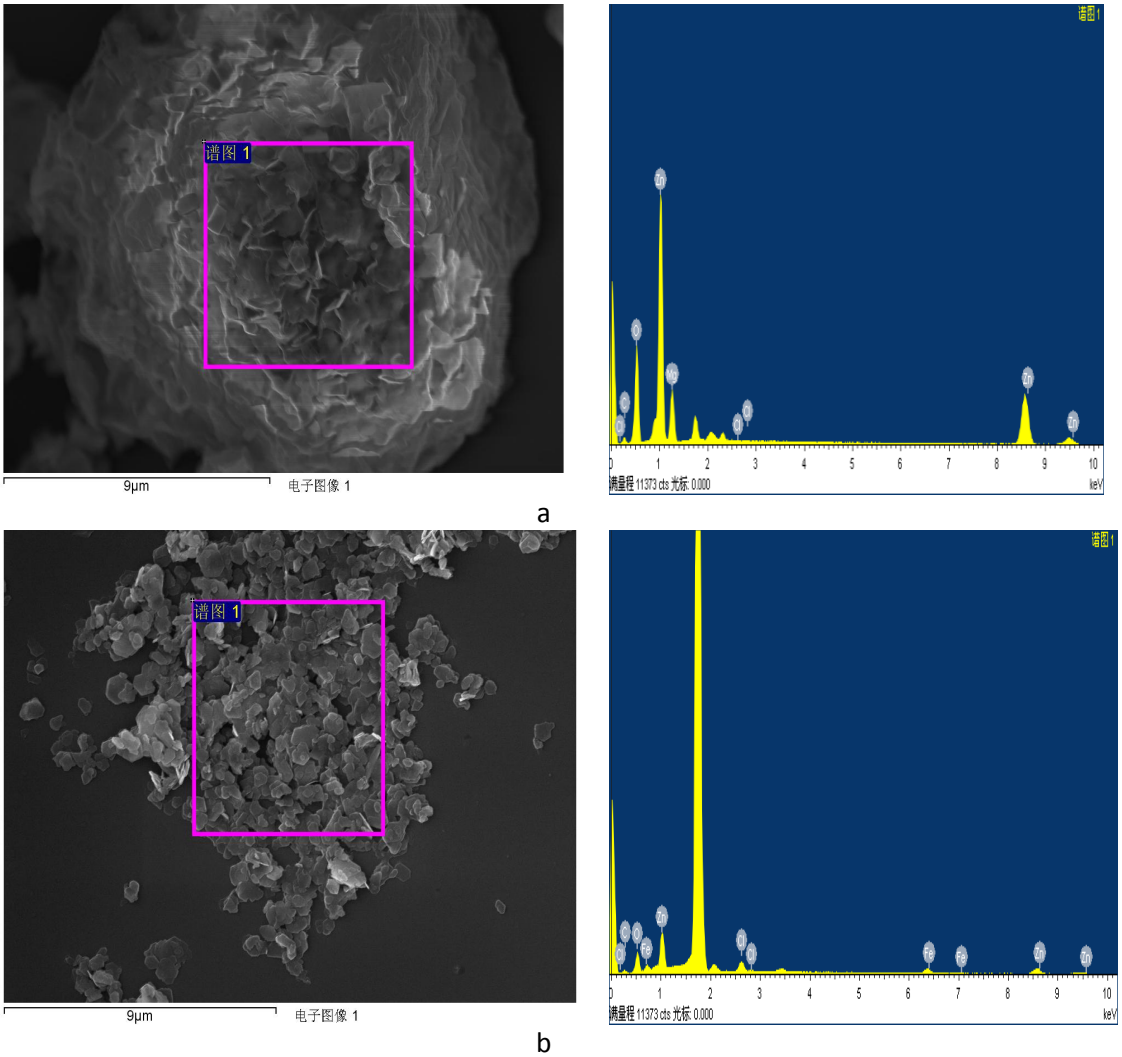

Figure 4.19: EDX spectra of **(a)** MgZn-Val and **(b)** FeZn-Val.

Table 4.7: The ratios of C, Zn, Fe, Mg and Cl from EDX data.

	C	Zn	Fe	Mg	Cl
FeZn-Val	9.1	2.1	1.0	-	1.6
MgZn-Val	1.3	0.9	-	1.0	0.0
FeZn-Nap	15.2	1.1	1.0	-	0.1

4.2.2.9. X-ray photoelectron spectroscopy

The XPS spectrum of the Fe 2p region (Figure 4.20) was used to provide information about the oxidation state of iron in the FeZn-Nap material. As for the pure HDS, the data show the Fe $2p_{1/2}$ main peak has a satellite peak, and thus it was fitted with two signals positioned at 725.9 and 731.3 eV. The other principal peak, $Fe2p_{3/2,}$ is located at 712.2 eV, and is associated with a small satellite peak at 719.2 eV. The B.E. difference between Fe $2p_{3/2}$ peak and its satellite is 7.0 eV. Thus, as discussed earlier in Section 4.2.2.7, the Fe is present in the Fe^{2+} oxidation state. There is a small peak visible at around 704 eV as well, which corresponds to Fe (iron metal).[68–71] Thus, the small particles seen in Figure 4.20 could be Fe particles (Fe^0). The mechanism of reduction of Fe^{2+} to Fe remains unclear, however, the redox potential of Nap may have contributed.[72–76] Peak fitting illustrates that 92 % of the iron present is Fe^{2+}, and 8 % is Fe^0.

To verify the iron oxidation state, the difference in binding energies was calculated: B.E. (Fe $2p_{3-2}$) – B.E. (O_{1s}) = 179.32 eV (Figure 4.20b). Comparing this value with the calibration curve reported by Hadnadjev and co-workers[46] reveals that there is mixture of Fe and Fe^{2+} present, but Fe^{2+} is much more abundant (> 90%). This is in harmony with the analysis above.

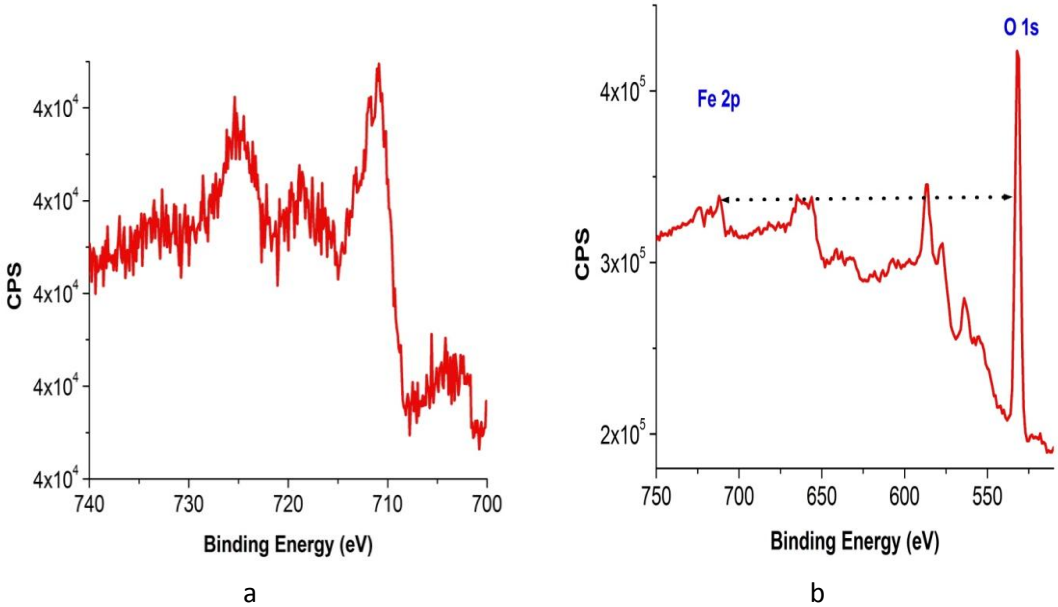

Figure 4.20: XPS of FeZn-Nap **(a)** Fe 2p region and **(b)** Section of the survey XPS spectrum showing the splitting between the O 1s and Fe $2p_{3/2}$ peaks.

4.2.3. Drug release

Dissolution tests for the HDS formulations have been carried out under experimental conditions as close as possible to the gastrointestinal tract and following pharmacopeia requirements.[77] The tablets were placed in 750 mL of 0.1 N hydrochloric acid in a vessel held at 37 ± 0.5 ºC and stirred at 50 r.p.m. After 2 hours of operation the pH of the medium was adjusted to 6.8 ± 0.05 by adding 250 mL of 0.20 M tribasic sodium phosphate. Experiments were carried out for 22 h at this pH. All the experiments were carried out in darkness (except for Val, where manual sampling was required). Dissolution tests were carried out in triplicate from the HDS formulations and 5 times from the commercial tablets. Additionally, one set of experiments was carried out in Phosphate-buffered saline (PBS, pH 7.4).

4.2.3.1. Issues faced with FeZn system

It proved impossible to effectively monitor drug release from the FeZn system as there was found to be interference with the UV/vis spectrum, even though the aliquots were filtered (filter 0.1 µm diameter) prior to measurement. This could be due to the presence of Fe in solution. [78–84] The percentage drug release calculated was often above 100 % and the data were normalised to permit detailed analysis.

4.2.3.2. Ibuprofen

In vitro dissolution of SI from the MgZn-SI powder and selected commercial tablets (Nurofen and Nurofen Express) was first explored; the results are depicted in Figure 4.21 and summarized in Table 4.8. Both commercial tablets disintegrated quickly but the SI embedded did not completely dissolve in the early stages of the experiment due to its low solubility in acidic media. On the other hand, some of the MgZn-SI material is thought to have dissolved in the acidic media, freeing SI in a gradual manner into the solution. Once the pH was adjusted to 6.8, the remaining SI from the commercial tablets dissolved with 5

min. However; SI release from MgZn-SI occurred slowly over 2 hours. The final concentration of SI in solution was higher than with the commercial tablets in the acidic media. It is believed that there are two release mechanisms which took place, firstly, weathering (at low pH), followed by ion exchange (at pH ≥ 6.8, and reliant on the anions in solution). The improvement in SI solubility could be related to the presence of the drug as individual ions in the HDS rather than in a high-lattice energy salt unit cell. Many release studies have been carried out from LDH-SI powder in phosphate buffer (pH ≥ 7),[85–89] but only a few studies were carried with LDH powder in acidic media (pH < 3) since it is known that LDHs dissolve at lower pH.[90] Barkhordari and co-workers reported that more than 80 % of an Mg/Al LDH-SI formulation was dissolved within 2 h at pH1.2.[91] Hence, the MgZn-SI HDS system appears to be somewhat more stable than Mg/Al LDH-SI in acidic media.

Table 4.8: Summary of drug release from MgZn-SI and commercial tablets (Nurofen).

	MgZn-SI	Nurofen Express	Nurofen
After 2h (%)	19.9	12.6	14.4
After 24h (%)	100	100	100
t50/min	125	121	121
t90/min	175	123	123

t50/min and t90/min: Time taken for 50 % and 90 % SI release from the MgZn-SI.

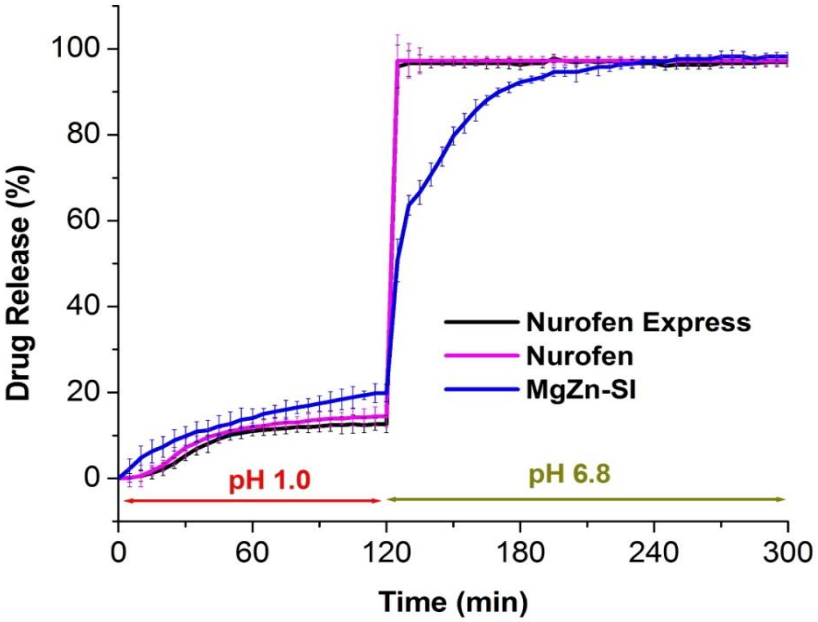

Figure 4.21: SI release from the MgZn-SI and two commercial formulations (Nurofen and Nurofen Express) at pH 1 and pH 6.8.

The Nurofen tablets have t_{max} :35 min and C_{max} : 41.47 µg/mL.[92] Most excipients have no direct pharmacological action but sometimes they can influence the diffusion of a drug. Solubility and bioavailability have a positive correlation and enhancement in the solubility results in the improvement of bioavailability.[93,94] It was demonstrated that an antacid such as magnesium hydroxide reduces the lag time of Ibuprofen and increases its diffusion rate.[95,96] Therefore, it is believed that the MgZn-SI would show quicker t_{max}, higher C_{max} and longer lasting effects than the commercial formulations. Which would be translated into enhancing pain relief with a smaller dose, inducing faster onset of analgesia without compromising safety and with longer duration of efficacy. In addition, it has a longer stability period, which results in longer shelf life (expiry date). The study could not be carried from FeZn-SI because of a lack of instrument availability.

4.2.3.3. Valproate

In vitro dissolution profiles of Val from MgZn-Val and FeZn-Val are depicted in Figure 4.22. After 1h, the FeZn-Val release only 50 % of its loading, versus 100 % from MgZn-Val (Table 4.9). FeZn-Val appears to be more resistant than MgZn-Val in the acidic milieu. Even so, MgZn-Val dissolved much more quickly in acidic media than MgZn-SI. This could be due to the higher solubility of Val compared to SI.

Table 4.9: Summary of drug release from MgZn-Val and FeZn-Val.

	MgZn-Val	**FeZn-Val**
t50/min	19	60
t90/min	48	131
After 2h (%)	100	70.8

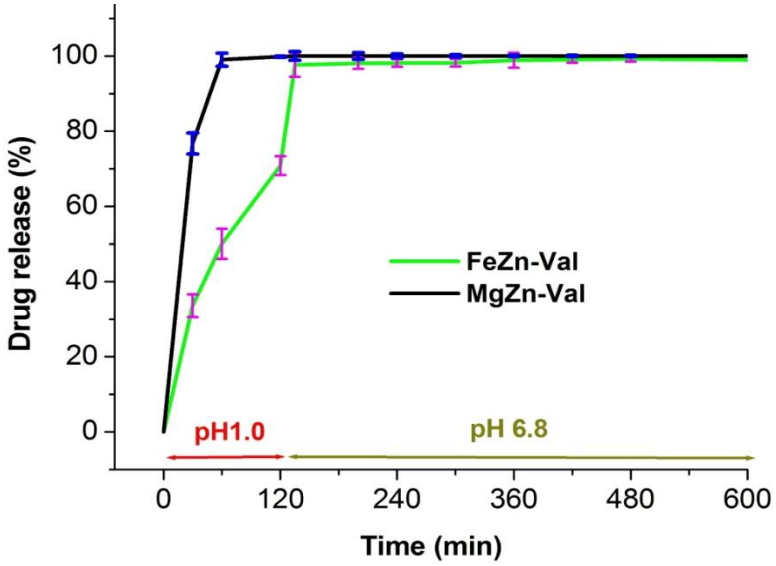

Figure 4.22: Val release from MgZn-Val and FeZn-Val at pH 1 and pH 6.8.

4.2.3.4. Diclofenac

In vitro dissolution profiles of Val from MgZn-Dic and FeZn-Dic are given in Figure 4.23. The FeZn-Dic and MgZn-Dic tends to be more resistant in acidic milieu. Since very little drug release was observed at low pH (Table 4.10), the release mechanism is expected to be ion exchange (at pH ≥ 6.8). MgZn-Val was observed to dissolve very quickly in acidic media, followed by MgZn-SI and MgZn-Dic which remained intact. The solubility order is Val > SI > Dic, so the solubility of the guest seems to control the fate of the HDS in acidic media.

Table 4.10: Summary of drug release from MgZn-Dic and FeZn-Dic.

	MgZn-Dic	FeZn-Dic
After 2h (%)	1.3	2.3
After 24h (%)	100	100
t50/min	150	145
t90/min	300	415

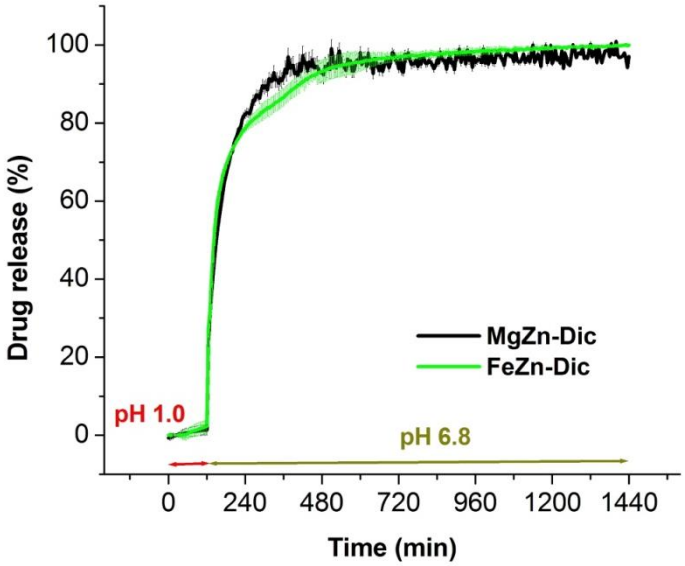

Figure 4.23: Dic release from MgZn-Dic and FeZn-Dic at pH 1 and pH 6.8.

4.2.3.5. Naproxen

4.2.3.5.1. pH1 and 6.8

In vitro dissolution of Nap from MgZn-Nap, FeZn-Nap and commercial tablets (Naprosyn ®) was investigated; the results are depicted in Figure 4.24. Naprosyn tablets disintegrated in a short period of time, but Nap did not completely dissolve in the acidic solution. On the other hand, Nap was gradually released from FeZn-Nap and MgZn-Nap. Once the pH was adjusted the remaining Nap from Naprosyn dissolved within 5 min. While MgZn-Nap behaved similarly to Naprosyn, the FeZn-Nap system gave a more sustained release profile (Table 4.11).

Table 4.11: Summary of drug release from HDSs and commercial tablet.

	MgZn-Nap	FeZn-Nap	Naprosyn
After 2h (%)	23.4	54.9	15
After 24 h (%)	100	100	100
t50/min	123	75	122
t90/min	145	505	130

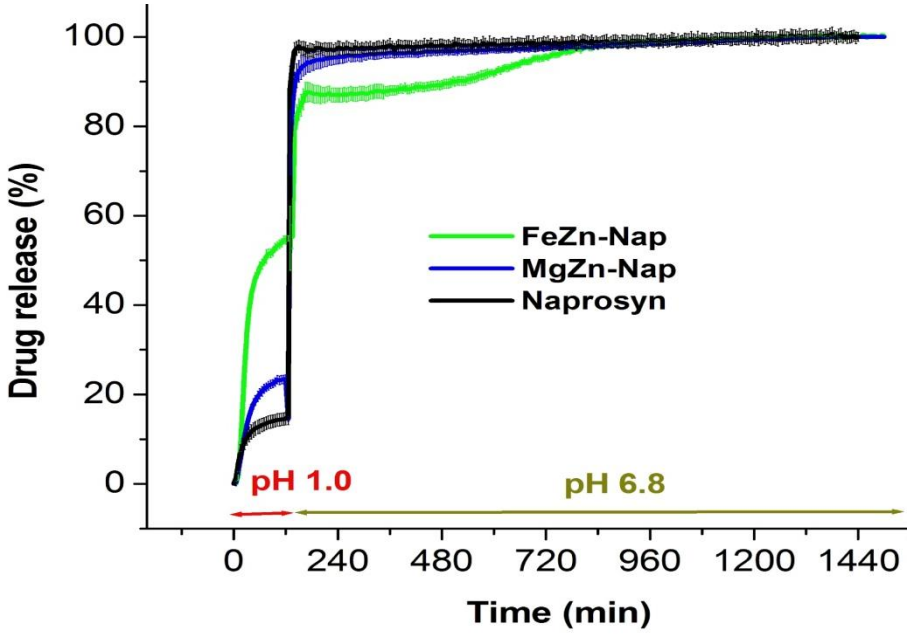

Figure 4.24: Nap release from FeZn-Nap, MgZn-Nap and commercial formulation (Naprosyn) at pH 1and pH 6.8.

The FeZn-Nap and MgZn-Nap dissolved in acidic media, resulting in the drug being released into solution. The concentration of Nap released in the acidic solution was higher for both HDSs compared to the Naprosyn tablets. This implies that the solubility of Nap in acidic media was enhanced in the presence of HDSs; a similar finding was reported by Rojas and coworkers from $Zn_5(OH)_8$/naproxen sodium (Zn-Nap).[97] The improvement could be related to the release of the drug in the ionic (rather than in a high-lattice energy salt unit cell) form from the dissolved FeZn-Nap and MgZn-Nap.[97] The FeZn-Nap appeared to be a little more stable than MgZn-Nap in acidic media, and more stable than the Zn-Nap reported by Rojas *el.al*.[97] Both weathering at low pH and then ion exchange (at pH ≥ 6.8) are believed to have contributed to release.

The Naprosyn tablets have t_{max}: 2-4 hours and C_{max} : 39.3-44.7 µg/mL.[98] Since HDSs have an antacid property and have increased the Nap solubility in acidic milieu, it is believed that the FeZn-Nap and MgZn-Nap should show quicker t_{max} and higher C_{max}. The FeZn-Nap and MgZn-Nap should show better effect than Naprosyn. Which would be translated into enhancing pain relief with a smaller dose, inducing faster onset of analgesia without compromising safety and with

longer duration. In addition, they have a longer stability period, which results in longer shelf life (expiry date) compared to the commercial tablets.

4.2.3.5.2. pH 7.4

The HDS-Nap release data were additionally compared to data available in the literature for controlled release naproxen tablets (Naprelan ®). The release study was carried out under the same conditions reported by the authors of the previous study (a type 2 dissolution paddle apparatus according to U.S (for a digital photograph, see Chapter 6). Pharmacopoeia XXII in PBS buffer pH 7.4 and at 50 r.p.m).[99,100] The results are shown in Figure 4.25. The release of the drug from Zn-Nap (prepared in Chapter 3), MgZn-Nap and Fe_{ox}Zn-Nap are within the interval of the drug release reported (Table 4.12).[99,100] The difference in the drug release from the various HDS is thought to be related to their metal compositions, since it is known that metals influence the release properties of LDHs.[101,102]

The drug release from MgZn-Nap showed 90 % of Nap was liberated after 8 h, which is slower than an analogous LDH system (Mg/Al-Nap) where 90 % of the drug was released after 4 h.[103,104] On the other hand, Carriazo et al and Gu et al found that 90 % of Nap was released from Mg/Al LDH after 35 min and 8 h; respectively.[55,105]

Fe_{ox}Zn-Nap and MgZn-Nap are expected to be suitable for patients with a rapid transit time, while FeZn-Nap should be appropriate for patients with a normal transit time.

Table 4.12: Summary of drug release from HDSs and commercial tablet (Naprelan ®).

Time (h)	Drug Release %				
	FeZn-Nap	Zn-Nap	Fe_{ox}Zn-Nap	MgZn-Nap	Naprelan® [91,92]
0.5	14.3	65.2	45.0	37.0	25 to 70
1	23.8	69.3	53.0	51.2	> 50
4	60.0	78.6	72.0	80.8	> 75

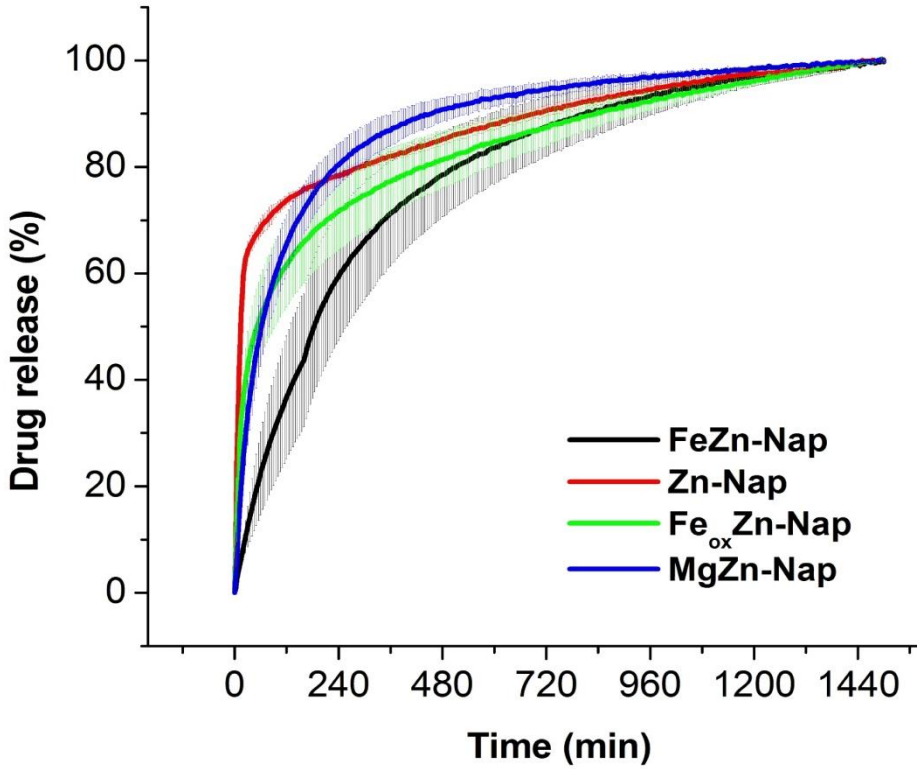

Figure 4.25: Nap release from different HDS at PBS pH 7.4.

The new HDSs released Nap in a sustained manner in phosphate buffer, which makes them good candidates for sustained drug delivery systems. Indeed, they appear to perform better than a commercially available naproxen sustained release formulation.

4.2.4. Tablet preparation

The above data clearly illustrate that new biocompatible HDSs have been prepared, and successfully loaded with a range of drugs. The HDS-drug intercalates were then formulated into tablets, as detailed in Chapter 6. In order to prepare tablets in large batches of 0.5 kg, it was first necessary to scale up the HDS preparation process. This was achieved successfully as detailed in Chapter 6. The scaled up products show same characteristics as those reported in Section 4.2.2. (Appendix III).

The HDS-drug intercalates were blended with excipients for successful tablet preparation. The recipe was based initially on a previous report,[56] with some variations in the excipient blend then introduced to explore the effect this had on drug release. The compositions of the various formulations prepared are detailed in Table 4.13. The effect of compression pressure on the tablet performance was also investigated in selected instances. The role of each excipient is shown in Table 4.14. All the tablets manufactured had smooth surfaces, and some are depicted in Figure 4.26.

Table 4.13: The HDS tablet formulations.

	HDS-Guest(%)	(Avicel® PH 101) (%)	PVP K44 (%)	(Pearlitol® 200) (%)	Mg stearate(%)
FeZn-Dic-Tab1	22.0	47.9	2.5	27.0	0.6
Fe_{ox}Zn-Dic-Tab1	19.3	46.4	4.2	27.2	2.9
FeZn-Dic-Tab	70.5	17.4	0.9	10.2	1.0
MgZn-Nap-Tab	60.0	24.1	1.3	14.1	0.5
FeZn-Nap-Tab	58.1	26.9	1.0	13.2	1.0
MgZn-Sl-Tab	70.7	17.3	0.9	10.2	0.9
FeZn-Sl-Tab	70.7	17.3	0.9	10.2	0.9
MgZn-Val-Tab	59.3	18.9	-	20.9	0.9
MgZn-Val-Tab2	59.3	18.9	-	20.9	0.9
MgZn-Val-Tab3	70.4	17.4	0.9	10.3	1.0
FeZn-Val-Tab	18.9	49.2	2.1	27.9	1.9
FeZn-Val-Tab2	18.9	49.2	2.1	27.9	1.9
FeZn-Val-Tab3	18.9	49.2	2.1	27.9	1.9

Table 4.14: List of the excipients used for tablet preparation and their role

Excipient	Role
Microcrystalline cellulose (Avicel® PH 101)	Diluent/filler
Spray dried (SD) mannitol (Pearlitol® 200)	
Polyvinyl pyrolidone (PVP K44)	Binder
Magnesium stearate	Lubricant

Figure 4.26: Photographs of the HDS tablets prepared.

4.2.5. Pharmacopoeial assessment

The US and British Pharmacopoeias sets strict guidelines for the physical properties that a tablet must have.[106–108] A summary of the key parameters evaluated is given in Table 4.15.

Tablets undergo repeated mechanical shocks or stress during their manufacturing, packing and transportation. This can cause attrition, capping or breakage of tablets. Thus, tablets are formulated to withstand such stress. To find out if the tablets have sufficient mechanical strength to withstand fracture, aberration and capping during the manufacture and handling process, two tests are usually carried out.[109]

The first is a hardness test, where the load required to crush a tablet is measured. It is important that a tablet is neither too hard nor too soft, because it

needs to be hard enough to withstand packaging, transportation, and so forth, but if it is too hard it will not break up in the body. A hardness test is performed to determine the required pressure parameters on the tableting machine. The hardness for oral tablets is usually between 40-100 N for immediate release and 100-200 N for sustained release tablets.[110]

The second test is a friability test, it is defined as the percentage (%) of weight loss by tablets as they roll and fall inside a set of rotating apparatus (for a digital photograph, see Chapter 6). The weight loss should be less than 1%, and after the test the tablets should not show any sign of breakage.[111]

All pharmaceutical preparations are also required to contain a constant dose of active ingredient, with small variations permitted within strict pharmacopeial limits, in all the tablets. In order to ensure that a patient receives the same amount of drug every time they take a tablet, it is vital to ensure that the tablet masses are consistent. For each batch of tablets prepared, the uniformity of active ingredient content is tested in two separate tests, namely a uniformity of weight (mass) study and quantification of the uniformity of active ingredient.[112]

The HDS tablets had a target mass between 150 - 650 mg, depending on the drug, and the observed masses can be seen in Table 4.15. The tablet masses were planned to match the amount of drug present in commercial formulations. The relative standard deviation (RSD) weight variation of the HDS tablets was found to range between 1.6 - 5.2 %, while measurements on commercially available tablets showed the RSDs on the masses to lie between 1- 17.4 %. The pharmacopoeia limit for percentage deviation of tablets of 80-250 mg is ± 7.5 % and above 250 mg is ± 5.0 %, and thus the formulation batches were found to pass according to the specifications given in the US and British pharmacopoeias.[106,107]

Excellent drug content uniformity was also found in the HDS tablets, with values between 92.6 ± 1.7 and 105.0 ± 3.4 % of the target content observed. These values lie above the USP and BP requirements of 100 ± 15 %. [106,107]

The values for hardness were found to be uniform and to range between 43 and 123.5 N. Friability values for the HDS tablets were found below 0.8 % (pharmacopeia requirement < 1 %). No sign of cracking, capping or breaking was seen. This implies that HDS tablets had sufficient strength to comply with pharmacopeia requirements.

Thus, all the HDS tablets were found to meet the pharmacopeia requirements, as is evident from the results shown in Table 4.15. All tablets in Table 4.15 were submitted to *in vitro* release studies in conditions which mimic the gastrointestinal tract, and monitored for 24 hours.

Table 4.15: Summary of pharmacopeial tests for HDSs and commercial tablets (the cell highlighted in green mean the tablets pass the test, and those in red failed).

Formulation	Drug	Weight variations (mg) (±SD), n=20	Hardness (N) (±SD), n=5	Friability (weight loss) (%)	Drug content (%) (±SD), n=4
FeZn-Dic-Tab	Dic	201.7 ± 3.4	123.5 ± 7.8	0.0	98.8 ± 2.5
FeZn-Dic-Tab1	Dic	190.1 ± 3.3	79.3 ± 3.7	0.2	92.6 ± 1.7
Fe_{ox}Zn-Dic-Tab1	Dic	151.2 ± 3.9	110.3± 4.6	0.3	99.3 ± 2.5
MgZn-Nap-Tab	Nap	200.3 ± 3.0	123.0 ±9.9	0.3	100.9 ± 2.8
FeZn-Nap-Tab	Nap	331.5 ± 5.0	119.2 ± 7.6	0.4	105.0 ± 3.4
MgZn-SI-Tab	SI	203.6 ± 4.3	43.0 ± 4.6	0.7	99.0 ± 1.2
FeZn-SI-Tab	SI	214.3 ± 5.2	53.0 ± 3.5	0.5	97.4 ± 3.3
MgZn-Val-Tab	Val	656.5 ± 4.5	77.0 ± 7.8	0.7	94.5 ±3.0
MgZn-Val-Tab2	Val	385.6 ± 4.1	93.0 ± 4.5	0.4	98.8 ±2.7
MgZn-Val-Tab3	Val	440.0 ± 2.5	120.0 ± 5.2	0.4	100.2 ± 3.3
FeZn-Val-Tab3	Val	645.7 ± 3.9	120.0 ± 6.3	0.5	105 ± 4.5
Clofenac 100 mg	Dic	218.9 ± 2.0	-	-	93.5 ± 5.4
Dicloflex 75mg	Dic	233.9 ± 6.0	-	-	86.3 ± 3.3
Rheumatac Retard 75 mg	Dic	251.5 ± 1.6	-	-	114.7 ± 1.2
Naprosyn 250 mg	Nap	269.1 ± 1.6	-	-	115.9 ± 1.2
Brufen 800mg	SI	1059.3± 17.4	-	-	107.8 ± 13.4
Nurofen	SI	476.2 ± 5.9	-	-	97.1 ± 4.9
Epilim 200mg	Val	295.6 ± 1.0	-	-	95 ± 1.5

(-)The hardness and friability of the commercial tablets were not measure.

4.2.6. Release study from HDS tablets

4.2.6.1. Diclofenac

Dissolution tests from samples MgZn-Dic-Tab, FeZn-Dic-Tab, FeZn-Dic-Tab1, Fe_{ox}Zn-Dic-Tab1, and commercial sustained release (SR) Dic tablets (Rheumatac Retard, Dicloflex and Clofenac) are included in Figures 4.27 and 4.28. All the tablets showed only low amounts of Dic release at pH 1, with FeZn-Dic-Tab1 releasing 9 % of its loading and the other tablets between 0-5 % during the first 2 h at this pH (these condition mimic the stomach milieu and transit time). The high amounts of release from FeZn-Dic-Tab1 may be caused by the destruction of some of the HDS layers; the tablets were observed to disintegrate before the pH was raised. The other tablets disintegrated after the adjustment of the pH to 6.8.

After 2 h, once the pH was adjusted to 6.8, the release rate from all the tablets increased. This is triggered by the anion exchange of the Dic located in the interlayer with phosphate anions in solution (see Table 4.16). The FeZn HDS remained green after the experiment, as can be seen in Figure 4.29 indicating that oxidation of Fe^{2+} does not occur to any significant extent.

Table 4.16: Summary of Dic release from the different tablets.

	FeZn-Dic-Tab	FeZn-Dic-Tab1	Fe_{ox}Zn-Dic-Tab1	MgZn-Dic-Tab	Rheumatec Retard	Dicloflex	Clofenac
After 2h (%)	4.1	9.0	5.3	0.1	2.1	0.1	0.2
After 24h (%)	100	100	100	100	100	100	100
t50/min	315	135	455	610	290	480	285
t90/min	885	360	1170	1205	660	1095	720

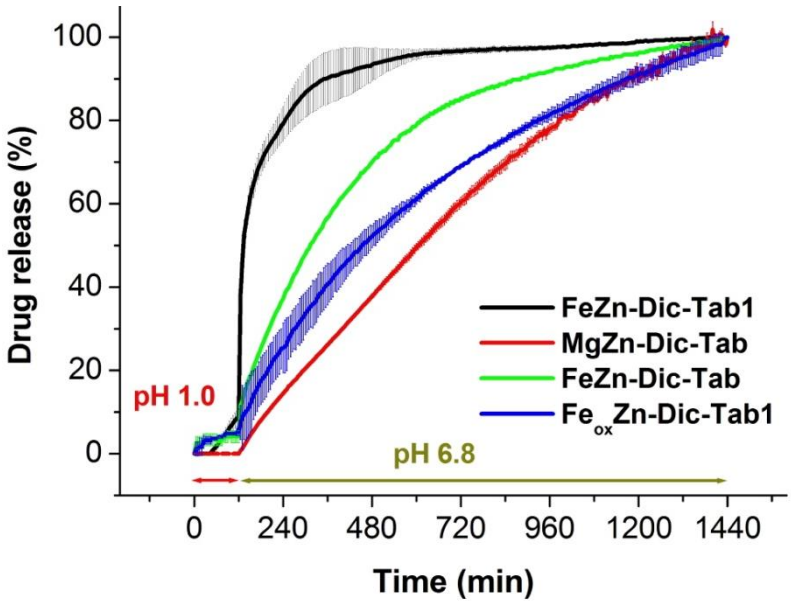

Figure 4.27: Dic release from the different HDS tablets formulations at pH 1 and pH 6.8. (There are error bar on green line but they are too small (< 1%) to be clearly visible).

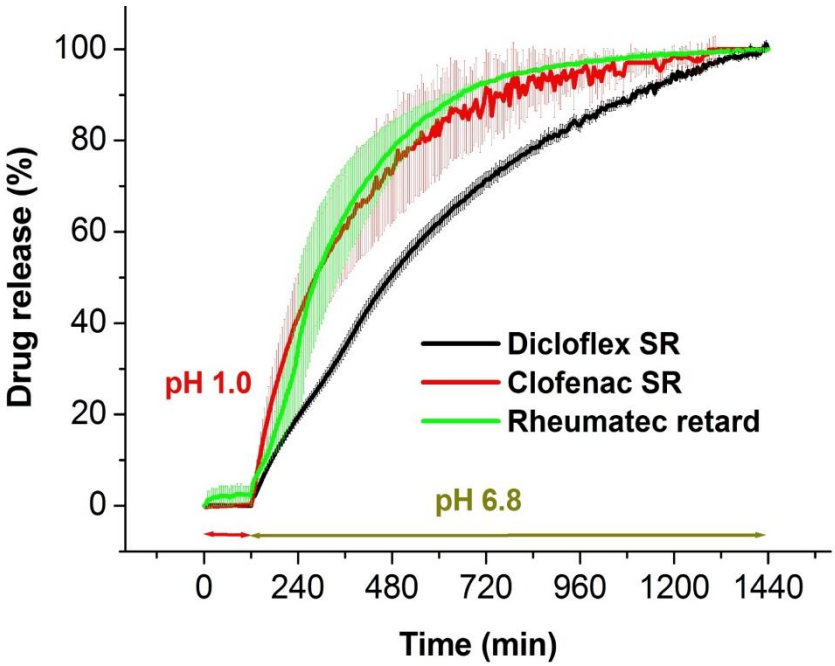

Figure 4.28: Dic release from 3 different commercial tablets at pH 1 and pH 6.8 (n=5).

Figure 4.29: A digital photograph of FeZn-Dic-Tab after drug release.

The release rate from FeZn-Dic-Tab and MgZn-Dic-Tab was consistent from tablet to tablet, with a standard deviation (SD) less than 1.8 % throughout all the experiment compared to other with SDs of up to 16 %. FeZn-Dic-Tab and MgZn-Dic-Tab should be hypothetically better than the commercial tablets in giving the same relief of symptoms on every application, since they have very consistent rates.[113]

The new HDS formulations meet the pharmacopeia requirements for delayed-release dosage forms as well as sustained release dosage forms: these specify that less than 10 % of the incorporated drug should be released in the acidic media and the drug is freed at a slow rate over a prolonged duration of time, respectively.[77,114] In addition, all the drug loading was liberated within 24 h. By meeting the pharmacopeia delayed-release dosage forms requirement, the new HDS tablets are expected to prevent stomach irritation which can be caused by Dic. By meeting the other requirement, the HDS tablets may contribute to improved patient compliance. The FeZn-Dic-Tab, Fe_{ox}Zn-Dic-Tab1 and MgZn-Dic-Tab showed a similar release profile to the commercial tablets, thus they are expected to be suitable for patients with normal transit times. FeZn-Dic-

Tab1 disintegrated quickly and showed a faster release profile and might be suitable for patients with faster transit times (due to a various factors for instance: Short bowel syndrome, diet).[115,116] If the transit time is rapid and drug release too slow, the tablets can be excreted from the human body before freeing all their loading, which leads to a decrease in bioavailability.[117,118] Therefore; there is a risk that the drug level does not attain the therapeutic window, resulting in no pharmacological effect (in this case no pain relief).

4.2.6.2. Naproxen

Dissolution tests from FeZn-Nap-Tab and MgZn-Nap-Tab are depicted in Figure 4.30. The FeZn-Nap-Tab and MgZn-Nap-Tab showed no release during the first 2 h at pH 1 (Table 4.17). Once the pH was adjusted, the Nap release started from FeZn-Nap-Tab and MgZn-Nap-Tab, which both displayed almost identical release profiles. The release from LDH-Nap tablets has been explored in a previous study, which used LDH-Nap compressed without additional excipients in the same conditions: for that formulation, it was found that there was no release in acidic milieu and only 27 % release after 24 h at pH 6.8.[119] LDH-Nap tablets, FeZn-Nap-Tab and MgZn-Nap-Tab thus behave in same manner in the acidic media. However, FeZn-Nap-Tab and MgZn-Nap-Tab show enhanced properties over LDH-Nap tablets, since they liberate all the loading within 24 h in a neutral environment.

It is believed that the only release mechanisms which took place from the two formulations is ion exchange (at pH ≥ 6.8). It appeared that no weathering at low pH occurred. Wanwimolruk and co-workers reported that an in vivo study of commercial Nap controlled release tablets, and found they released 9 % and 30 % in a fasted state during the first 1h and 2 h, respectively.[98] This can lead to stomach irritation, but would not be a problem with the HDS tablet formulations.

In vivo studies reported by many scientists showed that Nap sustained release tablets have better effect than normal tablets (immediate release).[98,120–122] The new HDS formulations meet the pharmacopeia requirements for delayed-release dosage forms as well as sustained release dosage forms. In addition, they released all their loading within 24 h. The FeZn-Nap-Tab and MgZn-Nap-Tab should be suitable for patients with normal transit time.

Table 4.17: Summary of Nap release from the different tablets.

	MgZn-Nap-Tab	FeZn-Nap-Tab
After 2h (%)	0	1.6
After 24h (%)	100	100
t50/min	335	295
t90/min	980	1040

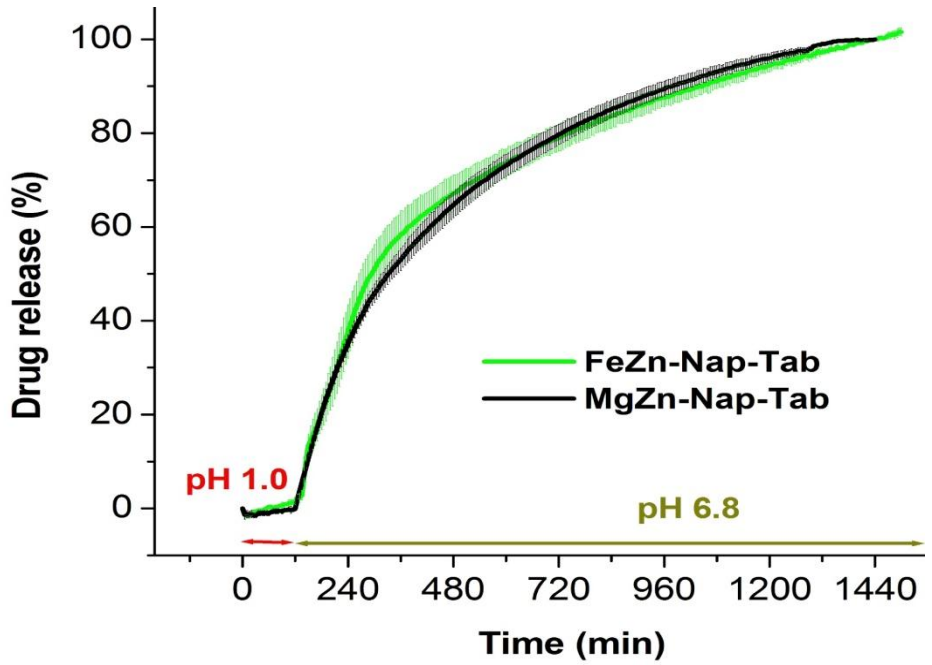

Figure 4.30: Nap release from FeZn-Nap-Tab and MgZn-Nap-Tab at pH 1and pH 6.8.

4.2.6.3. Ibuprofen

Dissolution tests from HDS tablets FeZn-SI-Tab, MgZn-SI-Tab and a commercial tablet (Brufen Retard) are displayed in Figure 4.31. All the tablets showed minimal release at low pH, with FeZn-SI-Tab releasing less than 8 %, and the other two tablets 3 % during the first 2 h at pH 1.0 (Table 4.18). Once the tablets were in a milieu mimicking the intestine (pH 6.8), there was a sharp burst of release from the MgZn-SI-Tab and Brufen Retard. In contrast, the SI release from FeZn-SI-Tab remained flat for 75 min and then was followed by a sharp release. The release rate from all the tablets slows and both HDS formulations behave very similarly from 5 h until the end of the experiments; the data are summarised in Table 4.18. After the initial burst release, drug was freed from the tablets in an almost linear fashion from all three types of tablets. In contrast, Rojas and co-workers reported that LDH-SI tablets (compressed LDH-SI without additional excipients) did not release at pH 1.2 and only 16.5 % was released after 24 h at pH 6.8.[119]

Table 4.18: Summary of SI release from the different tablets.

	MgZn-SI-Tab	FeZn-SI-Tab	Brufen retard
After 2h (%)	3.2	7.1	2.9
After 24h (%)	100	100	49.2
t50/min	255	325	1470
t90/min	1120	1160	-

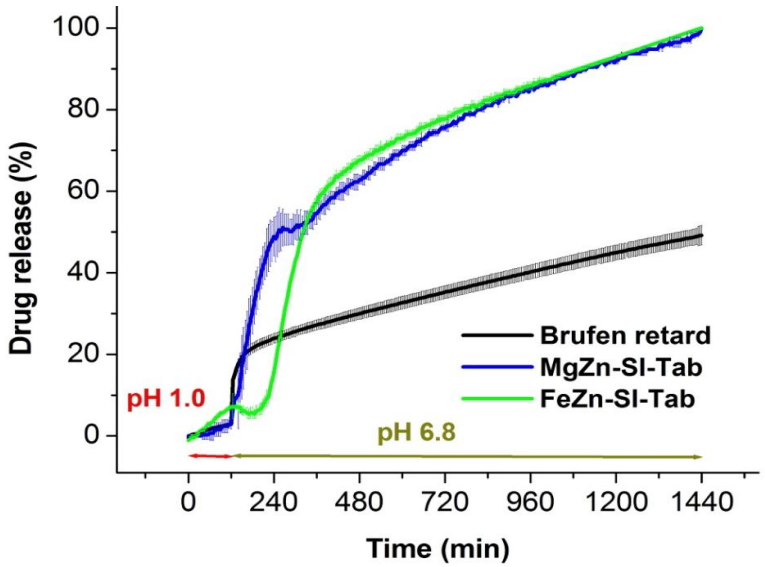

Figure 4.31: SI release from FeZn-SI-Tab, MgZn-SI-Tab and commercial formulation (Brufen Retard) at pH 1and pH 6.8.

Only 50 % of the SI content was release from the Brufen Retard tablet within 24 h and (79 % within 48 h, see Appendix III). After 24 h, there is risk that the remains of the tablet will have been excreted from the human body or be enrobed inside stools. This can halt release, and thus the remaining drug will not be freed. This is wasteful, since more drug is being used to make the medicine than is used in the body, and in addition the drug concentration may not be maintained within the therapeutic window with this type of formulation. The MgZn-SI-Tab and FeZn-SI-Tab showed a comparable solution drug concentration vs time profile to the commercial Brufen Retard tablet, but the HDS tablets free all their loading within 24 h; this is illustrated in Figure 4.32.

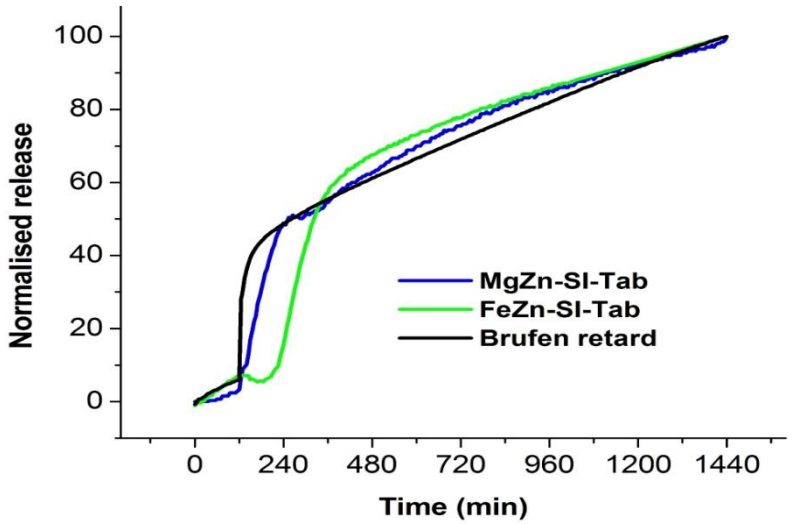

Figure 4.32: Normalised SI release from the FeZn-SI-Tab, MgZn-SI-Tab and Brufen retard releasing at pH 1and pH 6.8.

SI release from Zn-SI tablets (containing the same excipients as the new HDS tablets reported in this Chapter) has been reported by Taj *el al*,[56] in similar conditions. These authors found that *ca.* 10 % of the drug was released in an acidic media, and following transfer to neutral medium the rest of the drug was freed within 10 h. Shiyani and co-workers reported that LDH-SI tablets did not release in acidic milieu and all the SI was released after 10 h in the neutral medium.[123]

All data reported here, and previously by others scientists, showed a burst release of SI in the phosphate buffer (pH ≥ 6.8). Since it is known that the SI is absorbed quickly in the gastrointestinal tract of a healthy human being,[92] this initial release from the HDS tablets should bring its plasma concentration rapidly into the therapeutic window; the second, sustained, part of the release profile should maintain it within this window for a prolonged period of time.[124,125]

The MgZn-SI-Tab and FeZn-SI-Tab formulations meet the pharmacopeia requirements for both delayed-release dosage forms and sustained release dosage forms. Therefore, they are expected to prevent damage to the stomach caused by drug release in this low pH environment, as well as improving patient compliance. They showed a similar release profile to a commercial tablet, and thus should be suitable for patients with normal transit times. The new formulations are less wasteful of drug than the commercial tablets.

4.2.6.4. Valproate

Several different tablet formulations were prepared for the Val system. Dissolution test results from FeZn-Val-Tab, MgZn-Val-Tab, and commercial tablets (Epilim ®) are shown in Figure 4.33. To the best of our knowledge, outside the work reported in this thesis no one has studied Val release from HDS or LDH formulations. The release of Val from HDS tablets was slower compared to its release from the HDS-Val powder (Figure 4.22). In acidic media, the drug release was slower from MgZn-Val-Tab2 and Tab3 than MgZn-

Val-Tab and Epilim (see also Table 4.19). Once the pH was adjusted, the release rate slowed down from all 4 formulations. Epilim and MgZn-Val-tab released all their loading within 24h, while MgZn-Val-Tab2 and MgZn-Val-Tab3 released only 74.6% and 68.6%, respectively. MgZn-Val-Tab and Epilim showed very similar release profiles. Some trial experiments with the FeZn-Val tablet formulations were performed, and it appeared that release was slower than MgZn system, but this study could not be done in triplicate because of a lack of instrument availability.

The Val release in acidic conditions was much higher than the amount of drug release observed from the other HDS tablets, even though MgZn-Val-Tab contains the same excipients in the same amounts as MgZn-Dic-Tab, MgZn-SI-Tab and MgZn-Nap-Tab. This is, however, a positive thing. Val release in acidic media is preferable, since *in vivo* studies showed that Epilim tablets (which release in the stomach) are more effective in the long-term treatment of epilepsy than enteric-coated sodium valproate tablets (which do not).[126]

Table 4.19: Summary of Val release from the different tablets.

	MgZn-Val-Tab	MgZn-Val-Tab2	MgZn-Val-Tab3	Epilim®
After 2h	44.8	25.2	23.4	54.7
After 24h	100	74.6	68.6	100
t50/min	125	310	540	110
t90/min	845	1580	1640	625

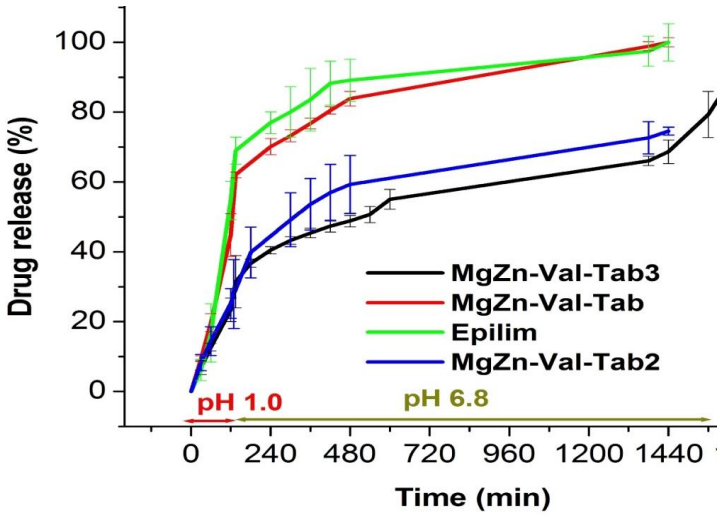

Figure 4.33: Val release from the MgZn-Val tablets and Epilim at pH 1 and pH 6.8.

This greater extent of release can be attributed the higher solubility of Val compared to the other drugs. The release rate difference between the three Val-loaded HDS tablets is thought to be due to porosity, which has an inverse correlation with hardness and a positive correlation with the release rate.[127–132] The hardness test showed that MgZn-Val-Tab3 was most resistant to crushing, followed by MgZn-Val-Tab2 and finally MgZn-Val-Tab (Table 4.15). The release mechanism is believed to be mainly due to weathering in acidic media. Once the pH was adjusted, there was a deceleration in the release rate, which suggested strongly that a new release mechanism became dominant, the ion exchange mechanism (which is highly dependent on the anions present).

The release rate could be tailored just by varying the ratio of excipients or the compressional force used to prepare the three tablets formulations (MgZn-Val-Tab, MgZn-Val-Tab2 and MgZn-Val-Tab3). It is known that antacids can increase the bioavailability of valproic acid,[133–136] and since HDSs can act in an antacid role MgZn-Val-Tab may be able to generate the same effect as Epilim with a smaller dose. MgZn-Val-Tab is expected to be suitable for patients with normal transit time, while MgZn-Val-Tab2 and MgZn-Val-Tab3 might be useful for those with a longer transit time.

4.2.7. Stability test

Stability studies were carried out by storing the formulated tablets and HDSs-drug powders under usual environmental conditions (temperature and humidity varied with the seasons). The tablets and HDS-drug intercalates were kept in glass vials and stability tests were performed at 0 days and after 1, 3, 6, 12, 15 18 and 24 months using FTIR, XRD, NMR and HPLC. The tests showed that all the drugs remained stable during these periods (FTIR is shown in Appendix III).

4.2.8. Kinetic analysis

In order to gain more insight into the mechanism involved in Nap release from the biocompatible HDSs (MgZn and FeZn), some widely used mathematical models were utilised. These models are summarised in Table 4.20. M_t and M_∞ are the amount of drug released at time t and the theoretical maximum amount of release possible; M_0 is the initial amount of drug present in solution (usually, $M_0 = 0$). k (the release constant) and n (the release exponent).

Table 4.20: Summary of kinetic equation models.

Model	Equation	References
Zero-order	$M_t = M_0 + k_0 t$	137
First-order	$\ln (Mt/ M_\infty) = -k_F t$	138
Korsmeyer-Peppas	$M_t / M_\infty = k_{KP} t^n$	139
Higuchi	$M_t / M_\infty = k_H t^{1/2}$	140–142
Bhaskar	$\ln(M_t / M_\infty) = k_B t^{0.65}$	143

The Higuchi and Korsmeyer-Peppas models are applicable only for the first 60 % of drug release. [144] Thus, the data were fitted up to this limit, and for the other models up to 90 % release.

The fitting results are shown in Figure 4.35 and the obtained data are summarised in Table 4.21. The Bhaskar and Higuchi models show a good fit to the data ($R^2 > 0.99$). Therefore, it is proposed that Nap release is a proactive diffusion process taking place via ion exchange and governed by the nature of the HDS matrix. Ambrogi and co-workers have observed the same release process from Mg/Al LDH-Dic.[145]

Table 4.21: Fitting parameters of different kinetic models for the release of Nap from the HDS in PBS (pH 7.4)

	Bhaskar		First order	
	R^2	k_B ($min^{-0.65}$)	R^2	k_1 (min^{-1})
Fe_{ox}Zn-Nap	0.9962	0.0232	0.7493	0.0034
FeZn-Nap	0.9983	0.0319	0.5313	0.0021
MgZn-Nap	0.9957	0.0434	0.4863	0.0075

	Higuchi		Korsmeyer-Peppas		
	R^2	k_H ($min^{-1/2}$)	R^2	n	k_{KP} (min^{-n})
Fe_{ox}Zn-Nap	0.9777	3.9721	0.9889	0.2939	0.1561
FeZn-Nap	0.9971	4.5379	0.9949	0.7814	0.8524
MgZn-Nap	0.9919	7.1902	0.9688	0.7125	0.0393

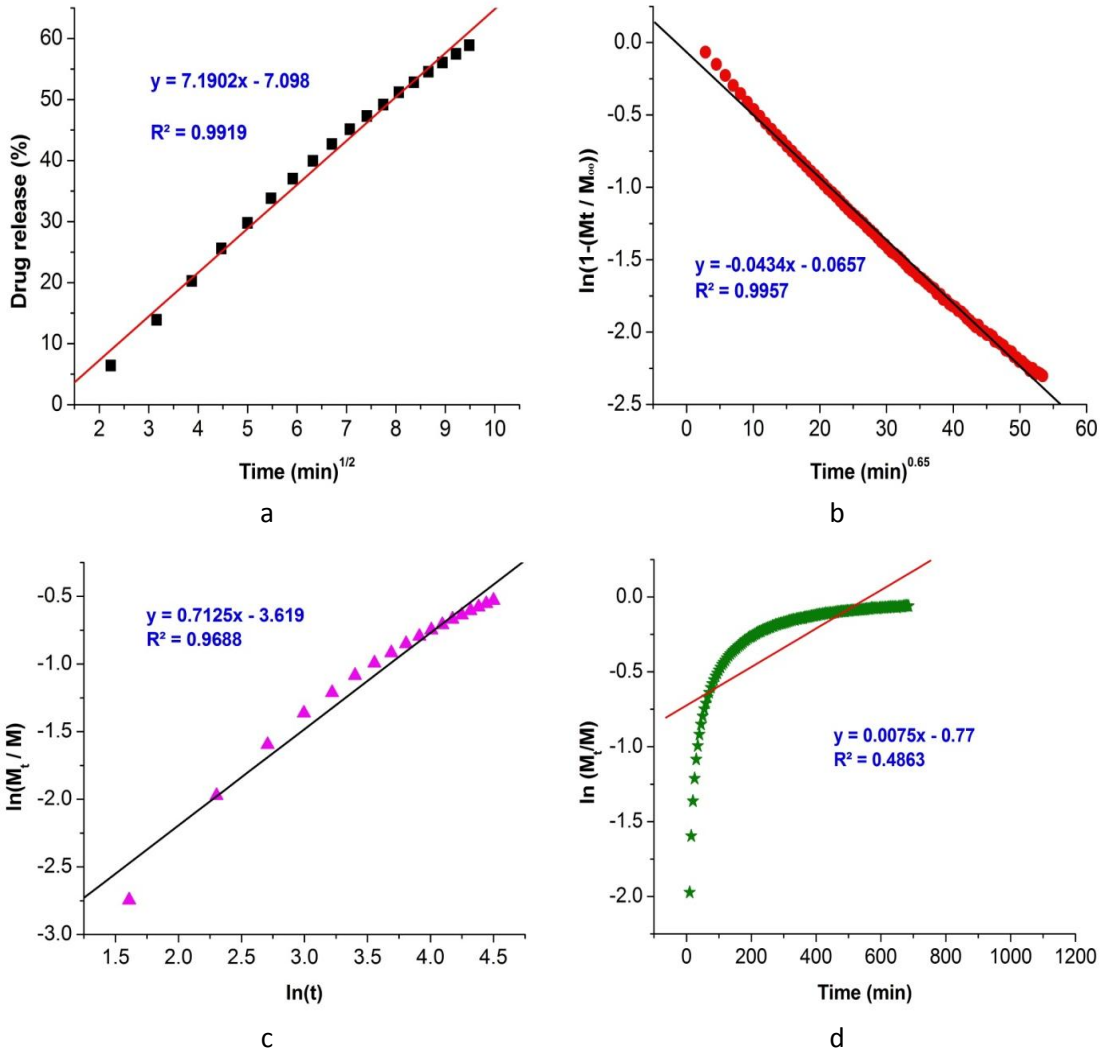

Figure 4.34: Kinetic models fitted to the experimental release data for MgZn-Nap. **(a)** Higuchi model, **(b)** Bhaskar model, **(c)** Korsmeyer-Peppas model **(d)** First order model.

Two kinds of mechanism were postulated during the investigation of drug release from HDS tablets: weathering or dissolution of HSDs layers in the HCl solution (pH ≥ 1.0) and an ion-exchange process in phosphate buffer (pH ≥ 6.8). To gain more insights into the mechanism of drug release, the same kinetics models (Table 4.20) were exploited.

Fits of the models to Dic and Nap release in pH ≥ 6.8 are given in Figure 4.36, and the results are summarised in Table 4.22. It is clear that the first order model does not describe Dic and Nap release, reflected by the fact that data clearly do not lie on a straight line.

The Higuchi model is not suitable to explain the release process from the HDS tables. They have been utilised inappropriately during last half century to analyse drug release kinetics, specially from tablets.[144] They were only plotted here to see if they can lead to the misinterpretation of the data. Korsmeyer-Peppas models showed most of the $R^2 > 0.96$, however, all the n values were beyond the boundary (> 1). This demonstrate that the models are not suitable for those tablets .

Meanwhile, the Bhaskar model fits the release profiles much better ($R^2 > 0.99$), except for MgZn-Dic-Tab and Fe_{ox}Zn-Dic-Tab, indicating that the release mechanism from HDS tablets in most cases is controlled by ion exchange. The release of Dic from MgZn-Dic-Tab appears to be zero order ($R^2 > 0.99$), with the release data lying on a straight line for the first 80 % of release ($R^2 > 0.998$).

Usually, zero-order release formulations are complex, expensive, time consuming, and challenging to manufacture.[146,147] Zero-order release formulations remain the ultimate aim of much research due their ability to release drug at a constant rate, leading to good control of plasma concentration.[148] The MgZn-Dic-Tab are easy, inexpensive and quick to

manufacture. This makes the formulation a good candidate for commercialisation.

Table 4.22: Fitting parameters for the release of Dic and Nap from the HDS Tablets.

	Zero order		**First order**		**Higuchi**	
	R^2	k_0	R^2	$K_1(min^{-1})$	R^2	$k_H\ (min^{-1/2})$
Fe_{ox}Zn-Dic-Tab1	0.9590	0.0739	0.8015	0.0015	0.9989	0.0409
FeZn-Dic-Tab	0.9153	0.0956	0.7662	0.0018	0.9992	5.7102
FeZn-Dic-Tab1	0.9075	0.1593	0.8421	0.0021	0.9987	13.882
MgZn-Dic-Tab	0.9919	0.0865	0.7654	0.0026	0.9935	3.8371
FeZn-Nap-Tab	0.8579	0.0696	0.6903	0.0076	0.9858	7.0196
MgZn-Nap-Tab	0.8984	0.0863	0.6106	0.0019	0.9825	6.0025

	Bhaskar		**Korsmeyer-Peppas**		
	R^2	$K_b(min^{-0.65})$	R^2	n	$K_{KP}\ (min^{-n})$
Fe_{ox}Zn-Dic-Tab1	0.9753	0.0284	0.9747	1.1551	0.0345
FeZn-Dic-Tab	0.9963	0.0385	0.9779	1.2972	0.0003
FeZn-Dic-Tab1	0.9974	0.0718	0.9979	1.4805	0.0004
MgZn-Dic-Tab	0.9428	0.0267	0.9860	1.4196	0.0000
FeZn-Nap-Tab	0.9940	0.0307	0.9618	1.6206	0.0000
MgZn-Nap-Tab	0.9950	0.0336	0.8404	1.8708	0.0067

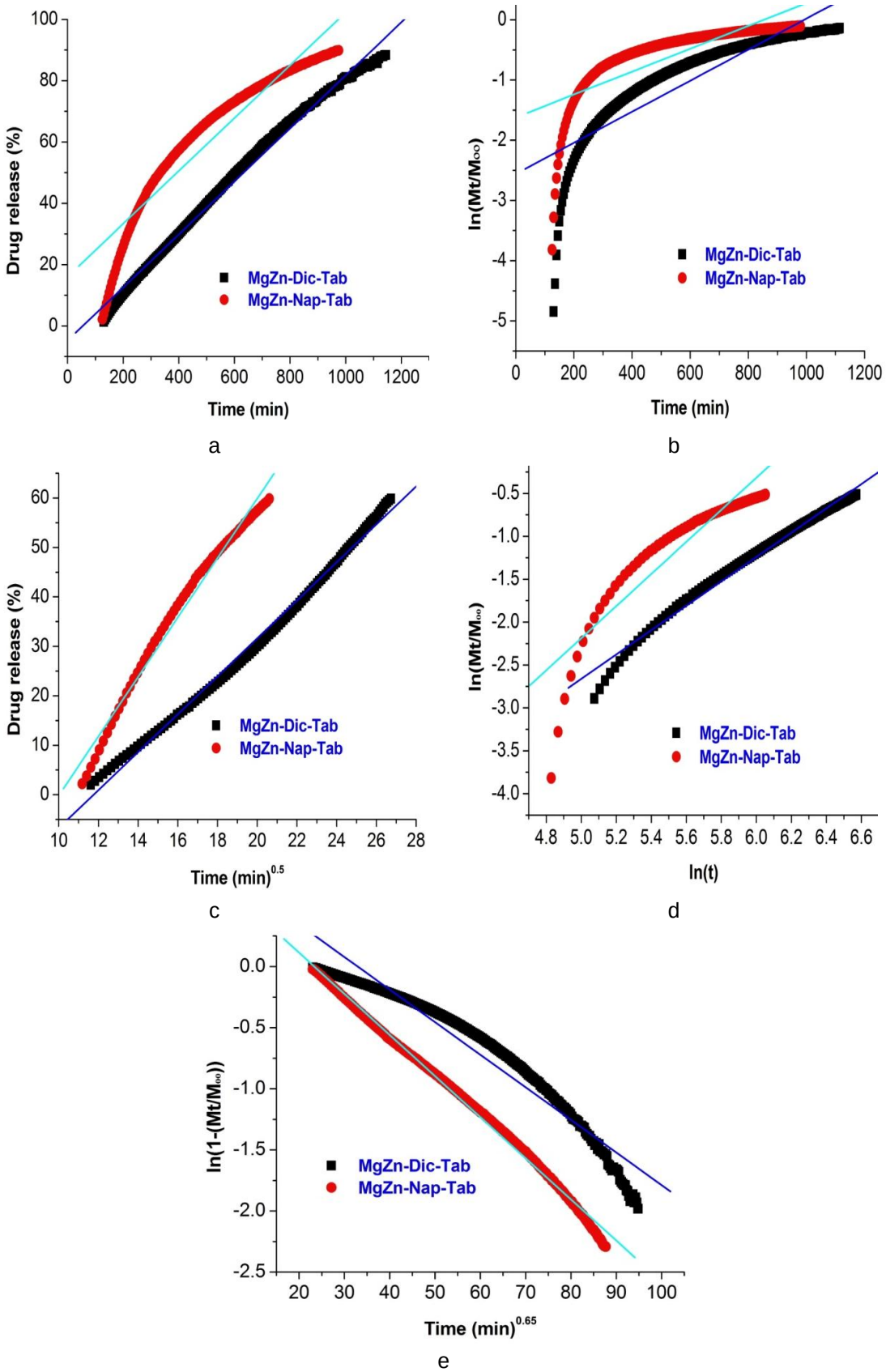

Figure 4.35: Kinetic models fitted to the experimental release data for MgZn-Dic-Tab and MgZn-Nap-Tab. **(a)** Zero order model, **(b)** First order model, **(c)** Higuchi model, **(d)** Korsmeyer-Peppas model **(e)** Bhaskar model.

Fits of the models to SI and Val release at pH ≥ 6.8 are given in Figure 4.37, and the fitting parameters in Table 4.23. It is clear that the Bhaskar model was the only model able to describe the SI release mechanism ($0.97 < R^2 < 0.99$). All the models indicate that there are two different segments of the SI release process, thus fitting was carried out individually for each segment. The resultant analysis suggests that the SI release mechanism from HDS tablets is controlled by an ion exchange mechanism. The release of SI showed slightly different behaviour from Dic and Nap, which could result from a variety of factors such as the interactions of the guests with the layers.

Table 4.23: Fitting parameters for the release of SI and Val from the HDS tablets

	Zero order		**First order**		**Higuchi**	
	R^2	K_0	R^2	$K_1(min^{-1})$	R^2	$k_H\ (min^{-1/2})$
FeZn-SI-Tab	0.7748	0.0710	0.4816	0.0057	0.9783	11.079
Segment 1	0.9813	0.3650	0.8721	0.0109	0.9783	11.079
Segment 2	0.9807	0.0392	0.9816	0.0020	-	-
MgZn-SI-Tab	0.9019	0.0576	0.6433	0.0011	0.8394	4.4824
Segment 1	0.9820	0.3954	0.9033	0.0150	0.9879	10.590
Segment 2	0.9821	0.0483	0.9551	0.0007	0.9739	2.8014
MgZn-Val-Tab	0.9953	0.0622	0.9873	0.0009	-	-
MgZn-Val-Tab2	0.7808	0.0265	0.6439	0.0005	0.9962	2.3432
MgZn-Val-Tab3	0.9463	0.0225	0.9001	0.0004	0.9931	1.3857

	Bhaskar		**Korsmeyer-Peppas**		
	R^2	$K_B(min^{-0.65})$	R^2	n	$K_{KP}\ (min^{-n})$
FeZn-SI-Tab	0.9766	0.0314	0.9491	3.7402	0.000
Segment 1	0.9946	0.0646	0.9491	3.7402	0.000
Segment 2	0.9890	0.0277	-	-	-
MgZn-SI-Tab	0.9813	0.0268	0.7602	1.1114	0.0466
Segment 1	0.9972	0.0550	0.9269	2.6044	0.0016
Segment 2	0.9886	0.0289	0.9720	0.4788	0.0328
MgZn-Val-Tab	0.9774	0.0269	-	-	-
MgZn-Val-Tab2	0.972	0.0093	0.9562	0.5443	0.0215
MgZn-Val-Tab3	0.9904	0.0080	0.9971	0.2872	0.0834

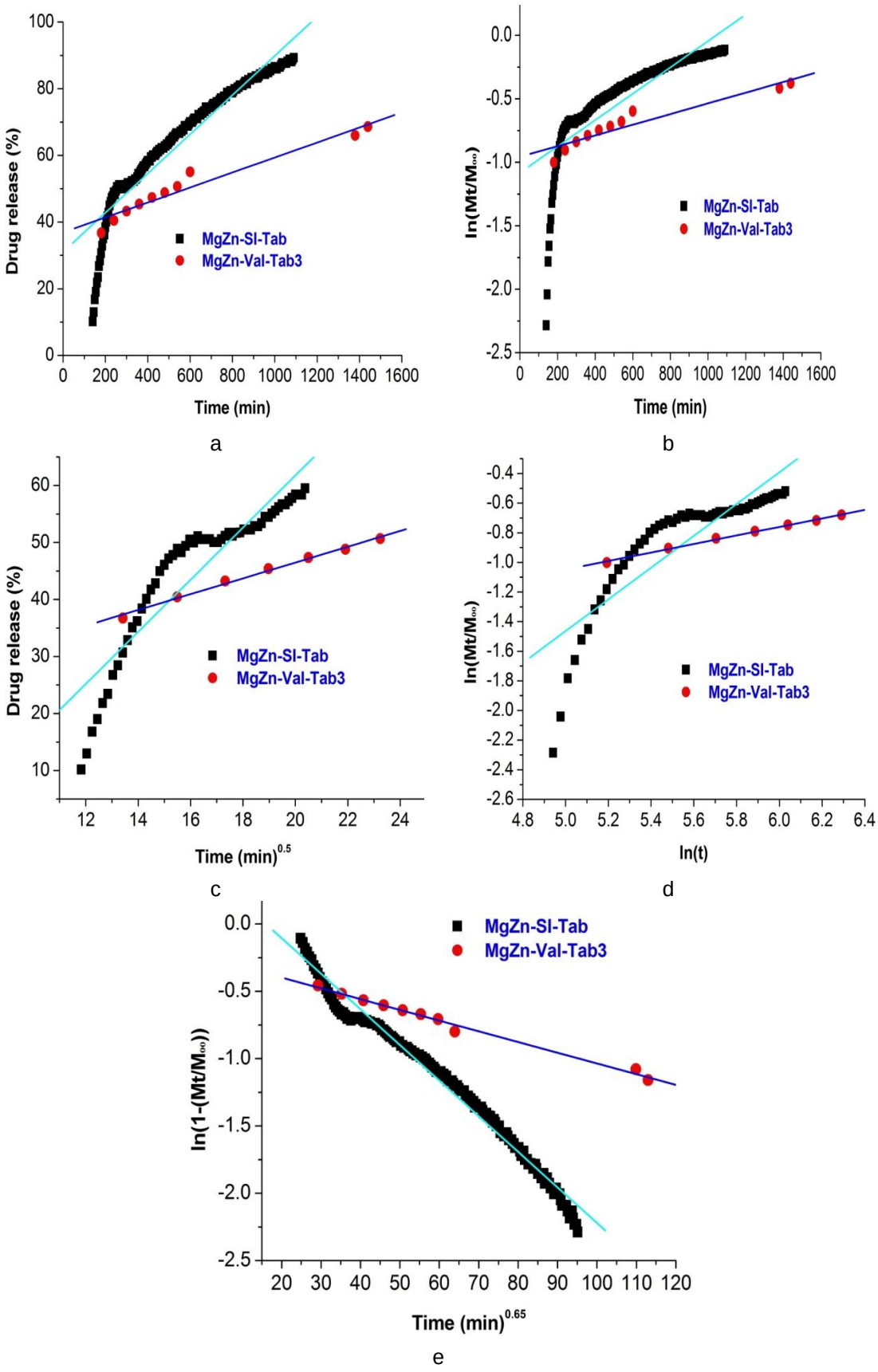

Figure 4.36: Kinetic models fitted to the experimental release data for MgZn-SI-Tab and MgZn-Val-Tab: **(a)** Zero order model, **(b)** First order model, **(c)** Higuchi model, **(d)** Korsmeyer-Peppas model and **(e)** Bhaskar model.

4.3. Conclusion

New biocompatible HDSs MgZn-Cl and FeZn-Cl were successfully synthesised. They comprise hexagonal platelets, and XPS data suggested that Mg^{2+} and Fe^{2+} occupy both octahedral and tetrahedral sites. The organic guests Dic, Nap, SI and Val have been successfully intercalated into the new HDSs. NMR and FTIR showed that the four guest structures remained intact after intercalation. It was found that the Dic and Nap ions are intercalated in an intertwined bilayer arrangement between the HDS layers, while the SI and Val adopt perpendicular bilayer arrangements of ions. Nap release in PBS (pH 7.4) from the various HDSs showed a sustained release profile, and as a result of these promising results tablets were prepared with the intercalated HDS systems.

The tablets prepared met the standard pharmacopeia requirements (weight consistency, hardness, friability and drug content). Drug release from the HDS tablets was investigated in conditions that mimic the human gastrointestinal tract. NSAID-loaded HDS tablets (containing Dic, Nap or SI) showed minimal release in acidic media, but freed all the loaded drug into a neutral medium within 24 h. Desirable delayed and sustained release profiles were often observed. This is believed to prevent the upset stomach, which is one of the commons side effects of the NSAIDs and generates longer duration of pain relief. The release profile from some of the HDSs tablets were similar to the commercial tablets and some of the HDSs tablets showed better release profile than the commercial tablets. The new NSAID-loaded HDS tablets formulations met the pharmacopeia delayed-release and sustained release requirements. The Val-loaded HDS tablets released significant amounts of drug at pH 1.0, but still met the pharmacopeia sustained release dosage form requirements.

4.4. References

1. Wu, C. Y. & Seville, J. P. K. A comparative study of compaction properties of binary and bilayer tablets. *Powder Technol.* **189,** 285–294 (2009).

2. Kagan, L. & Hoffman, A. Systems for region selective drug delivery in the gastrointestinal tract: biopharmaceutical considerations. *Expert Opin. Drug Deliv.* **5,** 681–692 (2008).

3. Koo, O. M. Y. Application challenges and examples of new excipients in advanced drug delivery systems. in *Am. Pharm. Rev.* **14,** 60–68 (2011).

4. Balbani, A. P. S., Stelzer, L. B. & Montovani, J. C. Pharmaceutical excipients and the information on drug labels. *Braz. J. Otorhinolaryngol.* **72,** 400–406 (2006).

5. Lee, B.-J. in *Pharm. Sci. Encycl.* 1–52 (John Wiley & Sons, Inc., 2010).

6. Hertrampf, A., Müller, H., Menezes, J. C. & Herdling, T. A PAT-based qualification of pharmaceutical excipients produced by batch or continuous processing. *J. Pharm. Biomed. Anal.* **114,** 208–215 (2015).

7. Gad, S. C. *Pharmaceutical Manufacturing Handbook: Production and Processes*. (John Wiley & Sons, Inc., 2008).

8. Santos, H. M. M. & Sousa, J. J. M. S. in *Pharm. Manuf. Handb.* 1133–1163 (John Wiley & Sons, Inc., 2000).

9. Karolewicz, B. A review of polymers as multifunctional excipients in drug dosage form technology. *Saudi Pharm. J.* (2015).

10. Abdul, S. & Poddar, S. S. A flexible technology for modified release of drugs: Multi layered tablets. *J. Control. Release* **97,** 393–405 (2004).

11. Deshpande, A. A., Rhodes, C. T., Shah, N. H. & Malick, A. W. Controlled-Release Drug Delivery Systems for Prolonged Gastric Residence: An Overview. *Drug Dev. Ind. Pharm.* **22,** 531–539 (1996).

12. Saks, S. R. & Gardner, L. B. The pharmacoeconomic value of controlled-release dosage forms. *J. Control. Release* **48,** 237–242 (1997).

13. Degen, L. P. & Phillips, S. F. Variability of gastrointestinal transit in healthy women and men. *Gut* **39,** 299–305 (1996).

14. WorsØe, J. *et al.* Gastric transit and small intestinal transit time and motility assessed by a magnet tracking system. *BMC Gastroenterol.* **11,** 145 (2011).

15. Gorard, D. a, Gomborone, J. E., Libby, G. W. & Farthing, M. J. Intestinal transit in anxiety and depression. *Gut* **39,** 551–555 (1996).

16. Bennett, E. J. *et al.* Psychological and sex features of delayed gut transit in functional gastrointestinal disorders. *Gut* **46,** 83–87 (2000).

17. Varum, F. J. O., Merchant, H. a. & Basit, A. W. Oral modified-release formulations in motion: The relationship between gastrointestinal transit and drug absorption. *Int. J. Pharm.* **395,** 26–36 (2010).

18. Yoshida, T., Lai, T. C., Kwon, G. S. & Sako, K. pH- and ion-sensitive polymers for drug delivery. *Expert Opin. Drug Deliv.* **10,** 1497–1513 (2013).

19. Balamurali, V. *et al.* pH Sensitive Drug Delivery Systems: A Review. *Am. J. Drug Discov. Dev.* **1,** 24–48 (2011).

20. Nykänen, P. *et al.* Organic acids as excipients in matrix granules for colon-specific drug delivery. *Int. J. Pharm.* **184,** 251–261 (1999).

21. Zhang, Z. *et al.* A novel pulsatile drug delivery system based on the physiochemical reaction between acrylic copolymer and organic acid: In vitro and in vivo evaluation. *Int. J. Pharm.* **462,** 66–73 (2014).

22. Kura, A., Hussein, M., Fakurazi, S. & Arulselvan, P. Layered double hydroxide nanocomposite for drug delivery systems; bio-distribution, toxicity and drug activity enhancement. *Chem. Cent. J.* **8,** 47 (2014).

23. Ladewig, K., Xu, Z. P. & Lu, G. Q. M. Layered double hydroxide nanoparticles in gene and drug delivery. *Expert Opin. Drug Deliv.* **6,** 907–922 (2009).

24. Arruebo, M. Drug delivery from structured porous inorganic materials. *Wiley Interdiscip. Rev. Nanomedicine Nanobiotechnology* **4,** 16–30 (2012).

25. Powlson, D. S. *et al.* When does nitrate become a risk for humans? *J. Environ. Qual.* **37,** 291–295

26. Espejo-Herrera, N. *et al.* Nitrate in drinking water and bladder cancer risk in spain. *Environ. Res.* **137C,** 299–307 (2015).

27. Sci, B. E. Original Article Nitrate-induced Biochemical and Histopathological Changes in the Liver of Rats: Ameliorative Effect of Hyparrhenia hirta *. *Oikos* **27,** 695–706 (2014).

28. Hill, L. L. Body composition, normal electrolyte concentrations, and the maintenance of normal volume, tonicity, and acid-base metabolism. *Pediatr. Clin. North Am.* **37,** 241–256 (1990).

29. HOLLANDER, W., CHOBANIAN, A. V. & BURROWS, B. A. Body fluid and electrolyte composition in arterial hypertension. I. Studies in

essential, renal and malignant hypertension. *J. Clin. Invest.* **40,** 408–415 (1961).

30. Chen, J., Zhang, H., Tomov, I. V. & Rentzepis, P. M. Electron transfer mechanism and photochemistry of ferrioxalate induced by excitation in the charge transfer band. *Inorg. Chem.* **47,** 2024–2032 (2008).

31. Testa, P. *et al.* Geometry Diagnostics of a Stellar Flare from Fluorescent X-rays. *Physics (College. Park. Md).* **9024,** 65–68 (2008).

32. Beamson, G. *et al.* High-energy monochromated Cu Kα1 x-ray source for electron spectroscopy of materials: Initial results. *Surf. Interface Anal.* **36,** 275–279 (2004).

33. Van Kuiken, B. E. & Khalil, M. Simulating picosecond iron K-edge X-ray absorption spectra by ab initio methods to study photoinduced changes in the electronic structure of Fe(II) spin crossover complexes. *J. Phys. Chem. A* **115,** 10749–10761 (2011).

34. Ziba, A., Pacuła, A., Serwicka, E. M. & Drelinkiewicz, A. Transesterification of triglycerides with methanol over thermally treated Zn5(OH)8(NO3)2×2H 2O salt. *Fuel* **89,** 1961–1972 (2010).

35. Delorme, F. *et al.* Synthesis and anion exchange properties of a Zn/Co double hydroxide salt. *Solid State Ionics* **187,** 93–97 (2011).

36. Zhang, M., Gao, B., Yao, Y. & Inyang, M. Phosphate removal ability of biochar/MgAl-LDH ultra-fine composites prepared by liquid-phase deposition. *Chemosphere* **92,** 1042–1047 (2013).

37. Markov, L., Petrov, K. & Petkov, V. On the thermal decomposition of some cobalt hydroxide nitrates. *Thermochim. Acta* **106,** 283–292 (1986).

38. Kandare, E. & Hossenlopp, J. M. Thermal degradation of acetate-intercalated hydroxy double and layered hydroxy salts. *Inorg. Chem.* **45,** 3766–3773 (2006).

39. Oriakhi, C. O., Farr, I. V & Lerner, M. M. Thermal characterization of poly(styrene sulfonate) layered double hydroxide nanocomposites. *Clays Clay Miner.* **45,** 194–202 (1997).

40. Wandelt, K. Photoemission studies of adsorbed oxygen and oxide layers. *Surf. Sci. Rep.* **2,** 1–121 (1982).

41. Wu, Y. *et al.* Effective removal of pyrophosphate by Ca-Fe-LDH and its mechanism. *Chem. Eng. J.* **179,** 72–79 (2012).

42. Kim, K. S. & Winograd, N. X-ray photoelectron spectroscopic binding energy shifts due to matrix in alloys and small supported metal particles. *Chem. Phys. Lett.* **30,** 91–95 (1975).

43. Biesinger, M. C., Lau, L. W. M., Gerson, A. R. & Smart, R. S. C. The role of the Auger parameter in XPS studies of nickel metal, halides and oxides. *Phys. Chem. Chem. Phys.* **14,** 2434 (2012).

44. Suchorski, Y. *et al.* Evolution of oxidation states in vanadium-based catalysts under conventional XPS conditions. *Appl. Surf. Sci.* **249,** 231–237 (2005).

45. Coulston, G. W., Thompson, E. A. & Herron, N. Characterization of VPO Catalysts by X-Ray Photoelectron Spectroscopy. *Catal* **163,** 8 (1996).

46. Hadnadjev, M., Vulic, T., Marinkovic-Neducin, R., Suchorski, Y. & Weiss, H. The iron oxidation state in Mg-Al-Fe mixed oxides derived from layered double hydroxides: An XPS study. *Appl. Surf. Sci.* **254,** 4297–4302 (2008).

47. Grosvenor, a. P., Kobe, B. a., Biesinger, M. C. & McIntyre, N. S. Investigation of multiplet splitting of Fe 2p XPS spectra and bonding in iron compounds. *Surf. Interface Anal.* **36,** 1564–1574 (2004).

48. Braski, D. N., Osborne, N. R. & Zurbuchen, J. M. Xps Study of Ni-Fe Manganite Thermistor Material. *MRS Proc.* **360,** (1994).

49. Swiatkowska-Warkocka, Z., Kawaguchi, K., Wang, H., Katou, Y. & Koshizaki, N. Controlling exchange bias in Fe3O4/FeO composite particles prepared by pulsed laser irradiation. *Nanoscale Res. Lett.* **6,** 226–233 (2011).

50. Corneille, J. S., He, J.-W. & Goodman, D. W. XPS characterization of ultra-thin MgO films on a Mo (100) surface. *Surf. Sci.* **306,** 269–278 (1994).

51. Valente, J. S. *et al.* Comprehending the thermal decomposition and reconstruction process of sol-gel MgAl layered double hydroxides. *J. Phys. Chem. C* **114,** 2089–2099 (2010).

52. Han, J. *et al.* Biomimetic design and assembly of organic-inorganic composite films with simultaneously enhanced strength and toughness. *Chem. Commun. (Camb).* **47,** 5274–5276 (2011).

53. Mattogno, G., Righini, G., Montesperelli, G. & Traversa, E. X-ray photoelectron spectroscopy investigation of MgAl 2 O 4 thin films for humidity sensors. *J. Mater. Res.* **9,** 1426–1433 (1994).

54. West, A. R. *Solid State Chemistry and its Applications*. (John Wiley & Sons, 1987).

55. Gu, Z., Wu, A., Li, L. & Xu, Z. Influence of Hydrothermal Treatment on Physicochemical Properties and Drug Release of Anti-Inflammatory Drugs of Intercalated Layered Double Hydroxide Nanoparticles. *Pharmaceutics* **6,** 235–248 (2014).

56. Taj, S. F., Singer, R., Nazir, T. & Williams, G. R. The first hydroxy double salt tablet formulation. *RSC Adv.* **3,** 358 (2013).

57. Wei, M., Shi, S., Wang, J., Li, Y. & Duan, X. Studies on the intercalation of naproxen into layered double hydroxide and its thermal decomposition by in situ FT-IR and in situ HT-XRD. *J. Solid State Chem.* **177,** 2534–2541 (2004).

58. Hayashi, A. & Nakayama, H. Simple Intercalation Reaction of Layered Double Hydroxide with Sodium Valproate under Solid Conditions. *Chem. Lett.* **39,** 1060–1062 (2010).

59. Nakayama, H. & Hayashi, A. Mixing Acid Salts and Layered Double Hydroxides in Nanoscale under Solid Condition. *Pharmaceutics* **6,** 436–446 (2014).

60. Gordijo, C. R., Barbosa, C. a S., Da Costa Ferreira, A. M., Constantino, V. R. L. & De Oliveira Silva, D. Immobilization of ibuprofen and copper-ibuprofen drugs on layered double hydroxides. *J. Pharm. Sci.* **94,** 1135–1148 (2005).

61. Jácome-Acatitla, G. *et al.* Photodegradation of sodium naproxen and oxytetracycline hydrochloride in aqueous medium using as photocatalysts Mg-Al calcined hydrotalcites. *J. Photochem. Photobiol. A Chem.* **277,** 82–89 (2014).

62. Mishra, B., Sahoo, J. & Dixit, P. K. Formulation and process optimization of naproxen nanosuspensions stabilized by hydroxy propyl methyl cellulose. *Carbohydr. Polym.* **127,** 300–308 (2015).

63. Tomasko, D. L. & Timko, M. T. Tailoring of specific interactions to modify the morphology of naproxen. *J. Cryst. Growth* **205,** 233–243 (1999).

64. Prevot, V. *et al.* Syntheses and Thermal and Chemical Behaviors of Tartrate and Succinate Intercalated Zn 3 Al and Zn 2 Cr Layered Double Hydroxides. **1669,** 4293–4301 (1998).

65. Bull, R. M. R., Markland, C., Williams, G. R. & O'Hare, D. Hydroxy double salts as versatile storage and delivery matrices. *J. Mater. Chem.* **21,** 1822 (2011).

66. Liu, J. *et al.* Preparation and structural characterization of zwitterionic surfactant intercalated into NiZn–layered Hydroxide Salts. *J. Phys. Chem. Solids* (2015).

67. ChemAxon. Marvin 6.0.1. (2013). at <http://www.chemaxon.com>

68. Graupner, H., Hammer, L., Heinz, K. & Zehner, D. M. Oxidation of low-index FeAl surfaces. *Surf. Sci.* **380,** 335–351 (1997).

69. Opitz, A. K. *et al.* Enhancing Electrochemical Water-Splitting Kinetics by Polarization-Driven Formation of Near-Surface Iron(0): An In Situ XPS

Study on Perovskite-Type Electrodes. *Angew. Chemie Int. Ed.* **54,** 2628–2632 (2015).

70. Graat, P. C. J. & Somers, M. a J. Quantitative analysis of overlapping XPS peaks by spectrum reconstruction : determination of the thickness and composition of thin iron oxide films. *Surf. interface Anal.* **26,** 773–782 (1998).

71. Yan, W., Ramos, M. a V, Koel, B. E. & Zhang, W.-X. Multi-tiered distributions of arsenic in iron nanoparticles: Observation of dual redox functionality enabled by a core-shell structure. *Chem. Commun. (Camb).* **46,** 6995–6997 (2010).

72. Santoyo-Cisneros, R., Cercado, B., Elías Razo, F. & Cházaro Ruiz, L. F. Effect of anodic poised potential on the removal of naproxen sodium using bioelectrochemical systems (BESs). in *64th Annu. Meet. Int. Soc. Electrochem.* 80 (International Society of Electrochemistry, 2013).

73. Stefano, J. S., Montes, R. H. O., Richter, E. M. & Muñoz, R. A. A. Flow-Injection Analysis with Multiple-Pulse Amperometry for Simultaneous Determination of Paracetamol and Naproxen Using a Homemade Flow Cell for Screen-Printed Electrodes. *J. Braz. Chem. Soc.* **25,** 484–491 (2014).

74. Norouzi, P., Dousty, F., Ganjali, M. R. & Daneshgar, P. Dysprosium nanowire modified carbon paste electrode for the simultaneous determination of naproxen and paracetamol: Application in pharmaceutical formulation and biological fluid. *Int. J. Electrochem. Sci.* **4,** 1373–1386 (2009).

75. Costa, D., Gomes, A., Lima, J. L. F. C. & Fernandes, E. Singlet oxygen scavenging activity of non-steroidal anti-inflammatory drugs. *Redox Rep.* **13,** 153–160 (2008).

76. Pekoe, G., Van Dyke, K., Peden, D., Mengoli, H. & English, D. Antioxidation theory of non-steroidal anti-inflammatory drugs based upon the inhibition of luminol-enhanced chemiluminescence from the myeloperoxidase reaction. *Agents Actions* **12,** 371–376 (1982).

77. US Pharmacopeia USP 38NF33. The United States Pharmacopeial Convention, (711) Dissolution. *Rockville,MD.* 486–496 (2015).

78. Klačanová, K. *et al.* Formation of Fe (0) -Nanoparticles via Reduction of Fe (II) Compounds by Amino Acids and Their Subsequent Oxidation to Iron Oxides. **2013,** (2013).

79. Siwach, O. P. & Sen, P. Fluorescence properties of Fe nanoparticles prepared by electro-explosion of wires. *Mater. Sci. Eng. B Solid-State Mater. Adv. Technol.* **149,** 99–104 (2008).

80. Schaffer, S., Gared, P., Dezael, C. & Richard, D. Direct determination of iron (II), iron (III) and total iron as UV-absorbing complexes by capillary electrophoresis. *J. Chromatogr. A* **740,** 151–157 (1996).

81. Maloney, K. O., Morris, D. P., Moses, C. O. & Osburn, C. L. The role of iron and dissolved organic carbon in the absorption of ultraviolet radiation in humic lake water. *Biogeochemistry* **75,** 393–407 (2005).

82. Kinoshita, T. *et al.* Magnetic evaluation of nanostructure of gold-iron composite particles synthesized by a reverse micelle method. *J. Alloys Compd.* **359,** 46–50 (2003).

83. Shauo, C.-N., Chao, C.-G., Wu, T. M. & Shy, H.-J. Magnetic and Optical Properties of Isolated Magnetite Nanocrystals. *Mater. Trans.* **48,** 1143–1148 (2007).

84. Ehrt, D. UV-absorption and radiation effects in different glasses doped with iron and tin in the ppm range. *Comptes Rendus Chim.* **5,** 679–692 (2002).

85. Lu, X. *et al.* Facile fabrication of ibuprofen–LDH nanohybrids via a delamination/reassembling process. *Mater. Res. Bull.* **48,** 1512–1517 (2013).

86. Ambrogi, V., Fardella, G., Grandolini, G. & Perioli, L. Intercalation compounds of hydrotalcite-like anionic clays with antiinflammatory agents - I. Intercalation and in vitro release of ibuprofen. *Int. J. Pharm.* **220,** 23–32 (2001).

87. Huang, W., Zhang, H. & Pan, D. Study on the release behavior and mechanism by monitoring the morphology changes of the large-sized drug-LDH nanohybrids. *AIChE J.* **57,** 1936–1946 (2011).

88. Gunawan, P. & Xu, R. Direct assembly of anisotropic layered double hydroxide (LDH) nanocrystals on spherical template for fabrication of drug-LDH hollow nanospheres. *Chem. Mater.* **21,** 781–783 (2009).

89. Gunawan, P. & Xu, R. Direct control of drug release behavior from layered double hydroxides through particle interactions. *J. Pharm. Sci.* **97,** 4367–4378 (2008).

90. Choy, J.-H., Park, J., Kwak, S.-Y. & Jeong, Y.-J. Inorganic Layered Double Hydroxides as Nonviral Vectors. *Angew. Chem. Int. Ed.* **39,** 4041–4045 (2000).

91. Barkhordari, S., Yadollahi, M. & Namazi, H. PH sensitive nanocomposite hydrogel beads based on carboxymethyl cellulose/layered double hydroxide as drug delivery systems. *J. Polym. Res.* **21,** 1–9 (2014).

92. Dewland, P. M., Reader, S. & Berry, P. Bioavailability of ibuprofen following oral administration of standard ibuprofen, sodium ibuprofen or

ibuprofen acid incorporating poloxamer in healthy volunteers. *BMC Clin. Pharmacol.* **9,** 1–10 (2009).

93. Savjani, K. T., Gajjar, A. K. & Savjani, J. K. Drug Solubility: Importance and Enhancement Techniques. *ISRN Pharm.* **2012,** 1–10 (2012).

94. Khadka, P. *et al.* Pharmaceutical particle technologies: An approach to improve drug solubility, dissolution and bioavailability. *Asian J. Pharm. Sci.* **9,** 1–13 (2014).

95. Neuvonen, P. J. The effect of magnesium hydroxide on the oral absorption of ibuprofen, ketoprofen and diclofenac. *Br. J. Clin. Pharmacol.* **31,** 263–266 (1991).

96. Shaw, L. R., Irwin, W. J., Grattan, T. J. & Conway, B. R. The influence of excipients on the diffusion of ibuprofen and paracetamol in gastric mucus. *Int. J. Pharm.* **290,** 145–154 (2005).

97. Rojas, R., Linck, Y. G., Cuffini, S. L., Monti, G. a. & Giacomelli, C. E. Structural and physicochemical aspects of drug release from layered double hydroxides and layered hydroxide salts. *Appl. Clay Sci.* **109-110,** 119–126 (2015).

98. Wanwimolruk, S., Lipschitz, S. & Roberts, M. S. Pharmacokinetics and bioavailability of Naprosyn CR 500 mg tablet, a new controlled-release formulation of naproxen, after single and multiple dosing. *Int. J. Pharm.* **75,** 55–62 (1991).

99. Alvogen Pharma US, I. NAPRELAN® Controlled-Release Tablets, 375mg, 500mg and 750mg. at <http://www.naprelanus.com>

100. Bourke, E. A. & Mulligan, S. Controlled absorption naproxen formulation for once-daily administration. (1997).

101. Ding, P., Tang, S. F. & Li, Z. Z. Influence of Metal Cations on the Structure and Release Property of Layered Double Hydroxide-Ibuprofen Host-Guest Materials. *Adv. Mater. Res.* **152-153,** 556–559 (2010).

102. Hussein, M. Z., Nasir, N. M. & Yahaya, A. H. Controlled release compound based on metanilate-layered double hydroxide nanohybrid. *J. Nanosci. Nanotechnol.* **8,** 5921–5928 (2008).

103. Rezvani, Z. & Sarkarat, M. Synthesis and characterization of magnetic composites: Intercalation of naproxen into Mg-Al layered double hydroxides coated on Fe 3O 4. *Zeitschrift fur Anorg. und Allg. Chemie* **638,** 874–880 (2012).

104. Arco, M., Fernández, A., Martín, C. & Rives, V. Applied Clay Science Release studies of different NSAIDs encapsulated in Mg , Al , Fe-hydrotalcites. *Appl. Clay Sci.* **42,** 538–544 (2009).

105. Carriazo, D., del Arco, M., Martín, C., Ramos, C. & Rives, V. Influence of the inorganic matrix nature on the sustained release of naproxen. *Microporous Mesoporous Mater.* **130,** 229–238 (2010).

106. Appendix XII C. Consistency of formulated Preparations. *British Pharmacopoeia*. (2014).

107. US Pharmacopeia USP 38NF33. The United States Pharmacopeial Convention, (905) Uniformity of dosage units. *Rockville,MD.* (2015).

108. US Pharmacopeia USP 38 NF33. The United States Pharmacopeial Convention, (1216) Tablet friability. *Rockville,MD.* (2015).

109. Huynh-Ba, K. Handbook of Stability Testing in Pharmaceutical Development. *Book* 390 (2009).

110. Moulali, S. *et al.* Invention and in Vitro Evaluation of Floating. *Int. J. Biol. Pharm. Res.* **3,** 339–346 (2012).

111. Qiu, Y., Chen, Y., Zhang, G., Liu, L. & Porter, W. *Developing Solid Oral Dosage Forms: Pharmaceutical Theory & Practice: Pharmaceutical Theory and Practice*. (Academic Press, 2009).

112. Aulton, M. E. & Taylor, K. M. G. *Aulton's Pharmaceutics: The Design and Manufacture of Medicines*. (Elsevier, 2013).

113. Labhasetwar, V., Underwood, T., Schwendeman, S. P. & Levy, R. J. Iontophoresis for modulation of cardiac drug delivery in dogs. *Proc. Natl. Acad. Sci. U. S. A.* **92,** 2612–2616 (1995).

114. US Pharmacopeia USP 38 NF33. The United States Pharmacopeial Convention, (1151) Pharmaceutical dosage forms. *Rockville,MD.* 1278–1231 (2015).

115. Nightingale, J. & Woodward, J. M. Guidelines for management of patients with a short bowel. *Gut* **55 Suppl 4,** iv1–v12 (2006).

116. Kashyap, P. C. *et al.* Complex interactions among diet, gastrointestinal transit, and gut microbiota in humanized mice. *Gastroenterology* **144,** 967–977 (2013).

117. Jayanthi, B., Manna, P. K., Madhusudhan, S., Mohanta, G. P. & Manavalan, R. Per oral extended release products - An overview. *J. Appl. Pharm. Sci.* **1,** 50–55 (2011).

118. Rathore, A. S., Jat1, R. C., Sharma1, N. & Tiwari1, R. AN OVERVIEW : MATRIX TABLET AS CONTROLLED DRUG DELIVERY SYSTEM. *Int. J. Res. Dev. Pharm. Life Sci.* **2,** 482–492 (2013).

119. Rojas, R., Jimenez-Kairuz, a. F., Manzo, R. H. & Giacomelli, C. E. Release kinetics from LDH-drug hybrids: Effect of layers stacking and

drug solubility and polarity. *Colloids Surfaces A Physicochem. Eng. Asp.* **463,** 37–43 (2014).

120. Ling, T. L. *et al.* A Multiple-Dose Pharmacokinetic Comparison of Naproxen as a Once-Daily Controlled-Release Tablet and a Twice-Daily Conventional Tablet. *J. Clin. Pharmacol.* **27,** 325–329 (1987).

121. Palazzini, E., Galli, G. & Babbini, M. Multiple-dose pharmacokinetics of naproxen from a controlled-release tablet in healthy volunteers. *Int. J. Clin. Pharmacol. Res.* **10,** 277–284 (1990).

122. Zhou, D., Zhang, Q., Lu, W., Xia, Q. & Wei, S. Single- and multiple-dose pharmacokinetic comparison of a sustained-release tablet and conventional tablets of naproxen in healthy volunteers. *J. Clin. Pharmacol.* **38,** 625–629 (1998).

123. Shiyani, B., Gattani, S. & Surana, S. Formulation and evaluation of bi-layer tablet of metoclopramide hydrochloride and ibuprofen. *AAPS PharmSciTech* **9,** 818–827 (2008).

124. Patra, C. N., Kumar, A. B., Pandit, H. K., Singh, S. P. & Devi, M. V. Design and evaluation of sustained release bilayer tablets of propranolol hydrochloride. *Acta Pharm.* **57,** 479–489 (2007).

125. Dumitriu, S. & Popa, V. *Polymeric Biomaterials: Medicinal and Pharmaceutical Applications, Volume 2, Third Edition*. (CRC Press, 2013).

126. Roberts, D., Easter, D. & O'Bryan-Tear, G. Epilim chrono: a multidose, crossover comparison of two formulations of valproate in healthy volunteers. *Biopharm. Drug Dispos.* **17,** 175–182 (1996).

127. Nordström, J., Persson, A. S., Lazorova, L., Frenning, G. & Alderborn, G. The degree of compression of spherical granular solids controls the evolution of microstructure and bond probability during compaction. *Int. J. Pharm.* **442,** 3–12 (2013).

128. Adolfsson, Å. & Nyström, C. Tablet strength, porosity, elasticity and solid state structure of tablets compressed at high loads. *Int. J. Pharm.* **132,** 95–106 (1996).

129. Higuchi, T., Rao, A. N., Busse, L. W. & Swintosky, J. V. The physics of tablet compression. II. The influence of degree of compression on properties of tablets. *J. Am. Pharm. Assoc.* **42,** 194–200 (1953).

130. Chopra, R., Alderborn, G., Podczeck, F. & Newton, J. M. The influence of pellet shape and surface properties on the drug release from uncoated and coated pellets. *Int. J. Pharm.* **239,** 171–178 (2002).

131. Schnieders, J., Gbureck, U., Vorndran, E., Schossig, M. & Kissel, T. The effect of porosity on drug release kinetics from vancomycin

microsphere/calcium phosphate cement composites. *J. Biomed. Mater. Res. - Part B Appl. Biomater.* **99 B,** 391–398 (2011).

132. Klose, D., Siepmann, F., Elkharraz, K., Krenzlin, S. & Siepmann, J. How porosity and size affect the drug release mechanisms from PLGA-based microparticles. *Int. J. Pharm.* **314,** 198–206 (2006).

133. Spratto, G. & Woods, A. *2009 Edition Delmar's Nurse's Drug Handbook*. (Cengage Learning, 2008).

134. May, C. A., Garnett, W. R., Small, R. E. & Pellock, J. M. Effects of three antacids on the bioavailability of valproic acid. *Clin. Pharm.* **1,** 244–247 (1982).

135. Washington, N. in *Antacids Anti Reflux Agents* 174 (CRC Press, 1991).

136. Spratto, G. & Woods, A. *Delmar Nurse's Drug Handbook 2012 Edition*. (Cengage Learning, 2011).

137. Costa, P. & Sousa Lobo, J. M. Modeling and comparison of dissolution profiles. *Eur. J. Pharm. Sci.* **13,** 123–133 (2001).

138. Gibaldi, M. & Feldman, S. Establishment of sink conditions in dissolution rate determinations. Theoretical considerations and application to nondisintegrating dosage forms. *J. Pharm. Sci.* **56,** 1238–1242 (1967).

139. Peppas, N. A. Analysis of Fickian and non-Fickian drug release from polymers. *Pharm. Acta Helv.* **60,** 110–111 (1985).

140. Roseman, T. J. & Higuchi, W. I. Release of medroxyprogesterone acetate from a silicone polymer. *J. Pharm. Sci.* **59,** 353–357 (1970).

141. Higuchi, T. Rate of release of medicaments from ointment bases containing drugs in suspension. *J. Pharm. Sci.* **50,** 874–875 (1961).

142. Higuchi, T. Mechanism of sustained- action medication. Theoretical analysis of rate of release of solid drugs dispersed in solid matrices. *J. Pharm. Sci.* **52,** 1145–1149 (1963).

143. Bhaskar, R., Murthy, R. S. R., Miglani, B. D. & Viswanathan, K. Novel method to evaluate diffusion controlled release of drug from resinate. *Int. J. Pharm.* **28,** 59–66 (1986).

144. Siepmann, J. & Peppas, N. a. Higuchi equation: Derivation, applications, use and misuse. *Int. J. Pharm.* **418,** 6–12 (2011).

145. Ambrogi, V. *et al.* Eudragit® and hydrotalcite-like anionic clay composite system for diclofenac colonic delivery. *Microporous Mesoporous Mater.* **115,** 405–415 (2008).

146. Abramson, S. *et al. Biomaterials Science (Third Edition)*. (Academic Press, 2013).

147. Pandit, A., Planell, J. & Navarro, M. *Biomaterials Science*. *Biomater. Sci. An Introd. to Mater. Med.* (2013).

148. Dash, A., Singh, S. & Tolman, J. *Pharmaceutics: Basic Principles and Application to Pharmacy Practice*. (Academic Press, 2013).

Chapter 5: Combined *in situ* and *in silico* studies of guest intercalation into the layered double hydroxide $[LiAl_2(OH)_6]X{\cdot}yH_2O$

5.1. Introduction

Understanding and predicting HDSs tablet behaviour in conditions that mimic the human body is important, and should help predict their behaviour in the human body. The drug release mechanism is a key factor, and hence its comprehension and prediction is crucial. The drug release is related to guest deintercalation; to understand this, it is important to understand first the intercalation process. Layered double hydroxides (LDHs) have been investigated deeply and considerable data have been reported on their intercalation processes, and for this reason LDHs were selected to begin this work.

LDHs, also known as hydrotalcite-like compounds, are a widely-studied class of ion exchange materials. They consist of positively charged metal hydroxide sheets and charge balancing anions in the interlayer region. The general formula of LDHs is $[M^{z}_{1-x}M^{3+}_{x}(OH)_2]^{q+}(X^{n-})_{q/n}{\cdot}yH_2O$. Generally z=2, and M^{2+} is a divalent metal such as Mg, Co, Ni, Cu, Zn or Ca; M^{3+} is a trivalent metal such as Al. There is also a unique family of LDHs for which $z = 1$, where $M^{+} = Li^{+}$ and $q = 2x - 1$. The common formula for this family of materials is $[LiAl_2(OH)_6]X{\cdot}yH_2O$ (LiAl-X), where y lies in the approximate range 0.5 – 4 and X is a generic anion (*e.g.* Cl, Br, and NO_3). [1] This family of materials is known to exist in hexagonal (2H) and rhombohedral (3R) polytypes; these differ in their layer stacking sequences, with 2H materials having a two-layer repeat *aba* stacking sequence and 3R possessing a three-layer *abca* repeat.[2] The layers stack in the c-direction, which means that a 2H unit cell contains two layers and a 3R cell has three.

Interest in LDHs has increased in recent years because of their utility as flame retardants,[3] catalysts and catalyst precursors,[4–6] water and air purifying agents,[7,8] adsorbents,[9–11] electrical and optical functional materials,[12] and for the separation of organic isomers.[13,14] They have also been shown to have potential as drug delivery systems,[15,16] and for the stabilisation of pharmaceutical salts of antipyretic, analgesic and anti-inflammatory drugs.[17] A range of organic species featuring different functional groups including carboxylates,[15,18–21] phosphonate,[22–26] and sulfonates[21,27–29] have been intercalated.

Although the intercalation of an enormously wide range of species into LDHs has been reported, the precise nanoscopic processes which take place during guest uptake remain poorly understood. This is in part because the most accessible method to obtain such insight, quenching the reaction, is invasive and known potentially to affect the outcome of the reaction. To gain reliable understanding of solid-state reaction processes, a non-invasive probe is required. Few such probes exist, but the technique of time-resolved *in situ* diffraction using a synchrotron X-ray source is one which permits us to obtain detailed information on solid state or solid/liquid reaction processes without affecting the course of the reaction. It has been used to great effect to begin to unravel the kinetics and mechanisms of intercalation processes.[30]

Time resolved X-ray diffraction (XRD) has been used to probe a range of LDH intercalation reactions; particularly interesting results have been obtained for the incorporation of carboxylate and phosphonate species. The intercalation of such species into the LiAl-X family of LDHs has revealed that the reactions in some cases proceed *via* so-called “second stage” intermediates, in which alternate interlayer spaces are occupied by the starting anion X and the incoming ion.[24,31,32] Whether the reaction proceeds directly from the host to the product or *via* a second stage intermediate has been shown to be dependent on the incoming ion, the layer stacking sequence of the LDH (*aba* hexagonal, or *abca* rhombohedral),[33] the initial interlayer ion,[33] the reaction temperature,[26] and the solvent system.[26] It has also been shown that if the second stage phases can

be isolated, then they exhibit selective ion exchange properties, with (in)organic guests preferentially replaced by other (in)organics.[34]

In this work, we sought to build on the earlier work exploring phosphonates and carboxylates, and investigated the intercalation of three bifunctional ions (phosphonoacetic acid, sulfoacetic acid, and diethylphosphonoacetic acid) into the hexagonal LiAl-Cl and LiAl-NO_3 LDH systems. These systems were selected because for organic phosphonates and carboxylates second stage intermediates have been reported to occur for the hexagonal form of LiAl-Cl, but not for its nitrate analogue. The final products obtained after incorporation of the bifunctional anions into the $[LiAl_2(OH)_6]X{\cdot}H_2O$ system were first synthesised and fully characterised. A range of *in situ* diffraction experiments were then used to probe the intercalation mechanisms. We coupled the use of *in situ* diffraction techniques with molecular dynamics (MD) simulations to provide additional insight into the phase transformations observed. MD is a valuable tool for complementing experimental work in terms of understanding of the interactions between the LDH layer and the guest ions. The technique allows the interlayer arrangements and dynamics of guest ions and water molecules to be evaluated. There have been several MD studies of LDH intercalates, for instance of amino-acids,[35] benzocarbazole,[36] lanthanide complexes,[37] organic luminescent materials,[38–40] and even DNA.[41,42]

Phosphonoacetic acid (PAA) has an antiviral activity by blocking DNA polymerase.[43] The reported data showed that PAA was active against various viruses such as: herpes virus, African swine fever virus and vaccinia virus.[43–45] and had minimal adverse effects on the animals themselves.[46] However, direct delivery of PAA is generally inefficient and the drug suffers from problems such as short half-life and nephrotoxicity. It is known that LDHs can help improve the drug efficacy.[47] In vitro tests were carried out to see if these disadvantages can be overcome by using LDHs as drug carrier.

5.2. Results and discussion

5.2.1. Intercalation

5.2.1.1. X-ray diffraction

Successful PAA intercalation was clearly evidenced by X-ray diffraction (XRD), IR spectroscopy, and elemental microanalysis. The XRD patterns of the reaction products (Figure 5.1) do not show any of the characteristic basal reflections of the starting material, and the *00l* basal reflections are observed to shift to lower angle. This corresponds to an increase in interlayer spacing, implying the incorporation of a larger anion. The intercalation of the three different PAA anions into LDHs thus appears to have been successful.

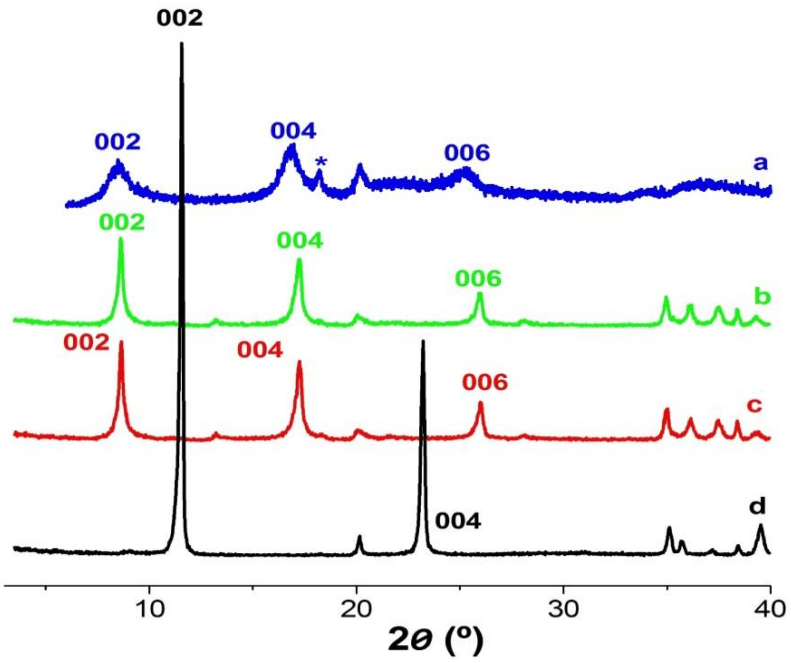

Figure 5.1: XRD patterns of **(a)** LiAl-PAA^{-}, **(b)** LiAl-PAA^{2-}, **(c)** LiAl-PAA^{3-} and **(d)** the LiAl-Cl starting material. The reflection marked * corresponds to gibbsite [γ-Al(OH)$_3$].

The LiAl-PAA^- material shows a slightly higher interlayer spacing (11.1 Å) than the PAA^{2-} and PAA^{3-} intercalates (for which d_{002} is 10.2 Å). There also appears to be a small reflection attributable to gibbsite in the pattern of LiAl-PAA^- and the overall crystallinity is much reduced, with broadened reflections clearly notable. We cannot be certain why this arises, but we believe it to be a result of the low pH (2.5) of the PAA^- solution causing some degradation of the sample. In addition, the lower charge density of the monoanionic guest may encourage turbostratic disorder in the material. A simple comparison of the interlayer spacings of the three PAA intercalates with the length of the molecules (calculated with Marvin),[48] suggests that the guests are aligned in a monolayer with their long axes perpendicular to the LDH layers. A summary of the data collected on the intercalates is presented in Chapter 6, Table 6.9. It appears that when two and three equivalents of NaOH are used to ionise PAA, a mixture of mono- and di- or di- and tri-anionic species are intercalated; this is sensible given that there will be an equilibrium between these species existing in solution. The materials prepared from LiAl-Cl and LiAl-NO_3 are virtually identical.

As for the PAA systems, the XRD patterns of LiAl-sulfoacetate (SAA) and LiAl-diethyl phosphonoacetate (DPA) show (002) reflections at lower angle than the starting material, confirming successful intercalation (Appendix IV). The DPA intercalate is poorly crystalline, and with the SAA-containing material it appears that a small amount of unreacted starting material is present alongside the product. On the basis of guest size and interlayer spacing comparisons, it is thought that the SAA anions adopt a perpendicular monolayer arrangement while the DPA guests are organised in a perpendicular bilayer arrangement in the interlayer space, with carboxylate groups facing the positively charged layers and diethyl groups in the centre of the interlayer region. Characterising data may be found in Table 5.1.

Table 5.1: A summary of key characterising data on the intercalated phases of $LiAl_2$-X.

ID	d_{002} (Å)		Formula[a]	Elemental analysis (%) Obsd (calcd)[b]
	X = Cl	X = NO_3		
LiAl-X	7.65	8.95	$[LiAl_2(OH)_6]X\cdot yH_2O$	
LiAl-PAA$^-$	11.1	11.0	$[Li_{0.8}Al_2(OH)_6](PO_3HCH_2CO_2H)_{0.8}\cdot 1.75H_2O$	C 5.73 (6.32) H 3.81 (4.21) H_2O 10.1(10.4)
LiAl-PAA^{2-}	10.2	10.4	$[Li_{0.95}Al_2(OH)_6](PO_3CH_2CO_2H)_{0.4}(PO_3HCH_2CO_2H)_{0.15}\cdot 2.0H_2O$	C 5.02 (4.81) H 4.46 (4.22) H_2O 11.5(13.1)
LiAl-PAA^{3-}	10.2	10.2	$[Li_{0.96}Al_2(OH)_6](PO_3CH_2CO_2H)_{0.3}(PO_3CH_2CO_2)_{0.12}\cdot 1.5H_2O$	C 4.23 (4.08) H 4.28 (4.13) H_2O 10.5(10.9)
LiAl-SAA	10.5	10.7	[c]	[c]
LiAl-DPA	18.6	19.2	$[Li_{0.9}Al_2(OH)_6](PO_3(C_2H_5)_2CH_2CO_2)_{0.4}Cl_{0.5}\cdot 2.5H_2O$	C 9.00 (9.51) H 4.71 (5.25) H_2O 11.2(14.9)

[a] Determined for the samples prepared from LiAl-Cl.
[b] C and H contents were determined by quantitative combustion, and the H_2O content from TGA.
[c] It proved impossible to analyse the LiAl-SAA material by quantitative combustion.

5.2.1.2. IR spectroscopy

Selected IR spectra are given in Figure 5.2. LiAl-Cl shows a broad band due to the H-bonded OH groups of the LDH layer (centred at *ca.* 3400 cm^{-1}), and an absorption at around 1640 cm^{-1} as a result of the δ-bend of interlayer water molecules. PAA^{2-} has carboxylate bands between 1380 and 1570 cm^{-1} and phosphate bands at 900 – 1250 cm^{-1}. Its intercalation compound LiAl-PAA^{2-} exhibits all of these features, indicating successful intercalation of the intact guest. The spectra of the other intercalation compounds similarly exhibit the characteristic bands from their guest ions: in all cases successful intercalation is confirmed by IR spectroscopy (data for DPA, PAA^- and PAA^{3-} may be found in Appendix IV).

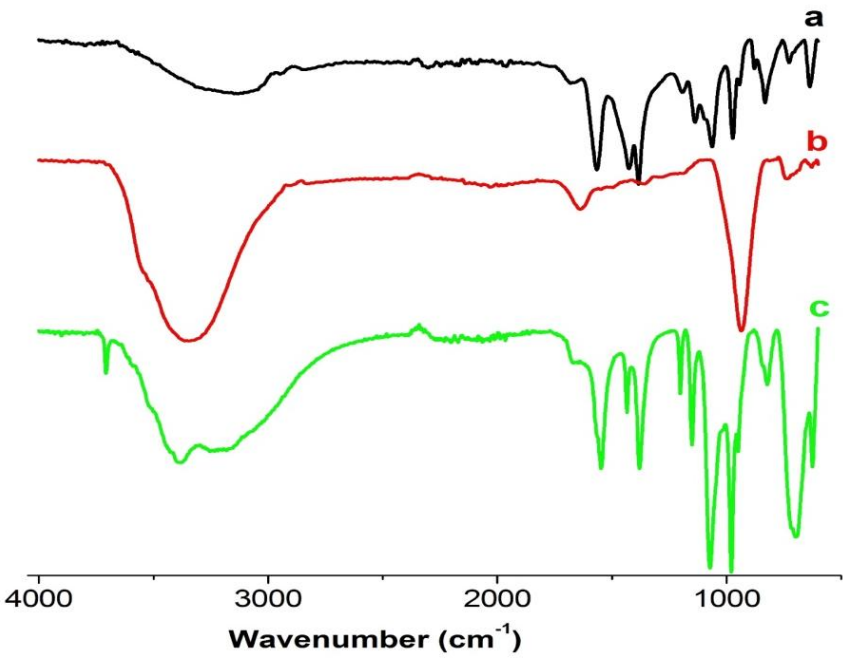

Figure 5.2: The FTIR spectra of **(a)** PAA^{2-}, **(b)** LiAl-Cl, and **(c)** LiAl-PAA^{2-}.

5.2.1.3. Guest recovery

Selected LiAl-PAA intercalates were reacted with Na_2CO_3 in D_2O, and NMR spectra recorded of the filtrate from these reactions. The spectra after deintercalation are observed to be identical to those of the PAA starting material, confirming that the structural integrity of the drug molecule is retained (Appendix IV).

5.2.2. The intercalation process

The intercalation of phosphonate and dicarboxylate guests has previously been shown to be interesting mechanistically, with second stage intermediates having been reported.[24,26,32–34] Experiments were thus performed to study the reaction of the PAA, SAA, and DPA anions with LiAl-Cl and LiAl-NO_3, with the intent of developing more understanding of the reaction mechanisms.

The intercalation of all three PAA anions was found to be very rapid, even at room temperature, and thus the reactions could not be followed satisfactorily. This has previously been reported by O'Hare and co-workers for similar systems.[24,32] In order to obtain mechanistic information, solutions of the PAA ions were added dropwise to aqueous suspensions of the LDH materials. Intercalation was studied at room temperature, and in some cases also with the LDH suspension heated to 70 °C.

5.2.2.1. Intercalation of PAA^{3-}

In situ diffraction data for the intercalation of PAA^{3-} are given in Figure 5.3. At both RT and 70 °C, a crystalline intermediate phase was observed in the diffraction data. This possesses a higher d-spacing than the final LiAl-PAA^{3-} product. It is clear from the raw experimental data given in Figure 5.3a and b that the intermediate and product appear at the same d-spacing regardless of which LDH starting material (LiAl-Cl or LiAl-NO_3) is used. The intensities of the LiAl-Cl and LiAl-PAA^{3-} (002) reflections and the intermediate reflection were integrated for each reaction, and converted to the extent of reaction, α:

$$\alpha = I_{hkl}(t)/I_{hkl}(max) \quad (1)$$

where $I_{hkl}(t)$ is the intensity of a reflection hkl at time t, and $I_{hkl}(max)$ is the maximum intensity of that reflection. Plots of α *vs.* time for intercalation into LiAl-Cl and LiAl-NO_3 are depicted in Figure 5.3c and d. The α *vs.* t curves of the starting material and final product cross close to α = 0, which confirms the presence of an intermediate phase. This crossing point indicates that the loss of diffracted intensity from the starting material is complete before any product reflections grow into the system. If there was not an intermediate phase, the curves should cross near α = 0.5. The LiAl-Cl/intermediate and intermediate/LiAl-PAA^{3-} curves both cross at α = 0.5, however, indicating that there are no additional phases present on the reaction coordinate.

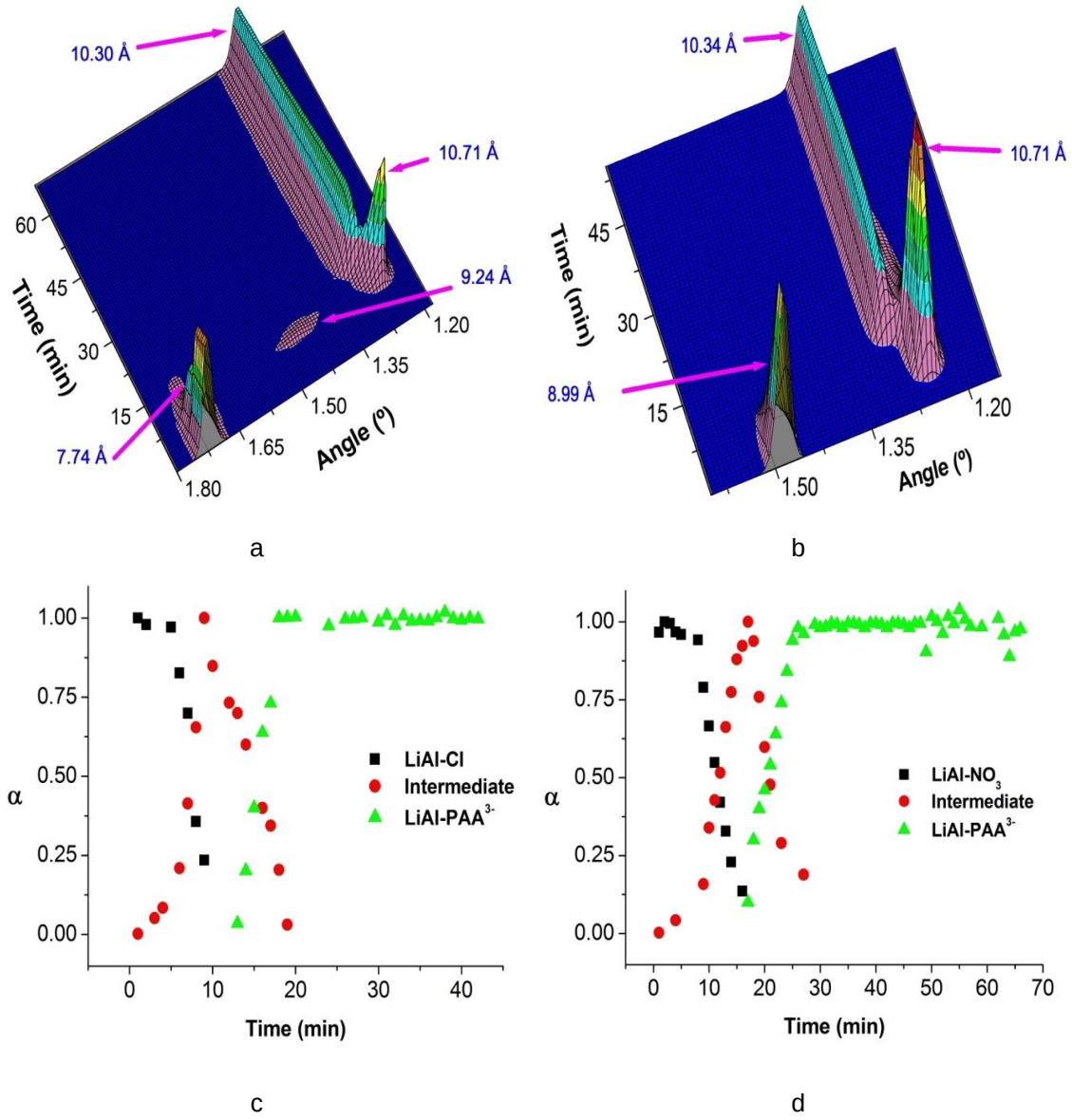

Figure 5.3: *In situ* XRD data for the intercalation of PAA^{3-} into LiAl-Cl and LiAl-NO_3. 3D stacked plots of the raw data obtained at Diamond are given for **(a)** LiAl-Cl and **(b)** LiAl-NO_3, together with α *vs.* time plots for **(c)** LiAl-Cl and **(d)** LiAl-NO_3.

Experiments were performed both at Diamond and DESY to ensure the reproducibility of the results obtained (data from DESY are not shown in the interests of brevity). In Figure 5.3a, a small reflection can be seen at 9.24 Å in the data for LiAl-Cl. This was not observed when the same experiment was performed at DESY, but a quenching experiment suggested that this is likely to be a real phase rather than an artefact, and thus we believe that this reflection may correspond to an additional, very transient, intermediate phase (see Appendix IV). The reflection at 9.24 Å is rather broad, typical of the very early

stages of intercalation where some galleries contain PAA^{3-} ions and others do not. It is uncertain why this is not observed with the nitrate system, but this could be a result of overlap with the LiAl-NO_3 starting material (002) reflection.

Second stage intermediates have previously been observed by O'Hare and co-workers for the intercalation of both organic phosphonates and carboxylates into LiAl-Cl,[24,32,33] but in this case it does not appear that the intermediates correspond to staged systems. The d_{002} value expected for a second stage intermediate of PAA^{3-} and LiAl-Cl would be [d_{002}(LiAl-Cl) + d_{002}(LiAl-PAA^{3-})] = 17.9 Å (probably too high to be observed using the experimental configuration used), giving d_{004} of 8.97 Å. For a third stage system d_{002} should be 25.7 Å, and d_{004} = 12.8 Å. For LiAl-NO_3, the equivalent d_{004} spacings would be 9.58 and 14.1 Å respectively. The major intermediate observed experimentally has a reflection at 10.71 Å, very different to those expected for a staged system. Staging is further ruled out when quenching studies were undertaken: no very low-angle reflections indicating the presence of a supercell were observed (see Appendix IV). Finally, use of both the chloride and nitrate starting materials results in the same intermediate, and thus staging cannot be operational (if it was, the intermediate should have different reflection positions).

To understand more about the intercalation process, a series of molecular dynamics (MD) simulations were undertaken (Figure 5.4) on the Cl-derived systems. The model was set-up using one water molecule per Li^+ ion and the interlayer spacing determined experimentally (Table 5.2).

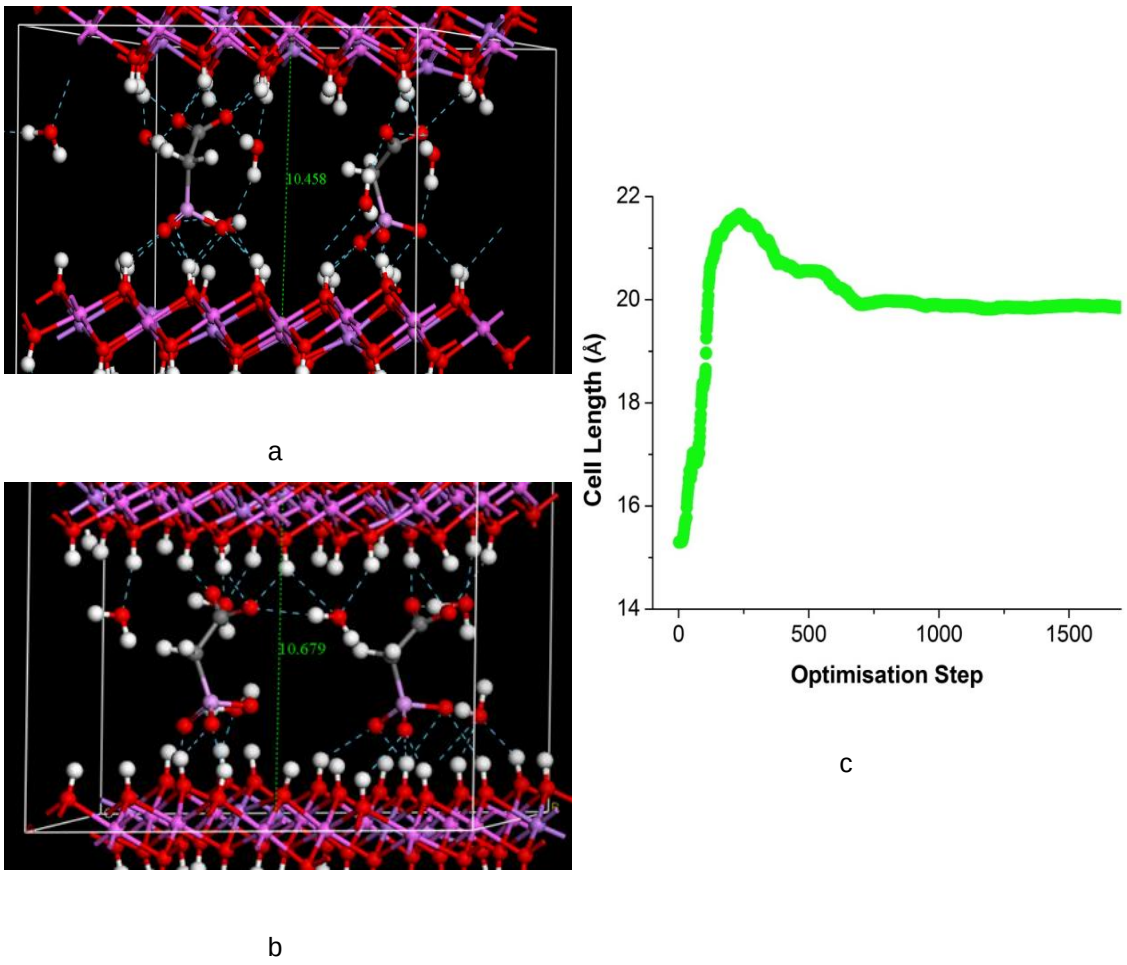

Figure 5.4: MD results for the intercalation of PAA^{3-} into LiAl-Cl. **(a)** the orientation of PAA^{3-} in the interlayer space of the energy minimised structure; **(b)** the orientation of PAA^{3-} in the intermediate phase; **(c)** the change in the unit cell c-parameter with optimisation step.

First, we allowed the simulation to run until the energy of the system was minimised. This resulted in the model given in Figure 5.4a. The PAA^{3-} ions can be seen to form a monolayer, resulting in an interlayer spacing of 10.45 ± 0.04 Å (the PAA^{3-} atomic positions are reported in Appendix IV). This result is in good agreement with the experimental values both *ex situ* and *in situ* (10.2 and 10.3 Å), with the small difference between experimental and simulation being well within the range of deviations reported in previous LDH modelling studies.[35,49–52] The PAA^{3-} ions adopt an almost perpendicular position, lying across the interlayer region to interact with two adjacent layers through H-bonding. We also modelled the orientation of the ions in the major intermediate phase, feeding the d_{002} value observed for this into the model. The arrangement

of molecules here is similar to the final product (see Figure 5.4b), but there are subtle differences in the orientation of the PAA^{3-} ions.

Next, we explored the simulation process in more detail, and plotted the change in cell c-parameter as a function of the optimisation cycle number (Figure 5.4c). This experiment was undertaken by reading the known structure for $[LiAl_2(OH)_6]Cl{\cdot}H_2O$ into Materials Studio, deleting the Cl ions, and manually inserting PAA^{3-} between the layers. The PAA^{3-} ions were inserted in the configuration which gave the lowest energy when the c-parameter was fixed at 15.3 Å. This model ("the unconstrained model") was then allowed to optimise without constraints. Remarkably, it can be seen that the changes in c-parameter observed track very closely what is observed *in situ*: the c-parameter increases from 15.3 Å (d_{002} = 7.65 Å) in the first optimisation step to 21.6 Å (d_{002} = 10.8 Å), where it remains at a plateau for a number of optimisation cycles (presumably the system is in a local energy minimum at this point in time). There is then a decrease in c-parameter to 20.0 Å (d_{002} = 10.0 Å), after which the system reaches an energy minimum. Furthermore, close inspection of the optimisation process suggests there is a brief point of inflection after around 100 optimisation cycles (Appendix IV), with a c-parameter of 17.1 Å, possibly corresponding to the very short-lived intermediate noted in Figure 5.3a.

It should be noted that there are small differences in the d-spacings observed experimentally and those calculated during the optimisation cycle. These can be attributed to differences in the amount of water in the model and in the interlayer in the real system (it is not possible to know the latter for all stages of the reaction), and also the fact that in the model we assumed the ions to comprise equal mixture, whereas in reality the mixture ratio of divalent and trivalent anions is different. However, these results strongly suggest that the intermediate observed is a result of the PAA ions first intercalating in a higher-energy orientation, before reorienting themselves to the most energetically favourable configuration. The sharp correlation between the MD and *in situ* results is striking, and to the best of our knowledge this is the first time that such observations have been reported. Our results suggest that MD simulations may be used not only to model the final product, but that the energy minimisations

which they use correspond closely to the molecular movements which take place in real reaction systems.

5.2.2.2. Intercalation of PAA^-

Data for the intercalation of PAA^- into LiAl-Cl and LiAl-NO_3 are depicted in Figure 5.5. With both host materials, crystalline intermediate phases with lower d-spacings than the final product are observed in the diffraction data.

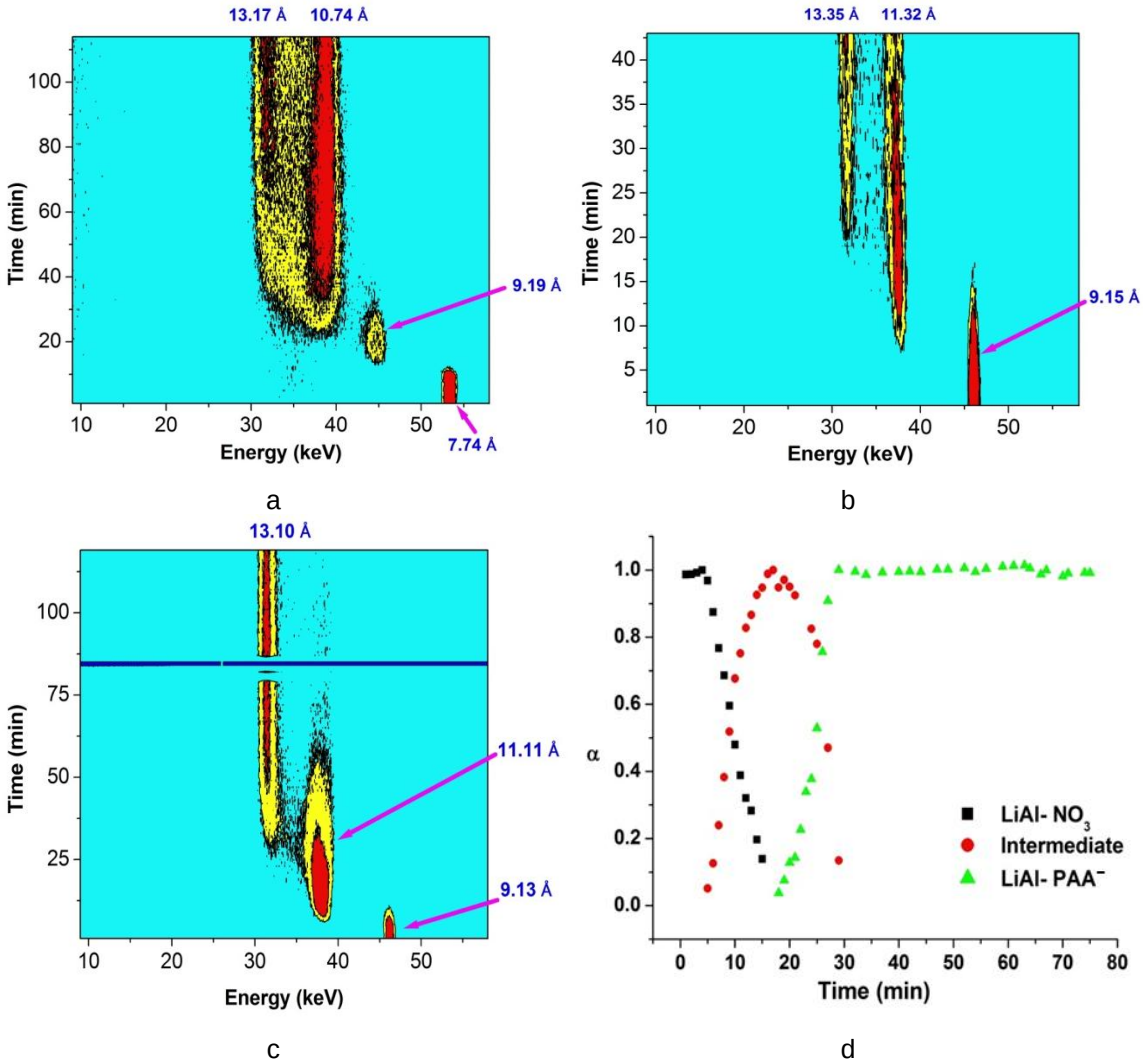

Figure 5.5: *In situ* XRD data obtained on DESY for the intercalation of PAA^-. Contour plots of the raw data obtained at RT for **(a)** LiAl-Cl and **(b)** LiAl-NO_3; **(c)** raw data and **(d)** the extent of reaction *vs.* time plot for intercalation into LiAl-NO_3 at 70 °C. The blue line across the centre of the image in **(c)** arises owing to a temporary loss of the X-ray beam. An α vs time plot could not be constructed satisfactorily for intercalation into LiAl-Cl, owing to poor crystallinity of the phases, and thus is not included.

The intercalation of PAA^- into LiAl-Cl proceeds *via* two intermediate phases: initially the starting material at 7.74 Å can be seen, before a material with a reflection at 9.19 Å emerges, followed by a second at 10.74 Å, and then the final product at 13.17 Å. It should be noted that the latter is a significantly higher d-spacing than that observed *ex situ* for the final product. Complete conversion of the 10.74 Å phase to the 13.17 Å material is not observed during the timescale over which the reaction was observed. The reaction product was recovered, filtered, and dried; XRD analysis of the resultant material showed it to have a d_{002} of *ca.* 11 Å. Therefore, the 13.17 Å phase observed *in situ* must be a highly hydrated material, which is converted to a material with an 11 Å interlayer spacing by drying.

In the case of LiAl-NO_3, in the room temperature reaction an initial reflection grows in at 11.32 Å, followed by the emergence of another reflection at around 13.4 Å. As in the LiAl-Cl case, both the 11.32 and 13.35 Å phases persist until reaction monitoring was ceased. To determine if the species around 11 Å is an intermediate or not, the reaction was repeated at 70 °C. At this elevated temperature, the 11 Å phase is clearly seen to grow in and then decline, leaving only a material with a d-spacing of 13.1 Å. The α *vs.* time curves for LiAl-NO_3 and the final product cross very close to zero, consistent with the presence of an intermediate. In contrast, the LiAl-NO_3/intermediate and intermediate/product sets of curves both cross at α = 0.5, showing that there are direct solid/solid transformations between these phases. The 70 °C reaction suspension was stored at RT for 24 h after monitoring ceased, and upon reanalysis d_{002} was shown to be 13.5 Å, The small increase in d-spacing over that observed during continuous monitoring can be ascribed to some additional hydration. As for LiAl-Cl, the final d-spacing observed *in situ* is higher than that observed *ex situ*. If the products are filtered and dried, then XRD shows the d-spacings of the dry products to be essentially the same as those prepared in the laboratory, indicating that the higher d-spacing phases are highly hydrated systems which are not stable to drying.

The reaction process for PAA^- intercalation can thus be summarised as follows:
LiAl-Cl (7.74 Å) → Intermediate 1 (9.19 Å) → Intermediate 2 (10.74 Å) → Product (13.17 Å).
LiAl-NO_3 (9.15 Å) → Intermediate 2 (11.1 – 11.3 Å) → Product (13.1 – 13.35 Å).

The similarity of d-spacings for the 11 Å phase from both LiAl-Cl and LiAl-NO_3 indicates that they are probably the same material, with small differences in hydration. Given the fact that the first intermediate seen during PAA intercalation into LiAl-Cl has the same d-spacing as $LiAl_2$-NO_3, it might be the case that this 9.19 Å phase also forms with the nitrate starting material, but cannot clearly be seen because the reflections overlap. As was the case with PAA^{3-}, the intermediates seen are not the result of staging (for LiAl-Cl, second and third stage intercalates with PAA^- would have d_{004} of 9.4 and 13.3 Å; for LiAl-NO_3 9.98 and 14.5 Å).

As for PAA^{3-}, MD simulations were performed for the LiAl-Cl starting material, and are presented in Figure 5.6. First, simulations for PAA^- were set up with one water molecule per Li^+ ion and the interlayer spacing observed for the dried *ex situ* product, and allowed to run until an energy minimum was reached. This reveals that in the final product observed *ex situ* the PAA^- ions form a monolayer between the LDH layers, with a *d*-spacing of 10.91 ± 0.01 Å (Figure 5.6a). This is in good agreement with the *ex situ* experimental value of 11.1 Å, and the 10.74 Å observed *in situ*. The PAA^- ions lie perpendicular across the interlayer regions (the detailed locations of the PAA^- ions are given in Appendix IV).

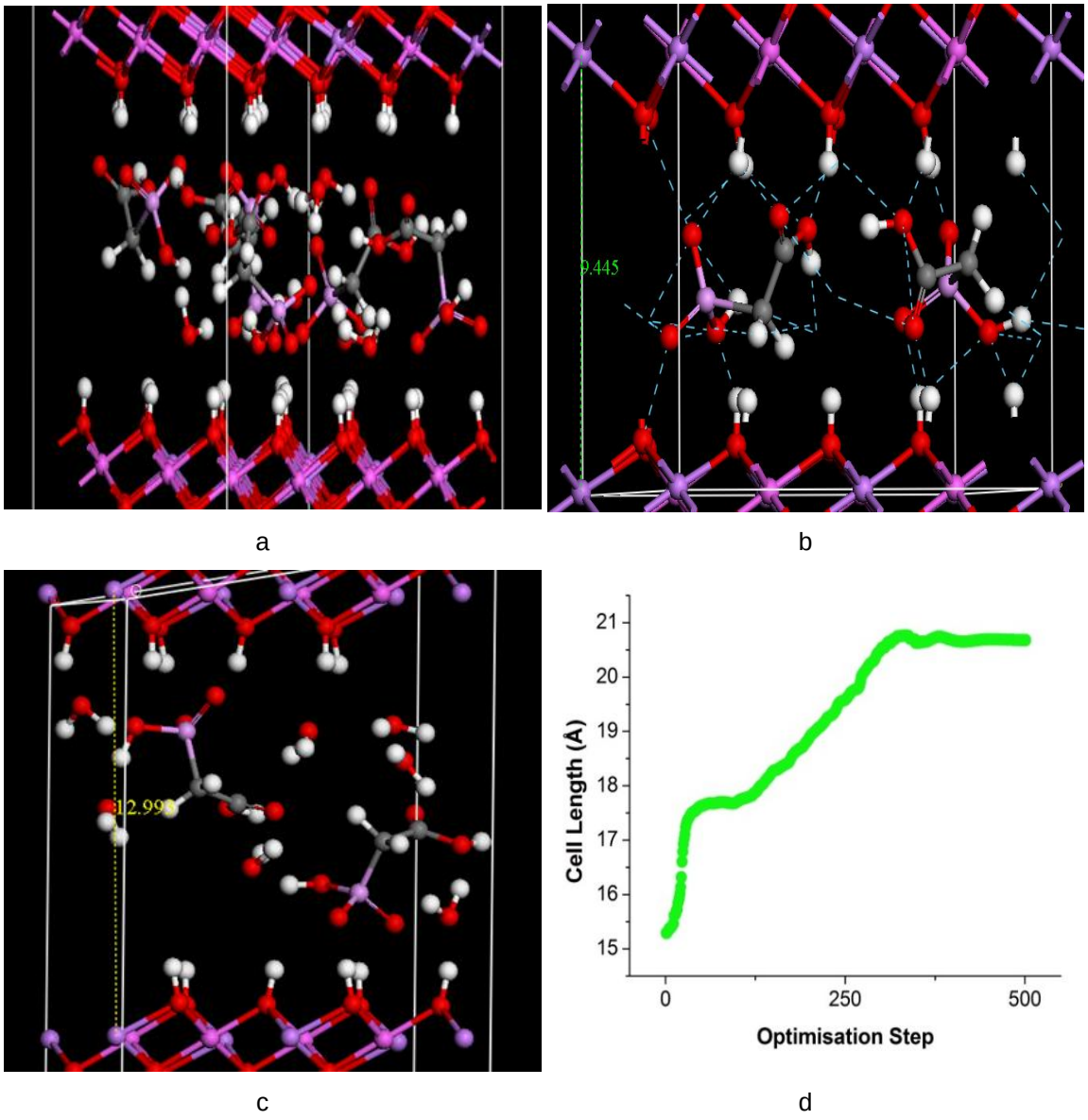

a b c d

Figure 5.6: MD simulations for the intercalation of PAA^- into LiAl-Cl. **(a)** the energy minimised final product; **(b)** the orientation of PAA^- in the 9.2 Å intermediate phase; **(c)** the results of adding more water to the simulations; and, **(d)** the variation in cell c-parameter with optimisation cycle.

In the same way, we modelled the intermediate phase observed *in situ* at *ca.* 9.2 Å for LiAl-Cl (Figure 5.6b). This suggests that the PAA^- ions are intercalated in a horizontal manner in this system; they presumably re-orient later to give the final product. Additionally, further simulations were performed in which we increased the amount of water in the system, in order to model the final, highly hydrated, material observed *in situ* at around 13 Å (see Figure 5.6c). When the simulations were rerun with six water molecules per unit cell, d_{002} is calculated to be 12.99 Å, in excellent agreement with the observed experimental value.

The PAA^- ions are vertically oriented here, but the interlayer space is expanded because of the large amount of water present.

To understand in more detail the interlayer spacing evolution during the intercalation of PAA^-, we again took the known structure for $[LiAl_2(OH)_6]Cl{\cdot}H_2O$, deleted the Cl ions and manually inserted PAA^- between the layers (in the lowest energy orientation possible), and permitted the model to optimise without constraints. A plot of c-parameter *vs.* optimisation step is given in Figure 5.6b; the c-parameter first increases rapidly to *ca.* 17.7 Å (d_{002} = 8.85 Å) before there is a plateau where despite further optimisation cycles running, no increase in c is seen. After around 125 cycles, the c-parameter again rises to 20.8 Å (d_{002} = 10.4 Å).

The d_{002} values calculated are a little different to those observed *in situ* (9.19 Å and 10.74 Å), for the same reasons as discussed above. However, the trend calculated by MD mirrors precisely what happens in the first stage of PAA^- intercalation *in situ*, with a lower d-spacing intermediate first forming and the d-spacing and then expanding. Re-running the model with varied amounts of water present (data not shown) led to changes in the absolute values of the d-spacings observed, but the variation of c-parameter with optimisation cycle follows the same trend in all cases there is an initial rapid increase in c, followed by a plateau, and a second region of expansion before the model reaches an optimal configuration. The final product observed *in situ* at around 13 Å is not accounted for in the unconstrained model when the amount of water included is restricted to the amounts determined experimentally (see Table 5.2), but can be simulated when very large amounts of water are added to the unit cell in the model.

As for the intercalation of PAA^{3-}, it is clear that MD simulations may be used not only to model the guest orientations in the final product, but also to understand the nanoscopic processes occurring along the reaction coordinate.

5.2.2.3. Intercalation of SAA

In situ data for the intercalation of SAA are given in Figure 5.7. Intercalation into both LiAl-Cl and LiAl-NO_3 proceed in an essentially identical fashion: the starting material declines in intensity before a phase grows in with d-spacing a little over 11 Å. There is then a distinct shift in the position of the latter reflection, to *ca.* 10.8 Å.

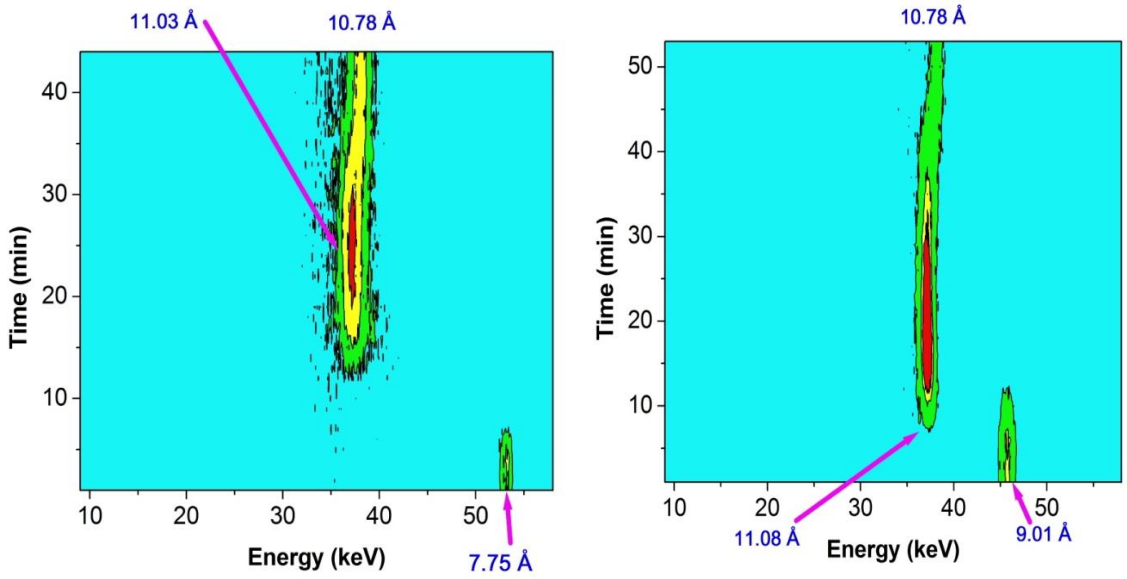

Figure 5.7: *In situ* XRD data for the intercalation of SAA into **(a)** LiAl-Cl and **(b)** LiAl-NO_3.

As was the case with PAA, the d-spacings of the phases observed are not consistent with staging, and MD simulations were performed to model the intercalation process into LiAl-Cl. The final energy minimised structure (calculated with constraints) showed SAA to form a monolayer in the interlayer space, with a d-spacing of 10.98 ± 0.01Å (Figure 5.8a). This is in good agreement with the *ex situ* experimental value of 10.5 Å, and the 10.78 Å seen *in situ*. The SAA ions lie perpendicular across the interlayer regions.

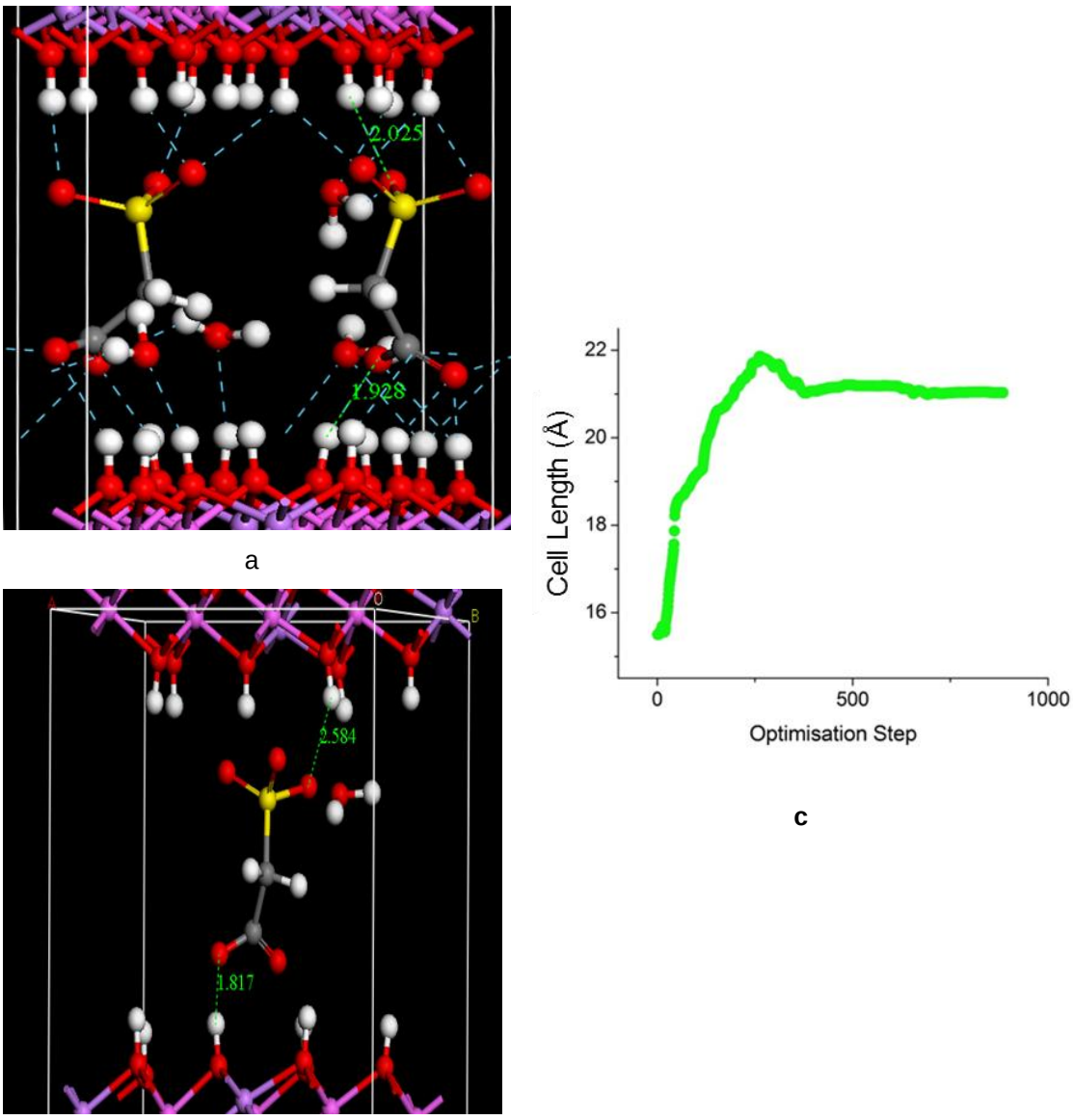

Figure 5.8: MD results for the intercalation of SAA into LiAl-Cl. **(a)** the proposed orientation of SAA in the interlayer space in the energy minimised system; **(b)** the orientation of SAA in the intermediate; and, **(c)** the change in the unit cell c-parameter with optimisation step.

The orientation of the SAA in the initial product with higher d-spacing was also modelled with constraints (Figure 5.8b), and looking at the guest orientations (see Figure 5.8a and b), the simulation study indicates that the SAA reorients itself after initial intercalation, presumably in order to maximise bonding interactions, and thus the initial d-spacing is higher than that observed at the end of the reaction.

Looking at the MD process run without constraints (Figure 5.8c), as increasing numbers of optimisation cycles are run, the simulation shows the c-parameter to rapidly increase to *ca.* 21.9 Å (d_{002} = 10.95 Å), which is very similar to the interlayer spacing of the initial material seen to form *in situ*. This subsequently declines to c = 21.1 Å (d_{002} = 10.6 Å) upon further optimisation cycles, again in excellent agreement with the reflection shift observed *in situ*. Beyond what is observed experimentally, the plot of cell length *vs.* optimisation cycle in Figure 5.8b includes a point of inflection at around 19 Å. This indicates that a very transient intermediate may exist, but the limitations of the *in situ* experiments do not allow this to be observed.

5.2.2.4 Intercalation of DPA

In situ data for DPA intercalation into LiAl-NO_3 are given in Figure 5.9. In these experiments, the pH of the DPA solution was adjusted to either 4.55 or 6.10 prior to the LDH being added.

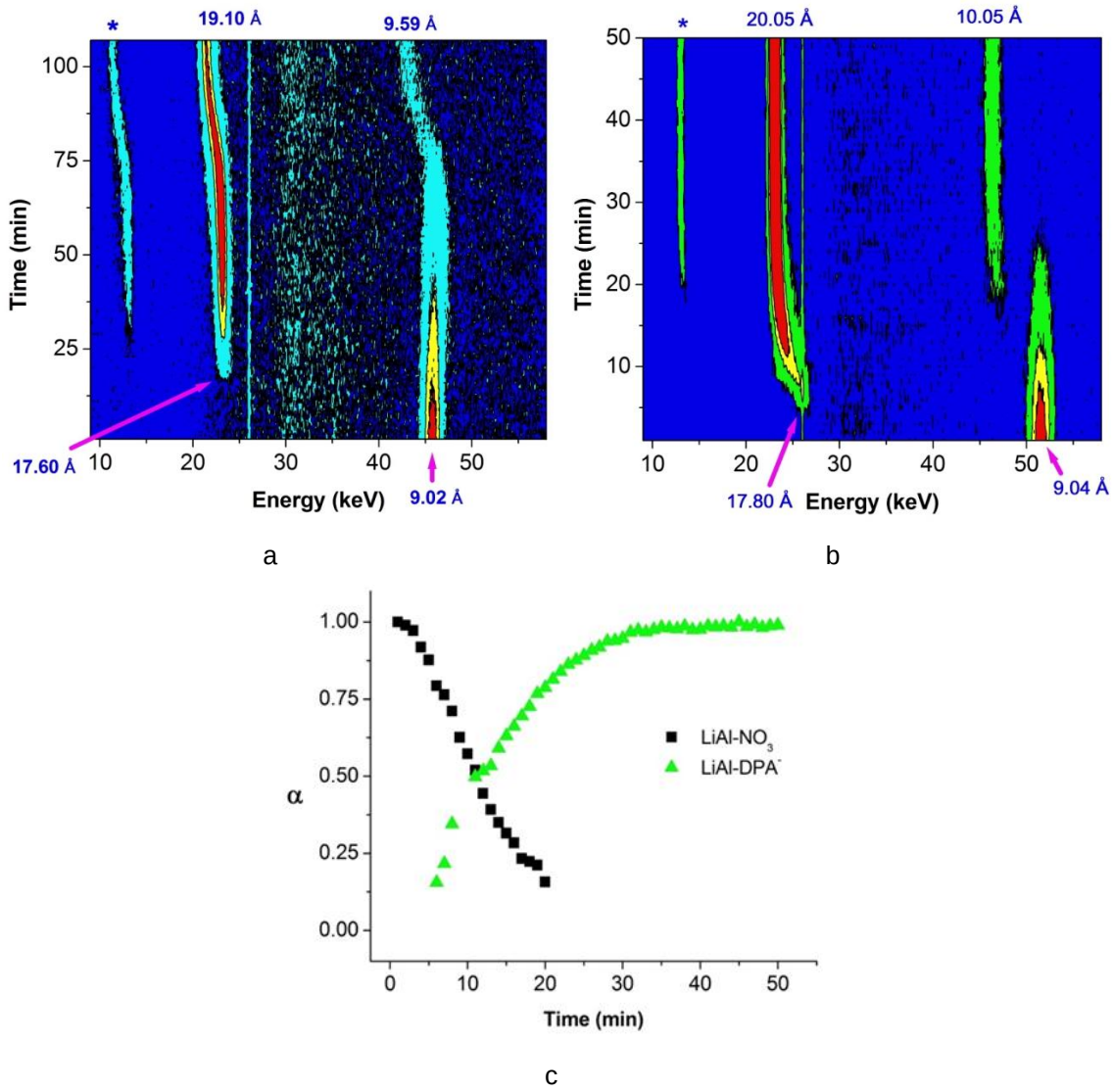

Figure 5.9: *In situ* XRD data collected on DESY for the intercalation of DPA into LiAl-NO_3 at **(a)** pH 4.55, and (b) pH 6.10; **(c)** the extend of reaction *vs.* time plot at pH 6.1 The reflections marked * in **(a)** and **(b)** are escape reflections from the detector.

No intermediates are observed for DPA intercalation: the starting material is converted directly to the product at both pH 4.55 and pH 6.10 (see Figure 5.9a and b). This is confirmed by the α *vs.* time curves in Figure 5.9c; these cross at α = 0.5, confirming that there is no intermediate phase present here. However, there is a gradual increase in d_{002} with time, from an initial 17.6 – 17.8 Å to 19.1 Å (pH 4.55) or 20.05 Å (pH 6.1). Similar shifts in position are seen in d_{004}.

Constrained MD simulations for DPA suggest the minimum energy structure is a bilayer arrangement with a *d*-spacing of 19.17 ± 0.02 Å (see Figure 5.10a). This

is in reasonable agreement with the *ex situ* value of 18.6 Å, and a little lower that the final *in situ* d-spacings of 19 – 20 Å. The DPA anions are oriented in a perpendicular fashion across the interlayer regions, with their carboxylates facing the LDH layer and the ethylene chains towards the centre. The simulation shows that H-bonding occurs between the COO^- group of DPA and the LDH layer. The variation in cell length with optimisation step (Figure 5.10b), simulated using the unconstrained model, shows a very rapid increase in c-parameter to around 30.0 Å (d_{002} = 15.0 Å). This is followed by a more gradual increase in c, with the final c-value levelling off at *ca.* 36 Å (d_{002} = 18 Å). As for the previous systems studied, the unconstrained model mirrors very closely what is observed *in situ*, albeit with some differences between the interlayer spacings between the calculations and experimental observations. These may be ascribed to differences in hydration state.

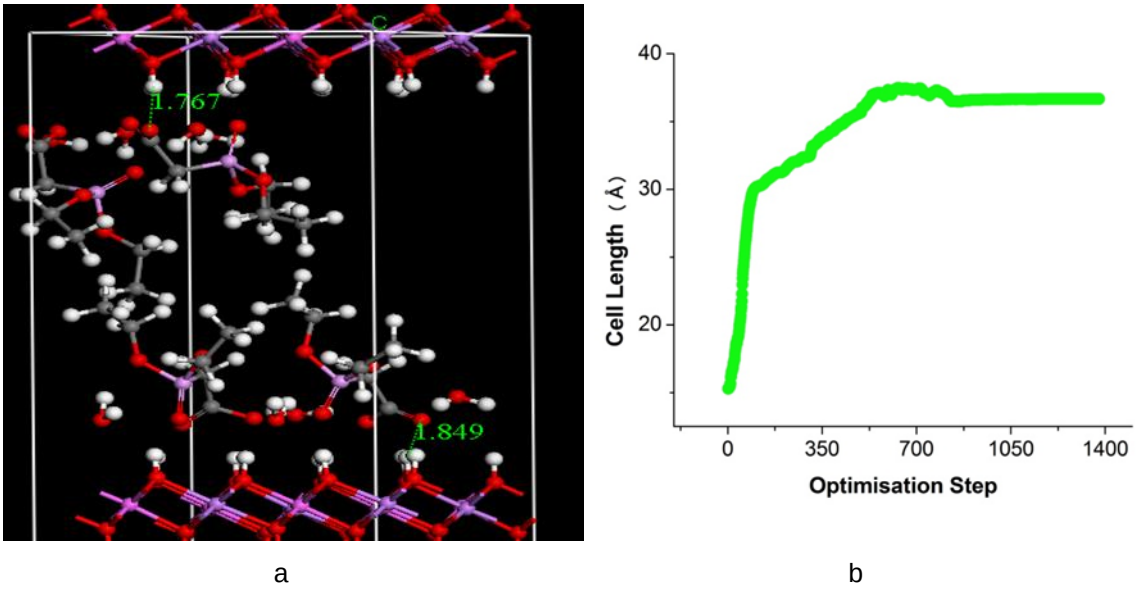

a b

Figure 5.10: (a) the energy minimised structure of LiAl-DPA; and, **(b)** the variation of cell length with optimisation step.

5.2.3. Drug release

Dissolution tests were performed under experimental conditions close to the human blood plasma, with the media composition being slightly modified from the one reported by Marques *et al.*[53] The drug release study was carried out from the PAA^{2-} and PAA^{3-} systems (0.1g in 1L of 2 M sodium carbonate solution in a vessel held at 37 ± 0.5 ºC and stirred at 50 r.p.m), since the pH of solutions of these ions are closer to physiological pH than the very acidic PAA^{-}, and thus less likely to cause irritation. PAA^{2-} release was very rapid, within the first 5 min almost all was released (Figure 5.11). However, this initial burst of release was followed by a strange phenomenon: the concentration of PAA^{2-} in the media was subsequently observed to decrease very quickly and only 5 % remained free in solution after 3h. PAA^{3-} behaves in the same manner as PAA^{2-} (Figure 5.12). It was postulated that PAA anions might have been adsorbed to the surface of the LDH or the glass wall of the conical flask in which the release experiment was undertaken. Alternatively, it may have been re-intercalated.

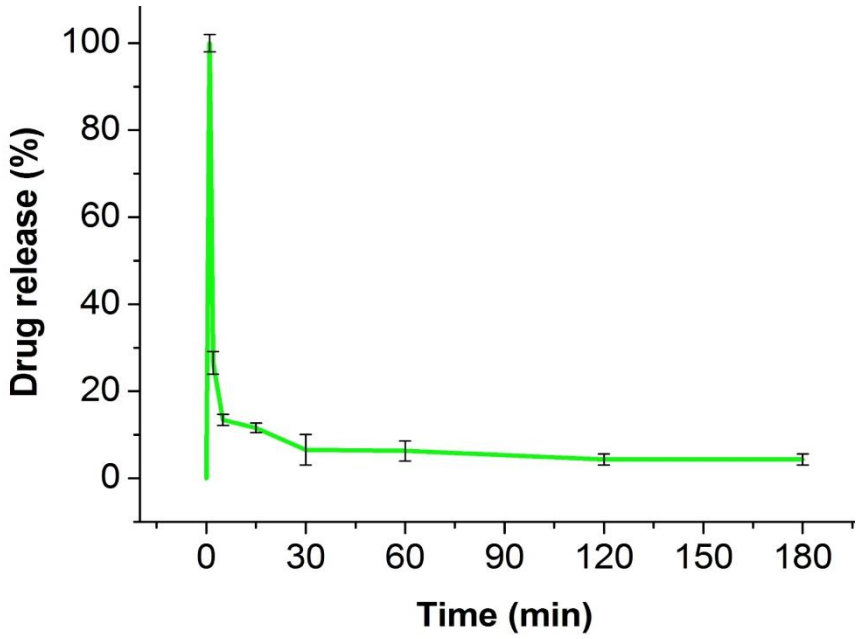

Figure 5.11: Drug release from LiAl-PAA^{2-}.

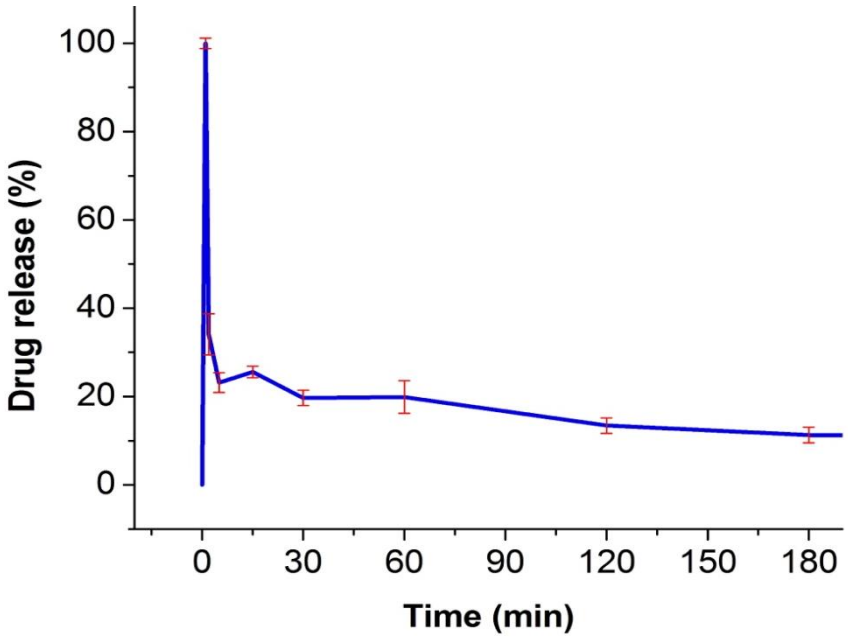

Figure 5.12: Drug release from LiAl-PAA^{3-}.

The solid material was recovered after the end of the LiAl-PAA^{2-} release experiment and explored by IR, XRD and XPS. The XRD and IR show that some PAA^{2-} ions remained intercalated (Figures 5.13 and 5.14). XPS can reveal if elements of interests are on the surface of the sample. PAA, LiAl-PAA^{2-} and LiAl-PAA^{2-} after release all show different background spectra. In this case, the spectrum of LiAl-PAA^{2-} after release suggests there is no P at the top layers of the LDH, suggesting that maybe some remains intercalated in the centres of the platelets (Figure 5.15), while the background spectra of the others (samples PAA and LiAl-PAA^{2-}) are similar; suggesting that PAA^{2-} is occupying the top layers (Appendix IV). This may arise as a result of the affinity of phosphorus for aluminium.[54–57]

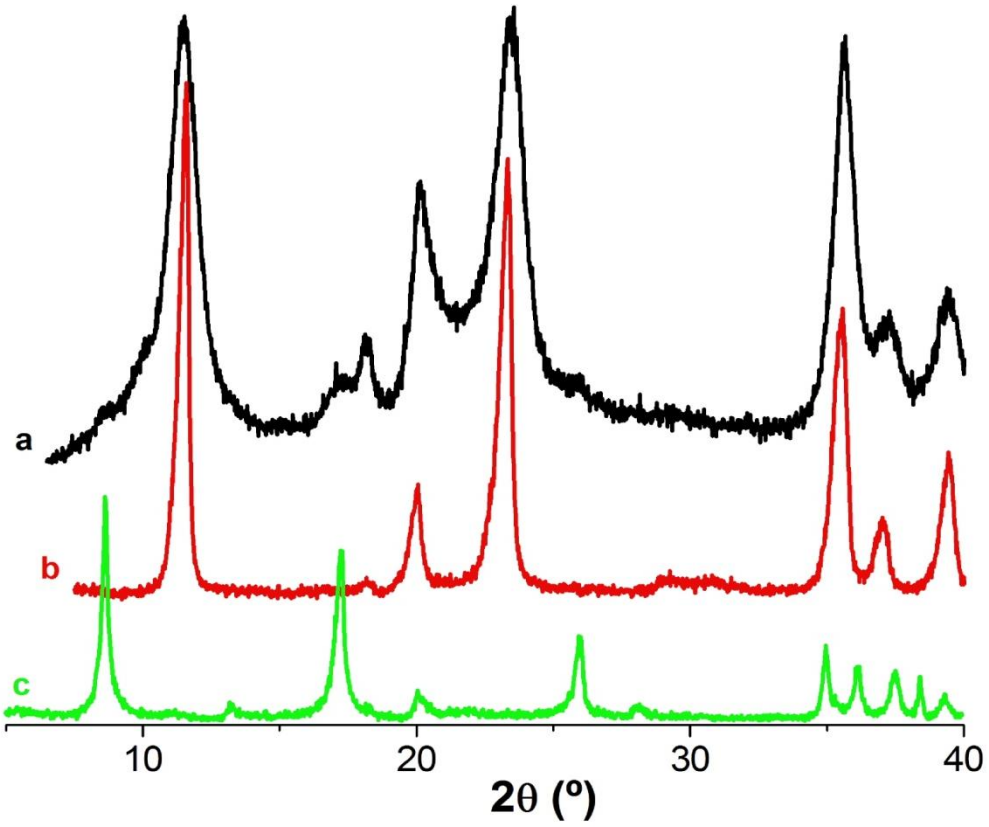

Figure 5.13: XRD patterns of **(a)** LiAl-PAA^{2-} after release, **(b)** LiAl-Cl and **(c)** LiAl-PAA^{2-}.

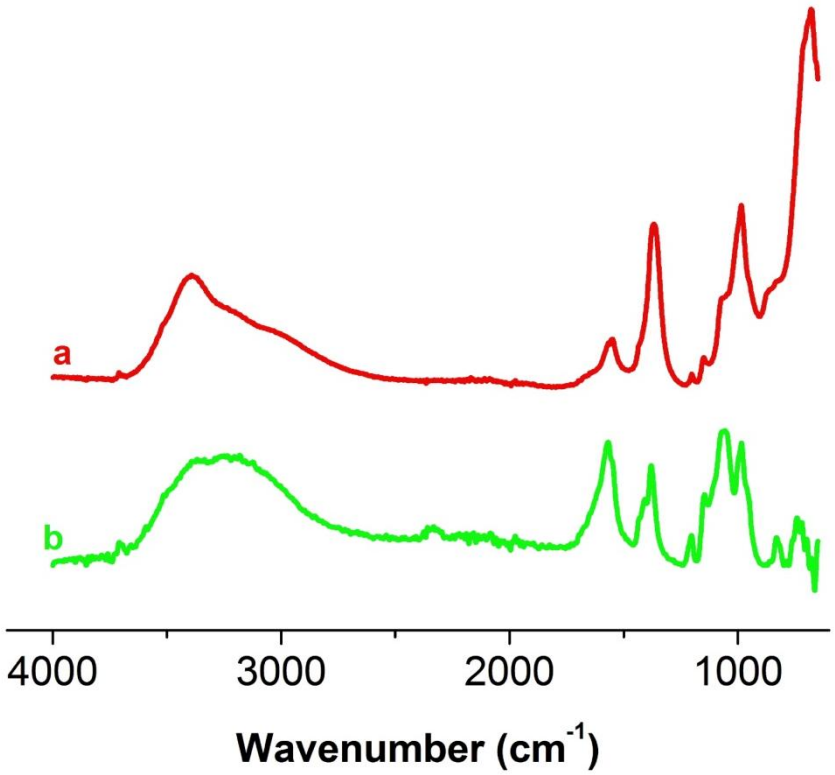

Figure 5.14: The FTIR spectra of **(a)** LiAl-PAA^{2-} after release and **(b)** LiAl-PAA^{2-}.

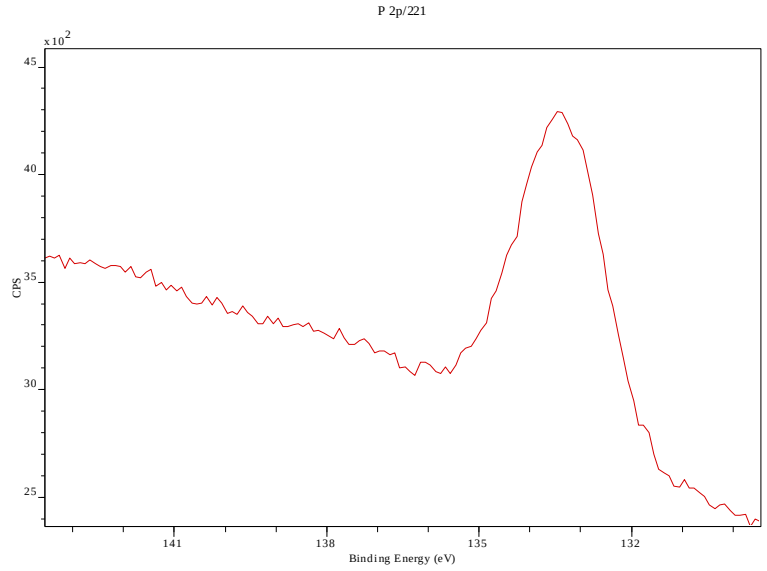

a

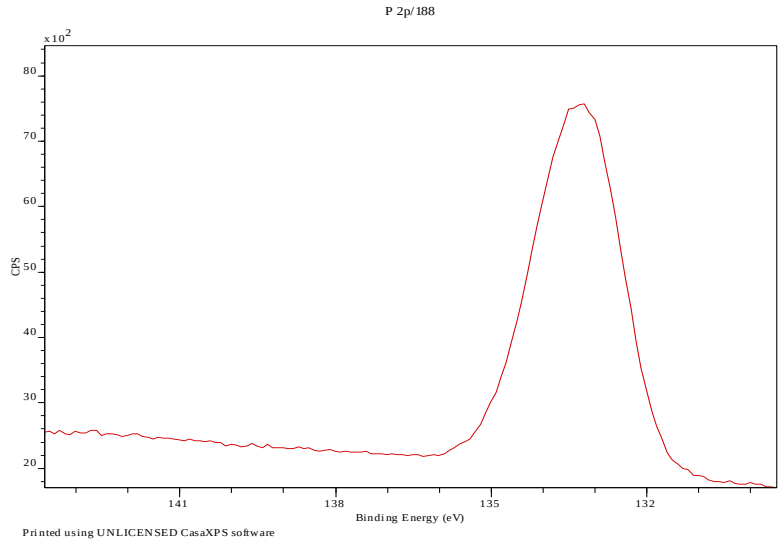

b

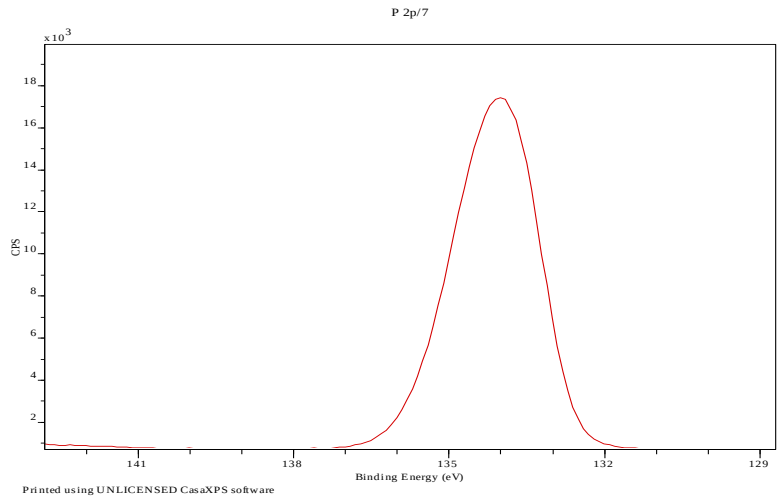

c

Figure 5.15: XPS of P spectra of **(a)** LiAl-PAA^{2-} after release; **(b)** LiAl-PAA^{2-} and **(c)** PAA.

PAA has antiviral activity, and can block the DNA polymerase.[46] However, direct delivery of PAA is generally inefficient and suffers from problems such as nephrotoxicity and a short half-life,[58,59] which can be translated to its unlikelihood to cross cell membrane. These disadvantages can be overcome by using LDH carriers that can improve bioavailability as well as reducing undesirable effects. Their positive surface charge facilitates cellular uptake and reduces renal clearance, which translates into a longer circulation time and increases their chance of crossing the cell membrane. *In vivo* tests have shown that the LDH–acetylsalicylic acid system improves the bioavailability and decreases the elimination rate of the drug, with the potential to increase its efficacy and reduce its adverse effects.[60] LiAl-PAA does not seem to be a good as drug delivery systems.

5.3 Conclusions

A systematic study into the intercalation of the ions of phosphonoacetic acid (PAA), sulfoacetic acid (SAA) and diethylphosphonoacetic acid (DPA) into the $[LiAl_2(OH)_6]X{\cdot}yH_2O$ (LiAl-X; X = Cl, NO_3) is reported. Three different anions of PAA, SAA^{2-} and DPA^- could easily be incorporated into the LDH. *In situ* time resolved X-ray diffraction experiments showed that the intercalation of PAA proceeds by very distinct intermediates, while reflection shifts were observed in the interlayer spacing of the SAA and DPA products. The intermediate phases observed were distinct from simple staged systems. *In silico* molecular dynamics (MD) simulations were employed to gain more insight into the arrangement of ions in the interlayer space, and it was found that the different phases observed *in situ* correspond closely to local energy minima in the MD results. The results presented here demonstrate that MD simulations can be used not only to probe the orientation and interaction of guest species in host lattices, but also can unravel details of the intimate steps along the reaction coordinate. The LiAl LDH does not seem to be a carrier for PAA.

5.4 References

1. Meyer, P. D. T. J. & Sauvage, H. W. R. J. *Layered Double Hydroxides*. *J. Infect. Dis.* **119,** (Springer-Verlag, 2006).

2. Fogg, A. M. & O'Hare, D. Study of the Intercalation of Lithium Salt in Gibbsite Using Time-Resolved in Situ X-ray Diffraction. *Chem. Mater.* **11,** 1771–1775 (1999).

3. Wang, Z., Han, E. & Ke, W. Influence of nano-LDHs on char formation and fire-resistant properties of flame-retardant coating. *Prog. Org. Coatings* **53,** 29–37 (2005).

4. Kagunya, W., Hassan, Z. & Jones, W. Catalytic Properties of Layered Double Hydroxides and Their Calcined Derivatives. *Inorg. Chem.* **35,** 5970–5974 (1996).

5. Gong, M. *et al.* An advanced ni-fe layered double hydroxide electrocatalyst for water oxidation. *J. Am. Chem. Soc.* **135,** 8452–5 (2013).

6. He, S., An, Z., Wei, M., Evans, D. G. & Duan, X. Layered double hydroxide-based catalysts: nanostructure design and catalytic performance. *Chem. Commun. (Camb).* **49,** 5912–20 (2013).

7. Theiss, F. L., Sear-Hall, M. J., Palmer, S. J. & Frost, R. L. Zinc aluminium layered double hydroxides for the removal of iodine and iodide from aqueous solutions. *Desalin. Water Treat.* **39,** 166–175 (2012).

8. Jin, S., Bland, A. E. & Brown, T. H. Bioagent Air Filtration Systems. (2005).

9. Dutta, P. K. & Robins, D. S. Pyrene Sorption in Organic-Layered Double-Metal Hydroxides. *Langmuir* **10,** 1851–1856 (1994).

10. Monash, P. & Pugazhenthi, G. Utilization of calcined Ni-Al layered double hydroxide (LDH) as an Adsorbent for removal of methyl orange dye from aqueous solution. *Environ. Prog. Sustain. Energy* **33,** 154–159 (2014).

11. Bruna, F. *et al.* Layered double hydroxides as adsorbents and carriers of the herbicide (4-chloro-2-methylphenoxy)acetic acid (MCPA): systems Mg-Al, Mg-Fe and Mg-Al-Fe. *J. Hazard. Mater.* **168,** 1476–81 (2009).

12. Ogawa, M. & Kuroda, K. Photofunctions of Intercalation Compounds. *Chem. Rev.* **95,** 399–438 (1995).

13. Millange, F., Walton, R. I., Lei, L. & O'Hare, D. Efficient Separation of Terephthalate and Phthalate Anions by Selective Ion-Exchange Intercalation in the Layered Double Hydroxide $Ca_2Al(OH)_6 \cdot (NO_3)_2 \cdot H_2O$. *Chem. Mater.* **12,** 1990–1994 (2000).

14. Ragavan, A., Khan, A. I. & O'Hare, D. Isomer selective ion-exchange intercalation of nitrophenolates into the layered double hydroxide $[LiAl_2(OH)_6]Cl{\cdot}xH_2O$. *J. Mater. Chem.* **16,** 602 (2006).

15. Khan, A. I., Lei, L., Norquist, A. J. & O'Hare, D. Intercalation and controlled release of pharmaceutically active compounds from a layered double hydroxide. *Chem. Commun. (Camb).* 2342–3 (2001).

16. Yang, J. *et al.* New Inorganic-Based Drug Delivery System of Indole-3-Acetic Acid-Layered Metal Hydroxide Nanohybrids with Controlled Release Rate. *Chem. Mater.* **19,** 2679–2685 (2007).

17. Ambrogi, V., Fardella, G., Grandolini, G. & Perioli, L. Intercalation compounds of hydrotalcite-like anionic clays with antiinflammatory agents--I. Intercalation and in vitro release of ibuprofen. *Int. J. Pharm.* **220,** 23–32 (2001).

18. Williams, G. R. *et al.* New insights into the intercalation chemistry of $Al(OH)_3$. *Dalton Trans.* **40,** 6012–22 (2011).

19. Khan, A. I., Williams, G. R., Hu, G., Rees, N. H. & O'Hare, D. The intercalation of bicyclic and tricyclic carboxylates into layered double hydroxides. *J. Solid State Chem.* **183,** 2877–2885 (2010).

20. Wei, M. *et al.* Intercalation of l -Dopa into Layered Double Hydroxides: Enhancement of Both Chemical and Stereochemical Stabilities of a Drug through Host−Guest Interactions. *Chem. Mater.* **20,** 5169–5180 (2008).

21. Markland, C., Williams, G. R. & O'Hare, D. The intercalation of flavouring compounds into layered double hydroxides. *J. Mater. Chem.* **21,** 17896 (2011).

22. Williams, G. R., Rees, N. H. & O'Hare, D. Incorporation of phosphorus oxyacids into layered double hydroxides. *Solid State Sci.* **11,** 1229–1238 (2009).

23. Jellicoe, T. C. & Fogg, A. M. Synthesis and characterization of layered double hydroxides intercalated with sugar phosphates. *J. Phys. Chem. Solids* **73,** 1496–1499 (2012).

24. Williams, G. R., Norquist, A. J. & O'Hare, D. Time-Resolved, In Situ X-ray Diffraction Studies of Staging during Phosphonic Acid Intercalation into $[LiAl_2(OH)_6]Cl{\cdot}H_2O$. *Chem. Mater.* **16,** 975–981 (2004).

25. Williams, G. R. & O'Hare, D. New phosphonate intercalates of $[Ca_2Al(OH)_6]NO_3{\cdot}yH_2O$: A synthetic and kinetic study. *Solid State Sci.* **8,** 971–980 (2006).

26. Williams, G. R., Fogg, A. M., Sloan, J., Taviot-Guého, C. & O'Hare, D. Staging during anion-exchange intercalation into $[LiAl_2(OH)_6]Cl.yH_2O$: structural and mechanistic insights. *Dalton Trans.* **2,** 3499–506 (2007).

27. Auxilio, A. R. *et al.* Adsorption and intercalation of Acid Blue 9 on Mg–Al layered double hydroxides of variable metal composition. *Polyhedron* **26,** 3479–3490 (2007).

28. Costa, F. R. *et al.* Alkyl sulfonate modified LDH: Effect of alkyl chain length on intercalation behavior, particle morphology and thermal stability. *Appl. Clay Sci.* **44,** 7–14 (2009).

29. Oriakhi, C. O., Farr, I. V & Lerner, M. M. Thermal characterization of poly(styrene sulfonate) layered double hydroxide nanocomposites. *Clays Clay Miner.* **45,** 194–202 (1997).

30. Williams, G. R., Khan, A. I. & O'Hare, D. Mechanistic and kinetic studies of guest ion intercalation into layered double hydroxides using time-resolved, in-situ X-ray power diffraction. *Struct. Bond.* **119,** 161–192 (2005).

31. Williams, G. R., Norquist, A. J. & O'Hare, D. The formation of ordered heterostructures during the intercalation of phosphonic acids into a layered double hydroxide. *Chem. Commun.* 1816 (2003).

32. Fogg, A. M., Dunn, J. S. & O'Hare, D. Formation of Second-Stage Intermediates in Anion-Exchange Intercalation Reactions of the Layered Double Hydroxide $[LiAl_2(OH)_6]Cl{\cdot}H_2O$ As Observed by Time-Resolved, in Situ X-ray Diffraction. *Chem. Mater.* **10,** 356–360 (1998).

33. Williams, G. R. & O'Hare, D. Factors influencing staging during anion-exchange intercalation into $[LiAl_2(OH)_6]X$ center dot mH_2O ($X = Cl^-$, Br^-, NO_3^-). *Chem. Mater.* **17,** 2632–2640 (2005).

34. Feng, Y. J., Williams, G. R., Leroux, F., Taviot-Gueho, C. & O'Hare, D. Selective anion-exchange properties of second-stage layered double hydroxide heterostructures. *Chem. Mater.* **18,** 4312–4318 (2006).

35. Newman, S. P., Di Cristina, T., Coveney, P. V. & Jones, W. Molecular Dynamics Simulation of Cationic and Anionic Clays Containing Amino Acids. *Langmuir* **18,** 2933–2939 (2002).

36. Yan, D., Lu, J., Wei, M., Evans, D. G. & Duan, X. Recent advances in photofunctional guest/layered double hydroxide host composite systems and their applications: experimental and theoretical perspectives. *J. Mater. Chem.* **21,** 13128 (2011).

37. Gao, R. *et al.* Ordered and flexible lanthanide complex thin films showing up-conversion and color-tunable luminescence. *J. Mater. Chem. C* **2,** 9579–9586 (2014).

38. Yan, D. *et al.* A combined study based on experiment and molecular dynamics: perylene tetracarboxylate intercalated in a layered double hydroxide matrix. *Phys. Chem. Chem. Phys.* **11,** 9200–9209 (2009).

39. Yan, D. *et al.* Near-infrared absorption and polarized luminescent ultrathin films based on sulfonated cyanines and layered double hydroxide. *J. Phys. Chem. C* **115,** 7939–7946 (2011).

40. Zhao, Y., Lin, H., Chen, M. & Yan, D. Niflumic anion intercalated layered double hydroxides with mechano-induced and solvent-responsive luminescence. *Ind. Eng. Chem. Res.* **53,** 3140–3147 (2014).

41. Thyveetil, M. A., Coveney, P. V, Greenwell, H. C. & Suter, J. L. Role of host layer flexibility in DNA guest intercalation revealed by computer simulation of layered nanomaterials. *J. Am. Chem. Soc.* **130,** 12485–12495 (2008).

42. Thyveetil, M., Coveney, P. V, Greenwell, H. C. & Suter, J. L. Computer simulation study of the structural stability and materials properties of DNA-intercalated layered double hydroxides. *J. Am. Chem. Soc.* **130,** 4742–4756 (2008).

43. Gordon, Y. J., Lahav, M., Photiou, S. & Becker, Y. Effect of phosphonoacetic acid in the treatment of experimental herpes simplex keratitis. *Br. J. Ophthalmol.* **61,** 506–9 (1977).

44. Smee, D. F., Bailey, K. W., Wong, M.-H. & Tarbet, E. B. Topical treatment of cutaneous vaccinia virus infections in immunosuppressed hairless mice with selected antiviral substances. *Antivir. Chem. Chemother.* **21,** 201–8 (2011).

45. Villinger, F., Genovesi, E. V, Gerstner, D. J., Whyard, T. C. & Knudsen, R. C. Inhibition of African swine fever virus in cultured swine monocytes by phosphonoacetic acid (PAA) and by phosphonoformic acid (PFA). *Arch. Virol.* **115,** 163–84 (1990).

46. Shipkowitz, N. L. *et al.* Suppression of herpes simplex virus infection by phosphonoacetic acid. *Appl. Microbiol.* **26,** 264–7 (1973).

47. Choy, J.-H., Oh, J.-M., Choi, S.-J. & Jung, H. in *Biomim. Bioinspired Nanomater.* (Kumar, C. S. S. R.) 213–250 (Wiley, 2010).

48. ChemAxon. Marvin 6.0.1. (2013). at <http://www.chemaxon.com>

49. Mohanambe, L. & Vasudevan, S. Anionic clays containing anti-inflammatory drug molecules: comparison of molecular dynamics simulation and measurements. *J. Phys. Chem. B* **109,** 15651–8 (2005).

50. Greenwell, H. C. *et al.* Interlayer Structure and Bonding in Nonswelling Primary Amine Intercalated Clays. *Macromolecules* **38,** 6189–6200 (2005).

51. Wang, J., Kalinichev, A. G. & Kirkpatrick, R. J. Effects of substrate structure and composition on the structure, dynamics, and energetics of water at mineral surfaces: A molecular dynamics modeling study. *Geochim. Cosmochim. Acta* **70,** 562–582 (2006).

52. Xu, S.-M. *et al.* Understanding the thermal motion of the luminescent dyes in the dye–surfactant cointercalated ZnAl-layered double hydroxides: a molecular dynamics study. *RSC Adv.* **4,** 47472–47480 (2014).

53. Marques, M. R. C., Loebenberg, R. & Almukainzi, M. Simulated Biological Fluids with Possible Application in Dissolution Testing. *Dissolution Technol.* **18,** 15–28 (2011).

54. Zheng, T.-T., Sun, Z.-X., Yang, X.-F. & Holmgren, A. Sorption of phosphate onto mesoporous γ-alumina studied with in-situ ATR-FTIR spectroscopy. *Chem. Cent. J.* **6,** 26 (2012).

55. Ramsier, R., Henriksen, P. & Gent, A. Adsorption of phosphorus acids on alumina. *Surf. Sci.* **203,** 72–88 (1988).

56. Lewis, J. M. & Kydd, R. A. Adsorption Mechanism of Phosphoric Acid on y-Alumina. *J. Catal.* 465–471 (1991).

57. Stanislaus, a., Absi-Halabi, M. & Al-Doloma, K. Effect of phosphorus on the acidity of γ-alumina and on the thermal stability of γ-alumina supported nickel—molybdenum hydrotreating catalysts. *Appl. Catal.* **39,** 239–253 (1988).

58. Chadwick, M. *et al.* Comparative physiological disposition of N-(phosphonacetyl)-L-aspartate in several animal species after intravenous and oral administration. *Cancer Res.* **42,** 627–632 (1982).

59. Bartlett, J. G., Auwaerter, P. G. & Pham, P. A. *Johns Hopkins ABX Guide 2012*. (Jones and Bartlett, 2012).

60. Dong, L., Gou, G. & Jiao, L. Characterization of a dextran–coated layered double hydroxide acetylsalicylic acid delivery system and its pharmacokinetics in rabbit. *Acta Pharm. Sin. B* **3,** 400–407 (2013).

Chapter 6: Experimental details

6.1. Analytical techniques

6.1.1. X-ray Diffraction

Powder X-ray diffraction (XRD) patterns were recorded using either a Philips PW 1830 (Philips, Amsterdam, Netherlands) or a MiniFlex 600 diffractometer (Rigaku, Tokyo, Japan) using Cu Kα radiation at 40 kV and 25 mA (PW1830) or 40 kV and 15 mA (MiniFlex).

6.1.2. Solution NMR spectroscopy

NMR experiments were carried out on *AV*-400 or 500 NMR Spectrometers *(*Bruker*,* Billerica, USA) operating at ^{1}H frequencies of 400.13 or 500.13 MHz. Samples were dissolved in D_2O for NMR analysis.

6.1.3. Infrared spectroscopy

Infrared spectra were recorded using a Spectrum 100 FTIR spectrometer, (Perkin Elmer, Waltham, MA, USA) over the range 650–4000 cm^{-1} with a resolution of 2 cm^{-1}.

6.1.4. Differential scanning calorimetry

The differential scanning calorimetry (DSC) apparatus used was a Q2000 instrument (TA Instruments Co., New Castle, DE, USA). Temperature calibration was performed using the melting point of indium at a heating rate of 10 ºC/min. A nitrogen purge of 50 mL/min was utilised for all measurements. Samples were loaded into T Zero pans and heated from 40–300 ºC at 10 ºC/min

6.1.5. Thermogravimetric analysis

Thermogravimetric analysis was carried out on a Discovery TGA instrument (TA Instruments Co., New Castle, DE, USA). The sample (*ca.* 5-10 mg) was mounted in an aluminium pan and heated at a rate of 10 ºC min^{-1} between 30 ºC and 400 ºC under a flow of nitrogen (10 ml/min).

6.1.6. Elemental microanalysis

Elemental microanalysis measurements were carried out by Stephen Boyer at London Metropolitan University. C, H and N contents were calculated using the quantitative combustion technique on a Carlo Erba CE1108 elemental analyser.

6.1.7. Scanning electron microscopy

Most scanning electron microscopy (SEM) was performed by Dr. Urszula Stachewicz at the SEM facility at the Nanovision Centre (QMUL), UK, on a JSM-5600LV instrument (JEOL, Tokyo, Japan), or by Mr. David McCarthy on a Quanta 200 FEG ESEM microscope (FEI, Hillsborough, OR, USA) at the UCL

School of Pharmacy. Samples were placed onto aluminium SEM stubs with carbon tape before being sputter coated with gold. Some further measurements were obtained on an EVO 18 microscope (Carl Zeiss AG, Oberkochen, Germany) at the Beijing University of Chemical Technology, China. These samples were mounted on silica and sputtered with platinum prior to measurement. Both the JSM-5600LV and EVO 18 microscopes are fitted with energy dispersive X-ray spectroscopy (EDX) detectors.

The images obtained were analysed using the ImageJ software (National Institutes of Health, Bethesda, MD,USA).[1]

6.1.8. Transmission electron microscopy (TEM)

Transmission electron micrographs were collected by Dr. Neil Young at the Department of Materials, University of Oxford, on a JEM-3000F HR (S)TEM microscope (JEOL, Tokyo, Japan) operating at 300 kV, or by Mr. David McCarthy at the UCL School of Pharmacy using a FEI CM120 Bio Twin microscope (Philips, Amsterdam, Netherlands) operating at 120kV. Samples were mounted onto lacey carbon coated copper grids for measurment.

6.1.9. X-ray photoelectron spectroscopy

X-ray photoelectron spectroscopy was performed by Dr. Naoko Sano at the NEXUS facility (Newcastle University). A K-alpha instrument (Thermo Scientific, East Grinsted, UK) equipped with a monochromated Al Kα X-ray source was used with a pass energy of 40 eV and step size of 0.1 eV. Spectra were processed using the CasaXPS software (Casa Software Ltd., Teignmouth, UK).

6.1.10. Drug release

Dissolution tests from various formulations have been carried out under experimental conditions as close as possible to the gastrointestinal tract and following pharmacopeia requirements.[2] Tablets were initially placed in 750 ml of 0.1 N hydrochloric acid in a vessel held at 37 ± 0.5 ºC, and stirred at 50 r.p.m. After 2 hours of operation, the pH of the medium was adjusted to 6.8 ± 0.05 by adding 250 ml of 0.20 M tribasic sodium phosphate. Experiments were carried out for 22 h at this pH. Dissolution tests were carried out in darkness (in triplicate with the new formulations prepared, and 5 times with the commercial tablets) from the various formulations in an automated apparatus (equipped with autosampler and inline UV spectrometer) to monitor release from the formulations which had a UV chromophore. A different protocol for Val was required: since it does not have a distinct UV chromophore, manual sampling was required, and HPLC used to measure the amount of Val released.

Some experiments were additionally carried out solely in PBS buffer (phosphate-buffered saline) at pH 7.4 and 37 ± 0.5 ºC, with stirring at 50 r.p.m. All the experiments were carried out on USP Apparatus 2 (paddle apparatus) (Figure 6.1).

a

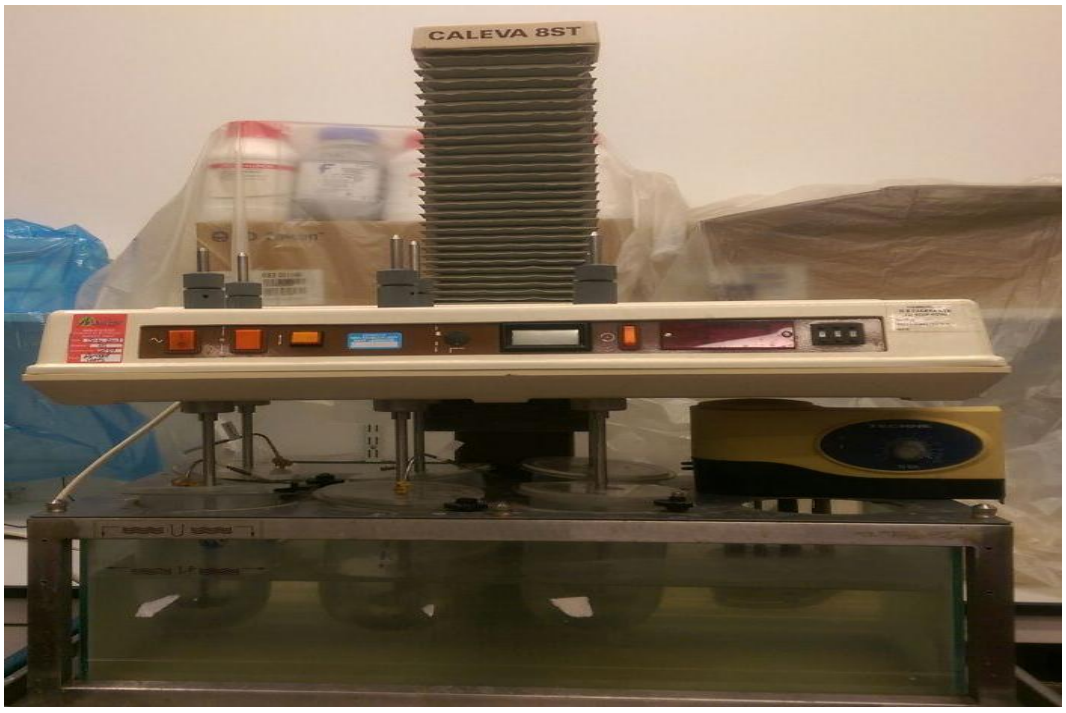

b

Figure 6.1: Photographs of the dissolution apparatus used for drug release :(a) automated dissolution apparatus ((1) a dissolution apparatus, (2) a temperature controller, (3) a pump (4)an UV spectroscopy)and (b) manual dissolution apparatus.

6.1.11. High-performance liquid chromatography

High-performance liquid chromatography (HPLC) was performed on an Agilent Technologies system (1260 Infinity, 1260 Quat Pump VL, Agilent Technologies, Santa Clara, CA, USA). The stationary phase was a Supelco® Discovery® HS F5-5 HPLC Column (5 µm particle size, L × I.D. 15 cm × 4.6 mm). The details of the experiments are summarised in Table 6.1.

The nanofibres' drug loading was evaluated by dissolving precisely weighed quantities in a known amount of deionised water and sonicating for about 10 min. The resulting solution was then filtered through a 0.22-µm filter and assayed by HPLC. For the drug release aliquots (1mL) were removed at regular intervals and filtered through a 0.1-µm filter. All experiments were performed in triplicate.

Table 6.1: Details of HPLC experiments.

Drug	Wavelength (nm)	Volume (µL)	Flow rate (mL/min)	T (ºC)	Mobile phase
Sodium ibuprofen	264	10	1.0	RT	Acetonitrile/ Trifluoroacetic acid (TFA) (0.1 %) in water (74/26)
Valproic acid	210	100	0.9	40	Acetonitrile/Phosphate buffer (pH 3.0) (60/40)
Phosphonoacetic acid	210	10	0.8	40	Methanol/Phosphate buffer (pH 7.0) (90/10)

6.1.12. *In situ* X-ray diffraction

The first series of *in situ* energy-dispersive X-ray diffraction (EDXRD) measurements was performed on Beamline F3 of the DORIS synchrotron at the Deutsches Elektronen-Synchrotron (DESY), Hamburg, Germany. The beamline was supplied with a white-beam of X-rays over the energy range 13.5 to 65 keV. Reactions were performed in borosilicate glass vessels using a purpose built furnace system; details of the apparatus used are given elsewhere.[3] The experimental set-up is depicted in Figure 6.2.

Figure 6.2: A photograph of the apparatus used on DESY beamline F3:(1) the syringe pump, (2) the borosilicate reaction tube mounted in a temperature-controlled furnace, (3) the temperature controller, (4) entrance of the X-ray beam, and (5) the detector.

In situ XRD was also undertaken at the Diamond Light Source, using Beamline I12. For these experiments, the X-ray beam was monochromated to *ca.* 53 keV, and data collected with a Thales Pixium RF4343 detector positioned 2 m from the reaction vessel. Experiments on I12 were conducted in glassy carbon tubes with the aid of the Oxford-Diamond *in Situ* Cell (ODISC).[4] The apparatus used is shown in Figure 6.3.

a b c

d

Figure 6.3: Photographs of the apparatus used on beamline I12 of Diamond: (a) the detector, (b) entrance of the X-ray beam, (c) the glassy C tube mounted in a temperature-controlling furnace (d) the overall assembly of the detector ,furnace and X-ray source assembly.

Diffraction patterns were recorded every 60 seconds (DESY) or 4 seconds (Diamond) until no further changes in these were observed. Data analysis was performed by integrating reflections of interest using the F3Tool software (DESY), or by employing Fit2D[5] to convert the as-collected images into one-dimensional patterns, subtracting the background, and applying in-house tools to integrate the reflections of interest (Diamond). Integrated data were subsequently probed using the Avrami–Erofe'ev model;[6–9] more details are given Sections 6.3.5 and 6.5.6.

6.1.13. Modelling

All MD simulations were performed adopting the LDHFF force field developed by Zhang *et al.* in an isothermal-isobaric (NPT) ensemble.[10] Temperature and pressure control were performed using the Andersen method and the Berendsen method, respectively.[11,12] The temperature was kept at 298 K, and the pressure was 0.1 MPa. Long-range Coulombic interactions were computed by the Ewald summation technique and van der Waals interactions using a "spline-cut off" method.[13] The time-step was set to be 1 fs, which is suitable for the characterisation of thermal motion,[14] and the simulation time was 5 ns. All models could reach equilibrium within 1 ns based on the observed temperature and pressure of each model. All MD simulations were carried out using the Forcite module in the Materials Studio v5.5 software package (Accelrys Software Inc, San Diego, CA, USA).[15]

6.2. Experimental details for Chapter 2

6.2.1. Materials

Materials were procured as follows: poly(ethylene oxide) (PEO) (Sigma; MW ca.400 000, St Louis, MO, USA); polyvinylpyrrolidone (PVP) (Sigma; MW ca. 360 000, St Louis, MO, USA); sodium alginate (SA) (Fisher; MW 120 000–190 000, Waltham, MA, USA); sodium ibuprofen (SI) (Sigma-Aldrich; 98%, St Louis, MO, USA); diclofenac sodium (Dic) (Cambridge Bioscience; 98 %, Cambridge, UK); naproxen sodium (Nap) (Sigma-Aldrich; 98-102 %, St Louis, MO, USA); and, valproate sodium (Val) (Sigma; ≥98%, St Louis, MO, USA). All chemicals were of analytical grade and used without further purification.

6.2.2. Preparation of spinning solutions

Solutions were prepared by dissolving PEO and SA in deionised water to give final concentrations of 5 % and 1.5 % w/v respectively. In the same way, solutions of PVP and SA were prepared with final concentrations of 20 % and 2 % w/v, respectively (again by dissolving both in water). 10 mL of each solution was then combined with certain amounts of SI, Nap, Val and Dic. In addition, a pure PVP solution at 10 % w/v was also prepared by dissolving it in ethanol. Details of the solutions prepared are given in Tables 6.2 and 6.3.

Table 6.2: The compositions of the PEO/SA solutions prepared in this study.

Fiber ID	Drug	% SA in solution (w/v)	% PEO in solution (w/v)	% Drug in solution (w/v)
F0	-	1.5	5.0	0
Fi10	SI	1.5	5.0	10.0
Fi2	SI	1.5	5.0	2.0
Fi1	SI	1.5	5.0	1.0
Fn10	Nap	1.5	5.0	10.0
Fn5	Nap	1.5	5.0	5.0
Fn1	Nap	1.5	5.0	1.0
Fv1	Val	1.5	5.0	1.0
Fv2	Val	1.5	5.0	2.0
Fv5	Val	1.5	5.0	5.0
Fv10	Val	1.5	5.0	10.0
Fd1	Dic	1.5	5.0	1.0

Table 6.3: The compositions of the PVP and PVP/SA solutions prepared in this study.

Fiber ID	Drug	% SA in solution (w/v)	% PVP in solution(w/v)	% SI solution (w/v)
FP	-	0	10.0	0
FPi1	SI	0	10.0	1.0
FPS	-	2.0	20.0	0
FPSi1	SI	2.0	20.0	1.0

6.2.3. Electrospinning

The electrospinning equipment includes a high voltage power supply (HCP 35-65000, Fug Elektronik, Rosenheim, Germany), a syringe pump (KDS100, Cole-Parmer, Vernon Hills, IL, USA), and a metal collector plate. The spinneret and collector plate were enclosed in a perspex box to minimise the effect of air currents on the trajectory of the electrospun jet and to ensure safe operation.[16] In the first experiments, electrospinning was carried out using a range of voltages, spinneret-to-collector distances, flow rates and polymer concentrations to study the effect of these parameters on the materials produced. Each solution was loaded into a 5 ml syringe fitted with a metal needle (0.5 mm diameter) and an electrode was attached to the needle (Figure 6.4).

Optimal parameters were found to be as follows. The PVP-SI solution was placed into a 5 mL syringe and all air bubbles purged prior to electrospinning. The needle tip was maintained at 13 cm above the metal collector. The pump pressure was set at 1 mL/h and a voltage of +20 kV was applied to the needle to initiate the jet. Experiments were performed under ambient conditions (Temperature between 20-25 ºC and humidity between 30-40 %). PVP/SA-SI and PEO/SA-drug (SI, Nap, Dic and Val) nanofibres were prepared similarly, but with a reduced feed rate of 0.5 mL/h, the humidity maintained below 20 % and the temperature kept at 37 ± 2 ºC.

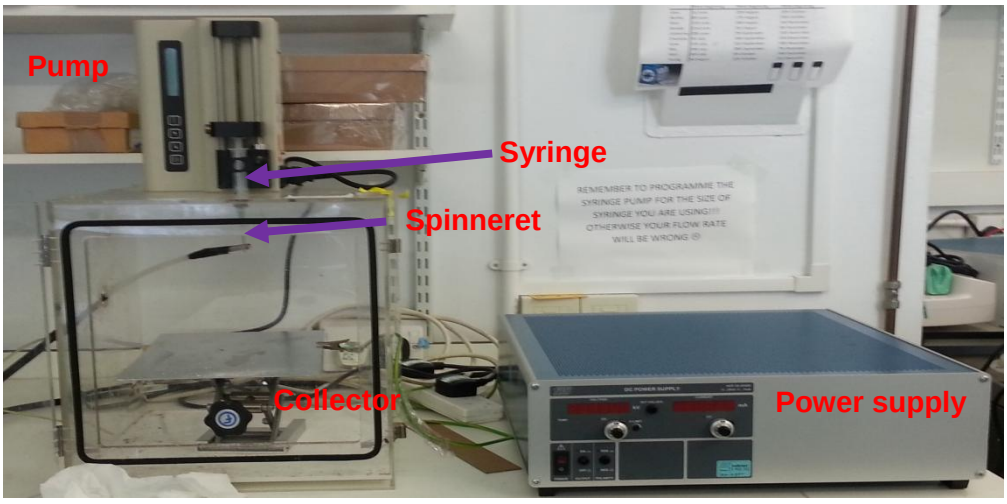

Figure 6.4: A digital photograph of the electrospinning step.

6.3. Experimental details for Chapter 3

6.3.1. Materials

Materials were procured as follows: Zinc oxide (ZnO) (Fisher Scientific; 99 %, Waltham, MA, USA), zinc chloride ($ZnCl_2$) (Fisher Scientific; 98 %, Waltham, MA, USA), zinc nitrate hexahydrate ($Zn(NO_3)_2{\cdot}6H_2O$) (Fisher Scientific; 98 %, Waltham, MA, USA), cobalt (II) nitrate hexahydrate ($Co(NO_3)_2{\cdot}6H_2O$) (Fisher Scientific; 99 %, Waltham, MA, USA), nickel (II) nitrate hexahydrate ($Ni(NO_3)_2{\cdot}6H_2O$) (Fisher Scientific; 99 %, Waltham, MA, USA), diclofenac sodium (Dic) (Cambridge Bioscience; 98 %, Cambridge, UK), naproxen sodium (Nap) (Sigma-Aldrich; 98-102 %, St Louis, MO, USA) and valproate sodium (Val) (Sigma; ≥98%, St Louis, MO, USA).

6.3.2. Hydroxy double salt synthesis

The hydroxy double salts (HDSs) were synthesised using methods reported previously.[17] The reaction mixtures detailed in Table 6.4 were stirred for 7 days at room temperature. The solid products (white Zn-NO_3 and Zn-Cl, green NiZn-NO_3 and pink CoZn-NO_3) were isolated by vacuum filtration, washed with copious amounts of deionised water and a tiny amount of acetone, then dried in an oven for 4 hours at 40 ºC.

Table 6.4: Summary of the HDS preparation methods

HDS	Starting materials	Solvent	Volume (mL)
$Zn_5(OH)_8(NO_3)_2.yH_2O$ [Zn-NO_3]	ZnO (4.2 g) + $Zn(NO_3)_2{\cdot}6H_2O$ (24.1 g)	water	60
$Zn_5(OH)_8(Cl)_2.yH_2O$ [Zn-Cl]	ZnO (3.0 g) and $ZnCl_2$ (7.26 g)	water	18
$Zn_3Ni_2(OH)_8(NO_3)_2.yH_2O$ [NiZn-NO_3]	ZnO (3.0 g) + $Ni(NO_3)_2{\cdot}6H_2O$ (8.73 g)	water	18
$Zn_{3.8}Co_{1.2}(OH)_8(NO_3)_2.yH_2O$ [CoZn-NO_3]	ZnO (3.0 g) + $Co(NO_3)_2{\cdot}6H_2O$ (8.73 g)	water	18

6.3.3. Intercalation

Intercalation of the organic anions was achieved by combining 0.4 mmol of an HDS with a 4-fold excess of the guest anions. 10 ml of deionised water was added to the solid materials, and the mixture stirred at 60 ºC for 3 days. The solid products were filtered under vacuum, washed with deionised water, and dried.

6.3.4. Guest recovery

The ability to recover the guest ions intact after intercalation was investigated in selected cases by reacting ca. 50 mg of the intercalate with approximately 100 mg of Na_2CO_3 in D2O overnight at 80 °C. The resultant suspension was filtered and the filtrate analysed by ^{1}H NMR.

6.3.5. *In situ* X-ray diffraction

In situ experiments were performed using the apparatus described in Section 6.1.12. Both at DESY and on I12, 0.4 mmol of the desired HDS was mixed with 1.6 mmol of the guest ion in 10 ml of deionised water and heated at temperatures between 60-90 ºC.

6.3.6. Modelling

Models of the Zn HDS systems were built in the space group C2/*m*, using the structure previously reported by Stahlin and Oswald.[18] In this symmetry, β = 93.28°, a = 19.48 Å, b = 6.238 Å and c = 5.517 Å.

6.4. Experimental details for Chapter 4

6.4.1. Materials

Materials were obtained as follows: Zinc oxide (ZnO) (Fisher Scientific; 99 %, Waltham, MA, USA), iron chloride ($FeCl_2$) (Sigma; 98 %, St Louis, MO, USA), magnesium chloride ($MgCl_2 \cdot 6H_2O$) (Fisher Scientific; 98 %, Waltham, MA, USA), potassium iodide (KI) (Sigma; ≥ 99 %, St Louis, MO, USA), diclofenac sodium (Dic) (Cambridge Bioscience; 98 %, Cambridge, UK), naproxen sodium (Nap) (Sigma-Aldrich; 98-102 %, St Louis, MO, USA), and valproate sodium (Val) (Sigma; ≥ 98%, St Louis, MO, USA), microcrystalline cellulose (Avicel® PH 101, Sigma, St Louis, MO, USA), spray dried mannitol (Pearlitol® 200) (a kind gift from Roquette-Pharma, Lestrem, France), Mg stearate (Sigma, St Louis, MO, USA) and polyvinylpyrrolidone (PVP) (Sigma; MW ca.44 000, St Louis, MO, USA). All chemicals were used without further purification. Commercial tablets as follow: Dicloflex 75 mg (Almus, Chessington, UK), Brufen® Retard 800 mg (Abbott, Chicago, IL, USA), Nurofen (Reckitt Benckiser, Slough, UK), Nurofen Express 200 mg (Reckitt Benckiser, Slough, UK) Rheumatac Retard 75 mg (Amdipharm Mercury, Oakville, Canada), Clofenac 100 mg (Squarepharma, Dhaka, Bangladesh) and Epilim 200 mg (Sanofi, Paris, France).

6.4.2. Biocompatible HDS synthesis

These HDSs were synthesised for the first time in this work. The reaction mixtures detailed in Table 6.5 were stirred for 3 days at room temperature in a sealed conical flask. The solid products were isolated by vacuum filtration, washed with copious amounts of deionised water, then dried in an oven at 40 ºC. The FeZn-Cl system tended to oxidise easily when in contact with air. It was hence handled with extra care to overcome this oxidation: during product recovery, the water was drained from the preparation rapidly quickly using a large filter funnel, and the HDS was then dried in a vacuum oven in the presence of silica gel at 40 ºC and 0 % humidity.

Table 6.5: Summary of biocompatible HDS preparation methods

HDSs	Starting materials	solvent	Volume (ml)
$Fe_{2.4}Zn_{2.6}(OH)_8(Cl)_2.yH_2O$ [FeZn-Cl]	ZnO (0.5 g) + $FeCl_2$ (1.18 g) +KI (0.5 g)	water	15
$Mg_2Zn_3(OH)_8(Cl)_2.yH_2O$ [MgZn-Cl]	ZnO (0.5 g) + $MgCl_2 \cdot 6H_2O$ (2.5 g)	water	5

6.4.3. Particle size and charge

The particle size and zeta potential of the MgZN-Cl and FeZn-Cl were recorded on a Zetasizer (Malvern Nano ZS, Malvern Instruments Ltd, Worcestershire, UK)

6.4.4. Intercalation

Intercalation of the organic anions was achieved by combining 0.4 mmol of an HDS with a 4-fold excess of the guest anions. 10 ml of deionised water was added to the solid materials, and the mixture stirred at 60 ºC for 4 days in a sealed glass vial. KI (0.2 mmol) was added to the mixture of FeZn-Cl and the organic guest anions to reduce the HDS oxidation. The solid products were filtered under vacuum, washed with deionised water and dried. The intercalates of the FeZn-Cl HDS were treated with extra care as described above in Section 6.4.2.

6.4.5. Guest recovery

The ability to recover the guest ions intact after intercalation was investigated in selected cases by reacting ca. 50 mg of the intercalate with approximately 100 mg of Na_2CO_3 in D_2O overnight at 80 ºC. The resultant suspension was filtered and the filtrate analysed by ^1H NMR.

6.4.6. Scale up

The large production of the new HDSs and their intercalation products was undertaken as detailed in Table 6.6. Reactions were performed in sealed Schlenk flasks fitted with an external rotator. The solid products were recovered as described in Section 6.4.2. To investigate the oxidation of the FeZn-Dic compound, some was left to dry in a normal oven and denoted Fe_{ox}Zn-Dic.

Table 6.6: Summary of large-scale biocompatible HDS preparation

HDSs	Starting materials	Solvent	Volume (ml)	Temperature	Time (day)
$Fe_2Zn_3(OH)_8(Cl)_2.yH_2O$ [FeZn-Cl]	ZnO (100.0 g) + $FeCl_2$ (240.0 g) + KI (166.0 g)	water	2500	RT	3
$Mg_2Zn_3(OH)_8(Cl)_2.yH_2O$ [MgZn-Cl]	ZnO (200.0 g) + $MgCl_2{\cdot}6H_2O$(700g)	water	1000	RT	3
FeZn-Drug	FeZn-Cl (0.5 mol) +Drug (2 mol) + KI (0.2 mol)	water	500	60 ºC	3
MgZn-Drug	MgZn-Cl (0.5 mol) + Drug (2 mol)	water	500	60 ºC	3

6.4.7. Tablet preparation

The HDS-drug intercalates were blended with excipients for tablet preparation. The recipe was based initially on a previous report by Taj and coworkers,[19] with some variations in the excipient blend then introduced to explore the effect this had on drug release. The compositions of the various formulations prepared are detailed in Table 6.7 and the role of each excipient is shown in Table 6.8. All the tablets formulation were compressed using a F3 tableting machine (Manestry, Liverpool, UK) (Figure 6.5). The effect of compression pressure on the tablet performance was also investigated in selected instances.

Table 6.7: The HDS tablet formulations

Formulations	HDS-Guest (%)	Avicel® (%)	PVP K44 (%)	SD mannitol (%)	Mg stearate (%)
FeZn-Dic-Tab1	22.0	47.9	2.5	27.0	0.6
FeZn-Dic-Tab	70.5	17.4	0.9	10.2	1.0
Fe_{ox}Zn-Dic-Tab1	19.3	46.4	4.2	27.2	2.9
MgZn-Nap-Tab	60.0	24.1	1.3	14.1	0.5
FeZn-Nap-Tab	58.1	26.9	1.0	13.2	1.0
MgZn-Sl-Tab	70.7	17.3	0.9	10.2	0.9
FeZn-Sl-Tab	70.7	17.3	0.9	10.2	0.9
MgZn-Val-Tab	59.3	18.9	-	20.9	0.9
MgZn-Val-Tab2	59.3	18.9	-	20.9	0.9
MgZn-Val-Tab3	70.4	17.4	0.9	10.3	1.0
FeZn-Val-Tab	18.9	49.2	2.1	27.9	1.9
FeZn-Val-Tab2	18.9	49.2	2.1	27.9	1.9
FeZn-Val-Tab3	18.9	49.2	2.1	27.9	1.9

Table 6.8: List of the excipients used for tablet preparation and their role

Excipient	Role
Microcrystalline cellulose (Avicel® PH 101)	Diluent/filler
Spray dried (SD) mannitol (Pearlitol® 200)	
Polyvinyl pyrolidone (PVP K44)	Binder
Magnesium stearate	Lubricant

Figure 6.5: A photograph of the tableting machine used in this work.

6.4.7.1. Friability

20 tablets were pre-weighed and placed in a friability tester (TBH 200, Copley Scientific, Nottingham, UK) (Figure 6.6). They were rotated 100 times, after which the tablets were recovered, any dust attached to them removed, and they were reweighed.

a b

Figure 6.6: The friability tester used in this work.

6.4.7.2. Hardness

The hardness of five tablets of each formulation was determined using a hardness tester (FR1000, Copley Scientific, Nottingham, UK) (Figure 6.7).

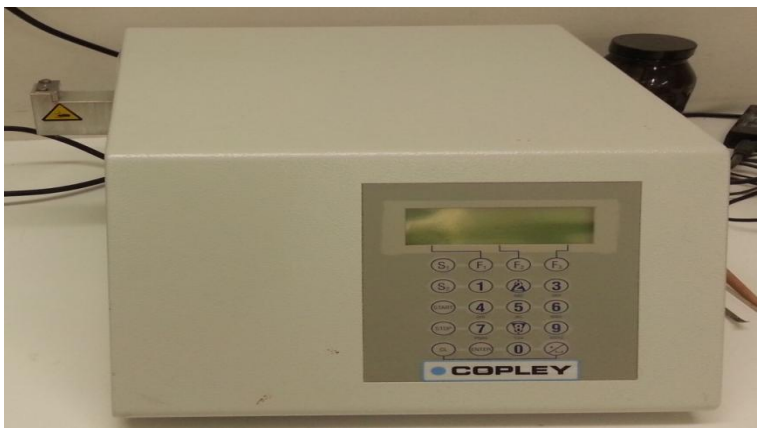

Figure 6.7: A tablet hardness tester.

6.4.7.3. Weight variation

20 tablets were weighted individually and the mean mass and standard deviation were calculated.

6.4.7.4. Drug content

Three tablets of each formulation were finely ground using a mortar and pestle. The powder was transferred into a volumetric flask containing an acidic solution (HCl), was shaken for 2 h at room temperature, then the pH was neutralised with NaOH and the final volume adjusted to 250ml with deionised water. The solution was filtered, suitable dilutions were made and UV absorbance were recorded using a U.V. spectrophotometer (UV 1800, Shimadzu, Kyoto, Japan)

6.4.7.5. Stability studies

Stability studies were carried out by storing the formulated tablets and HDSs-drug powders under usual environmental conditions (temperature and humidity varied with the seasons). The tablets and HDSs-drug intercalates were kept in glass vials and the stability was assessed at 0 day and after 3, 6, 12 and 18 months using FTIR, XRD, NMR and HPLC.

6.5. Experimental details for Chapter 5

6.5.1. Materials

Lithium chloride; lithium nitrate, phosphonoacetic acid (PAA), sulfoacetic acid (SAA), and diethyl phosphonoacetic acid (DPA) were purchased from Sigma Aldrich (St Louis, MO, USA). Gibbsite (γ-$Al(OH)_3$) was a kind gift from Prof Dermot O'Hare of Oxford University. All chemicals were of analytical grade and used without further purification.

6.5.2. Layered double hydroxide synthesis

The hexagonal polymorph of $[LiAl_2(OH)_6]Cl{\cdot}yH_2O$ (LiAl-Cl) was synthesised using methods reported previously.[20] In a standard experiment, 1g of γ-$Al(OH)_3$ was combined with a 6-fold molar excess of LiCl in 10mL deionised water. The reaction mixture was stirred and heated at 90 ºC for *ca.* 48 h in a sealed ampoule. The solid product was recovered by vacuum filtration, washed with copious amounts of deionised water, a small amount of acetone, and then allowed to dry under vacuum. The hexagonal form of $[LiAl_2(OH)_6]NO_3{\cdot}yH_2O$ (LiAl-NO_3) was prepared using analogous procedures but with $LiNO_3$ in place of LiCl.

6.5.3. Intercalation reactions

Three different PAA species were prepared by reacting one equivalent of PAA with 1, 2 or 3 equivalents of NaOH; these are respectively denoted PAA^-, PAA^{2-} and PAA^{3-}. Intercalation was achieved by combining 1 mmol of LiAl-Cl (or LiAl-NO_3) with a 2-fold excess of the guest. The LDH was added to 10 mm of a 40 mM guest solution, and the mixture stirred at room temperature for a pre-determined period of time (1h – 24h). The solid products were recovered by vacuum filtration, washed, and dried. SAA and DPA were intercalated in an

analogous manner: DPA was combined with 1 equivalent of NaOH and SAA with 2 equivalents of NaOH, before a two-fold excess of the ions was reacted with the LDH. The final products are denoted LiAl-X, where X = PAA^{3-}, PAA^{2-}, PAA^{-}, SAA or DPA.

6.5.4. Guest recovery

The ability to recover the guest ions intact after intercalation was investigated in selected cases by reacting *ca.* 50 mg of the intercalate with approximately 100 mg of Na_2CO_3 in D_2O overnight at 80 ºC. The resultant suspension was filtered and the filtrate analysed by ^1H NMR.

6.5.5. Modelling

Models of the LiAl LDH systems were built in the space group $P6_3/$, using the structure previously reported by O'Hare *et. al.*[19] In this symmetry, α = β = 90°, γ = 120°. The molar ratio of Li^+ to Al^{3+} is 1:2. The formulae of these five models are listed in Table 6.3.

Table 6.9: The formulae of the LiAl LDH models used for molecular dynamics work.

Material	Formula for constrained model	Formula for unconstrained model
LiAl-PAA^{3-}	$[LiAl_2(OH)_6]_{12}(C_2PO_5H_2)_4 \cdot 12H_2O$	$[LiAl_2(OH)_6]_{10}(C_2PO_5H_2)_2(C_2PO_5H_3)_2 \cdot 12H_2O$
LiAl-PAA^{-}	$[LiAl_2(OH)_6]_{12}(C_2PO_5H_4)_{12} \cdot 12H_2O$	$[LiAl_2(OH)_6]_6(C_2PO_5H_4)_6 \cdot 9H_2O$
LiAl-SAA	$[LiAl_2(OH)_6]_8(C_2SO_5H_2)_4 \cdot 8H_2O$	$[LiAl_2(OH)_6]_4(C_2SO_5H_2)_2 \cdot 4H_2O$
LiAl-DPA	$[LiAl_2(OH)_6]_8(C_6PO_5H_{12})_8 \cdot 16H_2O$	$[LiAl_2(OH)_6]_4(C_6PO_5H_{12})_4 \cdot 8H_2O$

6.5.6. *In situ* X-ray diffraction

In situ experiments were performed using the apparatus described in Section 6.1.12. Both at DESY and on I12, 2 mmol of the desired LDH was suspended under stirring in 5 mL of deionised water, and 10 ml of a solution containing 4 mmol of the guest ion was added dropwise using a syringe pump (KDS100, Cole-Parmer, Vernon Hills, IL, USA).

6.6. References

1. Schneider, C. A., Rasband, W. S. & Eliceiri, K. W. NIH Image to ImageJ: 25 years of image analysis. *Nat. Methods* **9,** 671–675 (2012).

2. US Pharmacopeia USP 38NF33. The United States Pharmacopeial Convention, (711) Dissolution. *Rockville,MD.* 486–496 (2015).

3. Williams, G. R., Norquist, A. J. & O'Hare, D. Time-Resolved, In Situ X-ray Diffraction Studies of Staging during Phosphonic Acid Intercalation into $[LiAl_2(OH)_6]Cl{\cdot}H_2O$. *Chem. Mater.* **16,** 975–981 (2004).

4. Moorhouse, S. J., Vranješ, N., Jupe, A., Drakopoulos, M. & O'Hare, D. The Oxford-Diamond In Situ Cell for studying chemical reactions using time-resolved X-ray diffraction. *Rev. Sci. Instrum.* **83,** 084101 (2012).

5. Hammersley, A. P. FIT2D V9.129 Reference Manual V123.121. (1998).

6. Avrami, M. Granulation, Phase Change, and Microstructure Kinetics of Phase Change. III. *J. Chem. Phys.* **9,** 177 (1941).

7. Avrami, M. Kinetics of Phase Change. I General Theory. *J. Chem. Phys.* **7,** 1103 (1939).

8. Avrami, M. Kinetics of Phase Change. II Transformation-Time Relations for Random Distribution of Nuclei. *J. Chem. Phys.* **8,** 212 (1940).

9. Erofe'ev, B. Generalized equation of chemical kinetics and its application in reactions involving solids. *Compt Rend Acad Sci USSR* 511–14 (1946).

10. Zhang, S. T., Yan, H., Wei, M., Evans, D. G. & Duan, X. Valence force field for layered double hydroxide materials based on the parameterization of octahedrally coordinated metal cations. *J. Phys. Chem. C* **116,** 3421–3431 (2012).

11. Andersen, H. C. Molecular dynamics simulations at constant pressure and/or temperature. *J. Chem. Phys.* **72,** 2384 (1980).

12. Berendsen, H. J. C., Postma, J. P. M., van Gunsteren, W. F., DiNola, A. & Haak, J. R. Molecular dynamics with coupling to an external bath. *J. Chem. Phys.* **81,** 3684–3690 (1984).

13. Allen, M. & Tildesley, D. *Computer simulation of liquids*. (Clarendon Press, 1987).

14. Casalini, T., Salvalaglio, M., Perale, G., Masi, M. & Cavallotti, C. Diffusion and aggregation of sodium fluorescein in aqueous solutions. *J. Phys. Chem. B* **115,** 12896–904 (2011).

15. Accelrys Software Inc. Materials Studio 5.5. *San Diego, USA* (2010).

16. Fennessey, S. F. & Farris, R. J. Fabrication of aligned and molecularly oriented electrospun polyacrylonitrile nanofibres and the mechanical behavior of their twisted yarns. *Polymer (Guildf).* **45,** 4217–4225 (2004).

17. Williams, G. R., Crowder, J., Burley, J. C. & Fogg, A. M. The selective intercalation of organic carboxylates and sulfonates into hydroxy double salts. *J. Mater. Chem.* **22,** 13600 (2012).

18. Stählin, W. & Oswald, H. R. The crystal structure of zinc hydroxide nitrate, Zn5(OH)8(NO3)2.2H2O. *Acta Crystallogr. Sect. B Struct. Crystallogr. Cryst. Chem.* **26,** 860–863 (1970).

19. Taj, S. F., Singer, R., Nazir, T. & Williams, G. R. The first hydroxy double salt tablet formulation. *RSC Adv.* **3,** 358 (2013).

20. Besserguenev, A. V *et al.* Synthesis and Structure of the Gibbsite Intercalation Compounds [$LiAl_2(OH)_6$]X {X = Cl, Br, NO_3} and [$LiAl_2(OH)_6$]Cl·H_2O Using Synchrotron X-ray and Neutron Powder Diffraction. *Chem. Mater.* **9,** 241–247 (1997).

Chapter 7: Conclusions and Future work

7.1. Conclusions

This work project explored two matrices for drug delivery: inorganic (hydroxy double salts (HDSs) and layered double hydroxide(LDH)) and polymeric (electrospun nanofibres). The knowledge and understanding gained by studying these matrices laid the foundation for the development of a novel drug delivery systems that combined both biocompatibility and sustained release.

7.1.1. Electrospun nanofibres (Chapter 2)

First; poly(ethylene oxide) (PEO)/ sodium alginate (SA), poly(vinyl pyrrolidone) (PVP)/ SA and PVP nanofibres were prepared using the electrospinnig technique. The PVP/SA and PVP fibres formed flat mats, however PEO/SA formed 3-dimensional “mountain” structures The analysis of PEO/SA nanofibres by electron microscopy indicated the presence of regions of high and low SA density in the fibres. It seems that the SA was present as very small strands (less than 20 nm in diameter) enrobed inside PEO nanofibres.

PEO/SA fibres could be loaded with the non-steroidal anti-inflammatory drugs diclofenac sodium (Dic), naproxen sodium (Nap) and sodium ibuprofen (SI). The fibres formed 3-dimensional “mountain” structures rather than the more typical flat mats, and crystals of the drugs could clearly be seen embedded in these structures. Valproate sodium (Val) loaded fibres could also be prepared; here, a flat mat of fibres was seen with higher concentrations of drug and crystallites could not been seen by scanning electron microscopy (SEM). However, X-ray diffraction (XRD) and differential scanning calorimetry (DSC) showed that Val is still present in the fibres in a crystalline form. Flat mats were

obtained from SI loaded PVP/SA and PVP fibres. No crystallites could be seen by SEM, XRD and DSC showed that SI is in amorphous form. The PVP and PVP/SA dissolved very quickly in aqueous media regardless of the pH. The PEO/SA nanofibres proved to be pH responsive delivery systems able to retard drug release in low pH conditions. The PEO dissolves first in acidic media and frees its drug loading, once the pH is adjusted to neutral, the SA dissolves, releasing the remaining drug. The PEO/SA/drug fibres thus comprise time-controlled drug delivery systems, where there is an “on/off” pattern of drug release (bursts of release with a lag period between them). The release profile may be precisely tuned by varying the drug contents of the fibres. The materials may hence be used for colon-targeted drug delivery, and/or to deliver a desired amount of drug into the stomach in the fed state.

7.1.2. Hydroxy double salts (Chapters 3 and 4)

Dic and Nap were intercalated into several Zn-based HDSs ($Zn_5(OH)_8$-$(NO_3)_2$ $2H_2O$ (Zn-NO_3), $Zn_5(OH)_8$-Cl_2 $2H_2O$ (Zn-Cl), $Ni_2Zn_3(OH)_8$-$(NO_3)_2$ $2H_2O$ (NiZn-NO_3) and $Co_{1.2}Zn_{3.8}(OH)_8$-$(NO_3)_2$ $2H_2O$ (CoZn-NO_3)) in Chapter 3. The intercalation of Val into Zn-NO_3 and Zn-Cl could not be achieved successfully, however, and led to the destruction of the HDS layers to yield ZnO. In contrast, the presence of Co^{2+} or Ni^{2+} in the HDS appears to stabilise the layers and resulted in the successful intercalation of Val into CoZn-NO_3 and NiZn-NO_3. *In situ* time resolved X-ray diffraction experiments showed that the intercalation of Dic and Nap into CoZn-NO_3 and Zn-NO_3 proceeds by distinct intermediates, while the intercalation of the three drugs into NiZn-NO_3 are simple one step reactions proceeding directly from the starting material to the product. Molecular Dynamics (MD) simulations found that the Dic and Nap ions were arranged in an “X” shape, forming a bilayer arrangement in the HDS interlayer space. Val was determined to adopt a position with its aliphatic groups parallel to the HDS layer, and again form a bilayer. Nap and Dic were released from the various HDSs in sustained manner in phosphate buffer saline at pH 7.4

Although it is not believed that the HDS intercalates reported in Chapter 3 would be toxic in the doses necessary to treat common conditions, in order to make the most patient friendly medicines possible it was decided to prepare new HDSs using more biocompatible metals (Mg^{2+} and Fe^{2+}) for further development of these formulations. New biocompatible HDSs ($Mg_2Zn_3(OH)_8(Cl)_2 \cdot 3.4H_2O$ (MgZn-Cl) and $Fe_{2.4}Zn_{2.6}(OH)_8(Cl)_2 \cdot 2H_2O$ (FeZn-Cl)) were successfully synthesised. The organic guests Dic, Nap, SI and Val successfully intercalated into the new HDSs. These intercalates were formulated into tablets and compared to commercial tablets. It was found that the tablets prepared met the strict US and British Pharmacopoeias guidelines for their physical properties. Drug release was investigated in conditions that mimic the human gastrointestinal tract. The HDS tablets containing Dic, Nap, showed negligible release in acidic media (and SI around 7%), but freed all the loaded drug into a neutral medium within 24 h. Desirable delayed and sustained release profiles were often observed. Such drug delivery patterns are believed to prevent the stomach irritation, one of the common side effects of the NSAIDs, and lead to a longer duration of pain relief. The release profile from some of the HDSs tablets were similar to the commercial tablets, while some showed better releases profile than their commercial analogues. The Val-loaded HDS tablets released significant amounts of drug at pH 1.0, in a similar manner to commercial Val tablets, but still met the pharmacopeia sustained release dosage form requirements.

7.1.3. Layered double hydroxides

Understanding and predicting HDSs tablet behaviour in conditions that mimic the human body is important, and should help predict their behaviour in the human body. The drug release mechanism is a key factor, and hence its comprehension and prediction is crucial. The drug release is related to guest deintercalation; to understand this, it is important to understand first the intercalation process. Layered double hydroxides (LDHs) have been investigated deeply and considerable data have been reported on their

intercalation processes, for this reason LDH were selected. A systematic study into the intercalation of the ions of phosphonoacetic acid (PAA), sulfoacetic acid (SAA) and diethylphosphonoacetic acid (DPA) into the $[LiAl_2(OH)_6]X{\cdot}yH_2O$ (LiAl-X; X = Cl, NO_3) was performed. *In situ* time resolved X-ray diffraction experiments showed that the intercalation of PAA proceeds by very distinct intermediates, while reflection shifts were observed in the interlayer spacing of the SAA and DPA products. *In silico* MD simulations were employed to gain more insight into the arrangement of ions in the interlayer space, and it was found that the different phases observed *in situ* correspond closely to local energy minima in the MD results. The results presented demonstrate that MD simulations can be used not only to probe the orientation and interaction of guest species in host lattices, but also can unravel details of the intimate steps along the reaction coordinate. The release of PAA – a potential potent anti-viral medicine – was explored, but found to be too rapid for practical application.

7.2. Future work

With the demand for novel drug delivery systems increasing and, with it, the complexity of bringing a new active pharmaceutical ingredient to market (which requires more than 12 years of *in vitro, in vivo* and clinical trials), it is easier to develop a new drug delivery system or modify existing ones to improve the effectiveness and reduce side-effects. Electrospun nanofibres and HDSs show great promise in this regard as has been demonstrated in this work. However, there remains much additional work to do to fully demonstrate their potential as future drug delivery systems, as follows:

7.2.1. Electrospun nanofibres

In future it will be interesting to perform Nap release from PEO/SA and compare the data with XPS, since it was shown that it can predicted the amount of the

drug in the first phase of drug release. The worked carried out in Chapter 2 was done using high positive voltage; negative voltages can be used as well, and in preliminary trials results with a negative voltage were completely different from those obtained with positive voltage. Further experiments would be helpful to understand the effect of the voltage on the 3D structure formation, crystallites shapes and geometries , and drug release properties. The next step would be the scale up of the nanofibre production and the preparation of pharmaceutical formulations from the scale up products. Beyond this, *in vivo* tests of the nanofibres formulations could be performed and if they show promise, they could be followed by clinical trials.

7.2.2. Hydroxy double salts

The HDSs tablets prepared in Chapter 4 showed good release profiles *in vitro*. The MgZn-Dic tablets showed zero order release, and experiments could usefully be performed to achieve zero order from the other HDS-drug systems by preparing further batches of tablets with varying excipients ratio and/or compression forces. More release studies on the FeZn-Val tablets, which trials showed have slower release than MgZn-Val tablets would be valuable to fully characterise this system. Additional stability tests are required to determine whether the intercalated drugs remain stable for long periods of time; accelerated aging studies would be beneficial here. The best performing tablets could be tested *in vivo.* If the *in vivo* results have promise, the next step would be clinical trials. Other types of biocompatible HDSs were synthesised as well including $Mg_5(OH)_8.Cl_2\cdot$and different Fe/Zn HDS (FeZn-$Cl_{m)}$ (their preparation require extra steps). FeZn-Cl_m was highly magnetic and almost has nil zeta potential. Both $Mg_5(OH)_8.Cl_2$ and FeZn-Cl_m could be good carriers for targeted delivery of anti-cancer drugs (some preliminary work was done on this as part of this thesis). *In vitro* and *in vivo* tests would then be required to verify their potential as selective targeted delivery systems.

7.2.3. Layered double hydroxide

MD could successfully be used to predict the intercalation mechanism of PAA, DPA and SAA, and in future it could be interesting to apply this technique to other *in situ* intercalation reactions with new guests in order to establish the wider applicability of this approach. The prediction of the drug release mechanism from HDSs formulations and comparison of MD and *in situ* diffraction results would also be interesting.

7.2.4. Combination of inorganic and organic matrices

Combination of LDH or HDS and nanofibres could also be explored These combinations might be used as local drug delivery systems, which could generate a cost effective and efficient drug delivery systems for instance delivery of antibiotic to an infected wound. The system can be used as well in the prevention or protection in many cases.

Appendices

Appendix I: Additional data for Chapter 2

Chemical Structures

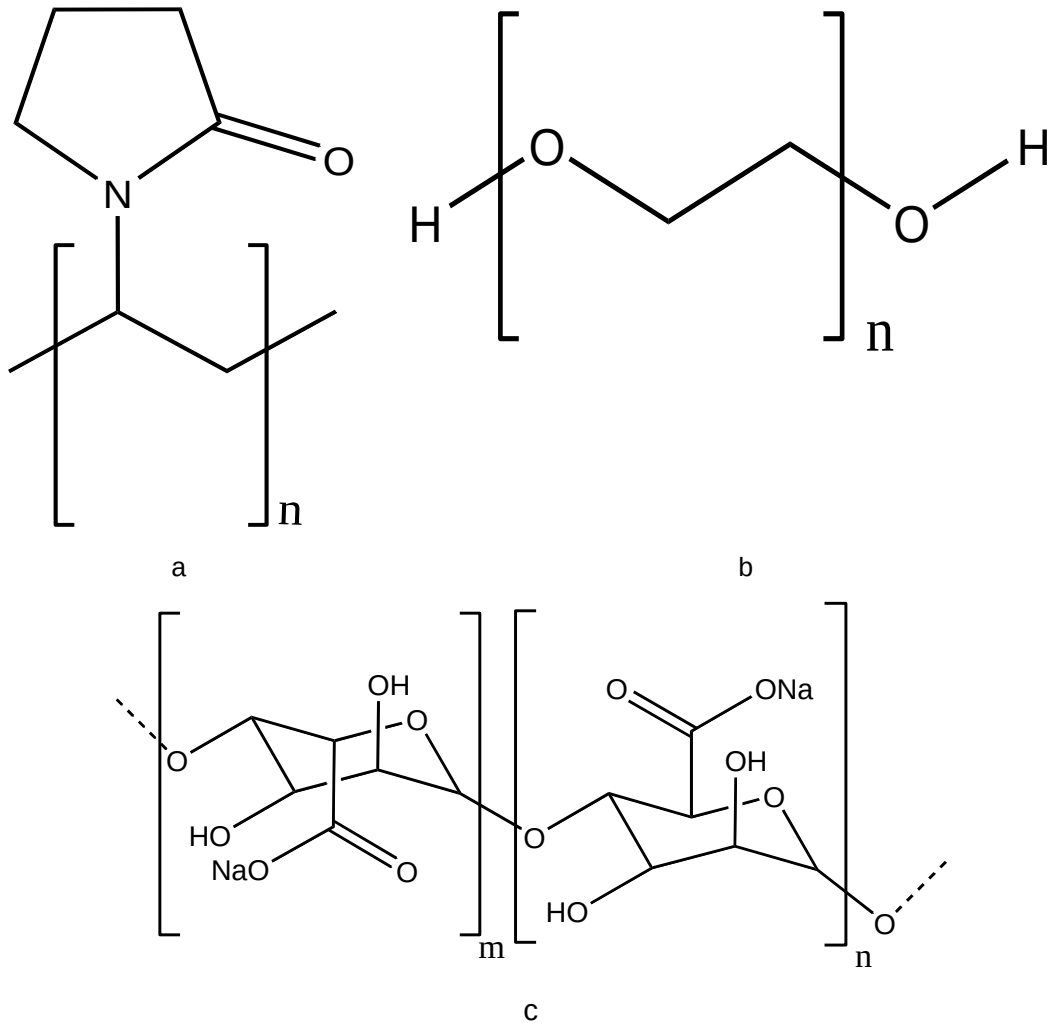

Figure AI-2.1: Polymers chemical structures of (a) PVP, (b) PEO and (c) SA

XRD

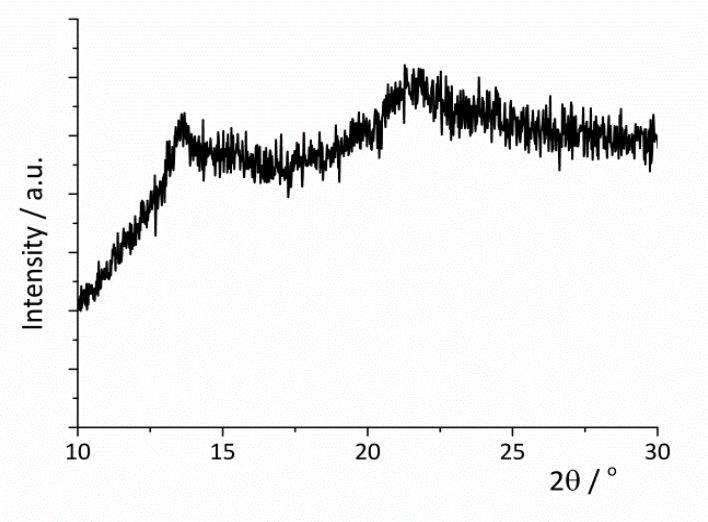

Figure AI-2.2: The XRD pattern of sodium alginate (SA).

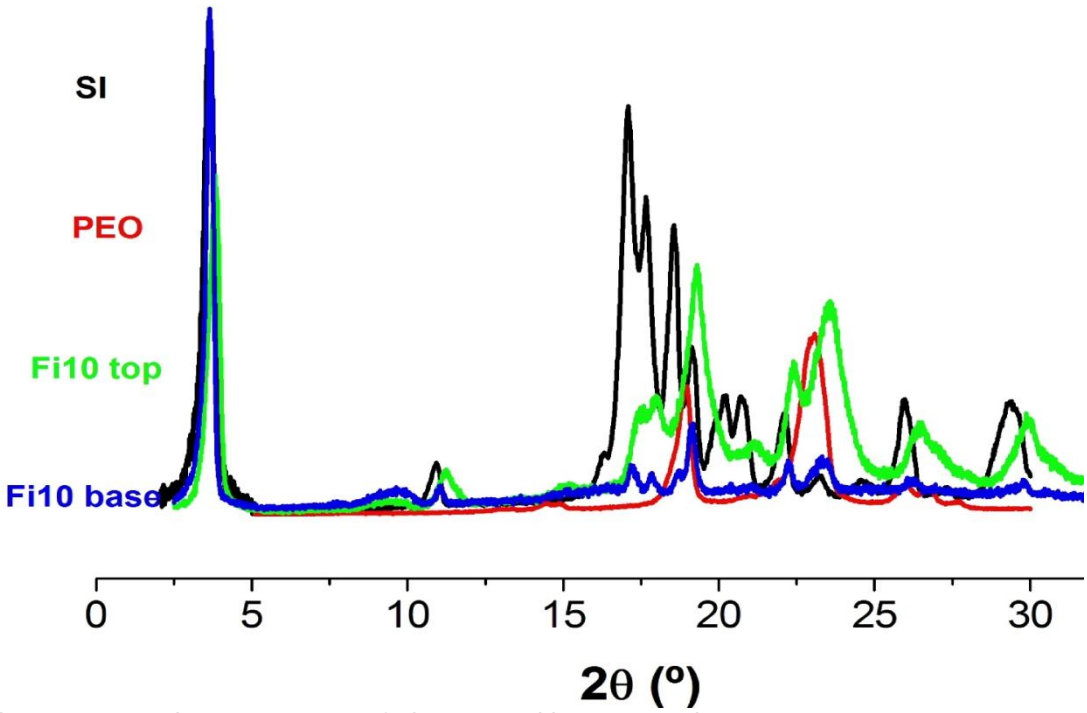

Figure AI-2.3: The XRD pattern of Fi10 top and base, SI and PEO.

SEM

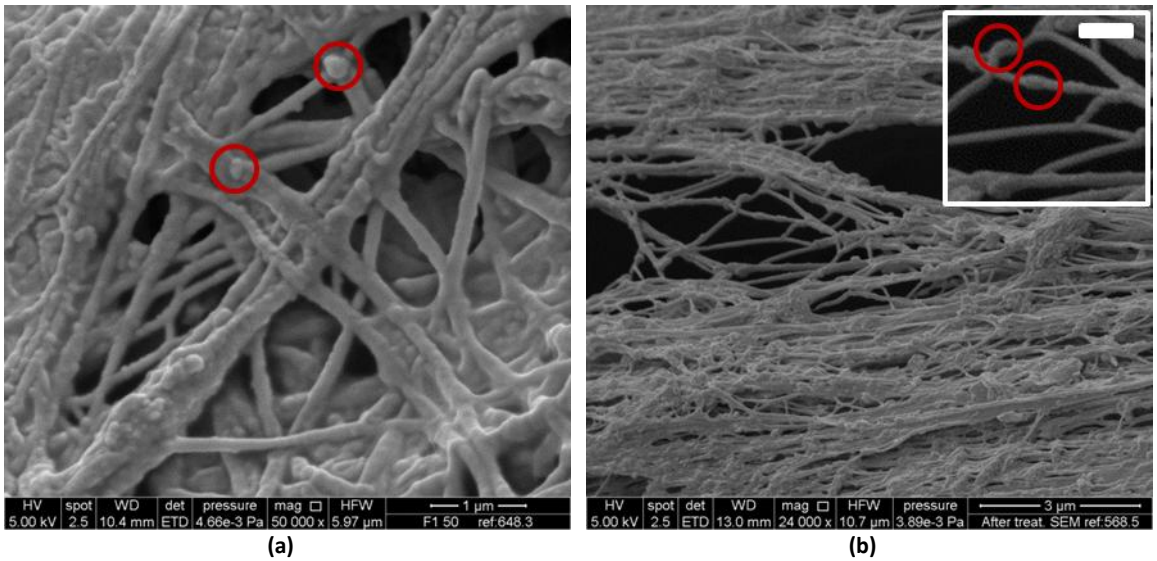

(a) (b)

Figure AI-2.4. SEM images of F1 fibres exposed to a pH 3 environment for 10 – 20 minutes. **(a)** The fibre mat after immersion in a few drops of acidic medium; **(b)** the mat after suspension in 1 L of medium. The inset in **(b)** is an enlargement of a section of the main image, and the scale bar represents 500 nm.

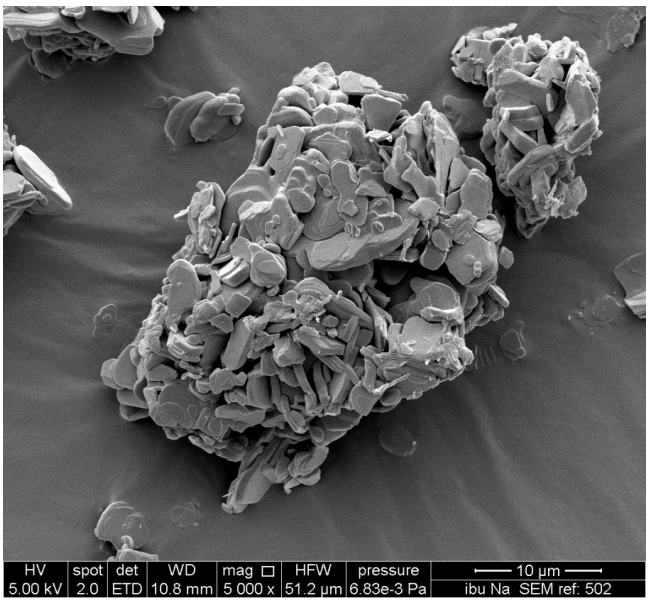

Figure AI-2.5: SEM image of SI raw material.

TEM

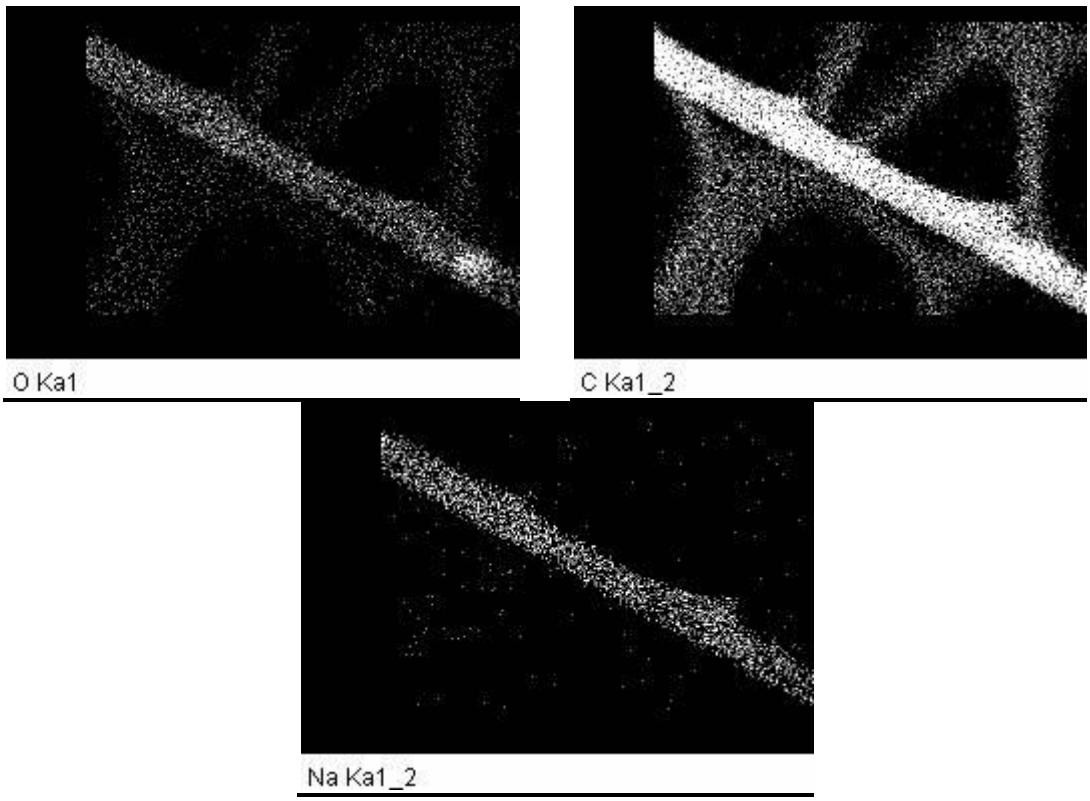

Figure AI-2.6 : Elements mapping of F0

FTIR

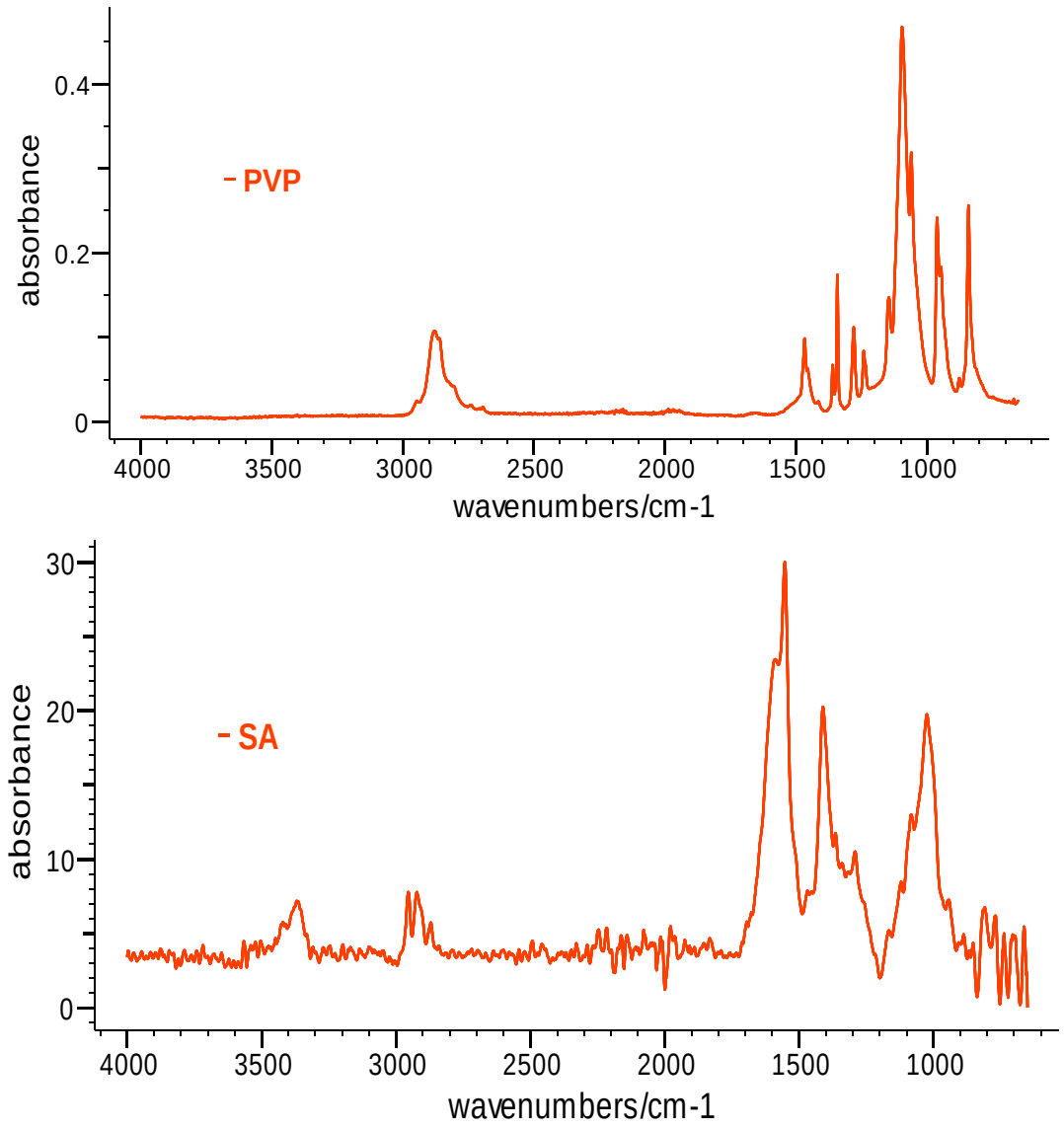

Figure AI-2.7: IR spectra of PVP and SA.

NMR

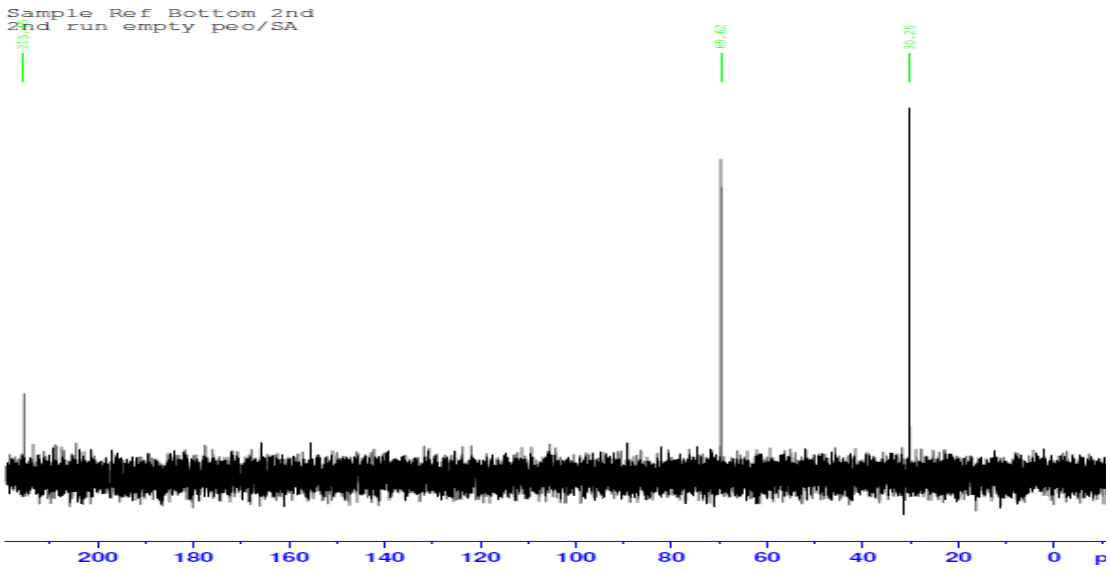

a

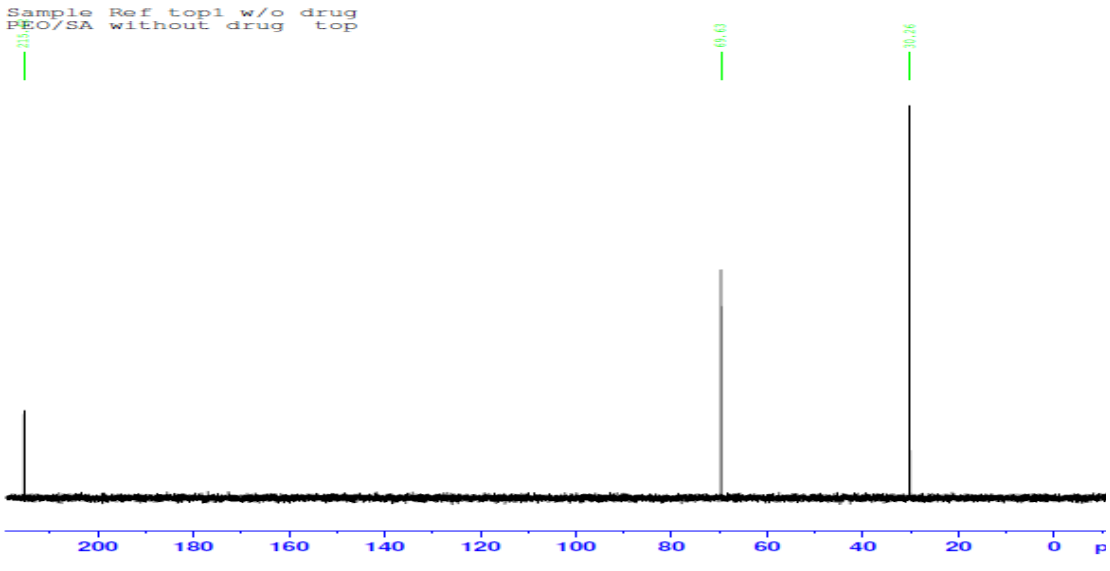

b

Figure AI-2.8: ^{13}C NMR spectra of (a) F0 base and (b) F0 top

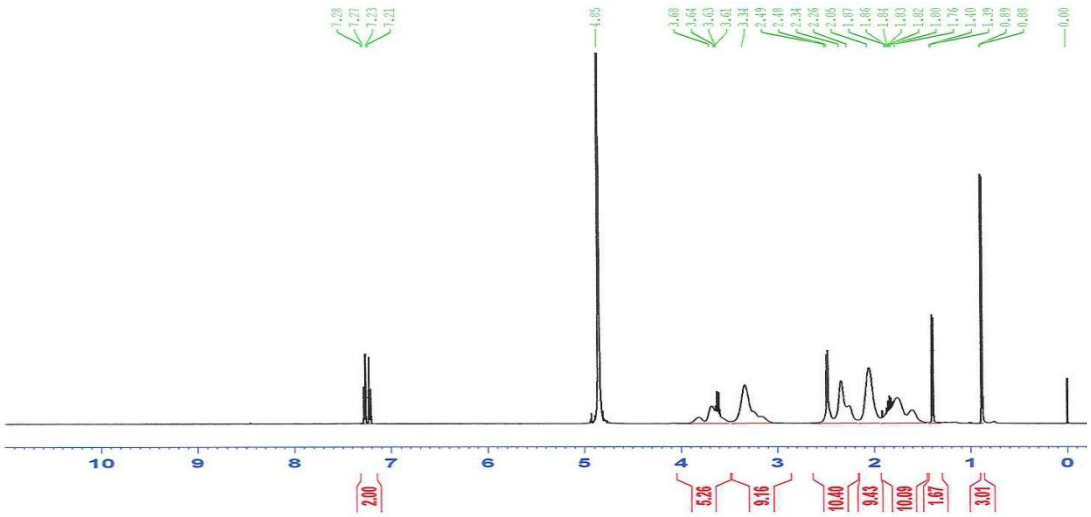

a

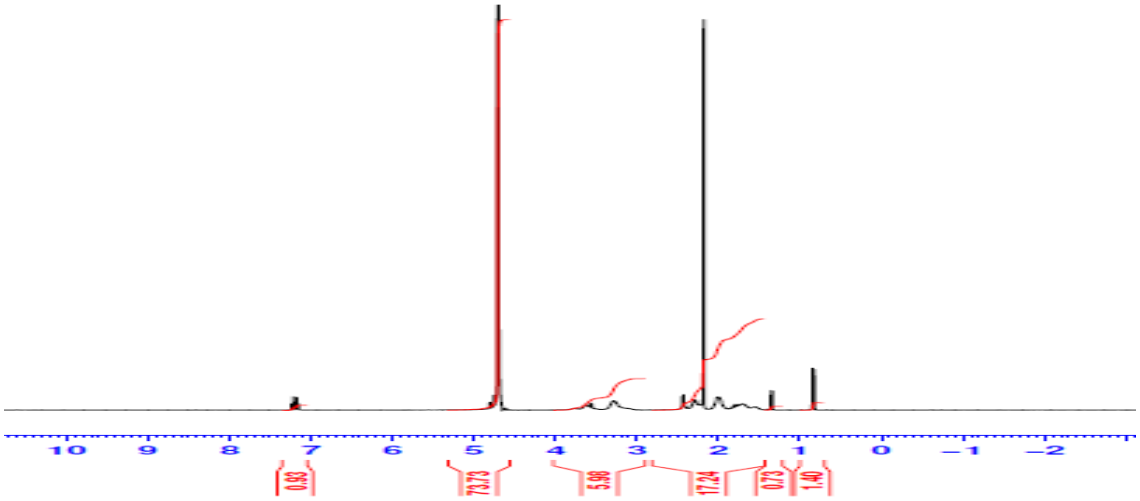

b

Figure AI-2.9: ^{1}H NMR spectra of (a) FPi1 and (b) FPSi1.

XPS

Table AI-2.1: The content of Dic and Val at the surface of the fibres, calculated from XPS data. Samples were taken from the top of the 3D fibre structure

Fibre ID	Drug Surface composition (%)
Fd1	10.0 ± 1.5
Fv1	46.3 ± 2.0

Appendix II: Additional data for Chapter 3.

XRD

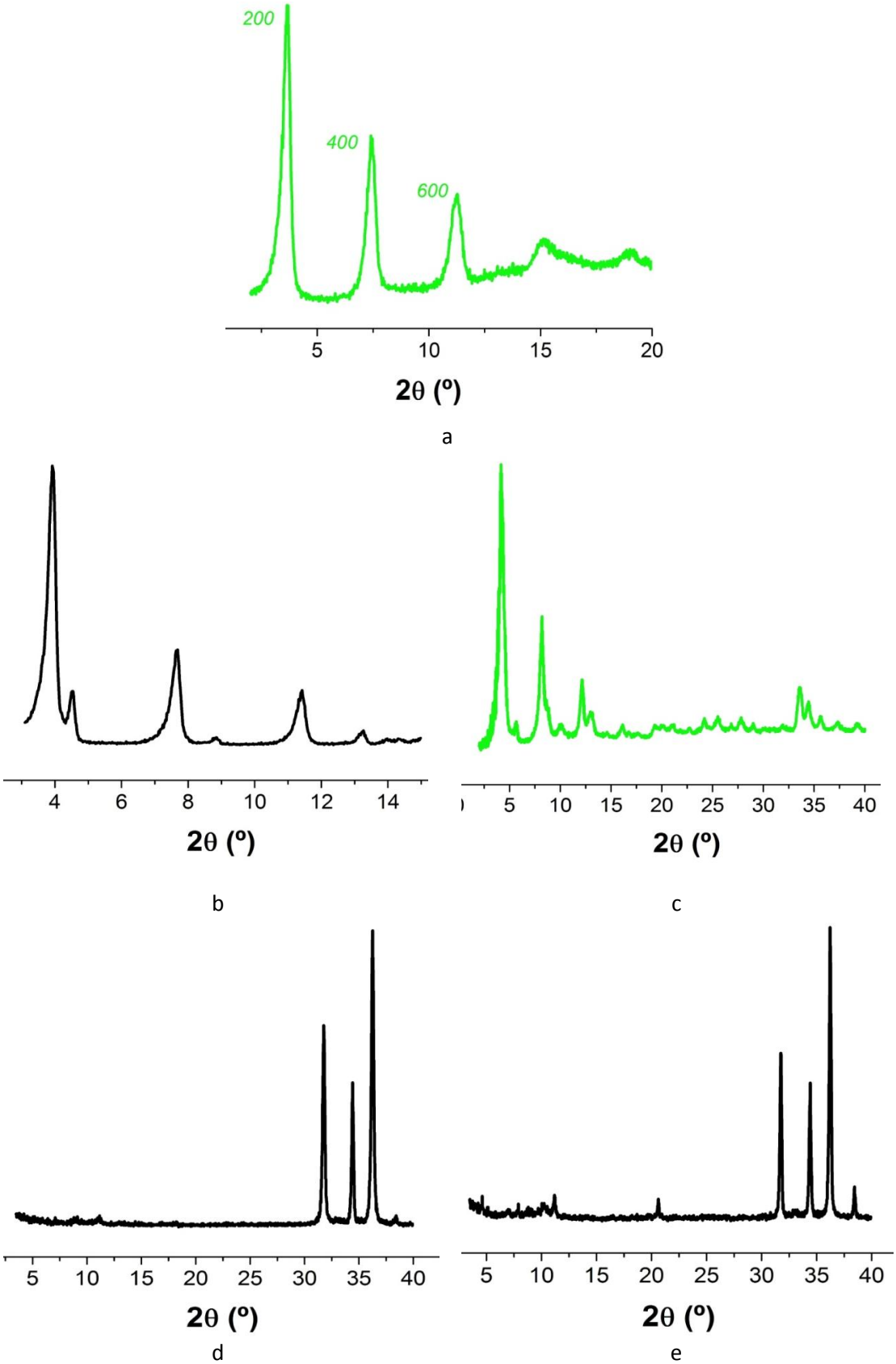

Figure AI-3.1: XRD patterns of (a) NiZn-Nap; (b) Zn-Dic; (c) NiZn-Dic; Zn-Val from (d) Zn-NO_3 and (e) Zn-Cl.

FTIR

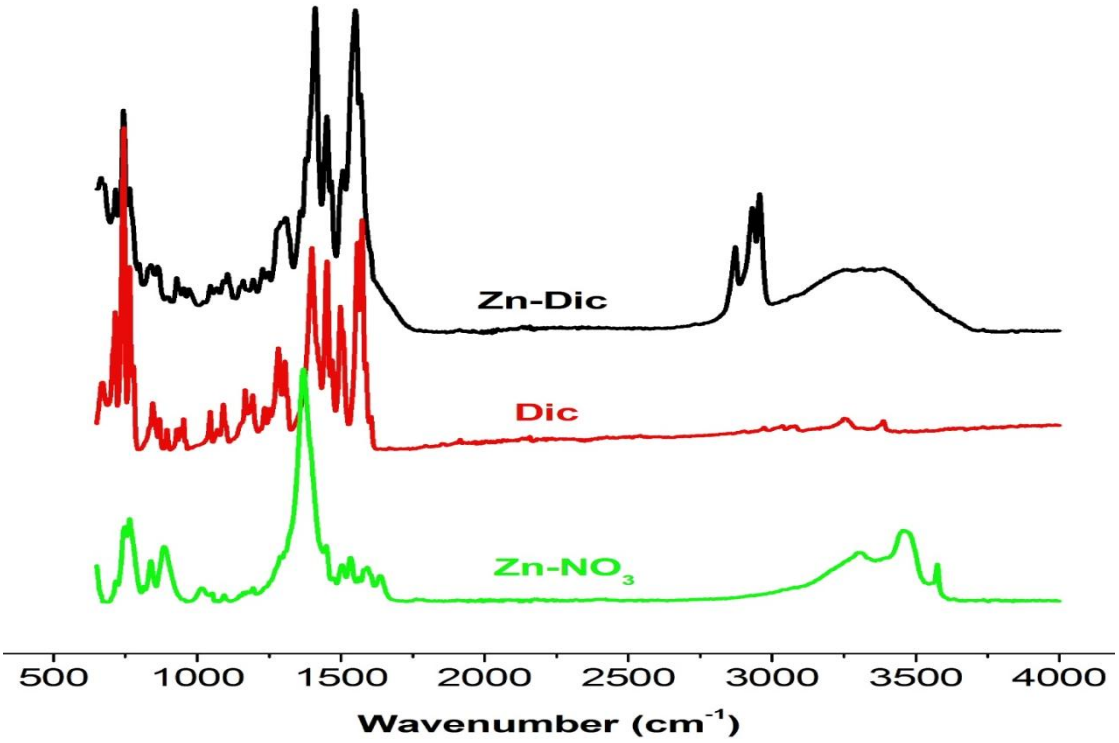

a

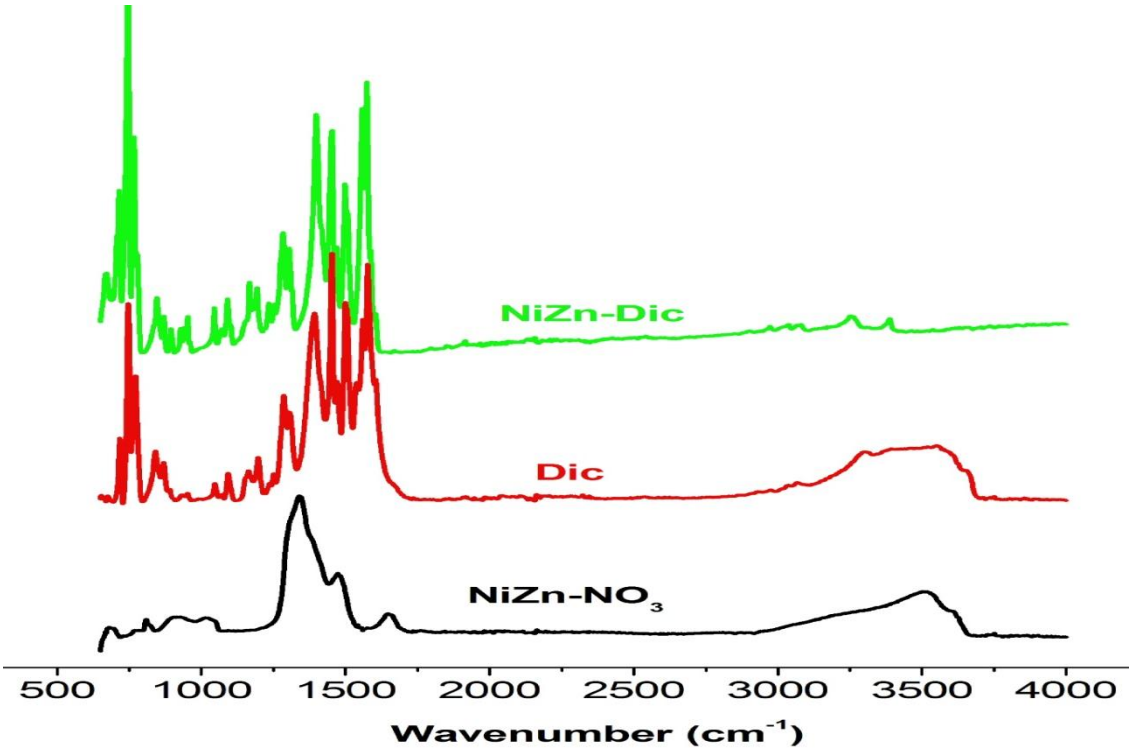

b

Figure AI-3.2: IR spectra of (a) Zn-NO_3, Zn-Dic and Dic; (b) NiZn-NO_3, NiZn-Dic and Dic

In Situ

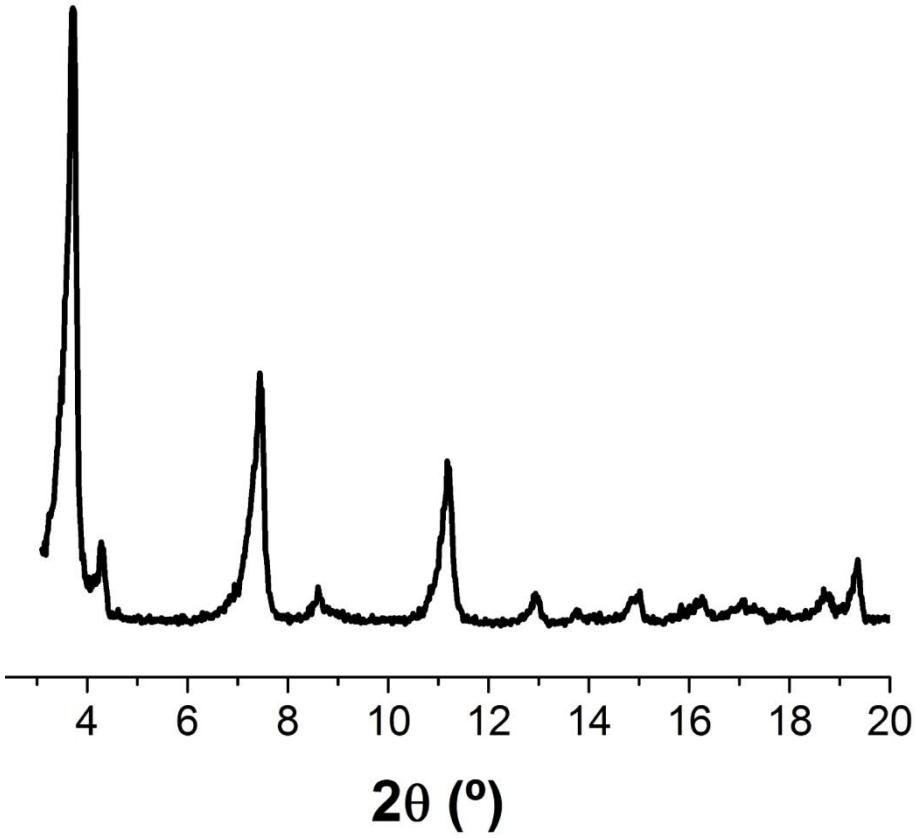

Figure AI-3.3: XRD pattern of Zn-Nap *in situ* product after drying.

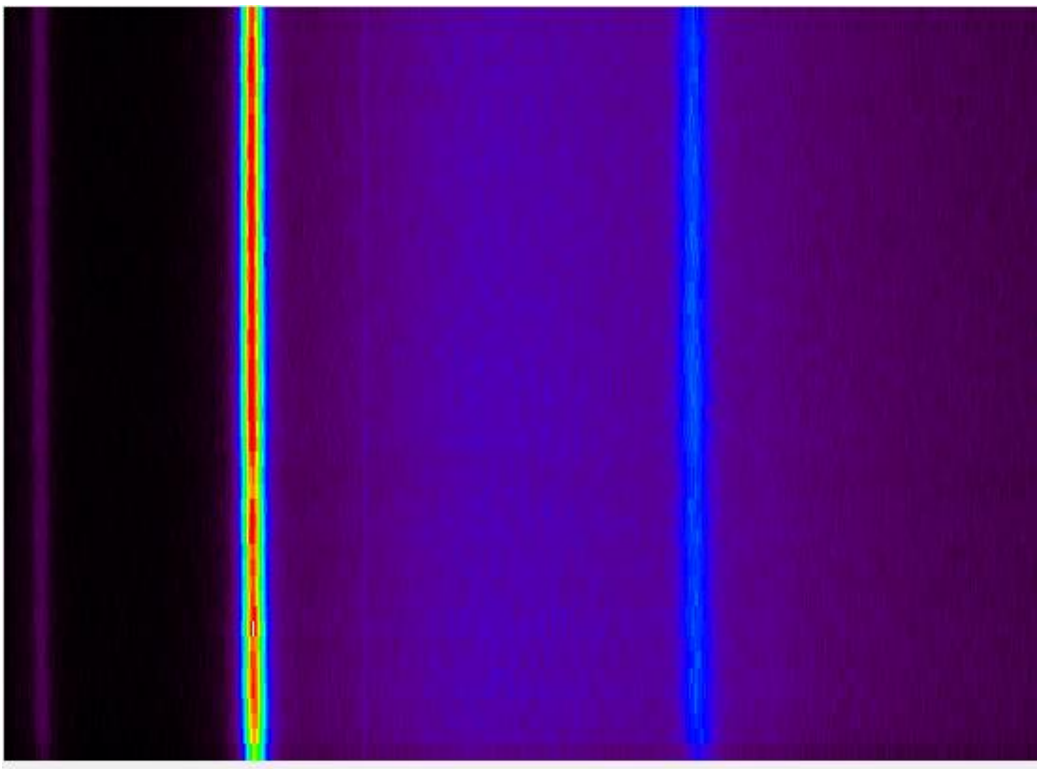

Figure AI-3.4: In situ data for the intercalation of Val into NiZn-NO_3 at 80 ºC.

XPS

The visual characterisation of CoZn-NO_3 shows it has a pink colour. Hydroxides of cobalt α and β $Co(OH)_2$ are similar systems to CoZn-NO_3, in the β form Co^{2+} is located in octahedral sites and has a characteristic pink. In the other form Co^{2+} is located in octahedral and tetrahedral sites, it has a characteristic green to green blue colour.[1,2]

The XPS data are shown in Table AI-3.1 and Figure AI-3.5. The data show peaks at binding energies (B.Es) 781.0 ± 0.02 eV and 796.6 ± 0.16 eV are attributed to core level transitions arising from the spin-orbit doublet of the Co 2p, with strong satellite (SS) features at 5.0 ± 0.05 eV and 6.4 ± 0.31 eV. The shape of Co 2*p* lines ($2p_{1/2}$ and $2p_{3/2}$) and the satellites structure on the high binding energy side of the principal $2p_{1/2}$ and $2p_{3/2}$ lines can reveal the oxidation state of the Co atoms, they are a typical characteristic of high spin Co^{2+}. The data of Co atoms in octahedral and tetrahedral sites are summarised in Table 3.7. The Co^{+2} has been suggested to be located in the octahedral position as well,[3,4] it is known that Co^{2+} is in octahedral positions in LDH Co/Al. Similar B.Es and SS values were reported for LDH Co/Al.[5,6] Therefore; the cobalt in the CoZn-NO_3 sample exists in one oxidation state and in octahedral coordination geometry.

The Ni 2p XPS spectrum shows two major peaks with binding energies at 873.9 and 856.1 eV, corresponding to Ni $2p_{1/2}$ and Ni $2p_{3/2}$, respectively, with a spin-energy separation of 17.8 eV. The corresponding satellite peaks are observed at 862.3 and 880.0 eV, respectively. This is typical characteristic of Ni^{2+} in octahedral sites.[7] This is in agreement with previous experiment by Choy and co-workers on $Ni_{1-x}Zn_{2x}(OH)_2(CH_3COO)_{2x}.nH_2O$ by X-ray absorption spectroscopic.[8] NiZn-NO_3 shows green colour similar to $Ni(OH)_2$.

It is believed that the metal composition of the HDS (from the experimental data) might be important in determining the reaction mechanism.

HDSs that contain mixture of divalent metal have different stability than those with a single divalent metal.[9] It is clear from the raw experimental data of the intercalation of Dic, Nap and Val in various types of HDSs, that the presence of Co^{2+} or Ni^{2+} inside the system and their absence has lead to different intercalation process. The Ni^{2+} is in octahedral position (in the main layer structure) and this has stabilised the system. Resulting in the successful intercalation of Val (the layers system remained intact) and one step reaction for Dic and Nap. The presence of Co^{2+} may have contributed to the stability of CoZn system and resulted as well in the successful intercalation of Val. It seems that the presence of only one atom of Co^{2+} in the CoZn-NO_3 system has not generated enough stability, since the intercalation of Dic and Nap was two steps reaction.

The XPS and EDX data show that there are very tiny metals leach after the intercalation of Dic into CoZn-NO_3 and NiZn-NO_3. The data show that the drug loading is slightly higher compared to the CHN analysis.

Table AI-3.1: XPS Binding Energies (B.E) (All values in eV).

Samples	$2p_{3/2}$		$2p_{1/2}$		Δ BE ($2p_{3/2}$-$2p_{1/2}$)	References.
	B.E	S.S	B.E.	S.S		
CoZn-NO_3	781.0	5.0	796.6	6.4	15.6	This work
NiZn-NO_3	856.1	6.2	873.9	6.1	17.8	This work
CoO	780.1	6.3	796	-	15.9	[10,11]
CoOOH	780.1	-	795.1	-	15.0	[12]
$Co(OH)_2$	781	5.8	797	-	16.0	[11]
$CoAl_2O_4$	780.9	4.7	796.7	6.3	15.7	[13]
Ni(OH)2	855.9	5.0	873.5	6.8	17.6	[14,15]
LDH Co/Al	781.3	6.1	797.3	6.0	16.0	[5,6]

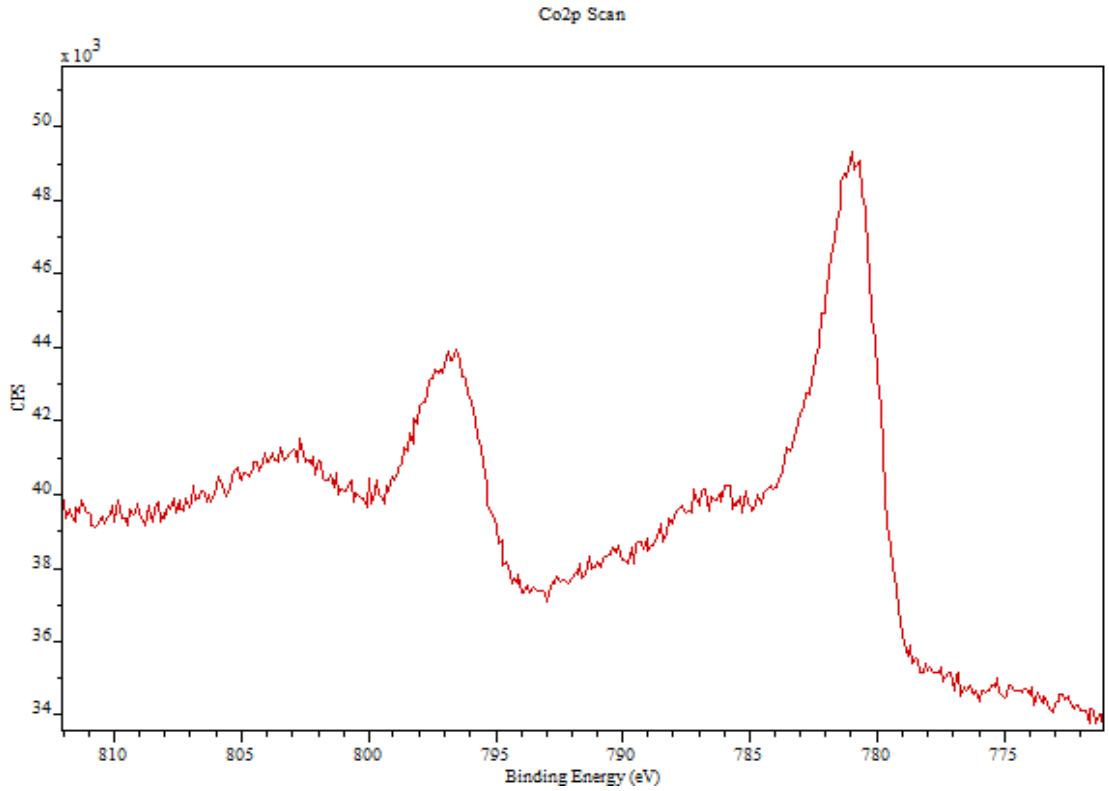

a

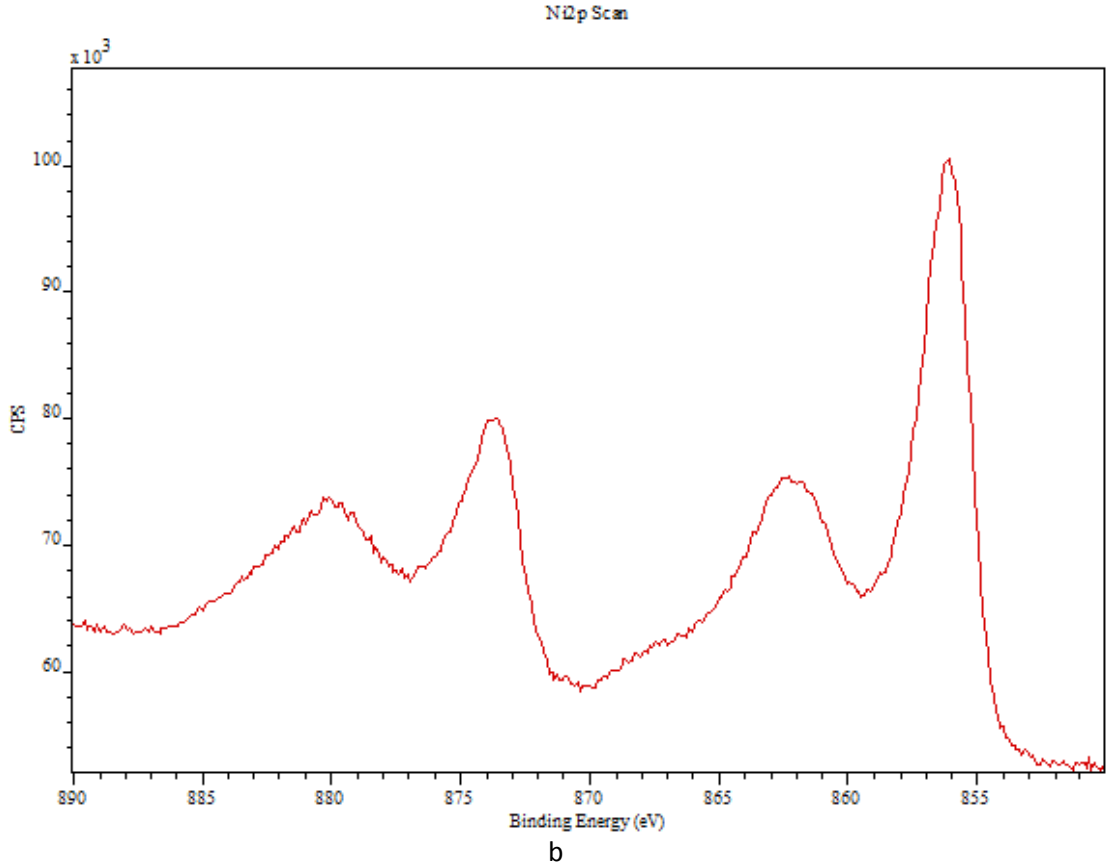

b

Figure AI-3.5: XPS spectra (a) Co^{2+} of CoZn-NO_3 and (b) Ni^{2+} of NiZn-NO_3.

Drug release

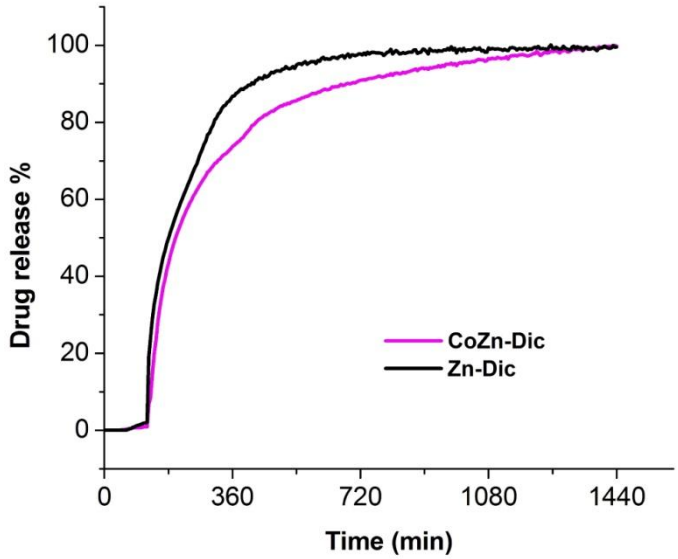

Figure AI-3.6: The results of an experiment to monitor Dic release from Zn-Dic and CoZn-Dic in pH=1.0 and 6.8 in under pharmacopoeial conditions (n=1).

References

1. Liu, Z., Ma, R., Osada, M., Takada, K. & Sasaki, T. Selective and controlled synthesis of - and -cobalt hydroxides in highly developed hexagonal platelets. *J. Am. Chem. Soc.* **127,** 13869–13874 (2005).

2. Ma, R. *et al.* Tetrahedral Co(II) Coordination in α-Type Cobalt Hydroxide: Rietveld Refinement and X-ray Absorption Spectroscopy. *Inorg. Chem.* **45,** 3964–3969 (2006).

3. Tronto, J., Leroux, F., Dubois, M., Taviot-Gueho, C. & Valim, J. B. Hybrid organic-inorganic materials: Layered hydroxy double salts intercalated with substituted thiophene monomers. *J. Phys. Chem. Solids* **67,** 978–982 (2006).

4. Rajamathi, J. T., Raviraj, N. H., Ahmed, M. F. & Rajamathi, M. Hexacyanoferrate-intercalated nickel zinc hydroxy double salts. *Solid State Sci.* **11,** 2080–2085 (2009).

5. Kishore, D. & Rodrigues, A. E. Liquid phase catalytic oxidation of isophorone with tert-butylhydroperoxide over Cu/Co/Fe-MgAl ternary hydrotalcites. *Appl. Catal. A Gen.* **345,** 104–111 (2008).

6. Dou, Y. *et al.* TiO_2 @Layered Double Hydroxide Core-Shell Nanospheres with Largely Enhanced Photocatalytic Activity Toward O_2 Generation. *Adv. Funct. Mater.* 1–7 (2015).

7. Davison, N. & Mcwhinnie, W. R. X-Ray Photoelectron Spectroscopic Study of Cobalt (Ii) and Nickel (Ii) Sorbed on Hectorite and Montmorillonite. **39,** 22–27 (1991).

8. Choy, J.-H., Kwon, Y.-M., Han, K.-S., Song, S.-W. & Chang, S. H. Intra- and inter-layer structures of layered hydroxy double salts, $Ni_{1-x}Zn_{2x}(OH)_2(CH_3CO_2)_{2x}\cdot nH_2O$. *Mater. Lett.* **34,** 356–363 (1998).

9. Ramesh, T. N. & Madhu, T. L. Thermal Decomposition Studies of Layered Metal Hydroxynitrates (Metal : Cu , Zn , Cu / Co , and Zn / Co). *Int. J. Inorg. Chem.* **2015,** 1–11 (2015).

10. Mekki, A., Holland, D., Ziq, K. & Mcconville, C. F. XPS and magnetization studies of cobalt sodium silicate glasses. *J. Non. Cryst. Solids* **220,** 267–279 (1997).

11. Biesinger, M. C. *et al.* Resolving surface chemical states in XPS analysis of first row transition metals, oxides and hydroxides: Cr, Mn, Fe, Co and Ni. *Appl. Surf. Sci.* **257,** 2717–2730 (2011).

12. Kelpšaite, I., Baltrušaitis, J. & Valatka, E. Electrochemical deposition of porous cobalt oxide films on AISI 304 type steel. *Medziagotyra* **17,** 236–243 (2011).

13. Dillard, J. G., Schenck, C. V & Koppelman, M. H. Surface Chemistry of Cobalt in Calcined Cobalt-Kaolinite Materials. *Clays Clay Miner.* **31,** 69–72 (1983).

14. Li, H. B. *et al.* Amorphous nickel hydroxide nanospheres with ultrahigh capacitance and energy density as electrochemical pseudocapacitor materials. *Nat. Commun.* **4,** 1894 (2013).

15. Yan, J. *et al.* Advanced asymmetric supercapacitors based on Ni(OH) 2/graphene and porous graphene electrodes with high energy density. *Adv. Funct. Mater.* **22,** 2632–2641 (2012).

Appendix III: Additional data for Chapter 4

UV measurement

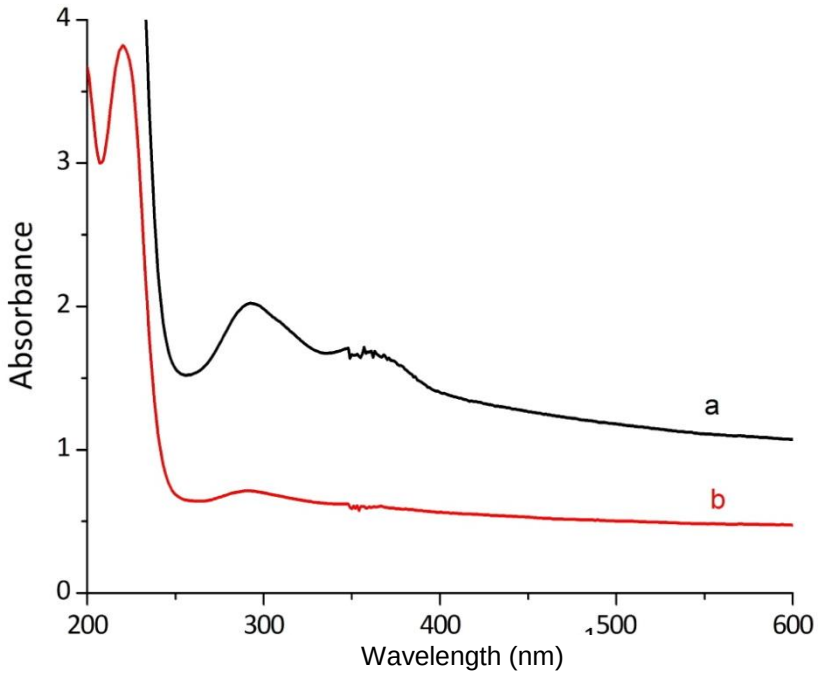

Figure AI-4.1: The UV spectra of FeZn-Cl dispersed in ethanol at **(a)** low **(b)** high concentration.

Size and zeta potential

Results

		Size (d.nm):	% Intensity:	St Dev (d.n...
Z-Average (d.nm): 325.2	Peak 1:	359.9	98.8	138.5
PdI: 0.165	Peak 2:	5064	1.2	571.1
Intercept: 0.875	Peak 3:	0.000	0.0	0.000

Result quality : Good

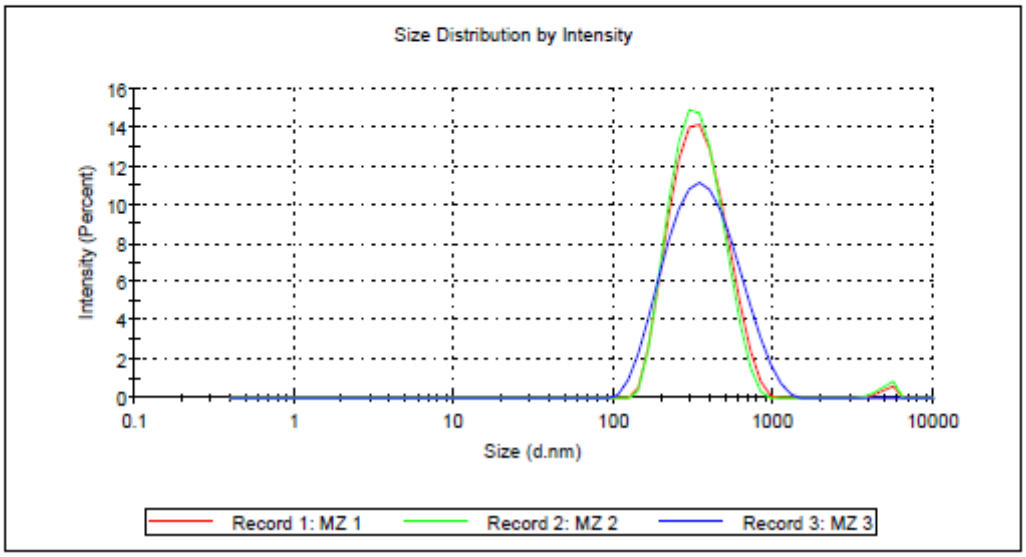

a

Results

		Mean (mV)	Area (%)	St Dev (mV)
Zeta Potential (mV): 43.0	Peak 1:	44.4	90.8	10.2
Zeta Deviation (mV): 13.9	Peak 2:	10.6	6.5	6.50
Conductivity (mS/cm): 0.311	Peak 3:	75.4	2.2	4.83

Result quality : See result quality report

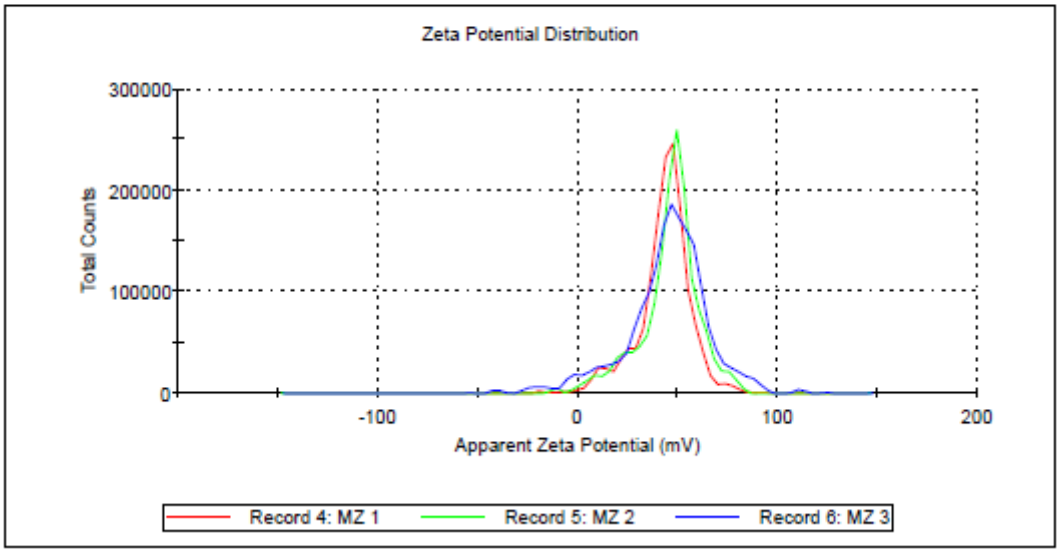

b

Figure AI-4.2: MgZn-Cl **(a)** size and **(b)** zeta potential distribution.

Results

		Size (d.nm):	% Intensity:	St Dev (d.n...
Z-Average (d.nm): 313.9	Peak 1:	403.5	100.0	238.9
PdI: 0.202	Peak 2:	0.000	0.0	0.000
Intercept: 0.913	Peak 3:	0.000	0.0	0.000

Result quality : Good

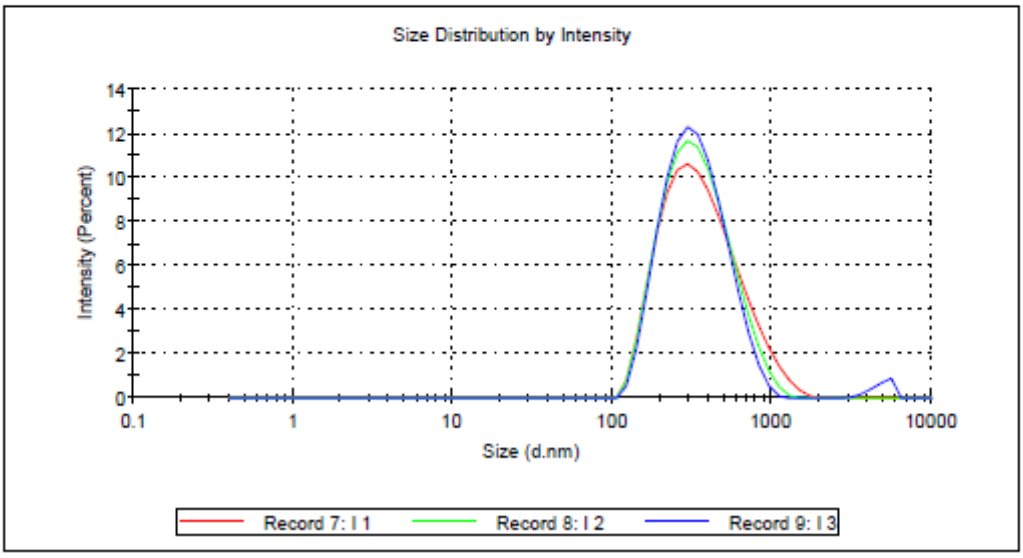

a

Results

		Mean (mV)	Area (%)	St Dev (mV)
Zeta Potential (mV): 45.1	Peak 1:	45.1	100.0	14.0
Zeta Deviation (mV): 14.0	Peak 2:	0.00	0.0	0.00
Conductivity (mS/cm): 0.606	Peak 3:	0.00	0.0	0.00

Result quality : See result quality report

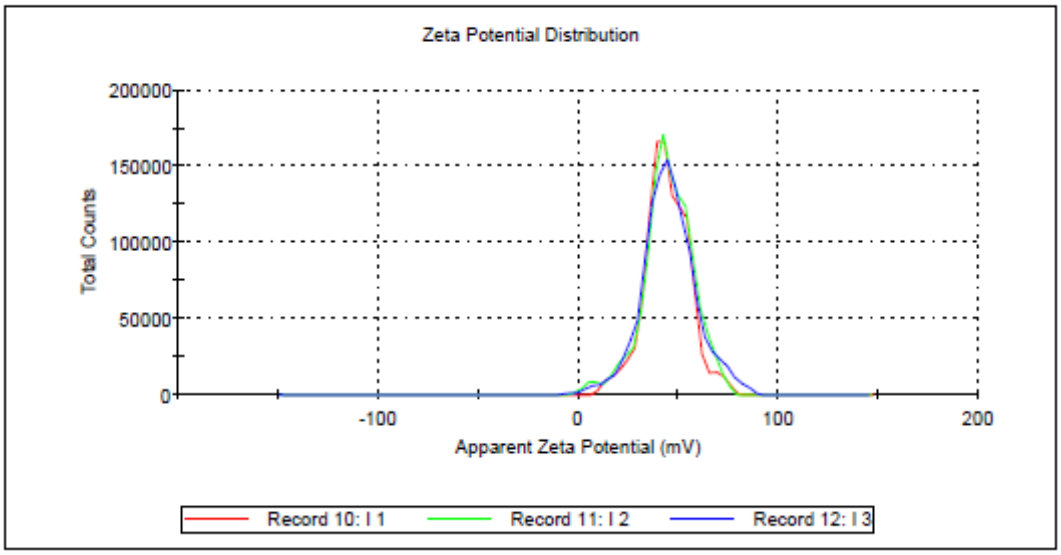

b

Figure AI-4.3: FeZn-Cl **(a)** size and **(b)** zeta potential distribution.

X-ray diffraction

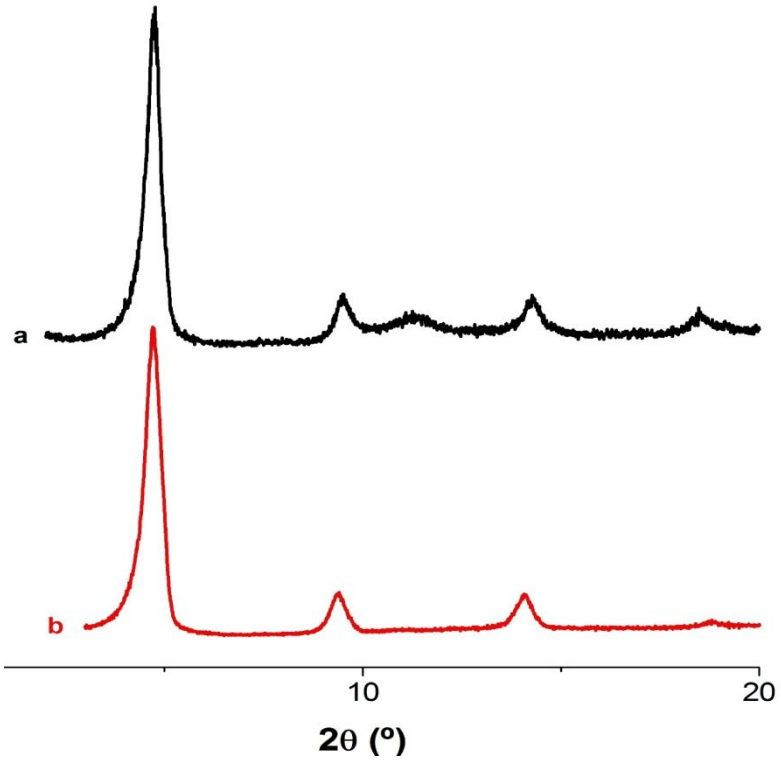

Figure AI-4.4: XRD patterns of FeZn-Val **(a)** small scale and **(b)** large scale up.

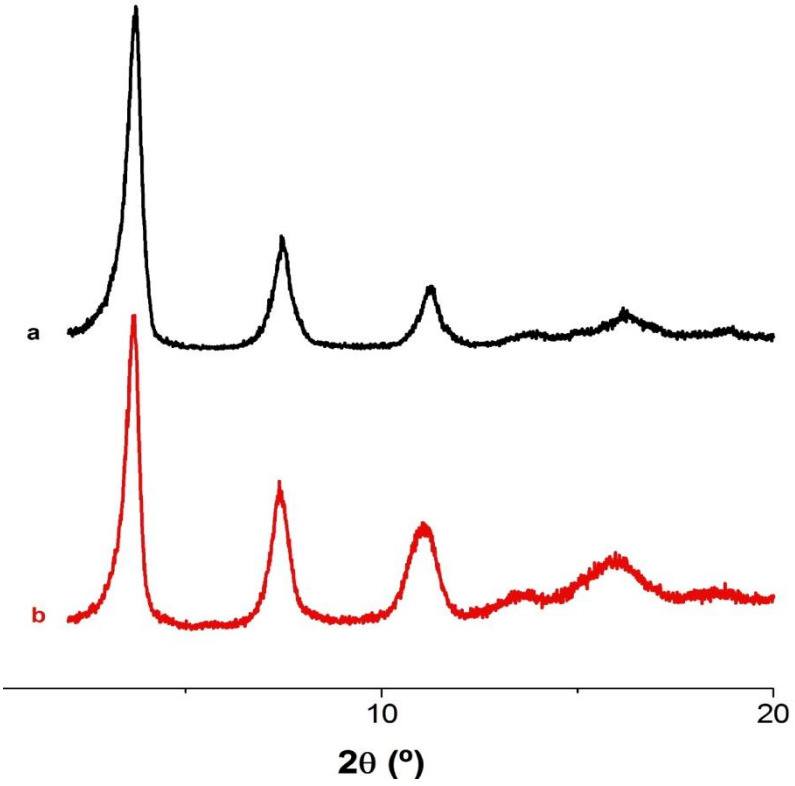

Figure AI-4.5: XRD patterns of FeZn-Nap **(a)** small scale and **(b)** large scale up.

Drug release

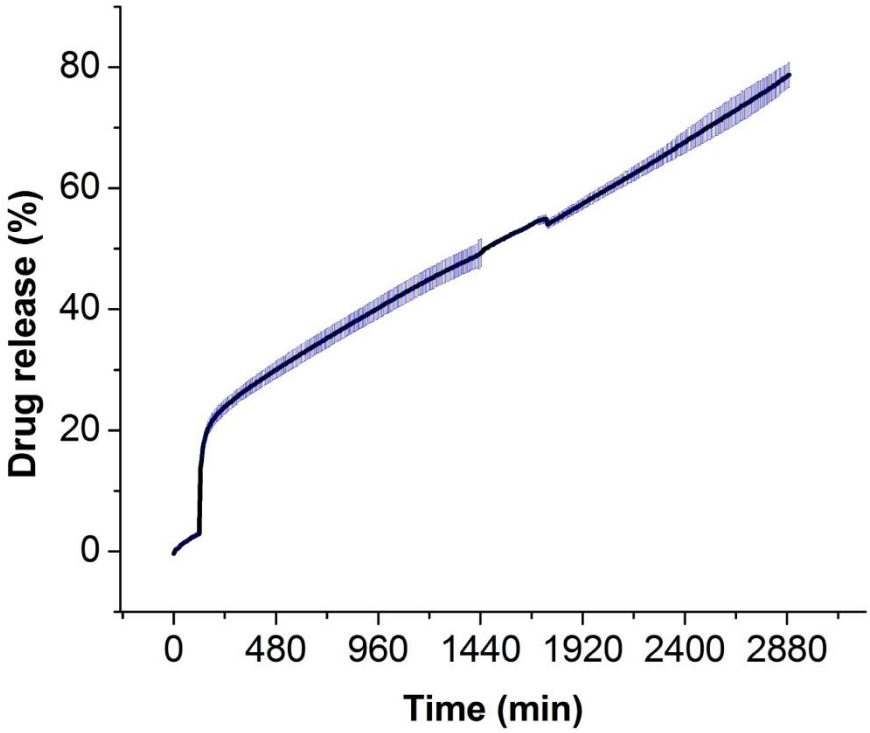

Figure AI-4.6: SI release from a commercial formulation (Brufen Retard) at pH 1 and pH 6.8.

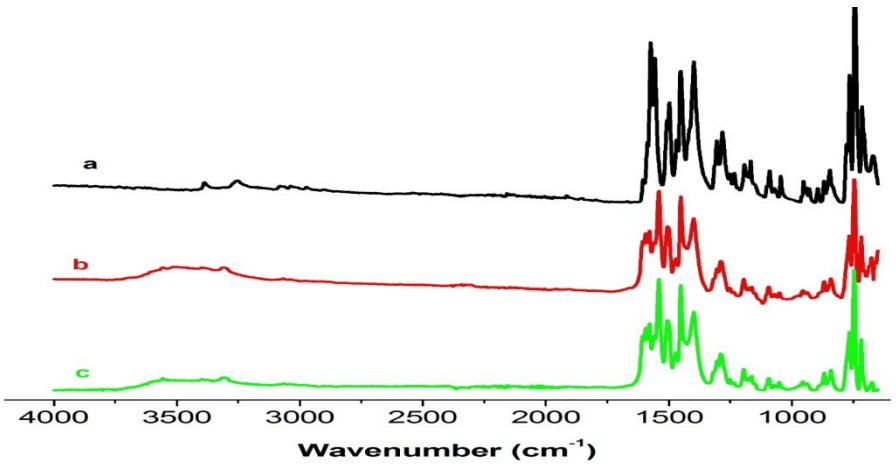

Figure AI-4.7: IR spectra of **(a)** Dic; MgZn-Dic after **(b)** 1 month, and **(c)** 15 months.

Appendix IV: Additional data for Chapter 5

XRD

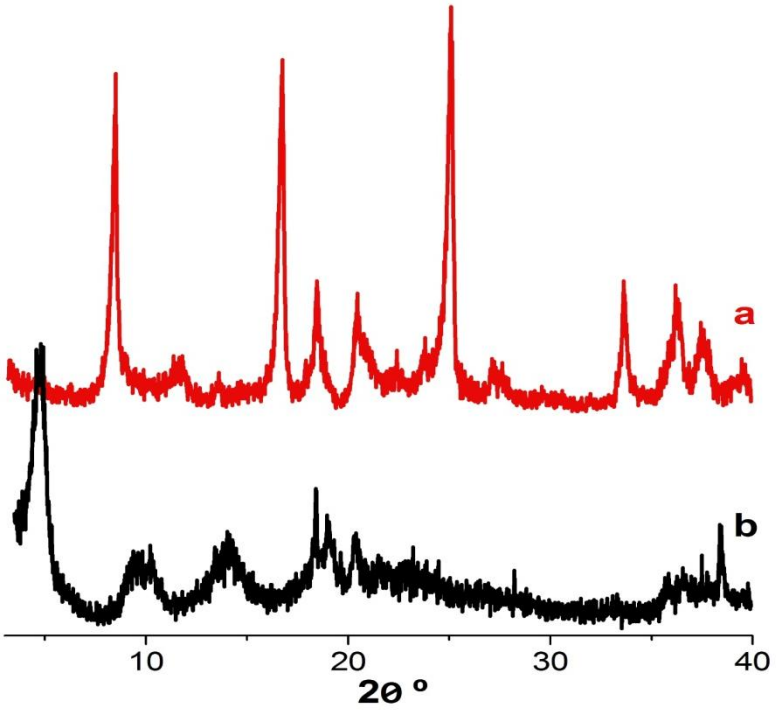

Figure AI-5.1: XRD patterns of (a) LiAl-SAA^{2-}, and (b) LiAl-DPA.

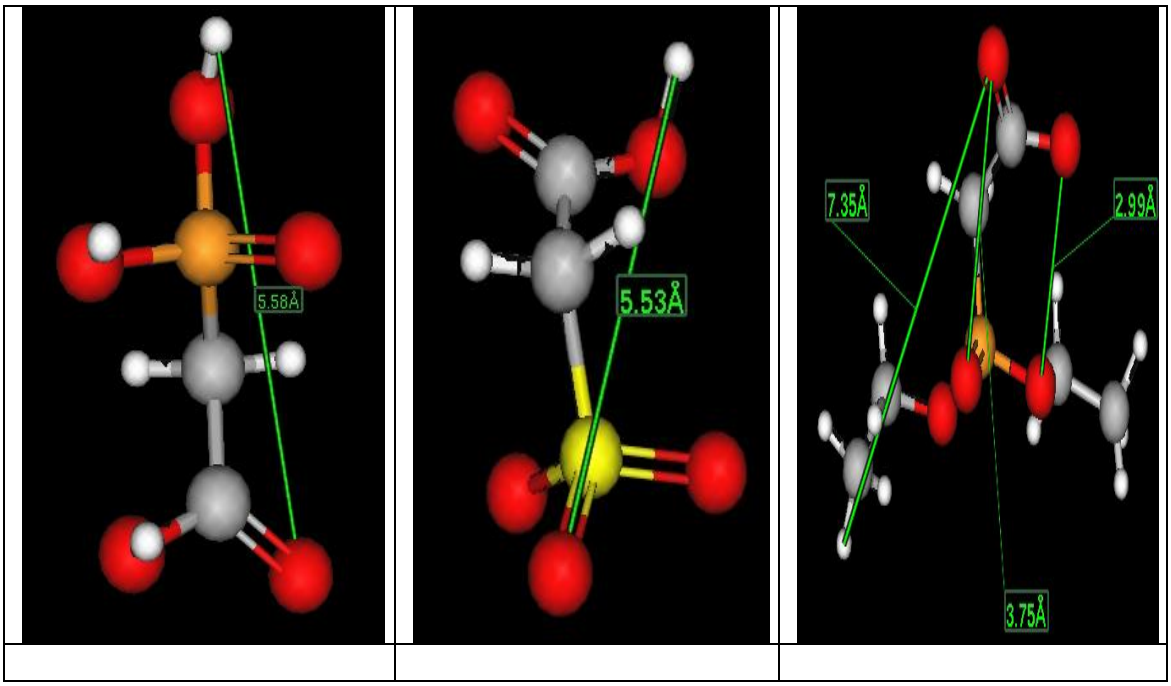

FTIR

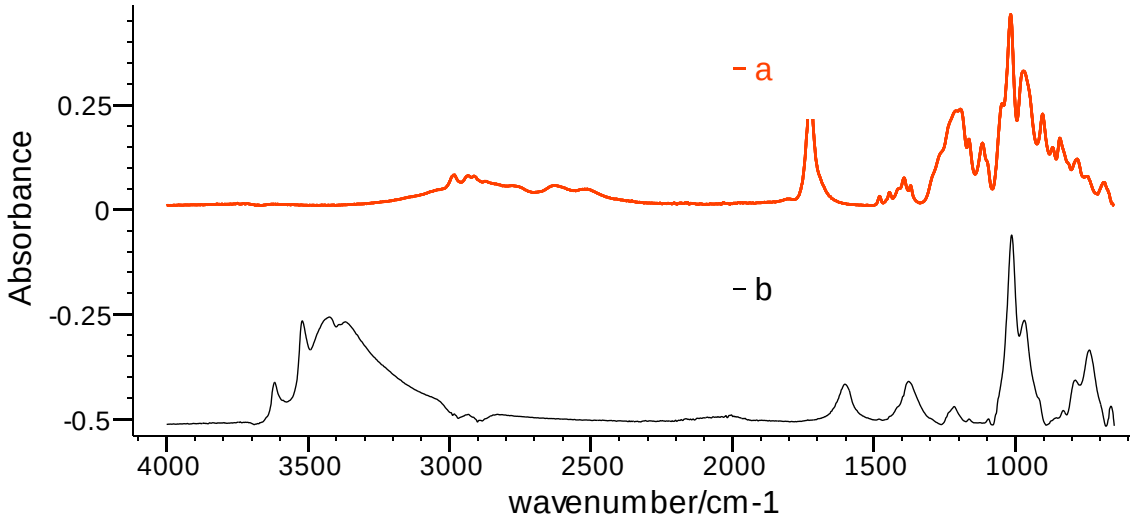

Figure AI-5.2: IR spectra of (a) DPA, and (b) LiAl–DPA.

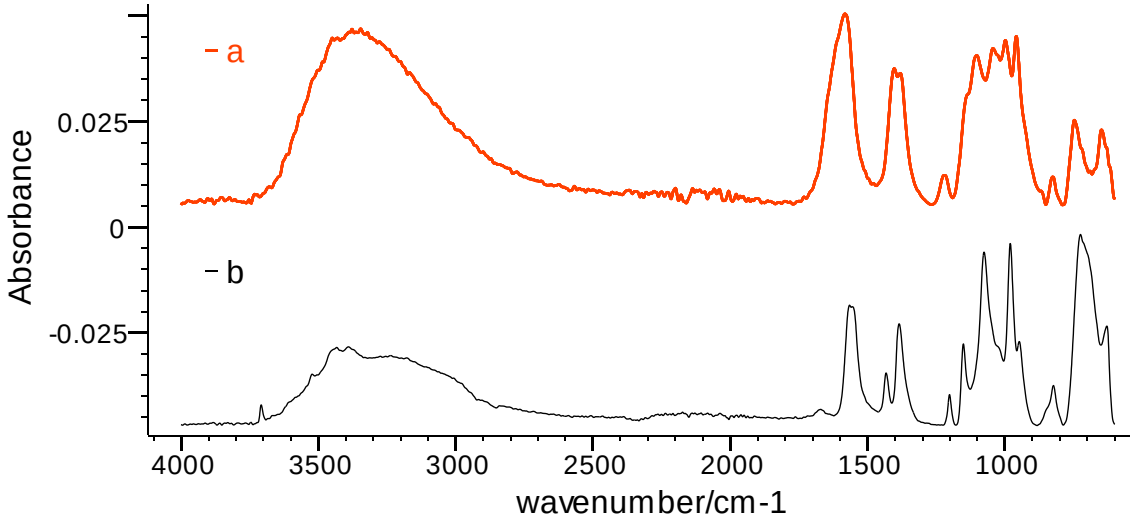

Figure AI-5.3: FT-IR spectra of (a) LiAl-PAA^{-} (a) and (b) LiAl–PAA^{3-}.

Quenching reactions

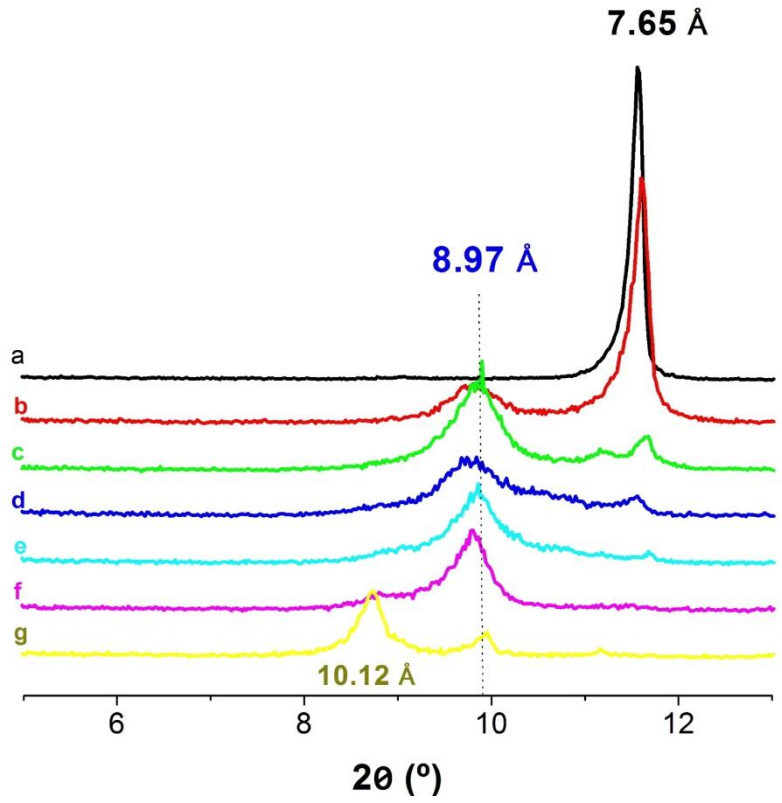

Figure AI-5.4: XRD patterns obtained from quenching the RT reaction between PAA^{-3} and LiAl-Cl after (a) 0 min, (b) 1 min, (c) 2 min, (d) 4 min, (e) 6 min, (f) 8 min and (g) 12 min.

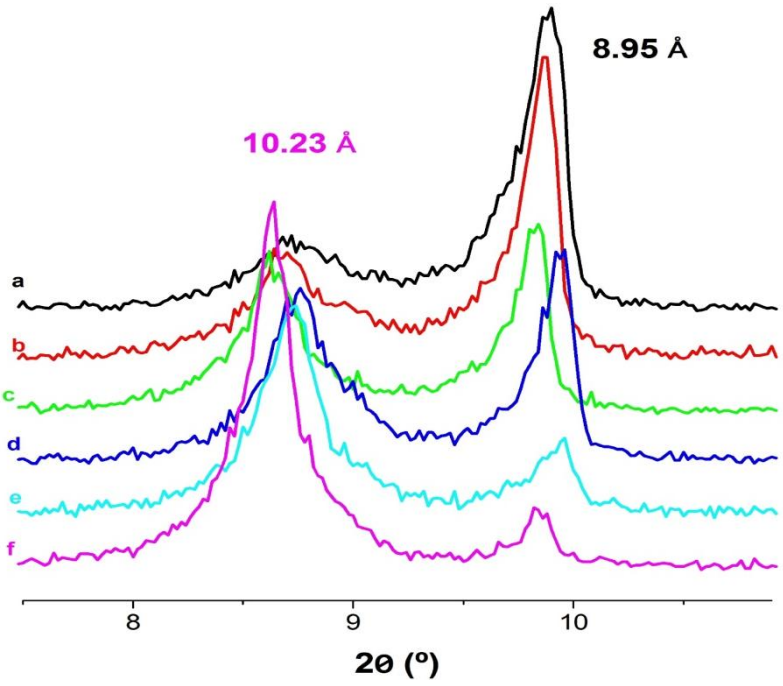

Figure AI-5.5: XRD patterns obtained from quenching the RT reaction between PAA^{-3} and LiAl-NO_3 after (a) 1 min, (b) 2 min, (c) 4 min, (d) 6 min, (e) 8 min and (f) 12 min.

XPS

The ratio between Al/P in LiAl-PAA^{2-} was around 73.27/26.73 and for LiAl-PAA^{2-} after release around 82.37/17.63

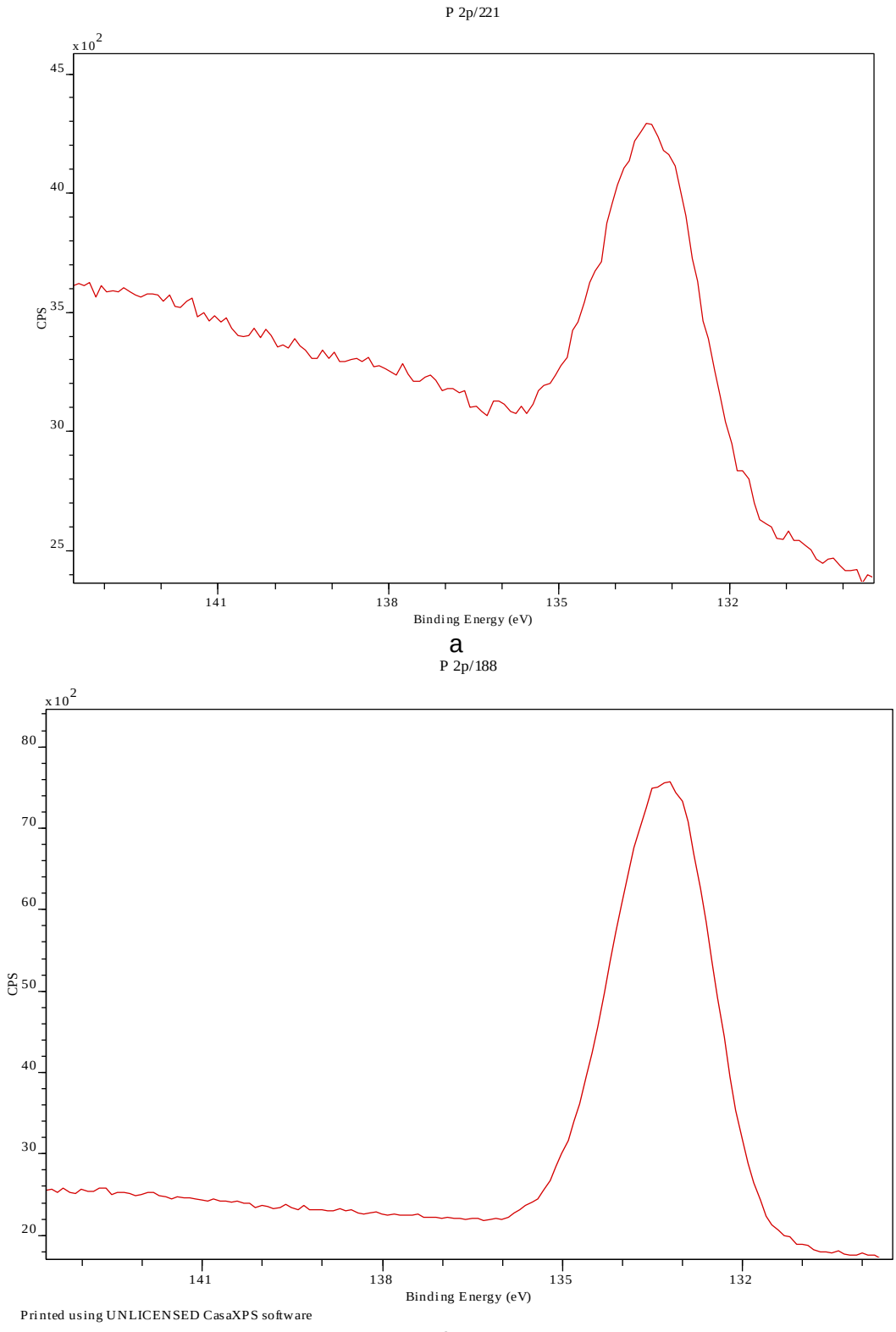

Figure AI-5.6: XPS spectra showing the P peak (a) LiAl-PAA^{2-} after release and (b) LiAl-PAA^{2-}.

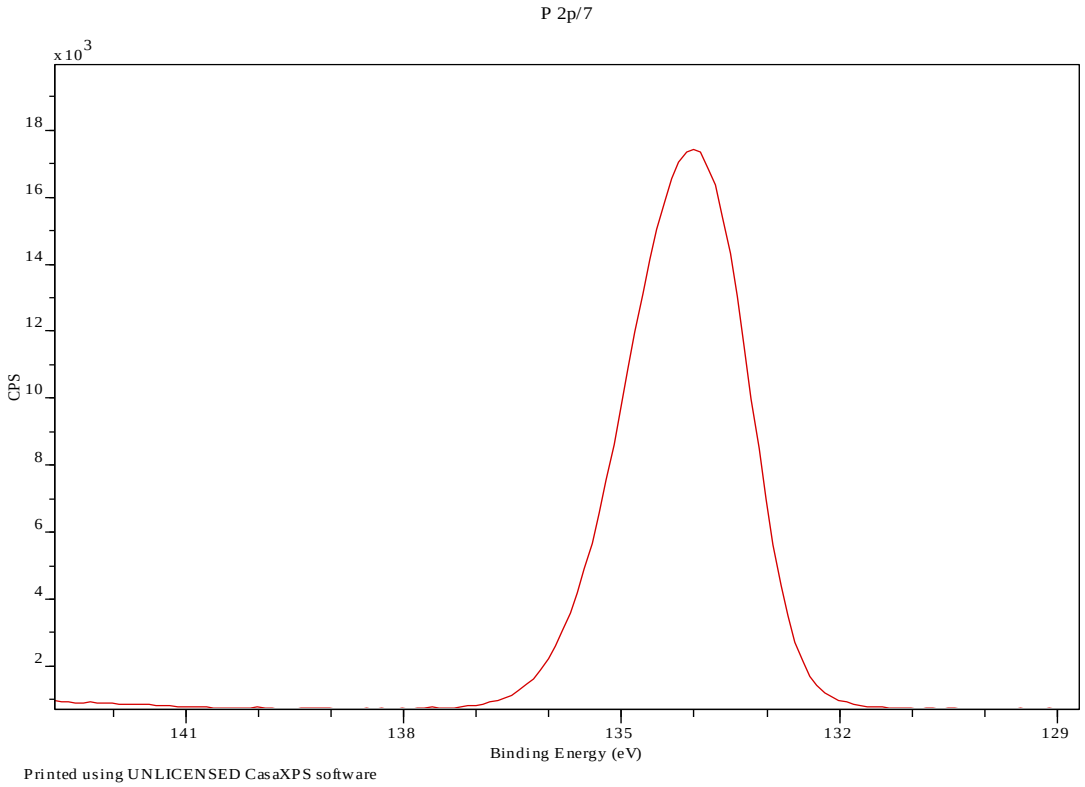

b

Figure AI-5.7: XPS spectra showing the P peak PAA.

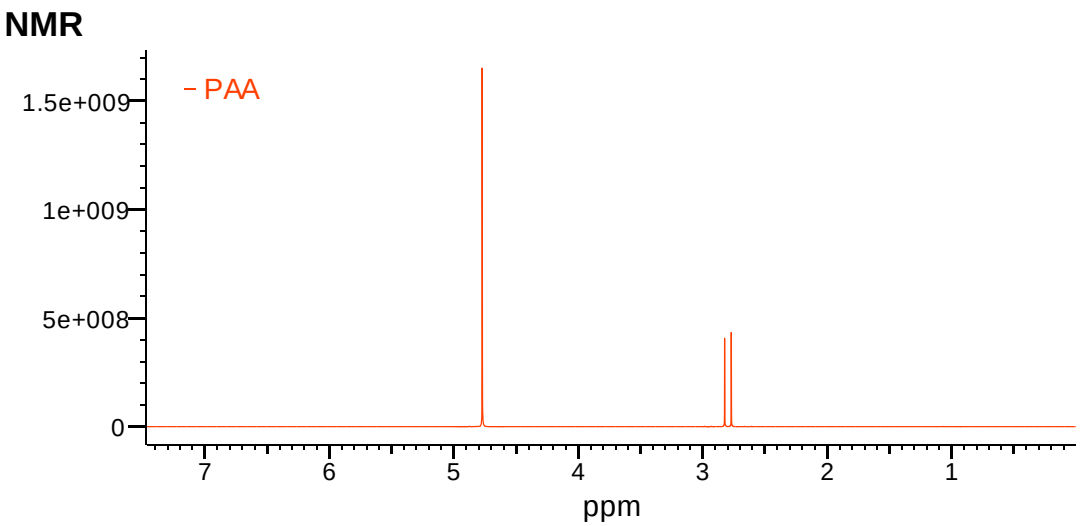

Figure AI-5.8: ^{1}H-NMR of PAA.

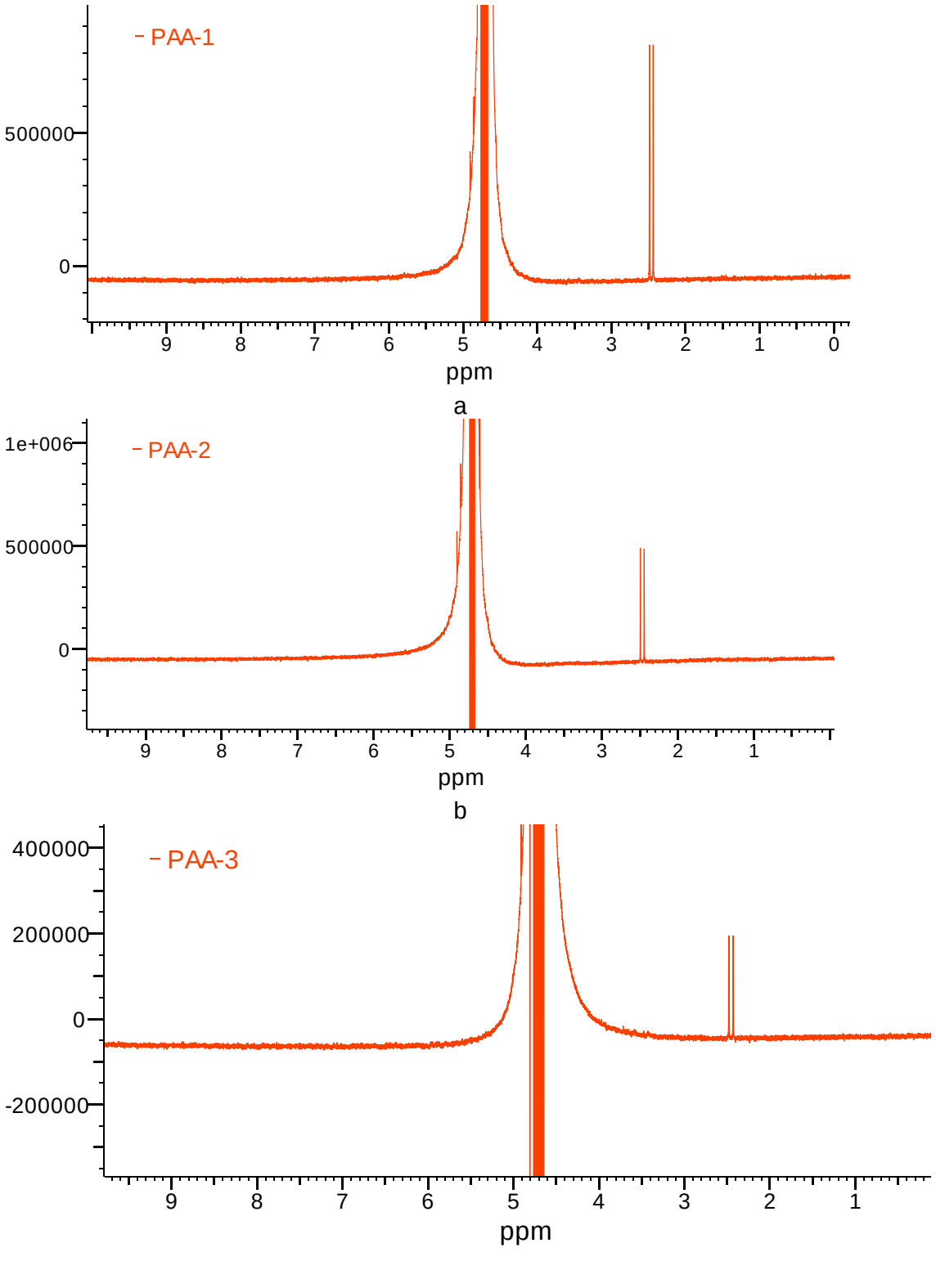

Figure AI-5.9: ^{1}H-NMR of PAA^{-1}, PAA^{-2} and PAA^{-3}.

MD

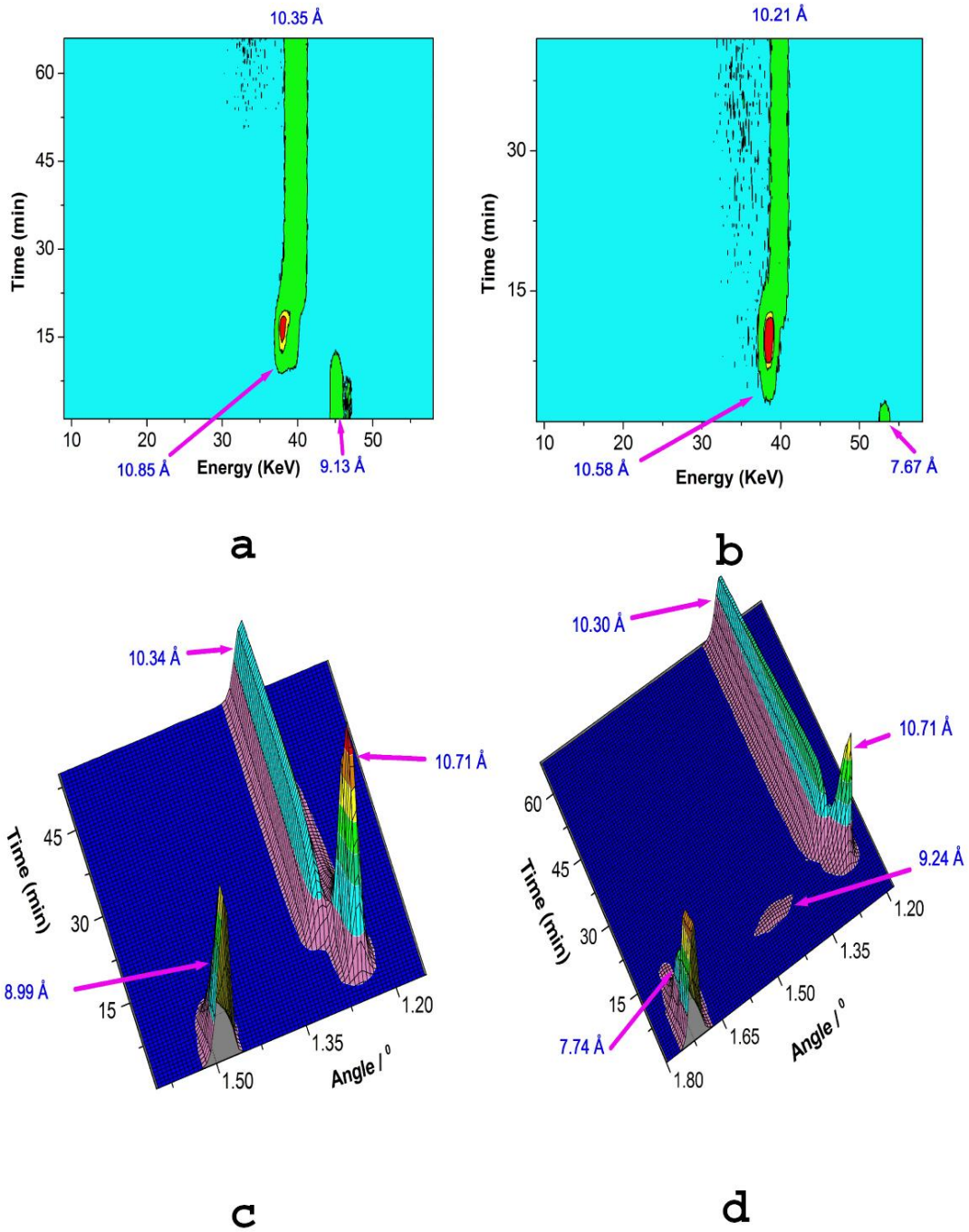

Figure AI-5.10: In situ XRD data for the intercalation of PAA^{3-} into LiAl-Cl **(a,c)** and LiAl-NO_3 **(b,d)** at DESY **(a,b)** and Diamond **(c,d).**

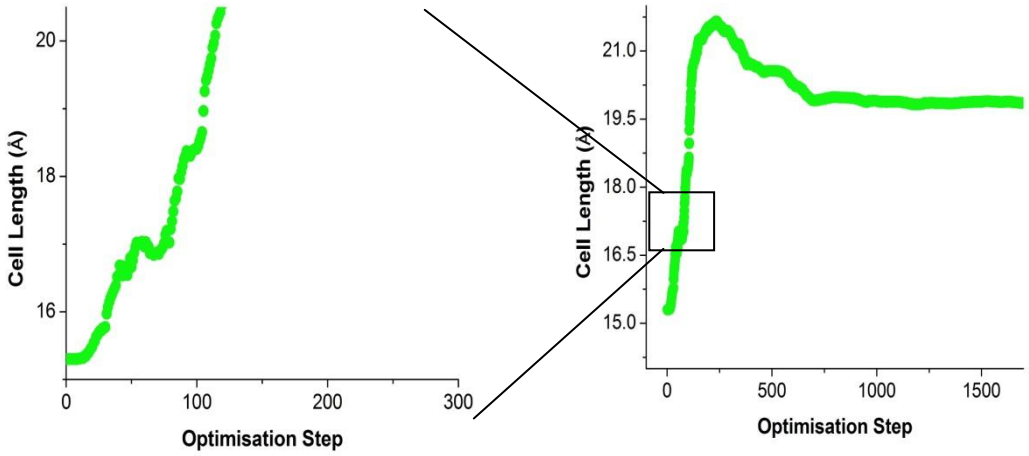

Figure AI-5.11: The change in the unit cell c-parameter with optimisation step for the intercalation of PAA^{3-} into LiAl-Cl.

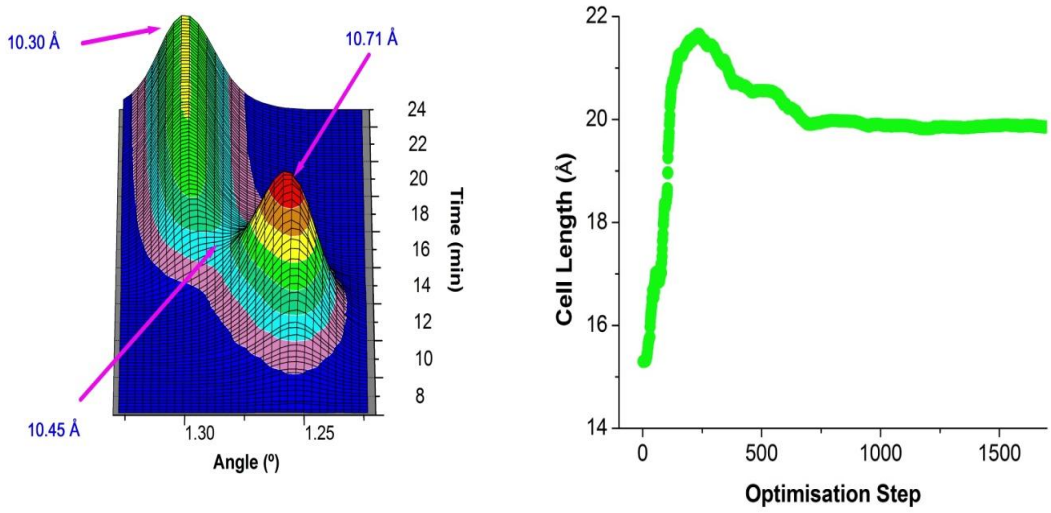

Figure AI-5.12: Time comparison between *in situ* and MD.

Considering the d-spacing of the system as observed in the in situ *and MD data gives the following:*

d-spacing	**In situ *max intensity seen at time of (min)***	***MD (step)***
10.71	*13.2*	*230*
10.45	*15.4*	*470*
10.30	*20.0*	*950*

If we now look at the time taken for the system to go from 10.71 → 10.45 and 10.45 → 10.30 Å we get:

#	Transition	Time taken for change in situ (min)	Time taken for change in MD (steps)
1	*10.71 → 10.45*	*2.2*	*240*
2	*10.45 → 10.30*	*4.5*	*480*
1/2	***Ratio***	***0.49***	***0.5***

Table AI-5.1: A summary of the C and P atom positions of PAA^{3-} at the average guest location the interlayer region of LiAl-PAA^{3-}.

x(C)	y(C)	z(C)	x(P)	y(P)	z(P)
5.671	3.4	5.755	4.508	0.96	5.35
6.412	3.091	5.577	4.85	0.759	5.186
6.472	2.864	5.48	4.831	0.665	5.236
6.484	2.922	5.497	4.764	0.786	5.245
6.251	3.321	5.619	4.491	1.131	5.476
6.296	3.378	5.843	4.859	1.031	5.502
6.317	3.367	5.599	4.759	0.97	5.292
6.568	2.758	5.588	4.472	0.88	5.428
6.033	3.203	5.709	4.543	0.91	5.432
5.79	3.091	5.557	4.717	0.7	5.257
14.104	-1.811	4.935	12.473	-4.027	4.665
14.254	-1.567	5.087	12.421	-3.652	4.702
14.498	-1.678	5.11	12.886	-3.817	4.746
14.322	-1.013	5.112	12.923	-3.462	4.736
14.481	-3.806	4.383	11.861	-4.844	4.396
14.592	-1.112	4.851	12.918	-3.271	4.567
14.035	-1.471	4.909	12.631	-3.888	4.599
13.789	-0.904	5.051	12.541	-3.517	4.702
13.784	-0.994	5.022	12.725	-3.58	4.657
14.171	-1.659	5.205	12.544	-3.775	4.716

The normal of the matrix is (1, 4.681, -19.364).

Table AI-5.2: A summary of the C and P atom positions of PAA^- at the average guest location the interlayer region of LiAl-PAA^-.

x(C)	y(C)	z(C)	x(P)	y(P)	z(P)
0.93	0.163	6.867	0.177	0.458	4.63
0.94	0.416	6.883	0.163	0.727	4.483
0.979	0.139	6.731	0.182	0.654	4.521
0.415	0.221	6.749	0.684	0.653	4.46
0.075	0.004	6.8	0.404	0.4	4.63
0.935	0.094	6.649	0.568	0.504	4.549
0.959	0.136	6.85	0.254	0.673	4.548
0.943	0.134	6.664	0.323	0.396	4.503
0.184	0.282	6.845	0.384	0.668	4.618
0.985	-0.316	6.689	0.096	0.467	4.532
3.612	3.664	7.149	4.392	6.05	6.946
3.705	3.526	7.015	4.556	6.039	6.879
4.06	3.628	7.161	4.462	6.202	6.845
3.591	3.54	7.077	4.585	5.988	6.911
3.814	3.743	7.035	4.558	6.044	6.944
3.873	3.661	6.872	4.569	6.046	6.912
3.53	3.203	7.134	4.284	5.94	6.859
3.648	3.468	7.184	4.515	5.873	6.786
3.923	3.349	7.143	4.358	5.953	6.891
3.683	3.127	7.177	4.431	5.773	6.935
6.459	0.13	6.812	7.108	1.821	4.884
6.723	0.077	6.948	6.933	1.776	4.863
6.466	0.072	6.797	6.807	1.878	4.77
6.366	0.06	6.894	6.877	1.786	4.899
6.453	0.136	6.943	6.712	1.915	4.896
6.565	0.339	6.854	6.845	2.045	4.788
6.606	-0.38	6.586	7.071	1.43	4.777
6.602	0.029	6.919	7.141	1.722	4.819
6.274	-0.106	6.693	7.241	1.575	4.723
6.537	-0.059	6.943	7.098	1.456	4.719
10.281	-2.206	7.487	9.934	-3.232	5.113
10.096	-2.501	7.797	9.741	-3.21	5.227
10.292	-2.386	7.634	10.026	-3.287	5.204
10.311	-2.082	7.791	9.714	-2.715	5.376
10.369	-2.142	7.637	9.66	-2.905	5.202
10.273	-2.391	7.863	10.006	-2.997	5.283
10.04	-2.31	7.679	9.932	-3.571	5.382
10.119	-2.228	7.637	9.566	-2.953	5.15
10	-2.335	7.699	9.792	-3.329	5.202
10.092	-2.303	7.75	9.588	-3.032	5.239
10.563	2.134	7.442	12.607	0.562	7.636
10.459	1.854	7.411	12.7	0.261	7.706
10.13	2.03	7.59	12.452	0.548	7.774

10.517	2.286	7.259	12.62	0.846	7.686
10.417	1.987	7.183	12.624	0.644	7.582
10.572	1.852	7.483	12.696	0.433	7.72
10.564	2.107	7.496	12.564	0.419	7.593
10.438	2.156	7.533	12.642	0.504	7.806
10.242	1.757	7.4	12.559	0.698	7.749
10.202	1.902	7.418	12.572	0.557	7.615

14.142	-5.33	6.003	16.422	-4.123	5.515
14.19	-5.476	5.81	16.499	-4.327	5.502
14.048	-5.308	5.898	16.477	-4.242	5.584
13.915	-5.093	5.64	16.377	-4.239	5.56
14.082	-5.14	5.862	16.538	-4.226	5.491
13.972	-5.203	5.847	16.321	-4.274	5.564
14.073	-5.432	5.769	16.458	-4.444	5.52
14.128	-5.161	6.056	16.467	-4.155	5.58
14.058	-5.242	5.836	16.463	-4.315	5.628
13.931	-5.216	5.599	16.314	-4.208	5.52

The normal of the matrix is (1, -9.34, 15.97).